Imaging and Therapeutic Radiotracers for Prostate Cancer

Young, Jennifer Denise

Awarding institution:
King's College London

Imaging and Therapeutic Radiotracers for Prostate Cancer

Jennifer Denise Young

PhD in Imaging Science

School of Biomedical Engineering and Imaging Sciences

King's College London

Abstract

Radiotracers that target glutamate carboxypeptidase II, also known as the prostate specific membrane antigen (GCP(II)/PSMA), have shown exceptional promise for prostate cancer imaging and molecular radiotherapy. A number of bioconjugates have been developed to target GCP(II)/PSMA which utilise the simple and robust targeting motif (Lys-C(O)-Glu) (referred to as PSMA ligand), functionalised with a chelator for radiometal incorporation. This work utilised and evaluated the tris(hydroxypyridinone) (THP) chelator due to the simplicity, speed and selectivity of its radiolabelling with gallium radioisotopes, and its potential to be developed into one-step radiopharmaceutical kits. [^{68}Ga]Ga-THP-PSMA was assessed as a PET imaging agent and [^{67}Ga]Ga-THP-PSMA for molecular radiotherapy due to its Auger electron emissions.

The first objective was to synthesise THP-PSMA and assess its radiolabelling with gallium-68. [^{68}Ga]Ga-THP-PSMA with over 95% radiochemical purity was produced at room temperature, and pH 7 in just 5 minutes. A one-step kit was developed, suitable for use with gallium-68 directly from a generator. [^{68}Ga]Ga-THP-PSMA exhibited specific uptake in GCP(II)/PSMA-expressing prostate cancer cells and 50% inhibition of binding at a concentration of 361 ± 60 nM. *In vivo* PET imaging showed specific uptake in GCP(II)/PSMA-expressing tumours, reaching 5.6 ± 1.2 percentage injected dose per cubic centimetre. Overall, [^{68}Ga]Ga-THP-PSMA had equivalent imaging properties but greatly simplified radiolabelling compared to other [^{68}Ga]Ga-PSMA tracers. Clinical studies were then conducted by collaborators which found that [^{68}Ga]Ga-THP-PSMA could delineate prostate cancer in both initial staging and biochemical recurrence.

The second objective was to assess [^{67}Ga]Ga-THP-PSMA for molecular radiotherapy. Extremely high molar activity was achieved: 326 MBq/nmol (22% chelator occupancy). Despite this, the activity delivered to GCP(II)/PSMA expressing cells was low (max 0.1 Bq/cell) and the tracer showed rapid efflux. These findings were confirmed with *in vivo* studies showing poor retention of [^{67}Ga]Ga-THP-PSMA in GCP(II)/PSMA-expressing prostate cancer tumours. These results suggest that the affinity and retention, but not the molar activity, limit the use of [^{67}Ga]Ga-THP-PSMA for molecular radiotherapy.

The third objective was to determine whether replacing the urea with a thiourea in the GCP(II)/PSMA targeting motif resulted in higher affinity. This was studied using the inhibitors Glu-C(O)-Glu and Glu-C(S)-Glu, the syntheses of which are described. The *in vitro* inhibition assays showed that the affinity was made much weaker by the presence of the thiourea (135 µM compared to 1.34 µM) and therefore this is not an effective strategy for improving affinity.

Overall the THP-PSMA bioconjugate shows excellent radiolabelling properties, with both gallium-68 and gallium-67. [^{68}Ga]Ga-THP-PSMA is a good PET imaging agent for prostate cancer however, improved affinity for GCP(II)/PSMA and retention of the tracer may potentially enhance the utility of [^{67}Ga]Ga-THP-PSMA for molecular radiotherapy.

Declaration

I Jennifer Denise Young confirm that no part of this thesis has been submitted in support of any other application for a degree or qualification of King's College London, or any other university or institute of learning. I confirm that this work is my own. Where information has been derived from other sources it has been indicated in this thesis.

Acknowledgements

Firstly, I would like to thank my supervisor Professor Phil Blower, I am privileged to have had the opportunity to complete my PhD under your supervision. Your support and guidance has challenged me to develop my scientific thinking and rigour, and you have enabled me to produce work I am really proud of. I also thank you for displaying confidence in my abilities throughout my PhD especially by putting me forward to present and conferences, encouraging me to set up collaborations and supervise students, asking me to write a lecture, and even sending me all the way to Australia to do research. I have learnt a huge amount from you, and I really appreciate all the time you have invested in my supervision, and the wonderful environment you have fostered in the department.

I would also like to thank Dr Greg Mullen, for the vision and passion he had for this project and being the driving force behind the clinical translation of this work. It has been exciting, and a great learning experience to work on a project that moved so quickly from bench to bedside. I would also like to thank the other people at Imaging Equipment Limited and Theragnostics Limited that have been involved in the project's industry partnership: Nick Stevens, Jeevan Virk, Gareth Smith and Levente Meszaros.

Thank you to my colleagues that have provided me with ideas for the synthesis and radiosynthesis involved in this project, and lent me their support in the lab: Vincenzo Abbate, Agostino Cilbrizzi, Yu-Lin Chen, Siham Memdouh, Michelle Ma, Brett Patterson, Ingebjorg Hungnes, Julia Blower, Jackie Lange, Mauricio Da Silva Morais, Peter Gawne, Truc Pham, Enrico Fantoni, Alex Khoshnevisan, Ruslan Cusnir, Edward Waters, Joseph Downey, Filipa Da Mota Quinteiro, Maggie Cooper, David Thakor, Barry Cook, Stephen Catchpole, Matthew Hutchings, and Cinzia Imberti.

Thank you to the team of wonderful scientists involved in the *in vitro* and *in vivo* aspects of this work: Levente Meszaros, Cinzia Imberti, Sam Terry, Jackie Lange, Muhamad Faiz Othman, Michelle Ma, Lindsay Lim, Amanda Smith, Florian Kampmeier, Kavitha Sunassee, Jayanta Bordoloi, Nisha Kuzhuppilly Ramakrishnan, Julia Baguna Torres, Floyd Laniyan and the rest of the BSU staff.

Thank you to the NMR experts who have contributed to this project: Thomas Eykyn, Andrew Atkinson, and Michelle Ma.

Thank you to everyone involved in the clinical studies in both Australia and the UK: Michael Hofman, Peter Eu, Price Jackson, Emily Hong, David Binns, Amir Iravani, Declan Murphy,

Catherine Mitchell, Shankar Siva, Rodney J. Hicks, Phil Blower, Greg Mullen, Gary Cook, Simon Hughes, Stephen Morris, Ben Challacombe, Paul Cathcart, Rick Popert, Christian Brown, Prokar Dasgupta, Joemon John, Andrew Mallia, Victoria Gibson, Scott Edmonds, and Victoria Warbey.

Thank you to those who have proofread this work for me: Phil Blower, Julia Blower, Joanna Bartnicka, Gemma Dias, Michelle Ma, Sam Terry, Gary Cook, and Maggie Cooper.

Thank you to everyone involved in the CDT, for my place in the first cohort and all of the support, opportunities, and extra training this has allowed me to access. Thank you especially for the additional funding that allowed me to go on a research trip to Australia in 2017. In particular, I would like to thank, Rob Miles, Nick Long, and Julia Schnabel.

I am very grateful for all the funding that has supported this work including King's College London and Imperial College London EPSRC Centre for Doctoral Training in Medical Imaging; Theragnostics Limited; KCL and UCL Comprehensive Cancer Imaging Centre funded by CRUK and EPSRC; NIHR Biomedical Research Centre awarded to Guy's and St Thomas' NHS Foundation Trust in partnership with King's College London and King's College Hospital NHS Foundation Trust; and the Wellcome/EPSRC Centre for Medical Engineering.

Additional special thanks go to the following people: Prof. Bob Hider, thank you for welcoming me into your lab, and for all of the valuable insights and encouragement you have given me. Vincenzo Abbate, a huge thank you for your input into the synthesis of THP-PSMA, your patience whilst training me and your openness to share your expertise. I have really enjoyed working with you. Cinzia Imberti, I couldn't have asked for a better person (and awesome scientist) to work so closely with over the last 4 years. Your enthusiasm and energy are contagious. Thanks for the hundreds of favours we've asked of each other, and the laughs and tears we've shared. Michelle Ma, thank you so much for your support, guidance and friendship. I have really appreciated having someone I trust to discuss science with (as well as have a good rant, and a laugh), and you have always given me excellent advice and encouragement. Sam Terry, thanks for teaching me about molecular radiotherapy and your invaluable input into these projects. You are a pleasure to work with, and an inspirational scientist. Levente Meszaros, thank you so much for helping me with my first *in vivo* experiments and all the advice and expertise you shared with me in this, and lots of other areas. David Thakor, thank you for being a wonderful lab manager and encouraging me to become an RPS. We have always had a great rapport, and I really appreciate all the help you have given me over the last 4 years (as well as all the goodies from your allotment).

Finally, I would also like to thank all of my family and friends who encouraged me to do a PhD and who have supported me throughout. I'm so excited to have much more time to spend with you again. To my brother Peter, thanks for always showing your support and interest in my work. Catherine, you are the best housemate, friend and sister. Thank you for always being there for me and always knowing how to make me laugh and let my hair down. To my partner, Marcus, thank you for always being so enthusiastic and encouraging about my PhD, and for having more confidence in my abilities than I do. We make a great team. Mum and Dad, thank you for nurturing my love of science, and always giving me your love and support. I couldn't have done this without you.

List of Abbreviations

ACN	Acetonitrile
Ala	Alanine
ALS	Amyotrophic lateral sclerosis
Arg	Arginine
Asn	Asparagine
Asp	Aspartic acid
ASTC2	Alanine serine cysteine transporter 2
CHT1	A high-affinity Na^+- and Cl^--dependent choline transporter
CI	Confidence interval
CIM	2,2'-(2,2'- (azanediylbis(methylene))bis(1H-imidazole-2,1-diyl))diacetic acid
CLT1	A lower affinity Na^+-independent choline transporter
COSY	Homonuclear correlation spectroscopy
CPM	Counts per minute
CPS	Counts per second
CT	Computed tomography
Dap	L-diaminopropanoic acid
DATA	6-amino-1,4-diazepine triacetate
DCFBC	(N-[N-[(S)-1,3-dicarboxypropyl] carbamoyl]-4-fluorobenzyl-L-cysteine
DCFPyL	2-(3-{1-carboxy-5-[(6-fluoro- pyridine-3-carbonyl)-amino]-pentyl}-ureido)-pentanedioic acid
DCIBzL	((S)-2-(3-((S)-1-carboxy-(4-iodobenzamido)pentyl)ureido)pentanedioic acid)
DCM	Dichloromethane
DFO	Desferrioxamine B
DIPEA	N,N-diisopropylethylamine
DIPEA	Diisopropylethylamine
DMF	Dimethylformamide
DMSA	Dimercaptosuccinic acid
DMSO	Dimethyl sulfoxide
DOTA	1,4,7,10-tetraazacyclododecane-1,4,7,10-tetraacetic acid
DOTAGA	1,4,7,10-tetraazacyclodocecane,1- (glutaric acid)-4,7,10-triacetic acid
DTPA	Diethylenetriaminepentaacetic acid
DU145	Cell line – human prostate carcinoma derived from a brain metastatic site
EANM	European Association of Nuclear Medicine
EAU	European Association of Urology
EC_{50}	50% maximal response concentration
EMA	European Medicines Agency
EPE	[(2S,3'S)-{[(3'-amino-3'-carboxy-propyl)-hydroxyphosphinoyl]methyl}-pentanedioic acid
FABC	Fluorocyclobutane-1-carboxylic acid
FACBC	Anti-1-amino-3-fluorocyclobutane-1-carboxylic acid or fluciclovine or trade name Axumin
FACS	Fluorescence-activated cell sorting

FDA	Food and drug administration
FDG	Fluorodeoxyglucose
FDHT	16β-fluoro-5α-dihydrotestosterone
FECH	Fluoro-ethyl choline
Fmoc	9-Fluorenylmethoxycarbonyl
FOLH1	Folate hydrolase 1
GCP(II)	Glutamate carboxypeptidase II
Gln	Glutamine
Glu	Glutamic acid
GLUT1	Glucose transporter 1
Gly	Glycine
GMP	Good manufacturing practice
GRPR	Gastrin-releasing peptide receptor
HATU	1-[bis(dimethylamino)methylene]-1*H*-1,2,3-triazolo[4,5-*b*]pyridinium 3-oxid hexafluorophosphate
HBED	Bis(2-hydroxybenzyl)ethylenediaminediacetic acid
HEPES	4-(2-hydroxyethyl)1-piperazineethanesulfonic acid
His	Histidine
HPLC	High pressure liquid chromatography
HSQC	Heteronuclear single quantum correlation
I&T	Imaging and therapy
IC_{50}	50% inhibition concentration
ID	Injected dose
IR	Infrared
iTLC	Instant thin layer chromatography
J591	Monoclonal antibody for the prostate specific membrane antigen
K_d	Dissociation constant
K_{GaL}	Ligand-gallium stability constant
K_i	Inhibitor constant
K_M	Michaelis constant
LC-ESIMS	Liquid chromatography electrospray ionisation mass spectrometry
LET	Linear energy transfer
LNCaP	Cell line - human prostate carcinoma derived from a left supraclavicular lymph node metastatic site
Lys	Lysine
m/z	Mass/charge
MAG3	Mercaptoacetyltriglycine
MDP	Methylene diphosphonate
MPE	2-[(3-{4-[(2-amino-4-hydroxy-pteridin-6- ylmethyl)-amino]-benzoylamino}-3-carboxy-pro- pyl)-hydroxy-phosphinoylmethyl]-pentanedioic acid
MRI	Magnetic resonance imaging
MW	Molecular weight
NAA	N-acetyl–aspartate
NAAG	N-acetyl-l-aspartyl-l-glutamate
NAALADase	N-acetylated-α-linked acidic dipeptidase
NICE	National Institute for Health and Care Excellence
NMR	Nuclear magnetic resonance
NODAGA	1,4,7-triazacyclononane,1-glutaric acid
NOESY	Nuclear Overhauser effect spectroscopy

NOPO	1,4,7-triazacy- clononane-1,4-bis[methylene(hydroxymethyl)phosphinic acid]-7-[methylene(2-carboxyethyl)phosphinic acid]
NOTA	1,4,7-triazacyclononane-1,4,7-triacetic acid
NOTP	1,4,7-triazacyclononane-N,N',N''-trimethylene-phosphonic acid
OCT	Octanol
PBDA	Phosphonic bis-dicarboxylic acid
PBS	Phosphate-buffered saline
PC3	Cell line- human prostate carcinoma derived from a bone metastatic site
PET	Positron emission tomography
PMPA	2-(phosphonomethyl)pentane-1,5-dioic acid
PPM	Parts per million
Pro	Proline
PSA	Prostate specific antigen
PSMA	Prostate specific membrane antigen
QC	Quality control
QM/MM	Quantum mechanics/molecular mechanics
RCP	Radiochemical purity
R_f	Retention factor
RM2	Bombesin-based peptide BAY 86-7548
ROI	Regions of interest
RT	Room temperature
R_t	Retention time
SCID	Severe combined immune-deficient
SD	Standard deviation
SNMMI	Society of Nuclear Medicine and Molecular Imaging
SPE	((2S)-2-{[(2-carboxy-ethyl)-hydroxy-phosphinoyl]methyl}-pentanedioic acid)
SPECT	Single photon emission computed tomography
SUV	Standard uptake value
TATE	D-Phe^1-Tyr^3-Thr^8-octreotate
TCA	Tricarboxylic acid
TFA	Trifluroacetic acid
THP	Tris(hydroxypyridinone)
TIM	2,2',2'',2'''-((2,2'-(2,2'- (azanediylbis(methylene))bis(1H-imidazole-2,1-diyl))bis(acetyl))bis(azanetriyl))tetraacetic acid
TIPS	Triisopropylsilane
TLC	Thin layer chromatography
TNM	Tumour, node, metastasis
TOC	D-Phe^1-Tyr^3-octreotide
TOSCY	Homonuclear total correlation spectroscopy
TRAP	1,4,7-triazacyclononane-1,4,7-tris[methyl(2-carboxyethyl)phosphinic acid]
Trp	Tryptophan
Tyr	Tyrosine
UK	United Kingdom
USA	United States of America

Table of Contents

1 Imaging Prostate Cancer

1.1 Prostate Cancer

In 2015, 11,819 men died of prostate cancer in the UK, making it the third most common cause of cancer death (*1*). The number of people diagnosed with prostate cancer has increased over the last 15 years, due to advances in detection, but also an ageing population, with the majority of prostate cancer cases in men over 50 (average age at diagnosis 65-69) (*2*). Medical imaging is an extremely important tool for the detection and staging of prostate cancer and it is vital that it gives an accurate and comprehensive account of disease burden, as this informs the patient's treatment plan, and inadequate data leads to over- or under-treatment. In this chapter, the current use of medical imaging in the diagnosis and staging of prostate cancer patients will be reviewed from a UK perspective and the clinical need for new imaging techniques within this pathway will be discussed.

1.2 Diagnosis, Staging and Biochemical Reoccurrence

If a patient presents with symptoms of prostate cancer, a prostate-specific antigen (PSA) blood test is carried out. PSA is excreted by the epithelial cells of the prostate and is elevated in cases of prostate cancer with blood serum levels increasing with tumour burden. Under 4 ng/mL is considered normal (*3*). The detected PSA level, a digital rectal examination, and the patient's comorbidities, risk factors and wishes are all used to determine whether a patient proceeds to prostate biopsy (*4*). In some cases, this will also be supported by pre-biopsy multi-parametric magnetic resonance imaging (MRI). Normally a transrectal ultrasound-guided biopsy is performed, where ultrasound is used to locate the prostate, measure its size and shape, and guide the 12 biopsy locations. Samples are analysed with histological techniques to diagnose and grade prostate cancer, using the Gleason scoring system which measures the extent of gland uniformity and cell differentiation. Higher Gleason scores indicate more poorly differentiated and aggressive cancer types (*5*). The multiple core biopsies give information on the location and extent of cancer in the prostate. If the cancer is suspected to have spread outside the prostate then computed tomography (CT) or MRI are used to size pelvic lymph nodes (enlarged lymph nodes > 8 mm indicates possible prostate cancer (*6*)) and bone scintigraphy or single-photon emission computed tomography (SPECT) imaging with technetium-99m-methylenediphosphonate ([^{99m}Tc]Tc-MDP), is used to detect osseous metastases. The normal course of disease progression for prostate cancer is from a primary tumour in the prostate to lymph nodes within the pelvis (pelvic, hypogastric, iliac, sacral), then distant lymph nodes (aortic,

common iliac, inguinal, supraclavicular, cervical) and then to the bone, with other organs (lung and liver) only involved at a very late stage (*7*). As shown in figure 1.1 the location and extent of prostate cancer determines the patient's clinical stage as defined by the tumour, node and metastasis (TNM) system (*7*), and this, combined with the PSA level and Gleason score, gives the patient's level of risk, which determines the treatments offered at the time of diagnosis. This is summarised in table 1.1.

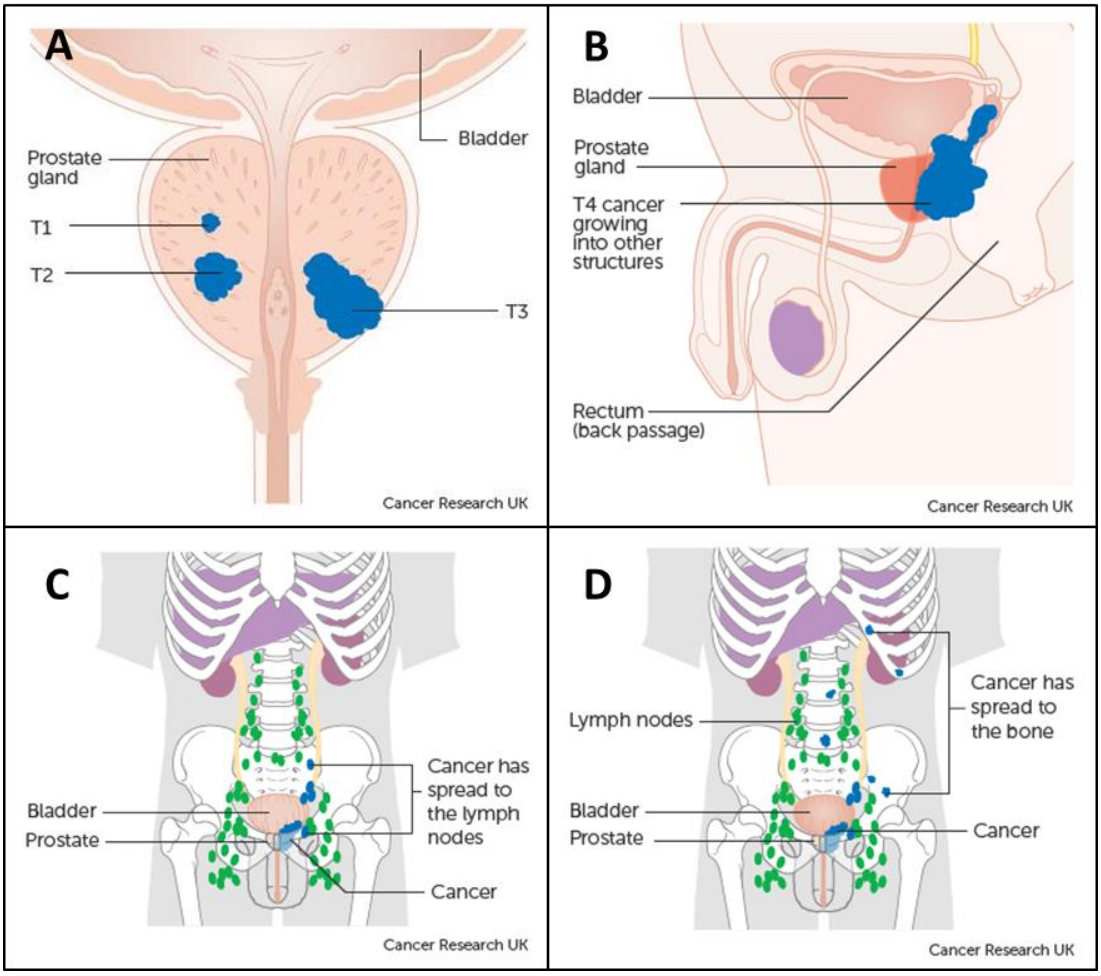

FIGURE 1.1: Clinical stages of prostate cancer: (A) Tumour (T) stages T1- T3. In stages T1 and T2 the tumour is contained within the prostate, in T3 the tumour extends outside of the prostate capsule; (B) Tumour stage T4, tumour has spread into adjacent organs; (C) Node (N) stage, cancerous lymph nodes present within the pelvis; (D) Metastasis (M) stage, cancer has spread beyond the pelvis, to distant lymph nodes, bone, or other organs. Reproduced from (8) (open source document).

Level of risk	PSA serum level		Gleason score		Clinical stage (TNM system (*7*))
Low risk	<10 ng/mL	And	≤ 6	and	T1-T2a
Intermediate risk	10-20 ng/mL	Or	7	or	T2b
High risk	>20 ng/mL	Or	8- 10	or	≥ T2c

TABLE 1.1: Summary of the different risk groups for patients diagnosed with prostate cancer and their dependence upon PSA serum level, Gleason score and clinical staging. Clinical stage 2a is defined as cancer detected in less than 50% of one lobe of the prostate gland, 2b as cancer detected in more than 50% of one lobe of the prostate gland and 2c as cancer detected in both lobes of the prostate gland. In stages 2a-2c the cancer is confined within the prostate. Table reproduced from (4) (open source document).

Patients with low-risk prostate cancer are likely to begin active surveillance, which entails a multi-parametric MRI to define the disease burden within the prostate, regular measurement of PSA levels and digital rectal examinations, and a repeat biopsy at 12 months (*4*). Such surveillance aims to avoid over-treatment of clinically insignificant prostate cancer, whilst ensuring disease progression is detected. Patients with intermediate-risk or high-risk prostate cancer will be offered radical prostatectomy or radical radiotherapy, when this would offer long-term disease control. If a patient has already progressed to having lymph node involvement or metastases, there is limited advantage in performing these radical treatments and they should instead start androgen therapy or chemotherapy. It is often difficult to correctly categorise these patients, because unless they have large enough lymph nodes to be detected by anatomical imaging (CT or MRI) or their bone scan indicates bone metastases, the spread of disease to lymph nodes cannot be detected with current imaging techniques and so risk tables are used to assess the likelihood of nodal involvement (*7*). Detection of such lymph nodes so that they can be removed during radical surgery, targeted with radiotherapy or categorise the patient as unsuitable for radical treatment, would be very beneficial. This creates a need to develop a suitable positron emission tomography (PET) scan that would allow detection of the primary tumour and involved lymph nodes throughout the whole body, providing a more accurate report of disease burden. There is precedence for the use of [^{18}F]fluorodeoxyglucose ([^{18}F]FDG) PET scans for staging in other cancers (breast cancer (*9*), lung cancer (*10*), and colorectal cancer (*11*)), however, studies evaluating the ability of [^{18}F]FDG to stage prostate cancer showed limited value for clinical practice (*12*)(*13*)(*14*)(*15*). Therefore [^{18}F]FDG scans are not recommended for the staging of prostate cancer by the UK's National Institute for Health and Care Excellence (NICE) (*4*). The reasons why [^{18}F]FDG is an unsuitable imaging agent for staging prostate cancer are explored in section 1.3.1. Alternative tracers are therefore required for imaging prostate cancer. Staging before radical treatment is the first of two scenarios where a PET scan specific for the detection of prostate cancer would serve a clinical need.

The second scenario where a PET scan suitable for prostate cancer would serve a clinical need is in patients with biochemical recurrence, indicated by a rising PSA after radical treatment (> 0.2 ng/mL after radical prostatectomy, > 2 ng/mL after radical external-beam radiation therapy or brachytherapy (*16*)). This happens in approximately 20% of men diagnosed with intermediate-risk disease within 8 years of radical surgery and 35% of men within 8 years of radical radiotherapy (*17*). In cases of biochemical recurrence imaging with bone scintigraphy or CT has only been shown effective in determining the site of relapse when patients have a PSA over 20 ng/mL (*16*), therefore in the majority of cases where the PSA levels are lower than this threshold there is a clinical need to determine the site of recurrence in order to inform the treatment decision. By definition, if a patient has rising PSA after radical treatment then they have biochemical recurrence, even if this is a very small volume of disease, and consequently, current techniques are unable to visualise it (*18*). Available treatments in cases of biochemical recurrence include: salvage radiotherapy, salvage prostatectomy, cryotherapy, high intensity focused ultrasound, orchiectomy, androgen therapy or chemotherapy (*4*)(*16*), and the most suitable choice will depend on the extent and location of disease.

In both scenarios, a PET scan would be an ideal imaging modality for detecting the presence of nodal and metastatic disease. It is a whole body scan with a high signal to noise ratio, which allows molecular rather than anatomical differences to be detected and quantified. An ideal tracer to detect these sites would have higher accumulation in prostate cancer than in normal prostate and other non-target organs, plus be suitable for the detection of well-differentiated through to undifferentiated prostate cancer, which would allow a primary tumour, lymph node involvement and soft tissue and bone metastases to all be identified, even if they are no longer androgen sensitive. Additionally, the choice of the positron-emitting radionuclide must be widely available and ensure high-quality images are produced within an acceptable patient dose, which favours the use of short half-life tracers with a high percentage of positron emission.

A number of different radiotracers have already been proposed and assessed for imaging prostate cancer for both initial staging and detection of disease sites after biochemical recurrence and some are clinically approved (*19*)(*20*). The key clinical need these tracers should address is an accurate identification of involved lymph nodes and metastatic disease. The design of such tracers falls into three major classes: metabolic, androgen, and receptor-based imaging and each of these approaches will be reviewed below.

1.3 Metabolic Tracers for Prostate Cancer

Metabolic PET tracers are radioactive analogues of small molecules vital for metabolism and cell proliferation. These tracers mimic sugars, amino acids, nutrients or small molecules that naturally occur in the body and they consequently localise in the same areas. Imaging with metabolic tracers therefore allows visualisation of this distribution. However, it is important that these radiotracers also have a trapping mechanism and are not fully metabolised by the same pathways, as this ensures that they accumulate intracellularly, providing enough signal to be detected on a PET scan and ensuring that the image shows only the distribution of the original tracer and rather than its radioactive metabolites. In cancer imaging, the changes in the metabolism of cancerous cells compared to normal cells, particularly when transporters are upregulated in order to aid proliferation, gives them different levels of tracer uptake to non-cancerous cells allowing them to be identified on a PET scan. All metabolic tracers will have endogenous uptake, as they target vital metabolic pathways that exist in both healthy and disease states (even though the extent of the process varies). This background uptake is therefore always an important consideration when using metabolic tracers as it impacts on both the signal to noise ratio and dosimetry of the procedure.

When using metabolic PET tracers in the context of prostate cancer it is also important to note that prostate cancer displays a wide range of proliferation rates (2 to 25 fold faster than matched normal tissue (*21*)), which will impact the extent of tracer uptake. In addition, the stage of the prostate cancer and therefore how well-differentiated it is, may also impact on its metabolism and therefore, on the uptake of the tracer (*22*). This is also likely to be influenced by any previous treatment the patient has received, in particular, androgen therapy (*23*), chemotherapy (*23*) and radiotherapy (*24*).

In this section the following metabolic tracers will be described briefly in the context of prostate cancer: [^{18}F]FDG, [^{11}C]acetate, [^{11}C]methionine, [^{11}C]choline, [^{18}F]fluoro-choline, and anti-1-amino-3-[^{18}F]fluorocyclobutane-1-carboxylic acid ([^{18}F]FACBC). The structure of all of these are shown in figure 1.2. [^{11}C]choline (*20*) and [^{18}F]FACBC (*19*) have been approved for prostate cancer patients with suspected prostate cancer recurrence based on elevated PSA levels by the U.S. Food and Drug Administration (FDA). [^{18}F]FDG, [^{11}C]methionine and [^{11}C]acetate are all FDA-approved agents (*25*), and therefore widely available, but in this context, it is important to remember that their use in prostate cancer was not part of the evidence that gained them this approval (*26*). All of these tracers utilise the short-lived radionuclides carbon-11 or fluorine-18,

which are suitable for PET imaging, and are cyclotron-produced. See table 1.2 for more detail of the properties of these radionuclides.

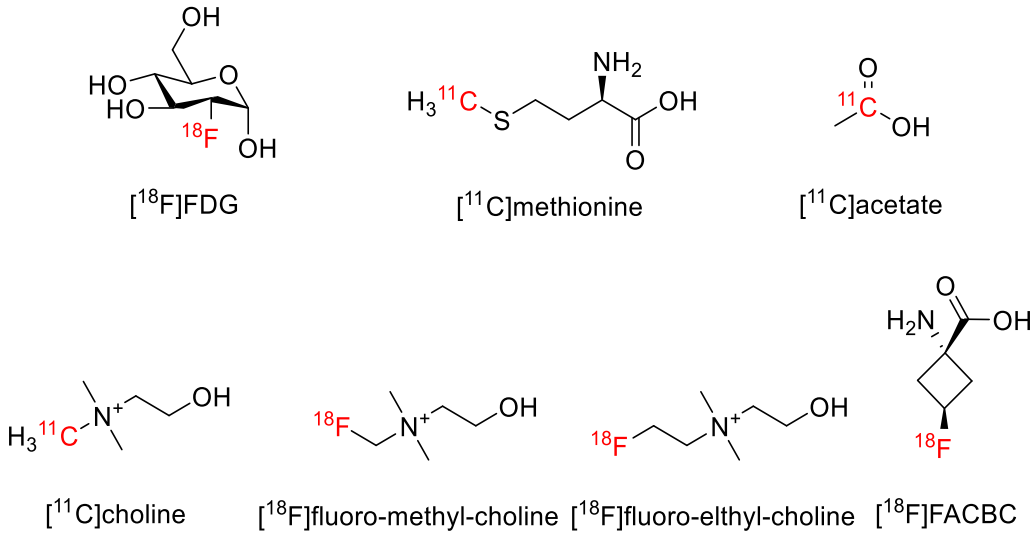

FIGURE 1.2: Structures of [18F]FDG, [11C]methionine, [11C]acetate, [11C]choline, [18F]fluoro-methyl-choline, [18F]fluoro-ethyl-choline, [18F]FACBC. Structures from (27)

Radionuclide	Non-metal / metal	PET/ SPECT	Emissions	Half-life	Production
Carbon-11	Non-metal	PET	99.8% β^+ 0.2% EC	20.4 min	Cyclotron
Copper-64	Metal	PET	39% β^- 18% β^+	12.7 hours	Cyclotron
Fluorine-18	Non-metal	PET	96.9% β^+ 3.1% EC	1.83 hours	Cyclotron
Gallium-68	Metal	PET	89% β^+ 11% EC	67.8 min	^{68}Ge/ ^{68}Ga generator or Cyclotron
Iodine-123	Non-metal	SPECT	97% γ 159 keV	13.27 hours	Cyclotron
Iodine-124	Non-metal	PET	70% EC 30% β^+	4.18 days	Cyclotron
Iodine-131	Non-metal	SPECT	89% β^- 81% γ 364.5 keV	8.02 days	Nuclear fission
Technetium-99m	Metal	SPECT	11.5% IC 88.5% γ 140.5 keV 142.6 keV	6.01 hours	^{99}Mo/^{99m}Tc Generator

TABLE 1.2: Properties of the radionuclides used for prostate cancer imaging. Data from (28–36).

1.3.1 [^{18}F]FDG

[^{18}F]FDG is the most widely used PET tracer with over 100,000 scans performed every year in the UK alone (*37*). Many hospitals only provide PET scans with [^{18}F]FDG. It is used for imaging a wide range of cancer types including breast cancer (*9*), lung cancer (*10*), and colorectal cancer (*11*) and the scans have become a vital tool in oncology. This has driven the large investment in PET scanners and production facilities seen over the last 20 years. [^{18}F]FDG is an analogue of glucose and the mechanism for detection of cancer with [^{18}F]FDG is through its increased glucose metabolism compared to normal tissue (the Warburg effect (*12*)). This is typically due to cancer cells upregulating the expression of glucose transporter 1 (GLUT1) on the cell membrane. Like glucose, [^{18}F]FDG is phosphorylated once it enters the cell but, due to its structural modification with fluorine-18, cannot be metabolised further, causing intracellular accumulation (*38*). GLUT1 is known to be upregulated in lung, stomach, thyroid, colon, oesophagus, bladder and breast cancer (*22*). However, the limited studies conducted on GLUT1 expression in prostate cancer suggest that the expression level is lower (*39*). It is known that the level of GLUT1 expression within prostate cancer cell lines varies between those that are well-differentiated and androgen-sensitive, such as LNCaP (where the expression is low), and the poorly-differentiated and less androgen-sensitive cell lines DU145 and PC3 (where the expression level increases (*22*)). Similarly, in clinical studies metastases which are more [^{18}F]FDG avid are considered indicative of more aggressive cancer (*13*)(*40*).

There have been many clinical studies examining the use of [^{18}F]FDG in prostate cancer, and overall they show it has limited value in clinical practice when compared to the utility of [^{18}F]FDG in other cancer types (*12*)(*13*)(*14*)(*15*). Due to this evidence, the UK NICE guidelines do not support the use of this tracer in prostate cancer (*4*). [^{18}F]FDG is particularly poor for primary tumour imaging as it cannot differentiate accurately between, normal tissue, prostatitis, and prostatic hyperplasia. Additionally, it is taken up in areas of inflammation or infection, making it prone to both false positive and false negative results (*40*)(*41*). Similar problems are seen when looking for reoccurrence in the prostate bed after radical prostatectomy, due to the uptake of [^{18}F]FDG in scar tissue (*13*). However, [^{18}F]FDG can be used for the detection of distant metastases particularly in biochemical recurrence, at PSA levels where bone scanning is unreliable (< 20 ng/mL (*16*)), in order to identify lymph node metastases or verify that enlarged lymph nodes detected by CT are malignant (*40*). A critical review summarising studies where patients with rising PSA after radical prostatectomy were imaged with [^{18}F]FDG showed a detection rate of 19% for prostate cancer in any location and of 6% for distant lymph node

involvement (*42*). This is a particularly low detection rate, as by definition all patients with rising PSA after radical treatment have reoccurrence (*18*).

Most of the alternative PET tracers for prostate cancer have been compared to [^{18}F]FDG and have shown improved detection rates (*42*). In the remainder of this section, other metabolic PET tracers will be discussed and compared to the performance of [^{18}F]FDG in prostate cancer.

1.3.2 [^{11}C]Acetate

Acetate is a common anion within the body and as [^{11}C]acetate has an identical chemical structure it will have identical behaviour. [^{11}C]acetate is actively transported across cell membranes via monocarboxylate transporters. It is then converted to [^{11}C]acetyl CoA in the mitochondria. From there it can either enter the tricarboxylic acid (TCA) cycle or be used in lipid or cholesterol synthesis (*41*)(*43*). The intracellular trapping of the radionuclide seen when [^{11}C]acetate enters prostate cancer cells suggests that it is converted into lipids. This theory is supported by the known upregulation of fatty acid synthase in prostate cancer, with higher levels associated with more aggressive tumours (*44*). In healthy volunteers, the biodistribution of [^{11}C]acetate showed uptake in the myocardium, pancreas, spleen, salivary glands and kidneys, but limited renal excretion, providing an advantage over [^{18}F]FDG when looking for uptake in the prostate bed (*45*). However, studies into the use of [^{11}C]acetate in the identification of primary prostate cancer showed no higher uptake in patients with cancer than in prostate hyperplasia or in healthy volunteers, making it unsuitable for this use (*46*). In metastatic prostate cancer, metastases were detected with [^{11}C]acetate and the detection rate correlated with PSA levels (*47*)(*48*). In studies where [^{11}C]acetate was compared to [^{18}F]FDG PET in the same patient population (*47*)(*48*), both studies showed [^{11}C]acetate was able to visualise local recurrences and regional lymph node metastases better than [^{18}F]FDG, (figure 1.3) but the two studies showed conflicting results for detection rates in distant metastases (*48*). This tracer also suffers from false positives when used to detect prostate cancer due to uptake within inflamed tissue and other cancer types, such as non-small cell lung cancer (*43*)(*49*).

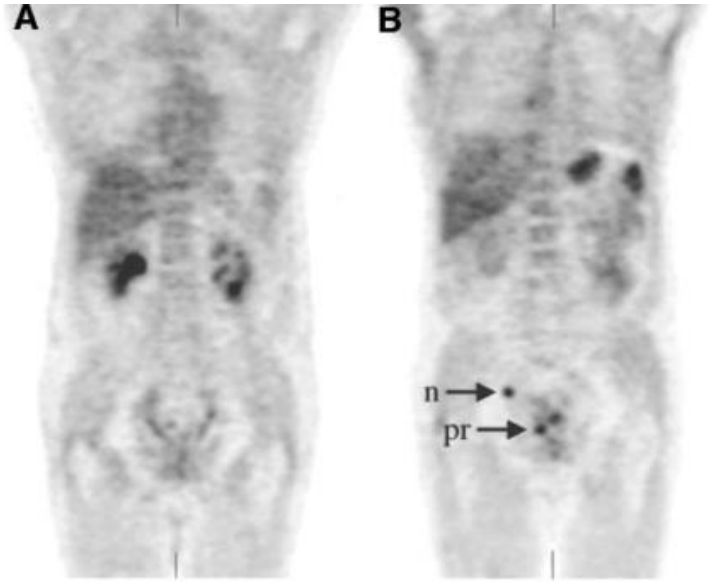

FIGURE 1.3 : Coronal images of the same patient scanned with (A) [^{18}F]FDG and (B) [^{11}C]acetate. This patient had histologically confirmed prostate cancer and biochemical recurrence after radical prostatectomy. [^{18}F]FDG is unable to detect any disease, [^{11}C]acetate shows uptake in the prostate bed (pr) and a pelvic lymph node (n). Reproduced with permission from (47).

1.3.3 [^{11}C] Methionine

Methionine is an essential amino acid and as [^{11}C]methionine has an identical chemical structure behaves identically *in vivo*. [^{11}C]methionine accumulation in tumour cells is attributed to increased amino acid transport and metabolism. Methionine is transported into cells through sodium-dependent amino acid transporter systems, where it is metabolised and incorporated into proteins (*50*). The first 30 minutes of a [^{11}C]methionine scan is believed to reflect methionine transport, with over 80% of [^{11}C]methionine unmetabolised, but by 60 minutes a different distribution is observed due to production of metabolites and their incorporation into proteins (40% of the radionuclide is protein bound (*50*)(*51*)). Both the complex range of metabolites and the unspecific transport mechanism into cells are disadvantages for [^{11}C]methionine as an imaging agent. [^{11}C]methionine imaging (10-60 minutes post-injection) has been compared to [^{18}F]FDG imaging and to conventional imaging, defined as a combination of CT, MRI and bone scans, in 12 patients with known metastatic prostate cancer and rising PSA levels (*38*). [^{11}C]methionine showed the ability to delineate both soft tissue and bone metastases and identified more sites than [^{18}F]FDG, but less than the combination of CT, MRI and bone scans that constituted the standard of care (72.1%). However, 37 additional metastatic sites were identified with [^{11}C]methionine which were absent on bone scans. Figure 1.4 shows [^{11}C]methionine and [^{18}F]FDG PET scans in the same patient 2 hours apart and demonstrates a

higher number of detected lesions plus a higher uptake of [^{11}C]methionine within them. Limited further studies into the effectiveness of [^{11}C]methionine have been conducted in prostate cancer patients and also showed no advantage over conventional imaging techniques (*52*)(*53*).

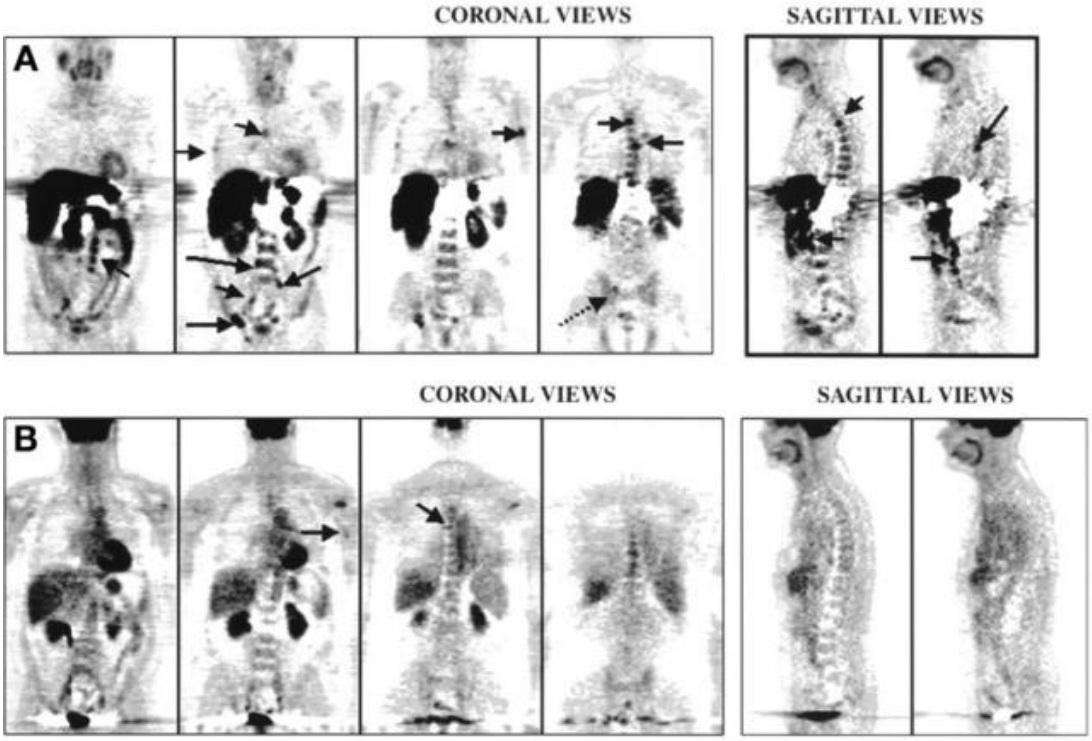

FIGURE 1.4: Imaging of patient who had presented with rising PSA levels (48.7 ng/mL). (A) [^{11}C]methionine PET, (B) [^{18}F]FDG PET. Reproduced with permission from (38).

1.3.4 [^{11}C]Choline, [^{18}F]Fluoro-choline and [^{18}F]FECH

[^{11}C]choline, [^{18}F]fluoro-choline ([^{18}F]fluoro-methyl choline) and [^{18}F]FECH ([^{18}F]fluoro-ethyl choline) are all radioactive analogues of the essential nutrient choline, and so accumulate in sites of high choline metabolism. Choline and its radioactive analogues are charged hydrophilic cations due to their quaternary amine and therefore need specific transporters to pass through cell membranes (*54*). Two key transporters are CHT1, a high-affinity Na^+- and Cl^--dependent choline transporter (*55*); and CLT1 a lower affinity Na^+-independent choline transporter (*23*). Both of these transporters have been detected at higher expression levels in prostate cancer alongside a higher transport rate (*54*). The trapping mechanism of [^{11}C]choline, [^{18}F]fluoro-choline and [^{18}F]FECH in cells is the incorporation of these radiotracers into phosphatidylcholine. As phosphatidylcholine is a key component in cell membranes the increased uptake of choline in prostate cancer is indicative of cell proliferation (*56*). However, proliferation is unlikely to be the only factor increasing uptake, as prostate cancer cells are also known to have abnormal

choline phospholipid metabolism which is implicated in cell signalling (*54*). Physiologic uptake of radio-choline is similar between the carbon-11 and fluorine-18 analogues, with high uptake in the pancreas, spleen, liver, kidneys, and salivary glands and variable uptake in the intestines (*57*). However, the fluorine-18 versions also accumulate in the urine, a disadvantage for the detection of small volume disease in the prostate bed, due to potential overlap with the signal from the urine. This difference in renal excretion occurs because of structural modifications required to accommodate radio-fluorination cause incomplete tubular reabsorption (*58*). The ability of [^{11}C]choline to localise cancer within the prostate in order to stage primary tumours (figure 1.5) was assessed in a study of 36 patients with known prostate cancer (*59*). The uptake of [^{11}C]choline in the prostate was correlated with histopathology after radical prostatectomy and showed that [^{11}C]choline identified the majority of sites containing prostate cancer (94/143), but failed to identify cancer in a third of regions (49/143). Uptake was also seen in areas without cancer, but with high-grade prostate intraepithelial neoplasm. These results show a high rate of false positives and false negatives and that [^{11}C]choline imaging is not a suitable technique for primary tumour staging. However, [^{11}C]choline/[^{18}F]fluoro-choline PET imaging is more suitable, than anatomical imaging and bone scans for detection of involved lymph nodes before radical surgery or radical radiation therapy, as determined by over 9 prospective studies. These were summarised by a meta-analysis in 2013 (*60*) which showed a pooled sensitivity of 49.2% (95% confidence interval (CI), 39.9–58.4%) and a pooled specificity of 95% (95% CI 92–97.1). In such meta-analyses, sensitivity is defined as the probability of a person with prostate cancer having a positive test result, and specificity as the probability of a person without the disease having a negative test result and so it is ideal for both numbers to be as high as possible (*61*). These results therefore mean that [^{11}C]choline/[^{18}F]fluoro-choline PET imaging will miss around half of the involved lymph nodes that would have shown positive for prostate cancer by histological analysis after pelvic lymph node dissection (the gold standard), but that false positives would be much less frequent (~5%). In biochemical recurrence [^{11}C]choline and [^{18}F]fluoro-choline PET have been evaluated in a range of meta-analyses (*62*)(*63*)(*64*) and shows a much improved sensitivity (pooled sensitivity 84%-91%) compared to anatomical lymph node staging and bone scans, whilst maintaining good specificity (79%-93%). This may be due in part to a shift in the gold standard used to define true positive results towards lymph node sizing by MRI and CT and bone scans rather than histological analysis which can detect much smaller areas of disease but are more difficult to obtain in cases of biochemical recurrence. The main application of [^{11}C]choline and [^{18}F]fluoro-choline is therefore in the detection of biochemical

recurrence. The use of [^{11}C]choline in this context has been approved by the FDA and therefore has become the benchmark for any novel tracers for prostate cancer.

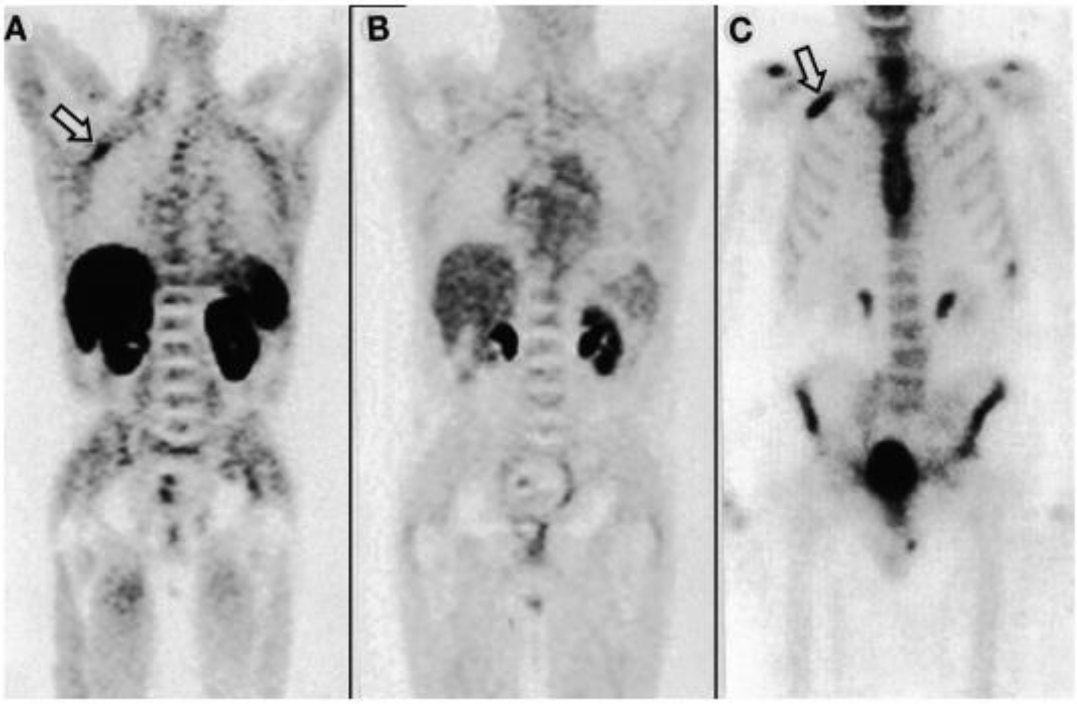

FIGURE 1.5: Imaging of a patient who has previously had a radical prostatectomy, and presented with rising PSA levels (6.2 ng/mL). (A) [^{11}C]choline PET, (B) [^{18}F]FDG PET (C) [^{99m}Tc]Tc-MDP bone scintigraphy. Reproduced with permission from (65).

1.3.5 [^{18}F]FACBC

[^{18}F]FACBC, also known as anti-1-amino-3-[^{18}F]fluorocyclobutane-1-carboxylic acid, [^{18}F]fluciclovine and by its trade name Axumin (*56*), is a fluorine-18 radiolabelled synthetic amino acid, which mimics the behaviour of glutamine in the body (figure 1.2). Glutamine can be transported into cells by a number of amino acid transporters, including alanine serine cysteine transporter 2 (ASTC2) (*66*) which is known to be upregulated in prostate cancer. Because of the differences in structure between glutamine and [^{18}F]FACBC, after entering the cell, [^{18}F]FACBC is not metabolised and intracellular accumulation occurs. Studies in healthy volunteers showed high physiological uptake in the liver (13.8 ± 3.3%), red bone marrow (11.1 ± 5.8%), lung (7.1 ± 1.3%), and pancreas (4.2 ± 0.7%), with minimal (~4%) urinary excretion (*67*). Clinical imaging in patients with recently diagnosed prostate cancer (n=9) or biochemical recurrence (n=6) showed the ability to delineate intra-prostatic cancer and involved regional lymph nodes, with good concordance with histological findings (*68*). The results showed higher SUVs and tumour to muscle ratios when imaged at 4.5 minutes post-injection compared to at 20 or 65 minutes, this

optimal time point is surprisingly early and suggests that either the uptake is rapid followed by a rapid washout from tumours, or that this is a blood flow effect. One study comparing [^{11}C]choline and [^{18}F]FACBC in the same patients has been published and showed a slightly higher metastases detection rate in biochemical recurrence for [^{18}F]FACBC (*69*), and example images are shown in figure 1.6. A meta-analysis (*70*) of clinical data for detection of biochemical recurrence with [^{18}F]FACBC had pooled sensitivity values of 87% (95% CI, 80–92%) but a lower 66% (95% CI, 56–75%) pooled specificity. The most recent studies of this tracer were not included in this meta-analysis but showed similar results (*71*)(*72*). This lower specificity indicates a larger number for false positive results compared to [^{11}C]choline or [^{18}F]fluoro-choline and was attributed to the uptake of [^{18}F]FACBC in non-cancerous conditions including but not limited to prostatic hyperplasia and inflammation. Unfortunately, inflammation can be caused by treatments for prostate cancer and so is likely to be present in a significant number of patients undergoing PET imaging for recurrence, limiting the utility of [^{18}F]FACBC. However, the strength of the evidence for the use [^{18}F]FACBC in prostate cancer patients with suspected prostate cancer recurrence based on elevated PSA levels meant it was approved by the FDA in 2016 (*19*) and the European Medicines Agency (EMA) in 2017 (*73*).

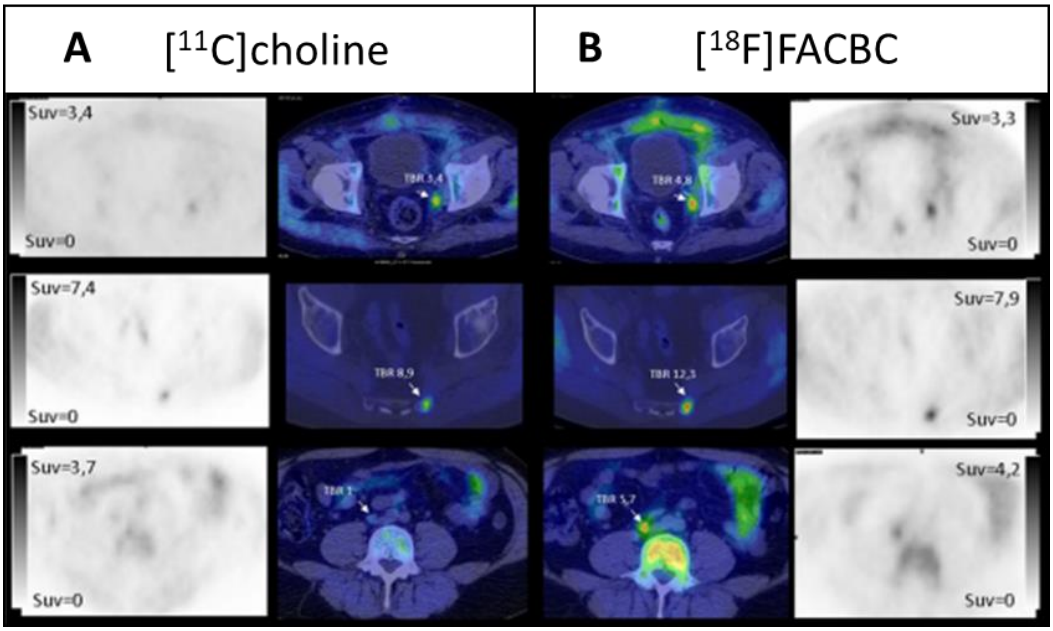

FIGURE 1.6: PET and PET/CT imaging in patients with biochemical recurrence with (A) [^{11}C]choline, (B) [^{18}F]FACBC. Modified with permission from (69).

1.4 Androgen Imaging

The androgen receptor is a steroid hormone receptor, specific for testosterone and dihydrotestosterone, and is found in primary and metastatic prostate cancer of all grades and in androgen-independent cancers (*74*). Chemical or surgical castration can induce apoptosis of androgen-sensitive prostate cancer cells (*74*), leading to improved patient outcomes, as can the use of androgen deprivation therapy where anti-androgens are administered to block the androgen receptor and inhibit its function (*16*). The ability to image the distribution of the androgen receptor may provide information for prostate cancer staging but it also may have a more specific role in validating the ability of novel androgen therapy drugs to block the androgen receptor.

1.4.1 16β-[^{18}F]fluoro-5α-dihydrotestosterone

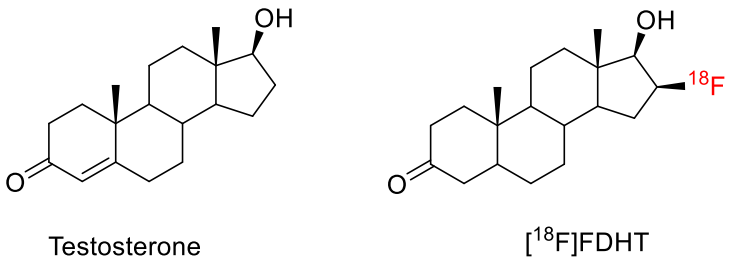

FIGURE 1.7: Structures of testosterone and [^{18}F]FDHT (16β-[^{18}F]fluoro-5α-dihydrotestosterone) (75).

The structure of 16β-[^{18}F]fluoro-5α-dihydrotestosterone ([^{18}F]FDHT) is very similar to that of testosterone as shown in figure 1.7 and so it behaves similarly *in vivo*. The first clinical study of [^{18}F]FDHT compared its performance to [^{18}F]FDG imaging in 7 patients with metastatic prostate cancer (*76*). A key finding was the rapid metabolism of the tracer with 80% conversion to more hydrophilic metabolites within 10 minutes of administration. Across the 12 patients studied the 59 lesions were detectable by CT, MRI or bone scan. [^{18}F]FDG was able to detect 97% of these metastatic sites, whereas [^{18}F]FDHT imaging at 1 hour post-injection was only able to detect 78%. A comparison of the two tracers' performance in the same patient is shown in figure 1.8. Despite these findings which suggest it unsuitable for use in clinical practice, two clinical trials for androgen therapies have utilised [^{18}F]FDHT to monitor response (*77*)(*78*). Although there is known rapid metabolism of [^{18}F]FDHT, making it most appropriate to choose a very short imaging time point such as 5 minutes, the imaging time point chosen in these studies was 30 minutes to 1 hour and these results were used to define the level of androgen receptor expression and binding capacity. In both studies the uptake of the tracer decreased after 4

weeks of androgen therapy in a dose dependent manner, suggesting the therapeutics bound to androgen receptors, blocking uptake of [^{18}F]FDHT.

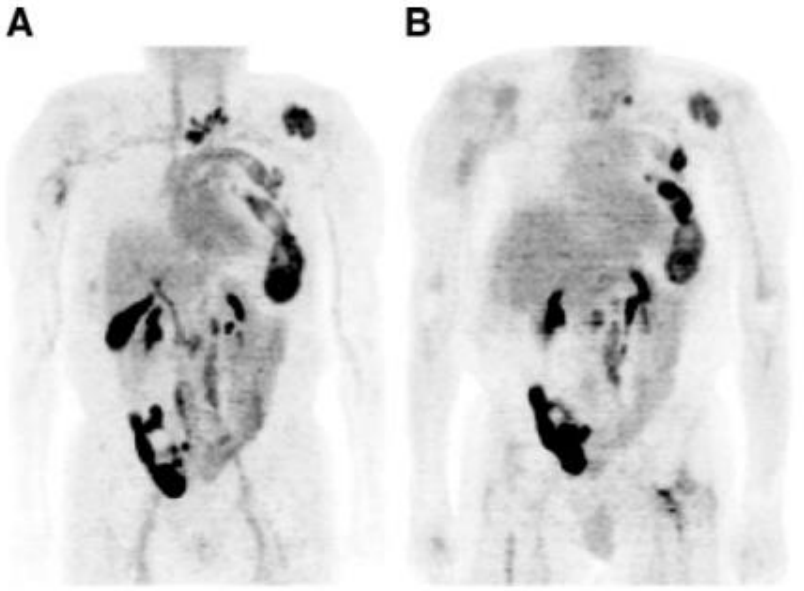

FIGURE 1.8: (A) [^{18}F]FDHT and (B) [^{18}F]FDG PET images in a patient with metastatic prostate cancer which showing heterogeneity between the tracer uptake. Reproduced with permission from (76).

1.5 Receptor-Based Imaging

Cell surface receptors that are highly expressed in prostate cancer but poorly expressed or absent in healthy tissue provide a means of detecting disease sites by utilising radiotracers which selectively target these receptors. Upon binding the receptor, the tracer should remain intact and bound to the receptor, or be internalised, so that the concentration of the radiotracer increases substantially enough to provide a good signal to noise ratio, that allows detection of disease sites. Two key receptors implicated in prostate cancer are the gastrin-releasing peptide receptor and the prostate specific membrane antigen, both of which can be targeted with low molecular weight peptide-based motifs.

1.5.1 Gastrin-Releasing Peptide Receptors

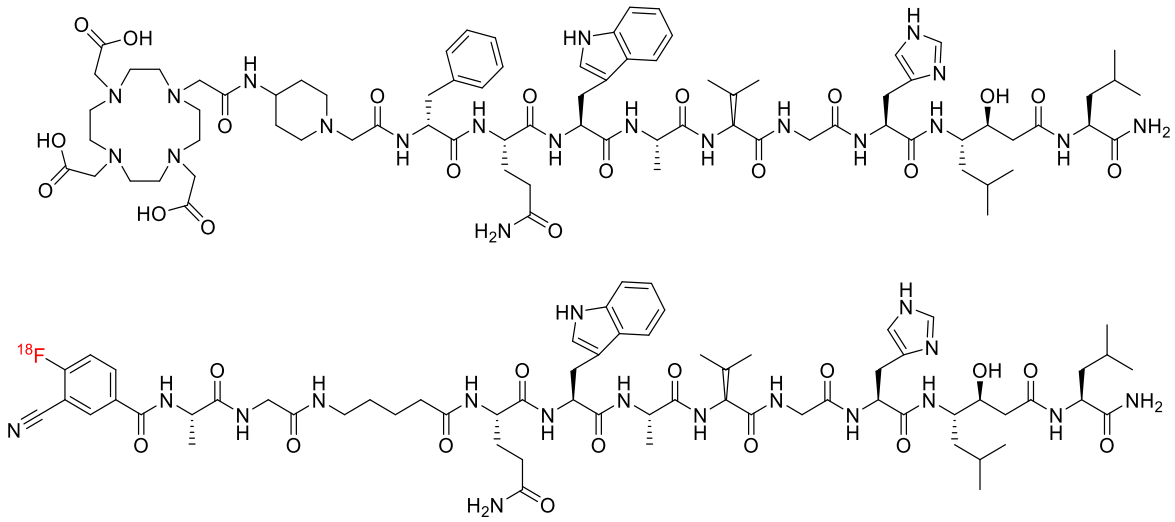

FIGURE 1.9: The structure the GRPR antagonist DOTA-RM2 suitable for radiolabelling to produce [^{68}Ga]Ga-DOTA-RM2(79) and the structure of [^{18}F]F-BAY 864367 with fluorine-18 in red (80).

Gastrin-releasing peptide receptors (GRPRs) belong to the bombesin receptor family and can be targeted by the 14 amino acid peptide bombesin. GRPR expression is upregulated in prostate cancer compared to the normal prostate but its expression level is highest in lower grade prostate cancer rather than higher grade undifferentiated prostate cancer (Gleason scores over 7 (*81*)). Radiotracers have been made from antagonists of these receptors and [^{68}Ga]Ga-DOTA-RM2 also known as BAY 867548 (*79*) as shown in

figure 1.9, has been evaluated in the most clinical studies. In healthy volunteers [^{68}Ga]Ga-DOTA-RM2 showed extensive uptake in normal tissues, with the highest uptake seen in the pancreas, kidneys and bladder, and moderate uptake in the liver, spleen, gastrointestinal tract, and colon (*80*). Plasma studies showed 3 radioactive-metabolites within 10 minutes of administration, due to the cleavage of amide bonds, with the intact radiotracer dropping from 92% ± 9% at 1 minute post-injection to 15% ± 2% after 150 minutes (figure 1.10). Such rapid metabolism is a major concern and means imaging should be restricted to short time-points when the majority of the tracer is intact. Despite this, clinical evaluation in prostate cancer patients showed uptake in both the primary tumour and in involved lymph nodes when imaged at 60 minutes post-injection with SUV_{max} in the primary tumour of 6.6 ± 4.7 (*81*)(*82*). A fluorine-18 labelled analogue has also been produced called [^{18}F]F-BAY 864367 and has been evaluated clinically, this showed the ability to delineate prostate cancer in the primary prostate and in lymph nodes, but the number of lymph nodes detected was lower than with [^{18}F]fluoro-choline, and no metabolite studies

were completed. As the structure of [^{18}F]F-BAY 864367 is very similar to that of [^{68}Ga]Ga-DOTA-RM2 (

figure 1.9), it is very probable that radioactive metabolites are also being produced so the PET images are not showing the distribution of just the desired tracer. Although the gastrin-releasing peptide receptors are interesting targets, the tracers that have been produced to image them in prostate cancer suffer from high background uptake and metabolic breakdown *in vivo*, suggesting that a new generation of tracers is required to observe the true distribution of this receptor in prostate cancer. However, even if this is achieved, the fact that the expression levels of this receptor decrease as the prostate cancer becomes more undifferentiated, will limit its ability to detect late-stage disease; a key requirement for clinical use.

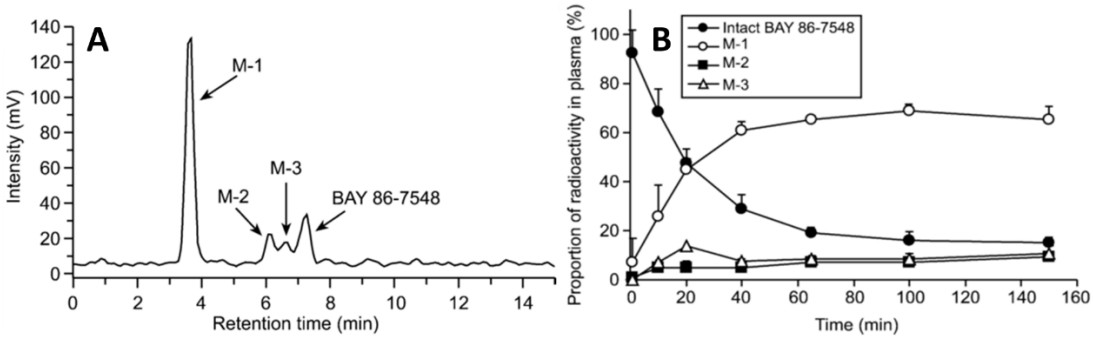

FIGURE 1.10: (A) Radio-HPLC of blood plasma 65 minutes after injection of [^{68}Ga]Ga-DOTA-RM2 (BAY 867548) showing the presence of three metabolites. (B) Graph showing the ratios of intact tracer to the three metabolites in plasma samples from 1 minutes post-injection to 150 minutes post-injection of [^{68}Ga]Ga-DOTA-RM2 (BAY 867548). Reproduced with permissions from (80).

1.5.2 The Prostate Specific Membrane Antigen/Glutamate Carboxypeptidase II

Pathological studies have revealed the prostate specific membrane antigen (PSMA), also known as glutamate carboxypeptidase II (GCP(II)), as a suitable target for imaging prostate cancer (*83*)(*84*)(*85*). This is a transmembrane zinc metalloenzyme that catalyses the cleavage of a terminal glutamate from its natural substrates N-Acetyl-l-aspartyl-l-glutamate (NAAG) and poly-γ-glutamated-folates (*86*) (figure 1.11). It is found naturally in prostate tissue, brain, kidneys, and intestinal tract but its expression is 100- 1000 times higher in prostate cancer cells (*87*)(*88*). A detailed description of the structure of GCP(II)/PSMA and its interaction with its natural inhibitors is described in chapter 6 and so will not be reproduced here.

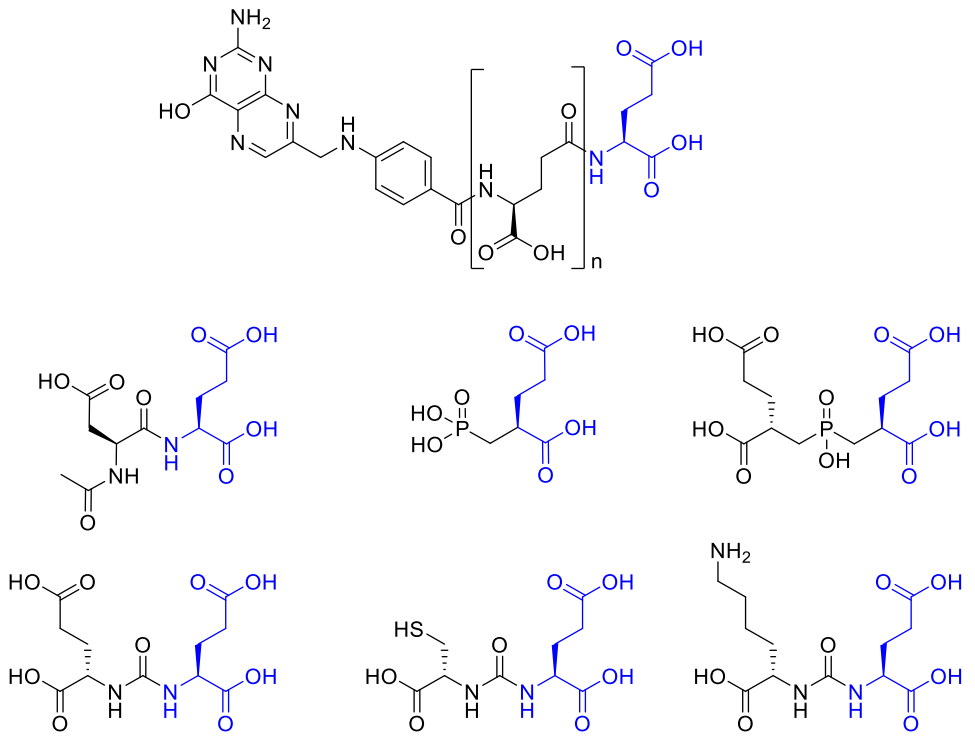

FIGURE 1.11: Structures of the natural substrates (A, B) and inhibitors (C-G) of GCP(II)/PSMA, with the conserved terminal glutamate structure shown in blue. (A) Poly-γ-glutamated folate, (B) NAAG, (C) PMPA, (D) PBDA, (E) Glu- Glu, (F) Cys-Glu, (G) Lys-Glu.

1.5.2.1 Imaging GCP(II)/PSMA with Antibodies

GCP(II)/PSMA has been imaged previously with the indium-111 radiolabelled antibody 7E11.C5 (ProstaScint). This targeted an internal epitope of GCP(II)/PSMA and so was suitable for the detection of GCP(II)/PSMA expressing non-viable or apoptotic cells, which only accumulate in quantities sufficient for imaging in larger solid tumours (*89*). Therefore the diagnostic performance of this radiolabelled antibody was limited. Monoclonal antibodies which recognise epitopes in the extracellular domain of GCP(II)/PSMA have also been identified and radiolabelled, most notably the monoclonal antibody J591 (*89*)(*90*). In addition, a number of smaller single chain fragments (*91*), and diabodies (*92*) of J591 have also been produced and used for imaging. A review of this work is outside the scope of this introduction and reviews are already available (*89*)(*90*).

1.5.2.2 Imaging GCP(II)/PSMA with Small Molecule Inhibitors

Generally, small molecule targeting agents offer comparable affinity to targeting with antibodies with a number of additional advantages. They typically accumulate quicker in tumours and have deeper penetration and faster blood clearance which results in shorter imaging time points and better signal to noise ratios (*93*). There are also fewer concerns about an immunogenic response

to small molecules (*94*), and they allow for the design of multiple analogues giving the opportunity to optimise properties such as binding affinity, pharmacokinetics and radiolabelling sites. Therefore, small molecule radiotracers have become the preferred approach for imaging GCP(II)/PSMA (*95*).

The first small molecule inhibitors of GCP(II)/PSMA were designed as neuroprotection agents. GCP(II)/PSMA in the brain converts NAAG into glutamate and N-acetylaspartate (NAA) and excessive glutamate transmission is found in a range of neurological disorders including ischaemia and stroke, central nervous system trauma and amyotrophic lateral sclerosis (ALS) (*86*). Inhibitors for GCP(II)/PSMA in the brain were therefore developed using NAAG as a starting point rather than the other natural substrate, poly-γ-glutamated folate. Initially, phosphonate derivatives were designed with the most successful structures being 2-(phosphonomethyl)pentane-1,5-dioic acid (PMPA) (*96*), and phosphonic bis-dicarboxylic acid (PBDA) (*97*)(*98*) (figure 1.11) which have low nM affinities (IC_{50} = 5.1 ± 0.6 nM (*98*), and EC_{50} 6.9 ± 0.7 nM (*97*) respectively). These studies also highlighted the importance of conserving a terminal L- glutamate (L-glutamic acid)-like structure in order to achieve high affinity, and that dipeptides gave enhanced inhibition (*86*). PMPA is still the small molecule inhibitor of choice for GCP(II)/PSMA and has been used as a blocking agent in order to demonstrate specific binding in a number of studies (*99*)(*100*)(*101*)(*102*), as well as to provide nephroprotection for GCP(II)/PSMA targeted therapies (*103*). However, PMPA cannot be functionalised whilst maintaining its high affinity and so urea-based GCP(II)/PSMA inhibitors were developed by further rational design (*98*). These utilise a urea as an amide bond mimic, allowing the structure of the terminal L-glutamic acid to be conserved, but stopping its enzymatic cleavage by GCP(II)/PSMA. The urea also allows for the addition of a second amino acid with a terminal amide (L-lysine) or thiol group (L-cysteine) allowing functionalisation (figure 1.11). In fact, this structure is extremely robust to functionalisation of this second amino acid and maintains excellent affinity to GCP(II)/PSMA with a wide range of modifications. As a results this urea-based motif has been chosen as the GCP(II)/PSMA targeting scaffold for many GCP(II)/PSMA targeting radiotracers, radiolabelled either covalently with $^{123/124/125/131}I$, ^{11}C or ^{18}F, or by means of an attached chelator allowing radiometals such as ^{68}Ga, ^{64}Cu, ^{99m}Tc, and ^{177}Lu to be incorporated. The key PSMA tracers that use this targeting motif that have reached clinical evaluation will be discussed in the following sections and are summarised in table 1.3. The properties of the radionuclides they utilise are summarised in table 1.2.

	Effective dose mSv/MBq	Injected activity	Molar activity	Moles injected	Imaging time point
[^{11}C]MCG (*99*)	Not available	370 MBq (Baboon study)	167 GBq/mmol	2 µmol (Baboon study)	Up to 90 minutes
[^{123}I]I-MIP-1072 (*104*)	0.022	370 MBq	148 GBq/ µmol (*95*)	2.5 nmol	Up to 72 hours
[^{123}I]I-MIP-1095 (*104*)	0.032	370 MBq	148 GBq/ µmol (*95*)	2.5 nmol	Up to 72 hours
[^{124}I]I-MIP-1095 (*105*)	0.58	67 MBq	55.5- 236.8 MBq/µmol	1.2-0.28 µmol	Up to 96 hours
[^{131}I]I-MIP-1095 (*105*)	0.54	4.8 GBq	55.5 - 236.8 MBq/µmol	12-50 nmol	7 days
[^{99m}Tc]Tc-MIP-1404 (*106*)	0.00878	784.4 ± 59.2 MBq	37–44.4 MBq/µg	20 nmol	3 to 6 hours
[^{99m}Tc]Tc-MIP-1405 (*106*)	0.00787	784.4 ± 59.2 MBq	37–44.4 MBq/µg	20 nmol	3 to 6 hours
[^{18}F]DCFBC (*93*)	0.0199	370 MBq	1,190 ± 894 GBq/µmol	0.3 nmol	2 hours
[^{18}F]DCFPyL (*107*)	0.0139	320.6 310.8–327.1 MBq	107.2 85.8–141.0 MBq/nmol	3 nmol	2 hours
[^{18}F]F-PSMA-1007 (*108*)	0.0220	200–250MBq	Not available	Not available	1 and 3 hours
[^{68}Ga]Ga-HBED-CC-PSMA (*109*)	0.0236 (±0.0036) (*110*)	121 MBq, 52–212 MBq (*109*)	26-106 MBq/nmol	2 nmol	1 and 3 hours
[^{68}Ga]Ga-DOTA-PSMA(617) (*111*)	0.0208 (*108*) (*112*)	288 MBq	14-140 GBq/nmol	2 nmol	1 hour
[^{68}Ga]Ga-DOTAGA-PSMA(I&T) (*113*)	Not available	98 ± 26 MBq	74 MBq/nmol	Up to 15 nmol	1 and 3 hours

TABLE 1.3: Properties of PSMA-based tracers for PET or SPECT imaging of prostate cancer

1.5.2.3 Carbon-11-Based Tracers

The first tracer to utilise the urea-based scaffold was [^{11}C]MCG (*99*) figure 1.12**.** This tracer was only evaluated in healthy mice and baboon studies but paved the way for the development of all other PSMA radiotracers with the same scaffold (*99*). [^{11}C]MCG has a low nanomolar affinity (K_i = 1.9 nM) for GCP(II)/PSMA and showed a bio-distribution which mirrored its known physiological expression, with the majority of uptake seen in the kidneys, which could be blocked by PMPA administration. There was minimal uptake in the brain, suggesting that the compound does not pass through the blood-brain barrier, probably due to its hydrophilicity, and so would not be suitable for imaging the distribution of GCP(II)/PSMA in the brain.

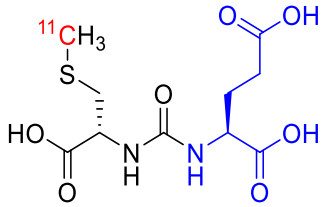

FIGURE 1.12: The structure of the radiotracer [^{11}C]MCG (99). The location of carbon-11 is shown in red and the conserved terminal glutamate is shown in blue.

1.5.2.4 Iodine-123-Based Tracers

Iodine-123-based PSMA tracers were the first to be developed for SPECT imaging of GCP(II)/PSMA. Iodine-123 has a half-life of 13.3 hours and major gamma emissions at 159 keV (*34*). Two analogues [^{123}I]I-MIP-1072 and [^{123}I]I-MIP-1095 figure 1.13 were synthesised, radiolabelled (*95*) and tested *in vitro*. They both showed specific uptake and internalisation in GCP(II)/PSMA expressing human prostate cancer cells (LNCaP) and affinity values (K_i values 4.6 ± 1.6 nM and 0.24 ± 0.14 nM respectively (*114*)). These compounds were then tested in a xenograft model of prostate cancer using the same cell line and had comparable tumour uptake values at 1 hour ([^{123}I]I-MIP-1072 17.4 ± 6.3 %ID/g, [^{123}I]I-MIP-1095 20.7 ± 5.8 %ID/g) however, [^{123}I]I-MIP-1095 had higher background tissue uptake than [^{123}I]I-MIP-1072 most likely due to its longer circulation time (*114*). These two tracers have also been assessed for safety, pharmacokinetics and ability to visualise prostate cancer. A phase 1 clinical study was conducted in which 6 patients were imaged with both tracers, with scans two weeks apart (*104*). The injected activity at each session was 370 MBq, and patients were imaged at time points up to 72 hours. The safety study reported 4 cases of mild adverse events including, chills, constipation, insomnia, and mild injection site irritation. SPECT imaging at 1 hour detected tracer uptake in metastatic bone and lymph node lesions, which correlated with bone scans and lymph node

sizing from CT. Uptake was also seen in the liver, spleen, bowel, kidneys, salivary and lachrymal glands. The liver and spleen are not known to express GCP(II)/PSMA and so uptake in these organs is probably not GCP(II)/PSMA-mediated (*115*)(*116*). The tumour-to-background ratio from SPECT imaging was the highest for both tracers 24 hours post-injection with ratios above 15:1. The calculated effective doses for [^{123}I]I-MIP-1072 and [^{123}I]I-MIP-1095 were 0.022 and 0.032 mSv/MBq respectively. In both cases, the dose-limiting organs were the kidney, salivary glands and thyroid. The high thyroid values are due to radioiodine-containing metabolites and radio-iodide localising in the thyroid due to its natural iodine avidity, and should be controllable with a thyroid blockade. These promising results suggest that either of these agents could be used for SPECT imaging of GCP(II)/PSMA-expressing prostate cancer, but no further studies demonstrating their use in this manner have been published. Instead, the iodine-124 and iodine-131 version of MIP-1095 have been explored for PET imaging and molecular radiotherapy (*105*)(*117*).

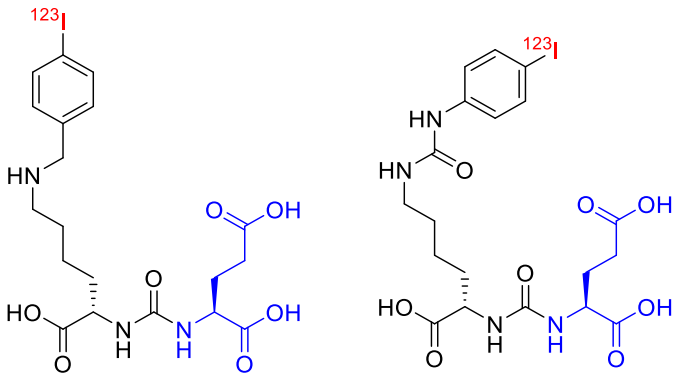

FIGURE 1.13: The structure of the radiotracers [^{123}I]I-MIP-1072 and [^{123}I]I-MIP- 1095. The location of iodine-123 is shown in red and the conserved terminal glutamate is shown in blue (95)(104).

1.5.2.5 Technetium-99m-Based Tracers

Technetium-99m tracers for SPECT imaging of GCP(II)/PSMA expressing prostate cancer were the first to demonstrate that the urea-based GCP(II)/PSMA targeting motif (Lys-C(O)-Glu) could be modified with a chelator and radiometal, whilst maintaining low nanomolar affinity (*102*)(*118*). The chelator choice and type of linker between the chelator and the GCP(II)/PSMA targeting motif were both found to influence affinity, and this knowledge was incorporated into future tracer design for a range of radiometals (*119*)(*120*)(*121*)(*122*). The two technetium-99m tracers that have progressed to clinical studies are [^{99m}Tc]Tc-MIP-1404 and [^{99m}Tc]Tc-MIP-1405, shown in figure 1.14, which incorporate [^{99m}Tc](Tc(CO)$_3$)$^+$ through their TIM and CIM chelators respectively (*123*). The tracers both have low nanomolar K_d values ([^{99m}Tc]Tc-MIP-1404 = 1.07 ± 0.89 nM, [^{99m}Tc]Tc-MIP-1405 = 4.35 ± 0.35 nM) and were shown in preclinical studies to have

uptakes of 10.3 ± 2.5 %ID/g and 12.4 ± 2.3 %ID/g in LNCaP tumour xenografts at 1 hour post-injection (*123*). The phase 1 clinical study for [^{99m}Tc]Tc-MIP-1404 and [^{99m}Tc]Tc-MIP-1405 utilised a 6 patient cross-over design, which meant that each patient was imaged with the first of 2 tracers and then, 2 weeks later, imaged with the other tracer (*106*). All patients had evidence of metastatic prostate cancer by CT and the average administered activity during each imaging session was 784 ± 59 MBq (20 µg of cold tracer). This phase 1 study showed that both tracers identified soft-tissue prostate cancer lesions including lymph nodes less than 10 mm in size (greater than 8 mm suggests lymph node involvement using anatomical imaging (*6*)) and were also able to detect the majority of bone metastasis when compared to bone scans with [^{99m}Tc]Tc-MDP. The two tracers showed different renal excretion patterns with a much higher percentage of [^{99m}Tc]Tc-MIP-1405 in the urine 24 hours after injection (25-30%) than [^{99m}Tc]Tc-MIP-1404 (5-10%). Non-target tissue uptake was seen was seen in the salivary glands, liver, kidneys, and gastrointestinal tract for both tracers but uptake was higher for [^{99m}Tc]Tc-MIP-1404.

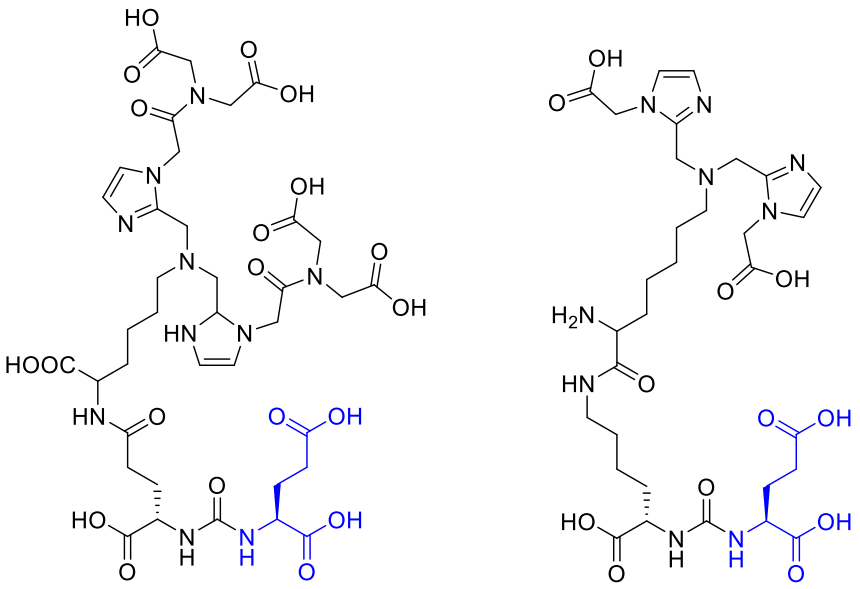

FIGURE 1.14: The structures of MIP-1404 and MIP-1405 for radiolabelling with [^{99m}Tc]$(Tc(CO)_3)^+$ to produce [^{99m}Tc]Tc-MIP-1404 and [^{99m}Tc]Tc-MIP-1405 respectively (106). The conserved terminal glutamate is shown in blue.

[^{99m}Tc]Tc-MIP-1404 was selected for further study, due to its higher uptake in metastatic sites and minimal activity in the bladder, which allowed better visualisation of the prostate and surrounding lymph nodes during initial staging. It has completed a phase 2 study, under the name [^{99m}Tc]Trofolastat, evaluating its use in staging before radical surgery in 105 patients with histologically proven prostate cancer (*124*). Imaging was undertaken 3-6 hours post-injection. The tracer identified prostate cancer in 94% of patients and detected local lymph node involvement with a sensitivity of 50% and specificity of 87%. There are two published studies

that have assessed [^{99m}Tc]Tc-MIP-1404 in biochemical recurrence (*125*)(*126*). Both showed a high detection rate (≥ 90%) in patients with PSA levels above 2 ng/mL but lower detection rates below this threshold (54% (*125*) and 40% (*126*)). A phase 3 clinical trial (clinical trial registry number, NCT02615067 (*127*)) was conducted in over 500 patients across 45 sites in the US and Canada between December 2015 and December 2017. However, results have not yet been published. This trial focuses on using the SPECT imaging with [^{99m}Tc]Tc-MIP-1404 in low-grade prostate cancer as a tool for active surveillance and will be validated against histological samples from either biopsy or prostatectomy taken within 42 days of imaging. It aims to determine the sensitivity and specificity of the tracer for the detection of prostate cancer in this context. This will be the first phase 3 trial completed for a PSMA-based tracer and its results will be instrumental in defining how PSMA agents gain regulatory approval.

1.5.2.6 Fluorine-18-Based Tracers

[^{18}F]DCFBC and [^{18}F]DCFPyL shown in figure 1.15 are first and second generation radiotracers from the Pomper research group and have both been evaluated *in vitro*, in a mouse xenograft model of prostate cancer and in clinical trials (*93*)(*107*)(*128*)(*129*). These tracers incorporate fluorine-18 through a terminal aromatic group - either an [^{18}F]fluorobenzyl or an [^{18}F]fluoropyridy substituent. The reported affinity values are not directly comparable as they were obtained by different techniques but were both in the low nanomolar range ([^{18}F]DCFBC, IC_{50} = 13.9 nM (*128*) and [^{18}F]DCFPyL, K_i = 1.1 ± 0.1 nM (*129*)). Despite their similar structure and affinity values, they showed differences in biodistribution. Tumour uptake values at 1 hour post-injection in a mouse xenograft model of GCP(II)/PSMA expressing prostate cancer (PC-3 PIP tumour) were 8.2 ± 2.5 %ID/g for [^{18}F]DCFBC (*128*) and 44.2 ± 9.7 %ID/g for [^{18}F]DCFPyL (*129*). The tracers had similar uptake in the kidney (41.6 ± 7.2, 42.3 ± 19.0 %ID/g) but [^{18}F]DCFBC had higher uptake in the liver (5.1 ± 0.8 %ID/g, 2.87 ± 0.92 %ID/g) and some activity also associated with the bone (1.7 ± 0.8 %ID/g) which suggests the presence of free fluoride, and therefore some instability or metabolism of the radiotracer (*130*).

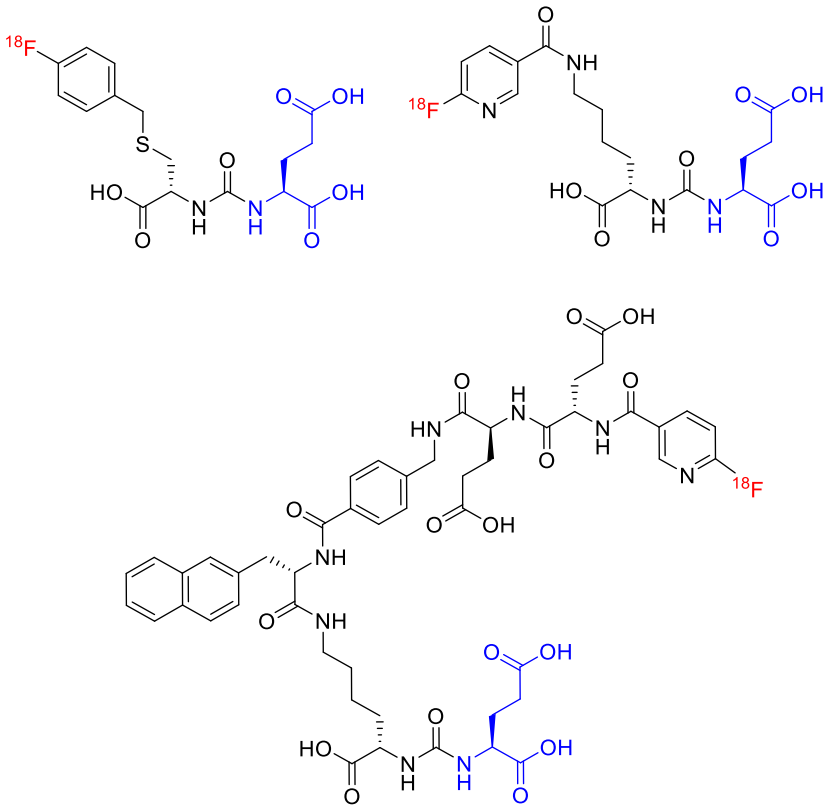

FIGURE 1.15: The structure of the radiotracers [^{18}F]DCFBC (128), [^{18}F]DCFPyL (107)(129), and [^{18}F]F-PSMA-1007 (108)(131). The location of fluorine-18 is shown in red and the conserved terminal glutamate is shown in blue.

The phase 1 studies for both tracers used patients with histologically confirmed prostate cancer and evidence of disease progression using conventional imaging techniques (*93*)(*107*). In the [^{18}F]DCFBC study patients were administered an average of 370 MBq and imaged up to 120 minutes post-injection. A similar protocol was used in [^{18}F]DCFPyL study with 320 MBq administered and imaging performed for 150 minutes. [^{18}F]DCFBC allowed detection of involved lymph nodes (median lymph node SUV_{max} = 5.6, 2 hours post-injection) and bone metastases (median bone lesion SUV_{max} = 3.6, 2 hours post-injection) and was able to detect smaller involved lymph nodes than detected by anatomical imaging. As defluorination was suspected in preclinical studies this was investigated in humans by taking patient plasma samples over time and analysing the ratio of [^{18}F]DCFBC to [^{18}F]fluoride levels. This was seen to be over 95% at the end of the 2 hour scan which was comparable to the administered radiochemical purity. The [^{18}F]DCFPyL study detected involved lymph nodes and bone metastases with improved visualisation due to higher SUV_{max} values (mean SUV_{max} = 45 bone lesions, and mean SUV_{max} = 25 for lymph nodes at 2 hours post-injection) and therefore better tumour to background ratios (*107*). Further studies have also confirmed the ability of [^{18}F]DCFBC to detect disease in primary prostate cancer (*132*) and shown that both tracers have superior detection of metastatic

prostate cancer compared to the conventional imaging modalities (*133*)(*134*). However, specific studies looking at the performance in detection rates in biochemical recurrence are not yet available.

Another important fluorine-18-based PSMA tracer is [^{18}F]F-PSMA-1007 which has a very similar structure to the DOTA-PSMA(617) tracer used for both [^{68}Ga]Ga-PSMA PET imaging and [^{177}Lu]Lu-PSMA beta therapy, discussed in detail later on and shown in figure 1.16. The GCP(II)/PSMA targeting scaffold (Lys-C(O)-Glu) is conserved between these tracers, as is the optimised lipophilic linker, however, in the fluorine-18 version the DOTA chelator is replaced by two glutamic acid residues and a [^{18}F]fluoropyridyl substituent. The glutamic acid residues are included in order to conserve the hydrophilicity provided by carboxylic acids of the DOTA chelator not used in metal binding. This radiotracer has been designed to have very similar biodistribution and performance to [^{68}Ga]Ga-DOTA-PSMA(617) so that it can act as replacement PET imaging agent. This is useful because fluorine-18 is a more amenable radionuclide than gallium-68 for the centralised production of radiotracers followed by shipping the tracer to a number of different hospitals for use, due to its longer half-life and the larger amounts of activity produced from one cyclotron run.

The pre-clinical studies of [^{18}F]F-PSMA-1007 showed high LNCaP cell internalisation ratios (67% ± 13%) and 8.0 ± 2.4 %ID/g uptake in LNCaP xenografts at 1 hour post-injection (*135*). This tracer has been assessed as a clinical tool for primary staging and excellent alignment was found between it and histological GCP(II)/PSMA staining and, when available, multiparametric MRI (*108*)(*136*). A 12 patient study evaluating the performance of [^{18}F]F-PSMA-1007 in biochemical recurrence detected metastases in 75% of patients, including metastases under 8 mm in size (*137*). The comparative performance of [^{18}F]DCFPyL and [^{18}F]F-PSMA-1007, in the same patient before undergoing radical prostatectomy has also recently been reported (*138*). The two tracers detected the same metastases with no statistical difference between their SUV_{max} values. However, differences were observed in non-target tissue, where [^{18}F]DCFPyL showed greater renal excretion with associated higher kidney and bladder signal, whereas [^{18}F]F-PSMA-1007 showed higher spleen, pancreas, liver and salivary gland background.

1.5.2.7 Gallium-68-Based Tracers

Gallium-68 is a radiometal with suitable positron (β^+) emissions for PET imaging (89% positron emissions with an energy of 1.9 MeV (*31*)). Unlike the majority of PET radionuclides, gallium-68 can be obtained from generators containing its parent isotope germanium-68 which has a half-life of 270.95 days (*139*). The elution of a modern clinical grade generator provides 1-1.85 GBq of gallium-68 in 1.1 - 5 mL of 0.1 M HCl, which can be used to manufacture radiopharmaceuticals at doses which allow high-quality images to be obtained. Additionally, the 67.8 minute half-life (*31*) of gallium-68 makes it particularly suited to radiolabelling peptides and small molecules with fast pharmacokinetics, such as the GCP(II)/PSMA targeting motif (Lys-C(O)-Glu).

The most widely studied PSMA radiotracer utilising gallium-68 is [^{68}Ga]Ga-HBED-CC-PSMA. The urea-based GCP(II)/PSMA targeting scaffold (Lys-C(O)-Glu) is conserved and is joined by an amide-based linker to the acyclic chelator HBED-CC as shown in figure 1.16. This tracer was evaluated *in vitro* and found to have specific uptake in GCP(II)/PSMA expressing cells and a high internalisation rate (*101*). The biodistribution of this tracer in mice with LNCaP xenografts showed a tumour uptake of 7.70 ± 1.45% ID/g at 1 hour post-injection. This coincided with high kidney (139.4 ± 21.4% ID/g) and spleen (17.90 ± 2.87% ID/g)) uptake and renal excretion. These promising results led to the tracer being evaluated in patients with biochemical recurrence after treatment (*109*). This initial study showed the ability to delineate local relapse lymph node, soft tissue and bone metastases (figure 1.17), and was cross-validated with samples from biopsy or surgery in 6 out of 37 patients (*109*). Non-target tissue accumulation was seen most strongly for the kidneys and the salivary glands with less intense uptake seen for the lacrimal glands, liver, spleen and intestinal tract as shown in figure 1.17. The lung uptake seen in the mouse model was not seen in humans. The urinary excretion could have been a disadvantage for this tracer, however, if the bladder is voided before a scan and PET/CT is used rather than PET alone, it is possible to differentiate metastatic lymph nodes from urinary excretion particularly when axial slices are used. Dosimetry studies have found the effective dose of [^{68}Ga]Ga-HBED-CC-PSMA to be 0.0236 ± 0.0036 mSv/MBq, with the highest dose delivered to the kidneys and bladder (*110*).

Since these initial studies, the use of this tracer has become widespread across research centres, and large patient populations have been imaged. For staging before treatment, two major studies have shown that [^{68}Ga]Ga-HBED-CC-PSMA is able to detect metastasis more accurately than morphological imaging (CT or MR) with postoperative histology used as the ground truth (*140*)(*141*). Both studies also reported high sensitivites and specificities (84%, 82% (*141*) and 65.9%, 98.9% (*140*)) which, when compared to CT (42%, 82% (*6*)) and [^{11}C]choline imaging

(49.2%, 95% (*60*)) show similar specificity but enhanced sensitivity, making it the best performing PET tracer for primary staging to date.

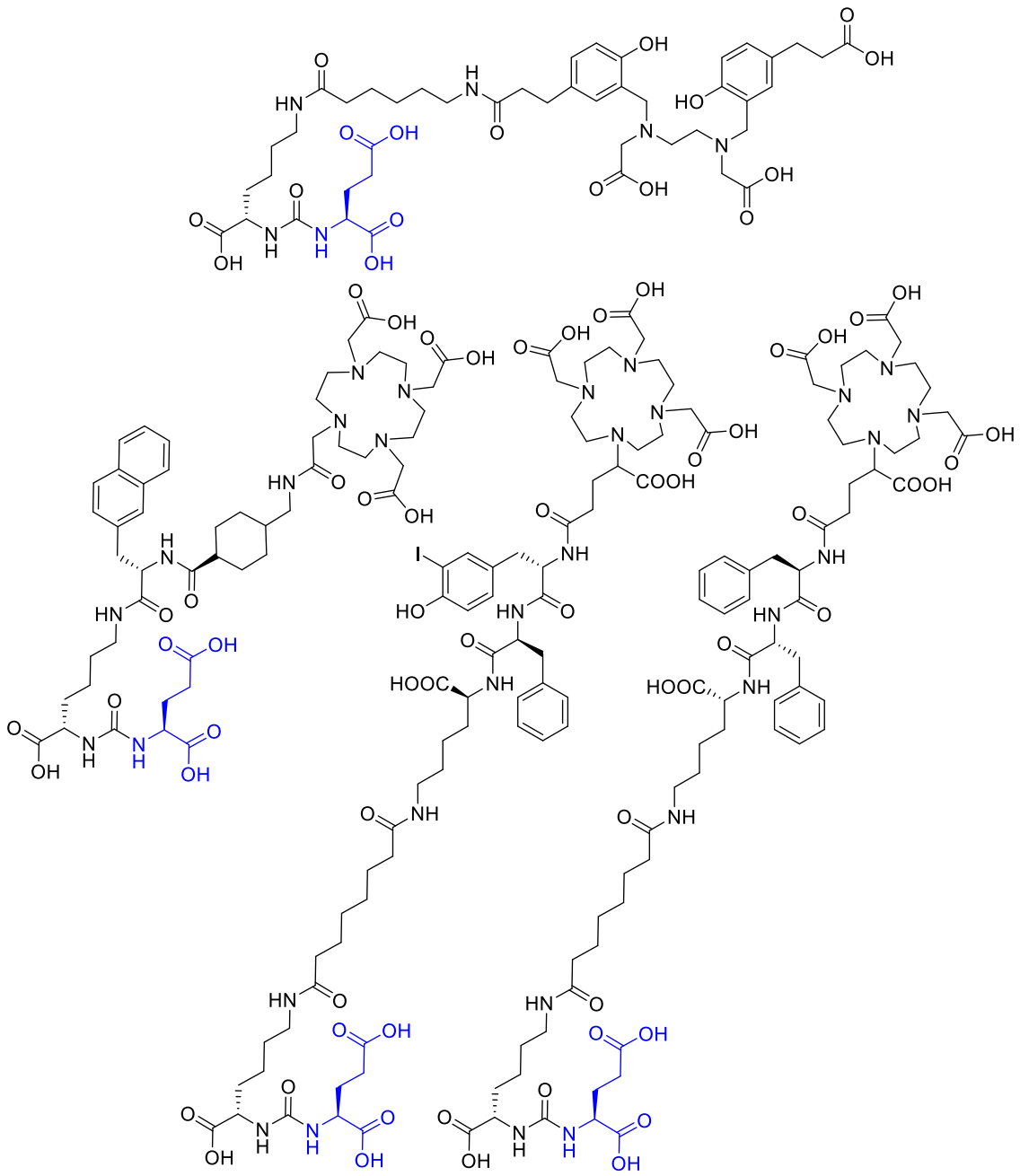

FIGURE 1.16: Structures of HBED-CC-PSMA (101), DOTA-PSMA(617) (111), DOTAGA-FFK(Sub-KuE) (121), DOTAGA-(I-y)fk (Sub-KuE) (142). The conserved terminal glutamate is shown in blue

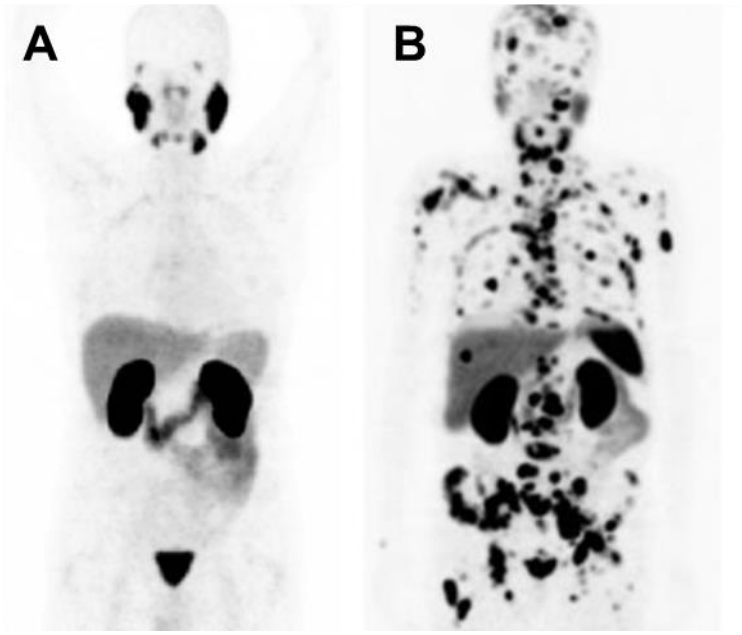

FIGURE 1.17: (A) A maximum intensity projection of a patient with a normal biodistribution of [^{68}Ga]Ga-HBED-CC-PSMA (B) A maximum intensity projection of a patient with disseminated lymph node and bone metastases imaged with [^{68}Ga]Ga-HBED-CC-PSMA at 1 hour post-injection. Non-target uptake is seen in the kidney, salivary glands, lacrimal glands, liver, spleen and intestinal tract. Reproduced with permissions from (109).

The majority of clinical studies of [^{68}Ga]Ga-HBED-CC-PSMA have focused on its use in biochemical recurrence. A meta-analysis of these results has been conducted and concluded that it had 86% sensitivity and 86% specificity on a per-patient basis (*143*), and that there was a clear correlation between detection rate using [^{68}Ga]Ga-HBED-CC-PSMA and PSA level as demonstrated in figure 1.18. It is important to note that the detection of metastases is possible at much lower PSA levels than the PSA level where evaluation with bone scans and CT become reliable (20 ng/mL (*16*)), thus providing much earlier detection of recurrence. A more recent study summarised the results of 1007 consecutive scans of patients with biochemical reoccurrence at Heidelberg University Hospital again confirmed this relationship, with detection rates increasing with PSA levels, but interestingly they did not find a significant correlation between detection rates and Gleason score, PSA doubling time or PSA velocity (*144*).

It is important to note that despite the excitement around [^{68}Ga]Ga-HBED-CC-PSMA imaging and its adoption into clinical decision making, evidence from prospective multicentre trials is not yet available. A number of clinical trials are ongoing (*145*) and although the majority of these are single centre trials, a multicentre phase 1 and 2 trial is ongoing in 11 sites across Germany, Switzerland and Austria (*146*). This study will evaluate [^{68}Ga]Ga-HBED-CC-PSMA in staging before radical prostatectomy, and findings will be correlated with histology. This study will

therefore provide key evidence for the clinical use of PSMA imaging agents and move them closer towards regulatory approval.

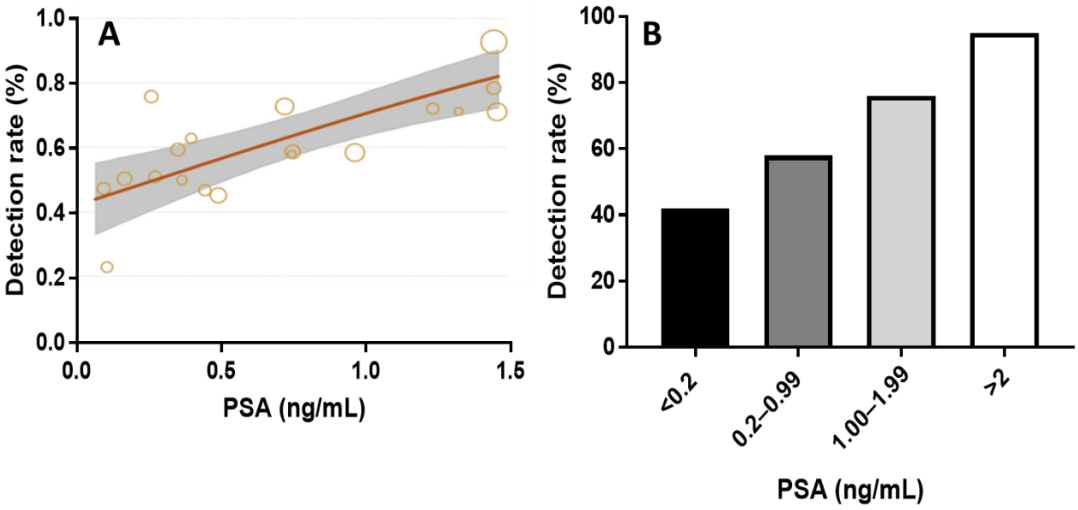

FIGURE 1.18: (A) Scatter plot of prostate specific antigen (PSA) level versus the detection rate for [68Ga]Ga-HBED-CC-PSMA in each study. The orange line is the meta-regression prediction with the shading showing the 95% confidence interval. The size of the circles is related to the inverse of the variance (B) Mean disease detection rate for [68Ga]Ga-HBED-CC-PSMA over the PSA levels (ng/mL) <0.2 (black), 0.2-0.99 (dark grey), 1.00-1.99 (light grey), >2 (white), modified with permissions from (143).

Another important gallium-68 tracer that has been studied clinically is the DOTA conjugate [^{68}Ga]Ga-DOTA-PSMA(617) (*111*). Unlike HBED-CC the DOTA chelator allows a range of radio-metals to be bound including those suitable for molecular radiotherapy such as lutetium-177 (*147*), yttrium-90 (*148*), bismuth-213 (*149*), and actinium-225 (*150*), so this tracer was designed with the dual purpose of imaging and therapy. This was achieved by screening a large number of different linker groups for the following properties: K_i value, specific cell binding, specific internalisation, tumour uptake and tumour to background ratios (*119*). It is interesting to note that these features were not as well correlated to each other as may be expected by intuition, with some tracers with low K_i (and therefore high affinity for GCP(II)/PSMA) showing lower specific cell binding and internalisation values than some of those with higher K_i values (and therefore lower affinity for GCP(II)/PSMA), and tracers with the highest tumour uptake not having the highest tumour to background ratio *in vivo*. This demonstrates the complexity of the GCP(II)/PSMA binding and internalisation mechanisms and that a screening protocol which looked at K_i values alone would not provide the optimal tracer for use *in vivo*. However, there was a correlation between the degree of specific internalisation *in vitro* and the tumour to background ratio seen *in vivo* with the same tracer having the best performance for both of these properties. This tracer, utilising a 2-naphthyl-L-alanine linker followed by a cyclohexanoic

acid between the GCP(II)/PSMA targeting moiety (Lys-C(O)-Glu) and the DOTA chelator (figure 1.16), was named DOTA-PSMA(617) and was selected for clinical translation (*111*)(*119*). This tracer showed a similar biodistrubution to [^{68}Ga]Ga-HBED-CC-PSMA and could delineate involved lymph nodes at one hour post-injection, however, there are limited further studies demonstrating its potential as an imaging agent.

A third important tracer for gallium-68 imaging is [^{68}Ga]Ga-DOTAGA-(I-y)fk (Sub-KuE) also referred to as [^{68}Ga]Ga-DOTAGA-PSMA(I&T) (*142*). With I&T standing for imaging and therapy. This is an optimised version of the previously developed DOTA-FFK(Sub-KuE) (*121*)(*151*)(*152*) shown in figure 1.16. The structures differ in their stereochemistry within the linker, the replacement of the final phenyl group with a 4-hydroxy-3-iodophenyl group and the replacement of the DOTA chelator by DOTAGA, creating one further pendant carboxylic acid available for metal chelation (*142*). However, there is no description of why these specific changes were selected. This tracer has been evaluated clinically and, in a limited number of patients, has shown similar results to [^{68}Ga]Ga-HBED-CC-PSMA (*113*)(*142*)(*153*)(*154*). A key study focused on detection rates in patients with biochemical recurrence over a range of PSA levels and these were found not to be statistically different from published results for [^{68}Ga]Ga-HBED-CC-PSMA (*154*).

[^{68}Ga]Ga-DOTA-PSMA(617) and [^{68}Ga]Ga-DOTAGA-PSMA(I&T) show similar results to [^{68}Ga]Ga-HBED-CC-PSMA for PET imaging of prostate cancer but no advantage over it. Therefore due to the larger body of evidence supporting the use of [^{68}Ga]Ga-HBED-CC-PSMA, it is likely to remain the most prevalent PSMA PET agent. The advantage of both [^{68}Ga]Ga-DOTA-PSMA(617) and [^{68}Ga]Ga-PSMA(I&T) should be their dual use for both imaging and therapy, but as the radiometal is different between the two versions, the complexes are inequivalent and will have slightly different biodistributions. This has been demonstrated for the gallium-68 and lutetium-177 versions of DOTAGA-PSMA(I&T) in mice bearing prostate cancer xenografts (*142*) as shown in figure 1.19. These results suggest there is no real advantage in using the same bioconjugate over using another that targets GCP(II)/PSMA with similar bio-distribution (i.e. [^{68}Ga]Ga-HBED-CC-PSMA or even [^{18}F]F-PSMA-1007) for therapeutic planning if a different radioactive element is to be used. These tracers have not been used in many published studies for PET imaging with gallium-68, and even when planning for therapy with their lutetium-177 analogues [^{68}Ga]Ga-HBED-CC-PSMA is more often used. This is probably less to do with the quality of the images produced by these tracers and more to do with the fact that [^{68}Ga]Ga-HBED-CC-PSMA was already established in many centres and had been shown suitable for planning for therapy so validating a new tracer for the same purpose was not deemed necessary.

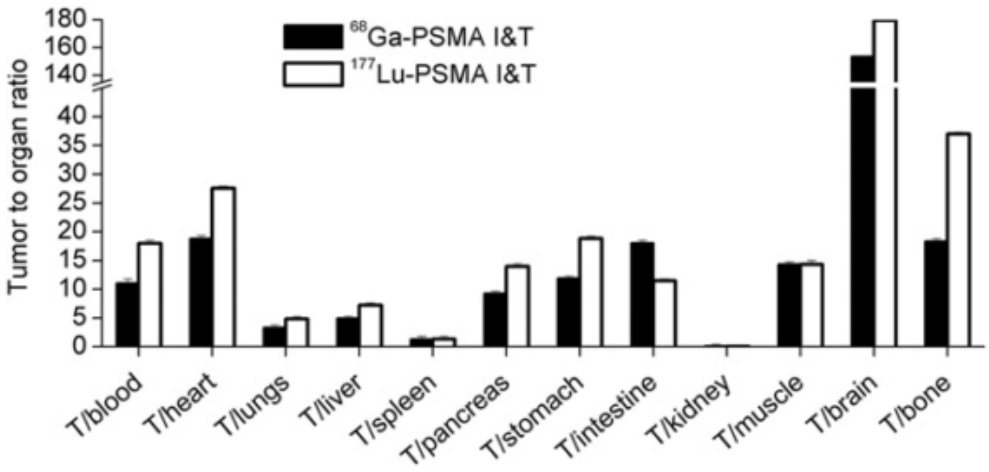

FIGURE 1.19: Tumour-to-organ ratios of dual-tracer biodistribution of [^{68}Ga]Ga-DOTAGA-PSMA(I&T) and [^{177}Lu]Lu-DOTAGA-PSMA(I&T) 1 hour after injection of 1 nmol tracer in CD-1 nu/nu mice with LNCaP xenografts (n = 4) Reproduced with permissions from (142).

1.5.2.8 Summary of PSMA Tracers

PET and SPECT GCP(II)/PSMA imaging are clearly promising techniques for more accurate staging of prostate cancer and detection of metastatic disease in biochemical recurrence, and the body of evidence supporting their use continues to grow. As the most widely used tracer, the most clinical evidence exists for [^{68}Ga]Ga-HBED-CC-PSMA, however, to date, no PSMA tracer has been approved by the EMA or FDA and therefore all current use of PSMA tracers must be within a research study or under regulations for non-approved radiopharmaceuticals (*155*). Large multicentre clinical trials will be required to obtain such approval, and these are ongoing for [^{99m}Tc]Tc-MIP-1404 (*127*) and [^{68}Ga]Ga-HBED-CC-PSMA (*146*). Further evidence will also be required before reimbursement is issued by health insurance companies or government bodies such as NICE or the Centres for Medicare and Medicaid Services, which would enable widespread use of PSMA tracers in clinical practice.

1.6 Comparison of All Tracers in Imaging Biochemical Recurrence

The performance of 5 different tracers in the detection of prostate cancer sites in cases of biochemical recurrence (rising PSA serum levels >0.1 ng/mL)) after radical surgery was compared in a critical analysis of published literature in 2014 (*42*). In order to ensure that different studies could be fairly compared, data were only used if it fitted with a pre-defined set of patient selection criteria and verification standards. The tracers included were: [^{18}F]FDG, [^{11}C]acetate, [^{11}C]choline or [^{18}F]fluoro-choline (the results for these two tracers were combined), [^{18}F]FACBC, and [^{68}Ga]Ga-HBED-CC-PSMA. This study found that [^{18}F]FDG had the

lowest detection rate with a positive scan in only 12% of patients and concluded that it was unsuitable for clinical detection of biochemical recurrence. [^{11}C]acetate, [^{11}C]choline/[^{18}F]fluoro-choline and [^{18}F]FACBC all had higher disease detection rates, (48%, 51%, and 40%, respectively) with no statistically significant differences in their performance. However, [^{68}Ga]Ga-PSMA showed the greatest disease detection in biochemical recurrence after radical prostatectomy (84%), and the highest rates of detection for extra-prostatic disease (77%), involved lymph nodes (45%) and bone lesions (25%). Similar findings were seen in patients who had biochemical recurrence after radical radiotherapy, confirming [^{68}Ga]Ga-HBED-CC-PSMA imaging as a very promising tool. In the last 4 years since that review, the field of prostate cancer PET imaging has evolved rapidly, especially with regards to GCP(II)/PSMA imaging, and there is now much more data available to use in such a comparison (the 2014 critical review only used two [^{68}Ga]Ga-HEBD-CC-PSMA papers (*156*)(*157*)). A 2018 review looked at results of meta-analyses and critical reviews published for the most promising tracers in the localisation of biochemical recurrence, [^{11}C]choline/[^{18}F]fluoro-choline, [^{68}Ga]Ga-HBED-CC-PSMA, and [^{18}F]FACBC and compared their sensitivity and specificity as well as their detection rates across a range of PSA levels (*56*). A summary of the meta-analysis is shown in table 1.4 with very similar sensitivity and specificity values for all three tracer types, except for [^{11}C]choline/[^{18}F]fluoro-choline showing an advantage in specificity. In contrast, when the detection rates were compared at different patient PSA levels, [^{68}Ga]Ga-HBED-CC-PSMA imaging showed markedly higher detection rates at all PSA levels (*56*). PSMA imaging therefore shows clear advantages over the other available tracers in both detection rates and sensitivity and specificity for primary staging, and detection rates at low PSA levels after biochemical reoccurrence.

Systematic review and meta-analysis	Number of studies	Number of patients	Sensitivity (per lesion) (95% CI)	Specificity (per lesion) (95% CI)	Sensitivity (per patient) (95% CI)	Specificity (per patient) (95% CI)
[^{11}C]choline/[^{18}F]fluoro-choline						
Fanti (*62*)	12	1270			89% (83-93)	89% (73-96)
Evangelista (*63*)	19	1555	86% (83-88)	93% (90-95)		
Umbehr (*64*)	12	1055	90% (74-97)	95% (94-97)	87% (79-93)	97% (93-99)
[^{18}F]FACBC						
Ren (*70*)	6	251			87% (80-92)	66% (56-75)
[^{68}Ga]Ga-HBED-CC-PSMA						
Perera (*143*)	16	1309	80% (66-80)	97% (92-99)	86% (37-98)	86% (3-100)

TABLE 1.4: Summary of sensitivity and specificity of meta-analyses evaluating [^{68}Ga]Ga-HBED-CC-PSMA, [^{11}C]choline/[^{18}F]fluoro-choline, and [^{18}F]FACBC PET/CT. CI = confidence interval. Modified from (56) with permission.

1.7 Impact on Management and Survival

PET scanning should provide additional information to ensure patients are on the correct treatment pathway. A limited number of studies have been conducted into change in management for [^{11}C]choline (*158*)(*159*) (retrospective studies), [^{68}Ga]Ga-HEBD-CC-PSMA (*160*) (*161*) (one retrospective and one prospective) and [^{18}F]FACBC (2 prospective studies (*162*)(*163*)). The [^{11}C]choline and [^{18}F]FACBC studies focused solely on the impact in patients presenting with biochemical relapse and showed the treatment approach was altered in 45-55% of the patients after receiving a [^{11}C]choline scan and in 40-62% after [^{18}F]FACBC (*162*). The retrospective study into [^{68}Ga]Ga-HEBD-CC-PSMA showed a 39% impact on treatment in biochemical relapse and the prospective study showed a higher impact in biochemical relapse rather than initial staging (62% and 21% respectively). These are all encouraging results which highlight the utility of the information provided by a PET scan with any of these 3 tracers, and that clinicians trust the results and are adjusting treatment accordingly. It is therefore important to validate that there is a relationship between the extent of disease detectable by the PET scan, and survival. Such analysis has only been attempted for [^{11}C]choline (*164*) and showed that patients with positive scans for prostate cancer had worse survival than those with negative scans as demonstrated in figure 1.20. After such analysis has been performed the next step is to

prove that having the information from a PET scan allowed patients to be put onto a different treatment which goes on to positively impacted survival rates.

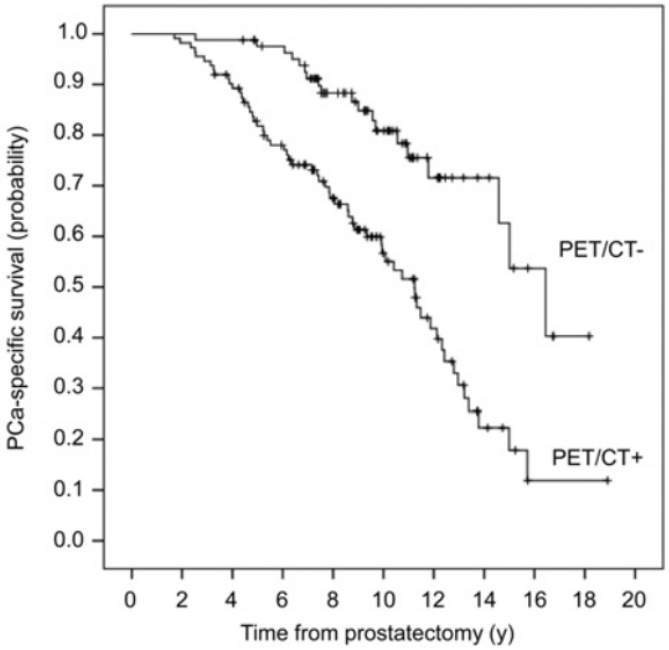

FIGURE 1.20: Kaplan–Meier survival probability curves in patients with negative [^{11}C]choline PET/CT and in patients with positive [^{11}C]choline PET/CT. reproduced with permission from (164).

1.8 GCP(II)/PSMA Targeted Radionuclide Therapy

Another key use for GCP(II)/PSMA imaging, for which the other tracers are not suitable, is planning for GCP(II)/PSMA targeted molecular radiotherapy, where the same targeting motif is used (Lys-C(O)-Glu), but a therapeutic radionuclide is incorporated instead of a radionuclide suitable for SPECT or PET imaging. Tracers currently under evaluation include [^{131}I]I-MIP-1095 (*105*), [^{177}Lu]Lu-DOTA-PSMA(617) (*165*) and [^{177}Lu]Lu-DOTAGA-PSMA(I&T) (*142*) for beta-based therapy, [^{225}Ac]Ac-DOTA-PSMA(617) (*150*), (2S)-2-(3-(1-carboxy-5-(4-[^{211}At]astatobenzamido) pentyl) ureido)-pentanedioic acid (*166*) and [^{213}Bi]Bi-DOTA-PSMA(617) (*149*) for alpha-based therapy, and 2-[3-[1-carboxy-5-(4-[^{125}I] iodo-benzoylamino)-pentyl]-ureido]-pentanedioic acid ([^{125}I]I-DCIBzL) (*167*) for therapy with Auger electrons. Of these the most studied clinically is [^{177}Lu]Lu-DOTA-PSMA(617), which has shown promising therapeutic results in patients with advanced metastatic prostate cancer. A typical protocol for [^{177}Lu]Lu-DOTA-PSMA(617) is 2 cycles of 6 GBq, 10 weeks apart (*168*). In 2017 a meta-analysis reviewed 7 small single centre clinical studies on the effect of therapy with [^{177}Lu]Lu-DOTA-PSMA(617) or [^{177}Lu]Lu-DOTGA-PSMA(I&T) on the PSA levels of patients with metastatic prostate cancer (*169*). Most patients in the studies used for this meta-analysis had disease progression after being treated with docetaxel and post-chemotherapy androgen deprivation therapy. The analysis showed that over

70% of patients had a reduction in PSA levels and 51% of patients showed at least a 50% reduction in PSA figure 1.21. These are very promising results, even though there was substantial heterogeneity across studies. The next step will be a focus on survival as the endpoint rather than PSA reduction and application for a phase 3 trial of [^{177}Lu]Lu-DOTA-PSMA(617) has been announced by the company Endocyte (*170*).

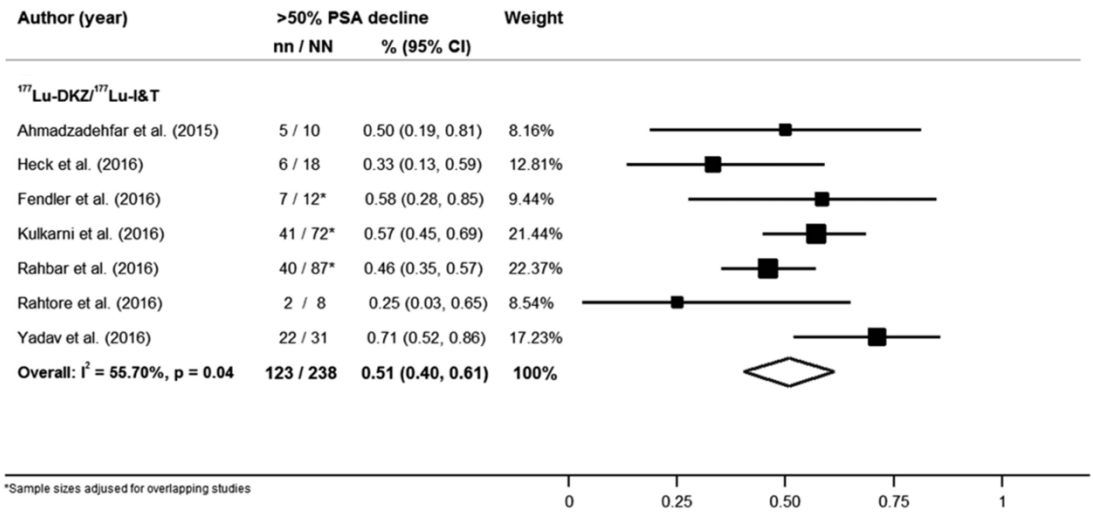

FIGURE 1.21: Forest plot for meta-analysis results of the proportion of patients with > 50% PSA decline after therapy with [^{177}Lu]Lu-DOTA-PSMA(617) or [^{177}Lu]Lu-DOTGA-PSMA(I&T). Reproduced from (169).

It is possible for a PSMA PET or SPECT scan to be used not only to assess the suitability of a patient for GCP(II)/PSMA targeted therapy (ensuring their metastatic sites express GCP(II)/PSMA) but also to monitor the effect of treatment as demonstrated in figure 1.22. In this example [^{68}Ga]Ga-HBED-CC-PSMA was used although other tracers would also have been suitable.

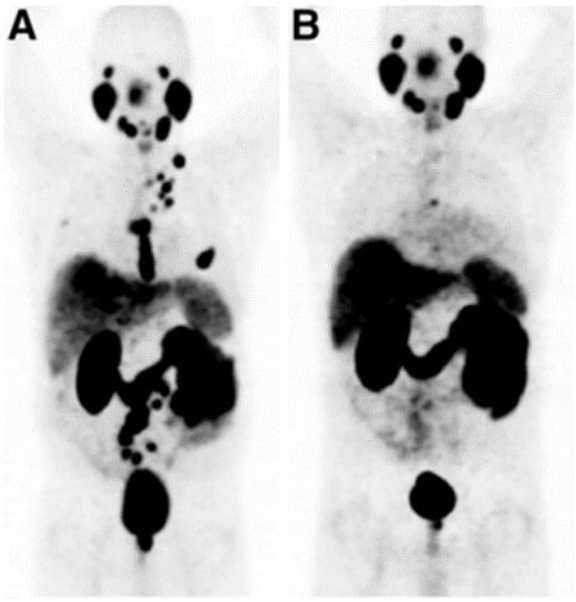

FIGURE 1.22: [^{68}Ga]Ga-HBED-CC-PSMA PET/CT images at 1 hour post-injection (175-180 MBq) for the same patient before (A) and three months after (B) therapy with [^{177}Lu]Lu-PSMA I&T therapy (8 GBq). Modified with permission from (142).

1.9 Concluding Remarks

There is a clear clinical need for improved imaging in prostate cancer. This need is not fulfilled by anatomical imaging, bone scans or [^{18}F]FDG PET. [^{11}C]choline and [^{18}F]FACBC offer significant advantages over these standard imaging techniques in biochemical recurrence and have therefore become FDA approved agents, but they are unproven for initial staging, and therefore their use is still limited to research sites rather than becoming integrated into standard clinical practice. The data available for [^{68}Ga]Ga-HBED-CC-PSMA imaging suggest that it provides improved performance for both initial staging and for disease detection in biochemical recurrence at low PSA levels, and that it therefore has the potential to become the standard of care for prostate cancer imaging. Other PSMA tracers have high potential but have not been evaluated as fully in clinical studies. The fact that PSMA agents can also be used for determining the suitability of patients for radionuclide therapy with [^{177}Lu]Lu-PSMA and monitoring response to this therapy is a further advantage which is likely to expedite translation into the clinic. It is clear that GCP(II)/PSMA is an excellent receptor for imaging the distribution of prostate cancer, at all stages of the disease, and the surprisingly simple and yet robust targeting motif (Lys-C(O)-Glu) allows for specific targeting of this receptor, however, it remains unclear which PSMA tracer will become the most used clinically. Aside from clinical performance, major factors which could affect the choice of PSMA tracer used include how easily and cost effectively hospitals can obtain these tracers, or the radionuclides required for their production, and how simply radiosynthesis

could be carried out within existing infrastructure. These issues, and the ability to overcome some of these barriers by designing radiopharmaceutical kits which provide ease of radiolabelling will be discussed in the following chapter.

1.10 References

1. Prostate Cancer UK Website. https://prostatecanceruk.org/about-us/news-and-views/2018/2/we-call-on-uk-to-step-up-as-new-figures-show-prostate-cancer-now-a-bigger-killer-than-breast-cancer. Updated Feb 2, 2018. Accessed Jun 25, 2018.
2. Prostate Cancer UK Website. https://prostatecanceruk.org/prostate-information/are-you-at-risk. Updated August, 2017. Accessed Jun 25, 2018.
3. Catalona WJ, Smith DS, Ratliff TL, Dodds KM, Coplen DE, Yuan JJJ, Petros JA, Andriole GL. Measurement of Prostate-Specific Antigen in Serum as a Screening Test for Prostate Cancer. *N Engl J Med*. 1991;324:1156-1161.
4. National Institute for Health and Care Excellence NICE Guidelines. Prostate Cancer: Diagnosis and Management. https://www.nice.org.uk/guidance/CG175. Updated Jan 8, 2014. Accessed Jun 25, 2018.
5. Gleason DF. Histologic Grading of Prostate Cancer: A Perspective. *Hum Pathol*. 1992;23:273-279.
6. Hövels AM, Heesakkers RAM, Adang EM, Jager GJ, Strum S, Hoogeveen YL, Severens JL, Barentsz JO. The Diagnostic Accuracy of CT and MRI in the Staging of Pelvic Lymph Nodes in Patients with Prostate Cancer: A Meta-Analysis. *Clin Radiol*. 2008;63:387-395.
7. American Joint Committee on Cancer. *AJCC cancer staging manual. Sixth Edit.* New York, NY: Springer; 2002.
8. Cancer Research UK Website. TNM Staging. http://www.cancerresearchuk.org/about-cancer/prostate-cancer/stages/tnm-staging. Updated Jul 06, 2016. Accessed Jun 25, 2018.
9. National Institute for Health and Care Excellence NICE Guidelines. Advanced Breast Cancer: Diagnosis and Treatment. http://nice.org.uk/guidance/cg81. Updated Feb 23, 2009. Accessed Jun 25, 2018.
10. National Institute for Health and Care Excellence NICE Guidelines. Lung Cancer: Diagnosis and Management. http://nice.org.uk/guidance/cg121. Updated April 21, 2011. Accessed Jun 25, 2018.
11. National Institute for Health and Care Excellence NICE Guidelines. Colorectal Cancer: Diagnosis and Management. http://nice.org.uk/guidance/cg131. Updated Nov 1, 2011. Accessed June 25, 2018.
12. Jadvar H. PET of Glucose Metabolism and Cellular Proliferation in Prostate Cancer. *J Nucl Med.* 2016;57:25S-29S.
13. Oyama N, Akino H, Suzuki Y, Kanamaru H, Sadato N, Yonekura Y, Okada K. The Increased Accumulation of [18F]Fluorodeoxyglucose in Untreated Prostate Cancer. *Jpn J Clin Oncol*. 1999;29:623-629.
14. Hofer C, Laubenbacher C, Block T, Breul J, Hartung R, Schwaiger M. Fluorine-18-Fluorodeoxyglucose Positron Emission Tomography Is Useless for the Detection of Local Recurrence after Radical Prostatectomy. *Eur Urol*. 1999;36:31-35.
15. Hillner BE, Siegel BA, Shields AF, Liu D, Gareen IF, Hunt E, Coleman RE. Relationship between Cancer Type and Impact of PET and PET/CT on Intended Management: Findings of the National Oncologic PET Registry. *J Nucl Med*. 2008;49:1928-1935.
16. Heidenreich A, Bastian PJ, Bellmunt J, Bolla M, Joniau S, Van Der Kwast T, Mason M, Matveev V, Wiegel T, Zattoni F, Mottet N. EAU Guidelines on Prostate Cancer. Part II: Treatment of Advanced, Relapsing, and Castration-Resistant Prostate Cancer. *Eur Urol*. 2014;65:467-479.
17. D'Amico A V., Whittington R, Malkowicz SB, Cote K, Loffredo M, Schultz D, Chen MH, Tomaszewski JE, Renshaw AA, Wein A, Richie JP. Biochemical Outcome after Radical Prostatectomy or External Beam Radiation Therapy for Patients with Clinically Localized Prostate Carcinoma in the Prostate Specific Antigen Era. *Cancer*. 2002;95:281-286.

18. Weber WA, Morris MJ. Molecular Imaging and Targeted Radionuclide Therapy of Prostate Cancer. *J Nucl Med*. 2016;57:S3-6.
19. FDA Approves 18F-Fluciclovine and 68Ga-DOTATATE Products. *J Nucl Med*. 2016;57:9N.
20. FDA Approves 11 C-Choline for PET in Prostate Cancer. *J Nucl Med*. 2012;52:11N.
21. Werahera PN, Glode LM, La Rosa FG, Lucia MS, Crawford ED, Easterday K, Sullivan HT, Sidhu RS, Genova E, Hedlund T. Proliferative Tumor Doubling Times of Prostatic Carcinoma. *Prostate Cancer*. 2011;301850:1-7.
22. Effert P, Beniers a J, Tamimi Y, Handt S, Jakse G. Expression of Glucose Transporter 1 (Glut-1) in Cell Lines and Clinical Specimens from Human Prostate Adenocarcinoma. *Anticancer Res*. 2004;24:3057-3063.
23. Müller SA, Holzapfel K, Seidl C, Treiber U, Krause BJ, Senekowitsch-Schmidtke R. Characterization of Choline Uptake in Prostate Cancer Cells Following Bicalutamide and Docetaxel Treatment. *Eur J Nucl Med Mol Imaging*. 2009;36:1434-1442.
24. Holzapfel K, Müller S a, Seidl C, Grosu A-L, Schwaiger M, Senekowitsch-Schmidtke R. Effects of Irradiation on the [Methyl-3H]Choline Uptake in the Human Prostate Cancer Cell Lines LNCaP and PC3. *Strahlenther Onkol*. 2008;184:319-324.
25. FDA website. Highlights of Prescribing Information Choline C-11 Injection. Reference ID: 3187688. https://www.accessdata.fda.gov/drugsatfda_docs/label/2012/203155s000lbl.pdf. Updated Sept, 2009. Accessed Jun 25, 2018.
26. FDA website. Highlights of Prescribing Information Fludeoxyglucose F-18 Injection. Reference ID: NDA 21-870. https://www.accessdata.fda.gov/drugsatfda_docs/label/2005/021870lbl.pdf. Updated 2005, Accessed Jun 25, 2018.
27. Challapalli A, Aboagye EO. Positron Emission Tomography Imaging of Tumor Cell Metabolism and Application to Therapy Response Monitoring. *Front Oncol*. 2016;6:1-20.
28. Chiste V, Bé M. Iodine-131. Laboratoire National Henri Becquerel. http://www.lnhb.fr/nuclides/I-131_tables.pdf. Updated Jan 20, 2014. Accesed Jun 25, 2018.
29. Chiste V, Kuzmenko NK, Bé M. Fluorine-18. Laboratoire National Henri Becquerel. http://www.lnhb.fr/nuclides/F-18_tables.pdf. Updated Aug 29, 2014. Accessed Jun 25, 2018.
30. Bé M, Helmer RG. Copper-64. Laboratoire National Henri Becquerel. http://www.lnhb.fr/nuclides/I-131_tables.pdf. Updated Jul 12, 2011. Accesed Jun 25, 2018.
31. Bé M, Schonfeld E. Gallium-68. Laboratoire National Henri Becquerel. http://www.lnhb.fr/nuclides/Ga-68_tables.pdf. Updated Jul 4, 2012. Accessed Jun 25, 2018.
32. Morillon C, Bé M, Chechev VP, Egorov A. Technetium-99m. Laboratoire National Henri Becquerel. http://www.lnhb.fr/nuclides/Tc-99m_tables.pdf. Updated Jan 19, 2004. Accessed Jun 25, 2018.
33. Bé M, Chisté V, Dulieu C, Chechev V, Kuzmennko N, Helmer R, Nichols A, Schönfeld E, Dersch R. Carbon-11. Laboratoire National Henri Becquerel. http://www.lnhb.fr/nuclides/C-11_tables.pdf. Updated Nov 3, 2011. Accessed Jun 25, 2018.
34. Chiste V, Bé M. Iodine-123. Laboratoire National Henri Becquerel. http://www.lnhb.fr/nuclides/I-123_tables.pdf. Updated Aug 5, 2004. Accesed Jun 25, 2018.
35. Theobald T. *Sampson's Textbook of Radiopharmacy, Fourth Edit*. London UK: Pharmaceutical Press; 2011.

36. P.A. Schubiger, L. Lehmann MF. *PET Chemistry The Driving Force in Molecular Imaging.* New York, NY: Springer; 2007.
37. NHS England website. Diagnostic Imaging Dataset Statistical Release. https://www.england.nhs.uk/statistics/wp-content/uploads/sites/2/2016/08/Statistical-Release-27th-October-PDF-613KB.pdf Updated Oct 27, 2016. Accessed Jun 25, 2018.
38. Nuñez R, Macapinlac HA, Yeung HWD, Akhurst T, Cai S, Osman I, Gonen M, Riedel E, Scher HI, Larson SM. Combined 18F-FDG and 11C-Methionine PET Scans in Patients with Newly Progressive Metastatic Prostate Cancer. *J Nucl Med*. 2002;43:46-55.
39. Chandler JD, Williams ED, Slavin JL, Best JD, Rogers S. Expression and Localization of GLUT1 and GLUT12 in Prostate Carcinoma. *Cancer*. 2003;97:2035-2042.
40. Salminen E, Hogg A, Binns D, Frydenberg M, Hicks R. Investigations with FDG-PET Scanning in Prostate Cancer Show Limited Value for Clinical Practice. *Acta Oncol (Madr)*. 2002;41:425-429.
41. Jadvar H. Prostate Cancer: PET with 18F-FDG, 18F- or 11C-Acetate, and 18F- or 11C-Choline. *J Nucl Med*. 2011;52:81-89.
42. Yu CY, Desai B, Ji L, Groshen S, Jadvar H. Comparative Performance of PET Tracers in Biochemical Recurrence of Prostate Cancer: A Critical Analysis of Literature. *Am J Nucl Med Mol Imaging*. 2014;4:580-601.
43. Johannes Czernin, MD, Matthias R. Benz, MD, and Martin S. Allen-Auerbach M. PET Imaging of Prostate Cancer with 11C-Acetate. *PET Clin*. 2009;4:163-172.
44. Vāvere AL, Kridel SJ, Wheeler FB, Lewis JS. 1-11C-Acetate as a PET Radiopharmaceutical for Imaging Fatty Acid Synthase Expression in Prostate Cancer. *J Nucl Med*. 2008;49:327-334.
45. Seltzer MA, Jahan SA, Sparks R, Stout DB, Satyamurthy N, Dahlbom M, Phelps ME, Barrio JR. Radiation Dose Estimates in Humans for 11C-Acetate Whole-Body PET. *J Nucl Med*. 2004;45:1233-1236.
46. Kato T, Tsukamoto E, Kuge Y, Takei T, Shiga T, Shinohara N, Katoh C, Nakada K, Tamaki N. Accumulation of [11C]Acetate in Normal Prostate and Benign Prostatic Hyperplasia: Comparison with Prostate Cancer. *Eur J Nucl Med*. 2002;29:1492-1495.
47. Oyama N, Miller TR, Dehdashti F. 11C-Acetate PET Imaging of Prostate Cancer: Detection of Recurrent Disease at PSA Relapse. *J Nucl Med*. 2003;44:549-556.
48. Fricke E, Machtens S, Hofmann M, Hoff J van den, Bergh S, Brunkhorst T, Meyer GJ, Karstens JH, Knapp WH, Boerner AR. Positron Emission Tomography with 11C-Acetate and 18F-FDG in Prostate Cancer Patients. *Eur J Nucl Med Mol Imaging*. 2003;30:607-611.
49. Sandblom G, Sörensen J, Lundin N, Häggman M, Malmström PU. Positron Emission Tomography with C11-Acetate for Tumor Detection and Localization in Patients with Prostate-Specific Antigen Relapse after Radical Prostatectomy. *Urology*. 2006;67:996-1000.
50. Leskinen S, Pulkki K, Knuuti J, Kirvelã O, Lehikoinen P, Nã K. Transport of Carbon-11-Methionine Is Enhanced by Insulin. *J Nucl Med*. 1997;38:1967-1970.
51. Ishiwata K, Kameyama M, Hatazawa J, Kubota K, Ido T. Measurement of L-[Methyl-11C]Methionine in Human Plasma. *Int J Radiat Appl Instrumentation Part A Appl Radiat Isot*. 1991;42:77-79.
52. Toth G, Lengyel Z, Balkay L, Salah M, Trom L, Toth C. Detection of Prostate Cancer with 11C-Methionine Positron Emission Tomography. *J Urol*. 2005;173:66-69.
53. Shiiba M, Ishihara ÁK, Kuwako ÁT, Yoshihara ÁN, Sato ÁH, Kumita ÁS, Kimura G, Kondo ÁY, Tsuchiya S. Evaluation of Primary Prostate Cancer Using 11C-Methionine-PET/ CT and 18F-FDG-PET/CT. *Ann Nucl Med*. 2012;26:138-145.
54. Awwad HM, Geisel J, Obeid R. The Role of Choline in Prostate Cancer. *Clin Biochem*. 2012;45:1548-1553.

55. Ribeiro FM, Black SAG, Prado VF, Rylett RJ, Ferguson SSG, Prado MAM. The “Ins” and “Outs” of the High-Affinity Choline Transporter CHT1. *J Neurochem*. 2006;97:1-12.
56. Evans JD, Jethwa KR, Ost P, Williams S, Kwon ED, Lowe VJ, Davis BJ. Prostate Cancer-Specific PET Radiotracers: A Review on the Clinical Utility in Recurrent Disease. *Pract Radiat Oncol*. 2018;8:28-39.
57. Kohlfürst S, Malle P, Igerc I, Gallowitsch HJ, Lind P. The Role of F-18 Choline PET and PET/CT in Prostate Cancer. *Imaging Decis MRI*. 2009;13:97-103.
58. Schuster DM, Nanni C, Fanti S. PET Tracers beyond FDG in Prostate Cancer. *Semin Nucl Med*. 2016;46:507-521.
59. Farsad M, Schiavina R, Castellucci P, Nanni C, Corti B, Martorana G, Canini R, Grigioni W, Boschi S, Marengo M, Pettinato C, Salizzoni E, Monetti N, Franchi R, Fanti S. Detection and Localization of Prostate Cancer: Correlation of 11C-Choline PET/CT with Histopathologic Step-Section Analysis. *J Nucl Med*. 2005;46:1642-9.
60. Evangelista L, Guttilla A, Zattoni F, Muzzio PC, Zattoni F. Utility of Choline Positron Emission Tomography/Computed Tomography for Lymph Node Involvement Identification in Intermediate- to High-Risk Prostate Cancer: A Systematic Literature Review and Meta-Analysis. *Eur Urol*. 2013;63:1040-1048.
61. Leeflang MMG. Systematic Reviews and Meta-Analyses of Diagnostic Test Accuracy. *Clin Microbiol Infect*. 2014;20:105-113.
62. Fanti S, Minozzi S, Castellucci P, Balduzzi S, Herrmann K, Krause BJ, Oyen W, Chiti A. PET/CT with 11C-Choline for Evaluation of Prostate Cancer Patients with Biochemical Recurrence: Meta-Analysis and Critical Review of Available Data. *Eur J Nucl Med Mol Imaging*. 2016;43:55-69.
63. Evangelista L, Zattoni F, Guttilla A, Saladini G, Zattoni F, Colletti PM, Rubello D. Choline PET or PET/CT and Biochemical Relapse of Prostate Cancer: A Systematic Review and Meta-Analysis. *Clin Nucl Med*. 2013;38:305-314.
64. Umbehr MH, Muntener M, Hany T, Sulser T, Bachmann LM. The Role of 11C-Choline and 18F-Fluorocholine Positron Emission Tomography (PET) and PET/CT in Prostate Cancer: A Systematic Review and Meta-Analysis. *Eur Urol*. 2013;64:106-117.
65. Picchio M, Messa C, Landoni C, Gianolli L, Sironi S, Brioschi M, Matarrese M, Matei D V., De Cobelli F, Del Maschio A, Rocco F, Rigatti P, Fazio F. Value of [11C]Choline-Positron Emission Tomography for Re-Staging Prostate Cancer: A Comparison with [18F]Fluorodeoxyglucose-Positron Emission Tomography. *J Urol*. 2003;169:1337-1340.
66. Rajendram R, Preedy VR, Patel VB. Glutamine in Clinical Nutrition.; 2015.
67. McParland BJ, Wall A, Johansson S, Sørensen J. The Clinical Safety, Biodistribution and Internal Radiation Dosimetry of [18F]Fluciclovine in Healthy Adult Volunteers. *Eur J Nucl Med Mol Imaging*. 2013;40:1256-1264.
68. Schuster DM, Votaw JR, Nieh PT, Yu W, Nye JA, Master V, Dubois Bowman F, Issa MM, Goodman MM. Initial Experience with the Radiotracer Anti-1-Amino-3-18F-Fluorocyclobutane-1-Carboxylic Acid with PET/CT in Prostate Carcinoma. *J Nucl Med*. 2007;48:56-63.
69. Nanni C, Schiavina R, Boschi S, Ambrosini V, Pettinato C, Brunocilla E, Martorana G, Fanti S. Comparison Of18F-FACBC And11C-Choline PET/CT in Patients with Radically Treated Prostate Cancer and Biochemical Relapse: Preliminary Results. *Eur J Nucl Med Mol Imaging*. 2013;40:11-17.
70. Ren J, Yuan L, Wen G, Yang J. The Value of Anti-1-Amino-3-18F-Fluorocyclobutane-1-Carboxylic Acid PET/CT in the Diagnosis of Recurrent Prostate Carcinoma: A Meta-Analysis. *Acta radiol*. 2016;57:487-493.
71. Odewole OA, Tade FI, Nieh PT, Savir-Baruch B, Jani AB, Master VA, Rossi PJ, Halkar RK, Osunkoya AO, Akin-Akintayo O, Zhang C, Chen Z, Goodman MM, Schuster DM. Recurrent Prostate Cancer Detection with Anti-3-[18F]FACBC PET/CT: Comparison with CT. *Eur J*

Nucl Med Mol Imaging. 2016;43:1773-1783.

72. Bach-Gansmo T, Nanni C, Nieh PT, Zanoni L, Bogsrud TV, Sletten H, Korsan KA, Kieboom J, Tade FI, Odewole O, Chau A, Ward P, Goodman MM, Fanti S, Schuster DM, Willoch F. Multisite Experience of the Safety, Detection Rate and Diagnostic Performance of Fluciclovine (18F) Positron Emission Tomography/Computerized Tomography Imaging in the Staging of Biochemically Recurrent Prostate Cancer. *J Urol*. 2017;197:676-683.
73. European Medicines Agency website. Assessment Report Axumin Procedure No. EMEA/H/C/004197/0000. http://www.ema.europa.eu/docs/en_GB/document_library/EPAR_-_Public_assessment_report/human/004197/WC500230836.pdf. Updated Mar 23, 2017. Accessed Jun 25, 2018.
74. Taplin ME, Balk SP. Androgen Receptor: A Key Molecule in the Progression of Prostate Cancer to Hormone Independence. *J Cell Biochem*. 2004;91:483-490.
75. Liu A, Dence CS, Welch MJ, Katzenellenbogen JA. Fluorine-18 Labeled Androgens: Radiochemical Synthesis and Tissue Distribution Studies on Six Fluorine-Substituted Androgens, Potential Imaging Agents for Prostatic Cancer. *J Nucl Med*. 1992;33:724-734.
76. Larson SM, Morris M, Gunther I, Beattie B, Humm JL, Akhurst T a, Finn RD, Erdi Y, Pentlow K, Dyke J, Squire O, Bornmann W, Mccarthy T, Welch M. Tumor Localization of 16beta-18F-Fluoro-5alpha-Dihydrotestosterone versus 18F-FDG in Patients with Progressive, Metastatic Prostate Cancer. *J Nucl Med*. 2004;45:366-374.
77. Scher HI, Anand A, Rathkopf D, Shelkey J, Morris MJ, Danila DC, Larson S, Humm J, Fleisher M, Sawyers CL, Beer TM, Alumkal J, Higano CS, Yu EY, Taplin ME, Efstathiou E, Hung D, Hirmand M, Seely L. Antitumour Activity of MDV3100 in Castration-Resistant Prostate Cancer: A Phase 1-2 Study. *Lancet*. 2010;375:1437-1446.
78. Rathkopf DE, Morris MJ, Fox JJ, Danila DC, Slovin SF, Hager JH, Rix PJ, Maneval EC, Chen I, Gönen M, Fleisher M, Larson SM, Sawyers CL, Scher HI. Phase I Study of ARN-509, a Novel Antiandrogen, in the Treatment of Castration-Resistant Prostate Cancer. *J Clin Oncol*. 2013;31:3525-3530.
79. Mansi R, Wang X, Forrer F, Waser B, Cescato R, Graham K, Borkowski S, Reubi JC, Maecke HR. Development of a Potent DOTA-Conjugated Bombesin Antagonist for Targeting GRPr-Positive Tumours. *Eur J Nucl Med Mol Imaging*. 2011;38:97-107.
80. Roivainen A, Kahkonen E, Luoto P, Borkowski S, Hofmann B, Jambor I, Lehtio K, Rantala T, Rottmann A, Sipila H, Sparks R, Suilamo S, Tolvanen T, Valencia R, Minn H. Plasma Pharmacokinetics, Whole-Body Distribution, Metabolism, and Radiation Dosimetry of 68Ga Bombesin Antagonist BAY 86-7548 in Healthy Men. *J Nucl Med*. 2013;54:867-872.
81. Mansi R, Minamimoto R, Iagaru AH. Bombesin-Targeted PET of Prostate Cancer. *J Nucl Med*. 2016;57:67S-73S.
82. Kahkonen E, Jambor I, Kemppainen J, Lehtio K, Gronroos TJ, Kuisma A, Luoto P, Sipila HJ, Tolvanen T, Alanen K, Silen J, Kallajoki M, Roivainen A, Schafer N, Schibli R, Dragic M, Johayem A, Valencia R, Borkowski S, et al. In Vivo Imaging of Prostate Cancer Using [68Ga]-Labeled Bombesin Analog BAY86-7548. *Clin Cancer Res*. 2013;19:5434-5443.
83. Bařinka C, Rojas C, Slusher B, Pomper M. Glutamate Carboxypeptidase II in Diagnosis and Treatment of Neurologic Disorders and Prostate Cancer. *Curr Med Chem*. 2012;19:856-870.
84. Tykvart J, Schimer J, Bařinková J, Pachl P, Poštová-Slavětínská L, Majer P, Konvalinka J, Šácha P. Rational Design of Urea-Based Glutamate Carboxypeptidase II (GCPII) Inhibitors as Versatile Tools for Specific Drug Targeting and Delivery. *Bioorganic Med Chem*. 2014;22:4099-4108.
85. Mesters JR, Barinka C, Li W, Tsukamoto T, Majer P, Slusher BS, Konvalinka J, Hilgenfeld R. Structure of Glutamate Carboxypeptidase II, a Drug Target in Neuronal Damage and Prostate Cancer. *EMBO J*. 2006;25:1375-1384.

86. Zhou J, Neale JH, Pomper MG, Kozikowski AP. NAAG Peptidase Inhibitors and Their Potential for Diagnosis and Therapy. *Nat Rev Drug Discov*. 2005;4:1015-1026.
87. Ghosh A, Heston WDW. Tumor Target Prostate Specific Membrane Antigen (PSMA) and Its Regulation in Prostate Cancer. *J Cell Biochem*. 2004;91:528-539.
88. O'Keefe DS, Bacich DJ, Heston WDW. Comparative Analysis of Prostate-Specific Membrane Antigen (PSMA) versus a Prostate-Specific Membrane Antigen-like Gene. *Prostate*. 2004;58:200-210.
89. Holmes EH. PSMA Specific Antibodies and Their Diagnostic and Therapeutic Use. *Expert Opin Investig Drugs*. 2001;10:511-519.
90. Ristau BT, O'Keefe DS, Bacich DJ. The Prostate-Specific Membrane Antigen: Lessons and Current Clinical Implications from 20 Years of Research. *Urol Oncol Semin Orig Investig*. 2014;32:272-279.
91. Nawaz S, Mullen GED, Sunassee K, Bordoloi J, Blower PJ, Ballinger JR. Simple, Mild, One-Step Labelling of Proteins with Gallium-68 Using a Tris(Hydroxypyridinone) Bifunctional Chelator: A 68Ga-THP-ScFv Targeting the Prostate-Specific Membrane Antigen. *EJNMMI Res*. 2017;7:86.
92. Kampmeier F, Williams JD, Maher J, Mullen GE, Blower PJ. Design and Preclinical Evaluation of a 99mTc-Labelled Diabody of MAb J591 for SPECT Imaging of Prostate-Specific Membrane Antigen (PSMA). *EJNMMI Res*. 2014;4:13.
93. Cho SY, Gage KL, Mease RC, Senthamizhchelvan S, Holt DP, Jeffrey-Kwanisai A, Endres CJ, Dannals RF, Sgouros G, Lodge M, Eisenberger M a, Rodriguez R, Carducci M a, Rojas C, Slusher BS, Kozikowski AP, Pomper MG. Biodistribution, Tumor Detection, and Radiation Dosimetry of 18F-DCFBC, a Low-Molecular-Weight Inhibitor of Prostate-Specific Membrane Antigen, in Patients with Metastatic Prostate Cancer. *J Nucl Med*. 2012;53:1883-91.
94. Imai K, Takaoka A. Comparing Antibody and Small-Molecule Therapies for Cancer. *Nat Rev Cancer*. 2006;6:714-727.
95. Maresca KP, Hillier SM, Femia FJ, Keith D, Barone C, Joyal JL, Zimmerman CN, Kozikowski AP, Barrett J a., Eckelman WC, Babich JW. A Series of Halogenated Heterodimeric Inhibitors of Prostate Specific Membrane Antigen (PSMA) as Radiolabeled Probes for Targeting Prostate Cancer. *J Med Chem*. 2008;52:347-357.
96. Jackson PF, Cole DC, Slusher BS, Stetz SL, Ross LE, Donzanti B a, Trainor D a. Design, Synthesis, and Biological Activity of a Potent Inhibitor of the Neuropeptidase N-Acetylated Alpha-Linked Acidic Dipeptidase. *J Med Chem*. 1996;39:619-622.
97. Nan F, Bzdega T, Pshenichkin S, Wroblewski JT, Wroblewska B, Neale JH, Kozikowski AP. Dual Function Glutamate-Related Ligands: Discovery of a Novel, Potent Inhibitor of Glutamate Carboxypeptidase II Possessing MGluR3 Agonist Activity. *J Med Chem*. 2000;43:772-774.
98. Kozikowski AP, Nan F, Conti P, Zhang J, Ramadan E, Bzdega T, Wroblewska B, Neale JH, Pshenichkin S, Wroblewski JT. Design of Remarkably Simple, yet Potent Urea-Based Inhibitors of Glutamate Carboxypeptidase II (NAALADase). *J Med Chem*. 2001;44:298-301.
99. Pomper MG, Musachio JL, Zhang J, Scheffel U, Zhou Y, Hilton J, Maini A, Dannals RF, Wong DF, Kozikowski AP. 11C-MCG: Synthesis, Uptake Selectivity, and Primate PET of a Probe for Glutamate Carboxypeptidase II (NAALADase). *Mol Imaging*. 2002;1:96-101.
100. Wüstemann T, Bauder-Wüst U, Schäfer M, Eder M, Benesova M, Leotta K, Kratochwil C, Haberkorn U, Kopka K, Mier W. Design of Internalizing PSMA-Specific Glu-Ureido-Based Radiotherapeuticals. *Theranostics*. 2016;6:1085-1095.
101. Eder M, Schäfer M, Bauder-Wüst U, Hull W-E, Wängler C, Mier W, Haberkorn U, Eisenhut M. 68Ga-Complex Lipophilicity and the Targeting Property of a Urea-Based PSMA Inhibitor for PET Imaging. *Bioconjug Chem*. 2012;23:688-697.

102. Banerjee SR, Foss CA, Castanares M, Mease RC, Byun Y, Fox JJ, Hilton J, Lupold SE, Kozikowski AP, Pomper MG. Synthesis and Evaluation of Technetium-99m-and Rhenium-Labeled Inhibitors of the Prostate-Specific Membrane Antigen (PSMA). *J Med Chem*. 2008;51:4504-4517.
103. Kratochwil C, Giesel FL, Leotta K, Eder M, Hoppe-Tich T, Youssoufian H, Kopka K, Babich JW, Haberkorn U. PMPA for Nephroprotection in PSMA-Targeted Radionuclide Therapy of Prostate Cancer. *J Nucl Med*. 2015;56:293-298.
104. Babich W, Armor JT, Stubbs JB, Maresca KP, Stabin MG, Joyal JL, Eckelman WC, Barrett JA, Coleman RE, Goldsmith SJ, Vallabhajosula S, Petry NA, Cho S, Armor T, Babich JW. Prostate Cancer First-in-Man Evaluation of 2 High-Affinity PSMA-Avid Small Molecules for Imaging First-in-Man Evaluation of 2 High-Affinity PSMA-Avid Small Molecules for Imaging Prostate Cancer. *J Nucl Med*. 2013;54:380-387.
105. Zechmann CM, Afshar-Oromieh A, Armor T, Stubbs JB, Mier W, Hadaschik B, Joyal J, Kopka K, Debus J, Babich JW, Haberkorn U. Radiation Dosimetry and First Therapy Results with a 124I/ 131I-Labeled Small Molecule (MIP-1095) Targeting PSMA for Prostate Cancer Therapy. *Eur J Nucl Med Mol Imaging*. 2014;41:1280-1292.
106. Vallabhajosula S, Nikolopoulou A, Babich JW, Osborne JR, Tagawa ST, Lipai I, Solnes L, Maresca KP, Armor T, Joyal JL, Crummet R, Stubbs JB, Goldsmith SJ. 99mTc-Labeled Small-Molecule Inhibitors of Prostate-Specific Membrane Antigen: Pharmacokinetics and Biodistribution Studies in Healthy Subjects and Patients with Metastatic Prostate Cancer. *J Nucl Med*. 2014;55:1791-1798.
107. Szabo Z, Mena E, Rowe SP, Plyku D, Nidal R, Eisenberger M a., Antonarakis ES, Fan H, Dannals RF, Chen Y, Mease RC, Vranesic M, Bhatnagar A, Sgouros G, Cho SY, Pomper MG. Initial Evaluation of [18F]DCFPyL for Prostate-Specific Membrane Antigen (PSMA)-Targeted PET Imaging of Prostate Cancer. *Mol Imaging Biol*. 2015;17:565-74.
108. Giesel FL, Hadaschik B, Cardinale J, Radtke J, Vinsensia M, Lehnert W, Kesch C, Tolstov Y, Singer S, Grabe N, Duensing S, Sch??fer M, Neels OC, Mier W, Haberkorn U, Kopka K, Kratochwil C. F-18 Labelled PSMA-1007: Biodistribution, Radiation Dosimetry and Histopathological Validation of Tumor Lesions in Prostate Cancer Patients. *Eur J Nucl Med Mol Imaging*. 2017;44:678-688.
109. Afshar-Oromieh A, Malcher A, Eder M, Eisenhut M, Linhart HG, Hadaschik BA, Holland-Letz T, Giesel FL, Kratochwil C, Haufe S. PET Imaging with a [68Ga] Gallium-Labelled PSMA Ligand for the Diagnosis of Prostate Cancer: Biodistribution in Humans and First Evaluation of Tumour Lesions. *Eur J Nucl Med Mol Imaging*. 2013;40:486-495.
110. Afshar-Oromieh A, Hetzheim H, Kübler W, Kratochwil C, Giesel FL, Hope TA, Eder M, Eisenhut M, Kopka K, Haberkorn U. Radiation Dosimetry of 68Ga-PSMA-11 (HBED-CC) and Preliminary Evaluation of Optimal Imaging Timing. *Eur J Nucl Med Mol Imaging*. 2016;43:1611-1620.
111. Benešová M, Schäfer M, Bauder-Wüst U, Afshar-Oromieh A, Kratochwil C, Mier W, Haberkorn U, Kopka K, Eder M. Preclinical Evaluation of a Tailor-Made DOTA-Conjugated PSMA Inhibitor with Optimized Linker Moiety for Imaging and Endoradiotherapy of Prostate Cancer. *J Nucl Med*. 2015;56:914-920.
112. Afshar-Oromieh A, Hetzheim H, Kratochwil C, Benesova M, Eder M, Neels OC, Eisenhut M, Kubler W, Holland-Letz T, Giesel FL, Mier W, Kopka K, Haberkorn U. The Theranostic PSMA Ligand PSMA-617 in the Diagnosis of Prostate Cancer by PET/CT: Biodistribution in Humans, Radiation Dosimetry, and First Evaluation of Tumor Lesions. *J Nucl Med*. 2015;56:1697-1705.
113. Schmuck S, Nordlohne S, von Klot CA, Henkenberens C, Sohns JM, Christiansen H, Wester HJ, Ross TL, Bengel FM, Derlin T. Comparison of Standard and Delayed Imaging to Improve the Detection Rate of [68Ga]PSMA I&T PET/CT in Patients with Biochemical Recurrence or Prostate-Specific Antigen Persistence after Primary Therapy for Prostate

Cancer. *Eur J Nucl Med Mol Imaging*. 2017;44:960-968.
114. Hillier SM, Maresca KP, Femia FJ, Marquis JC, Foss C a., Nguyen N, Zimmerman CN, Barrett J a., Eckelman WC, Pomper MG, Joyal JL, Babich JW. Preclinical Evaluation of Novel Glutamate-Urea-Lysine Analogues That Target Prostate-Specific Membrane Antigen as Molecular Imaging Pharmaceuticals for Prostate Cancer. *Cancer Res*. 2009;69:6932-6940.
115. Silver DA, Pellicer I, Fair WR, Heston WDW, Cordon-Cardo C. Prostate-Specific Membrane Antigen Expression in Normal and Malignant Human Tissues. *Clin Cancer Res*. 1997;3:81-85.
116. Mhawech-Fauceglia P, Zhang S, Terracciano L, Sauter G, Chadhuri A, Herrmann FR, Penetrante R. Prostate-Specific Membrane Antigen (PSMA) Protein Expression in Normal and Neoplastic Tissues and Its Sensitivity and Specificity in Prostate Adenocarcinoma: An Immunohistochemical Study Using Mutiple Tumour Tissue Microarray Technique. *Histopathology*. 2007;50:472-483.
117. Afshar-Oromieh A, Haberkorn U, Zechmann C, Armor T, Mier W, Spohn F, Debus N, Holland-Letz T, Babich J, Kratochwil C. Repeated PSMA-Targeting Radioligand Therapy of Metastatic Prostate Cancer with 131I-MIP-1095. *Eur J Nucl Med Mol Imaging*. 2017;44:950-959.
118. Kularatne SA, Zhou Z, Yang J, Post CB, Low PS. Design, Synthesis, and Preclinical Evaluation of Prostate-Specific Membrane Antigen Targeted 99mTc-Radioimaging Agents. *Mol Pharm*. 2009;6:790-800.
119. Benesova M, Bauder-Wust U, Schafer M, Klika KD, Mier W, Haberkorn U, Kopka K, Eder M. Linker Modification Strategies to Control the Prostate-Specific Membrane Antigen (PSMA)-Targeting and Pharmacokinetic Properties of DOTA-Conjugated PSMA Inhibitors. *J Med Chem*. 2016;59:1761-1775.
120. Banerjee SR, Pullambhatla M, Foss CA, Nimmagadda S, Ferdani R, Anderson CJ, Mease RC, Pomper MG. 64Cu-Labeled Inhibitors of Prostate-Specific Membrane Antigen for PET Imaging of Prostate Cancer. *J Med Chem*. 2014;57:2657-2669.
121. Banerjee SR, Pullambhatla M, Byun Y, Nimmagadda S, Green G, Fox JJ, Horti A, Mease RC, Pomper MG. 68Ga-Labeled Inhibitors of Prostate-Specific Membrane Antigen (PSMA) for Imaging Prostate Cancer. *J Med Chem*. 2010;53:5333-5341.
122. Banerjee SR, Pullambhatla M, Foss C a, Falk A, Byun Y, Nimmagadda S, Mease RC, Pomper MG. Effect of Chelators on the Pharmacokinetics of 99mTc-Labeled Imaging Agents for the Prostate-Specific Membrane Antigen (PSMA). *J Med Chem*. 2013;56:6108-6121.
123. Hillier SM, Maresca KP, Lu G, Merkin RD, Marquis JC, Zimmerman CN, Eckelman WC, Joyal JL, Babich JW. 99mTc-Labeled Small-Molecule Inhibitors of Prostate-Specific Membrane Antigen for Molecular Imaging of Prostate Cancer. *J Nucl Med*. 2013;54:1369-1376.
124. Goffin KE, Joniau S, Tenke P, Slawin K, Klein EA, Stambler N, Strack T, Babich J, Armor T, Wong V. Phase 2 Study of 99m Tc-Trofolastat SPECT/CT to Identify and Localize Prostate Cancer in Intermediate- and High-Risk Patients Undergoing Radical Prostatectomy and Extended Pelvic Lymph Node Dissection. *J Nucl Med*. 2017;58:1408-1413.
125. Schmidkonz C, Hollweg C, Beck M, Reinfelder J, Goetz TI, Sanders JC, Schmidt D, Prante O, Bäuerle T, Cavallaro A, Uder M, Wullich B, Goebell P, Kuwert T, Ritt P. 99mTc-MIP-1404-SPECT/CT for the Detection of PSMA-Positive Lesions in 225 Patients with Biochemical Recurrence of Prostate Cancer. *Prostate*. 2018;78:54-63.
126. Reinfelder J, Kuwert T, Beck M, Sanders JC, Ritt P, Schmidkonz C, Hennig P, Prante O, Uder M, Wullich B, Goebell P. First Experience with SPECT/CT Using a 99mTc-Labeled Inhibitor for Prostate-Specific Membrane Antigen in Patients with Biochemical Recurrence of Prostate Cancer. *Clin Nucl Med*. 2017;42:26-33.
127. NIH U.S. National Library of Medicine, Clinical Trials Website. https://clinicaltrials.gov/ct2/show/NCT02615067. Updated January 5, 2018. Accessed

Feb 21, 2018.
128. Mease RC, Dusich CL, Foss C a, Ravert HT, Dannals RF, Seidel J, Prideaux A, Fox JJ, Sgouros G, Kozikowski AP, Pomper MG. N-[N-[(S)-1,3-Dicarboxypropyl]Carbamoyl]-4-[18F]Fluorobenzyl-L-Cysteine, [18F]DCFBC: A New Imaging Probe for Prostate Cancer. *Clin Cancer Res*. 2008;14:3036-3043.
129. Chen Y, Pullambhatla M, Foss CA, Byun Y, Nimmagadda S, Senthamizhchelvan S, Sgouros G, Mease RC, Pomper MG. 2-(3-{1-Carboxy-5-[(6-[18F]Fluoro-Pyridine-3-Carbonyl)-Amino]- Pentyl}-Ureido)-Pentanedioic Acid, [18F]DCFPyL, a PSMA-Based PET Imaging Agent for Prostate Cancer. *Clin Cancer Res*. 2011;17:7645-7653.
130. Kuchar M, Mamat C. Methods to Increase the Metabolic Stability of 18F-Radiotracers. *Molecules*. 2015;20:16186-16220.
131. Giesel FL, Cardinale J, Schafer M, Neels O, Bene??ov?? M, Mier W, Haberkorn U, Kopka K, Kratochwil C. 18F-Labelled PSMA-1007 Shows Similarity in Structure, Biodistribution and Tumour Uptake to the Theragnostic Compound PSMA-617. *Eur J Nucl Med Mol Imaging*. 2016;43:1929-1930.
132. Rowe SP, Gage KL, Faraj SF, Macura KJ, Cornish TC, Gonzalez-Roibon N, Guner G, Munari E, Partin a. W, Pavlovich CP, Han M, Carter HB, Bivalacqua TJ, Blackford A, Holt D, Dannals RF, Netto GJ, Lodge M a., Mease RC, et al. 18F-DCFBC PET/CT for PSMA-Based Detection and Characterization of Primary Prostate Cancer. *J Nucl Med*. 2015;56:1003-1010.
133. Rowe SP, Macura KJ, Ciarallo A, Mena E, Blackford A, Nadal R, Antonarakis ES, Eisenberger MA, Carducci MA, Ross AE, Kantoff PW, Holt DP, Dannals RF, Mease RC, Pomper MG, Cho SY. Comparison of Prostate-Specific Membrane Antigen-Based 18F-DCFBC PET/CT to Conventional Imaging Modalities for Detection of Hormone-Naive and Castration-Resistant Metastatic Prostate Cancer. *J Nucl Med*. 2016;57:46-53.
134. Rowe SP, Macura KJ, Mena E, Blackford AL, Nadal R, Antonarakis ES, Eisenberger M, Carducci M, Fan H, Dannals RF, Chen Y, Mease RC, Szabo Z, Pomper MG, Cho SY. PSMA-Based [18F]DCFPyL PET/CT Is Superior to Conventional Imaging for Lesion Detection in Patients with Metastatic Prostate Cancer. *Mol Imaging Biol*. 2016;18:411-419.
135. Cardinale J, Schäfer M, Benešová M, Bauder-Wüst U, Leotta K, Eder M, Neels OC, Haberkorn U, Giesel FL, Kopka K. Preclinical Evaluation of [18F]PSMA-1007: A New PSMA-Ligand for Prostate Cancer Imaging. *J Nucl Med*. 2017;58:425-431.
136. Kesch C, Vinsensia M, Radtke JP, Schlemmer HP, Heller M, Ellert E, Holland-Letz T, Duensing S, Grabe N, Afshar-Oromieh A, Wieczorek K, Schäfer M, Neels OC, Cardinale J, Kratochwil C, Hohenfellner M, Kopka K, Haberkorn U, Hadaschik BA, et al. Intra-Individual Comparison of 18F-PSMA-1007-PET/CT, Multi-Parametric MRI and Radical Prostatectomy Specimen in Patients with Primary Prostate Cancer - a Retrospective, Proof of Concept Study. *J Nucl Med*. 2017:jnumed.116.189233.
137. Giesel F, Will L, Kesch C, Freitag M, Kremer C, Merkle J, Neels O, Cardinale J, Hadaschik B, Hohenfellner M, Kopka K, Haberkorn U, Kratochwil C. Biochemical Recurrence of Prostate Cancer: Initial Results with 18F-PSMA-1007 PET/CT. *J Nucl Med*. 2018;59:632-635.
138. Giesel F, Will L, Lawal I, Lengana T, Kratochwil C, Vorster M, Neels O, Reyneke F, Haberkon U, Kopka K, Sathekge M. Intra-Individual Comparison of 18F-PSMA-1007 and 18F-DCFPyL PET/CT in the Prospective Evaluation of Patients with Newly Diagnosed Prostate Carcinoma: A Pilot Study. *J Nucl Med*. 2017.
139. Bé M, E. S. Germanium-68. Laboratoire National Henri Becquerel. http://www.lnhb.fr/nuclides/Ge-68_tables.pdf. Updated Feb 27, 2012. Accessed 25 Jun, 2018.
140. Maurer T, Gschwend JE, Rauscher I, Souvatzoglou M, Haller B, Weirich G, Wester HJ, Heck M, Kübler H, Beer AJ, Schwaiger M, Eiber M. Diagnostic Efficacy of 68-Gallium-PSMA Positron Emission Tomography Compared to Conventional Imaging for Lymph Node Staging of 130 Consecutive Patients with Intermediate to High Risk Prostate Cancer. *J*

Urol. 2016;195:1436-1442.
141. Herlemann A, Wenter V, Kretschmer A, Thierfelder KM, Bartenstein P, Faber C, Gildehaus FJ, Stief CG, Gratzke C, Fendler WP. 68Ga-PSMA Positron Emission Tomography/Computed Tomography Provides Accurate Staging of Lymph Node Regions Prior to Lymph Node Dissection in Patients with Prostate Cancer. *Eur Urol*. 2016;70:553-557.
142. Weineisen M, Schottelius M, Simecek J, Baum RP, Yildiz A, Beykan S, Kulkarni HR, Lassmann M, Klette I, Eiber M, Schwaiger M, Wester H-J, Rp-hplc A. 68Ga- and 177Lu-Labeled PSMA I&T: Optimization of a PSMA-Targeted Theranostic Concept and First Proof-of-Concept Human Studies. *J Nucl Med*. 2015;56:1169-1176.
143. Perera M, Papa N, Christidis D, Wetherell D, Hofman MS, Murphy DG, Bolton D, Lawrentschuk N. Sensitivity, Specificity, and Predictors of Positive 68Ga–prostate-Specific Membrane Antigen Positron Emission Tomography in Advanced Prostate Cancer: A Systematic Review and Meta-Analysis. *Eur Urol*. 2016;70:926-937.
144. Afshar-Oromieh A, Holland-Letz T, Giesel FL, Kratochwil C, Mier W, Haufe S, Debus N, Eder M, Eisenhut M, Schäfer M, Neels O, Hohenfellner M, Kopka K, Kauczor H-U, Debus J, Haberkorn U. Diagnostic Performance of 68Ga-PSMA-11 (HBED-CC) PET/CT in Patients with Recurrent Prostate Cancer: Evaluation in 1007 Patients. *Eur J Nucl Med Mol Imaging*. 2017;44:1781-1781.
145. NIH U.S. National Library of Medicine. Clinical Trials Website. https://www.clinicaltrials.gov/ct2/results?term=68Ga&recr=&rslt=&type=&cond=Prostate&intr=&titles=&outc=&spons=&lead=&id=&state1=&cntry1=&state2=&cntry2=&state3=&cntry3=&locn=&gndr=&rcv_s=&rcv_e=&lup_s=&lup_e=. Updated 25 Jun, 2018. Accessed 25 Jun, 2018.
146. NIH U.S. National Library of Medicine, Clinical Trials Website. https://www.clinicaltrials.gov/ct2/show/NCT03362359?term=68Ga&cond=Prostate&draw=5&rank=36. Updated January 9, 2018, Accessed Jun 25, 2018.
147. Kabasakal L, AbuQbeitah M, Aygün A, Yeyin N, Ocak M, Demirci E, Toklu T. Pre-Therapeutic Dosimetry of Normal Organs and Tissues of 177Lu-PSMA-617 Prostate-Specific Membrane Antigen (PSMA) Inhibitor in Patients with Castration-Resistant Prostate Cancer. *Eur J Nucl Med Mol Imaging*. 2015;42:1976-1983.
148. Banerjee SR, Foss CA, Pullambhatla M, Wang Y, Srinivasan S, Hobbs RF, Baidoo KE, Brechbiel MW, Nimmagadda S, Mease RC, Sgouros G, Pomper MG. Preclinical Evaluation of Y-86 Labeled Inhibitors of Prostate Specific Membrane Antigen for Dosimetry Estimates. *J Nucl Med*. 2015;56:628-634.
149. Sathekge M, Knoesen O, Meckel M, Modiselle M, Vorster M, Marx S. 213Bi-PSMA-617 Targeted Alpha-Radionuclide Therapy in Metastatic Castration-Resistant Prostate Cancer. *Eur J Nucl Med Mol Imaging*. 2017;44:1099-1100.
150. Kratochwil C, Bruchertseifer F, Rathke H, Bronzel M, Apostolidis C, Weichert W, Haberkorn U, Giesel FL, Morgenstern A. Targeted Alpha Therapy of MCRPC with 225 Ac-PSMA-617: Dosimetry Estimate and Empirical Dose Finding. *J Nucl Med*. 2017;58:1624-1631.
151. Weineisen M, Simecek J, Schottelius M, Schwaiger M, Wester H-J. Synthesis and Preclinical Evaluation of DOTAGA-Conjugated PSMA Ligands for Functional Imaging and Endoradiotherapy of Prostate Cancer. *EJNMMI Res*. 2014;4:1-15.
152. Schuchardt C, Weineisen M, Wiessalla S, Schottelius M, Kulkarni H, Mueller D, Klette I, Wester H, Baum R. Biodistribution and Dosimetry of Lu-177 PSMA in Metastasized Castrate Resistant Prostate Cancer Patients. *J Nucl Med*. 55:S641--641.
153. Derlin T, Weiberg D, von Klot C, Wester HJ, Henkenberens C, Ross TL, Christiansen H, Merseburger AS, Bengel FM. 68Ga-PSMA I&T PET/CT for Assessment of Prostate Cancer: Evaluation of Image Quality after Forced Diuresis and Delayed Imaging. *Eur Radiol*.

2016;26:4345-4353.
154. Berliner C, Tienken M, Frenzel T, Kobayashi Y, Helberg A, Kirchner U, Klutmann S, Beyersdorff D, Budäus L, Wester HJ, Mester J, Bannas P. Detection Rate of PET/CT in Patients with Biochemical Relapse of Prostate Cancer Using [68Ga]PSMA I&T and Comparison with Published Data of [68Ga]PSMA HBED-CC. *Eur J Nucl Med Mol Imaging*. 2017;44:670-677.
155. Fendler WP, Eiber M, Beheshti M, Bomanji J, Ceci F, Cho S, Giesel F, Haberkorn U, Hope TA, Kopka K, Krause BJ, Mottaghy FM, Schöder H, Sunderland J, Wan S, Wester HJ, Fanti S, Herrmann K. 68Ga-PSMA PET/CT: Joint EANM and SNMMI Procedure Guideline for Prostate Cancer Imaging: Version 1.0. *Eur J Nucl Med Mol Imaging*. 2017;44:1014-1024.
156. Afshar-Oromieh A, Zechmann CM, Malcher A, Eder M, Eisenhut M, Linhart HG, Holland-Letz T, Hadaschik B a., Giesel FL, Debus J, Haberkorn U. Comparison of PET Imaging with a 68Ga-Labelled PSMA Ligand and 18F-Choline-Based PET/CT for the Diagnosis of Recurrent Prostate Cancer. *Eur J Nucl Med Mol Imaging*. 2014;41:11-20.
157. Afshar-Oromieh A, Haberkorn U, Schlemmer HP, Fenchel M, Eder M, Eisenhut M, Hadaschik BA, Kopp-Schneider A, Röthke M. Comparison of PET/CT and PET/MRI Hybrid Systems Using a 68Ga-Labelled PSMA Ligand for the Diagnosis of Recurrent Prostate Cancer: Initial Experience. *Eur J Nucl Med Mol Imaging*. 2014;41:887-897.
158. Ceci F, Herrmann K, Castellucci P, Graziani T, Bluemel C, Schiavina R, Vollmer C, Droll S, Brunocilla E, Mazzarotto R, Buck AK, Fanti S. Impact of 11C-Choline PET/CT on Clinical Decision Making in Recurrent Prostate Cancer: Results from a Retrospective Two-Centre Trial. *Eur J Nucl Med Mol Imaging*. 2014;41:2222-2231.
159. Goldstein J, Even-Sapir E, Ben-Haim S, Saad A, Spieler B, Davidson T, Berger R, Weiss I, Appel S, Lawrence YR, Symon Z. Does Choline PET/CT Change the Management of Prostate Cancer Patients with Biochemical Failure? *Am J Clin Oncol*. 2017;40:256-259.
160. Afaq A, Alahmed S, Chen S, Lengana T, Haroon A, Payne H, Ahmed H, Punwani S, Sathekge M, Bomanji J. 68 Ga-PSMA PET/CT Impact on Prostate Cancer Management. *J Nucl Med*. 2018;59:89-92.
161. Roach PJ, Francis R, Emmett L, Hsiao E, Kneebone A, Hruby G, Eade T, Nguyen Q, Thompson B, Cusick T, McCarthy M, Tang C, Ho B, Stricker P, Scott A. The Impact of 68 Ga-PSMA PET/CT on Management Intent in Prostate Cancer: Results of an Australian Prospective Multicenter Study. *J Nucl Med*. 2018;59:82-88.
162. Akin-Akintayo OO, Jani AB, Odewole O, Tade FI, Nieh PT, Master VA, Bellamy LM, Halkar RK, Zhang C, Chen Z, Goodman MM, Schuster DM. Change in Salvage Radiotherapy Management Based on Guidance with FACBC (Fluciclovine) PET/CT in Post-Prostatectomy Recurrent Prostate Cancer. *Clin Nucl Med*. 2017;42:e22-e28.
163. Teoh E, Bottomley D, Scarsbrook A, Payne H, Afaq A, Bomanji J, van As N, Chua S, Hoskin P, Chambers A, Cook GJ, Warbey VS, Chau A, Ward P, Miller MP, Stevens DJ, Wilson L, Gleeson FV. Impact of 18 F-Fluciclovine PET/CT on Clinical Management of Patients with Recurrent Prostate Cancer: Results from the Phase 3 FALCON Trial. *Int J Radiat Oncol*. 2017;99:1316-1317.
164. Giovacchini G, Picchio M, Garcia-Parra R, Briganti A, Abdollah F, Gianolli L, Schindler C, Montorsi F, Messa C, Fazio F. 11C-Choline PET/CT Predicts Prostate Cancer-Specific Survival in Patients with Biochemical Failure during Androgen-Deprivation Therapy. *J Nucl Med*. 2014;55:233-241.
165. Ahmadzadehfar H, Rahbar K, Kürpig S, Bögemann M, Claesener M, Eppard E, Gärtner F, Rogenhofer S, Schäfers M, Essler M. Early Side Effects and First Results of Radioligand Therapy with 177Lu-DKFZ-617 PSMA of Castrate-Resistant Metastatic Prostate Cancer: A Two-Centre Study. *EJNMMI Res*. 2015;5:36.
166. Kiess AP, Minn IIL, Vaidyanathan G, Hobbs RF, Josefsson A, Brummet M, Chen Y, Choi J, Koumarianou E, Baidoo K, Brechbiel MW, Mease RC, Sgouros G, Zalutsky MR, Martin G,

Shen C, Brummet M, Chen Y, Choi J, et al. (2S)-2-(3-(1-Carboxy-5-(4-[211At]Astatobenzamido)Pentyl)Ureido)-Pentanedioic Acid for PSMA-Targeted α -Particle Radiopharmaceutical Therapy. *J Nucl Med*. 2016;57:1569-1575.

167. Kiess A, Minn I, Chen Y, Hobbs RF, Sgouros G, Mease RC, Pullambhatla M, Shen C, Foss C, Pomper M. Auger Radiopharmaceutical Therapy Targeting Prostate-Specific Membrane Antigen. *J Nucl Med*. 2015;56:1401-1407.
168. Ahmadzadehfar H, Eppard E, Kürpig S, Fimmers R, Schlenkhoff CD, Gärtner F, Rogenhofer S, Essler M. Therapeutic Response and Side Effects of Repeated Radioligand Therapy with 177 Lu-PSMA-DKFZ-617 of Castrate-Resistant Metastatic Prostate Cancer. *Oncotarget*. 2016;7:12477-12488.
169. Calopedos RJS, Chalasani V, Asher R, Emmett L, Woo HH. Lutetium-177-Labelled Anti-Prostate-Specific Membrane Antigen Antibody and Ligands for the Treatment of Metastatic Castrate-Resistant Prostate Cancer: A Systematic Review and Meta-Analysis. *Prostate Cancer Prostatic Dis*. 2017;20:352-360.
170. Endocyte Website. http://endocyte.com/pipeline/advanced-prostate-cancer-treatment/. Updated Jan 2018, Accessed Jun 25, 2018.

2 Ideal Radiolabelling: Generator Produced Radionuclides Combined with a One-Step Radiopharmaceutical Kit

2.1 The Prevalence of Technetium-99m

The majority of radiopharmaceuticals used to image patients every year are based on technetium-99m, a radio-metal which emits gamma radiation and has a half-life of 6.01 hours (*1*). This prevalence can be attributed to a number of factors, some clinical, others due to infrastructure and economics. These include but are not limited to: 1) The wide availability of SPECT and gamma cameras in hospitals; 2) The 140 keV gamma emissions of technetium-99m which are optimal for SPECT imaging and its 6.01 hour half-life (*1*) which allows imaging within an acceptable patient dose and minimal waste handling issues (*2*); 3) The wide range of technetium-99m radiopharmaceuticals clinically approved and commercially available (*2*)(*3*); 4) The relatively low production costs of tracers due to the generator production of technetium-99m and easy to label kit preparations (*2*)(*3*). This chapter will focus on the advantages of radiopharmaceutical production based on a generator-produced radionuclide incorporated into a radiopharmaceutical by reconstitution of a one-step kit, and how this technology could also be applied to gallium-68 PET radiopharmaceuticals.

2.1.1 Molybdenum-99/Technetium-99m Generators and Their Advantages

Molybdenum-99/technetium-99m generators provide a convenient way to produce high molar activity technetium-99m on demand in a radiopharmacy for the manufacture of radiopharmaceuticals (*4*). These generators consist of an aluminium oxide column onto which the parent isotope molybdenum-99 in the form $[^{99}Mo][Mo(VI)O_4^{2-}]$ is adsorbed (*2*). The molybdenum-99 on the column decays to technetium-99m producing $[^{99m}Tc][Tc(VII)O_4^{-}]$, which due to its lower charge has a lower affinity for the column. Saline can be used to elute the generator and separate the two radionuclides by removing $[[^{99m}Tc]Tc(VII)O_4^{-}]$ from the column without displacing the $[[^{99}Mo]Mo(VI)O_4^{2-}]$ (*4*). Clinical generators are commonly eluted with 0.9% saline and produce 2-150 GBq of technetium-99m per elution (*2*). A clinical generator is a benchtop-sized piece of equipment that weighs around 20 kg due to the required shielding (*5*). Generators are normally stored within hospital radiopharmacies in a customised lead drawer on a reinforced bench or in an isolator. The 66.02 hour half-life of molybdenum-99 means that generators have a lifetime of 1-2 weeks, giving plenty of time for transport from the manufacturer to radiopharmacies. This provides a big advantage over the nuclear reactor or cyclotron production of short half-life radionuclides, which can only be transported short

distances, limiting the number of sites that can utilise them. Molybdenum-99/technetium-99m generators can be eluted multiple times a day, depending on demand; this provides flexibility for scheduling. Additionally, as hospitals are charged per generator rather than for each batch of technetium-99m, the more the generator is used the lower the cost of each batch becomes. Generally, there is also a consistent supply of generators and the infrastructure is in place for their weekly delivery to radiopharmacies. However, as this supply relies on a small number of reactors for the production of molybdenum-99, and as limited excess capacity currently exists, any shut-down at these sites can cause world-wide generator shortages (*6*)(*7*).

2.1.2 Typical Radiolabelling Procedure for a Technetium-99m Single Vial Kit Radiopharmaceutical

Within a radiopharmacy, a diverse range of technetium-99m pharmaceuticals can be produced by eluting the generator and using the eluent to reconstitute commercially available radiopharmaceutical kits. This is typically a high-throughput environment where speed, simplicity, volume, and reproducibility of radiolabelling are essential, and would not be sustainable if complex radiolabelling procedures were required.

A radiopharmaceutical kit consists of a vial containing all the non-radioactive chemical components required for radiolabelling (*4*). The kit manufacturer is responsible for ensuring that kits meet the required standards in terms of good manufacturing practice (GMP), chemical purity and sterility. In most cases all that is required to prepare the radiopharmaceutical is the addition of technetium-99m pertechnetate in saline to the kit vial, inverting or shaking to ensure the contents have fully dissolved, and then leaving it at ambient temperature for the reaction to proceed (usually no more than a few minutes). In some cases, heating is also required to improve radiochemical yield and is done by heating the sealed kit vial on a hot plate, or in a water bath (*3*). As manipulation of radioactive substances is minimal, the process is quick (typically taking less than 10 minutes) and the radiation dose to the operator producing the tracer is minimised. A small sample can then be removed from the vial for quality control (QC), which typically involves analysis of pH, radiochemical purity (RCP) using instant thin layer chromatography (iTLC), and in some cases sterility testing. The methods will follow the monograph for the specific radiopharmaceutical defined within the pharmacopoeia for the relevant governed region or the methods described in the summary of product characteristics within the documentation provided for marketing authorisation. Simple kit-based radiolabelling procedures supported by well-defined QC procedures allow tracers to be produced consistently and reproducibly across all hospitals, with minimal extra training for staff members.

2.1.3 A Typical Technetium-99m Radiopharmaceutical Kit

A kit for a technetium-99m radiopharmaceutical is typically a single vial, containing a lyophilised powder made up of all the non-radioactive components required for radiolabelling of the desired complex at high radiochemical purity. The kits will be sterile and septum-sealed under an inert atmosphere (*4*). Most kits have a shelf life of 1 year (*3*) meaning a radiopharmacy can have a stock of kits that are used in response to demand. Some kits have been designed for single patient doses and others are suitable for multiple doses. Each type of kit contains a unique active ingredient, which will form the final complex with technetium. In order for complexation to be possible technetium-99m pertechnetate ($[^{99m}Tc][TcO_4]^-$), the form in which technetium is eluted from the generator, must be reduced to a lower oxidation state (Tc(VI), Tc(V), Tc(IV), Tc(III), Tc(II) or Tc(I)) (*2*). This is achieved with a reducing agent, most commonly tin(II) chloride ($SnCl_2$) and the quantity used and the pH and temperature affect the oxidation state achieved (*2*)(*3*). Kits may also include other components, such as antioxidants to minimise autoradiolysis, and weak chelating agents to create stable intermediates with technetium before it is chelated with the active ingredient, avoiding $[^{99m}Tc]TcO_2$ colloid formation (*2*). Additionally, buffers are often used to create the optimal pH and ensure complexation of the desired species, as well as bulking agents to aid the lyophilisation process (*4*). Once radiolabelled, kits are usually stable for 4-12 hours (*3*) and this combined with the 6.01 hour half-life of technetium-99m, gives a wide time period within which the tracer can be administered to a patient.

An example of a one-step kit is the $[^{99m}Tc]$Tc-MDP kit (*3*). This tracer is used to image bone metastasis and is an important and widely used clinical tracer for prostate cancer staging as described in chapter 1. These lyophilised GMP kits contain 10 mg MDP (methylene diphosphonic acid), 1 mg tin chloride dihydrate and 2 mg ascorbic acid (*3*). Radiolabelling is carried out by the addition of 4 mL of technetium-99m pertechnetate to the kit, shaking for 1 minute and QC after 5 minutes. The kit should then have a pH of 5-7, and a radiochemical purity (RCP) over 95% as measured by iTLC.

2.1.4 Disadvantages of Existing Kits and Challenges in Developing New Ones

Despite the extremely simple radiolabelling of $[^{99m}Tc]$Tc-MDP and its clinical utility, the chemical structure of this complex remains unknown (*4*)(*8*)(*9*)(*10*). Multiple species are formed upon radiolabelling which can be separated by high pressure liquid chromatography (HPLC) and the ratios formed are dependent upon the exact radiolabelling conditions (*8*)(*9*). These individual species have been shown to have different biodistributions in animal studies, in particular,

differences in bone-seeking ability were observed (*8*). This finding raises concerns about the tracer's consistency in the detection of bone metastases in clinical practice. Poorly understood species formed upon binding technetium-99m is not a problem unique to [^{99m}Tc]Tc-MDP. Other technetium tracers produced with a one-step kit produce multiple species or distinct stereoisomers upon binding. These include: [^{99m}Tc]Tc-DMSA (*11*)(*12*)(*13*), [^{99m}Tc]Tc-DTPA (*4*)(*14*), and [^{99m}Tc]Tc-MAG3 (*4*)(*15*). When these radiotracers were granted regulatory approval in the 1970's and 1980's full understanding of the complexes produced was not a requirement, but the process to gain regulatory and marketing approval is now much more rigorous and evidence that only one species is formed upon radiolabelling is likely to be a requirement. This can only be achieved by taking into account the coordination chemistry of technetium and careful design of ligands which will bind this radiometal in just one configuration without producing any chiral centres or other isomerism (*6*).

An additional challenge to producing one-step kits for novel radiopharmaceuticals is that, thus far, kits have only be developed for small molecule technetium-99m tracers. However, the field of nuclear medicine has moved on from functional to receptor-based imaging which often requires more complex bioconjugates, labelled at high molar activity. This presents further challenges for designing kit-based radiopharmaceuticals. At the moment bioconjugates utilising technetium-99m are mainly HYNIC (*2*)(*4*)(*16*) or tricarbonyl complexes (*2*)(*3*)(*17*), neither of which are currently amenable to one-step kit-based production. HYNIC is only a bidentate chelator and so requires a co-ligand to fully coordinate technetium; this leads to isomerism and it is difficult to characterise the complexes formed especially as these are sensitive the reaction conditions (*6*). In the case of tricarbonyl-based tracers, the radiolabelling process always requires two steps, one to generate the $[[^{99m}Tc]Tc(CO)_3(H_2O)_3]^+$ intermediate and the second to chelate it (*3*)(*17*).

As an example, the radiolabelling procedure for the PSMA tracer [^{99m}Tc]Tc-MIP-1404 which is currently undergoing a phase 3 clinical trial in the USA (*18*), is a tricarbonyl complex. Compared to one-step kits the radiolabelling procedure for this tracer is more lengthy and complex. The structure of MIP-1404 consists of a GCP(II)/PSMA targeting Lys-C(O)-Glu motif attached by a linker to the TIM chelator as shown in figure 2.1. Radiolabelling is performed in two stages and takes over 90 minutes to complete (*19*). A summary of this process is shown in figure 2.2. The first stage is the generation of the tricarbonyl intermediate $[[^{99m}Tc]Tc(CO)_3(H_2O)_3]^+$, by adding generator eluate to a commercially available kit (IsoLink, Covidien) containing sodium tartrate, sodium tetraborate, sodium carbonate and sodium boranocarbonate and heating to 100°C for 20-30 minutes (*3*)(*17*). These components ensure an alkaline pH, the reduction of Tc(VII) to Tc(I)

and the production of carbon monoxide ligands which stabilise technetium in this oxidation state. The second stage is to add the cold precursor MIP-1404 into this vial (100 µg in 100 µl) and heat at 100°C for 1 hour. Once complete the reaction mixture is neutralised and loaded onto a C_{18} column. The final radiolabelled complex is then eluted from the column with 1 mL ethanol, diluted with 9 mL saline and sterile filtered before QC and patient administration. Fortunately, multiple patient doses can be made with each synthesis, but the process is much longer, more labour intensive and therefore would require more training to perform than a one-step kit-based labelling procedure, and so is far from ideal. Clearly, the development of one-step technetium-99m kits has not kept pace with the development of receptor-based molecular imaging.

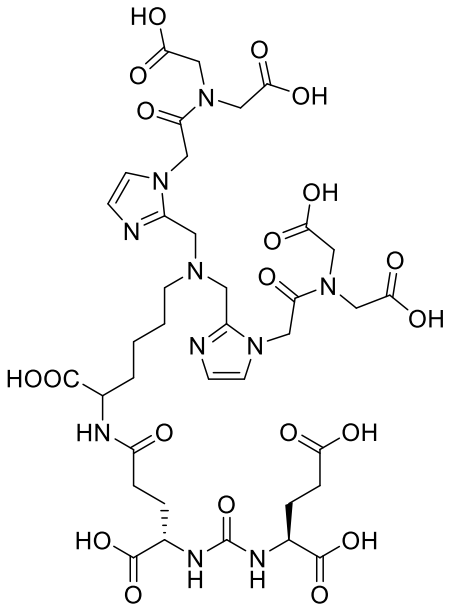

FIGURE 2.1: The structure of MIP-1404 used to make [^{99m}Tc]Tc-MIP-1404 (19).

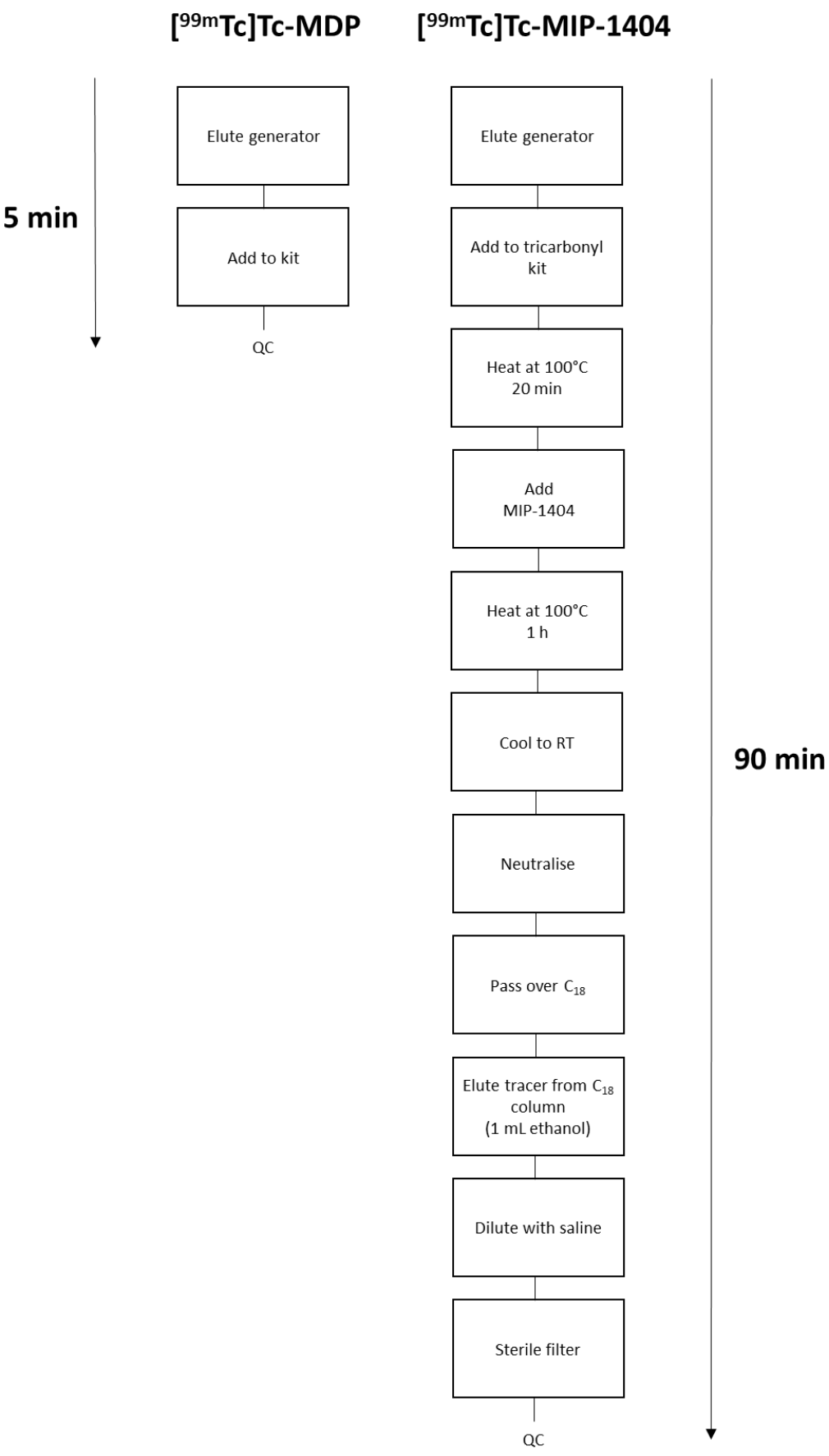

FIGURE 2.2: Radiolabelling steps for [^{99m}Tc]Tc-MDP (*3*) and [^{99m}Tc]Tc-MIP-1404 (19).

2.2 Applying One-Step Kits to PET Tracers

The advantages of the generator and one-step kit model have led to widespread use of technetium-99m radiopharmaceuticals. However, a kit and generator model is not compatible for the majority of clinically approved PET tracers because of the focus on fluorine-18 and carbon-11 tracers (*20*)(*21*). These short-lived radionuclides are produced in a cyclotron, rather than a generator, limiting production of tracers to sites with these facilities and delivery to a small area around the production site. As non-metals, they require complex synthetic chemistry to be incorporated into a radiotracer (*21*) that is usually incompatible with a kit. However, radiometals with suitable emissions can also be used for PET imaging and these have the potential to be developed into one-step kits. This would allow extremely simple radiolabelling procedures to be combined with the advantages of PET imaging: higher sensitivity which leads better signal to noise ratio, more accurate quantification of images, and the possibility to perform dynamic scans (*22*). Gallium-68 is the PET radiometal that is currently most appropriate for designing one-step kits. It is generator-produced and well-suited for PET imaging as 90% of its emissions are positrons (β^+) with an average energy of 1.9 MeV (*23*). The 67.8 minute half-life of gallium-68 also makes it particularly well-matched to the short pharmacokinetics of peptides and small molecules, and even small proteins, and means high-quality imaging can be achieved with similar injected activity to fluorine-18 tracers, with similar radiation doses to patients.

2.2.1 Germanium-68/Gallium-68 Generators

Like molybdenum-99/technetium-99m generators, germanium-68/gallium-68 generators are bench top sized, produce gallium-68 within a radiopharmacy on demand, and can be eluted multiple times a day. Germanium-68/gallium-68 generators in clinical use that are manufactured to GMP compliant conditions and produce gallium-68 elute that reaches the standards for human injection (>99.9% gallium-68, <0.001% germanium-68 (*24*)) include the Galli-Eo (IRE, Fleurus, Belgium), the iThemba (IDB Holland BV, Netherlands), the ITG (Isotope Technologies Garching GmbH, Garching, Germany) and the Galliapharm (Eckert & Ziegler, Berlin, Germany). However, only the Galliapharm generator has been granted marketing authorisation in Europe (13 counties (*25*)) and is the only generator approved for the manufacture of [^{68}Ga]Ga-DOTA-TATE in the USA (*26*). Therefore it will be focused on here for the development of one-step kits. Most germanium-68/gallium-68 generators including the Galliapharm uses a titanium dioxide column onto which germanium-68 is adsorbed. When this decays [^{68}Ga]Ga^{3+} is formed which has a lower affinity for the column and so can be eluted from it using hydrochloric acid (HCl).

The Galliapharm generator provides a maximum of 1.85 GBq of gallium-68 in 5 mL 0.1 M HCl, which can be used to manufacture radiopharmaceuticals. The generator has a 1 year lifetime; however, over this period the amount of activity produced in each elution drops considerably as shown in figure 2.3 (*27*).

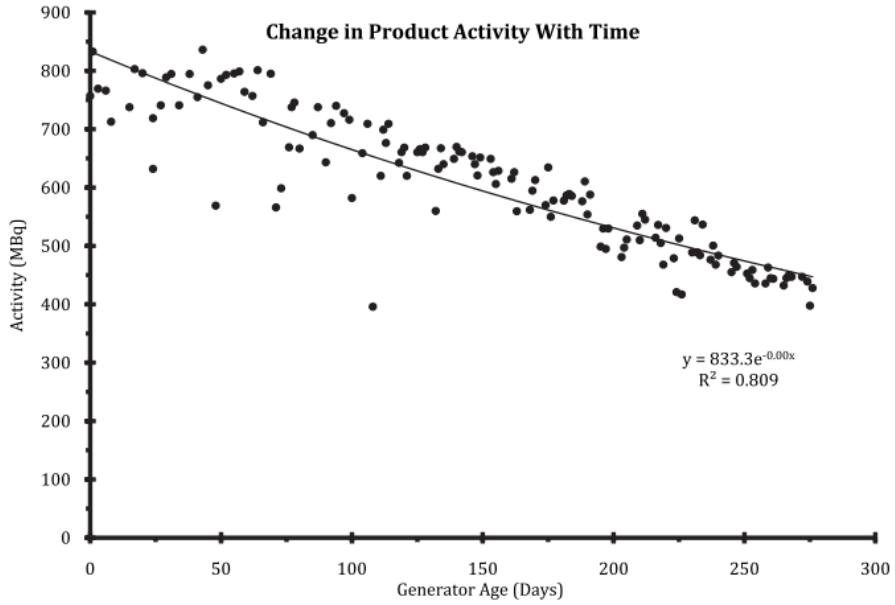

FIGURE 2.3: Change in the activity obtained over time from a 1.85 GBq Galliapharm germanium-68/gallium-68 generator. Reproduced with permission from (27).

Molybdenum-99/technetium-99m generators and germanium-68/gallium-68 generators can be compared in table 2.1. There are three big differences between a germanium-68/gallium-68 generator and a molybdenum-99/technetium-99m generator: 1) The solution used to elute the generator: technetium-99m is eluted in saline at near-neutral pH, and can therefore be injected directly into patients (it is used for thyroid imaging due to its affinity for the sodium iodine symporter (*28*)) whereas gallium-68 is eluted in 0.1 M HCl and so the pH must be raised to both allow coordination of the ligand to a chelator and to produce a suitable pH for injection; 2) The generator's lifetime is 2 weeks for a molybdenum-99/technetium-99m generator and 1 year for a germanium-68/gallium-68 generator. This is an advantage for germanium-68/gallium-68 generators as radiopharmacies are not reliant on a weekly supply but introduces concerns about maintaining sterility and apyrogenicity over this timeframe; 3) The activity per elution is much lower for germanium-68/gallium-68 generators than molybdenum-99/technetium-99m generators - a maximum of 1.85 GBq compared to 703 GBq. The impact of this is that many fewer patient doses can be made per gallium-68 elution, an issue exacerbated by its shorter half-life.

	Tc-99m	Gallium-68
Name	Ultra-Technekow™ V4	Galliapharm
Supplier	Mallinckrodt Pharmaceuticals	Eckert & Zeigler
Parent isotope	Molybdenum-99	Germanium-68
Half-life of parent	66.02 hours (*29*)	270.95 days (*30*)
Lifetime of generator	2 weeks	1 year
Elution solvent	0.9% saline	0.1 M HCl
Eluted complex	$Tc(VII)O_4^-$	$Ga(III)Cl_3$
Elution volume	5-20 mL	5 mL
Activity per elution	max 703 GBq	max 1.85 GBq
Activity concentration	max 35.15 GBq/mL	max 0.37 GBq/mL
Mininum time between elution	1 hour	2 hours
Maximum time between elution	24 hours	24 hours
Number of elutions per day	2	4
Doses per elution	> 100	1-4
Column sorbent	Aluminium oxide, ion exchange (Al_2O_3)	Titanium dioxide on borosilicate (TiO_2)
Possible contaminating radionuclides	Mo-99 Tc-99	Ge-68
Limits for contaminating radionuclides	0.1% Mo-99	0.001% Ge-68
GMP compliant	Yes	Yes
Cost per generator	~£1,000-1,500 (replaced weekly)	~£40,000-60,000 (replaced yearly)
Marketing approval	Yes	Yes

TABLE 2.1: Properties of a molybdenum-99/technetium-99m (31) and a germanium-68/gallium-68 (32) generator.

2.2.2 Ideal Kits for Gallium-68

In this section, the ideal properties of a kit for radiolabelling gallium-68 will be defined and justified. Overall the simplicity of labelling will be the focus for optimisation here, but of course, this must not come at the expense of the clinical utility. Here we will assume that the tracer that will be radiolabelled is a bioconjugate with a small peptide or pharmacophore, attached to a chelator for gallium-68. The kit should be a single vial, and the radiolabelling process should simply be the addition of gallium-68 eluate directly from a generator into the kit. Radiolabelling then should reach completion (> 95%) quickly (< 5 minutes) at room temperature and, after

passing QC, should be suitable for administering directly to patients. In order for such a simple process to be possible, not only does the kit vial need to be designed carefully but the generator used also needs to be controlled. The Galliapharm generator has marketing authorisation and therefore is the most appropriate to design a kit for. It will be assumed that this generator has been well-maintained, is sterile and has been tested for contaminating radiometals (germanium-68 <0.001%) before use with the kit.

2.2.2.1 Kit Design

It would be ideal to design a one-step kit to accommodate the whole elution volume from the generator (5 mL, 0.1 M HCl). This means the generator could be eluted directly into the kit, minimising the number of manipulations and any loss of activity from transferring between vials. This should also allow multiple patient doses to be produced at once, reducing the number of radiolabelling and QC procedures required per day, minimising cost. Once reconstituted, the kit should be at a pH and osmolality suitable for injection directly into patients, without any further dilution. The pH range for intravenous administration is pH 2-13 however, a physiological pH between 7.35-7.45 would be ideal as this is less likely to cause irritation at the site of injection (*33*). The acceptable osmolality limit is 1000 mOsm/kg, but again for patient comfort, it would be most preferable if the kit components were isotonic (300 mOsm/kg) (*34*).

2.2.2.2 Excipients

The only excipients vital to a gallium-68 kit should be a neutralising agent or buffer to modify the pH, as unlike technetium kits no reducing agent is required to change the oxidation state of the radiometal. There may also be the need for an antioxidant to reduce autoradiolysis and a bulking agent to improve lyophilisation or adjust osmolality. All components used should be pharmaceutical grade, already approved for human use and suitable for lyophilisation, as lyophilised kits typically have a much longer stability than solution-based ones.

2.2.2.3 Active Ingredient/Bioconjugate Design

The active ingredient design is the most important factor that will allow a one-step kit to be achieved. This active ingredient should be either a chelating agent which also provides a targeting mechanism (such as [^{67}Ga]Ga-citrate for lymphoma staging), or a bioconjugate that combines a pharmacophore, which targets it to a disease site, and a chelator with excellent properties for labelling with gallium-68 as well as *in vivo* stability. When these two parts are combined the presence of the chelator should not compromise the targeting ability of the pharmacophore, nor should the presence of the pharmacophore compromise the radiolabelling.

An ideal chelator for use in such a bioconjugate would bind gallium-68 quantitatively, quickly (< 5 minutes), at room temperature, and at low concentrations (< 10 μM). This allows the tracer to be produced at high molar activity, whilst ensuring that over 95% RCP is consistently achieved. The molar activity required for a high-quality image will depend on the target disease and the density of the transporter or receptor being imaged. If molar activity is not high enough, the excess cold tracer will act as an inhibitor and block uptake of the radiolabelled tracer *in vivo*, reducing signal (*35*). High molar activity is difficult to achieve for gallium-68 ratiotracers for a number of reasons including the high elution volume of generators, low activity concentration, and the presence of metal impurities in the generator eluate. Therefore the active ingredient should also utilise a chelator which is specific for gallium and does not bind to other metal impurities. Generator eluate does not only contain gallium-68, it also contains its decay product zinc-68 as well as a range of metals derived from the acid, the generator's column, lead shielding and plastic tubing (*36*). Figure 2.4 and figure 2.5 shows a summary of the metals found in the eluate of a Galliapharm generator by inductively coupled plasma mass spectroscopy (ICP-MS). However, it should be noted that the generator was over 1 year old which may have affected leaching from the column (*36*). As these generators use a titanium dioxide on borosilicate column, titanium becomes the major contaminant from this source with levels at 2 μM. Additional metal ions present in high concentrations (0.1 μM to 5 μM) are Al, Fe, Zn, Ga and Pb (*36*). (Note that when detected by ICP-MS the oxidation state of each metal is unknown). By selecting or designing a chelator that is very specific to gallium and no other metal, and binds gallium quickly, competition for binding the chelator is minimised and higher molar activity should be achievable.

The final requirement is that once the active ingredient binds the radio-metal a single, well-characterised complex should be formed with no evidence of diastereomers, enantiomers, or geometric isomers. This is important as each isomer may have a different affinity for the target or a different biodistribution. The presence of multiple isomers is also likely to be a barrier to gaining regulatory approval and hence to widespread use for the tracer.

2.2.2.4 Quality Control (QC)

Due to the short half-life of gallium-68, it would be ideal for not only the radiolabelling but also the QC processes to be as fast as possible. When a batch of kits is manufactured, a sample of these kits are used to confirm sterility and apyrogenicity for the whole batch. This means the cold kit is guaranteed sterile and pyrogen free, which means once marketing authorisation has been granted for that kit, radiopharmacies do not need to carry out these tests on every kit.

Additionally, if it is only possible to form one complex upon radiolabelling, only an iTLC method that could differentiate between bound and unbound gallium-68 would be required to assess radiochemical purity, whereas HPLC would be needed if multiple complexes are possible, in order to ensure the ratio of these is known and remains consistent between batches. This is of particular importance if different complexes are expected or known to have different *in vivo* properties, and the ratio of complexes formed changes depending on labelling conditions.

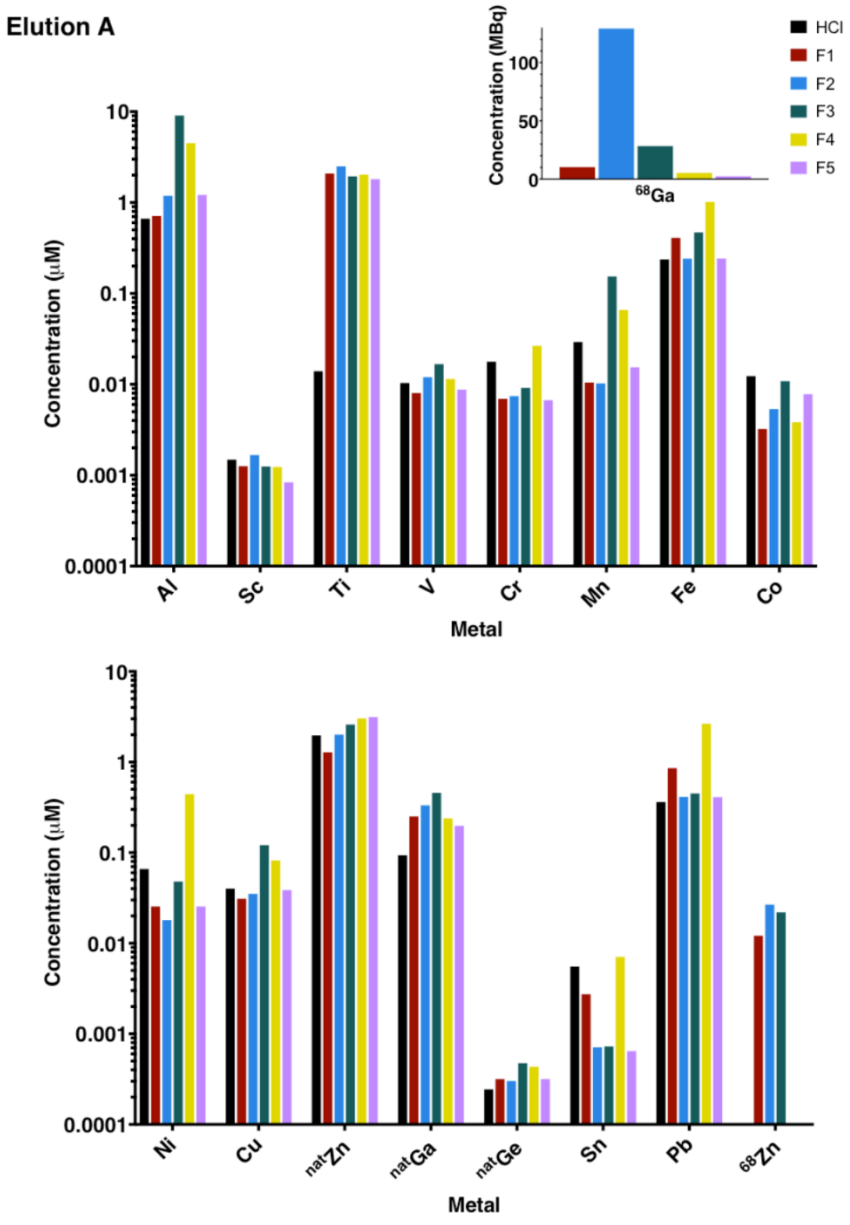

FIGURE 2.4: The concentrations of selected metals in each fraction of the Galliapharm germanium-68/gallium-68 generator eluate, and in the HCl used to elute the generator as measured by ICP-MS. The elution analysed was obtained 5 hours after the previous elution. Reproduced with permission from the supplementary material for (36).

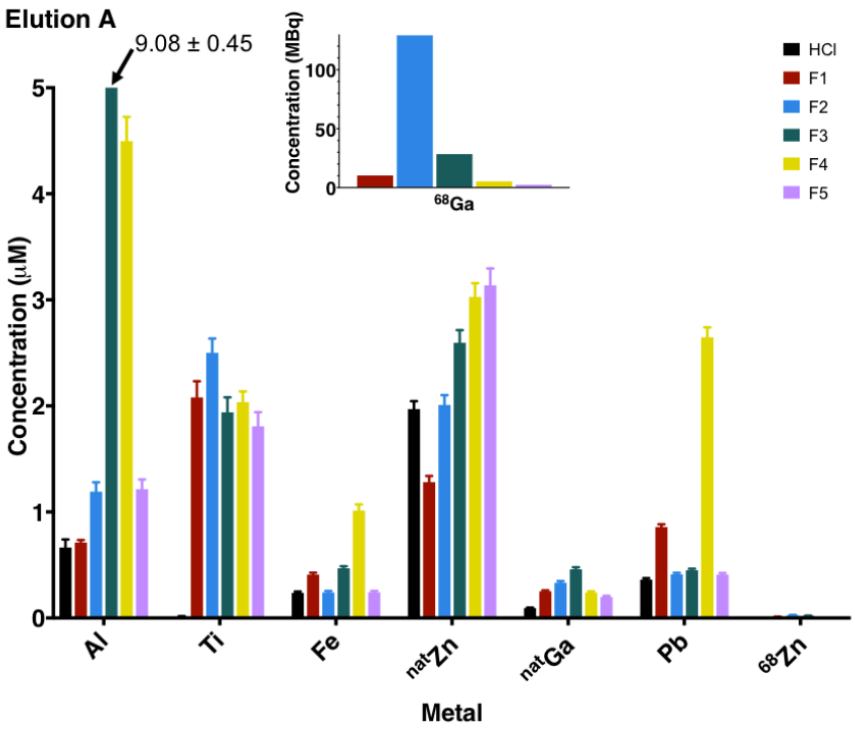

FIGURE 2.5: The concentrations of selected metals in each fraction of the Galliapharm germanium-68/gallium-68 generator eluate, and in the HCl used to elute the generator as measured by ICP-MS. The elution analysed was obtained 5 hours after the previous elution. Reproduced with permission from the supplementary material for (36).

2.2.2.5 Advantages of a Kit

Kits that fulfil the criteria outlined above would have the following advantages over multistep radiolabelling. 1) Radiolabelling will take 5 minutes to perform. This would allow many labelling procedures to be done per day, with minimal extra staffing. The speed is particularly important for gallium-68-based radiopharmaceuticals due to the 67.8 minute half-life, the low activity produced by the generator and the drop off in activity from the generator over time. One-step kit-based preparations would therefore maximise the activity available for administration and should allow multiple patient doses to be produced per kit. 2) A generator and one-step kit method removes the need for multiple manual manipulations or complex automated equipment with multiple moving parts, controlled by software. This means radiolabelling is consistent, and the possibility of radiolabelling failures is minimised. A kit-based radiotracer can easily be produced in the same manner across a number of sites if the same generator and kit are used. This is vital when conducting clinical trials, for gaining regulatory approval, and when creating a commercial product. 3) The low number of manipulations also minimises dose for the staff reconstituting the kit. This is an important safety consideration, especially as PET isotopes produce higher energy gamma rays (511 keV (*23*)) compared to typically used SPECT isotopes

(technetium-99m has major emissions at 140 keV (*1*)). 4) Sterility is easier to control with a kit and therefore endotoxin testing does not need to be tested before the release of every batch. This means one-step kits not only reduce the radiolabelling time but also the time required for QC. 5) Costs are likely to be significantly lower with a generator and one-step kit-based production. This includes personnel costs, as well as lower infrastructure investment compared to manual or automated multiple step synthesis, or cyclotron produced radionuclides.

2.2.3 Chelators for Gallium-68

The ability to design a bioconjugate that can be radiolabelled in a one-step kit is dependent on the selection of an appropriate chelator. The ideal chelator for a one-step kit would be water soluble, able to incorporate gallium into the radiotracer rapidly, at room temperature, neutral pH and low concentration, forming a single (non-isomeric) well-characterised complex, with high stability *in vivo*. For bioconjugates it is also important that the chelator does not adversely affect the biodistribution. In this section, the most clinically relevant chelators for gallium-68 will be discussed alongside their suitability for use in a one-step kit.

The design of chelators for gallium needs to reflect its chemistry. Gallium is a p-block element in group 13 of the periodic table, with the electronic configuration $[Ar]3d^{10}\ 4s^2\ 4p^1$. Due to its full d orbitals, the chemistry of gallium is relatively simple compared to its neighbouring transition metals. It is a hard Lewis acid, with an ionic radius (Ga^{3+}) of 0.62 Å. Gallium is predominantly trivalent and only stable as gallium(III) in aqueous solution, plus ligand-field effects play no role in its chemistry (*6*). As gallium(III) is a hard Lewis acid, it favours binding to hard Lewis bases such as nitrogen and oxygen. Its small radius means that gallium(III) is most stable as a six-coordinate (distorted) octahedron (*6*). It can also form four and five coordinate complexes but these are more sensitive to hydrolysis (*6*). Chelators for gallium that are to be used as radiopharmaceutical agents must form complexes with high kinetic inertness to ensure the stability of the complex *in vivo*. The chelator must also be able to rapidly complex gallium-68 at low concentration in aqueous solution, due to the constraints of radiopharmaceutical preparation. Another challenge is that chelators need to be able to compete with the formation of insoluble gallium colloid [$Ga(OH)_3$] which is produced in aqueous solution when the pH is above 3 (*37*). Figure 2.6 shows the distribution of gallium-hydroxide species in aqueous solution as a function of pH. Often stabilising ligands such as citrate, acetate or oxalate are used to reduce [$Ga(OH)_3$] formation; these are all weakly coordinating ligands and can therefore be easily exchanged for stronger chelating ligands, giving complexes with higher kinetic stability (*38*).

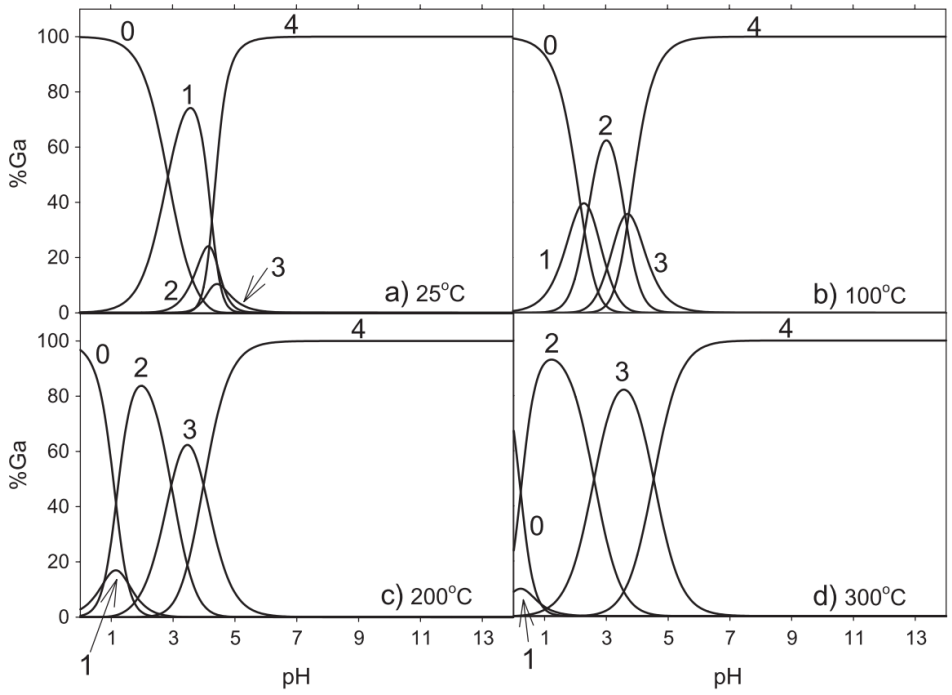

FIGURE 2.6: Distribution of mononuclear Ga–hydroxide species as a function of temperature and pH at saturated water vapour pressure and infinite dilution. The species shown are: 0 = $[Ga]^{3+}$; 1 = $[Ga(OH)]^{2+}$; 2 = $[Ga(OH)_2]^{+}$; 3 = $[Ga(OH)_3]$ and 4 = $[Ga(OH)_4]^{-}$. Reproduced with permission from (37).

2.2.3.1 DOTA

DOTA (1,4,7,10-tetraazacyclododecane-1,4,7,10-tetraacetic acid) is a macrocyclic chelator with a 12-membered ring containing 4 amine nitrogen atoms and has 4 pendant carboxylic acids (Figure 2.7). DOTA is the most clinically-used chelator for radiometals, and can form stable complexes with a large range of metals in different oxidation states (e.g. Ac(III), Al(III), Bi(III), Cu(II), Co(II), Fe(II), Fe(III), Ga(III), In(III), Lu(III), Pb(II), Sc(III), Y(III) Zn(II) (*39*)(*40*)). This allows imaging and therapy to be performed using the same bioconjugate, bound to different radiometals. DOTA was designed for metals with larger ionic radii than gallium and a larger coordination number, but is still suitable for binding gallium, and does so as a N_4O_2 donor. However, this produces steric strain in the backbone of DOTA and leaves two of its pendant carboxylic acids uninvolved in coordinating the metal (*6*). These pendant carboxylic acids can be used to functionalise the chelator. Alternatively, the DOTAGA derivative can be used if it is necessary to preserve them both. See figure 2.7 for the structure DOTAGA. Radiolabelling of DOTA with gallium-68 is optimal at pH 3.5-4 (*41*) with heating to 90-95°C for 5 minutes (*41*)(*42*)(*43*). Under such conditions quantitative radiolabelling can occur at concentrations of 5-70 µM (*42*)(*44*), however, post-labelling purification methods are commonly used to remove any remaining unchelated gallium-68 (*42*)(*43*). Because DOTA can bind a range of metals, it is very

sensitive to metal contaminants in gallium generator eluate and this restricts the molar activity that can be achieved. Figure 2.8 demonstrates how the radiolabelling of [^{68}Ga]Ga-DOTA-TATE is affected by the presence of a range of contaminating metals (*40*). For this reason, a number of pre-labelling purification methods have been developed for use when labelling DOTA with gallium-68 (*45*)(*46*)(*47*)(*48*)(*49*). Both the requirement for a heating step at concentrations appropriate for radiolabelling and the sensitivity of DOTA to metal impurities, make it unsuitable for development into a one-step kit.

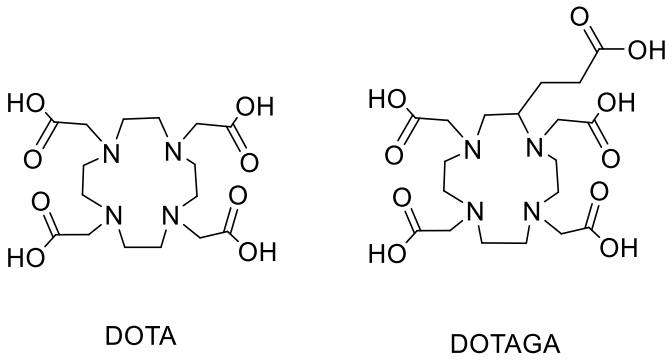

FIGURE 2.7: The structures of DOTA and DOTAGA (39).

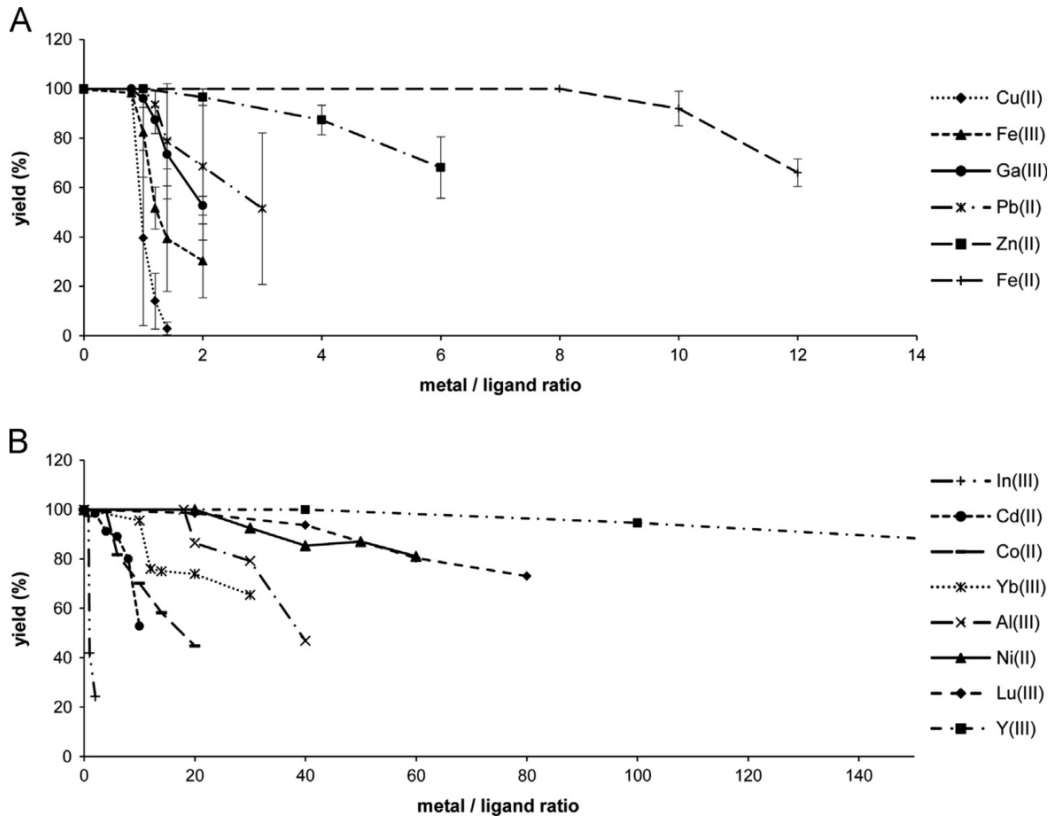

FIGURE 2.8: Effect of metal ion addition to reaction solution on [^{68}Ga]Ga-DOTA-TATE yield (pH 4, 95°C, 10 minutes, 5 nmol DOTATATE). Error bars in chart B have been left out for clarity. Reproduced with permission from (40).

Chelator	Log K_{GaL}
DOTA (*50*)	21.3
NOTA (*51*)	31.0
TRAP (*52*)	26.24
HBED (*53*)	38.5
DFO (*54*)	28.65
THP*	35.1
$DATA^m$ (*55*)	21.7

TABLE 2.2: Log K_{GaL} values for a range of chelators. * = unpublished work courtesy of Cinzia Imberti, manuscript in preparation.

2.2.3.2 NOTA

NOTA (1,4,7-triazacyclononane-1,4,7-triacetic acid) has a 9 membered ring containing 3 amine nitrogen and 3 pendant carboxylic acids, which matches the size, coordination number and geometry of gallium(III) and binds it as a N_3O_3 donor. Consequently, Ga-NOTA has a high stability constant with a log K_{GaL} of 31.0 compared to 21.3 for Ga-DOTA (*55*) (see table 2.2 which shows a comparison of log K_{GaL} values for all the chelators discussed). However, NOTA cannot retain this high-affinity binding for gallium if one of the pendant carboxylic acid arms is used for functionalisation with a targeting agent. Therefore the NODAGA bifunctional chelator was developed to preserve all pendant carboxylic acids. The structures of both chelators are shown in figure 2.10. Radiolabelling for NOTA or NODAGA with gallium-68 is optimal when carried out at pH 3.5 (*56*). Complex formation does not require heating, but complexation at 10 µM takes over 10 minutes to become quantitative at room temperature and at concentrations of 5 µM or below does not reach over 95% radiolabelling by 20 minutes (*56*). Therefore heating steps are often used to speed up the process or improve molar activity (*55*)(*57*). The stability of [^{67}Ga]Ga-NODAGA-TOC has been assessed through serum studies, mouse studies and metabolite analysis which all showed excellent stability for up to 4 hours (*58*). Particularly when radiolabelling is performed at high temperature, NOTA and NODAGA are sensitive to metal contaminants especially those with a smaller ionic radius such as Zn(II), Cu(II) and Fe(III) as shown in figure 2.9 (*59*). The kinetics of NOTA and NODAGA and their sensitivity to metal contaminants mean that radiolabelling with unprocessed eluate is unlikely to be possible at high molar activity and therefore these chelators are unsuitable for one-step kits with gallium-68.

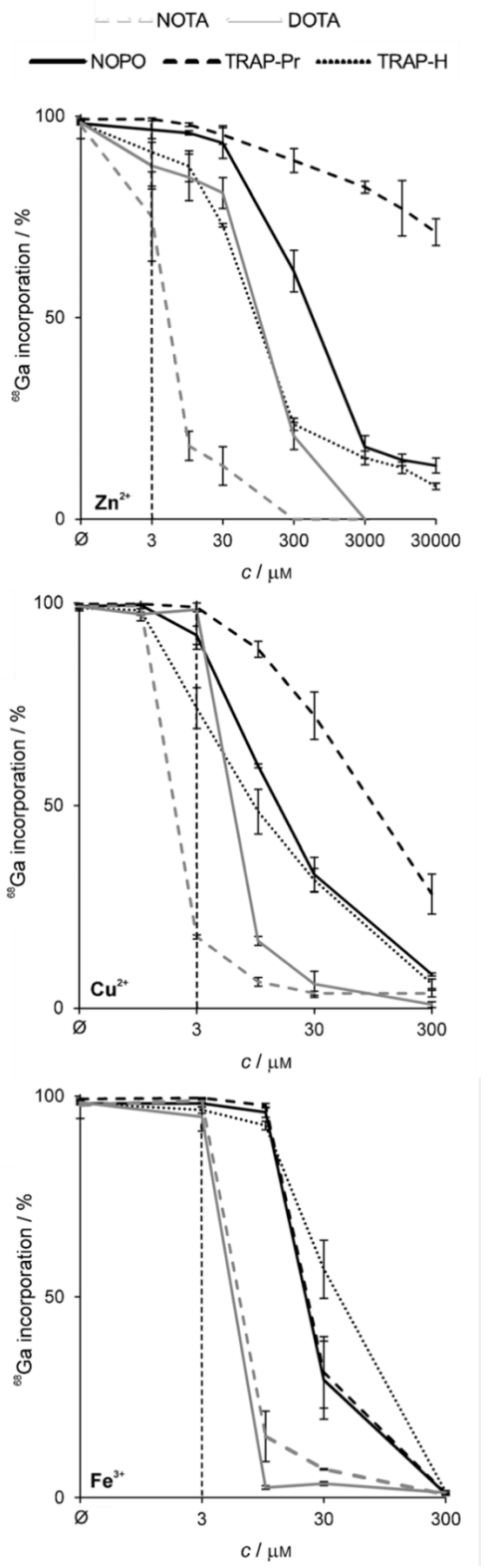

FIGURE 2.9: Incorporation of gallium-68 (10–20 MBq, 95°C, pH 3) by NOPO, TRAP-Pr, TRAP-H, NOTA, and DOTA as functions of increasing concentrations (*c*) of metal ions (Zn^{2+}, Cu^{2+}, Fe^{3+}). Vertical dashed lines indicate equal concentrations of chelator and contaminant (3 µM). Reproduced with permission from (59)

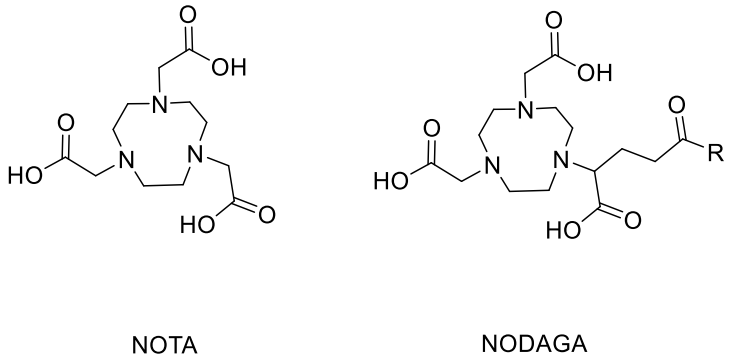

FIGURE 2.10: The structures of NOTA and NODAGA (55).

2.2.3.3 TRAP, NOTP and NOPO

TRAP, NOTP and NOPO are derivatives of NOTA where the carboxylic acid arms have been replaced with phosphinic or phosphonic acid groups, as shown in figure 2.11. They bind gallium as N_3O_3 donors and have higher stability constants than DOTA but lower than NOTA table 2.2. These modifications improve both molar activity and the ability to bind gallium-68 in the presence of metal impurities as shown in figure 2.9 (*59*). To date NOTP, has only been optimised with gallium-67 (*60*)(*61*) but gallium-68 labelling with modern generators has been optimised for TRAP and NOPO (*62*)(*63*). Radiolabelling for TRAP is optimal at a pH of 3-5 but possible over a broader range of pH 1-5. When radiolabelling is performed at room temperature (20°C), pH 3.3 and with 90 μM chelator concentration, over 90% labelling is achieved within 10 minutes (*52*). Heating the reaction mixture increases the speed, molar activity and RCP of radiolabelling and is the published method used for most TRAP bioconjugates (*62*). Radiolabelling for NOPO has an optimal pH of 3-4 when performed at room temperature, and quantitative radiolabelling can be achieved within 5 minutes at a concentration of 30 μM (*63*). If a 95°C heating step is included the concentration required to obtain over 95% radiolabelling drops to 1 μM (*63*). The advantages of TRAP and NOPO over DOTA and NOTA in terms of molar activity are therefore most stark when radiolabelling is performed at low pH and high temperature, conditions incompatible with a one-step kit. When radiolabelling is performed at room temperature, relatively high concentrations of chelator (30-100 μM) are required to achieve quantitative radiolabelling (*62*)(*63*), and so it is unlikely that high enough molar activity could be achieved for the development of one-step kits.

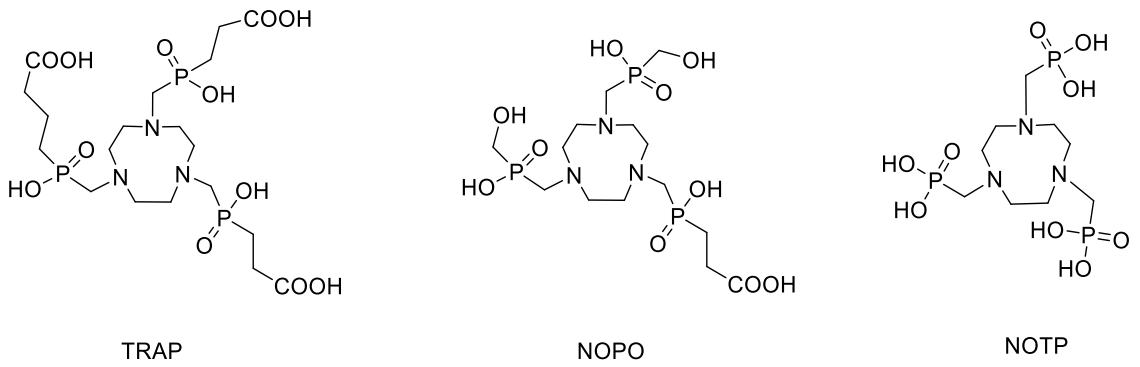

FIGURE 2.11: The structures of TRAP (62), NOPO (63) and NOTP (60).

2.2.3.4 HBED

HBED (bis(2-hydroxybenzyl)ethylenediaminediacetic acid) binds gallium through its phenol, amine and carboxyl groups as an N_2O_4 donor, and has exceptionally high log K_{GaL} value of 38.5 (*53*). However, the drawback of this chelator is that the 3 different donor groups allow for the formation of multiple geometric isomers upon binding, as shown in figure 2.13**.** These are distinguishable by HPLC and nuclear magnetic resonance spectroscopy (NMR) (*36*)(*64*). The ratio of these geometric isomers can change depending on the temperature and pH of complexation (figure 2.15) (*36*)(*64*)(*65*). It has been proposed that the most thermodynamically stable of these is the RR conformation where the phenol groups are mutually *trans*, as this is the least sterically hindered. Therefore it is presumed that this is the geometric isomer formed in the highest quantity after heating the reaction mixture. It should also be noted that each geometric isomer will be a racemic mixture of its lambda and delta enantiomers, but these are likely to interconvert rapidly on the biological timescale, and so will not be considered further here. If the chelator HBED was to be functionalised using one of its carboxylic acids used to bind gallium this would impede binding and so the HBED-CC bifunctional chelator has been developed to avoid this, as shown in figure 2.12. At physiological pH, the pendant carboxylic acid not used for functionalisation will add an additional negative charge to this region of the molecule, not present in the Ga-HBED complex. The radiolabelling conditions for quantitative radiolabelling with HBED-CC are pH 4.2, room temperature 5-10 minutes at a concentration of 25 μM (*57*). When compared to NOTA, the kinetics of complexation are much faster as demonstrated in figure 2.14. However, due to the geometric isomers formed a heating step is often used to provide 90% RCP of the most thermodynamically favoured species. Such a heating step would make HBED and HBED-CC incompatible with a one-step kit. If radiolabelling was instead performed at room temperature the presence of multiple isomers means that HPLC QC is required before batch release, along with validation that both isomers have the same targeting

properties *in vivo*, and this still may not satisfy the requirements of the regulators. Therefore it would be prudent to avoid this chelator when designing novel bioconjugates for one-step kits.

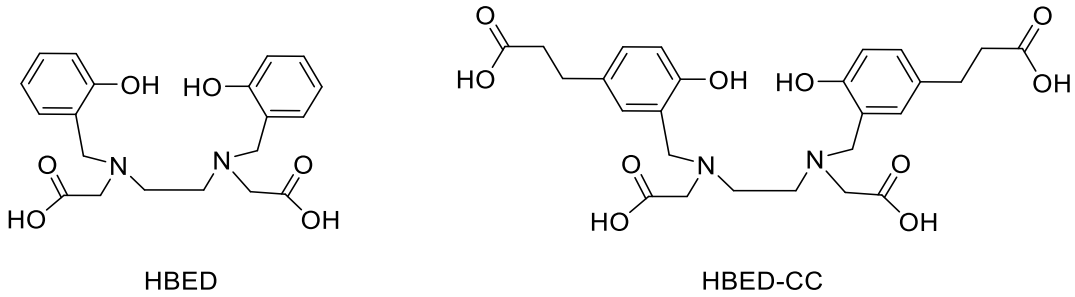

FIGURE 2.12: The structures of the HBED and HBED-CC chelators (36).

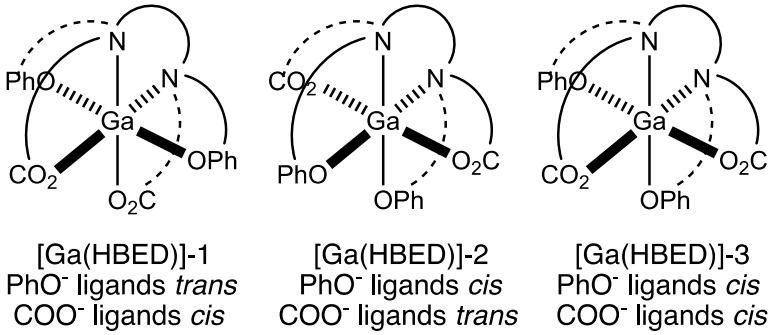

FIGURE 2.13: Possible geometric isomers for hexadentate [Ga(HBED)]. Note that each isomer depicted here is one of a pair of enantiomers [Ga(HBED)]-1 is the RR conformation, [Ga(HBED)]-2 the SS conformation and [Ga(HBED)]-3 the SR/RS conformation. Reproduced with permission from (36).

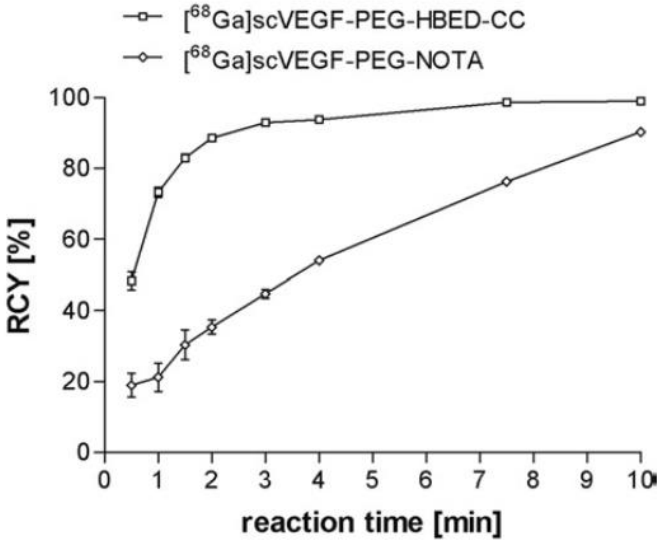

FIGURE 2.14: The difference in radiochemical yield for HBED-CC and NOTA conjugates at 25 µM bioconjugate, pH 4.2 and room temperature. Reproduced with permission from (57).

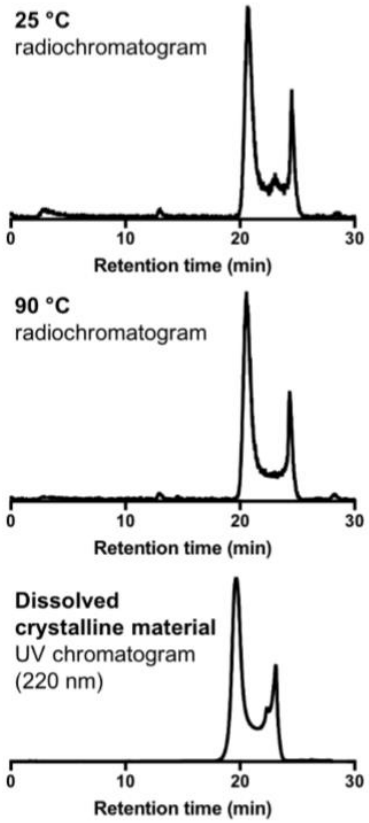

FIGURE 2.15: Reverse phase C_{18} HPLC radiochromatograms of [^{68}Ga]Ga-HBED after radiolabelling at 25°C (top) and 90°C (middle). At 25°C at least three distinct signals can be distinguished but at 90°C, only two distinct signals are observed. The same species were observed when radiolabelling was performed at pH 3.5 and pH 6.5. UV chromatogram (bottom) of a solution of dissolved crystalline [Ga(HBED)(H_2O)].CH_3CN. Reproduced from the supplementary material section of (36).

2.2.3.5 DFO

Desferrioxamine B (DFO) is an acyclic chelator, originally derived from bacteria, which binds gallium as an O_6 donor through its 3 hydroxamates (figure 2.16). However, its flexible structure means it has eight possible geometric isomers (*66*) as shown in figure 2.17. NMR studies of the Ga-DFO complex have shown that there are 2 major geometric isomers in solution, thought to be the N-cis, cis and C-trans, trans conformations (*66*). HPLC analysis of [^{68}Ga]Ga-DFO also showed multiple peaks (*36*). Quantitative radiolabelling with processed eluate from a germanium-68/gallium-68 generator has been demonstrated with DFO-bioconjugates at 12 µM within 10 minutes at pH 5.2 (*67*). The production of multiple species upon binding gallium, despite its mild radiolabelling conditions, show that the DFO chelator is incompatible with the criteria outlined above for a one-step kit.

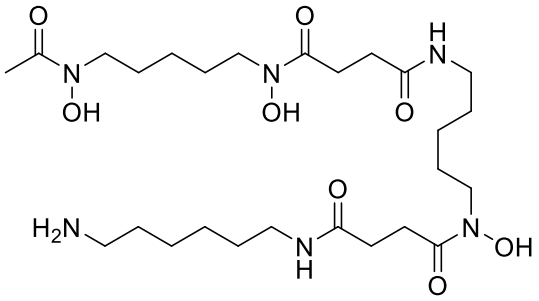

DFO

FIGURE 2.16: The structure of the DFO chelator (66).

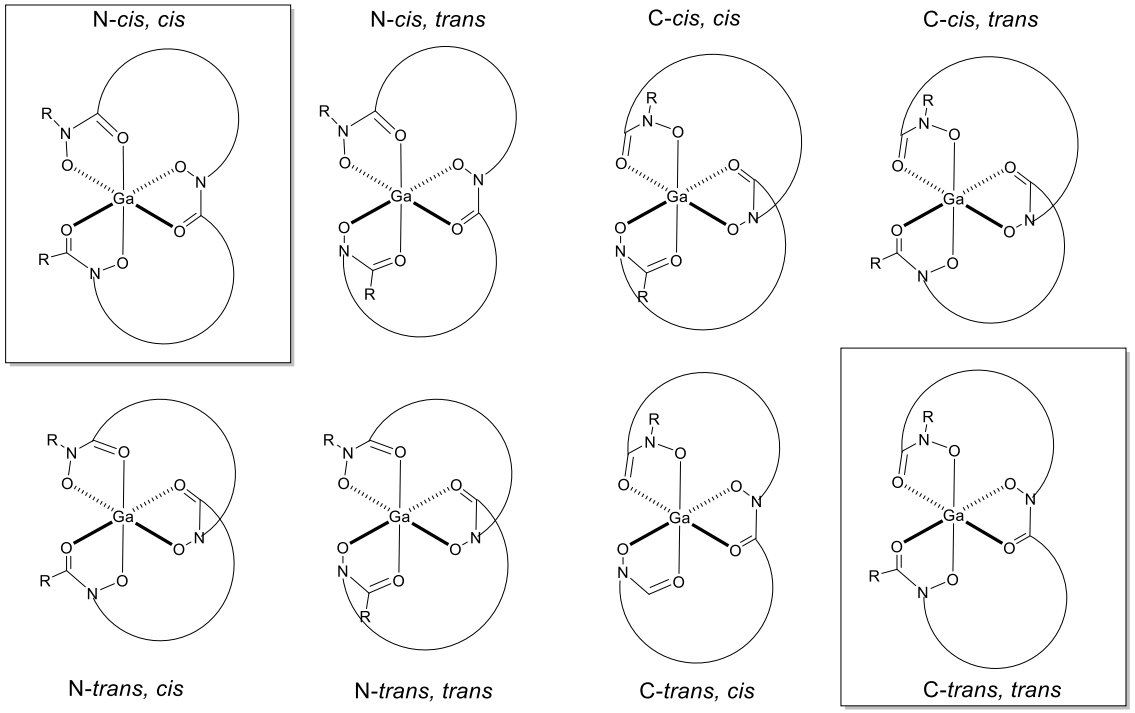

FIGURE 2.17: Structure of the eight possible Ga-DFO geometric isomers. The two geometric isomers believed to be present in solution are N-*cis, cis* and C- *trans,* trans (66).

2.2.3.6 DATA

The DATA (6-amino-1,4-diazepine triacetate) series of chelators form distorted octahedral complexes with gallium (III) as a N_3O_3 donor (*68*). The structures of a number of these variants are shown in figure 2.18. The 7 membered ring common to all of these chelators can form different conformations (chair, twist-chair, twist-boat, boat (*69*)) and so variants have been designed to favour only one of these conformations upon binding gallium. This has been achieved by the addition of sterically bulky substituents in the C6 position (Me or Ph group) which favours the equatorial positioning of this group and therefore the twist-chair

conformation (*68*). However, although the majority of DATA variants only produce one species upon binding gallium, the DATA^{M} variant also produces a second minor species at a ratio of 9:1 (*70*). The DATA series of chelators all show rapid (< 5 minutes), room temperature, quantitative labelling at pH 5 at concentrations of 5 µM (*71*). However, increases in pH to 7 or decreases to 4 reduced the radiochemical yield significantly, demonstrating the importance of precise pH control for these chelators (*71*). However, the DATA^{PPh} variant can still reach 95% RCP at 5 µM in 10 minutes at pH 7, whereas the RCP was < 85% for all other DATA variants tested under the same conditions. As these radiolabelling conditions were optimised with pre-processed eluate (acetone method) it is not known if these excellent radiolabelling properties could be achieved without such processing. However, it has been shown that a DATA^{M}-TOC conjugate can achieve 95% RCP after 1 minute at a concentration of 12 µM, pH 5, using fractionated eluate from a germanium-68/gallium-68 generator (*72*). The DATA chelators have also been shown to be sensitive to some metal contaminants, with radiochemical yields falling to under 95% at 4 equivalents of iron(III) and 1.25 equivalents of copper(II) (*71*). These chelators therefore provide a number of qualities required for use in a one-step kit.

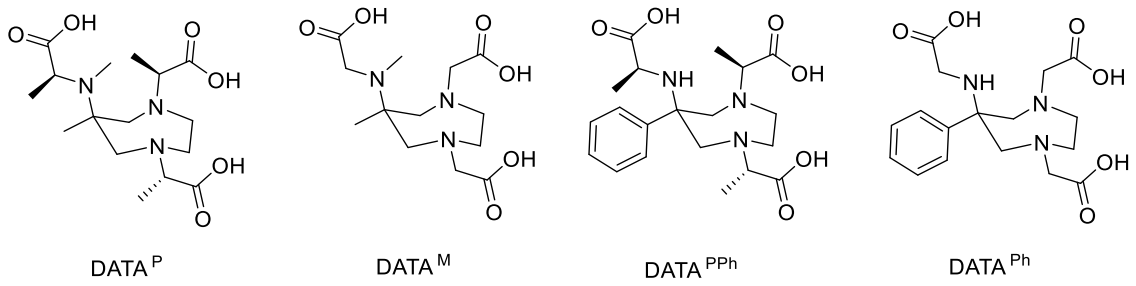

FIGURE 2.18: Structures of the DATA chelators (71).

2.2.3.7 THP

The THP (tris(hydroxypyridinone) chelator is a hexadente O_6 donor through its three 1,6-dimethyl-3-hydroxypyridin-4-ones, with each acting as a bidentate ligand. When their hydroxyl groups are deprotonated these 3,4-hydroxypyridinone units are electron rich oxygen donors due to the delocalisation of electrons over the pyridinone ring and are therefore well suited for binding hard Lewis acids such as gallium. The lengths of the three arms of the chelator are well matched to the ionic radius and coordination sphere of gallium and upon binding an uncharged complex is formed, which has a high Log K_{GaL} value (table 2.2). The tripodal design of THP with its three identical arms and C_3 symmetry avoids the formation of geometric isomers upon chelating gallium. It would allow the formation of delta and lambda enantiomers associated with all hexadentate tripodal chelators, but these would be expected to rapidly interconvert on the

biological timescale. THP can be converted into a bifunctional derivative by functionalisation at the hub of the tripodal scaffold, which is distant from the 3,4-hydroxypyridinone units and so does not affect gallium binding. A number of bifunctional derivatives have been developed which are shown in figure 2.19. Gallium-68 radiolabelling with THP and its derivatives can be performed using unprocessed generator eluate at room temperature, pH 6.5 and is complete within 5 minutes at concentrations of 0.5-10 μM (*36*)(*73*)(*74*). RCP was determined to be over 95% by iTLC and HPLC and showed a single species (*73*). Metal competition studies have shown that the THP chelator is very specific for gallium and radiolabelling is only affected by the presence of Fe, Al and Ti. These results are shown in figure 2.20. Additionally, its optimal radiolabelling conditions are near neutral pH which enables biological targeting agents that are sensitive to low pH, such as antibodies and single-chain fragments, to be radiolabelled with gallium-68 or gallium-67 (*73*)(*75*). [^{67}Ga]Ga-THP has also been shown to be resistant to transchelation to transferrin and human serum proteins for up to 4 hours (*73*). The stability of this complex has also been assessed in mice with the bioconjugates, [^{68}Ga]Ga-THP-mal-C2A (*73*), [^{68}Ga]Ga-THP-Ph-NCS-RGD (*76*), [^{68}Ga]Ga-THP-NCS-RGD (*76*), [^{68}Ga]Ga-THP-TATE (*74*) and none showed evidence of the presence of non-chelated gallium up to 60 or 90 minutes *in vivo,* the expected timeframe for imaging with gallium-68. Therefore THP demonstrates near-ideal properties for a chelator to be formulated into a one-step kit.

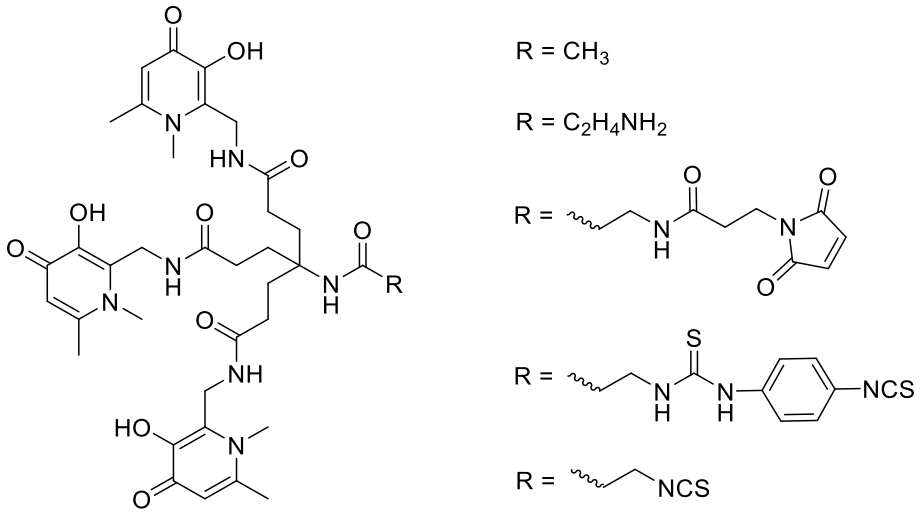

FIGURE 2.19: Structure of THP derivatives. Modified with permission from (77).

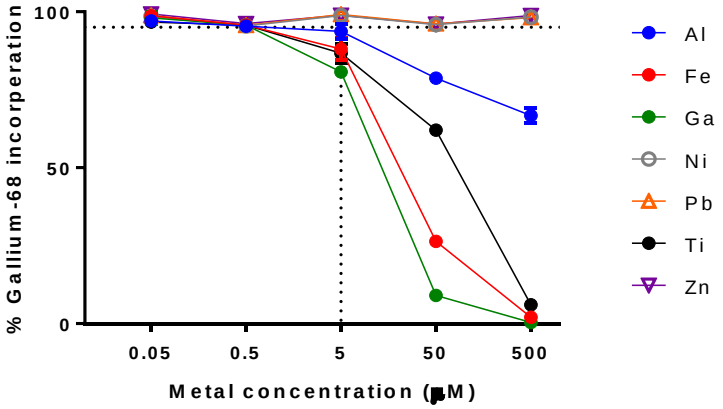

FIGURE 2.20: Incorporation of gallium-68 (2-6 MBq, room temperature, pH 6-7) by THP in the presence of increasing concentrations of metal ions (Al, Fe, Ga, Ni, Pb, Ti, Zn). The vertical dashed line indicates equal concentrations of chelator and contaminant (5 μM), horizontal dashed line indicates 95% radiochemical purity. Figure courtesy of Ruslan Cusnir, manuscript in preparation.

2.2.3.8 Comparative Studies

It is almost impossible to compare fairly the performance of different chelators using literature data, tested by different groups, in different experiments with gallium-68 from different sources, before or after pre-processing steps. Therefore well-designed comparative studies are essential to assess the performance of different chelators. This has been addressed in two studies, one where a range of chelators (DOTA, NOTA, HBED, THP) were assessed with their own optimal radiolabelling conditions over a range of ligand concentrations (figure 2.21) (*73*), and the second where a range of chelators (DOTA, NOTA, NOTP, TRAP, HBED, DFO, THP) were assessed over a range of concentrations under specific conditions (figure 2.22) (*36*). The first experiment showed that the RCP of all chelators tested dropped off at ligand concentrations below 10 μM but that [^{68}Ga]Ga-THP had the highest RCP of all chelators at 1 μM, even though it had the mildest radiolabelling conditions (pH 6.5, 5 minutes). In the second study, a broader range of ligands were studied (DOTA, NOTA, NOTP, TRAP, HBED, DFO, THP). Unfortunately, DATA chelators could not be included due to the lack of a commercial source. Radiolabelling was performed at pH 3.5 at 25°C, pH 6.5 at 25°C, pH 3.5 at 90°C and pH 6.5 at 90°C and the results are shown in figure 2.22. In assessing which chelators would be appropriate for one-step radiolabelling, the experiments performed at 25°C are the most informative. These investigations showed that all chelators performed poorly under 1 μM at a pH of 3.5, but that at pH 6.5 the chelators THP, DFO, NOTP and HBED performed well down to a concentration of 0.5 μM, with THP and DFO both achieving over 95% radiolabelling. This suggests that these two chelators would be the most suitable for a one-step kit. However, as discussed above of these

two chelators only THP produces a single species upon radiolabelling with gallium-68 and so would be the most appropriate to incorporate into a bioconjugate for a one-step kit.

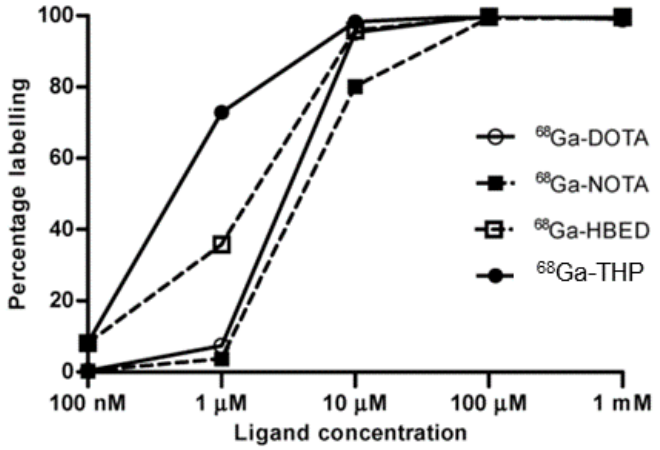

FIGURE 2.21: Radiochemical yield as a function of ligand concentration for [^{68}Ga]Ga-DOTA (pH 4.4, 30 min, 100°C), [^{68}Ga]Ga-NOTA (pH 3.6, 10 minutes, room temp), [^{68}Ga]Ga-HBED (pH 4.6, 10 minutes, room temp) and [^{68}Ga]Ga-THP (pH 6.5, 5 minutes). All experiments were conducted with the same batch of unprocessed gallium-68 eluate. All radiolabelling buffers were made with 0.2 M acetic acid/sodium acetate. Figure modified with permission from (73).

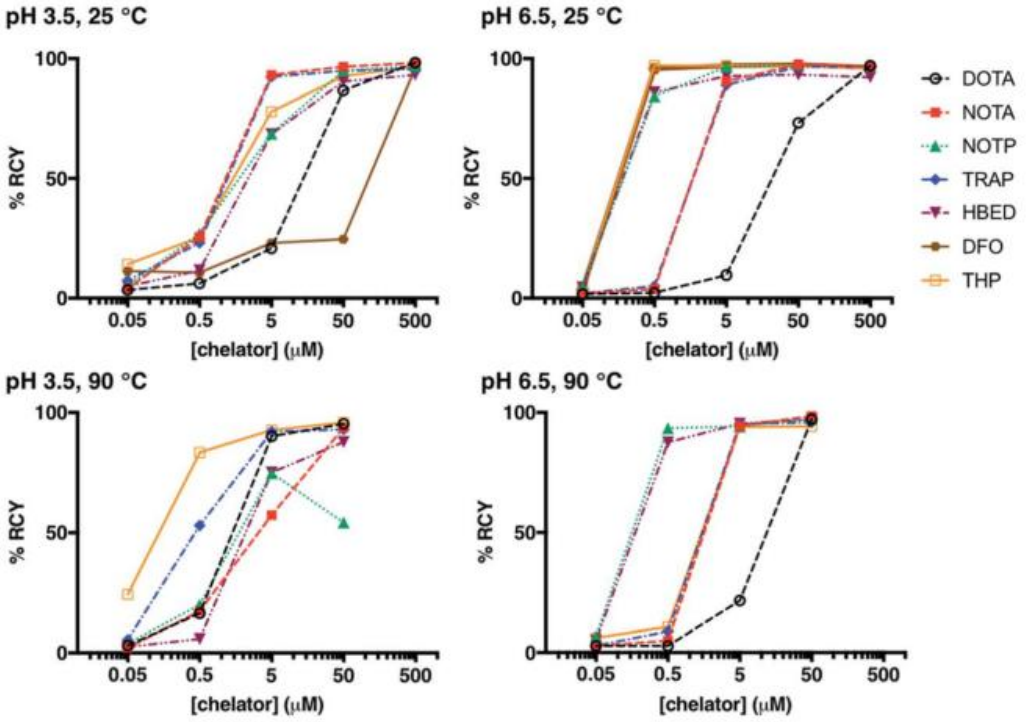

FIGURE 2.22: Radiochemical yields for the reaction of [^{68}Ga]Ga^{3+} with DOTA, NOTA, NOTP, TRAP, HBED, DFO and THP under different concentrations of chelator (500 mM to 50 nM), different pH conditions (pH 3.5 or pH 6.5), and different temperatures (25°C or 90°C), after 10 minutes reaction. Reproduced with permission from (36).

2.3 Applications for Gallium-68 One-Step Kits.

The two major applications of gallium-68 tracers are for imaging somatostatin-expressing neuroendocrine tumours and GCP(II)/PSMA-expressing prostate cancer. In this section, the current radiolabelling practices are discussed alongside the steps that have been taken towards one-step kit-based radiolabelling.

2.3.1 Gallium-68 Neuroendocrine Imaging

The only FDA- (*78*) and EMA-approved (*79*) clinical applications for gallium-68 PET imaging agents are [^{68}Ga]Ga-DOTA-TATE (in the US) and [^{68}Ga]Ga-DOTA-TOC (in Europe) for detection and staging of somatostatin receptor–positive neuroendocrine tumours. This approval, which was granted in 2016, was expedited by the tracer receiving an orphan drug designation in 2014 due to the rarity of neuroendocrine tumours (*80*). The structures of these bioconjugates are shown in figure 2.23. The FDA and EMA have granted the marketing approval to Advanced Accelerator Applications (Saint-Genis-Pouilly, France) who have commercialised [^{68}Ga]Ga-DOTA-TATE in the USA under the name NetSpot and [^{68}Ga]Ga-DOTA-TOC in Europe as SomaKit-TOC. It is available in two forms. The first as a ready-to-use dose of [^{68}Ga]Ga-DOTA-TATE delivered directly to hospitals, however, this is restricted to a select number of urban areas in the USA. Secondly, it is available as a two-vial kit for reconstitution in a radiopharmacy using the GalliaPharm generator (*44*).

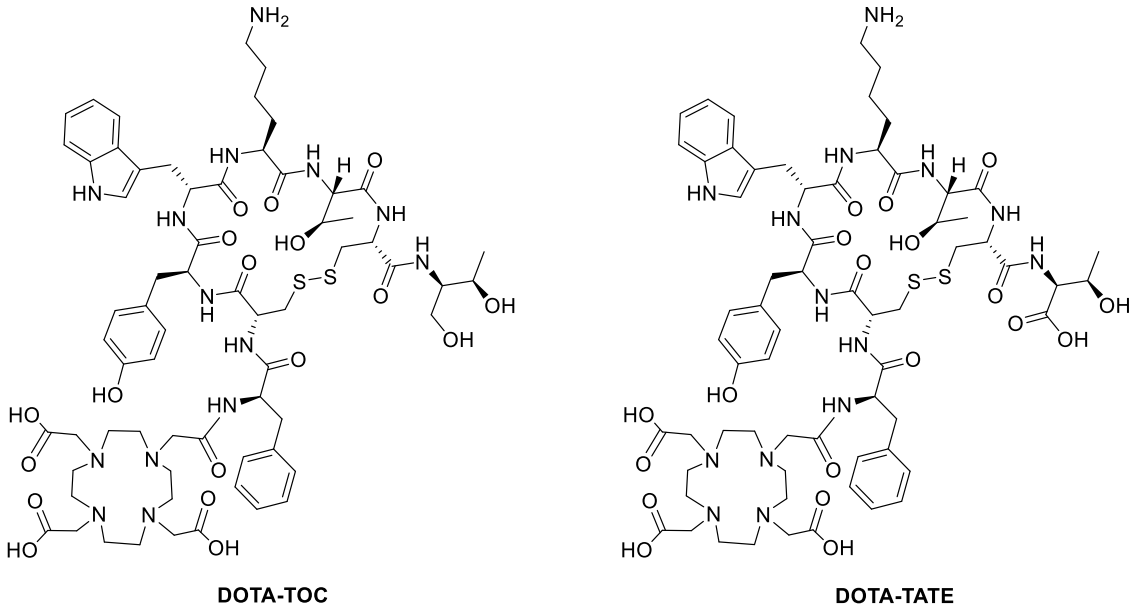

FIGURE 2.23: The structures of DOTA-TOC and DOTA-TATE (81).

2.3.1.1 Radiolabelling with an Automated Synthesis Module

Before the marketing approval of NetSpot or SomaKit-TOC kits, it was most common for radiolabelling of [^{68}Ga]Ga-DOTA-TATE or [^{68}Ga]Ga-DOTA-TOC to be carried out with an automated synthesis module and this will remain the favoured method for many sites. Such synthesis can be used to generate these tracers for use within research studies or under regulations for non-approved radiopharmaceuticals and so are worth discussing here. There are a number of different automated synthesis methods described in the literature (*27*)(*82*), and the most appropriate choice depends on the generator and automated synthesis module available and is therefore likely to be different at every site.

An example methodology from Royal North Shore Hospital, Sydney, Australia is described below. This method has been used for 500 runs over 3 years and the radiochemical yields and purity obtained have been reported alongside synthesis failure rates (*27*). A Modular Lab PharmTracer® (Eckert & Ziegler, Berlin, Germany) automated synthesis system controlled by the Modular Lab PharmTracer® (Eckert & Ziegler) software was used along with single-use synthesis cassettes (C4-GA68-PP Eckert & Ziegler) and the Galliapharm germanium-68/gallium-68 generator (Eckert & Ziegler). The setup for the automated synthesis model required the removal of the cassette from its sterile packaging and attachment to the module, followed by a 5 minute cassette pressure test. The high purity pharmaceutical grade reagents (0.9% saline, ethanol, pre-processing eluent (0.02 M HCl in 98% acetone) and DOTA-TATE peptide in acetate buffer) and cartridges (one ion-exchange and one C_{18} reverse phase) were then added to the cassette and the generator attached. Once setup was complete the automated synthesis was initiated and took 33 minutes to run. The radiolabelling involved the following automated steps: 1) The generator was eluted with 0.1 M HCl and the eluate concentrated on an ion exchange cartridge; 2) The ion exchange cartridge was then eluted with 0.02 M HCl in 98% acetone and transferred into the reaction vial which already contained 40 μg DOTA-TATE peptide in acetate buffer; 3) The reaction mixture was heated at 95°C for 400 seconds to form [^{68}Ga]Ga-DOTA-TATE and evaporate the acetone; 4) The contents of the reaction vial were removed and passed through a C_{18} cartridge, trapping the [^{68}Ga]Ga-DOTA-TATE; 5). The C_{18} cartridge was then eluted with ethanol through a sterile filter into the product vial followed by a saline wash. Once radiosynthesis was completed QC procedures were conducted before batch release. Each run produced [^{68}Ga]Ga-DOTA-TATE with a RCP of over 95% by HPLC and iTLC and decay corrected radiochemical yields of at least 81.8 ± 0.4%.

Because of the complicated set-up of an automated synthesis rig and the number of moving parts, there is a broad range of issues that can cause the automated synthesis to fail. In 1.6% of synthesis over the 3 years of the study, the problems were so major that production had to be cancelled for that day and no patients could be scanned. Reasons for these failures included leaks within the cassette, the ion exchange cartridge failing to elute, the syringe driver breaking, and high retention of activity on the C_{18} cartridge. On top of this figure 2.24 summarises additional more minor failures that occurred over the same 3 year period and their frequency.

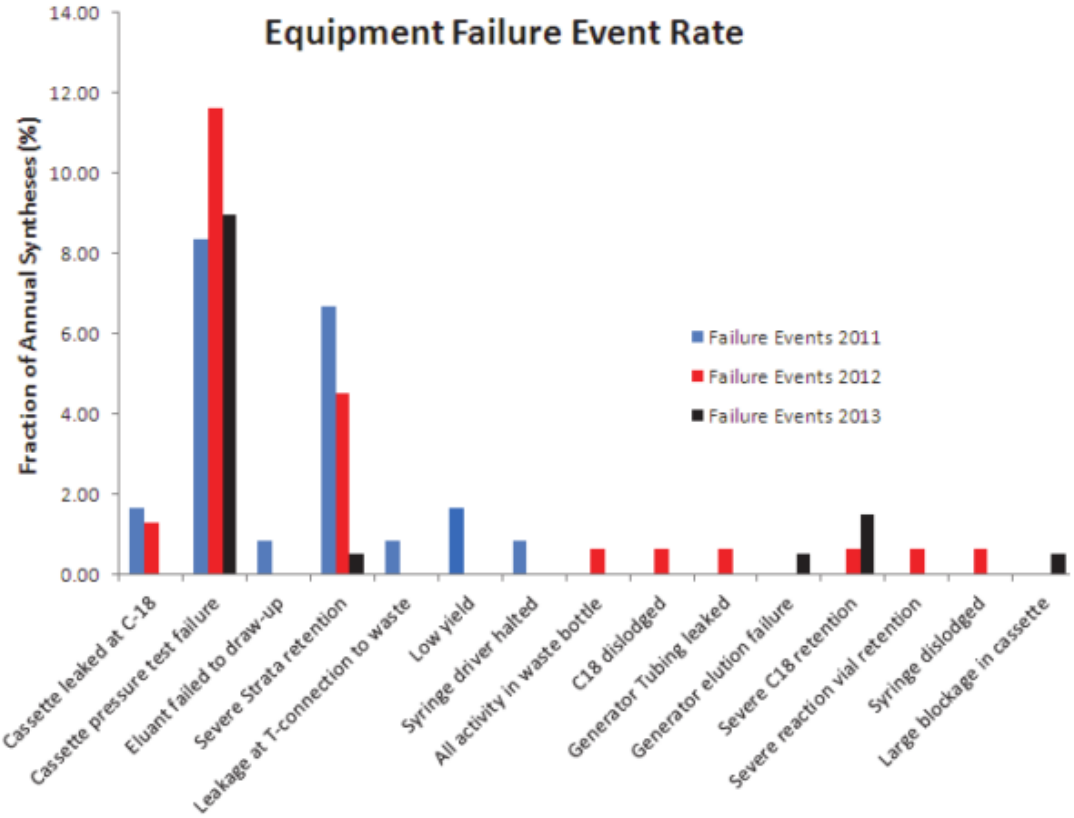

FIGURE 2.24: Rate and type of radio-synthesis failures for an automated synthesis rig, used to produce [^{68}Ga]Ga-DOTA-TATE over three years. These failures were due to either cassettes or the automated synthesis rig not performing as required. Reproduced with permission from (27).

2.3.1.2 Radiolabelling with Commercially Available Kits

As discussed above, there are two commercially available kits for neuroendocrine imaging, NetSpot and Somakit-TOC, both from Advanced Accelerator Applications. The NetSpot kit contains DOTA-TATE and the Somakit-TOC kit contains DOTA-TOC as the active ingredients. All other aspects of the kits are the same and so the contents and reconstruction process described below are applicable to both kits (*44*). As the kits do not have a pre-processing step they must be used only with the GalliaPharm generator (*32*). The kits consist of two vials and a silica

cartridge. Both vials are septum-sealed and sterile. The first becomes the reaction vial and contains the following lyophilised components: 40 µg DOTA-TATE or DOTA-TOC, 5 µg 1,10-phenanthroline, 6 µg gentisic acid and 20 mg mannitol (*44*). The second contains a buffer solution, consisting of 60 mg formic acid, 56.5 mg sodium hydroxide and 1 mL water for injection (*44*). The cartridge contains 660 mg porous silica, and is used to reduce the amount of germanium-68 in the generator eluate (although this should already be < 0.001%). The radiolabelling process using these kits proceed as follows (*44*). The generator is eluted with 5 mL of 0.1 M HCl which is passed through the silica cartridge (USA only) and into vial 1, which must be vented. Then 0.5 mL of the buffer within vial 2 is added to vial 1 which is then heated to 95°C for 7 minutes in a heating block. Then the vial is removed and allowed to cool to room temperature for 10 minutes. A sample is then removed for QC. This process is summarised in figure 2.25 and takes at least 20 minutes to perform.

With these kits the process is shorter, requires much less equipment, is much simpler to set up, and is likely to be better controlled and give more consistent results than using the automated synthesis rig. However, the process still requires 2 vials and a heating step, and so needs to be simplified further to reach the ideal one-step kit process.

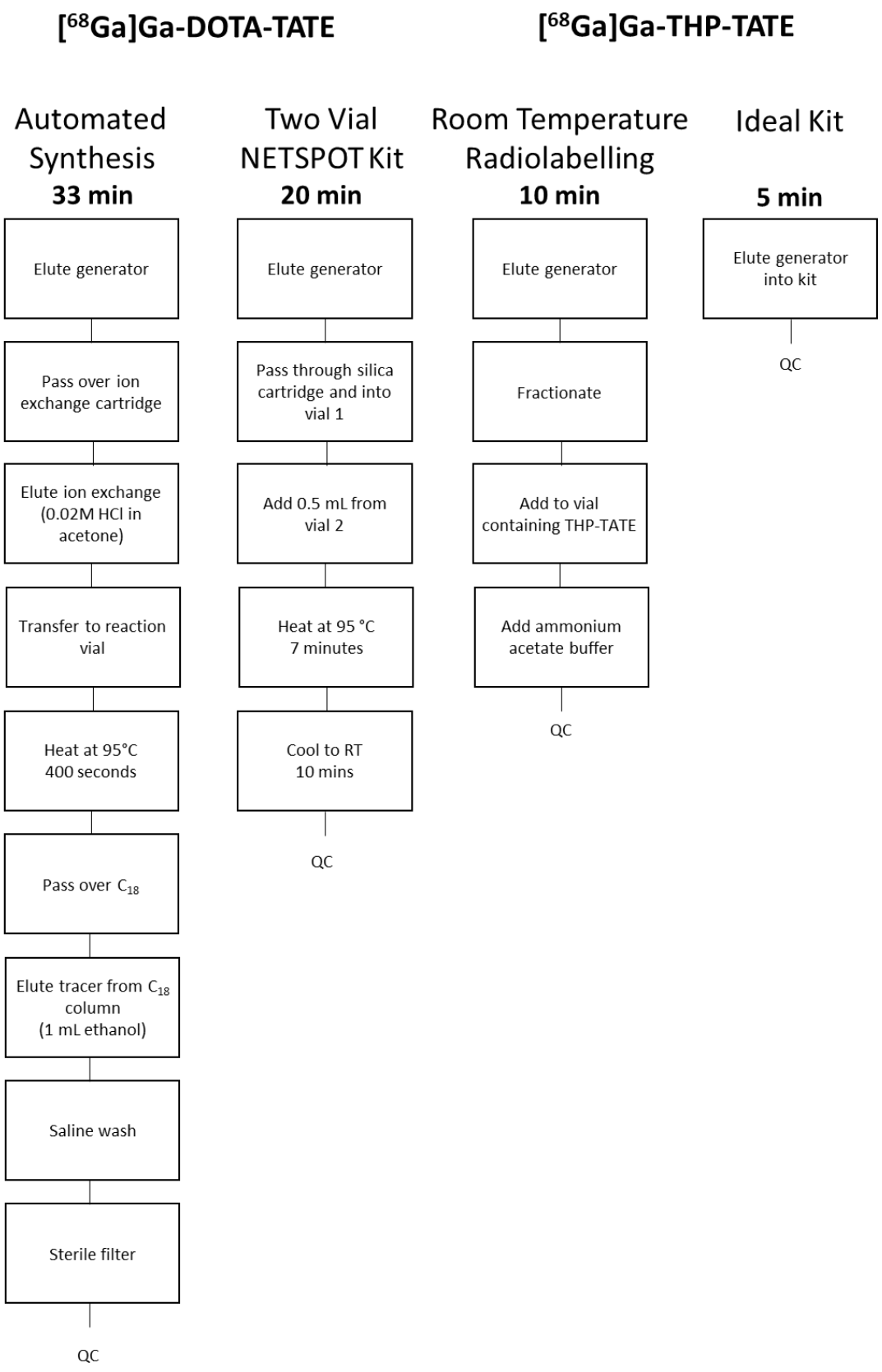

FIGURE 2.25: Flowchart describing the radiolabelling process for [^{68}Ga]Ga-DOTA-TATE or [^{68}Ga]Ga-THP-TATE, compared to the ideal one-step kit.

2.3.1.3 Single Vial Kits for Neuroendocrine Tumours

It has been demonstrated that a single rather than a two-vial kit can be used for radiolabelling of gallium-68-based tracers for neuroendocrine tumours with DOTA-TOC (*83*) DOTA-TATE (*84*), DOTAGA-TOC (*81*) and DOTAGA-TATE (*81*). The structures of these bioconjugates are shown in figure 2.23 and figure 2.26. These studies demonstrated that the correct pH for radiolabelling can be reached with a lyophilised single kit, but a heating step to 95°C is still required for radiolabelling to proceed. These studies used amounts of bioconjugate similar to that in the commercial kits (30-50 µg) and the radiolabelled product passed all QC tests.

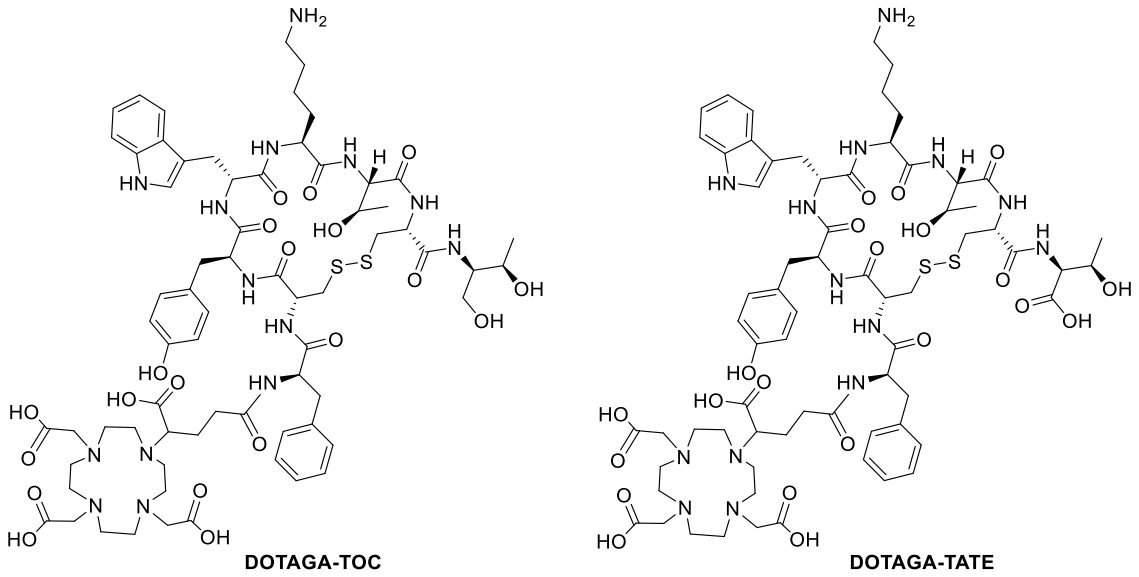

FIGURE 2.26: The structure of DOTAGA-TOC and DOTAGA-TATE (81).

2.3.1.4 Alternative Bioconjugates for Imaging Neuroendocrine Tumours

In order to avoid the heating step required for DOTA and DOTAGA, alternative chelators which bind gallium-68 quantitatively at room temperature in 10 minutes or less have been conjugated to TOC or TATE peptides. NODAGA-TATE (*56*), DATA-TOC (*72*) and THP-TATE (*74*) (figure 2.27) all show simple, room temperature radiolabelling, however, none have yet demonstrated they can be formulated into in a lyophilised one-step kit. Additionally, the pH required for such radiolabelling differs between the conjugates (NODAGA-TATE pH 3.5, DATA-TOC pH 4.2, THP-TATE pH 6). Room temperature radiolabelling for [^{68}Ga]Ga-NODAGA-TATE was performed in a two-step process (*56*). Firstly the gallium-68 from the generator (0.1 M HCl) was neutralised with sodium acetate buffer, and then NODAGA-TATE was added and the mixture incubated at room temperature for 10 minutes. The minimum final concentration of NODAGA-TATE required to obtain a RCP better than 95% as analysed by HPLC, was 10 µM. The simplest radiolabelling

procedure described for DATA-TOC (*72*) was conducted as follows: 13 nmol of DATA-TOC was dissolved 0.2 mL 1 M ammonium acetate and then 0.9 mL of fractionated gallium-68 eluate (0.1 M HCl) was added to the reaction vial. The solution was briefly vortexed and left to stand at ambient temperature for 10 minutes giving a final pH of 4.2 and a DATA-TOC concentration of 12 µM. [^{68}Ga]Ga-DATA-TOC was produced in over 95% radiochemical yield as determined by iTLC. The simplest radiolabelling described for THP-TATE (*74*) was again very similar. 1 mL of fractionated gallium-68 eluate (0.1 M HCl) was added to a 50 µL solution of THP-TATE (50:50 ethanol/water, 12 nmol) immediately followed by ammonium acetate buffer (2 M, 200 µL). The solution was left to stand at ambient temperature for 2-5 minutes which gave a final pH of 5-6 and a THP-TATE concentration of 10 µM. [^{68}Ga]Ga-THP-TATE was produced in over 95% radiochemical yield as determined by iTLC and HPLC. All three conjugates therefore demonstrate, simple, quantitative radiolabelling processes at similar concentrations (10-12 µM) close to those suitable for one-step kit preparation with adequate molar activity (<10 µM).

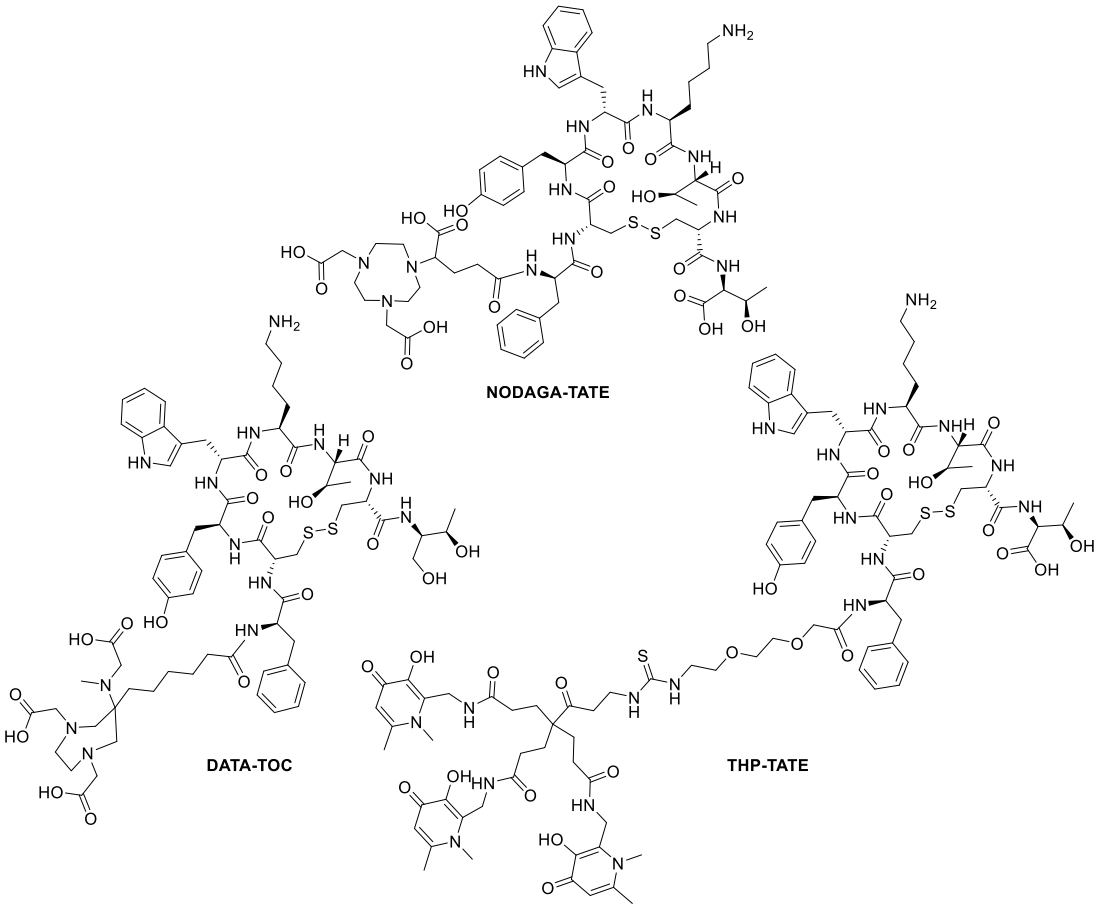

FIGURE 2.27: The structures of NODAGA-TATE (56), DATA-TOC (85) and THP-TATE (74)

The radiolabelling methods for DATA-TOC and THP-TATE relied on ammonium acetate as the neutralising and buffering agent, which is not an excipient approved for human use and is also

volatile and therefore unsuitable for lyophilisation, meaning reformulation of this buffer would be required before a true one-step kit can be developed. It would also be ideal for any kit developed to be able to cope with the full elution volume of a generator to remove the need for a fractionation process and creating a one-step radiolabelling procedure.

In order to ensure that the change of chelator did not impact the somatostatin targeting of the tracers both [^{68}Ga]Ga-DATA-TOC (*85*) and [^{68}Ga]Ga-THP-TATE (*74*) have been evaluated in a mouse model of neuroendocrine cancer, but surprisingly [^{68}Ga]Ga-NODAGA-TATE has not progressed to preclinical studies. Both [^{68}Ga]Ga-DATA-TOC (*85*) and [^{68}Ga]Ga-THP-TATE (*74*) demonstrated targeting to somatostatin-expressing tumours which could be specifically blocked by the co-injection of TATE peptide. However, when [^{68}Ga]Ga-DATA-TOC and [^{68}Ga]Ga-THP-TATE were compared to their DOTA analogues in a mouse model, the biodistributions observed were not identical, confirming the chelator portion of a bioconjugate can impact on the biological properties of a tracer. [^{68}Ga]Ga-DATA-TOC is currently undergoing clinical evaluation (*86*) and it will be interesting to see if these differences in biodistribution or targeting ability occur in human studies as well.

2.3.1.5 Conclusion on Neuroendocrine Labelling with Gallium

The marketing approval of and commercialisation of two-vial kits for [^{68}Ga]Ga-DOTA-TATE and [^{68}Ga]Ga-DOTA-TOC production demonstrate the appeal of kit-based formulations. Alternative bioconjugates have shown that simplified radiolabelling can be achieved with the right chelator but that chelator choice can influence targeting efficiency. These results move the field towards the development of one-step kits for gallium-68-based radiopharmaceuticals. Now that DOTA-TATE and DOTA-TOC have been approved by regulatory authorities it is unlikely that novel conjugates will replace them due to the time and costs involved. However, this idea could be applied to new gallium-68 tracers which show clinical promise but have not yet received regulatory approval, and may in fact, expedite their translation into the clinic.

2.3.2 Gallium-68 PSMA Tracers

As discussed in chapter 1 GCP(II)/PSMA targeted radiopharmaceuticals show great clinical promise for imaging prostate cancer, and have demonstrated utility in both initial staging and in cases of biochemical recurrence. Here the radiolabelling for the gallium-68 PSMA tracers that have already been developed will be reviewed in the context of one-step kit development to determine whether novel bioconjugates would be required to achieve this. The three most important gallium-based PSMA tracers are [^{68}Ga]Ga-HBED-CC-PSMA, [^{68}Ga]Ga-DOTA-

PSMA(617) and [^{68}Ga]Ga-DOTAGA-PSMA(I&T). Radiolabelling of DOTA-based PSMA tracers [^{68}Ga]Ga-DOTA-PSMA(617) and [^{68}Ga]Ga-DOTAGA-PSMA(I&T) has only been described using automated synthesis modules (*87*)(*88*)(*89*). The automated synthesis of [^{68}Ga]Ga-DOTA-PSMA(617) and [^{68}Ga]Ga-DOTAGA-PSMA(I&T) is extremely similar to those used for [^{68}Ga]Ga-DOTA-TOC and [^{68}Ga]Ga-DOTA-TATE discussed above because they all utilise the DOTA chelator. Therefore the individual protocols of these tracers will not be discussed here. Instead, this section will focus on the most widely used [^{68}Ga]Ga-PSMA tracer, [^{68}Ga]Ga-HBED-CC-PSMA, which utilises the HBED-CC chelator and therefore has its own unique considerations for radiolabelling.

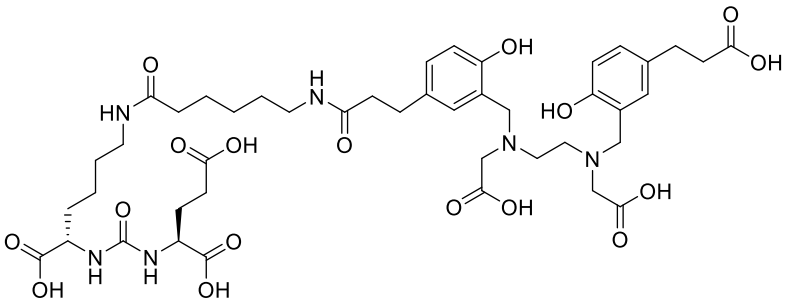

FIGURE 2.28: The structure of HBED-CC-PSMA (90).

2.3.2.1 Explanation of Isomers of [^{68}Ga]Ga-HBED-CC-PSMA

As discussed above HBED is an acyclic chelator with optimal radiolabelling at room temperature and pH 4. However, its structure, consisting of 6 groups of 3 different donor types means that upon binding at least 3 HBED isomers can form, the RR, RS, and SS**.** Rather than the HBED chelator, [^{68}Ga]Ga-HBED-CC-PSMA utilises the HBED-CC chelator which has an additional pendant carboxylic acid group attached to each of the phenol rings allowing the chelator to be functionalised. In HBED-CC-PSMA one of these additional carboxylic acid groups is attached to an aminohexanoic acid linker and which is in turn attached to the side chain of the lysine within the GCP(II)/PSMA targeting pharmacophore (Lys-C(O)-Glu) and the other remains free as shown in figure 2.28. The functionalisation of HBED-CC with PSMA makes the two phenol donor groups of the chelator inequivalent; one is attached to the GCP(II)/PSMA targeting moiety and the other has a pendant carboxylic acid. This means the RS and SR conformations also become inequivalent increasing the number of possible geometric isomers from 3 to 4 as shown in figure 2.29. Each of these geometric isomers will be present as a racemic mixture of its two enantiomers (lambda and delta with respect to metal binding).

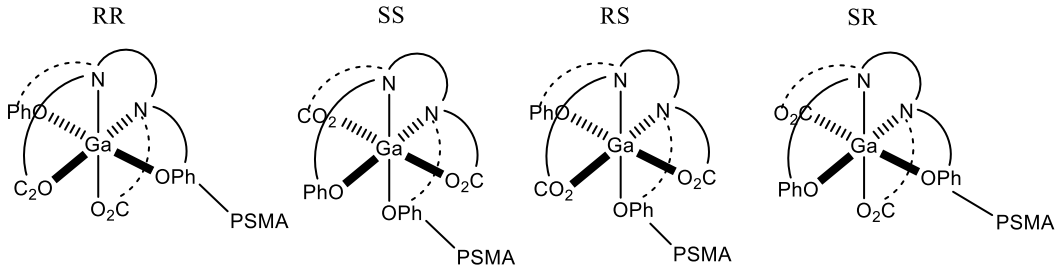

FIGURE 2.29: The possible geometric isomers for hexadentate Ga-HBED-CC-PSMA RR, SS, RS and SR. Note that SR and RS are not equivalent, unlike [Ga-HBED]. Each isomer depicted here is one of a pair of enantiomers.

Despite the complexities described above, only two separable species were observed in the HPLC of [^{68}Ga]Ga-HBED-CC-PSMA when radiolabelling was performed at room temperature (figure 2.30) (*65*). However, it is important to note that this could be due to the HPLC conditions used and does not prove there were only two species present. The two peaks observed occur in a ratio of 1:1 (area under the radio-peak). However, when radiolabelling was performed at 95°C the ratio changed to 9:1 as shown in figure 2.30. The major species is proposed from NMR studies (*64*) to be the RR conformation, which due to minimised steric hindrance should be the most thermodynamically favoured as the phenol donor groups are *trans*. When this mixture was left for 3 hours in the buffer used for patient injection, in order to mimic the maximum time between synthesis and patient injection, the ratio of these two peaks stayed at this 9:1 ratio (figure 2.31). This demonstrates that further interconversion does not occur and suggests that the major peak is the more thermodynamically stable. Conversion from the 1:1 ratio to the 9:1 ratio can also be achieved by controlling the pH. If [^{68}Ga]Ga-HBED-CC-PSMA is radiolabelled at room temperature producing the 1:1 ratio and then stored at pH 4 and pH 7 for 3 hours the sample stored at pH 7 remains at the 1:1 ratio but the one at pH 4 converts to the 9:1 ratio (figure 2.32). This finding is confirmed by earlier observations where interconversion of [^{67}Ga]Ga-HBED-CC at pH 7 into the most stable geometric isomer took 7 days. However, this was at a concentration of >2 mM which appears to encourage the formation of the less thermodynamically stable species (*91*).

These results suggest that there are at least two geometric isomers that are favoured by kinetics at room temperature with micromolar concentrations of HBED-CC-PSMA and therefore form rapidly (~2 minutes) (*65*). However, the thermodynamically favoured species can be preferentially formed by incubation at pH 3.5 or 95°C. Of these the much quicker method, and therefore the only one suitable for radiochemical synthesis with gallium-68 is heating to 95°C for 10 minutes. However, this only produces ~90% of the most favoured complex, rather than a single species. For comparison in clinical radiolabelling procedures for [^{68}Ga]Ga-DOTA-TATE, the

minimum RCP required for administration is higher at 91% with the remaining activity known to be only unchelated gallium-68, rather than an alternative radiolabelled complex (*24*). In technetium-99m kits the RCP required is normally >95% but this is only measured by iTLC and it is known that in some cases many species are formed, as discussed earlier.

The concerns surrounding the presence of multiple species is that these may have different GCP(II)/PSMA targeting abilities or biodistributions that would impact on detection rates, the quality of the image produced or other clinically-relevant parameters. The performance of [^{68}Ga]Ga-HBED-CC-PSMA and [^{nat}Ga]Ga-HBED-CC-PSMA, made at room temperature and those made at 95°C have only been compared *in vitro* (*65*). These results showed minimal differences between IC_{50} values of [^{nat}Ga]Ga-HBED-CC-PSMA produced by these two methods (27.4 ± 1.3 nM and 24.8 ± 1.2 nM) or between the uptake of [^{68}Ga]Ga-HBED-CC-PSMA in GCP(II)/PSMA expressing cells as shown in figure 2.33**.** These results suggest there would be no difference in affinity between the tracers made by the two methods. However, no comparative studies have been done in animal models or clinical studies and geometric isomers could behave differently under these conditions to what is seen *in vitro*. In order to minimise concerns about having two major species present the majority of published clinical studies for [^{68}Ga]Ga-HBED-CC-PSMA use a heating step of 95°C for 10 minutes to obtain ~90% of the major species (*65*)(*92*)(*93*).

Presently it is unknown what stance the regulatory bodies will take on the presence of multiple isomers of [^{68}Ga]Ga-HBED-CC-PSMA, and whether the heating step provides a high enough radiochemical purity to overcome any concerns. However, it is very likely that this issue would be raised during the approval process and that more extensive evidence into the complexes formed, and any differences in their performance will be required. These multiple species may therefore create a large barrier to gaining regulatory approval or marketing authorisation for [^{68}Ga]Ga-HBED-CC-PSMA and any other tracers incorporating the HBED or HBED-CC chelator. This would mean that access to these tracers would remain restricted to larger research hospitals which can produce it within research studies or under regulations for non-approved radiopharmaceuticals, rather than it becoming the standard of care and a reimbursable diagnostic tool.

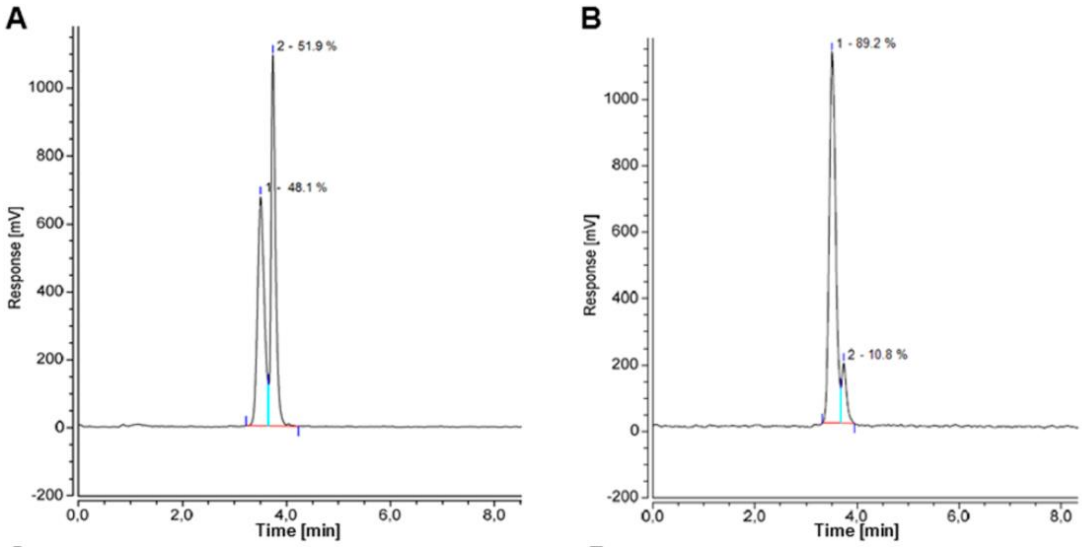

FIGURE 2.30: Radio-HPLC traces of [^{68}Ga]Ga-HBED-CC-PSMA radiolabelled (A) room temperature radiolabelling (B) 95 °C radiolabelling. The peaks correspond to (**1**), the thermodynamically more stable, and (**2**), the thermodynamically less stable geometric isomer. Modified with permission from (65).

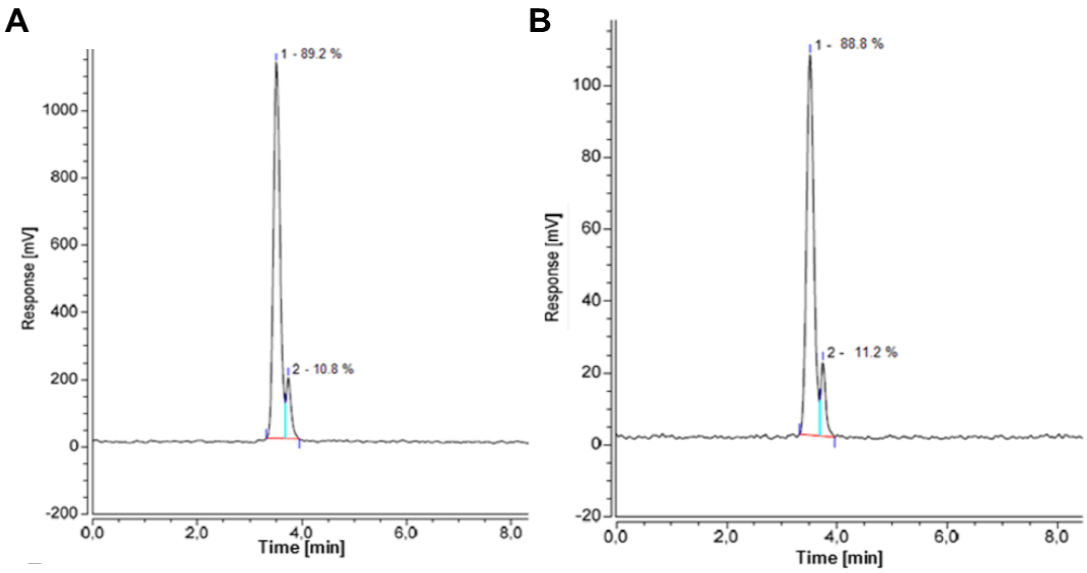

FIGURE 2.31: Radio-HPLC traces of [^{68}Ga]Ga-HBED-CC-PSMA radiolabelled at 95 °C (A) just after radiolabelling is complete (B) and after subsequent storage in the injection buffer (2 mL ethanol, 8 mL phosphate buffered saline (PBS)) for 3 hours. The peaks correspond to (**1**), the thermodynamically more stable, and (**2**) the thermodynamically less stable geometric isomer. These graphs demonstrate that the ratio of the peaks remains the same for 3 hours under these conditions. Modified with permission from (65).

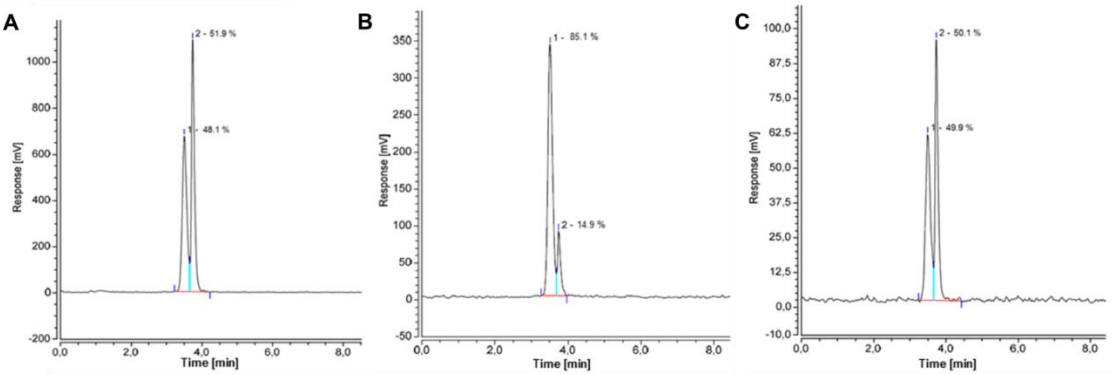

FIGURE 2.32: Radio-HPLC traces of [^{68}Ga]Ga-HBED-CC-PSMA radiolabelled at room temperature (A) radiolabelling just after radiolabelling is complete, (B) after subsequent storage at pH 4 for 3 hours (showing its conversion to the more thermodynamically stable geometric isomer and (C) after storage at pH 7 for 3 hours; under the latter conditions no conversion of the isomers is seen. The peaks correspond to (**1**), the thermodynamically more stable, and (**2**) the thermodynamically less stable geometric isomer. Modified with permission from (65).

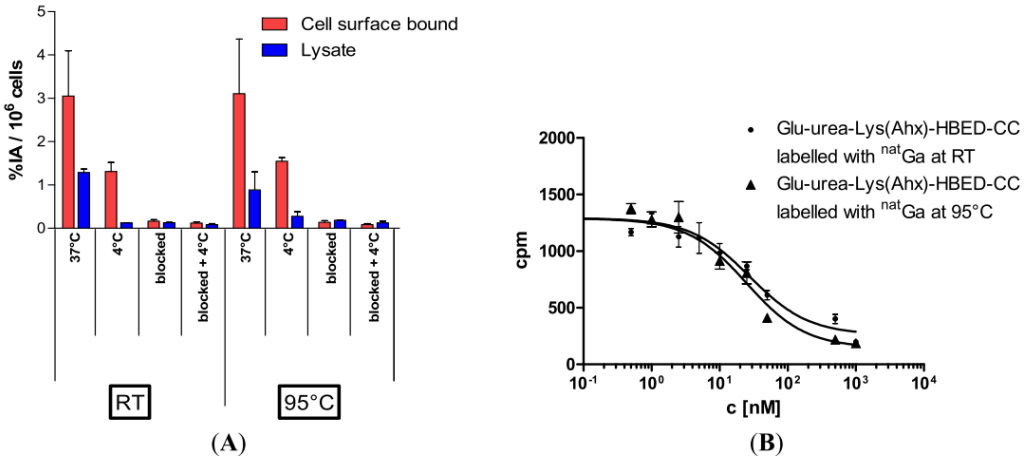

FIGURE 2.33: (A) LNCaP-cell binding and internalisation of [^{68}Ga]Ga-PSMA-HBED-CC labelled at room temperature or 95 °C, respectively. 500 µM 2-PMPA was used for blocking studies. Data are expressed as mean ± SD (n = 3); (B) IC_{50} determination for [^{nat}Ga]Ga-PSMA-HBED-CC labelled at room temperature and at 95 °C. [^{68}Ga]Ga-HBED-CC-PSMA was used as the probe. Reproduced with permission from (65).

When considering the development of [^{68}Ga]Ga-HBED-CC-PSMA into a one-step kit these questions around the different species formed also need to be addressed. If the multiple isomers are an issue then a heating step becomes mandatory and it is not possible to develop this bioconjugate into a one-step kit. As the majority of the clinical work has been done with this heating step, clinical studies would need to be repeated with a mixture of the two geometric isomers formed at room temperature. Therefore it would be ideal to have a one-step kit, without a heating step which did not produce multiple geometric isomers. For this, an alternative bioconjugate would be required.

2.3.2.2 Automated Synthesis of [^{68}Ga]Ga-HBED-CC-PSMA (*65*)

The most-referenced automated synthesis methodology for [^{68}Ga]Ga-HBED-CC-PSMA (*65*) is summarised below but other variations exist and methods are likely to vary significantly from site to site due to the range of generators and synthesisers used. A Scintomics GRP (Fürstenfeldbruck, Germany) fully automated synthesis module with a control centre and GRP-interface software were used along with disposable cassette kits (ABX advanced biochemical compounds) and the IDB-Holland BV generator (Baarle-Nassau, The Netherlands). The setup for the automated synthesis module required the removal of the cassette from its sterile packaging and attachment to the module, followed by a cassette pressure test. The high purity pharmaceutical grade reagents (5 M NaCl solution, ultrapure water, ethanol:water (1:1, v:v), and HBED-CC-PSMA peptide in acetate buffer containing ascorbic acid) and cartridges (one cation exchange and one C_{18} reverse phase) were then added to the cassette and the generator attached. Once setup was complete the automated synthesis was initiated and took 35 minutes to run. The radiolabelling involved the following automated steps: 1) The generator was eluted with 10 mL of 0.6 M HCl which was diluted with 9 mL of ultrapure water and passed through an ion exchange cartridge; 2) The ion exchange cartridge was then eluted with 5 M NaCl solution into the pre-heated reaction vial which contained HBED-CC-PSMA (1.9 µg, 2 nmol) in acetate buffer and ascorbic acid; 3) The reaction mixture was heated at 100°C for 10 minutes to form [^{68}Ga]Ga-HBED-CC-PSMA; 4) The contents of the reaction vial were removed and passed through a C_{18} cartridge, trapping [^{68}Ga]Ga-HBED-CC-PSMA; 5) 9 mL ultrapure water was used to rinse the reaction vessel and the C_{18} cartridge, and the C_{18} cartridge was washed with a further 5 mL of ultrapure water; 6) The C_{18} cartridge was then eluted with 2 mL of a 1:1 (v:v) ethanol:water mix through a sterile filter and then diluted in 8 mL phosphate buffered saline (PBS). Once this radio-synthesis was completed QC procedures were conducted before batch release. Each run produced [^{68}Ga]Ga-HBED-CC-PSMA with decay-corrected radiochemical yields of 80% ± 5% and RCP over 99% by HPLC and iTLC if the two diastereomers were combined and 89% if only the more thermodynamically stable isomer was included (the two isomers were distinguishable by HPLC but not iTLC).

2.3.2.3 Single Vial Kits for [^{68}Ga]Ga-HBED-CC-PSMA Imaging

The need for an automated synthesis rig for [^{68}Ga]Ga-HBED-CC-PSMA radiolabelling has been questioned in recent publications (*94*), especially when using generator eluate which has low germanium-68 breakthrough. Instead, formulations for single vial kits have been developed and shown to achieve suitable radiochemical yields (*95*)(*96*). Only some of these kits retained the

heating step. The radiolabelling procedure for a kit which included a heating step can be summarised as follows. Lyophilised vials containing 21 nmol (20 µg) HBED-CC-PSMA and 98 mg sodium acetate were prepared and then radiolabelling was performed by the addition of 2 mL of the fractionated eluate from an ITG germanium-68/gallium-68 generator (0.05 M HCl) to the vial followed by heating at 85 °C for 10 minutes (*95*) and QC. A published method without a heating step (*96*) used very similar lyophilised kits, containing 5 nmol (5 µg) HBED-CC-PSMA and 98 mg sodium acetate trihydrate. These were radiolabelled by adding 1 mL of fractionated eluent from an iThemba germanium-68/gallium-68 generator (0.6 M HCl) and allowed to incubate at room temperature for 15 minutes before QC.

2.3.2.4 Commercial Single Vial Kit Radiolabelling for [^{68}Ga]Ga-HBED-CC-PSMA

The manufacturer ANMI (Liege, Belgium) has developed a one-step kit for labelling of [^{68}Ga]Ga-HBED-CC-PSMA at room temperature (*97*)(*98*) which has now been tested in a clinical study (*99*) but does not have FDA or EMA approval. This lyophilised kit contains 25 µg (26 nmol) HBED-CC-PSMA. The rest of the kit contents have not been disclosed for commercial reasons, but must contain a neutralising agent or buffer to modify the pH to 4-5. The kit was reconstructed with 1.1 mL (the total eluate volume) of 0.1 M HCl eluted from an IRE-Elit germanium-68/gallium-68 generator (Fleurus, Belgium) (*99*). After this addition, the kit was shaken and left to stand at room temperature for 5 minutes before a sample is removed for QC. The final concentration of HBED-CC-PSMA was 23 µM. RCP was over 98% when measured by iTLC. Some radio-HPLC validation was performed but this was not deemed necessary for every batch. [^{68}Ga]Ga-HBED-CC-PSMA made with the ANMI kits has been tested in a clinical study of fifty prostate cancer patients (25 for initial staging, and 25 with biochemical recurrence) and showed the ability to detect primary tumours, cancerous lymph nodes and bone metastases (*99*). As there is no heating step in this method the two major isomers of [^{68}Ga]Ga-HBED-CC-PSMA would have been formed. This is not discussed in the clinical paper but was mentioned in previously published abstracts about these kits which stated the ratio of isomers was 1:1 (*97*)(*98*). The isomeric composition is therefore different from the majority of clinical studies where the heating step will have been used to ensure ~90% of one isomer. The two production methods were not compared in the same patients within the clinical study for the kit and so it is not possible to ascertain if there are any significant differences in biodistribution or detection rates between the methods.

2.4 Concluding Remarks

PSMA tracers show exceptional clinical promise for imaging prostate cancer, but to date, no PSMA tracers have been approved by the FDA or EMA. Because of the large number of prostate cancer patients that could benefit from a PSMA scan each year it would be ideal if the PSMA tracer that became established in routine clinical practice was accessible to a wide range of hospitals: a radiolabelling procedure based on a generator-produced radionuclide and a one-step kit could enable this to happen, and the germanium-68/gallium-68 generator makes this possible for PET imaging. The [^{68}Ga]Ga-PSMA tracers clinically assessed so far do not meet the ideal properties for a one-step kit and therefore there is an opportunity to develop novel bioconjugates that can achieve this. After reviewing the chelators available for gallium-68, THP stands out as the chelator with the potential to achieve a one-step kit for [^{68}Ga]Ga-PSMA imaging.

2.5 References

1. Morillon C, Bé M, Chechev VP, Egorov A. Technetium-99m. Laboratoire National Henri Becquerel. http://www.lnhb.fr/nuclides/Tc-99m_tables.pdf. Updated Jan 19, 2004. Accessed Jun 25, 2018.
2. Zolle I. *Technetium-99m Pharmaceuticals*. New York, NY: Springer; 2007.
3. International Atomic Energy Agency. *Technical Reports Series No. 466, Technetium-99m Radiopharmaceuticals: Manufacture of Kits.* Vienna, Austria: Sales and Promotion, Publishing Section International Atomic Energy Agency; 2008.
4. Theobald T. *Sampson's Textbook of Radiopharmacy, Fourth Edit*. London UK: Pharmaceutical Press; 2011.
5. Australasian Health Facility Guidelines Website. Part B - Health Facility Breifing and Planning: 0500- Nuclear Medicine/ PET Unit. https://www.healthfacilityguidelines.com.au/health-planning-units. Updated May 23, 2016. Accessed Jun 25, 2018.
6. Bartholomä MD, Louie AS, Valliant JF, Zubieta J. Technetium and Gallium Derived Radiopharmaceuticals: Comparing and Contrasting the Chemistry of Two Important Radiometals for the Molecular Imaging Era. *Chem Rev*. 2010;110:2903-2920.
7. Metello LF. 99mTc-Technetium Shortage: Old Problems Asking for New Solutions. *J Med Imaging Radiat Sci*. 2015;46:256-261.
8. Tanabe S, Zodda JP, Libson K, Deutsch E, Heineman WR. The Biological Distributions of Some Technetium-MDP Components Isolated by Anion Exchange High Performance Liquid Chromatography. *Int J Appl Radiat Isot*. 1983;34:1585-1592.
9. Hoch DJ, Pinkerton TC. Reversed-Phase HPLC of 99mTc Methylene Diphosphonate Bone Imaging Kits with Quantification of Pertechnetate. *Int J Radiat Appl Instrum Part A*. 1986;37:593-598.
10. Handeland Å, Lindegaard MW, Heggli DE. Biodistribution of Anionic Separated MDP Complexes from Different MDP Preparations. *Eur J Nucl Med*. 1989;15:609-611.
11. Blower PJ, Singh J, Clarke EM. The Chemical Identity of Pentavalent Technetium-99m Dimercaptosuccinic Acid. *J Nucl Med*. 1991;32:854-9.
12. Ikeda I, Inoue O, Kurata K. Chemical and Biological Studies on 99mTc-DMS-II: Effect of Sn(II) on the Formation of Various Tc-DMS Complexes. *Int J Appl Radiat Isot*. 1976;27:681-688.
13. Staník R, Světlík J, Benkovský I. DMSA and Its Complexes with Radioisotopes: Review. *J Radioanal Nucl Chem*. 2012;293:545-554.
14. Nosco DL, Beaty-Nosco JA. Chemistry of Technetium Radiopharmaceuticals 1: Chemistry behind the Development of Technetium-99m Compounds to Determine Kidney Function. *Coord Chem Rev*. 1999;184:91-123.
15. Coveney JR, Robbins MS. Comparison of Tc-99m MAG3 Kit with HPLC-Purified Tc-99m Mag3 and OIH in Rats. *J Nucl Med*. 1987;28:1881-1887.
16. Ming Z, Zhixin L. A Single-Step Kit Formulation for the 99mTc Labelling of HYNIC-Duramycin. *Nucl Med Biol*. 2012;39:997-1003.
17. Badar A, Williams J, de Rosales RTM, Tavaré R, Kampmeier F, Blower PJ, Mullen GED. Optimising the Radiolabelling Properties of Technetium Tricarbonyl and His-Tagged Proteins. *EJNMMI Res*. 2014;4:1-8.
18. NIH U.S. National Library of Medicine, Clinical Trials Website. https://clinicaltrials.gov/ct2/show/NCT02615067. Updated January 5, 2018. Accessed Feb 21, 2018.
19. Vallabhajosula S, Nikolopoulou A, Babich JW, Osborne JR, Tagawa ST, Lipai I, Solnes L, Maresca KP, Armor T, Joyal JL, Crummet R, Stubbs JB, Goldsmith SJ. 99mTc-Labeled Small-Molecule Inhibitors of Prostate-Specific Membrane Antigen: Pharmacokinetics and

Biodistribution Studies in Healthy Subjects and Patients with Metastatic Prostate Cancer. *J Nucl Med*. 2014;55:1791-1798.
20. The royal college of radiologists website. Evidence-Based Indications for the Use of PET-CT in the United Kingdom 2016. https://www.rcr.ac.uk/publication/evidence-based-indications-use-pet-ct-united-kingdom-2016. Updated 2016. Accessed Jun 25, 2018.
21. Bailey DL, Townsend DW, Valk PE, Maisey MN. Positron Emission Tomography: Basic Sciences.; 2005.
22. Rahmim A, Zaidi H. PET versus SPECT: Strengths, Limitations and Challenges. *Nucl Med Commun*. 2008;29:193.
23. Bé M, Schonfeld E. Gallium-68. Laboratoire National Henri Becquerel. http://www.lnhb.fr/nuclides/Ga-68_tables.pdf. Updated Jul 4, 2012. Accessed Jun 25, 2018.
24. Gallium (68Ga) Edotreotide Injection. *Br Pharmacop*. 2016;Monograph:2482.
25. European Medicines Agency website. List of Nationally Authorised Medicinal Products. Active Substance: Germanium (68Ge) Chloride / Gallium (68Ga) Chloride. Procedure No.: PSUSA/00010364/201603. http://www.ema.europa.eu/docs/en_GB/document_library/Periodic_safety_update_single_assessment/2016/11/WC500216013.pdf. Updated Oct 27, 2016. Accessed Jun 25, 2018.
26. FDA website. Division Director Summary Review for Regulatory Action: Netspot Kit Application Number: 208547Orig1s000. Center for Drug Evaluation and Research. https://www.accessdata.fda.gov/drugsatfda_docs/nda/2016/208547Orig1s000SumR.pdf. Updated May 30, 2016. Accessed Jun 25, 2018.
27. Aslani A, Snowdon GM, Bailey DL, Geoffrey P, Bailey EA, Roach PJ. Gallium-68 DOTATATE Production with Automated PET Radiopharmaceutical Synthesis System : A Three Year Experience. *Asia Ocean J Nucl Med Biol*. 2014;2:75-86.
28. Riesco-Eizaguirre G, Santisteban P. A Perspective View of Sodium Iodide Symporter Research and Its Clinical Implications. *Eur J Endocrinol*. 2006;155:495-512.
29. Bé M, E. S. Molybdenum-99. Laboratoire National Henri Becquerel. http://www.lnhb.fr/nuclides/Mo-99_tables.pdf. Updated Nov 3, 2011. Accessed Jun 25, 2018.
30. Bé M, E. S. Germanium-68. Laboratoire National Henri Becquerel. http://www.lnhb.fr/nuclides/Ge-68_tables.pdf. Updated Feb 27, 2012. Accessed 25 Jun, 2018.
31. FDA website. Ultra-Technekow™ V4. (Technetium Tc 99m Generator) Reference ID: 3455606. https://www.accessdata.fda.gov/drugsatfda_docs/label/2014/017243s043lbl.pdf. Updated Nov, 2015. Accessed Jun 26, 2018.
32. Imaging Equipment Ltd website. Eckert and Zeigler GalliaPharm® 68 Ge/68 Ga Generator Data Sheet. http://imagingequipment.co.uk/wp-content/uploads/2017/10/EZ-Galliapharm-Radionuclide-Generator-7132-0025.pdf. Updated Mar, 2017, Accessed Jun 25, 2018.
33. Klement W, Arndt JO. Pain on I.V. Injection of Some Anaesthetic Agents Is Evoked by the Unphysiological Osmolality or PH of Their Formulations. *Br J Anaesth*. 1991;66:189-195.
34. Wang W. Tolerability of Hypertonic Injectables. *Int J Pharm*. 2015;490:308-315.
35. Velikyan I, Sundin A, Eriksson B, Lundqvist H, Sörensen J, Bergström M, Långström B. In Vivo Binding of [68Ga]-DOTATOC to Somatostatin Receptors in Neuroendocrine Tumours—impact of Peptide Mass. *Nucl Med Biol*. 2010;37:265-275.
36. Tsionou MI, Knapp CE, Foley CA, Munteanu CR, Cakebread A, Imberti C, Eykyn TR, Young JD, Paterson BM, Blower PJ, Ma MT. Comparison of Macrocyclic and Acyclic Chelators for Gallium-68 Radiolabelling. *RSC Adv*. 2017;7:49586-49599.

37. Wood SA, Samson IM. The Aqueous Geochemistry of Gallium, Germanium, Indium and Scandium. *Ore Geol Rev*. 2006;28:57-102.
38. McInnes LE, Rudd SE, Donnelly PS. Copper, Gallium and Zirconium Positron Emission Tomography Imaging Agents: The Importance of Metal Ion Speciation. *Coord Chem Rev*. 2017;352:499-516.
39. Price EW, Orvig C. Matching Chelators to Radiometals for Radiopharmaceuticals. *Chem Soc Rev*. 2014;43:260-90.
40. Oehlke E, Le VS, Lengkeek N, Pellegrini P, Jackson T, Greguric I, Weiner R. Influence of Metal Ions on the 68Ga-Labeling of DOTATATE. *Appl Radiat Isot*. 2013;82:232-238.
41. Meyer G-J, Macke H, Schuhmacher J, Knapp WH, Hofmann M. 68Ga-Labelled DOTA-Derivatised Peptide Ligands. *Eur J Nucl Med Mol Imaging*. 2004;31.
42. Hofmann M, Maecke H, Börner A, Weckesser E, Schöffski P, Oei M, Schumacher J, Henze M, Heppeler A, Meyer G, Knapp W. Biokinetics and Imaging with the Somatostatin Receptor PET Radioligand 68Ga-DOTATOC: Preliminary Data. *Eur J Nucl Med*. 2001;28:1751-1757.
43. Notni J, Pohle K, Wester H-JJ. Comparative Gallium-68 Labeling of TRAP-, NOTA-, and DOTA-Peptides: Practical Consequences for the Future of Gallium-68-PET. *EJNMMI Res*. 2012;2:2-6.
44. Highlights of Prescribing Information NETSPOT (Kit for the Preparation of Gallium Ga 68 Dotatate Injection), for Intravenous Use. Reference ID: 3939719. https://www.accessdata.fda.gov/drugsatfda_docs/label/2016/208547s000lbl.pdf Updated Jun, 2016. Accessed Jun 25, 2018.
45. Larenkov AA, Bruskin AB, Kodina GE. Preparation of Highly Purified 68Ga Solutions via Ion Exchange in Hydrochloric Acid–ethanol Mixtures. *J Radioanal Nucl Chem*. 2015;305:147-160.
46. Zhernosekov KP, Filosofov D V, Baum RP, Aschoff P, Bihl H, Razbash A a, Jahn M, Jennewein M, Rösch F. Processing of Generator-Produced 68Ga for Medical Application. *J Nucl Med*. 2007;48:1741-1748.
47. Eppard E, Wuttke M, Nicodemus PL, Rosch F, Rösch F. Ethanol-Based Post-Processing of Generator-Derived 68Ga toward Kit-Type Preparation of 68Ga-Radiopharmaceuticals. *J Nucl Med*. 2014;55:1023-1028.
48. He P, Burke BP, Clemente GS, Brown N, Pamme N, Archibald SJ. Monolith-Based ^{68} Ga Processing: A New Strategy for Purification to Facilitate Direct Radiolabelling Methods. *React Chem Eng*. 2016;1:361-365.
49. Mueller D, Klette I, Baum RP, Gottschaldt M, Schultz MK, Breeman W a P. Simplified NaCl Based 68Ga Concentration and Labeling Procedure for Rapid Synthesis of 68Ga Radiopharmaceuticals in High Radiochemical Purity. *Bioconjug Chem*. 2012;23:1712-1717.
50. T.Clarke E, Martell AE. Stabilities of Trivalent Metal Ion Complexes of the Tetraacetate Derivatives of 12-, 13- and 14-Membered Tetraazamacrocycles. *Inorganica Chim Acta*. 1991;190:37-46.
51. T.Clarke E, Martell AE. Stabilities of the Fe(III), Ga(III) and In(III) Chelates of N,N',N''-Triazacyclononanetriacetic Acid. *Inorganica Chim Acta*. 1991;181:273-280.
52. Notni J, Hermann P, Havlíčková J, Kotek J, Kubíček V, Plutnar J, Loktionova N, Riss PJ, Rösch F, Lukeš I. A Triazacyclononane-Based Bifunctional Phosphinate Ligand for the Preparation of Multimeric 68Ga Tracers for Positron Emission Tomography. *Chem - A Eur J*. 2010;16:7174-7185.
53. Ma R, Motekaitis RJ, Martell AE. Stability of Metal Ion Complexes of N,N'-Bis(2-Hydroxybenzyl)Ethylenediamine-N,N'-Diacetic Acid. *Inorganica Chim Acta*. 1994;224:151-155.
54. Evers A, Hancock RD, Martell AE, Motekaitis RJ. Metal Ion Recognition in Ligands with

Negatively Charged Oxygen Donor Groups: Complexation of Fe(III), Ga(III), In(III), Al(III), and Other Highly Charged Metal Ions. *Inorg Chem*. 1989;28:2189-2195.
55. Spang P, Herrmann C, Roesch F. Bifunctional Gallium-68 Chelators: Past, Present, and Future. *Semin Nucl Med*. 2016;46:373-394.
56. Velikyan I, Maecke H, Langstrom B. Convenient Preparation of 68Ga-Based PET-Radiopharmaceuticals at Room Temperature. *Bioconjug Chem*. 2008;19:569-573.
57. Eder M, Krivoshein A V., Backer M, Backer JM, Haberkorn U, Eisenhut M. ScVEGF-PEG-HBED-CC and ScVEGF-PEG-NOTA Conjugates: Comparison of Easy-to-Label Recombinant Proteins for [68Ga]PET Imaging of VEGF Receptors in Angiogenic Vasculature. *Nucl Med Biol*. 2010;37:405-412.
58. Eisenwiener KP, Prata MIM, Buschmann I, Zhang HW, Santos AC, Wenger S, Reubi JC, Mäcke HR. NODAGATOC, a New Chelator-Coupled Somatostatin Analogue Labeled with [67/68Ga] and [111In] for SPECT, PET, and Targeted Therapeutic Applications of Somatostatin Receptor (Hsst2) Expressing Tumors. *Bioconjug Chem*. 2002;13:530-541.
59. Simecek J, Hermann P, Wester H, Notni J. How Is 68Ga Labeling of Macrocyclic Chelators Influenced by Metal Ion Contaminants in 68Ge/68Ga Generator Eluates? *ChemMedChem*. 2013;8:95-103.
60. Prata MIM, André JP, Kovács Z, Takács AI, Tircsó G, Tóth I, Geraldes CFGC. Gallium(III) Chelates of Mixed Phosphonate-Carboxylate Triazamacrocyclic Ligands Relevant to Nuclear Medicine: Structural, Stability and in Vivo Studies. *J Inorg Biochem*. 2017;177:8-16.
61. Prata MIM, Santos AC, Geraldes CFGC, Lima JJPD. Characterisation of 67Ga3+ Complexes of Triaza Macrocyclic Ligands: Biodistribution and Clearance Studies. *Nucl Med Biol*. 1999;26:707-710.
62. Notni J, Šimeček J, Hermann P, Wester HJ. TRAP, a Powerful and Versatile Framework for Gallium-68 Radiopharmaceuticals. *Chem - A Eur J*. 2011;17:14718-14722.
63. Simecek J, Zemek O, Hermann P, Notni J, Wester HJ. Tailored Gallium(III) Chelator NOPO: Synthesis, Characterization, Bioconjugation, and Application in Preclinical Ga-68-PET Imaging. *Mol Pharm*. 2014;11:3893-3903.
64. Tumors N, Klivhny G, Hull WE, Matys R, Hauser H, Kalthofp H, Schmiegel WH. A Bifunctional HBED-Derivative for Labeling of Antibodies with 67Ga, 111In and 59Fe. Comparitive Biodistribution with 111In-DPTA and 131-I-Labeled Antibodies in Mice Bearing Antibody Internalizing and Non-Internalizing Tumors. *Comp Gen Pharmacol*. 1992;19.
65. Eder M, Neels O, Müller M, Bauder-Wüst U, Remde Y, Schäfer M, Hennrich U, Eisenhut M, Afshar-Oromieh A, Haberkorn U. Novel Preclinical and Radiopharmaceutical Aspects of [68Ga]Ga-PSMA-HBED-CC: A New PET Tracer for Imaging of Prostate Cancer. *Pharmaceuticals*. 2014;7:779-796.
66. Borgias B, Hugi AD, Raymond KN. Isomerization and Solution Structures of Desferrioxamine B Complexes of Al3+ and Ga3+. *Inorg Chem*. 1989;28:3538-3545.
67. Gourni E, Del Pozzo L, Bartholomä M, Kiefer Y, T. Meyer P, Maecke HR, Holland JP. Radiochemistry and Preclinical PET Imaging of 68Ga-Desferrioxamine Radiotracers Targeting Prostate-Specific Membrane Antigen. *Mol Imaging*. 2017;16:1-11.
68. Parker D, Waldron BP, Yufit DS. Crystallographic and Solution NMR Structural Analyses of Four Hexacoordinated Gallium(III) Complexes Based on Ligands Derived from 6-Amino-Perhydro-1,4-Diazepine. *Dalt Trans*. 2013;42:8001.
69. Parker D, Waldron BP. Conformational Analysis and Synthetic Approaches to Polydentate Perhydro-Diazepine Ligands for the Complexation of Gallium(III). *Org Biomol Chem*. 2013;11:2827.
70. Waldron BP, Parker D, Burchardt C, Yufit DS, Zimny M, Roesch F. Structure and Stability of Hexadentate Complexes of Ligands Based on AAZTA for Efficient PET Labelling with

Gallium-68. *Chem Commun*. 2013;49:579-581.
71. Seemann J, Waldron BP, Roesch F, Parker D. Approaching 'Kit-Type' Labelling with 68Ga: The DATA Chelators. *ChemMedChem*. 2015;10:1019-1026.
72. Seemann J, Waldron B, Parker D, Roesch F. DATATOC: A Novel Conjugate for Kit-Type 68Ga Labelling of TOC at Ambient Temperature. *EJNMMI Radiopharm Chem*. 2017;1:4.
73. Berry DJ, Ma Y, Ballinger JR, Tavaré R, Koers A, Sunassee K, Zhou T, Nawaz S, Mullen GED, Hider RC, Blower PJ. Efficient Bifunctional Gallium-68 Chelators for Positron Emission Tomography: Tris(Hydroxypyridinone) Ligands. *Chem Commun (Camb)*. 2011;47:7068-70.
74. Ma MT, Cullinane C, Waldeck K, Roselt P, Hicks RJ, Blower PJ. Rapid Kit-Based (68)Ga-Labelling and PET Imaging with THP-Tyr(3)-Octreotate: A Preliminary Comparison with DOTA-Tyr(3)-Octreotate. *EJNMMI Res*. 2015;5:52.
75. Nawaz S, Mullen GED, Sunassee K, Bordoloi J, Blower PJ, Ballinger JR. Simple, Mild, One-Step Labelling of Proteins with Gallium-68 Using a Tris(Hydroxypyridinone) Bifunctional Chelator: A 68Ga-THP-ScFv Targeting the Prostate-Specific Membrane Antigen. *EJNMMI Res*. 2017;7:86.
76. Ma MT, Cullinane C, Imberti C, Baguna Torres J, Terry SY a., Roselt P, Hicks RJ, Blower PJ, Bagunya Torres J, Terry SY a., Roselt P, Hicks RJ, Blower PJ. New Tris (Hydroxypyridinone) Bifunctional Chelators Containing Isothiocyanate Groups Provide a Versatile Platform for Rapid One-Step Labeling and PET Imaging with 68Ga3+. *Bioconjug Chem*. 2015;27:309-318.
77. Cusnir R, Imberti C, Hider R, Blower P, Ma M. Hydroxypyridinone Chelators: From Iron Scavenging to Radiopharmaceuticals for PET Imaging with Gallium-68. *Int J Mol Sci*. 2017;18:116.
78. FDA Approves 18F-Fluciclovine and 68Ga-DOTATATE Products. *J Nucl Med*. 2016;57:9N.
79. European Medicines Agency website. Assessment Report: SomaKit TOC. Procedure No: EMEA/H/C/004140/0000. http://www.ema.europa.eu/docs/en_GB/document_library/EPAR_-_Public_assessment_report/human/004140/WC500221924.pdf. Updated Oct 13, 2016. Accessed Jun 25, 2018.
80. FDA Grants Orphan Drug Designation for Ga-68-DOTATOC. *J Nucl Med*. 2014;55:10N.
81. Satpati D, Shinto A, Kamaleshwaran KK, Sarma HD, Dash A. Preliminary PET/CT Imaging with Somatostatin Analogs [68Ga]DOTAGA-TATE and [68Ga]DOTAGA-TOC. *Mol Imaging Biol*. 2017;19:878-884.
82. Decristoforo C, Knopp R, von Guggenberg E, Et Al. A Fully Automated Synthesis for the Preparation of 68Ga-Labelled Peptides. *Nucl Med Commun*. 2007;28:870-5.
83. Asti M, Iori M, Pier Cesare C, Sara R, Fraternali A, Versari A, Capponi PC, Rubagotti S, Fraternali A, Versari A. Development of a Simple Kit-Based Method for the Preparation of Pharmaceutical Grade 68Ga-DOTATOC. *Nucl Med Commun*. 2015;36:502-510.
84. Mukherjee A, Pandey U, Chakravarty R, Sarma HD, Dash A. Development of Single Vial Kits for Preparation of 68Ga-Labelled Peptides for PET Imaging of Neuroendocrine Tumours. *Mol Imaging Biol*. 2014;16:550-557.
85. Nock BA, Kaloudi A, Nagel J, Sinnes J-P, Roesch F, Maina T. Novel Bifunctional DATA Chelator for Quick Access to Site-Directed PET 68Ga-Radiotracers: Preclinical Proof-of-Principle with [Tyr3]Octreotide. *Dalt Trans*. 2017;46:14584-14590.
86. Maina T, Nock B, Nagel J, Sinnes J-P, Baum R, Roesch F. In Vitro Binding Affinities and Initial in Vivo Evaluation of Ga-68-DATA-TOC. *J Nucl Med*. 2016;57:S1112.
87. Weineisen M, Schottelius M, Simecek J, Baum RP, Yildiz A, Beykan S, Kulkarni HR, Lassmann M, Klette I, Eiber M, Schwaiger M, Wester H-J, Rp-hplc A. 68Ga- and 177Lu-Labeled PSMA I&T: Optimization of a PSMA-Targeted Theranostic Concept and First Proof-of-Concept Human Studies. *J Nucl Med*. 2015;56:1169-1176.

88. Benešová M, Schäfer M, Bauder-Wüst U, Afshar-Oromieh A, Kratochwil C, Mier W, Haberkorn U, Kopka K, Eder M. Preclinical Evaluation of a Tailor-Made DOTA-Conjugated PSMA Inhibitor with Optimized Linker Moiety for Imaging and Endoradiotherapy of Prostate Cancer. *J Nucl Med*. 2015;56:914-920.
89. Afshar-Oromieh A, Hetzheim H, Kratochwil C, Benesova M, Eder M, Neels OC, Eisenhut M, Kubler W, Holland-Letz T, Giesel FL, Mier W, Kopka K, Haberkorn U. The Theranostic PSMA Ligand PSMA-617 in the Diagnosis of Prostate Cancer by PET/CT: Biodistribution in Humans, Radiation Dosimetry, and First Evaluation of Tumor Lesions. *J Nucl Med*. 2015;56:1697-1705.
90. Eder M, Schäfer M, Bauder-Wüst U, Hull W-E, Wängler C, Mier W, Haberkorn U, Eisenhut M. 68Ga-Complex Lipophilicity and the Targeting Property of a Urea-Based PSMA Inhibitor for PET Imaging. *Bioconjug Chem*. 2012;23:688-697.
91. Schuhmacher J, Klivényi G, Matys R, Stadler M, Regiert T, Hauser H, Doll J, Maier-Borst W, Zöller M. Multistep Tumor Targeting in Nude Mice Using Bispecific Antibodies and a Gallium Chelate Suitable for Immunoscintigraphy with Positron Emission Tomography. *Cancer Res*. 1995;55:115-123.
92. Eiber M, Maurer T, Souvatzoglou M, Beer a. J, Ruffani a., Haller B, Kubler H, Haberkorn U, Eisenhut M, Wester H-J, Gschwend JE, Schwaiger M. Evaluation of Hybrid 68Ga-PSMA-Ligand PET/CT in 248 Patients with Biochemical Recurrence after Radical Prostatectomy. *J Nucl Med*. 2015;56:668-674.
93. Afshar-Oromieh A, Holland-Letz T, Giesel FL, Kratochwil C, Mier W, Haufe S, Debus N, Eder M, Eisenhut M, Schäfer M, Neels O, Hohenfellner M, Kopka K, Kauczor H-U, Debus J, Haberkorn U. Diagnostic Performance of 68Ga-PSMA-11 (HBED-CC) PET/CT in Patients with Recurrent Prostate Cancer: Evaluation in 1007 Patients. *Eur J Nucl Med Mol Imaging*. 2017;44:1781-1781.
94. Chakravarty R, Chakraborty S, Radhakrishnan ER, Kamaleshwaran K, Shinto A, Dash A. Clinical 68Ga-PET: Is Radiosynthesis Module an Absolute Necessity? *Nucl Med Biol*. 2017;46:1-11.
95. Satpati D, Shinto A, Kamaleshwaran KK, Sane S, Banerjee S. Convenient Preparation of [68Ga]DKFZ-PSMA-11 Using a Robust Single-Vial Kit and Demonstration of Its Clinical Efficacy. *Mol Imaging Biol*. 2016;18:420-427.
96. Ebenhan T, Vorster M, Marjanovic-Painter B, Wagener J, Suthiram J, Modiselle M, Mokaleng B, Zeevaart J, Sathekge M. Development of a Single Vial Kit Solution for Radiolabeling of 68Ga-DKFZ-PSMA-11 and Its Performance in Prostate Cancer Patients. *Molecules*. 2015;20:14860-14878.
97. Maus S, Schreckenberger M, Kartamihardja H. Ga-68-PSMA Lyophilized Ready to Use Kit for Diagnosis of Prostate Cancer by PET/CT. *J Nucl Med*. 2016;57:S2,518.
98. Maus S, Schreckenberger M. GMP Ga-68-PSMA Cold Kit Cost Effective Alternative to Synthetizer Based Method. *J Nucl Med*. 2016;57:S2,1537.
99. Beheshti M, Paymani Z, Brilhante J, Geinitz H, Gehring D, Leopoldseder T, Wouters L, Pirich C, Loidl W, Langsteger W. Optimal Time-Point for 68 Ga-PSMA-11 PET / CT Imaging in Assessment of Prostate Cancer : Feasibility of Sterile Cold-Kit Tracer Preparation? *Eur J Nucl Med Mol Imaging*. 2018.

3 The Development of [^{68}Ga]Ga-THP-PSMA and Its Use in Imaging Prostate Cancer

The content of this chapter has been published in the form of an original research article in the Journal of Nuclear Medicine (*1*)

3.1 Introduction

As outlined in chapter 2, there is a desire and a need to have simple and robust radiolabelling procedures for all radiopharmaceuticals, and one-step, kit-based radiopharmaceuticals offer the greatest ease of GMP production. For years kit-based radiopharmaceuticals have dominated technetium-99m tracer production (*2*) but despite this history within nuclear medicine, the same approach has not been adopted for PET radiotracers, even though this concept has been proposed for over 20 years (*3*)(*4*). This was initially due to the prevalence of the fluorine-18 and carbon-11-based PET tracers which, as non-metals, are covalently incorporated into radiotracers, and so require complex multi-step synthetic chemistry, incompatible with a kit. However, interest has increased in the metal-based PET radionuclides, including copper-64, zirconium-89, gallium-68, scandium-44, and yttrium-96, where there is the opportunity to use chelating agents to incorporate the radiometal (*5*). If chelators with optimal properties can be designed, this opens the possibility for a one-step kit. Of these radiometals the most suitable for PET imaging of small molecules and peptides with fast pharmacokinetics is gallium-68, due to its well-matched 67.8 minute half-life, and the 89.14% positron decay which allows high-quality images to be obtained with acceptable patient dose (*4*)(*6*)(*7*)(*8*)(*9*).

In addition to these advantages, gallium-68 is available from a generator, which means it is potentially accessible to a wider range of hospitals than cyclotron-produced radionuclides. The germanium-68/gallium-68 generator is based on the parent radioisotope germanium-68 ($t_{1/2}$ = 270.95 days (*10*)), which decays via electron capture to gallium-68. The elution of the Galliapharm pharmaceutical grade generator (Eckert and Ziegler, Radiopharma, GmbH) which has marketing authorisation across Europe (*11*), provides up to 1.85 GBq of gallium-68 in 5 mL of 0.1 M HCl. This is enough activity for between 1 and 4 patient doses depending on the age of the generator and the radiosynthesis method. Additionally, the generator can be eluted several times a day (up to every 2 hours), and only needs replacing once a year (*8*). The GMP-compatible eluate meets all the British and European Pharmacopeia monograph standards, including germanium-68 breakthrough (< 0.001%) and can be used clinically without any purification steps

(*12*) (although purification steps are typically needed to improve subsequent radiolabelling of conventional bifunctional chelator conjugates).

The chemical properties of gallium also lend themselves to single step kit-based radiolabelling. In fact, one might expect that it should be simpler to design a kit for gallium-68 than technetium-99m, due to its strongly preferred oxidation state of gallium(III), whereas technetium-99m is eluted from the generator as ^{99m}Tc-pertechnetate(VII) and has to be reduced to a lower oxidation state (Tc(VI), Tc (V), Tc(IV), Tc(III) or Tc(I)) before it can be chelated (*2*). This brings the disadvantage of requiring the inclusion of a reducing agent such as tin chloride, which in a gallium-68 kit, could be avoided. No-carrier-added gallium-68 is eluted from the generator in a solution of hydrochloric acid, in the form of $[Ga(H_2O)_6]^{3+}$ which is stabilised by the low pH (*13*)(*14*). As the pH is increased ligands containing oxygen or nitrogen donors, can be used to chelate gallium-68. These properties demonstrate that, in theory, a gallium-68 radiopharmaceutical kit could be extremely simple, containing just a pH modifier and the metal-free pharmaceutical.

To achieve such a kit, the chelator used to incorporate gallium into the bio-conjugate must meet several criteria (*4*): its labelling should reach completion (> 95% radiochemical yield) quickly (< 5 minutes) at room temperature and be unaffected by common trace metals in the generator eluate, without additional steps to concentrate, heat, buffer, or purify. Its complex should resist *in vivo* transchelation (e.g. by transferrin or serum proteins), and conjugation and radiolabelling should not induce mixtures of diastereomers, enantiomers, or geometric isomers, nor adverse pharmacokinetics, (for example, delayed clearance or non-specific binding). The current generation of clinically assessed gallium-68 chelators, such as DOTA and HBED-CC, do not meet these criteria, as discussed in chapter 2.

A class of chelator with the potential to meet the requirements for kit-based labelling outlined above and in chapter 2 is the tris(hydroxypyridinone) (THP) system, which has been shown to bind gallium-68 rapidly at room temperature and neutral pH, with high yield and purity, without the need to process the generator eluate (*15*)(*16*)(*17*)(*18*)(*19*). The structure of THP-Ac is shown in figure 2.19 alongside its functionalised derivatives. The THP (*tris*(hydroxypyridinone) chelator is an acyclic ligand and an O_6 donor through its three hydroxyl groups and three carbonyl groups on its 1,6-dimethyl-3-hydroxypyridin-4-one arms, and forms a neutral complex with gallium(III). Such a complex would be predicted to have a (distorted) octahedral geometry. This tripodal design aimed to avoid the formation of geometric isomers upon binding but would allow the formation of delta and lambda enantiomers associated with all hexadentate tripodal chelators.

The performance of THP has been evaluated against a range of common chelators and demonstrated superior radiolabelling properties under milder conditions (*15*)(*16*).

THP has also been functionalised and conjugated to peptides and proteins (THP-Tyr3-octreotate, THP-RDG and THP-αvβ3 integrin) and retains both its mild radiolabelling and *in vivo* targeting properties (*16*)(*17*)(*20*)(*21*). This provides an excellent starting point to develop one step radiopharmaceutical kits which utilise the THP technology.

As the advantages of kit-based radiolabelling are only fully realised when applied to clinical production, efforts should be focused on developing such radiolabelling for radiotracers which serve a clinical need. Prostate cancer is the most prevalent type of cancer where [^{18}F]FDG imaging is unsuitable for staging and detection of disease recurrence, and so alternative PET imaging agents are required (*22*). The over-expression of the prostate specific membrane antigen (GCP(II)/PSMA) on the majority of prostate cancers provides a way to specifically target radiotracers to disease sites (*22*)(*23*), and a small urea-based inhibitor can be used to target GCP(II)/PSMA. This is a versatile scaffold which is suitable for conjugation to chelators without dramatically changing its affinity (*24*)(*25*)(*26*). A [^{68}Ga]Ga-labelled conjugate of this targeting moiety with HBED-CC as the chelator (figure 3.1) has shown outstanding clinical promise in several trials in patients with prostate cancer (*27*)(*28*) as described in chapter 1 and has established itself rapidly in routine use in research hospitals across the world. Studies have been carried out in Germany (*27*), UK (*29*), Australia (*30*), India (*31*), South Africa (*32*), mainly driven by demand from clinicians and patients, demonstrating that GCP(II)/PSMA imaging fulfils a clinical need (*33*). Recently published studies have also shown the impact of [^{68}Ga]Ga-PSMA scans on patient management (*29*)(*30*) and further studies into the effect on patient outcomes are underway, and will be critical for gaining regulatory approval.

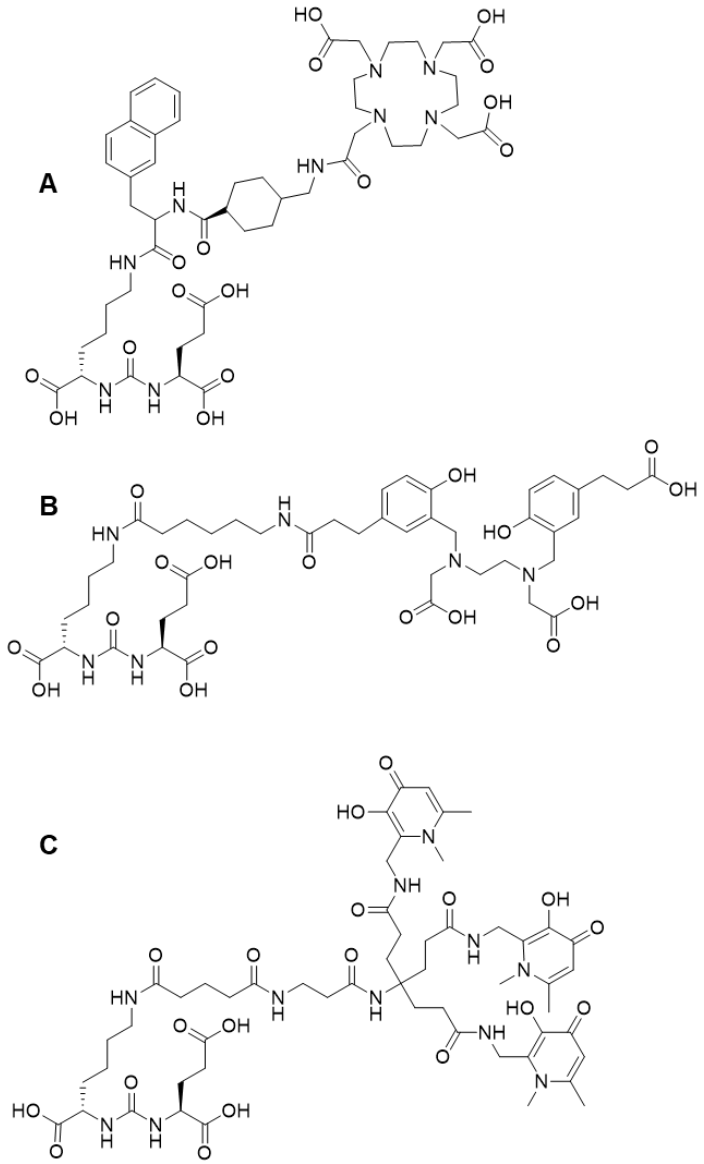

FIGURE 3.1: Structures of (A) DOTA-PSMA (PSMA-617) (34); (B) HBED-CC-PSMA (DKFZ-PSMA-11) (25); (C) THP-PSMA

The choice of HBED-CC as the chelator makes radiolabelling of [^{68}Ga]Ga-HBED-CC-PSMA possible at room temperature, but the labelling produces an undesirable mixture of cis/trans geometric isomers distinguishable by HPLC (*25*)(*31*)(*32*)(*35*)(*36*). Thus, a heating step is still required, to reduce the number of isomers and increase the yield of one of these to approximately 90%, as it has been suggested that these isomers may have different *in vivo* properties (*35*). Clinical radiosynthesis of tracers based on these chelators is currently performed on cartridge-based synthesis modules, taking 35 minutes and typically affording 80 ± 5% decay-corrected radiochemical yield (*35*). Such production requires a high level of radiochemical expertise and infrastructure rarely available outside research hospitals. Switching from this to a one-step kit-based process would ensure that tracer production is simple, robust, and a less labour-intensive

process which is quicker to validate. All these features should lead to faster and wider adoption across radiopharmacies and consequently better access for patients.

In this study a THP bioconjugate targeting GCP(II)/PSMA, incorporating the (Lys-C(O)-Glu) pharmacophore has been evaluated (figure 3.1) (*24*)(*25*)(*34*). The aims of this work were to determine the potential of [^{68}Ga]Ga-THP-PSMA to achieve one-step kit-based labelling and to evaluate the resulting tracer *in vitro* and in a preclinical prostate cancer model.

3.2 Experimental Aims

The experimental aims of this chapter are:

- Synthesise a THP-PSMA conjugate
- Assess radiolabelling of [^{68}Ga]Ga-THP-PSMA without pre- or post-processing
- Develop a one-step kit for [^{68}Ga]Ga-THP-PSMA suitable for use with the Galliapharm germanium-68/gallium-68 generator (Eckert and Ziegler)
- Evaluate the uptake of [^{68}Ga]Ga-THP-PSMA in prostate cancer cells that over-express GCP(II)/PSMA, and compare its affinity for GCP(II)/PSMA to the established tracers [^{68}Ga]Ga-HBED-CC-PSMA (DKFZ-11) and [^{68}Ga]Ga-DOTA-PSMA (PSMA-617)
- Evaluate the biodistribution and tumour uptake of [^{68}Ga]Ga-THP-PSMA in a preclinical mouse model with a subcutaneous prostate cancer xenograft and compare to the biodistribution of [^{68}Ga]Ga-HBED-CC-PSMA (DKFZ-11)

3.3 Materials and Methods

All reagents and consumables were purchased from Sigma Aldrich or Fischer Scientific, with the exception of Fmoc-Lys-Dde-COOH (Bachem AG, Bubendorf, Switzerland), 2-(phosphonomethyl)pentane-1,5-dioic acid (PMPA) (Enzo Life Sciences, Exeter, UK), Anti-PSMA-VioBright-FITC and REA-(control)-VioBright FITC (MACS Milenyi Biotec, Bisley, UK), DOTA-PSMA (PSMA 617), and HBED-CC-PSMA (DKFZ-11) (ABX, Radeberg, Germany). Severe combined immunodeficient (SCID)/beige mice were purchased from Charles River (Margate, UK). DU145 and DU145-PSMA cell lines were provided by Dr. Florian Kampmeier (*37*).

3.3.1 Instrumentation

NMR: Nuclear magnetic resonance (NMR) ^{1}H- and ^{13}C- spectra were acquired on a Bruker Avance III 700 spectrometer operating at 700 MHz (^{1}H frequency), equipped with a quadruple-resonance QCI cryoprobe.

LC-ESIMS: High-resolution liquid chromatography electrospray ionisation mass spectrometry (LC-ESIMS) was performed in positive ion mode on an Agilent 6520 Accurate-Mass Q-TOF LC/MS connected to an Agilent 1200 HPLC.

HPLC: All high-resolution liquid chromatography (HPLC) utilised an Agilent 1200 LC with in-line radio (sodium iodide gamma-detector) and ultraviolet detection (220 nm analytical, 280 nm preparative). Data were analysed using Laura software (version 4.0.2.75; LabLogic Systems Ltd.).

HPLC methods: The chemical purity of THP-PSMA and radiolabelling of [$^{68/67}$Ga]Ga-THP-PSMA were assessed using an Agilent Eclipse XDB C_{18} 5 µm 4.6 × 150 mm column with an isocratic mobile phase (87.5% H_2O, 12.5% acetonitrile (ACN), 0.075% trifluoroacetic acid (TFA), 0.05% triethylamine), with a flow rate of 1 mL/minute. [$^{68/67}$Ga]Ga radiolabelling of HBED-CC-PSMA and DOTA-PSMA(617) was assessed with the same HPLC equipment but an alternative mobile phase: A = H_2O with 0.05% TFA, B = ACN with 0.05% TFA, gradient: 0-5 minutes = 90% A, 5-15 minutes = ramp to 50% B (4%/min), 15-20 minutes = 90% A, with a flow rate of 1 mL/minute. Serum stability was assessed using size-exclusion chromatography with a Phenomenex BioSep 5 mm size-exclusion chromatography s2000 column (300 × 7.8 mm) with phosphate-buffered saline (PBS) as the mobile phase and a flow rate of 1 mL/minute.

iTLC: Instant thin-layer chromatography Radiolabelling for all [$^{67/68}$Ga]Ga-PSMA radiotracers was assessed by iTLC utilising Varian ITLC SGI0001 strips (10 cm length) with a mobile phase of

1 M ammonium acetate in water/methanol (1:1). iTLC plates were scanned with a LabLogic miniScan TLC reader and analysed with Laura software.

3.3.2 Synthesis of THP-PSMA

Synthesis of H-Lys-(Dde)-2CT-resin (compound 3): 2-Chlorotrityl resin (350 mg equivalent to a loading of 0.35 mmol) was inserted in a fritted polypropylene syringe, and a solution of Fmoc-Lys-DdeCOOH (600 mg, 1.1 mmol) (**compound 1,** reaction scheme 3.1) and excess N,N-diisopropylethylamine (DIPEA) in dichloromethane (DCM) was added. After being stirred overnight to form **compound 2**, the resin was washed with DCM and subsequently treated with methanol for 10 minutes. Thereafter, the resin was washed with dimethylformamide (DMF) and DCM and finally dried under vacuum. Resuspension of the beads in a solution of piperidine/DMF (20:80) for 20 minutes followed by separation of the resin from the supernatant by suction filtration and washing with DMF and DCM produced resin-bound **compound 3**.

Synthesis of resin-bound THP-PSMA (compound 9): Bis(tert-butyl) ester L-glutamate hydrochloride (444 mg, 1.5 mmol) was dissolved in anhydrous DCM (100 mL) containing DIPEA (750 µL, 4.3 mmol). This solution was added dropwise to a 3-neck round bottom flask containing a solution of triphosgene (150 mg, 0.5 mmol) in anhydrous DCM (5 mL) at 0°C under a nitrogen atmosphere. The reaction solution was then allowed to warm to room temperature and stirred for 1 hour. The previously prepared H-Lys-(Dde)-2CT-resin **compound 3** (reaction scheme 3.1) (250 mg, equivalent to a loading of 0.25 mmol) was added and stirred overnight to form **compound 6** (reaction scheme 3.1). The resin was separated from the supernatant by suction filtration in a fritted polypropylene syringe, washed, and dried. The resin was suspended in a mixture of 2% (v/v) hydrazine hydrate in 2 mL of DMF and stirred for 15 minutes, and then washed with DMF. This step was repeated 4 times to produce **compound 7** (reaction scheme 3.1). **Compound 7** (100 mg equivalent to a loading of 0.1 mmol) was added to a solution of glutaric anhydride (114 mg, 1 mmol) and DIPEA (358 µL, 2 mmol) dissolved in 2 mL of DMF, and the mixture was stirred for 3 hours to produce **compound 8** (reaction scheme 3.1). **Compound 8** (50 mg, equivalent to a loading of 0.05 mmol) was suspended in a solution of HATU (20 mg, 0.05 mmol) and DIPEA (18 µL, 0.1 mmol) in anhydrous DMF (0.5 mL), and *in situ* activation of the carboxylate was allowed to proceed for 10 minutes. A solution of THP-NH_2 (70 mg, 0.09 mmol), synthesised by a previously published method (*38*), in DMF/DMSO (2.5 mL/2 mL) containing DIPEA (18 µL, 0.1 mmol) was then added to this suspension and stirred for 36 hours, to produce **compound 9** (reaction scheme 3.1).

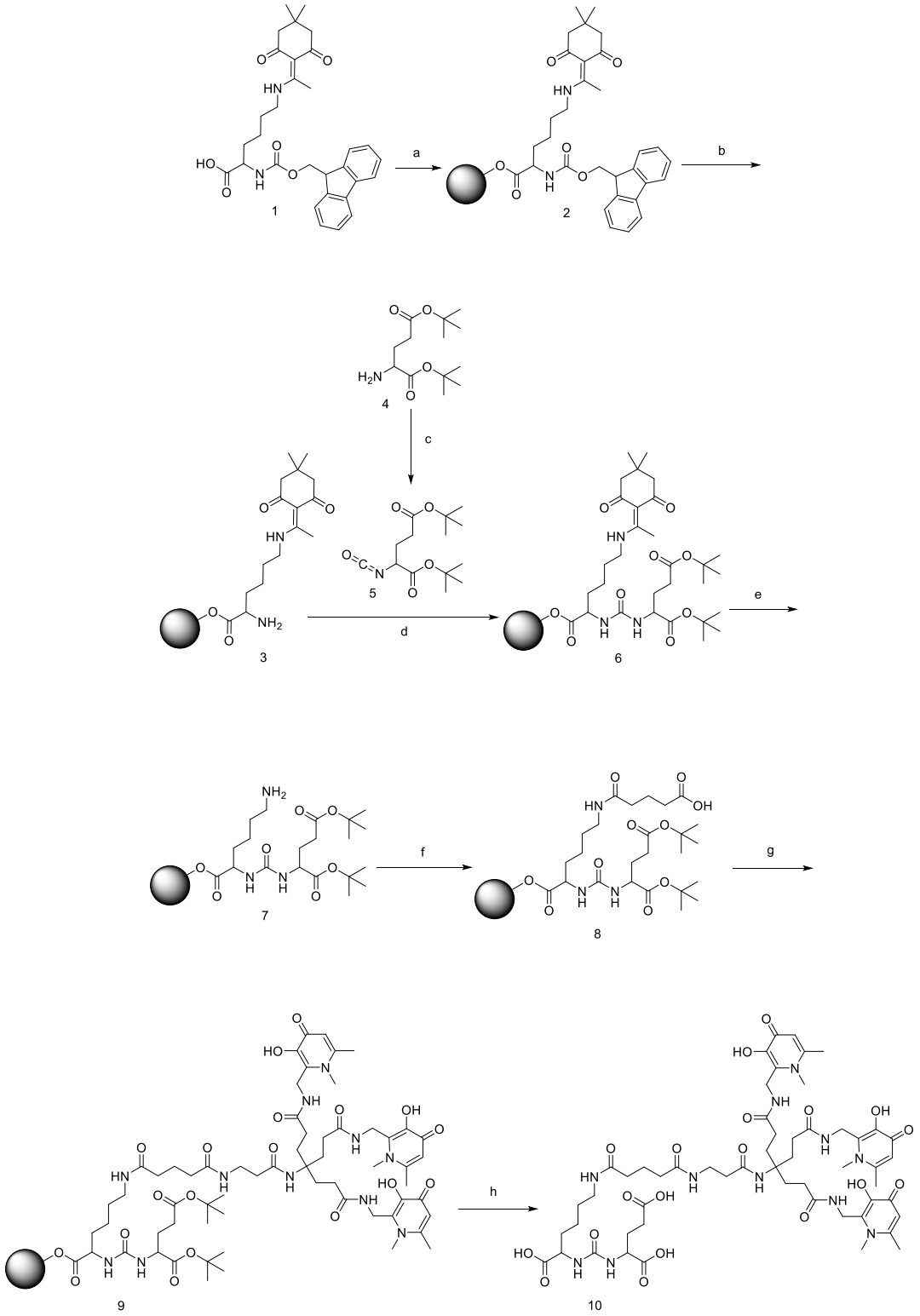

REACTION SCHEME 3.1: Reaction scheme for the synthesis of THP-PSMA. a. 2-chlorotrityl polymer-bound resin beads, DIPEA, DCM; b. Piperidine, DMF; c. Triphosgene, DIPEA, DCM, 0°C; d. Compound 3, Compound 5, DCM; e. Hydrazine hydrate, DMF; f. Glutaric anhydride, DIPEA, DMF; g. THP-NH_2, HATU, DIPEA, DMF, DMSO; h. TFA, phenol, TIPS, H_2O.

Cleavage of THP-PSMA (compound 10) from resin: Cleavage and removal of the side-chain protecting groups were performed by treating the resin-bound **compound 9** with TFA for 3 hours at room temperature in the presence of phenol (5% w/v), water (5% v/v), and triisopropylsilane (2% v/v) as scavengers. The filtrate was collected and the resin washed with TFA and DCM. The solution was concentrated to less than 0.5 mL at 40°C under a gentle stream of nitrogen. Ice-cold diethyl ether was added to precipitate THP-PSMA (**compound 10,** reaction scheme 3.1). The suspension was centrifuged, the supernatant decanted off, the precipitate washed with diethyl ether, and then dissolved in aqueous ACN and lyophilised. Crude THP-PSMA was purified by semi-preparative reversed-phase HPLC to give a TFA salt ($C_{54}H_{77}N_{11}O_{19}.(CF_3COO)_3$) (molecular weight (MW), 1,526.33). Semi-preparative reversed-phase HPLC was conducted using an Agilent Eclipse XDB C_{18} 5 µm 21.2 × 150 mm column with the concentration of mobile phase B increasing at a rate of 1 %/minute (A = H_2O with 0.2% TFA, B = ACN with 0.2% TFA, starting from 100% A at time 0; flow rate, 5 mL/minute). The yield of THP-PSMA$(CF_3COO)_3$ was 4 mg, 2.6 mmol, 5.2% yield from resin loading. The analytical HPLC retention time (R_t) was 13 minutes 23 seconds, and purity was greater than 98% assuming equal extinction coefficients for product and impurities. Analytical data can be found in the results section.

3.3.3 [^{nat}Ga]Ga-THP-PSMA NMR

Varying the gallium to THP-PSMA ratio: Solutions of THP-PSMA (3 mg/mL, MW 1526.33, 2 mM), [^{nat}Ga]Ga$(NO_3)_3.X(H_2O)$ (10 mg/mL, MW anhydrous basis 255.74, < 39 mM) and sodium bicarbonate (0.5 M) were prepared in deuterium oxide (D_2O). [^{nat}Ga]Ga-THP-PSMA was produced by the addition of the gallium nitrate solution to the THP-PSMA solution and neutralising to pH 7 with the sodium bicarbonate solution. 1D ^{1}H NMR spectra of three different samples were obtained: one without gallium (2 mM THP-PSMA, sample 1) one with THP-PSMA in excess (1.9 mM THP-PSMA, < 0.8 mM ^{nat}Ga, sample 2) and a third with gallium in excess (1.3 mM THP-PSMA, < 5.2 mM ^{nat}Ga, sample 3). All concentrations of natural gallium here are a maximum level as they were calculated using the molecular mass of [^{nat}Ga]Ga$(NO_3)_3$ rather than the hydrate.

Stability over time: NMR sample 3 containing excess gallium was kept at 4° C for 3 weeks and monitored with 1D ^{1}H NMR spectroscopy.

Variable temperature NMR spectroscopy: This study was carried out with sample 3, [^{nat}Ga]Ga-THP-PSMA containing excess gallium, to observe the fluxionality of the system. The sample was

evaluated over a range of bore temperatures (5°C, 25°C, 50°C, and 70°C) and was acclimatised for 10 minutes prior to the acquisition of 1D ^{1}H NMR spectra.

3.3.4 Preparation of Lyophilised Kits

One step kits were prepared either in-house, named here "type-A" or by ROTOP Pharmaka GmbH (Dresden-Rossendorf, Germany) named here "type-B". Type A kits for one-step radiolabelling were made by lyophilising an aqueous solution (5.25 mL) containing sodium bicarbonate (44 µg), sodium phosphate monobasic (8.6 mg), sodium phosphate dibasic heptahydrate (8.9 mg), and THP-PSMA (40 mg, 26 nmol) in a plastic vial affording a white powder. Type-B lyophilised kits used with the clinical generator for one-step radiolabelling were The GMP compliant GalliProst™ kits by ROTOP Pharmaka GmbH (Dresden-Rossendorf, Germany) for Theragnostics Ltd. (Bracknell, UK) in radiopharmaceutical grade glass vials, with septum seals. The exact formulation of this kit is confidential, but they contained 40 µg of THP-PSMA (*39*).

3.3.5 Radiolabelling

Radiolabelling and radioanalysis (HPLC and iTLC) of [$^{67/68}$Ga]Ga-DOTA-PSMA (PSMA-617) (*34*), [$^{67/68/nat}$Ga]Ga-HBED-CC-PSMA (DKFZPSMA-11) (*25*)(*35*), and [$^{68/67/nat}$Ga]Ga-THP-PSMA were performed as follows.

[^{68}Ga]Ga-THP-PSMA radiolabelling: Initial gallium-68 radiolabelling optimisation was performed with a Galliapharm (Eckert and Ziegler) germanium-68/gallium-68 generator, producing 120–400 MBq of gallium-68. Eluates (0.1 M HCl, 5 mL, Sigma Aldrich, high-performance capillary electrophoresis grade) were fractionated (10 × 0.5 mL) but not preconditioned to concentrate gallium-68 or remove trace metal contaminants. Typically, gallium-68 (5-75 MBq, 250 µL of the hottest fraction second mL) was added to a solution containing THP-PSMA at a range of concentrations (5-0.01 µg in 3 µL) in sodium bicarbonate solution (1 M, 26 µL), producing a solution with a pH of 6.5-7.5. Radiochemical yield was evaluated after 5 minutes at room temperature using HPLC and iTLC (HPLC: [^{68}Ga]Ga-THP-PSMA retention time (R_t) = 10.9 minutes, unbound [^{68}Ga]Ga^{3+} R_t = 2.32 minutes; iTLC: [^{68}Ga]Ga-THP-PSMA retention factor (R_f) = 0.8–1, unbound [^{68}Ga]Ga^{3+} R_f = 0). For *in vivo* studies, THP-PSMA (2 µg) was labelled with gallium-68 as described above; a greater than 95% radiochemical purity was consistently achieved.

To evaluate labelling using the entire eluate without fractionation, Galliapharm (Eckert and Ziegler) germanium-68/gallium-68 generator eluate (5 mL 0.1 M HCl, 122–202 MBq) or Galli E_O

(IRE ELiT) germanium-68/gallium-68 generator eluate (1.1 mL eluate diluted to 5 mL with 0.1 M HCl, 600–660 MBq) was added directly into a the vented, type-A, freeze-dried, kit vial. After being mixed, carbon dioxide evolution visibly ceased after 15 seconds, providing a transparent, colourless solution at pH 6-7 with a final concentration of 5.25 µM THP-PSMA. ITLC was performed at 5 minutes and HPLC at 10 minutes after reconstitution. Decay-corrected radiochemical yield determined by each method were greater than 95% (n = 3 per generator).

Labelling was also evaluated using type-B kits manufactured by ROTOP Pharmaka GmbH using a pharmaceutical grade Galliapharm (Eckert and Ziegler) germanium-68/gallium-68 generator within a radiopharmacy. The generator was less than 1 month old, produced 1100-1200 MBq of gallium-68, had been validated for clinical use and was pre-eluted 24 hours prior. The generator was eluted with 5 mL clinical grade 0.1 M HCl, directly into the kit vial, which was vented with a needle. The kit was then mixed until the generation of carbon dioxide ceased. 10 minutes after the addition of gallium-68 the activity was 1156 MBq, the pH 6, and the radiochemical purity 97.3%, as assessed by iTLC.

3.3.6 Preparation of PSMA Tracers for Biological Evaluation.

Conversion of [^{67}Ga]Ga-citrate to [^{67}Ga]Ga-chloride: This step is required because the presence of citrate reduces the radiolabelling efficiency of gallium-67 with a number of chelators (*40*). [^{67}Ga]Ga-citrate (6.49 mM citrate; Mallinckrodt) was passed over a Silica Light Sep-Pak cartridge (120 mg sorbent, 55-105 µm particle size) at 1 mL/minute to capture the radio-metal on the cartridge. This process was repeated 3 times whereupon approximately 90% of the activity remained on the cartridge. After being washed with 5 mL of H_2O, the gallium-67 was eluted with 400 µL of 0.1 M HCl and collected in 50 µL fractions. The 5th and 6th fractions which had the highest activity concentration (75 MBq/50 µL) were used for labelling (activity concentration, 1.5 GBq/mL).

[^{67}Ga]Ga-THP-PSMA for *in vitro* studies: 10 µL of a 2 mg/mL solution (20 µg, 13.1 nmol THP-PSMA, molecular weight 1,526.33) was added to 50 µL of [^{67}Ga]Ga^{3+} in 0.1 M HCl (converted from [^{67}Ga]Ga-citrate as described above) and the pH adjusted to 6.5–7.5 with 4.5 µL of 1 M sodium bicarbonate. Labelling was assessed after 5 minutes at room temperature by iTLC and HPLC. Before being added to cells, the tracer was diluted to 50 nM in PBS.

[$^{68/67}$Ga]Ga-DOTA-PSMA(617) for *in vitro* studies: 50 µL of [^{67}Ga]Ga^{3+} or [^{68}Ga]Ga^{3+} in 0.1 M HCl, 5.25 µL of 1 M HCl, and 20 µL of 2.1 M 4-(2-hydroxyethyl)1-piperazineethanesulfonic acid (HEPES) were combined, producing a solution at pH 3.5. For gallium-67 labelling, 20 µg (13.3

nmol) of DOTA-PSMA(617) (ABX; molecular weight, 1,498.18) were added; for gallium-68 labelling, 2 μg (1.3 nmol) of DOTA-PSMA(617) were added. The solution was heated to 95°C for 30 minutes, and then labelling was assessed by iTLC and HPLC. Before being added to cells, the tracer was diluted to 50 nM total ligand concentration in PBS.

[$^{68/67}$Ga]Ga-HBED-CC-PSMA for *in vitro* studies: 50 μL of [^{67}Ga]Ga^{3+} or [^{68}Ga]Ga^{3+}in 0.1 M HCl, 5 μL of 1 M HCl, and 50 μL of 2.1 M HEPES were combined, producing a solution at pH 4.5. For gallium-67 labelling, 29 μg (20.6 nmol) of HBED-CC-PSMA (ABX; molecular weight, 1,403.09) were added; for gallium-68 labelling, 2 μg (1.4 nmol) of HBED-CC-PSMA were added. The solution was heated to 95°C for 10 minutes, and then labelling was assessed by iTLC and HPLC. Before being added to cells, the tracer was diluted to 50 nM total ligand concentration in PBS.

[^{68}Ga]Ga-HBED-CC-PSMA for *in vivo* studies: Gallium-68 eluate (200 μL, 35-50 MBq) was added to a pre-prepared solution of HBED-CC-PSMA (15 μL, 105 μM, 2.2 μg of HBED-CC-PSMA) and sodium bicarbonate (19 μL, 1 M) and heated at 90°C for 10 minutes (pH 3-4). A radiochemical yield of greater than 95% was achieved consistently.

3.3.7 Preparation of Natural Gallium Chelated PSMA Complexes.

[^{nat}Ga]Ga-THP-PSMA: 124 μL of 0.93 mM THP-PSMA were added to 93 μL of 6.4 mg/mL [^{nat}Ga]$Ga(NO_3)_3.X(H_2O)$ dissolved in 0.1 M HCl (a 20-fold excess of gallium over THP-PSMA). The pH was adjusted to 6.5–7.5 with 14 μL of 1 M sodium bicarbonate, and 231 μL of PBS was then added. The solution was sonicated for 15 minutes, producing a final solution of 0.25 mM [^{nat}Ga]Ga-THP-PSMA. This solution was diluted in PBS to produce the range of concentrations required for the inhibition assay (50% inhibition constant, IC_{50}). This complex was characterised by LC-ESIMS as shown in table 3.2**.**

[^{nat}Ga]Ga-HBED-CC-PSMA: 124 μL of 0.93 mM HBED-CC-PSMA were added to 93 μL of 6.4 mg/mL [^{nat}Ga]$Ga(NO_3)_3.X(H_2O)$ dissolved in 0.1 M HCl (a 20-fold excess of gallium over HBED-CC-PSMA). The pH was adjusted to 4 with 13 μL of 1 M sodium bicarbonate, and the solution was heated to 95°C for 10 minutes. The pH was adjusted to 6.5-7.5 with 1 M sodium bicarbonate followed by sonication for 15 minutes, producing a final solution of 0.5 mM [^{nat}Ga]Ga-HBED-CC-PSMA. This solution was diluted in PBS to produce the range of concentrations required for the IC_{50} measurement.

3.3.8 Stability of [^{68}Ga]Ga-THP-PSMA and [^{68}Ga]Ga-DOTA-PSMA(617) in the presence of unchelated gallium

[^{68}Ga]Ga-THP-PSMA or [^{68}Ga]Ga-DOTA-PSMA(617) (molar activity 30.81 and 4 MBq/nmol respectively) was added to a solution of [^{nat}Ga]Ga(NO_3)$_3$.X(H_2O) in PBS. Final radiotracer total ligand concentration was 1 nM, final concentration of [^{nat}Ga]Ga(NO_3)$_3$.X(H_2O) ranged from 0 mg/mL to 0.5 mg/mL. Stability was monitored up to 2 hours by iTLC.

3.3.9 Log D $_{OCT/PBS}$ measurement

Each [^{67}Ga]Ga-labelled radiotracer (50 µL, 10 µM; molar activity, 1.5 MBq/nmol) was added to a pre-equilibrated mixture of 500 µL of octanol (OCT) and 450 µL of PBS (pH 7.4). The mixture was mixed for 30 minutes with a shaker plate and the phases separated by centrifugation (10,000 rpm, 10 minutes). Aliquots from each phase were analysed on a gamma counter.

3.3.10 Serum Stability

[^{68}Ga]Ga-THP-PSMA was labelled at 5 MBq/nmol and 20 µL were added to 180 µL of human serum, giving a final THP-PSMA concentration of 2.5 µM. Samples were incubated at 37°C and monitored over 6 hours by size-exclusion HPLC. [^{68}Ga]Ga-THP-PSMA without serum and unchelated [^{68}Ga]Ga^{3+} incubated with serum were analysed similarly.

3.3.11 Cell Lines

The GCP(II)/PSMA negative cell line chosen was DU145, a human carcinoma prostate cancer cell line derived from a brain metastatic site, which does not express GCP(II)/PSMA. The GCP(II)/PSMA-expressing cell line chosen was a genetically modified daughter cell line of DU145, DU145-PSMA. This cell line had previously been transduced to express full-length human GCP(II)/PSMA, following a published method (*37*). These cells were cultured in RPMI 1640 medium supplemented with 10% foetal bovine serum, 2 mM L-glutamine, and penicillin/streptomycin. To prepare for experiments, cells were grown at 37°C in an incubator with humidified air equilibrated with 5% CO_2.

3.3.12 Flow Cytometry

Expression of GCP(II)/PSMA in the DU145-PSMA cell line and the absence of this receptor in the DU145 cell line was assessed using flow cytometry. 1×10^6 cells were suspended in 100 µL PBS

containing 0.5% bovine serum albumin and then incubated with 10 µL of either Anti-PSMA-VioBright-FITC antibody (MACS Milenyi Biotec CAT 130-106-612), REA-control-VioBright-FITC (MACS Milenyi Biotec CAT 130-113-455) or PBS, for 15 minutes on ice. After this time the cells were washed twice with PBS and then analysed on a FACS Calibur (FL1 channel, voltage 525). Gating and analysis were performed using Flowing Software (version 2.5.1, Turku Centre for Biotechnology, University of Turku, Finland).

3.3.13 Gamma Counting

Radioactivity counting was performed with a gamma-counter (LKB Wallac; PerkinElmer) for log $P_{OCT/PBS}$ measurement, cell studies and *in vivo* biodistribution. The emissions from gallium-67 and gallium-68 for each detection window of the LKB Wallac gamma-counter (PerkinElmer) were measured and are shown in figure 3.2, including the measurement windows set during the measurements.

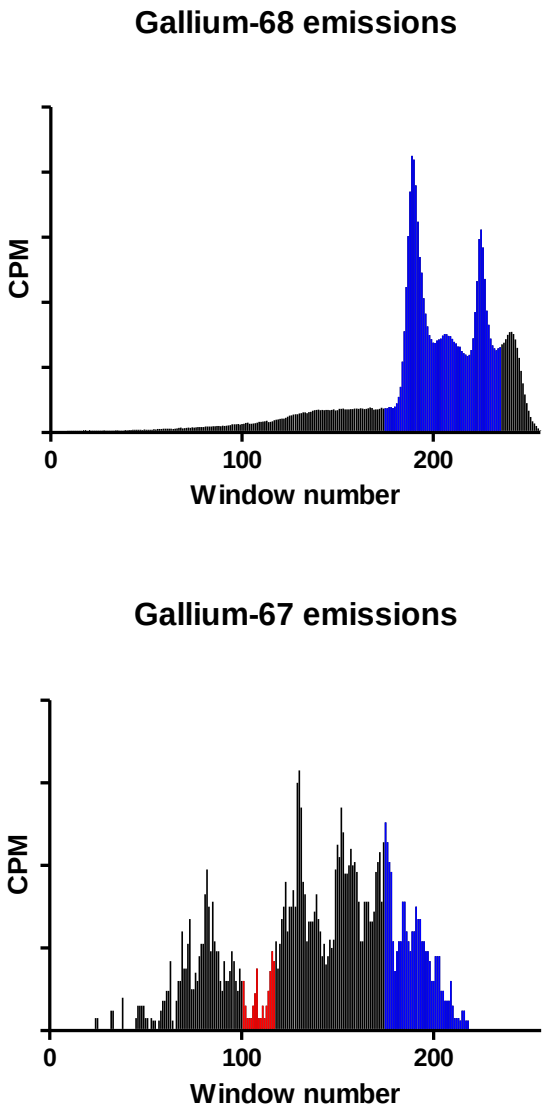

FIGURE 3.2: Emissions from (top) gallium-68 and (bottom) gallium-67 across all energy windows detectable by the gamma-counter. The range of windows used to measure the presence of gallium-67 (101-117) in red and gallium-68 (175-235) are shown in blue, highlighting the overlap in emissions.

3.3.14 Cell Uptake and IC_{50} Assays

Cell uptake: To determine the specificity of [^{68}Ga]Ga-THP-PSMA for GCP(II)/PSMA-expressing cells, the cellular uptake was determined in GCP(II)/PSMA-expressing cells DU145-PSMA and non–GCP(II)/PSMA-expressing cells DU145 (*37*). The two cell lines were seeded in a 6 well plate (1 x 10^6 cells/well) 1 day before the assay. Prior to incubation, the medium was replaced with 980 µL of fresh complete medium and then 20 µL of [^{68}Ga]Ga-THP-PSMA was added (radiolabelling mixture diluted in PBS) to give a 1 nM total ligand concentration on cells. Plates were incubated at 37°C for 1 hour. Then the supernatant was removed and the cells were washed with 2 × 1 mL PBS to determine the unbound fraction, followed by an acid wash (0.5 M glycine, pH 2.5, at 4°C, 5 minutes) to determine cell surface-bound activity. Attached cells were lysed with 1 M NaOH to determine activity internalised by the cells. Fractions were then gamma-counted.

Cell uptake over time: To determine the cellular uptake of each tracer at 37°C and 4°C over time DU145-PSMA DU145 were seeded in a 24-well plate (0.25 × 10^6 cells/well), 1 day before the assay. Two minutes before incubation, the medium was replaced with 245 µL of fresh complete medium at 37°C or 4 °C, then 5 µL of one of the [^{67}Ga]Ga-PSMA tracers (molar activity, 0.75–2.2 MBq/nmol) were added, giving a final total ligand concentration of 1 nM. Plates were incubated at 37°C or 4°C. At each time point, the supernatant was removed and cells were washed with 3 × 250 µL of PBS to determine the unbound fraction, followed by an acid wash (0.5 M glycine, pH 2.5, at 4°C, 5 minutes) to determine cell surface–bound activity. Cells were lysed with 1 M NaOH to determine activity internalised by the cells. Fractions were gamma-counted.

IC_{50}: To determine the IC_{50}, competitive binding studies were performed with DU145-PSMA cells with 1 nM [^{68}Ga]Ga-DOTA-PSMA(617) as the probe, blocked with [^{nat}Ga]Ga-THP-PSMA or [^{nat}Ga]Ga-HBED-CC-PSMA over a range of concentrations. Cells (0.25 × 10^6 per well) were seeded in a 24-well plate, 1 day before the assay. Before incubation, the medium was replaced with 240 µL of fresh complete medium. Increasing concentrations of [^{nat}Ga]Ga-THP-PSMA or [^{nat}Ga]Ga-HBED-CC-PSMA (5 µL) followed by 1 nM [^{68}Ga]Ga-DOTA-PSMA(617) (5 µL, molar activity, 5–7.5 MBq/nmol ligand, diluted in PBS) were added to the cells (total volume, 250 µL). After 30 minutes incubation at 37°C, the cells were washed with PBS (3 × 250 µL), lysed with NaOH (1 M, 250 µL), and the wells washed with PBS (250 µL). The activity present in supernatant and lysate was measured by gamma-counting. Data were analysed using GraphPad Prism (version 5.04, GraphPad Software) and a 1-site-fit log IC_{50} algorithm.

3.3.15 *Relative* Affinity Measurements

Due to the poor solubility of [^{nat}Ga]Ga-THP-PSMA above 0.25 mM, an alternative measure of affinity was developed, allowing the *relative* affinity of 2 gallium PSMA tracers to be determined simultaneously without the need for the natural gallium complex, therefore mitigating any solubility difficulties. The assay was designed based on Clark's theory of classical ligand-receptor interactions (*41*) and allowed the *relative* affinity of the 2 tracers to be determined. The assumptions and equations on which this assay was based on are detailed in section 3.8. In brief these equations show that in order to calculate the *relative* affinity (dissociation constant = K_d) of two tracers, they must be incubated at the same time with the same receptor and their specific binding determined once the uptake has reached equilibrium. The cell uptake over time assay described above was used to determine that equilibrium was reached after incubation at 4°C for 2 hours (figure 3.17). The 2 isotopes of gallium, gallium-67 and gallium-68, with their different half-lives (3.2613 days and 67.83 minutes respectively (*9*)(*42*)) and different emission profiles make it possible for two radiotracers to be incubated at the same time with the same receptor and their individual emissions and therefore uptake to be determined. The tracers compared in this study were: [$^{67/68}$Ga]Ga-DOTA-PSMA, [$^{67/68}$Ga]Ga-HBED-CC-PSMA, and [$^{67/68}$Ga]Ga-THP-PSMA. Each [^{67}Ga]Ga-PSMA tracer was compared to each [^{68}Ga]Ga-tracer (table 3.1) and affinity ratios were obtained by measuring total and non-specific binding for each tracer (gamma counting) and calculating the ratio of their specific binding.

The *relative* affinity measurements were carried out using the following methodology. DU145-PSMA cells were seeded with 1.5 x 10^6 cells/well in a 6 well plate, one day before the assay. Two minutes prior to incubation with tracer, the cell medium was replaced by 1410 µL fresh complete medium at 4°C. 30 µL of [^{67}Ga]Ga-PSMA tracer (50 nM, molar activity 0.75-2.2 MBq/nmol), and 30 µL [^{68}Ga]Ga-PSMA tracer (50 nM, molar activity 4-26 MBq/nmol, diluted in PBS) and 30 µL PBS were added, giving a total volume of 1.5 mL and final concentrations of 1 nM [^{67}Ga]Ga-PSMA tracer and 1 nM [^{68}Ga]Ga-PSMA tracer (total labelled and unlabelled PSMA conjugate concentration 2 nM). Additionally, non-specific uptake was determined by using non-GCP(II)/PSMA-expressing cells (DU145) or by blocking GCP(II)/PSMA-expressing cells (DU145-PSMA) with 750 µM PMPA (30 µL in place of the PBS added 2 minutes before the radiotracers). After 2 hours incubation at 4°C, the cells were washed with 3 × 250 µL 4°C PBS to determine the unbound fraction. They were then incubated with 0.5 M glycine pH 2.5 at 4°C for 5 minutes to determine the cell surface-bound fraction and then lysed with 1 M NaOH and the well washed with PBS to determine the fraction internalized by the cells. The activity from the [^{67}Ga]Ga-PSMA

tracer and the [^{68}Ga]Ga-PSMA tracer present in each fraction was measured by gamma counting (gallium-68 values were corrected for their gallium-67 component and gallium-67 was measured once the gallium-68 within the sample had decayed (> 10 half-lives) and all values were decay corrected). Specific binding was calculated by subtracting the non-specific binding (binding of the tracer to DU145 cells or to DU145-PSMA cells in the presence of PMPA) from the total binding percentage of activity associated with the DU145-PSMA cells when no blocking agent is present. Ratios of specific binding were calculated pair-wise for tracers incubated in the same well.

	[^{67}Ga]Ga-DOTA-PSMA(617)	[^{67}Ga]Ga-HBED-CC-PSMA	[^{67}Ga]Ga-THP-PSMA
[^{68}Ga]Ga-DOTA-PSMA(617) DU145-PSMA		9	18
[^{68}Ga]Ga-DOTA-PSMA(617) DU145		3	9
[^{68}Ga]Ga-DOTA-PSMA(617) DU145-PSMA + 750 mM PMPA		3	9
[^{68}Ga]Ga-HBED-CC-PSMA DU145-PSMA	9		18
[^{68}Ga]Ga-HBED-CC-PSMA DU145	3		9
[^{68}Ga]Ga-HBED-CC-PSMA DU145-PSMA + 750 mM PMPA	3		9
[^{68}Ga]Ga-THP-PSMA DU145-PSMA	18	18	
[^{68}Ga]Ga-THP-PSMA DU145	9	9	
[^{68}Ga]Ga-THP-PSMA DU145-PSMA + 750 mM PMPA	9	9	

TABLE 3.1: Number of wells incubated with each combination of tracers and blocking agents for the *relative* affinity measurements.

3.3.16 Mouse Model of Prostate Cancer

Animal studies complied with the guidelines on responsibility in the use of animals in bioscience research of the U.K. Research Councils and Medical Research Charities, under U.K. Home Office project and personal licences. Subcutaneous prostate cancer xenografts were produced in SCID/beige mice (male, 5-12 weeks old) by injecting 4×10^6 DU145-PSMA or DU145 cells suspended in serum-free media the right flank. Imaging was performed once a tumour had

reached 5-10 mm in diameter (1-4 weeks after injection). In order to provide a further control, one SCID beige mouse was injected with 4 × 10^6 DU145-PSMA into the right flank and an additional 4 × 10^6 DU145 cells into the left flank. Imaging was performed when the diameter of each tumour was 5 mm ensuring that the total tumour was below the 11 mm diameter project licence limit (3 weeks after inoculation).

3.3.17 PET/CT scanning

PET imaging was performed on mice under isoflurane anaesthesia with a BioScan nanoPET-CT PLUS (Mediso Medical Imaging Systems, Budapest, Hungary)

Mice without prostate cancer xenografts: A SCID/beige male mouse without a prostate cancer xenograft, was anaesthetised, positioned on the scanner, and its tail vein cannulated. A CT scan was performed and then a PET scan was initiated as [^{68}Ga]Ga-THP-PSMA (10.6 MBq, 114 µL, 0.5 µg) was administered. This ensured that the first pass of the tracer was imaged. The PET scan was acquired for a total of 4 hours and was a terminal procedure.

Mice with a single prostate cancer xenograft: PET/CT imaging was performed on 4 groups of mice (n = 3 each). Before radiotracer administration, CT was performed, the tracer was then injected through the cannulated tail vein and dynamic PET data was collected for the first hour after injection. Mice were then euthanised by cervical dislocation and organs harvested, weighed, and gamma-counted. Mice bearing DU145-PSMA tumours were administered either [^{68}Ga]Ga-THP-PSMA (5-15 MBq, 50-140 µL, 0.4-0.9 µg, group 1) or [^{68}Ga]Ga-HBED-CC-PSMA (5-15 MBq, 50-140 µL, 0.6-1.3 µg, group 2) by tail vein injection. A third group (group 3) was co-administered [^{68}Ga]Ga-THP-PSMA and the GCP(II)/PSMA-inhibitor, PMPA (50 µg) (*43*)(*44*) for blocking studies. Mice bearing DU145 tumours were administered [^{68}Ga]Ga-THP-PSMA (group 4).

Mouse with two prostate cancer xenografts: A 1 hour PET scan was acquired after tail vein administration of [^{68}Ga]Ga-THP-PSMA (104 µL, 8.7 MBq, 0.7 µg), a CT scan was then performed, and after completion, the mouse was culled by cervical dislocation.

Imaging protocol: The PET/CT scans were obtained on a BioScan nanoPET-CT PLUS (Mediso Medical Imaging Systems, Budapest, Hungary) scanner using their proprietary acquisition software (Nucline, version 2.00). CT was performed with an X-ray tube voltage of 45 kVp, 600 ms of exposure time, and 360° projections. This scan took 10 minutes to obtain. All dynamic PET scans were acquired within a 94.7 mm field of view from 0 to 60 minutes after tail vein injection of the [^{68}Ga]Ga-PSMA tracer, for the non-tumour bearing mouse that was imaged for 4 hours, 4

× 60 minute scans were performed. Acquisition took place in 1-5 coincidence mode with a coincidence window of 5 ns and a 400-600 keV energy window. The dynamic PET data were reconstructed using Nucline software (version 2.00). Data were allocated to both 20 and 2 minute bins using 0.4 mm^3 voxels for PET and 0.21 mm^3 voxels for CT.

Image processing: Image processing and analysis were performed using Vivoquant software (version 1.23). Before analysis, both CT and PET images were realigned and processed to a voxel size of 0.21 mm^3 and the PET output calibrated to display MBq per voxel. Regions of interest (ROIs) for each data file were produced using 3 different techniques: fixed-volume ROIs, Otsu thresholding, and freehand segmentation from the CT image. Fixed-volume ROIs were used for muscle (a 17.2 mm^3 sphere within the thigh muscle) and blood pool (a 2.2 mm^3 sphere in the left ventricle). These ROIs were positioned manually and drawn in triplicate within each organ. Otsu thresholding was used to determine the total activity deriving from the kidneys or the bladder. This method was not suitable for tumour uptake because of the close proximity of kidney signal. Total tumour volume was drawn manually from the CT image, defined 3 times per animal, and the average value from these 3 ROIs determined. Percentage injected dose per cubic centimetre (%ID/cm^3) values for each ROI were calculated using the activity and volume of the ROI and the injected dose (ID) as the total activity within the image, excluding activity within the tail. Time-activity curves were produced from the 2 minute bins, and total uptake was determined from the 20 minute binned data at the 40-60 minute time point. Static images were produced from dynamic data between 40 and 60 minutes and scaled between 0 and 25 %ID/cm^3. The images of the mice without prostate cancer xenografts and the mouse with two prostate cancer xenografts were analysed in the same manner but the images were scaled between 0 and 10 %ID/cm^3.

3.3.18 Biodistribution Studies

Additional [^{68}Ga]Ga-THP-PSMA biodistribution and blocking studies were performed in mice bearing DU145 or DU145-PSMA tumours without imaging or continuous anaesthesia. [^{68}Ga]Ga-THP-PSMA (3.5–12.7 MBq, 0.7–0.9 mg THP-PSMA) was administered via tail vein injection under isoflurane anaesthesia. After injection anaesthesia ceased and 1 hour after injection the animals were euthanized by cervical dislocation and organs harvested, weighed, and counted (n = 3 for each group).

3.3.19 Statistical Analysis

Data were analysed in GraphPad Prism 5 (version 5.04 or version 7.04) and expressed as mean ± standard deviation (SD). Student t tests were used to determine statistical significance; a P value of less than 0.05 was considered significant.

3.4 Results

3.4.1 Synthesis of THP-PSMA

Reaction Scheme 3.1 shows the route used to synthesise THP-PSMA. The resin-bound PSMA inhibitor (**compound 7**) was prepared by *in situ* formation of a bis(tert-butyl) glutamate isocyanate (**compound 5**) followed by coupling with resin-bound protected lysine (**compound 3**). After deprotection and coupling with glutaric anhydride, the intermediate bearing a pendant carboxylate (**compound 8**) was activated with HATU and formed an amide bond with the free amine of a THP derivative (*38*). Cleavage from the solid support and glutamate deprotection using trifluoroacetic acid (TFA) formed THP-PSMA (figure 3.1 and reaction scheme 3.1). Purification by semi-preparative HPLC afforded THP-PSMA as a TFA salt, yield 4 mg, 2.6 µmol, 5.2% yield, ($C_{54}H_{77}N_{11}O_{19}.(CF_3COO)_3$) calculated molecular weight of TFA salt 1526.33, HPLC: R_t = 13.4 minutes, greater than 98% purity. LC-ESIMS data are shown in figure 3.3, figure 3.4 and table 3.2. ^{1}H NMR: (D_2O, pH 3, 700 MHz): 1.37 (m, 2H), 1.50 (m, 2H), 1.7 (m, 1H), 1.78 (m, 2H), 1.85 (m, 1H), 1.92 (t, *J* = 8.09, 6H), 1.96 (m, 1H), 2.14 (m, 1H), 2.18 (dd, *J*= 6.59, 4H), 2.22 (t, *J* = 8.09, 6H), 2.35 (t, *J* =6.64, 2H), 2.49 (t, *J* = 7.49, 2H), 2.57 (s, 9H), 3.13 (t, *J* = 6.98, 2H), 3.36 (t, *J* = 6.64, 2H), 3.91 (s, 9H), 4.15 (dd, *J* = 8.99, 5.59 1H), 4.23 (dd, *J* = 8.70, 4.97 1H), 4.67 (s, 9H), 7.00 (s, 3H) ^{13}C[^{1}H] NMR: (D_2O, pH 3, 175 MHz): 20.5, 21.9, 22.4, 26.5, 27.8, 29.3, 29.4, 30.1, 30.7, 34.8, 35.5, 35.9, 36.1, 38.5, 39.0, 52.8, 113.6, 138.1, 143.2, 149.9, 159.4, 161.0, 173.2, 175.5, 175.7, 176.2, 176.6, 177.4. Additional ^{1}H, and ^{13}C NMR data are shown in figure 3.5, table 3.3, table 3.4 and table 3.5.

Ion	Calculated monoisotopic peak (m/z values)	Observed monoisotopic peak (m/z values)
$[C_{54}H_{77}N_{11}O_{19} + 2H]^{+2}$	592.77714	592.77689
$[C_{54}H_{77}N_{11}O_{19} + 3H]^{+3}$	395.52052	395.52027
$[C_{54}H_{74}N_{11}O_{19}Ga + H]^{+}$	1250.44910	1250.45092
$[C_{54}H_{74}N_{11}O_{19}Ga + 2H]^{+2}$	625.72819	625.72846

TABLE 3.2: Observed and calculated ESI-MS data from LCMS for THP-PSMA and [^{nat}Ga]Ga-THP-PSMA.

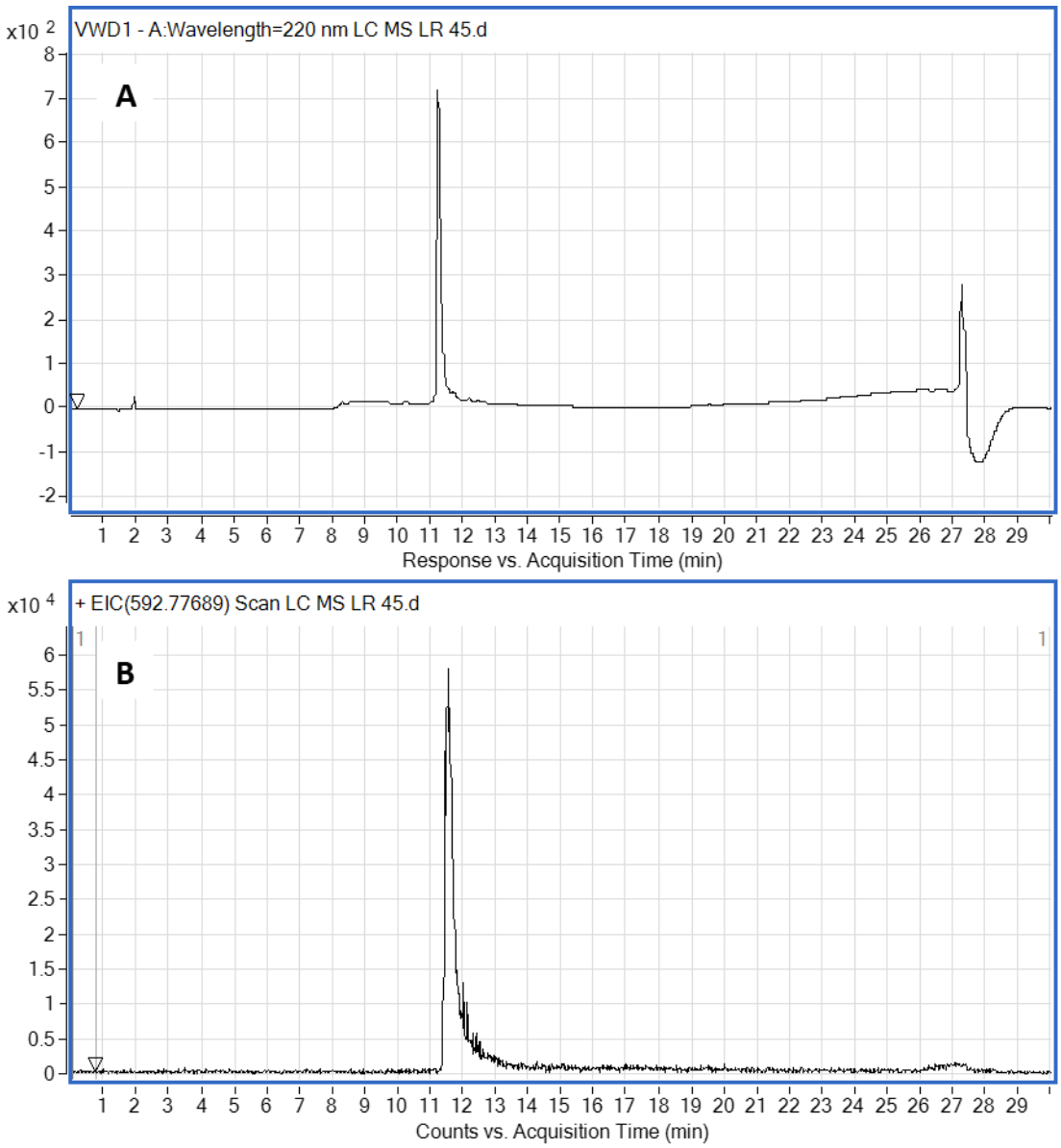

FIGURE 3.3: LC-MS (A) UV 220 nm and (B) extracted ion chromatogram of THP-PSMA.

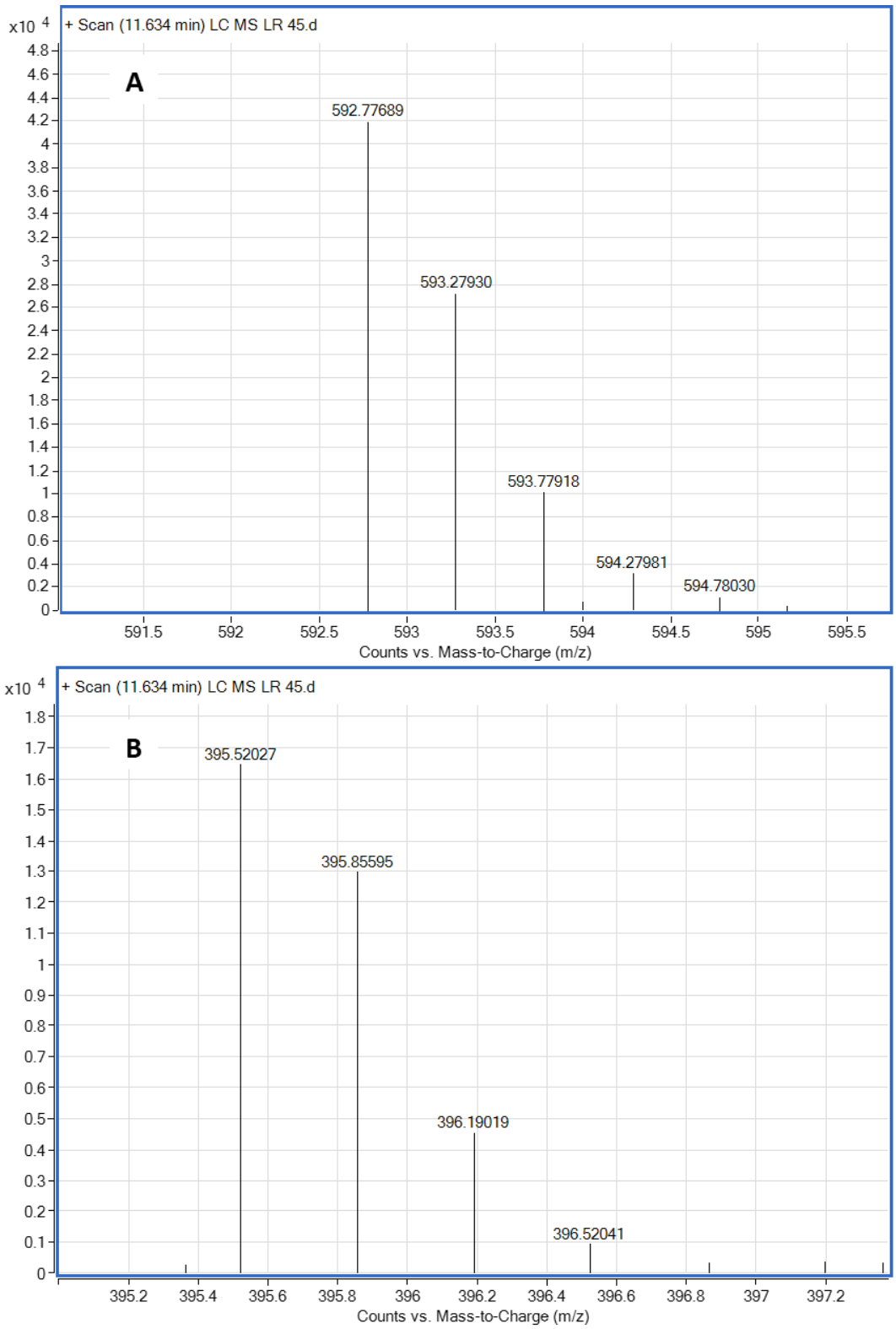

FIGURE 3.4: Mass spectrum of THP-PSMA (A) $[C_{54}H_{77}N_{11}O_{19} + 2H]^{+2}$ and (B) $[C_{54}H_{77}N_{11}O_{19} + 3H]^{+3}$ both obtained from different regions of the same LC-MS spectrum at a retention time of 11.6 minutes.

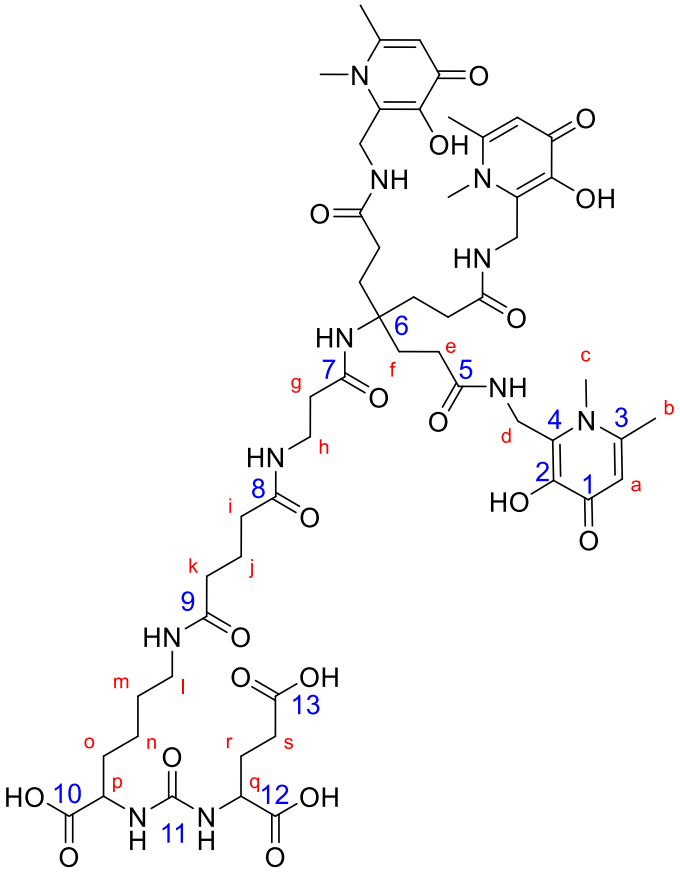

FIGURE 3.5: Structure of THP-PSMA with protons detectable in D_2O labelled a- s (red) and additional carbon atoms labelled 1-13 (blue).

Atom label	No. ^{1}H in each enviro-nment	Number of adjacent protons	PPM	Integration	Splitting	^{1}H COSY	^{1}H TOSCY Strong corr.	^{1}H TOSCY Weaker corr.
m	2	4	1.36	2.23	m			
n	2	4	1.50	2.26	m	l		
o_2	1	4	1.70	1.10	m		n,m	p
j	2	4	1.78	2.53	m	i+k	i+k	
o_1	1	4	1.85	0.75	m		n,m	p
f	6	2	1.93	6.53	t		e	
r_2	1	4	1.96	0.94	m			
r_1	1	4	2.14	1.04	m			
k+i	4	2	2.18	4.47	dd	j	j	
e	6	2	2.22	6.36	t		f	
g	2	2	2.35	2.23	t	h	h	
s	2	2	2.49	2.33	t	r_1, r_2	r_1, r_2	
c	9	0	2.57	9.67	s			
l	2	2	3.13	2.16	t	m	m	n
h	2	2	3.36	2.12	t	g	g	
un-known			3.71	1.60	s			
b	9	0	3.91	9 (calibrated to 9)	s			
p	1	2	4.14	1.01	dd	o_1, o_2	o_1, o_2	n, m
q	1	2	4.23	1.06	dd	r_1, r_2	r_1, r_2	s
d	6	0	4.67	2.62	s			
a	3	0	7.00	2.84	s			

TABLE 3.3: Assignment of ^{1}H NMR (400 MHz, D_2O) spectra, and summary of correlations detected in 2D ^{1}H COSY and 2D ^{1}H TOCSY spectra of THP-PSMA pH 3. Integration calibrated to the height of the peak corresponding to the 9 methyl hydrogens in position 'b'. s = singlet, d = doublet, t = triplet, dd = doublet of doublets, m = multiplet.

Atom Label	Number of ^{13}C in each environment	ppm	Integration	HSQC correlation observed
1	3	177.40	2.91	
13	1	176.62	1.38	
5	3	176.15	3.13	
10	1	175.74	1.06	
12	1	175.45	0.91	
7	1	173.21	0.85	
8,9	2	161.02	2.87	
11	1	159.38	1 (calibrated to 1)	
3	3	149.95	3.23	
2	2	143.17	2.85	
4	3	138.15	2.49	
a	3	113.61	5.91	A
unknown		69.68	1.64	unknown ^{1}H at 3.7ppm
6	1	58.23	0.95	
p	1	53.54	1.34	p
q	1	52.78	1.72	q
l	1	39.02	1.67	l
b	3	38.50	4.93	b
g	1	36.07	1.26	g
h	1	35.96	1.50	h
d	3	35.53	4.90	d
k + i	2	34.88	4.35	k + i
o	1	30.72	1.79	o
s	1	30.11	2.45	s
e	3	29.43	4.32	e
f	3	29.27	5.07	f
m	1	27.78	2.12	m
r	1	26.48	1.87	r1 + r2
n	1	22.38	1.93	n
j	1	21.91	1.85	j
c	3	20.52	5.93	c

TABLE 3.4: Assignment of signals within the ^{13}C spectra of THP-PSMA (175 MHz, D_2O) pH 3 and HSQC correlation. Integration calibrated to the height of the peak corresponding to the 1 urea carbon in position 11.

Atom label	No. ^{1}H in each environment	Number of adjacent protons	PPM	Integration	Splitting
m	2	4	1.33	2.25	m
n	2	4	1.48	2.08	m
o_2	1	4	1.61	1.07	m
o_1	1	4	1.71	0.97	m
j	2	4	1.76	2.08	t
r_2	1	4	1.84	1.27	m
f	6	2	1.94	5.70	t
r_1	1	4	1.99	1.34	m
k+i	4	2	2.16	4.05	q
e + g	6	2	2.22	8.05	t
s	2	2	2.37	2.20	t
c	9	0	2.39	8.73	s
l	2	2	3.11	8.73	t
h	2	2	3.37	3.12	t
unknown			3.72	1.52	s
b	9	0	3.66	9 (calibrated to 9)	s
p+q	1	2	3.99	1.96	q
d	6	0	4.54	3.73	s
a	3	0	6.45	2.70	s

TABLE 3.5: Assignment of ^{1}H NMR spectra of THP-PSMA (400 MHz, D_2O) pH 7. Integration calibrated to the height of the peak corresponding to the 9 methyl hydrogens in position b.

3.4.2 [^{nat}Ga]Ga-THP-PSMA NMR

Varying gallium to ligand ratio: The change to the ^{1}H spectrum of THP-PSMA upon adding gallium to form [^{nat}Ga]Ga-THP-PSMA was studied using 3 different samples, all in D_2O at pH 7 (neutralised with sodium bicarbonate). Sample 1 contained THP-PSMA, sample 2 contained THP-PSMA plus [^{nat}Ga]Ga-THP-PSMA with THP-PSMA in excess and sample 3 contained [^{nat}Ga]Ga-THP-PSMA plus excess gallium. Changes in the ^{1}H spectra were observed at both levels of gallium. In sample 2, the signal deriving from THP-PSMA remained stable, but a set of new peaks with lower intensity, corresponding to the signal from [^{nat}Ga]Ga-THP-PSMA, were observed as shown in figure 3.6. In sample 3 when ^{nat}Ga was in excess, the peaks from THP-PSMA disappeared and the [^{nat}Ga]Ga-THP-PSMA peaks increased in intensity (figure 3.6). Therefore there is only evidence of two species in solution, the free ligand and the complexed ligand. There was no change to the shape or shift of the [^{nat}Ga]Ga-THP-PSMA signal with further addition of gallium, only the intensity increased, suggesting the structure of the [^{nat}Ga]Ga-THP-PSMA complex formed does not change between the two concentrations, and it is assumed that this represents the 1:1 stoichiometry as seen in the MS results.

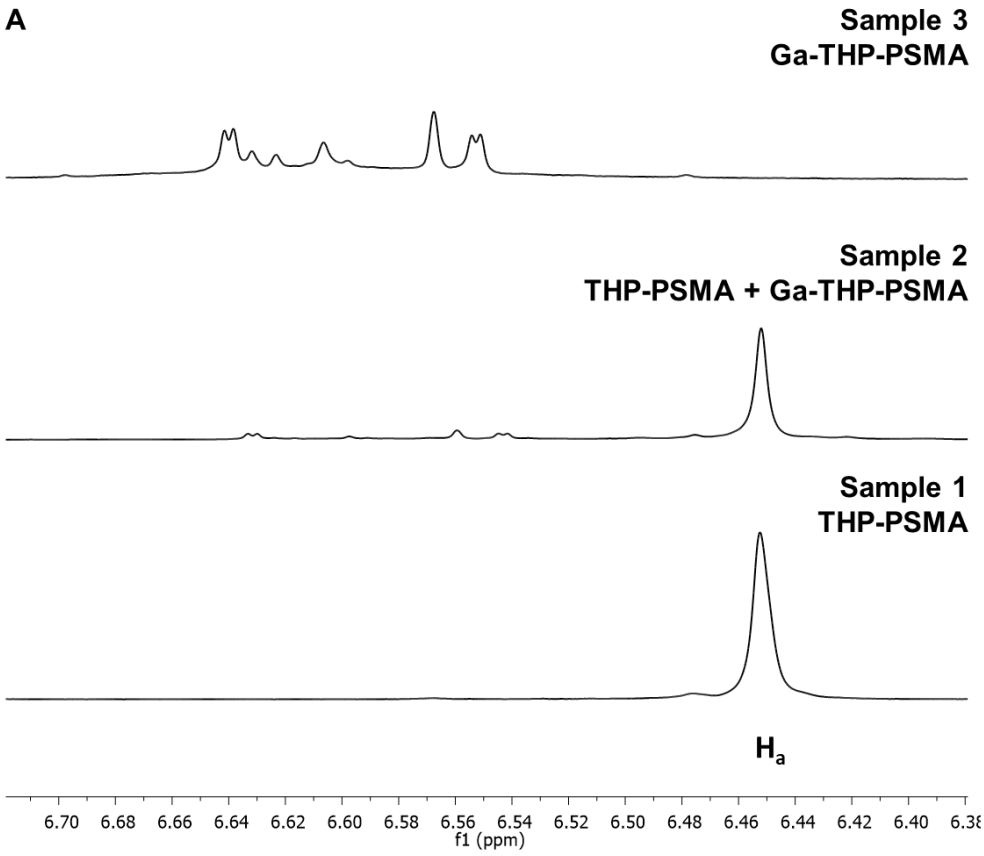
A
Sample 3
Ga-THP-PSMA
Sample 2
THP-PSMA + Ga-THP-PSMA
Sample 1
THP-PSMA
Ha
6.70 6.68 6.66 6.64 6.62 6.60 6.58 6.56 6.54 6.52 6.50 6.48 6.46 6.44 6.42 6.40
f1 (ppm)

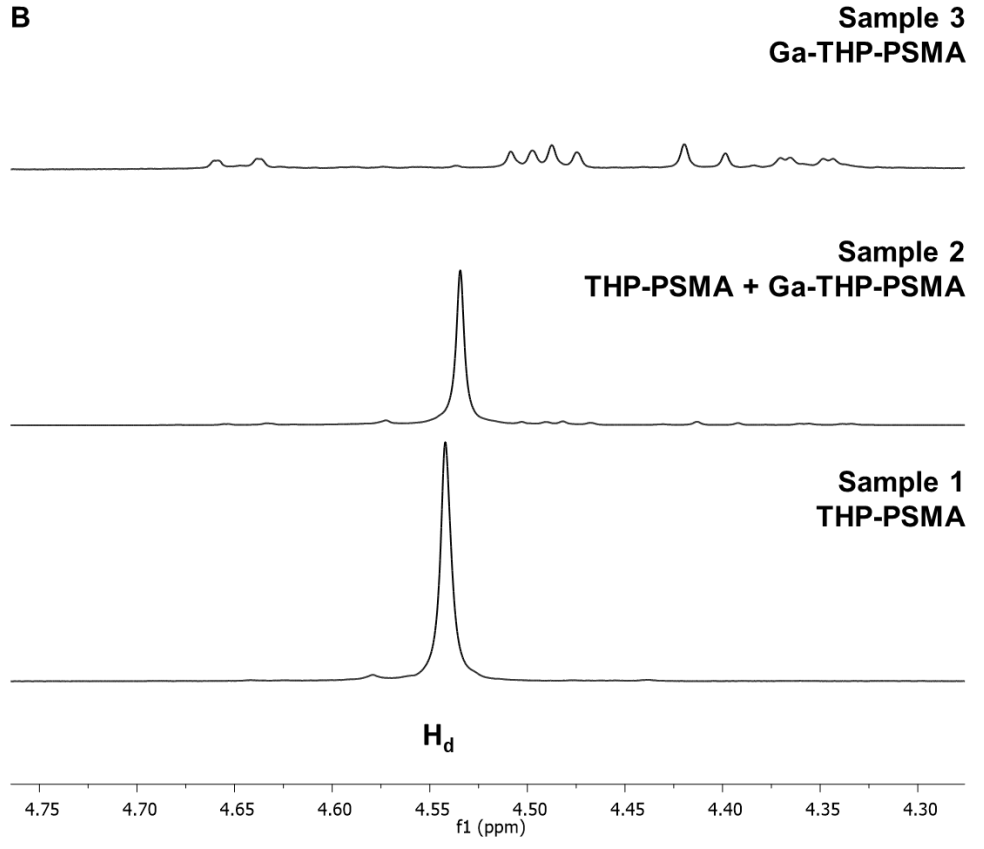
B
Sample 3
Ga-THP-PSMA
Sample 2
THP-PSMA + Ga-THP-PSMA
Sample 1
THP-PSMA
Hd
4.75 4.70 4.65 4.60 4.55 4.50 4.45 4.40 4.35 4.30
f1 (ppm)

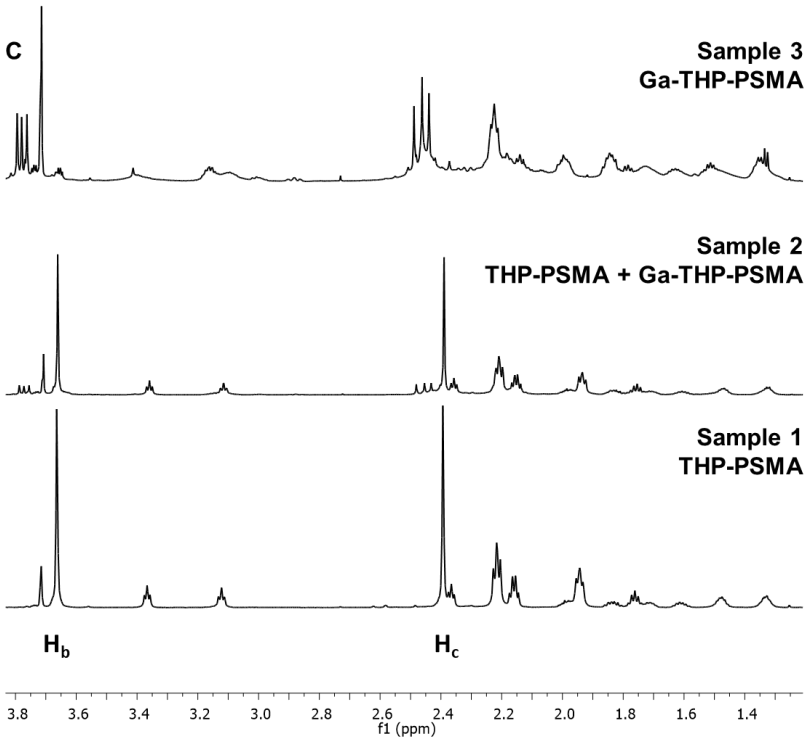

FIGURE 3.6: Change in ^{1}H NMR spectrum as gallium is added to THP-PSMA. Sample 1, THP-PSMA; sample 2, THP-PSMA plus Ga-THP-PSMA with THP-PSMA in excess; sample 3, Ga-THP-PSMA excess Ga. (A) NMR spectrum between 6.3 and 6.7 ppm showing signal from H_a protons; (B) NMR spectrum between 4.2 and 4.75 ppm showing signal from H_d protons; (C) NMR spectrum between 1.2 and 3.8 ppm showing signal from H_b and H_c protons.

As expected the signals from the THP portion of the molecule showed the most dramatic changes upon gallium binding (signals H_a–H_f), compared to signals from the urea-based inhibitor or the linker (H_g-H_s, see figure 3.5 for proton labelling scheme). In particular, the signal from the methyl groups on the pyridinone rings H_b and H_c (at 2.39 ppm and 3.66 ppm) were split into 3 singlets, as shown in figure 3.6C. This suggests each ring was in a different environment after gallium binding and that the C_3 symmetry that might have been expected intuitively (but superficially) was not present in the complex. Further confirmation of this comes from the singlet at 4.5 ppm (H_d) which arises from the CH_2 of the 3 ligand arms, splits into 6 doublets in the region 4.0-5.2 ppm upon binding (5 doublets were observable at 25°C with 1 masked by the water suppression, but all 6 were revealed at 5°C, figure 3.7). These all have similar *J* values (14.7-16.1 Hz) typical of $^{2}J_{H\text{-}H}$ geminal coupling constants for -N-CH_2-C= groups (*45*). This shows each proton in the three H_d CH_2 groups are in a distinct environment, again suggesting the three arms of THP are not equivalent upon binding gallium. The aromatic proton on each pyridinone ring (H_a), which gave rise to a singlet at 6.45 ppm in the THP-PSMA spectrum, was also split into a number of smaller peaks in the region 6.5-6.7 ppm, upon binding gallium as shown in figure 3.6A. There are 3 strong peaks and then 3 smaller more poorly defined peaks within this region.

These protons are in very close proximity (4 bonds) to the bound gallium, which is likely the cause of this more complicated splitting pattern.

Stability over time: The only change in spectrum after storing sample C (excess gallium) at 4°C for 3 weeks was a new singlet that developed at 3.36 ppm, believed to be an impurity. No change in assigned peaks was observed. This suggests an equilibrium state was reached rapidly upon binding ^{nat}Ga and maintained over time.

Variable temperature study: ^{1}H NMR analysis was performed at 4 different temperatures on [^{nat}Ga]Ga-THP-PSMA (sample 3, gallium in excess) and the spectra compared see figure 3.7. The variable temperature NMR spectra show that the relative intensity of peaks did not change with temperature suggesting the same species are present at all temperatures and that the system was at equilibrium, in agreement with the stability studies. Some spectral changes were observed upon varying the temperature; lower temperatures (5°C) caused peaks to sharpen and there was an increased detection of fine splitting. As the temperature increased, broadening and averaging of peaks was observed; demonstrating the system was dynamic.

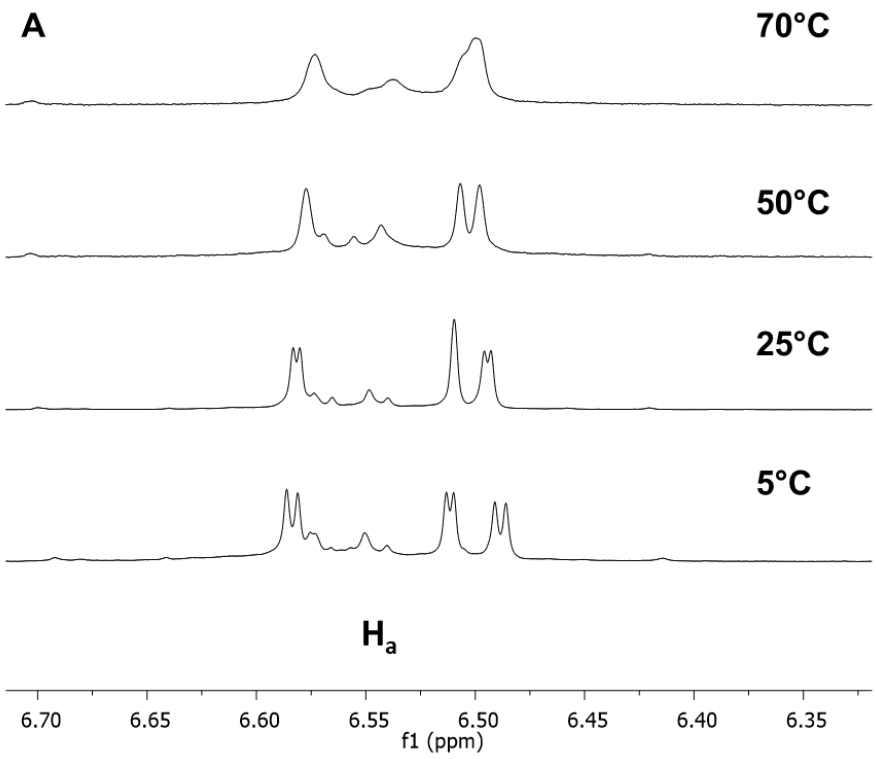

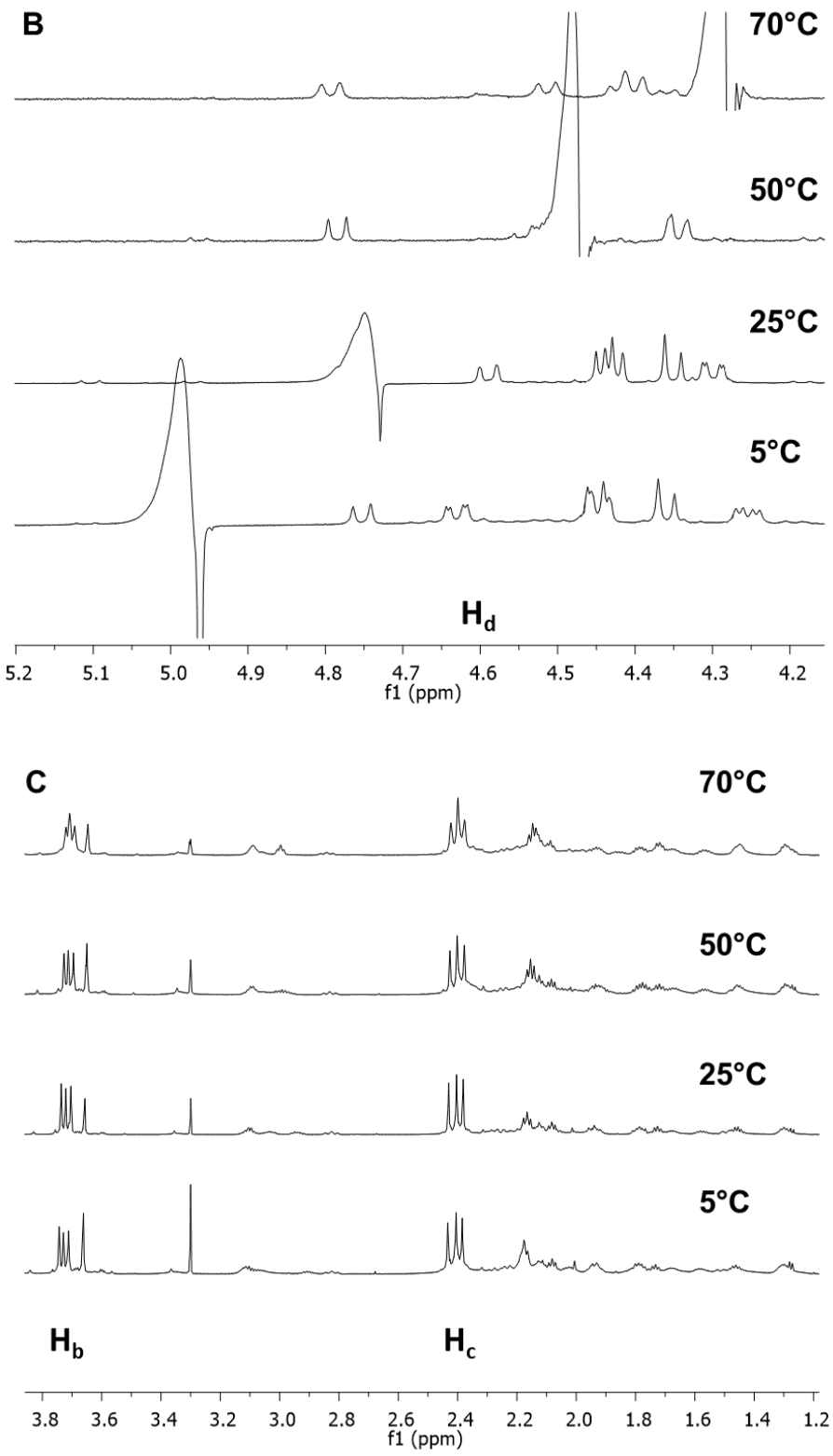

FIGURE 3.7: NMR spectra of [^{nat}Ga]Ga-THP-PSMA (sample 3, [^{nat}Ga]Ga-THP-PSMA excess gallium) when bore temperature was set to 5°C, 25°C, 50°C and 70°C. (A) NMR spectrum between 6.3 and 6.7 ppm showing signal from H_e protons; (B) NMR spectrum between 4.1 and 5.2 ppm showing signal from H_d protons; (C) NMR spectrum between 1.2 and 3.8 ppm showing signal from H_b and H_c protons of the chelator as well as signal from the rest of the linker and GCP(II)/PSMA targeting motif.

3.4.3 Radiolabelling

[^{68}Ga]Ga-THP-PSMA initial optimisation: The THP chelator enabled radiolabelling with unmodified generator eluate, in a single step. [^{68}Ga]Ga^{3+} (5-75 MBq) in aqueous HCl (0.1 M, 250 µL) was added to pre-prepared THP-PSMA (5-0.01 µg in 3 µL of H_2O) in sodium bicarbonate solution (1 M, 27 µL). After 5 minutes, pH was 6.5-7.5. Radiochemical purity (RCP), determined by HPLC and iTLC, as a function of THP-PSMA concentration is shown in figure 3.8. Molar activities between 15 and 45 MBq/nmol were consistently achieved with the labelling conditions used for *in vivo* work (2 µg, 1.3 nmol THP-PSMA, 250 µL 20–60 MBq of gallium-68 eluate, 95% radiochemical purity).

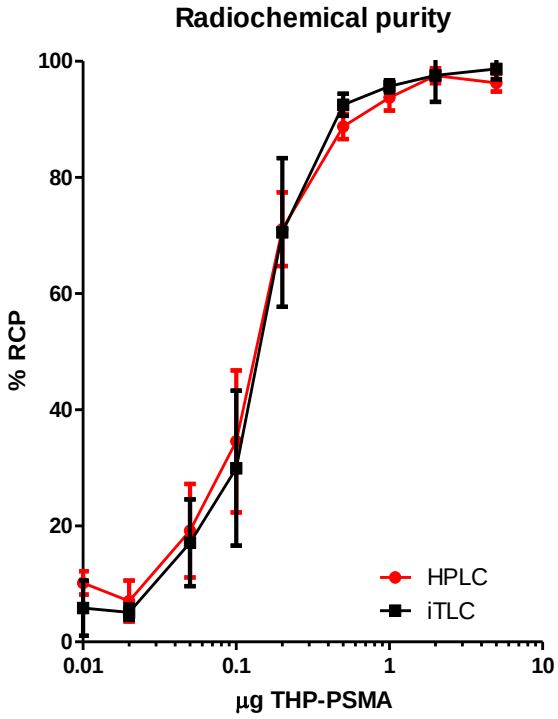

FIGURE 3.8: Dependence of radiochemical purity of [^{68}Ga]Ga-THP-PSMA on the mass of THP-PSMA in 280 µL, as measured by HPLC (red) and iTLC (black) after 5 minutes; n = 3, mean ± SD.

One-step kit for radiolabelling: When kit vials containing lyophilised THP-PSMA (40 µg, 26 nmol), sodium bicarbonate (44 mg), and sodium phosphate buffer (17.5 mg) were used (kit A), radiosynthesis of [^{68}Ga]Ga-THP-PSMA was achieved in one-step by direct addition of 5 mL of generator eluate (0.1 M HCl, 122-202 MBq from the Galliapharm (Eckert and Ziegler) generator, or 600-660 MBq from the Galli E_O (IRE ELiT) generator). After 5 minutes, the pH was 6–7 and iTLC confirmed radiochemical purity above 95% with molar activities of up to 22 MBq/nmol using the Galli E_O (IRE ELiT) generator (figure 3.9). HPLC at 10 minutes confirmed there was only 1

radioactive species (figure 3.10). ITLC analysis up to 3 hours after reconstitution showed no instability or autoradiolysis (figure 3.11).

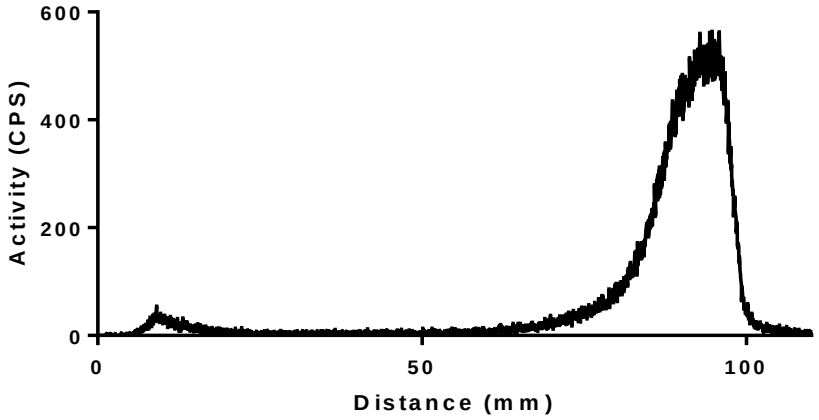

FIGURE 3.9: Radio-iTLC of [^{68}Ga]Ga-THP-PSMA labelled using one-step kit, analysed 5 minutes after reconstitution (R_f unchelated [^{68}Ga]Ga^{3+} = 0, R_f [^{68}Ga]Ga-THP-PSMA = 0.8–1).

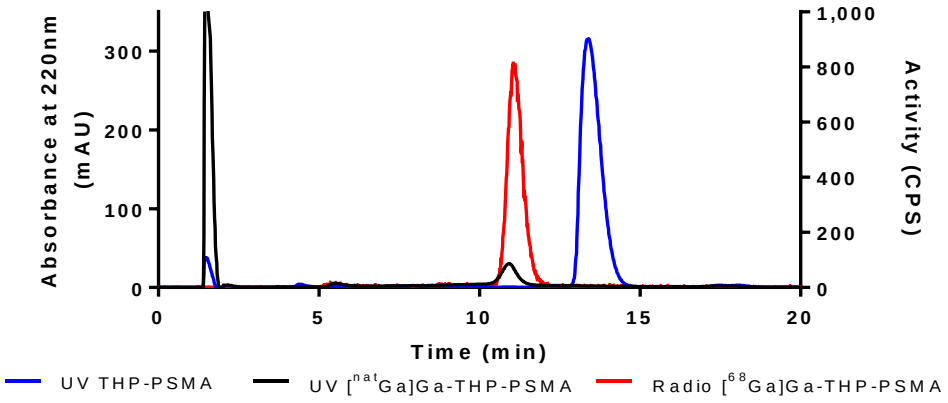

FIGURE 3.10: HPLC (λ = 220 nm) of THP-PSMA (blue, R_t = 13.38 minutes) and [^{nat}Ga]Ga-THP-PSMA (black, R_t = 10.92 min, excess [^{nat}Ga]$Ga(NO_3)_3.X(H_2O)$ was present with R_t = 1.47 minutes), and radio-HPLC of [^{68}Ga]Ga-THP-PSMA (red, R_t = 11.05 minutes) labelled using one-step kit and analysed 10 minutes after reconstitution.

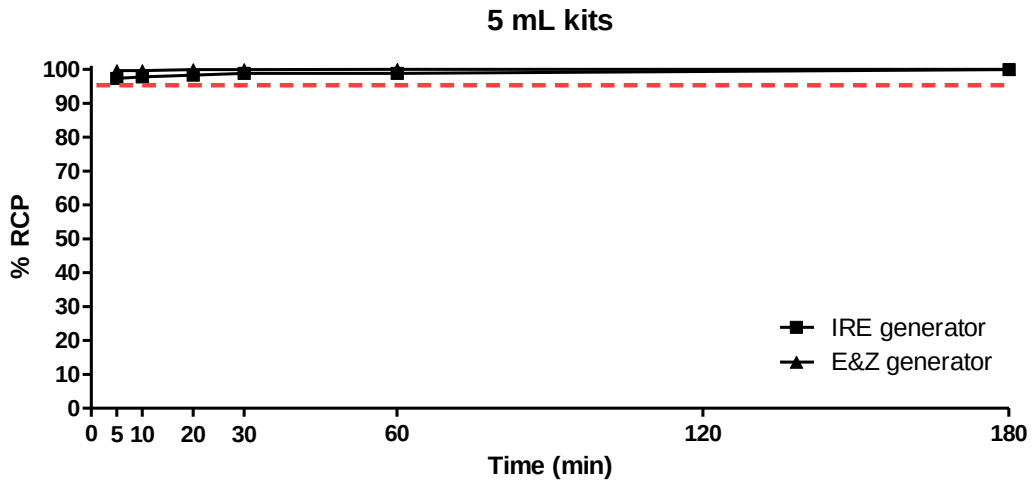

FIGURE 3.11: Radiochemical purity as measured by iTLC of [^{68}Ga]Ga-THP-PSMA labelled with 5 mL one-step kits as a function of incubation time at room temperature, with both the Galli E_0 (IRE ELiT) generator and Galliapharm (Eckert and Ziegler) generator. The broken red line represents quality control threshold of 95% (n = 3, mean ± SD).

One-step kit radiolabelling with pharmaceutical grade germanium-68/gallium-68 generator: The radiolabelling of a 40 µg THP-PSMA kit (kit B) produced to radiopharmaceutical standards by ROTOP Pharmaka GmbH was performed in one-step using the eluate from a pharmaceutical grade Galliapharm (Eckert and Ziegler) generator. The full elution volume from the generator was added directly to the kit (5 mL, 0.1M HCl, 1156 MBq) and after 10 minutes the pH was 6. The radiochemical purity of [^{68}Ga]Ga-THP-PSMA was confirmed above 97% with iTLC and a molar activity of 43 MBq/nmol was achieved.

3.4.4 Radiochemical Stability in the Presence of Excess Gallium

The stability in the presence of unchelated gallium was monitored for [^{68}Ga]Ga-THP-PSMA and [^{68}Ga]Ga-DOTA-PSMA(617) up to 2 hours. The presence of excess gallium had no effect on the radiochemical purity of [^{68}Ga]Ga-DOTA-PSMA(617) (>99% RCP maintained for all concentrations tested) but [^{68}Ga]Ga-THP-PSMA showed a drop to 76 ± 3.5% over 2 hours at 0.5 mg/mL [^{nat}Ga]Ga$(NO_3)_3$.X(H_2O) (figure 3.12) showing exchange between chelated and unchelated gallium.

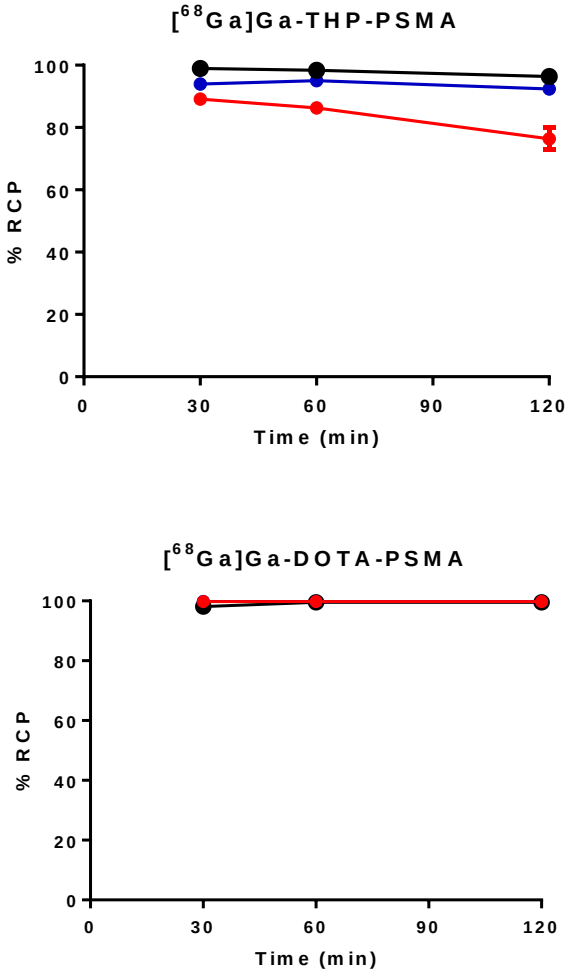

FIGURE 3.12: Effect of [^{nat}Ga]Ga$(NO_3)_3$.X(H_2O) concentration on the stability of (top) [^{68}Ga]Ga-THP-PSMA and (bottom) [^{68}Ga]Ga-DOTA-PSMA(617) over time. Black = 0 mg/mL, blue = 0.005 mg/mL, red = 0.5 mg/mL. (n = 3 for each time point)

3.4.5 Lipophilicity and Serum Stability

The log $D_{OCT/PBS}$ values of the 3 [^{68}Ga]Ga-PSMA complexes at pH 7.4 were similar: -5.35 ± 0.1 for [^{67}Ga]Ga-THP-PSMA (n = 6), -5.40 ± 0.2 for [^{67}Ga]Ga-HBED-CC-PSMA (n = 6), and -5.40 ± 0.1 for [^{67}Ga]Ga-DOTA-PSMA(617) (n = 5), indicating that all tracers are hydrophilic and lipophilicity is unlikely to underlie differences in *in vivo* performance (figure 3.13). In serum, [^{68}Ga]Ga-THP-PSMA (figure 3.14) showed minimal transchelation (< 2%) to proteins after a 6 hour incubation.

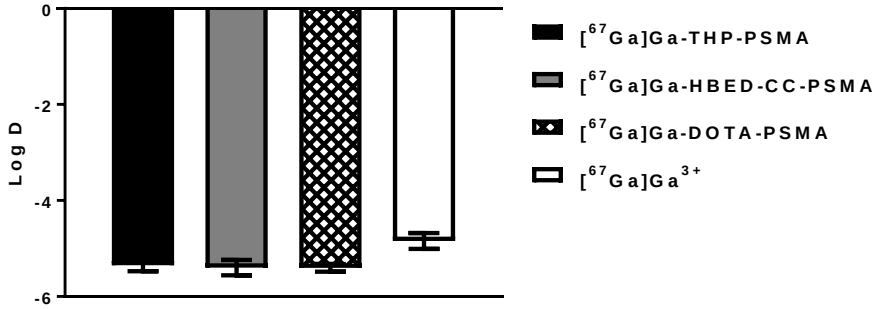

FIGURE 3.13: Octanol:PBS log D values at pH 7.4 for [^{67}Ga]Ga-THP-PSMA (black), [^{67}Ga]Ga-HBED-CC-PSMA (grey) [^{67}Ga]Ga-DOTA-PSMA(617) (hatched) [^{67}Ga]Ga^{3+} (white).

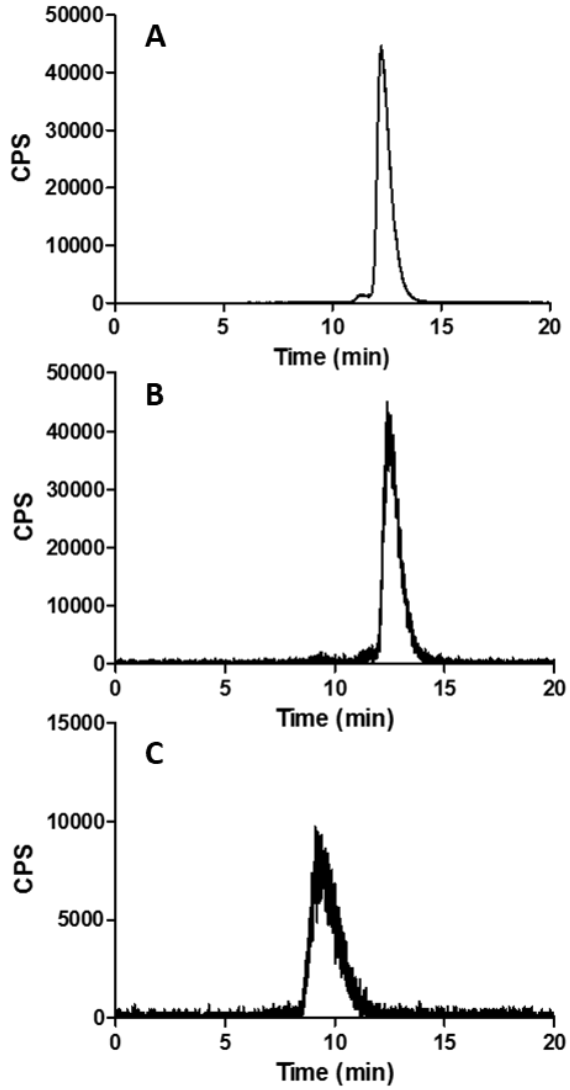

FIGURE 3.14: Size exclusion HPLC radiochromatograms of (A) [^{68}Ga]Ga-THP-PSMA; (B) [^{68}Ga]Ga-THP-PSMA after 6 hours incubation in human serum at 37°C; showing < 2% transchelation to serums; protein (C) [^{68}Ga]Ga^{3+} incubated in human serum for 6 hours. All chromatograms have been decay corrected.

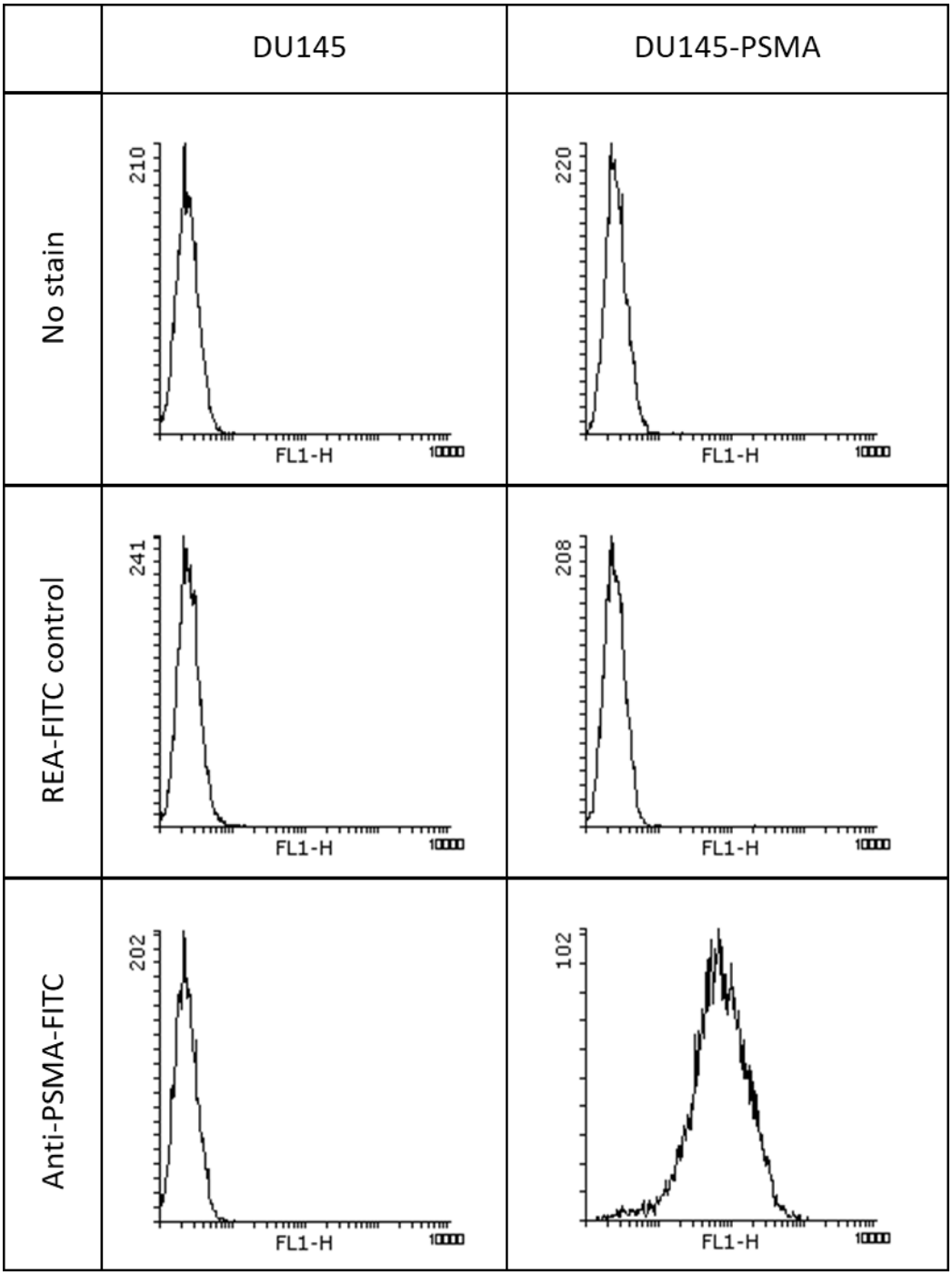

FIGURE 3.15: Flow cytometry results for DU145 and DU145-PSMA cells without staining (top), after staining with recombinant engineered antibody (REA) conjugated to FITC as a control (middle) and after staining with Anti-PSMA-FITC (bottom). These results confirm that DU145 cells do not express GCP(II)/PSMA and that > 97% of the cells in the DU145-PSMA population express GCP(II)/PSMA.

3.4.6 Flow Cytometry

Incubation of DU145 and DU145-PSMA cells with Anti-PSMA-VioBright-FITC followed by analysis by flow cytometry showed no expression of GCP(II)/PSMA in DU145 cells and that over 97% of the population of DU145-PSMA cells expressed GCP(II)/PSMA (figure 3.15).

3.4.7 *In Vitro* Cell Uptake and Binding Affinity Assays

The percentage uptake of [^{68}Ga]Ga-THP-PSMA in GCP(II)/PSMA-expressing DU145-PSMA cells and non GCP(II)/PSMA-expressing DU145 cells after 1 hour at 37°C is shown in figure 3.16. These results confirm the uptake of [^{68}Ga]Ga-THP-PSMA was GCP(II)/PSMA-mediated, and that this tracer has low non-specific uptake. They also demonstrate the tracer was not only bound to the surface of GCP(II)/PSMA-expressing cells but was also internalised. Uptake of [^{67}Ga]Ga-DOTA-PSMA(617), [^{67}Ga]Ga-HBED-CC-PSMA, and [^{67}Ga]Ga-THP-PSMA in DU145-PSMA and DU145 cells at 37°C and 4°C is shown in figure 3.17. All 3 tracers showed time-dependent accumulation in GCP(II)/PSMA-expressing cells, but low uptake in non GCP(II)/PSMA-expressing cells. At 37°C, uptake continued to increase with time, preventing measurement of equilibrium binding parameters such as the dissociation constant (K_d), but at 4°C, a plateau was reached for all tracers after approximately 2 hours. *Relative* affinity was therefore measured after 2 hours at 4°C. Results showed that the K_d of [$^{67/68}$Ga]Ga-THP-PSMA was 10.4 ± 3.4 times higher than that of [$^{67/68}$Ga]Ga-HBED-CC-PSMA and 8.6 ± 3.4 times higher than that of [$^{67/68}$Ga]Ga-DOTA-PSMA(617) (figure 3.18). This is in agreement with directly measured IC_{50} values of [^{nat}Ga]Ga-THP-PSMA (361 ± 60 nM) and [^{nat}Ga]Ga-HBED-CC-PSMA (34.3 ± 4.1 nM) (figure 3.19) and validates this newly developed "*relative* affinity" method.

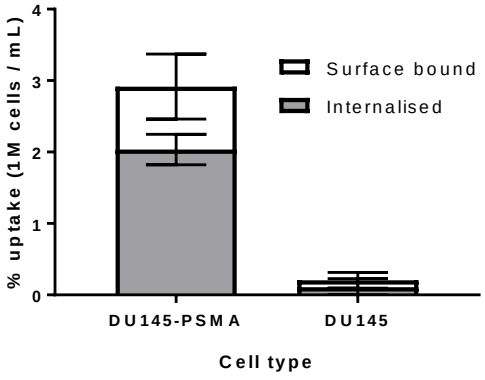

FIGURE 3.16: Percentage uptake of 1 nM [^{68}Ga]Ga-THP-PSMA in DU145-PSMA and DU145 cells at 1×10^6 cells/mL after 1 hour incubation at 37°C. Surface-bound activity (white) and internalised activity (grey) are shown (mean ± SD, n = 6).

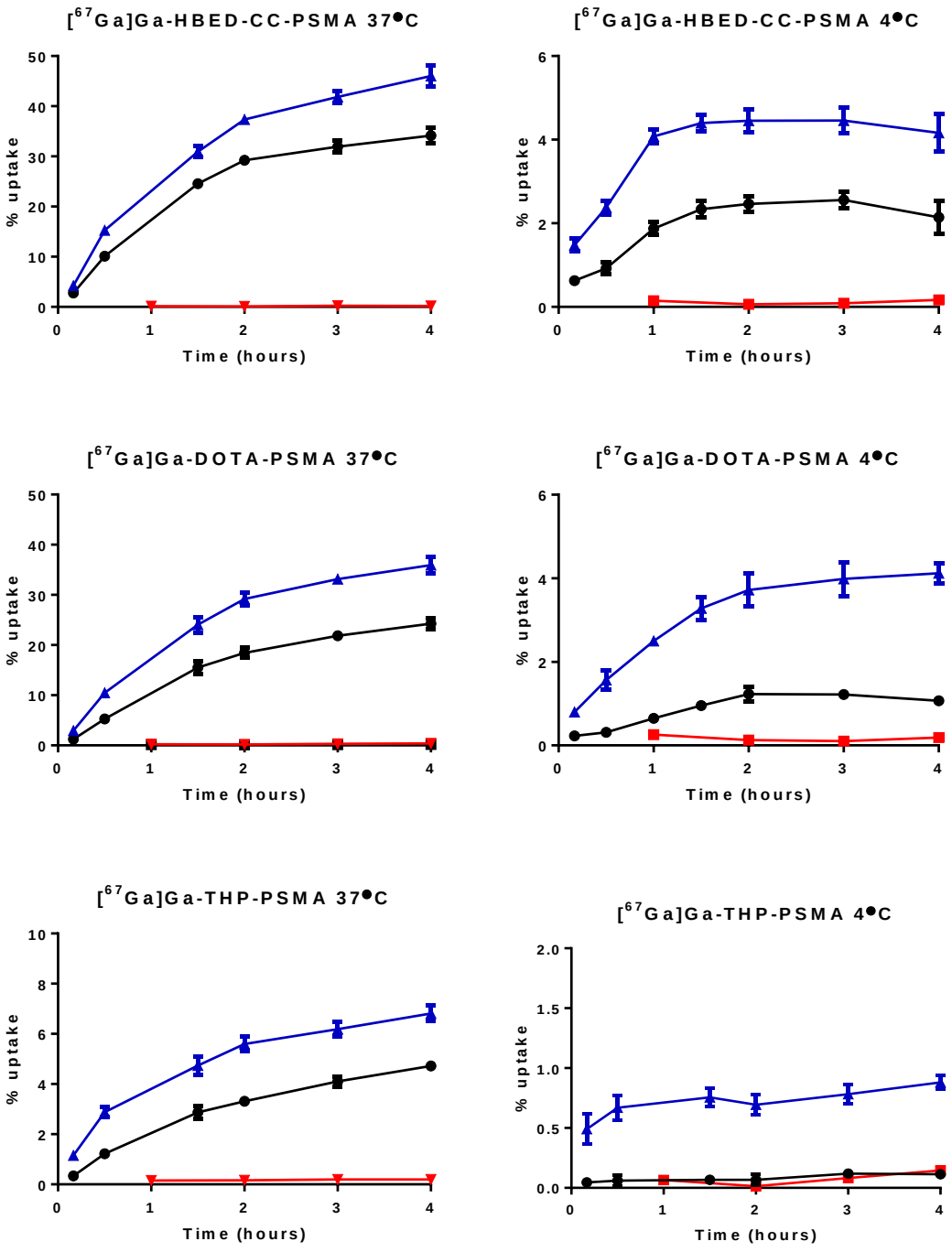

FIGURE 3.17: Uptake of 1 nM [^{67}Ga]Ga-HBED-CC-PSMA (top), [^{67}Ga]Ga-DOTA-PSMA(617) (middle) and [^{67}Ga]Ga-THP-PSMA (bottom) over time at 4°C (right) and 37°C (left), 1×10^{6} cells/mL. Combined internalised and cell surface-bound activity of DU145-PSMA cells (blue); internalised activity of DU145-PSMA cells (black); internalised and cell surface-bound activity of DU145 cells (red) (mean ± SD, n = 4 per time point per tracer).

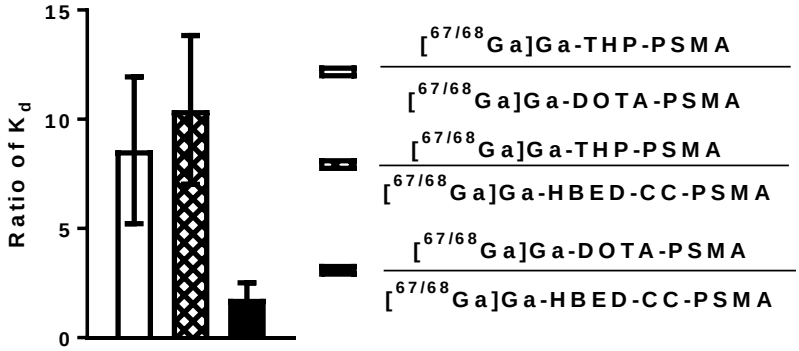

FIGURE 3.18: Ratio of K_d of 2 tracers incubated at 1 nM with DU145-PSMA cells at 4°C for 2 hours. Ratios were calculated from specific binding obtained by incubating the gallium-67 labelled tracer in the same well as its gallium-68 labelled comparator, and *vice versa*. Total number of wells was n = 34 for comparison of [$^{67/68}$Ga]Ga-THP-PSMA with [$^{67/68}$Ga]Ga-HBED-CCPSMA or [$^{67/68}$Ga]Ga-DOTA-PSMA(617) and n = 18 for comparison of [$^{67/68}$Ga]Ga-HBED-CC-PSMA with [$^{67/68}$Ga]Ga-DOTA-PSMA(617); mean ± SD.

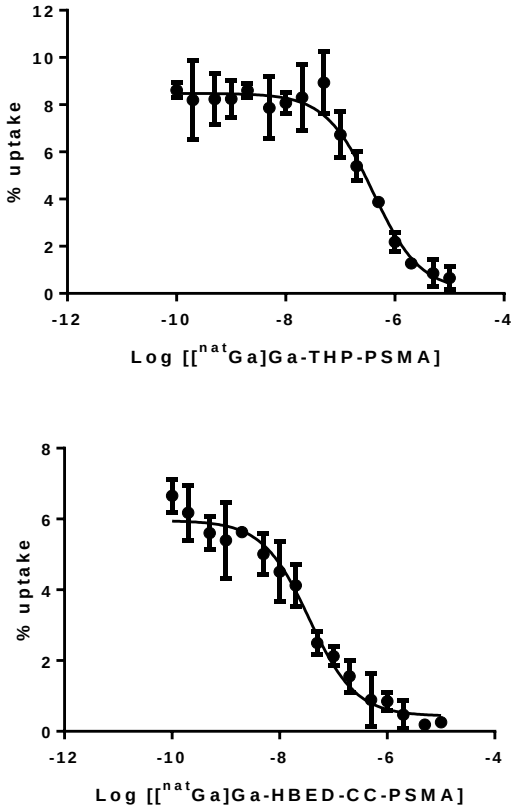

FIGURE 3.19: Representative IC_{50} experiments for (top) [^{nat}Ga]Ga-THP-PSMA and (bottom) [^{nat}Ga]Ga-HBED-CC-PSMA with 1 nM [^{68}Ga]Ga-DOTA-PSMA(617) as the probe (n = 4 for each concentration). IC_{50} values in the main text are the mean of at least 3 experiments.

3.4.8 PET Imaging and Biodistribution

PET/CT scanning of [^{68}Ga]Ga-THP-PSMA in a non-tumour bearing SCID/beige mouse for 4 hours, (figure 3.20) showed that excretion of [^{68}Ga]Ga-THP-PSMA was rapid and exclusively renal, with very low spleen and liver uptake. This confirms the stability of [^{68}Ga]Ga-THP-PSMA *in vivo*, as unchelated gallium-68 is known to be distributed throughout the body with uptake in the bone, liver, spleen, kidneys and intestine (*13*)(*16*).

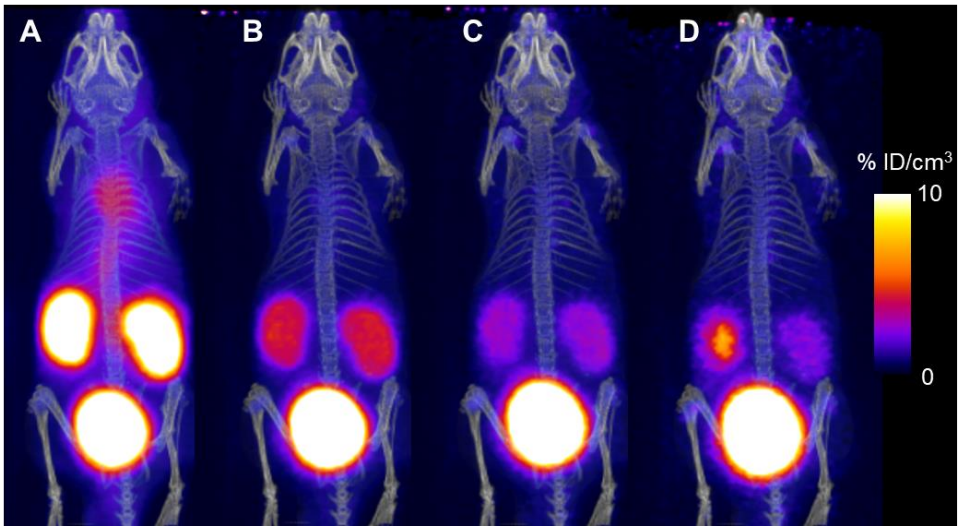

FIGURE 3.20: PET/CT images of SCID mouse without a prostate cancer xenograft administered with [^{68}Ga]Ga-THP-PSMA with PET images scaled from 0-10 %ID/cm^3: (A) 0-1 hours; (B) 1-2 hours; (C) 2-3 hours; (D) 3-4 hours.

In SCID/beige mice bearing GCP(II)/PSMA-positive xenografts (DU145-PSMA, group 1) PET/CT showed that most of the activity was associated with bladder and kidneys by 60 minutes figure 3.21 and figure 3.22. Blood clearance, represented by the blood pool in the left ventricle, was rapid, decreasing to 1 %ID/cm^3 within 30 minutes (figure 3.23). With images scaled between 0 and 25 %ID/cm^3, tumours were clearly delineated (figure 3.21)**.** Analysis of the 40 to 60 minute post-injection images gave a tumour uptake value of 5.6 ± 1.2 %ID/cm^3 (figure 3.24). Specificity was confirmed both by mice bearing a GCP(II)/PSMA-negative but otherwise similar tumour (DU145, group 4) with uptake of 1.5 ± 1.2 %ID/cm^3 ($P < 0.05$ compared with group 1), and by blocking experiments in mice bearing a DU145-PSMA tumour where PMPA was co-administered with [^{68}Ga]Ga-THP-PSMA (group 3), giving a tumour uptake of 1.0 ± 0.4 %ID/cm^3 ($P < 0.05$ compared with group 1). A further control was performed by imaging a mouse bearing one DU145 and one DU145-PSMA tumour with [^{68}Ga]Ga-THP-PSMA. This showed significant differences between tracer uptake in these two tumours (1.6 %ID/cm^3 compared to 0.2 %ID/cm^3) (figure 3.25).

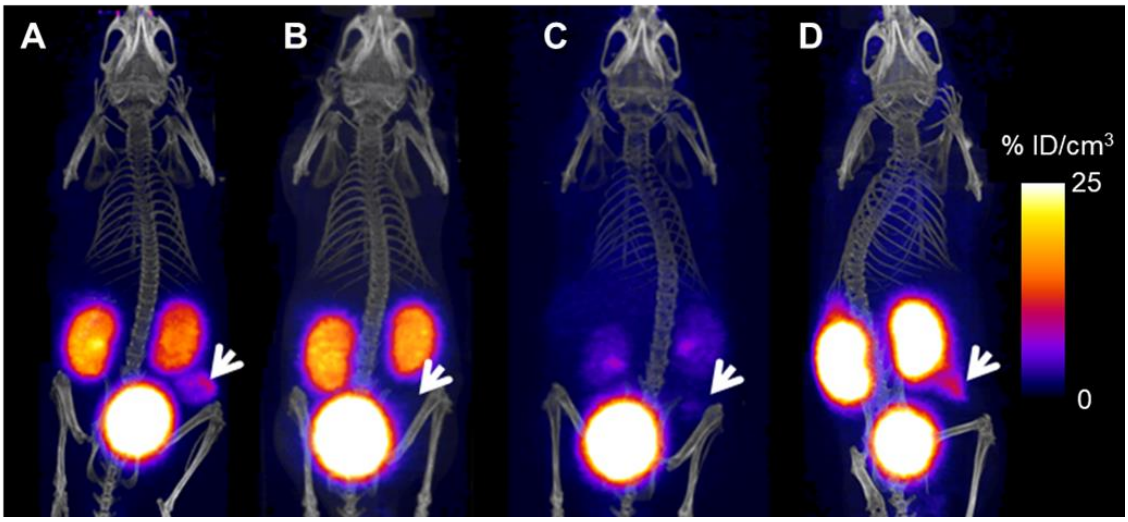

FIGURE 3.21: Representative PET/CT images of mice bearing xenografts at 40–60 minutes after injection with PET images scaled from 0–25 %ID/cm^3. White arrows indicate the location of tumour. (A) [^{68}Ga]Ga-THP-PSMA in DU145-PSMA tumour (group 1). (B) [^{68}Ga]Ga-THP-PSMA in DU145 tumour (group 4). (C) [^{68}Ga]Ga-THP-PSMA in DU145-PSMA tumour blocked with PMPA (group 3). (D) [^{68}Ga]Ga-HBED-CC-PSMA in DU145-PSMA tumour (group 2).

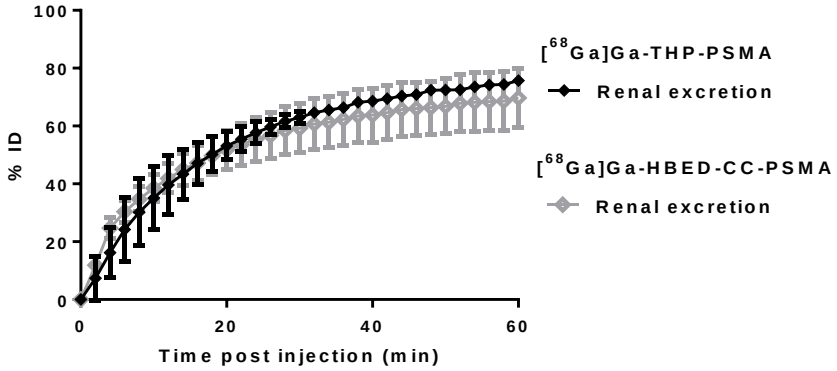

FIGURE 3.22: Time-activity curves of SCID/beige mice bearing DU145-PSMA tumours, derived from PET imaging data from mice imaged with [^{68}Ga]Ga-THP-PSMA or [^{68}Ga]Ga-HBED-CC-PSMA during the first hour post-injection. Plotted data are the mean and standard deviation of three mice calculated from the total %ID in the kidneys and bladder combined.

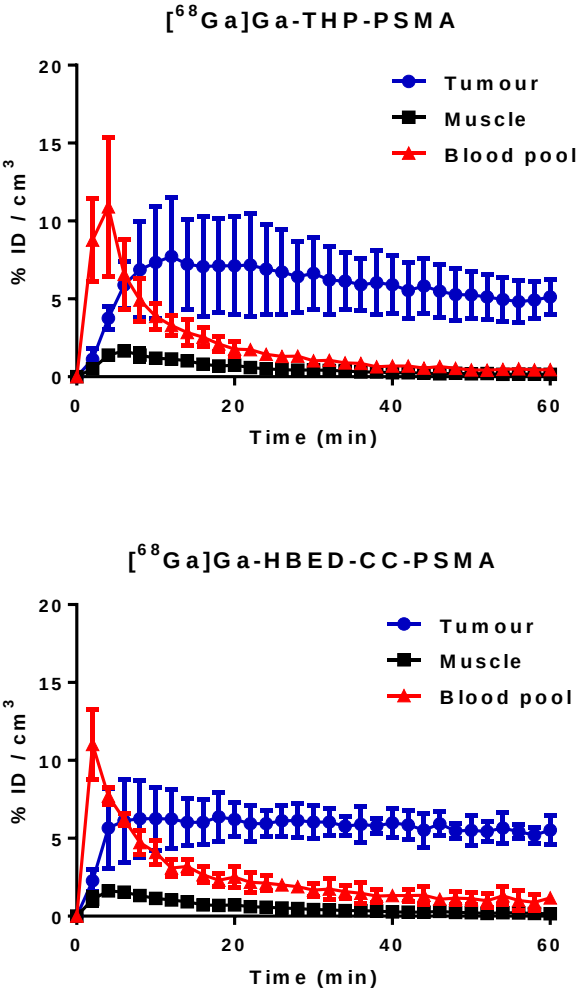

FIGURE 3.23: PET-derived time activity curves of tumour, muscle and blood pool of SCID/beige mice bearing DU145-PSMA tumours, imaged with (top) [^{68}Ga]Ga -THP-PSMA or (bottom) [^{68}Ga]Ga -HBED-CC-PSMA for 1 hour after injection: blood pool (left ventricle) (red), tumour (blue), and leg muscle (black); (n = 3, mean ± SD).

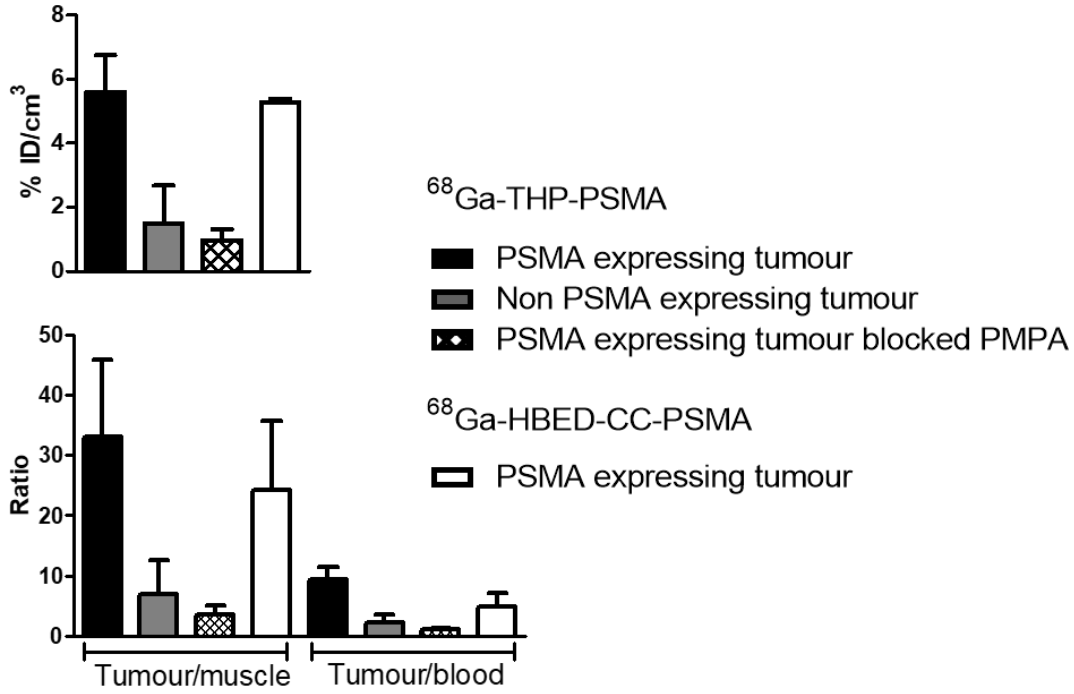

FIGURE 3.24: PET/CT-derived %ID/cm^3 in tumour and tumour-to-blood and tumour-to-muscle ratio 40–60 minutes after injection. [^{68}Ga]Ga-THP-PSMA in DU145-PSMA tumour, (group 1, black), [^{68}Ga]Ga-THP-PSMA in DU145-PSMA, [^{68}Ga]Ga-THP-PSMA in DU145 tumour, (group 4, grey), tumour blocked with PMPA, (group 3, hatched), or [^{68}Ga]Ga-HBED-CC-PSMA in DU145-PSMA tumour, (group 2, white) (n = 3, mean ± SD).

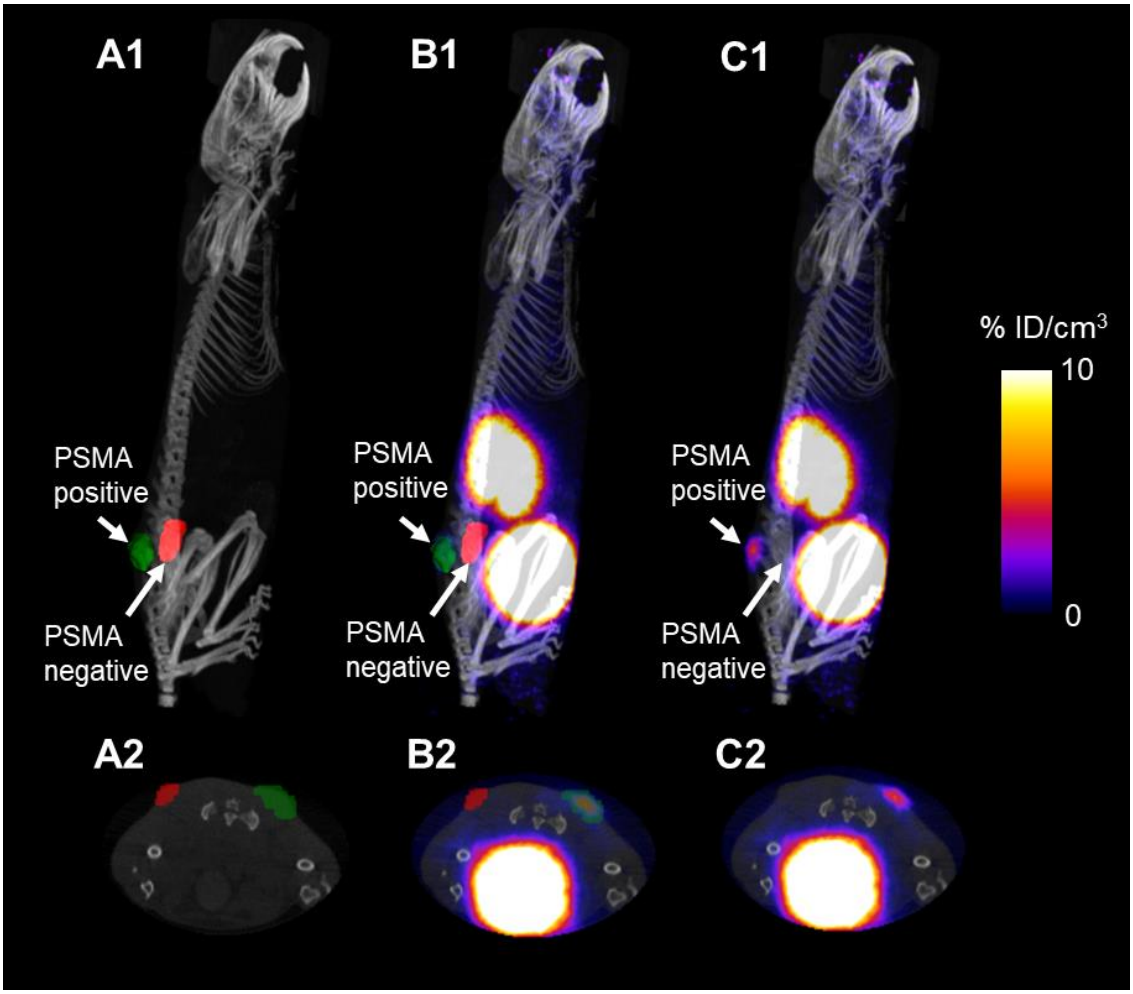

FIGURE 3.25: CT and PET/CT images of SCID mouse with two prostate cancer tumours imaged with [^{68}Ga]Ga-THP-PSMA: One xenograft of DU145 cells (left flank) and another of DU145-PSMA cells (right flank). PET images were acquired 40-60 minutes post-injection and scaled from 0-10 %ID/cm^3. Both maximum intensity projections (1) and axial slices (2) slices are shown. (A) CT image showing ROIs of the DU145-tumour (red) and the DU145-PSMA tumour (green) (B) PET/CT image showing ROIs of the DU145-tumour (red) and the DU145-PSMA tumour (green) (C) PET/CT image showing difference in uptake between the GCP(II)/PSMA-expressing (DU145-PSMA) and the non GCP(II)/PSMA-expressing (DU145) tumours.

For comparison with an established PET tracer, mice bearing DU145-PSMA tumours were imaged with [^{68}Ga]Ga-HBED-CC-PSMA (group 2) (*25*)(*27*)(*35*). Time-activity curves for [^{68}Ga]Ga-HBED-CCPSMA (group 2) and [^{68}Ga]Ga-THP-PSMA (group 1) showed similar blood clearance, tumour uptake, and renal excretion (figure 3.21, figure 3.22 and figure 3.23). Image analysis of 40-60 minutes PET images revealed that tumour uptake of [^{68}Ga]Ga-THP-PSMA (5.3 ± 0.1 %ID/cm^3) was not significantly different from that of [^{68}Ga]Ga-HBED-CC-PSMA (5.6 ± 1.2 %ID/cm^3). *Ex vivo* biodistribution data, summarised in figure 3.26 and table 3.6, were consistent with PET image analysis, confirming renal excretion and excellent specificity of [^{68}Ga]Ga-THP-PSMA for GCP(II)/PSMA-expressing tumours. [^{68}Ga]Ga-THP-PSMA showed *ex vivo* biodistribution similar to [^{68}Ga]Ga-HBED-CC-PSMA, apart from markedly lower spleen uptake (3.7 ± 1.3 and 17.6 ± 6.1 %ID/g respectively) (table 3.6). Importantly, anaesthesia appeared to severely affect tracer uptake in the kidney and excretion to the bladder, with large variation in kidney uptake across all groups, so comparison of kidney activity should be interpreted with caution.

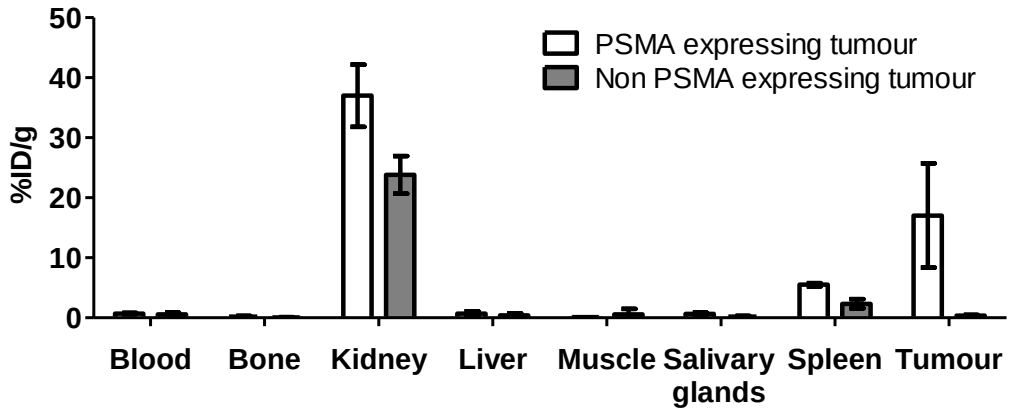

FIGURE 3.26: *Ex vivo* biodistribution of [^{68}Ga]Ga-THP-PSMA in mice with DU145-PSMA (white) or DU145 tumour (grey), culled 1 hour after injection (n = 3, mean ± SD). Unlike PET-imaged animals, these were not anesthetised between injection and euthanasia.

Tumour type	[^{68}Ga]Ga-THP-PSMA			[^{68}Ga]Ga-HBED-CC-PSMA
	Group 1 DU145-PSMA (n=3)	Group 4 DU145 (n=3)	Group 3 DU145-PSMA Blocked PMPA (n=3)	Group 2 DU145-PSMA (n=3)
Tumour	16.4 ± 7.4	0.69 ± 0.7	1.40 ± 0.2	19.5 ± 7.6
Blood	0.73 ± 0.4	1.23 ± 1.7	1.11 ± 0.7	2.18 ± 1.2
Intestines	0.35 ± 0.1	0.64 ± 0.6	0.71 ± 0.3	1.20 ± 0.5
Kidney	40.4 ± 34	52.3 ± 77	5.20 ± 5.0	63.4 ± 23
Liver	0.45 ± 0.2	0.59 ± 0.7	0.60 ± 0.2	0.69 ± 0.1
Lungs	0.50 ± 0.2	0.94 ± 1.3	0.72 ± 0.3	1.29 ± 0.4
Muscle	0.51 ± 0.4	0.31 ± 0.4	0.21 ± 0.1	0.26 ± 0.1
Salivary glands	0.28 ± 0.1	0.48 ± 0.7	0.33 ± 0.2	0.76 ± 0.1
Spleen	3.70 ± 1.3	3.61 ± 3.1	0.75 ± 0.1	17.6 ± 6.1
Tumour to organ ratios				
Tumour to blood	30.8 ± 28	0.93 ± 0.4	1.64 ± 0.9	11.0 ± 6.0
Tumour to muscle	44.6 ± 28	3.16 ± 1.1	9.79 ± 6.8	77.0 ± 34
Tumour to spleen	4.38 ± 0.8	0.17 ± 0.1	1.87 ± 0.3	1.16 ± 0.42

TABLE 3.6: *Ex vivo* biodistribution at 1 hour post-injection for PET-imaged mice. Mice bearing DU145-PSMA tumours were injected with [^{68}Ga]Ga-THP-PSMA, [^{68}Ga]Ga-THP-PSMA plus the blocking agent PMPA, or [^{68}Ga]Ga-HBED-CC-PSMA. Mice bearing control DU145 tumours were imaged with [^{68}Ga]Ga-THP-PSMA only.

3.5 Discussion

The aim of this study was to develop a gallium-68 radiotracer that targets GCP(II)/PSMA with radiolabelling procedures suitable for development into a single-step kit-formulated radiopharmaceutical, which required only the addition of unprocessed, unfractionated generator eluate to a single vial. The latter requirement was met by incorporating the THP chelator. A THP-PSMA conjugate has been synthesised and characterised and could be quantitatively radiolabelled with gallium-68 (and gallium-67). Radiolabelling yields of greater than 95% and molar activity of 15–45 MBq/nmol with unprocessed generator-produced gallium-68 were achieved in one-step at pH 7 and room temperature within 5 minutes without further purification. On the basis of this, a lyophilised kit was developed, which could be labelled/reconstituted simply by adding 5 mL of raw generator eluate. One-step kits can only be used with generators with less than 0.001% germanium-68 breakthrough, the limit for human injection as set within the European pharmacopoeia (*12*). Of such generators, the Galliapharm (Eckert and Ziegler) is the only one with marketing authorisation across Europe (*11*), and it incidentally has the largest elution volume (5 mL, 0.1 M HCl) and so the kit was designed to be compatible with this generator. Kits made in-house were proven to consistently produce [^{68}Ga]Ga-THP-PSMA with radiochemical purity over 95% within 5 minutes, using both the Galliapharm (Eckert and Ziegler) and the Galli E_O (IRE ELiT) generators, and the radiolabelled product was shown to be stable for 3 hours. Pharmaceutical grade kits were then produced by ROTOP Pharmaka GmbH which allowed them to be assessed within a radiopharmacy, with an entire (5 mL) elution from a pharmaceutical grade Galliapharm (Eckert and Ziegler) generator. In these conditions [^{68}Ga]Ga-THP-PSMA was produced within 10 minutes with a radiochemical purity of 97% and molar activity of 43 MBq/nmol. These radiolabelling properties demonstrate that kit-based radiolabelling of gallium-68 tracers is entirely feasible with an appropriate chelator. Additionally, the kit was designed exclusively with excipients approved for human use and after labelling the solution was at near neutral pH and suitable osmolality for direct administration to patients.

As well as rapid and simple radiolabelling, the coordination properties of THP endow its conjugates with other properties well suited to radiopharmaceutical application. It is highly selective for tripositive metal ions with an ionic radius similar to that of iron(III) and gallium(III) (*19*), potentially reducing the need to remove contaminating metal ions in raw generator eluate through purification steps. Unlike HBED-CC, the tripodal design of THP restricts the number of geometric isomers that form on Ga^{3+} coordination and on reversed-phase HPLC, [^{68}Ga]Ga-THP-

PSMA elutes as a single radioactive species (figure 3.10), shown by LC-MS to be a 1:1 complex with gallium (table 3.2). Initial NMR experiments also provide evidence of the formation of a single complex. However, it also suggests that upon binding gallium each arm of THP was in a different environment. This could be explained by hydrogen bonding between two adjacent arms of THP, which could occur between the C=O of one and the NH of the second, as shown in figure 3.27 and figure 3.28 and would make each arm inequivalent as the first would be a H-bond donor, the second a H-bond acceptor and the third neither. If this hydrogen bond was present it may also provide an energy barrier for interconversion of the delta and lambda isomers. However, such isomerism is subject to equilibration that is rapid compared with the timescale of HPLC and *in vivo* processes, and is therefore unlikely to be biologically relevant.

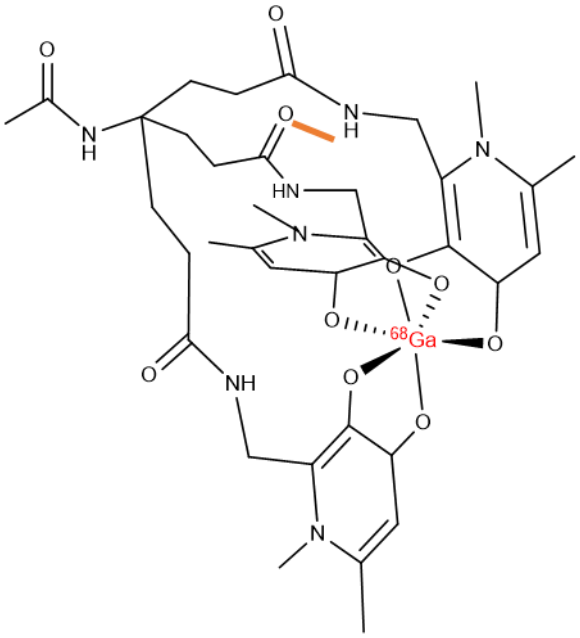

FIGURE 3.27: Structure showing possible hydrogen bonding interaction that could cause non-equivalence in the 3 ligand arms.

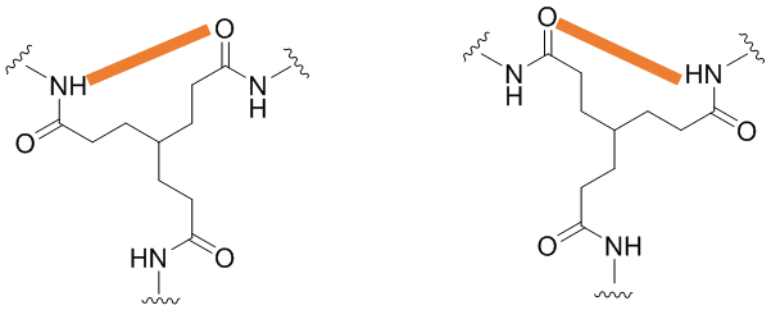

FIGURE 3.28: Schematic showing how the presence of a hydrogen bond between 2 arms of THP could cause non-equivalence in the 3 ligand arms and give rise to 2 distinct left- and right-handed species.

The lipophilicity of [^{68}Ga]Ga-THP-PSMA is low (log $D_{oct/PBS}$ = -5.35 ± 0.1) and comparable to that of established [^{68}Ga]Ga-PSMA ligands. *In vitro* experiments demonstrate that [^{68}Ga]Ga-THP-PSMA binds specifically to GCP(II)/PSMA, although with approximately 10-fold weaker affinity than [^{68}Ga]Ga-HBED-CC-PSMA and [^{68}Ga]Ga-DOTA-PSMA(617). The method developed to assess *relative* affinity for GCP(II)/PSMA allowed the radioactive versions of 2 gallium-tracers to be evaluated at low concentration (1 nM) without excess gallium, avoiding issues with solubility and the values obtained agreed with established IC_{50} methods. The *relative* affinity method is also a valuable new tool for screening gallium-68 ligands as it requires much less ligand than IC_{50} measurements and can be performed quickly at a single ligand concentration. However, there may be an advantage in performing this method with an isolated NAALADase-based assay, as is typically used for measuring K_i values (*25*)(*34*)(*46*), rather than a cell-based assay, as this would avoid the complications caused by internalisation and retention of tracers within the cells.

Although THP-PSMA was rationally designed on the basis of previous literature (*25*)(*44*)(*47*)(*48*), no optimisation was carried out on the specific target affinity of THP-PSMA bioconjugates and so there remains an opportunity to develop higher affinity bioconjugates incorporating THP. This topic is explored fully in chapters 6 and 7. However, the simplicity of radiolabelling, excellent serum stability, and *in vitro* GCP(II)/PSMA binding justified further evaluation of the new tracer *in vivo*. Assessment in SCID/beige mice bearing prostate cancer xenografts showed that incorporation of THP into bio-conjugates confers no THP-specific adverse pharmacokinetics. The rapid renal excretion, low non-specific uptake of [^{68}Ga]Ga-THP-PSMA in non-target tissues, and high radioactivity concentration in GCP(II)/PSMA-expressing tumours are clinically desirable features. In the preclinical model used here, tumour uptake and pharmacokinetic properties of [^{68}Ga]Ga-THP-PSMA and [^{68}Ga]Ga-HBED-CC-PSMA are indistinguishable except that spleen uptake of [^{68}Ga]Ga-THP-PSMA was lower, by almost a factor of 5. Although GCP(II)/PSMA-targeting radiopharmaceuticals generally appear to share high uptake in spleen in mice, murine spleen is not believed to express GCP(II)/PSMA (*49*). It seems likely therefore that some other target capable of binding the PSMA tracers is present in the spleen and that [^{68}Ga]Ga-THP-PSMA has enhanced ability to distinguish GCP(II)/PSMA from this alternative target.

3.6 Conclusion

Use of THP as the gallium-68 chelator facilitates rapid chelation under mild conditions and produces a GCP(II)/PSMA-targeted bioconjugate that can be labelled in one-step by reconstitution of a kit with unprocessed generator eluate. This is the first time that a one-step kit has been demonstrated for a [^{68}Ga]Ga-bioconjugate. Labelling requires only a generator, a lyophilised kit, a syringe, quality control facilities, and PET shielding. Kit-based labelling can be performed in a few minutes, using the full volume of unprocessed generator eluate (5 mL), without post synthesis purification and achieve a greater than 95% radiochemical purity. *In vivo*, [^{68}Ga]Ga-THP-PSMA accumulates in GCP(II)/PSMA-expressing tumours, with good tumour-to-background ratio and delineation of GCP(II)/PSMA-positive tumour lesions similar to [^{68}Ga]Ga-HBED-CC-PSMA. One-step kit-based radiolabelling of gallium-68 radiopharmaceuticals has been shown to be feasible with THP and would facilitate wider and more economical use of gallium-68 in hospitals, hence benefitting more patients.

3.7 References

1. Young JD, Abbate V, Imberti C, Meszaros LK, Ma MT, Terry SYAA, Hider RC, Mullen GE, Blower PJ. 68Ga-THP-PSMA: A PET Imaging Agent for Prostate Cancer Offering Rapid, Room-Temperature, 1-Step Kit-Based Radiolabeling. *J Nucl Med*. 2017;58:1270-1277.
2. Zolle I. *Technetium-99m Pharmaceuticals*. New York, NY: Springer; 2007
3. Deutsch E. Clinical PET: Its Time Has Come? *J Nucl Med*. 1993;34:1132-1134.
4. Rösch F. 68Ge/68Ga Generators and 68Ga Radiopharmaceutical Chemistry on Their Way into a New Century. *Postgrad Med Educ Res*. 2013;47:18-25.
5. Price EW, Orvig C. Matching Chelators to Radiometals for Radiopharmaceuticals. *Chem Soc Rev*. 2014;43:260-90.
6. Velikyan I. Continued Rapid Growth in 68Ga Applications: Update 2013 to June 2014. *J Label Compd Radiopharm*. 2015;58:99-121.
7. Velikyan I. Prospective of 68Ga-Radiopharmaceutical Development. *Theranostics*. 2014;4:47-80.
8. Breeman W a P, Verbruggen AM. The 68Ge/68Ga Generator Has High Potential, but When Can We Use 68Ga-Labelled Tracers in Clinical Routine? *Eur J Nucl Med Mol Imaging*. 2007;34:978-981.
9. Bé M, Schonfeld E. Gallium-68. Laboratoire National Henri Becquerel. http://www.lnhb.fr/nuclides/Ga-68_tables.pdf. Updated Jul 4, 2012. Accessed Jun 25, 2018.
10. Bé M, E. S. Germanium-68. Laboratoire National Henri Becquerel. http://www.lnhb.fr/nuclides/Ge-68_tables.pdf. Updated Feb 27, 2012. Accessed 25 Jun, 2018.
11. European Medicines Agency website. List of Nationally Authorised Medicinal Products. Active Substance: Germanium (68Ge) Chloride / Gallium (68Ga) Chloride. Procedure No.: PSUSA/00010364/201603. http://www.ema.europa.eu/docs/en_GB/document_library/Periodic_safety_update_single_assessment/2016/11/WC500216013.pdf. Updated Oct 27, 2016. Accessed Jun 25, 2018.
12. Gallium (68Ga) Edotreotide Injection. *Br Pharmacop*. 2016;Monograph:2482.
13. McInnes LE, Rudd SE, Donnelly PS. Copper, Gallium and Zirconium Positron Emission Tomography Imaging Agents: The Importance of Metal Ion Speciation. *Coord Chem Rev*. 2017;352:499-516.
14. Wood SA, Samson IM. The Aqueous Geochemistry of Gallium, Germanium, Indium and Scandium. *Ore Geol Rev*. 2006;28:57-102.
15. Tsionou MI, Knapp CE, Foley CA, Munteanu CR, Cakebread A, Imberti C, Eykyn TR, Young JD, Paterson BM, Blower PJ, Ma MT. Comparison of Macrocyclic and Acyclic Chelators for Gallium-68 Radiolabelling. *RSC Adv*. 2017;7:49586-49599.
16. Berry DJ, Ma Y, Ballinger JR, Tavaré R, Koers A, Sunassee K, Zhou T, Nawaz S, Mullen GED, Hider RC, Blower PJ. Efficient Bifunctional Gallium-68 Chelators for Positron Emission Tomography: Tris(Hydroxypyridinone) Ligands. *Chem Commun (Camb)*. 2011;47:7068-70.
17. Ma MT, Cullinane C, Imberti C, Baguna Torres J, Terry SY a., Roselt P, Hicks RJ, Blower PJ, Bagunya Torres J, Terry SY a., Roselt P, Hicks RJ, Blower PJ. New Tris (Hydroxypyridinone) Bifunctional Chelators Containing Isothiocyanate Groups Provide a Versatile Platform for Rapid One-Step Labeling and PET Imaging with 68Ga3+. *Bioconjug Chem*. 2015;27:309-318.
18. Ma MT, Cullinane C, Waldeck K, Roselt P, Hicks RJ, Blower PJ. Rapid Kit-Based (68)Ga-Labelling and PET Imaging with THP-Tyr(3)-Octreotate: A Preliminary Comparison with DOTA-Tyr(3)-Octreotate. *EJNMMI Res*. 2015;5:52.
19. Cusnir R, Imberti C, Hider R, Blower P, Ma M. Hydroxypyridinone Chelators: From Iron

Scavenging to Radiopharmaceuticals for PET Imaging with Gallium-68. *Int J Mol Sci*. 2017;18:116.
20. Imberti C, Terry SYAA, Cullinane C, Clarke F, Cornish GH, Ramakrishnan NK, Roselt P, Cope AP, Hicks RJ, Blower PJ, Ma MT. Enhancing PET Signal at Target Tissue in Vivo: Dendritic and Multimeric Tris(Hydroxypyridinone) Conjugates for Molecular Imaging of Avβ3 Integrin Expression with Gallium-68. *Bioconjug Chem*. 2017;28:481-495.
21. Dubey RD, Klippstein R, Wang JT-W, Hodgins N, Mei K-C, Sosabowski J, Hider RC, Abbate V, Gupta PN, Al-Jamal KT. Novel Hyaluronic Acid Conjugates for Dual Nuclear Imaging and Therapy in CD44-Expressing Tumors in Mice in Vivo. *Nanotheranostics*. 2017;1:59-79.
22. Bouchelouche K, Choyke PL, Capala J. Prostate Specific Membrane Antigen- a Target for Imaging and Therapy with Radionuclides. *Discov Med*. 2010;9:55-61.
23. Zhou J, Neale JH, Pomper MG, Kozikowski AP. NAAG Peptidase Inhibitors and Their Potential for Diagnosis and Therapy. *Nat Rev Drug Discov*. 2005;4:1015-1026.
24. Kozikowski AP, Nan F, Conti P, Zhang J, Ramadan E, Bzdega T, Wroblewska B, Neale JH, Pshenichkin S, Wroblewski JT. Design of Remarkably Simple, yet Potent Urea-Based Inhibitors of Glutamate Carboxypeptidase II (NAALADase). *J Med Chem*. 2001;44:298-301.
25. Eder M, Schäfer M, Bauder-Wüst U, Hull W-E, Wängler C, Mier W, Haberkorn U, Eisenhut M. 68Ga-Complex Lipophilicity and the Targeting Property of a Urea-Based PSMA Inhibitor for PET Imaging. *Bioconjug Chem*. 2012;23:688-697.
26. Wüstemann T, Bauder-Wüst U, Schäfer M, Eder M, Benesova M, Leotta K, Kratochwil C, Haberkorn U, Kopka K, Mier W. Design of Internalizing PSMA-Specific Glu-Ureido-Based Radiotherapeuticals. *Theranostics*. 2016;6:1085-1095.
27. Eiber M, Maurer T, Souvatzoglou M, Beer a. J, Ruffani a., Haller B, Kubler H, Haberkorn U, Eisenhut M, Wester H-J, Gschwend JE, Schwaiger M. Evaluation of Hybrid 68Ga-PSMA-Ligand PET/CT in 248 Patients with Biochemical Recurrence after Radical Prostatectomy. *J Nucl Med*. 2015;56:668-674.
28. Afshar-Oromieh A, Zechmann CM, Malcher A, Eder M, Eisenhut M, Linhart HG, Holland-Letz T, Hadaschik B a., Giesel FL, Debus J, Haberkorn U. Comparison of PET Imaging with a 68Ga-Labelled PSMA Ligand and 18F-Choline-Based PET/CT for the Diagnosis of Recurrent Prostate Cancer. *Eur J Nucl Med Mol Imaging*. 2014;41:11-20.
29. Afaq A, Alahmed S, Chen S, Lengana T, Haroon A, Payne H, Ahmed H, Punwani S, Sathekge M, Bomanji J. 68 Ga-PSMA PET/CT Impact on Prostate Cancer Management. *J Nucl Med*. 2018;59:89-92.
30. Roach PJ, Francis R, Emmett L, Hsiao E, Kneebone A, Hruby G, Eade T, Nguyen Q, Thompson B, Cusick T, McCarthy M, Tang C, Ho B, Stricker P, Scott A. The Impact of 68 Ga-PSMA PET/CT on Management Intent in Prostate Cancer: Results of an Australian Prospective Multicenter Study. *J Nucl Med*. 2018;59:82-88.
31. Satpati D, Shinto A, Kamaleshwaran KK, Sane S, Banerjee S. Convenient Preparation of [68Ga]DKFZ-PSMA-11 Using a Robust Single-Vial Kit and Demonstration of Its Clinical Efficacy. *Mol Imaging Biol*. 2016;18:420-427.
32. Ebenhan T, Vorster M, Marjanovic-Painter B, Wagener J, Suthiram J, Modiselle M, Mokaleng B, Zeevaart J, Sathekge M. Development of a Single Vial Kit Solution for Radiolabeling of 68Ga-DKFZ-PSMA-11 and Its Performance in Prostate Cancer Patients. *Molecules*. 2015;20:14860-14878.
33. Czernin J, Eiber M. Acceleration of PSMA-Targeted Theranostics to the Clinic: Can Common Sense Prevail? *J Nucl Med*. 2017;58:1186-1187.
34. Benešová M, Schäfer M, Bauder-Wüst U, Afshar-Oromieh A, Kratochwil C, Mier W, Haberkorn U, Kopka K, Eder M. Preclinical Evaluation of a Tailor-Made DOTA-Conjugated PSMA Inhibitor with Optimized Linker Moiety for Imaging and Endoradiotherapy of Prostate Cancer. *J Nucl Med*. 2015;56:914-920.

35. Eder M, Neels O, Müller M, Bauder-Wüst U, Remde Y, Schäfer M, Hennrich U, Eisenhut M, Afshar-Oromieh A, Haberkorn U. Novel Preclinical and Radiopharmaceutical Aspects of [68Ga]Ga-PSMA-HBED-CC: A New PET Tracer for Imaging of Prostate Cancer. *Pharmaceuticals*. 2014;7:779-796.
36. Chakravarty R, Chakraborty S, Radhakrishnan ER, Kamaleshwaran K, Shinto A, Dash A. Clinical 68Ga-PET: Is Radiosynthesis Module an Absolute Necessity? *Nucl Med Biol*. 2017;46:1-11.
37. Kampmeier F, Williams JD, Maher J, Mullen GE, Blower PJ. Design and Preclinical Evaluation of a 99mTc-Labelled Diabody of MAb J591 for SPECT Imaging of Prostate-Specific Membrane Antigen (PSMA). *EJNMMI Res*. 2014;4:13.
38. Zhou T, Neubert H, Liu DY, Liu ZD, Ma YM, Kong X Le, Luo W, Mark S, Hider RC. Iron Binding Dendrimers: A Novel Approach for the Treatment of Haemochromatosis. *J Med Chem*. 2006;49:4171-4182.
39. Hofman MS, Eu P, Jackson P, Hong E, Binns D, Iravani A, Murphy D, Mitchell C, Siva S, Hicks RJ, Young JD, Blower P, Mullen GE. Cold Kit PSMA PET Imaging: Phase I Study of 68Ga-THP-PSMA PET/CT in Patients with Prostate Cancer. *J Nucl Med*. 2018;59:625-631.
40. Othman MF bin, Mitry NR, Lewington VJ, Blower PJ, Terry SYA. Re-Assessing Gallium-67 as a Therapeutic Radionuclide. *Nucl Med Biol*. 2017;46:12-18.
41. Chapter 7. Theory of binding data analysis. In: *Fluorescence Polarization Technical Resource Guide*. Madison, WI: Invitrogen Corporation; 2008: 7.1-7.18.
42. Mougeot X, Chechev VP. Gallium-67. Laboratoire National Henri Becquerel. http://www.lnhb.fr/nuclides/Ga-67_tables.pdf. Updated Sept 20, 2000. Accessed Jun 25, 2018.
43. Jackson PF, Tays KL, Maclin KM, Ko YS, Li W, Vitharana D, Tsukamoto T, Stoermer D, Lu XCM, Wozniak K, Slusher BS. Design and Pharmacological Activity of Phosphinic Acid Based NAALADase Inhibitors. *J Med Chem*. 2001;44:4170-4175.
44. Chen Y, Foss C a, Byun Y, Nimmagadda S, Pullambhatla M, Fox JJ, Castanares M, Lupold SE, Babich JW, Mease RC, Pomper MG. Radiohalogenated Prostate-Specific Membrane Antigen (PSMA)-Based Ureas as Imaging Agents for Prostate Cancer. *J Med Chem*. 2008;51:7933-7943.
45. Cahill R, Cookson RC, Crabb TA. Geminal Coupling Constants in Methylene Groups—II : J in CH2 Groups α to Heteroatoms. *Tetrahedron*. 1969;25:4681-4709.
46. Banerjee SR, Foss CA, Castanares M, Mease RC, Byun Y, Fox JJ, Hilton J, Lupold SE, Kozikowski AP, Pomper MG. Synthesis and Evaluation of Technetium-99m-and Rhenium-Labeled Inhibitors of the Prostate-Specific Membrane Antigen (PSMA). *J Med Chem*. 2008;51:4504-4517.
47. Hillier SM, Maresca KP, Lu G, Merkin RD, Marquis JC, Zimmerman CN, Eckelman WC, Joyal JL, Babich JW. 99mTc-Labeled Small-Molecule Inhibitors of Prostate-Specific Membrane Antigen for Molecular Imaging of Prostate Cancer. *J Nucl Med*. 2013;54:1369-1376.
48. Chen Y, Pullambhatla M, Banerjee SR, Byun Y, Stathis M, Rojas C, Slusher BS, Mease RC, Pomper MG. Synthesis and Biological Evaluation of Low Molecular Weight Fluorescent Imaging Agents for the Prostate-Specific Membrane Antigen. *Bioconjug Chem*. 2012;23:2377-2385.
49. Bacich DJ, Pinto JT, Tong WP, Heston WDW. Cloning, Expression, Genomic Localization, and Enzymatic Activities of the Mouse Homolog of Prostate-Specific Membrane Antigen/NAALADase/Folate Hydrolase. *Mamm Genome*. 2001;12:117-123.
50. Xiang B, Dong DW, Shi NQ, Gao W, Yang ZZ, Cui Y, Cao DY, Qi XR. PSA-Responsive and PSMA-Mediated Multifunctional Liposomes for Targeted Therapy of Prostate Cancer. *Biomaterials*. 2013;34:6976-6991.

3.8 Theory to Support the Assay Design for *Relative* Affinity Measurements

According to Clark's theory (*41*) classical ligand-receptor interactions can be studied in systems where the following assumptions hold: 1) All the receptor molecules are equivalent and independent; 2) The response measured is proportional to the number of occupied receptor sites; 3) The interaction between ligand and receptor is reversible; 4) The ligand does not degrade or react during the experiment, and only exists as the free ligand or bound to the receptor; 5) The number of occupied ligand sites is determined at equilibrium.

A method that satisfies these requirements has therefore been proposed. In this experiment the ligand will be the [$^{67/68}$Ga]Ga-PSMA radiotracer ([$^{67/68}$Ga]Ga-DOTA-PSMA(617), [$^{67/68}$Ga]Ga-HBED-CC-PSMA, or [$^{67/68}$Ga]Ga-THP-PSMA) and the receptor will be GCP(II)/PSMA expressed on the surface of DU145-PSMA cells, all of these receptors should be identical as this cell line was genetically engineered to express this receptor (*37*). This satisfies assumption 1. The use of a radioactive tracer to measure the number of occupied sites is a well-established, direct and accurate method, in line with assumption 2. The interaction between the urea-based motif, used in all these tracers to target GCP(II)/PSMA, and the receptor is known to be reversible satisfying assumption 3, as the interaction does not involve the creation of covalent bonds between the substrate and the protein or the cleavage of the substrate: it is purely an inhibitor. Additionally, efflux from the protein/cells is seen when the concentration of tracer in the medium is reduced, further confirming the interaction is reversible. These tracers have been shown to be stable within the conditions proposed and in order to ensure any off-site reactions/interactions are taken into account, the experimental procedure proposed has 2 different controls for unspecific binding (blocking GCP(II)/PSMA sites with the known inhibitor PMPA, and the use of non GCP(II)/PSMA-expressing cells DU145). This should satisfy assumption 4. Importantly, assumption 5 states that the measurements must also be performed at equilibrium for the models to hold. In line with previously published studies, in this experiment it is assumed that an equilibrium state is reached once the uptake of tracer over time plateaus (*41*). Graphs displaying uptake over time for the three [^{67}Ga]Ga-PSMA tracers show that a plateau is not reached within 4 hours at 37°C, but at 4°C, a temperature where internalisation of the tracer would be dampened (*26*)(*50*), the plateau is reached by 2 hours (figure 3.17). With all these constraints satisfied we can use the classical ligand-receptor interactions to determine *relative* affinity values of tracers as outlined below.

Classical ligand-receptor interactions can be shown as:

$$Ligand_{free} + Receptor_{free} \underset{k_{-1}}{\overset{k_1}{\rightleftharpoons}} Ligand{:}Receptor$$

At equilibrium, the dissociation constant K_d can be defined as:

$$\frac{[Ligand_{free}][\,Receptor_{free}]}{[Ligand{:}Receptor]} = \frac{[L_F][\,R_F]}{[LR]} = \frac{k_{-1}}{k_1} \quad = K_d$$

If two different tracers are considered; tracer 1 and tracer 2, their individual dissociation constants (K_d) can be defined as:

$$K_{d1} = \frac{[L_{F1}][\,R_{F1}]}{[LR_1]} \qquad K_{d2} = \frac{[L_{F2}][\,R_{F2}]}{[LR_2]}$$

Which can be rearranged as:

$$R_{F1} = \left(\frac{[LR_1]}{[L_{F1}]}\right) K_{d1} \qquad R_{F2} = \left(\frac{[LR_2]}{[L_{F2}]}\right) K_{d2}$$

If these two tracers are incubated in the same experiment with the same receptor, then the total number of receptors, and the number of free receptors is controlled and becomes equivalent for the two tracers and so $R_{F1} = R_{F2}$.

When:

$$R_{F1} = R_{F2}$$

Then:

$$\left(\frac{[LR_1]}{[L_{F1}]}\right) K_{d1} = \left(\frac{[LR_2]}{[L_{F2}]}\right) K_{d2}$$

Therefore the *relative* affinity is equivalent to the ratio of the two tracers' dissociation constants and this can be calculated from:

$$\frac{K_{d1}}{K_{d2}} = \frac{\left(\frac{LR_2}{L_{F2}}\right)}{\left(\frac{LR_1}{L_{F1}}\right)}$$

This requires the specific binding of the two tracers to be determined, which can be calculated as shown below.

$$\frac{K_{d1}}{K_{d2}} = \frac{\left(\frac{[100 - \ \% \ specific \ binding_1]}{[\% \ specific \ binding_1]}\right)}{\left(\frac{[100 - \% \ specific \ binding_2]}{[\% \ specific \ binding_2]}\right)}$$

$$\frac{K_{d1}}{K_{d2}} = \frac{\left(\frac{100 - [\% \ total \ binding_1 \ - \% \ non \ specific \ binding_1]}{[\% \ total \ binding_1 \ - \% \ non \ specific \ binding_1]}\right)}{\left(\frac{100 - [\% \ total \ binding_2 \ - \% \ non \ specific \ binding_2]}{[\% \ total \ binding_2 \ - \% \ non \ specific \ binding_2]}\right)}$$

From these equations, we have determined that in order to calculate the *relative* affinity (K_d) of two tracers, they must be incubated at the same time with the same receptor (and so in this experiment in the same well, containing DU145-PSMA cells) and their specific binding determined. This was achieved by utilising the 2 isotopes of gallium, gallium-67 and gallium-68, which have different half-lives (3.26 days (*42*) and 68 minutes (*9*) respectively) and different emission profiles as shown in figure 3.2. The [^{67}Ga]Ga-PSMA tracer and the [^{68}Ga]Ga-PSMA tracer were incubated in the same well, and then the cells were washed, lysed and prepared for gamma-counting. The gamma-emissions from the gallium-68 tracer were measured directly after the experiment using a pre-selected emission window and then the samples were left to decay for at least 12 hours (ten half-lives) to ensure only gallium-67 remained in the sample. The samples were then gamma-counted for with the optimal window for gallium-67, which was used to determine the uptake of the gallium-67 tracer. Then the sample was counted with the window as used for gallium-68 so that the contribution of the gallium-67 present in the sample to the values measured for gallium-68 could be determined and decay corrected. These were then subtracted from the [^{68}Ga]Ga-PSMA uptake values obtained directly after the experiment providing the true [^{68}Ga]Ga-PSMA uptake values. Each gallium-67 tracer was compared with

each gallium-68 tracer in the same well in order to compensate for any differences caused by the labelling procedures with the 2 gallium isotopes.

The tracer concentration chosen was 1 nM with 1 million cells per mL as this was below the IC_{50} of all three tracers (figure 3.19). This ensured that there was a large excess of receptors and the non-radioactive constituent of the tracer was at a low enough concentration not to block uptake of the radioactive tracer. The assessment of the non-specific uptake of the tracer was determined by 2 methods, the use of DU145 cells which do not express GCP(II)/PSMA but are the mother cell line of DU145-PSMA and so should be identical in other features, and by using PMPA, a known inhibitor, in large excess (750 μM) to block all the GCP(II)/PSMA sites.

4 Clinical studies with [^{68}Ga]Ga-THP-PSMA

Since the development of [^{68}Ga]Ga-THP-PSMA, this tracer has been evaluated in a phase 1 clinical trial at Peter MacCallum Cancer Centre, Melbourne, Australia (*1*)(*2*), two clinical research studies at Hannover Medical School, Hannover, Germany (*3*)(*4*), and a clinical research study at Guy's and St Thomas' Hospital, London, UK (*5*). In this chapter, the published work on the clinical translation of [^{68}Ga]Ga-THP-PSMA will be summarised and discussed.

4.1 Overview of Phase 1 Clinical Study, Peter MacCallum Cancer Centre, Melbourne Australia

A phase 1 study which aimed to establish the safety profile of [^{68}Ga]Ga-THP-PSMA and its ability to delineate GCP(II)/PSMA-expressing prostate cancer using PET/CT, was conducted at the Peter MacCallum Cancer Centre in 2016 (*2*) and the results published in 2017 (*1*).

4.1.1 Radiochemistry

The GMP compliant GalliProst™ radiopharmaceutical kits produced by ROTOP Pharmaka GmbH, were used for the radiolabelling [^{68}Ga]Ga-THP-PSMA within this study. A Galliapharm generator (Eckert & Zeigler, Berlin, Germany), for which the one-step kits were designed for, was not available for these studies and instead two different generators were used: the iThemba (IDB Holland BV, Netherlands) which elutes with 5 mL of 0.5 M HCl and the Galli Eo (IRE-Elit, Fleurus, Belgium) which elutes with eluted with 1.1 mL 0.1 M HCl. Therefore these kits could not be reconstructed in a one-step process, as is possible with the GalliaPharm generator. However, the radiolabelling was still extremely simple and rapid when compared to the automated synthesis required for [^{68}Ga]Ga-HBED-CC-PSMA and over >99% RCP was consistently achieved.

4.1.2 Patient Selection and Imaging Protocols

Overall 14 patients were included in the phase 1 study and were grouped into 2 cohorts. Cohort A contained 8 patients with prior multi-parametric MRI and biopsy-proven prostate cancer, and were scheduled for prostatectomy but had not received any other treatment. These patients were administered 228-270 MBq [^{68}Ga]Ga-THP-PSMA (35 µg cold compound) and imaged with CT and a dynamic PET up to 90 minutes, then with static scans at 2 and 3 hours. Histological samples from these patients' prostatectomies and lymph node dissections were stained for GCP(II)/PSMA (Dako (Agilent) clone 3E6) which allowed the uptake of the tracer to be correlated with GCP(II)/PSMA-expression. Cohort B contained 6 patients who were selected because they

had metastatic prostate cancer which had previously shown [^{68}Ga]Ga-HBED-CC-PSMA uptake. These patients were also imaged with [^{68}Ga]Ga-THP-PSMA within 22 days of their original scan allowing the biodistribution and lesion uptake of the two tracers to be compared. These patients were administered 172-275MBq [^{68}Ga]Ga-THP-PSMA and imaged at 15 minutes, 1 and 2 hours.

4.1.3 Safety

No adverse events were seen in any of the patients administered with [^{68}Ga]Ga-THP-PSMA.

4.1.4 Biodistribution and Dosimetry

[^{68}Ga]Ga-THP-PSMA showed rapid renal excretion and very low background uptake in non-target tissues as demonstrated in figure 4.1. The majority of the activity was associated with the kidneys and the bladder within 15 minutes. The dosimetry results reflect this distribution with the highest absorbed dose to the urinary bladder and kidneys. The mean effective dose determined for [^{68}Ga]Ga-THP-PSMA was 0.021 mSv/MBq, a very similar value to those found for [^{68}Ga]Ga-HBED-CC-PSMA (0.024 mSv/MBq (*6*)), [^{68}Ga]Ga-DOTA-PSMA 617 (0.021 mSv/MBq (*7*)) [^{18}F]F-PSMA-1007 (0.022 mSv/MBq (*8*)) and [^{18}F]DCFPyL (0.0139 mSv/MBq (*9*)). When the two tracers were compared in the same patient there were clear differences in background uptake as shown in figure 4.2. In particular, lower uptake was seen for [^{68}Ga]Ga-THP-PSMA in the salivary glands (parotid), spleen, and liver, which was quantified using SUV_{max} values (table 4.1). In the [^{68}Ga]Ga-THP-PSMA images there was notable uptake in the urinary tract between kidneys and the bladder which may have been difficult to distinguish from pelvic lymph nodes if only PET was performed, but the two could clearly be differentiated on PET/CT axial slices.

		[^{68}Ga]Ga-THP-PSMA				[^{68}Ga]Ga-HBED-CC-PSMA			
	Patient	Parotid	Liver	Spleen	Blood Pool	Parotid	Liver	Spleen	Blood Pool
Cohort B	**9**	5.0	2.6	2.7	1.8	20.0	8.2	9.3	1.8
	10	3.5	4.8	4.8	1.6	18.3	72	9.8	1.2
	11	4.4	2.1	2.1	1.7	16.7	4.8	8.8	1.4
	12	3.9	2.2	3.2	1.9	18.7	6.3	15.9	1.7
	13	2.9	2.4	3.2	2.3	14.2	6.2	14.5	1.9
	14	4.2	1.9	1.6	1.9	27.0	5.1	4.4	0.6
	Mean	**4.0**	**2.7**	**2.9**	**1.9**	**19.2**	**17.1**	**10.5**	**1.4**

TABLE 4.1: Physiologic uptake (SUV_{max}) of [^{68}Ga]Ga-THP-PSMA compared to [^{68}Ga]Ga-HBED-CC-PSMA for Cohort B in the Phase 1 study. Modified with permissions from (1).

4.1.5 Performance of [^{68}Ga]Ga-THP-PSMA in Initial Staging

The results from cohort A showed the ability of [^{68}Ga]Ga-THP-PSMA to specifically delineate primary tumours with had high levels of GCP(II)/PSMA-expression (defined as immunohistochemistry ranking of +3) as shown in figure 4.1. Patients without high levels of expression of GCP(II)/PSMA in their primary tumour (n = 2) did not show [^{68}Ga]Ga-THP-PSMA uptake, demonstrating the selectivity of this tracer. In this set of patients, lymph node involvement was only detected by [^{68}Ga]Ga-THP-PSMA in one patient, but histological analysis of dissected lymph nodes showed the presence of cancer in the lymph nodes of two further patients. However, these lymph nodes were 0.6 mm and 0.1 mm in size; much smaller than the 8 mm detection limit of conventional imaging (*10*). [^{68}Ga]Ga-HBED-CC-PSMA imaging is also known to miss a proportion of lesions of a similar size when correlated with histology prior to prostatectomy (*11*).

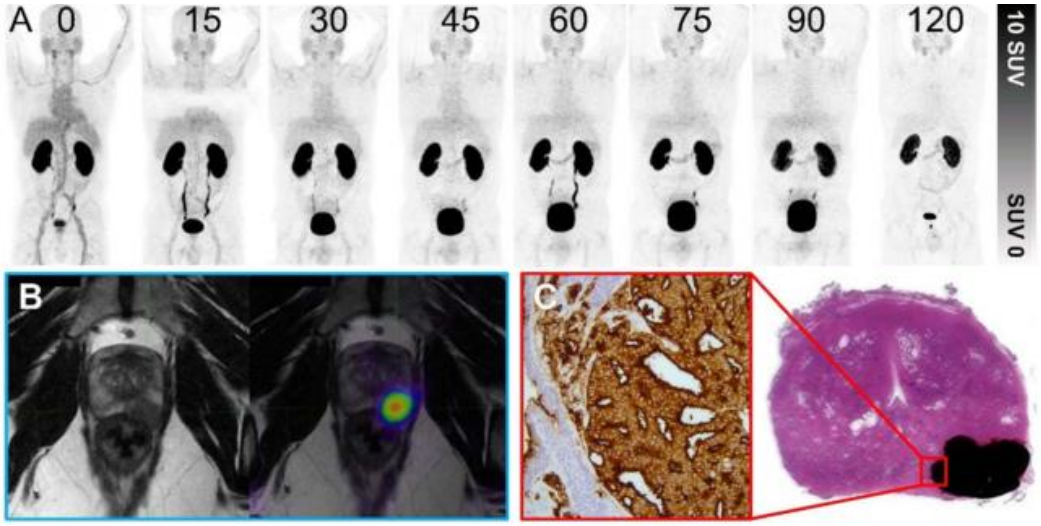

Figure 4.1: A prostate adenocarcinoma patient with a Gleason score of 4 + 4 = 8. (A) [^{68}Ga]Ga-THP-PSMA PET multi-time point PET images from 0 to 120 minutes demonstrating rapid blood pool clearance and low background activity. (B) 120 minute PET image after voiding fused to multi- parametric MRI T2 sequence demonstrating focal uptake in the left posterior mid-zone lesion. (C) Histopathologic correlation following prostatectomy with area of adenocarcinoma shaded in black, and zoomed-in area demonstrating 3+ staining with GCP(II)/PSMA immunohistochemistry. Reproduced with permission from (1).

4.1.6 Comparison of [^{68}Ga]Ga-THP-PSMA with [^{68}Ga]Ga-HBED-CC-PSMA in Metastatic Prostate Cancer

[^{68}Ga]Ga-THP-PSMA was able to successfully identify metastatic sites in all patients, including those within the prostate bed, pelvic and distant lymph nodes and bone. Statistically significant differences in SUV_{max} were seen between the same metastases imaged with [^{68}Ga]Ga-THP-PSMA

and with [^{68}Ga]Ga-HBED-CC-PSMA with mean values of 10.7 and 30.3 respectively (P <0.01). Example patient scans can be seen in figure 4.2. Although the tumour to background ratio was maintained, the lower intensity within cancerous lesions may mean that smaller areas of disease do not reach the threshold for detection and are consequently missed. This problem could explain why within this study, although the majority of scans showed a concordant number of disease sites, in one patient only 2 lesions were detected on the [^{68}Ga]Ga-THP-PSMA scan compared to 4 with the [^{68}Ga]Ga-HBED-CC-PSMA scan. However, these differences were not followed up with histology and so conclusions about which tracer gave a more accurate distribution of prostate cancer sites cannot be drawn. An optimal PSMA tracer would combine the low background uptake of [^{68}Ga]Ga-THP-PSMA with the high SUV_{max} values in GCP(II)/PSMA-expressing prostate cancer seen for [^{68}Ga]Ga-HBED-CC-PSMA.

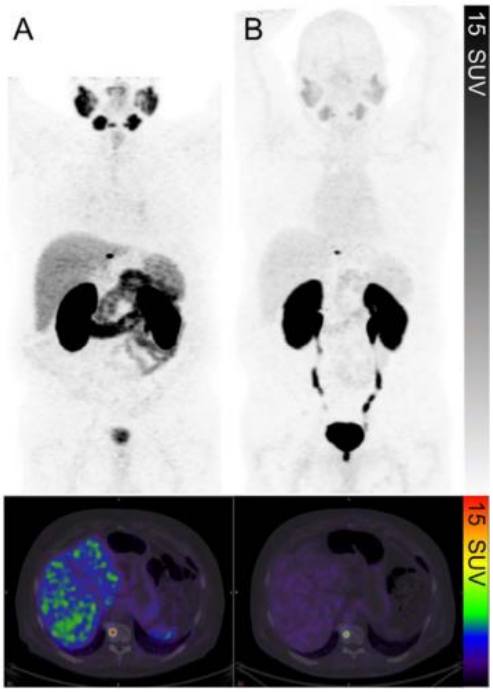

FIGURE 4.2: Comparison of (A) [^{68}Ga]Ga-HBED-PSMA PET/CT (177MBq, 56 minute uptake period) to (B) [^{68}Ga]Ga-THP-PSMA PET/CT (232 MBq, 60 minute uptake period) in the same patient. A solitary focal bone metastasis in the vertebra is well-visualised on both images. Image reproduced with permission from (1).

4.1.7 Conclusions from Phase 1 Study

The phase 1 study showed [^{68}Ga]Ga-THP-PSMA is safe and can be used to identify GCP(II)/PSMA-expressing prostate cancer in both initial staging and metastatic cancer. When imaging was performed in the same patient with both [^{68}Ga]Ga-THP-PSMA and [^{68}Ga]Ga-HBED-CC-PSMA the uptake in both the background tissues and prostate cancer was lower for [^{68}Ga]Ga-THP-PSMA, however, interpretation of either scan provided the same staging information, showing similar

clinical utility. Further studies in larger patient populations would be required to evaluate whether the differences in the images produced by the two tracers would impact on patient management.

4.2 Studies from Hannover Medical School, Hannover, Germany

Both studies from Hannover Medical School looked at the performance of [^{68}Ga]Ga-THP-PSMA in patients with biochemical recurrence after radical prostatectomy. The first looked at 25 patients and focused on comparing [^{68}Ga]Ga-THP-PSMA to [^{68}Ga]Ga-DOTAGA-PSMA(I&T) in similar patient populations (but not the same patients) (*3*), and the second was a larger study of 99 patients where the detection rate across a range of blood PSA levels was determined (*4*).

4.2.1 Radiochemistry

The radiolabelling for both studies was performed with GalliProst™ kits. These were reconstituted by the elution of an ITG gallium-68 generator (Isotope Technologies Garching GmbH, Garching, Germany) directly into the radiopharmaceutical kit in a one-step process. The eluate from these ITG generators was 5 mL of 0.05 M HCl. As the kits were designed for 5 mL 0.1 M HCl the pH is likely to have been higher than 7 with the ITG eluate, but this was not commented on in the papers (*3*)(*4*). Over 95% radiochemical purity was achieved and each 40 µg kit (THP-PSMA content) was used for two patients. This process was carried out in around 5 minutes, much faster than the 37 minutes required for the synthesis module production of [^{68}Ga]Ga-DOTAGA-PSMA(I&T) at the same radiopharmacy. This gave the advantage that more activity was available for patient imaging (*3*).

4.2.2 Patient Selection and Imaging Protocols

All patients recruited in the two studies had biochemical recurrence defined as a PSA of 0.01 ng/mL or more after radical prostatectomy (range in study 1: 0.05–19.0 ng/mL, range study 2: 0.01 – 8400 ng/mL). However, this is a very low PSA level at which to define biochemical recurrence. The European Association of Urology (EAU) guidelines on prostate cancer management define recurrence 0.2 ng/mL or above (*12*) over 4 times that used in this study. Additionally, the European Association of Nuclear Medicine (EANM) and Society of Nuclear Medicine and Molecular Imaging (SNMMI) procedure guidelines for prostate cancer imaging also recommend [^{68}Ga]Ga-PSMA imaging only in patients with PSA levels over the 0.2 ng/mL threshold (*13*) so most published studies use this value (*14*)(*15*). Patients were administered

with 150 MBq [^{68}Ga]Ga-THP-PSMA using one GalliProst™ kit for two patients (~20 µg THP-PSMA per patient) and then imaged at 1 hour post-injection after voiding the bladder.

4.2.3 Biodistribution

The biodistribution of [^{68}Ga]Ga-THP-PSMA in these studies matched that observed in the phase 1 trial. When the distribution was compared to [^{68}Ga]Ga-DOTAGA-PSMA(I&T) in a similar patient population (but not the same patients) [^{68}Ga]Ga-DOTAGA-PSMA(I&T) showed higher non-target uptake and higher uptake in prostate cancer metastases as shown in figure 4.3. SUV_{max} uptake values in different prostate cancer lesions cannot be fairly used to compare tracers and neither can the number of lesions detected. This is because the true number of metastases in each patient and the extent of GCP(II)/PSMA-expression in those metastases is not known. Therefore, limited conclusions can be drawn from these result as two small populations of patients where used and each group was only imaged with one tracer.

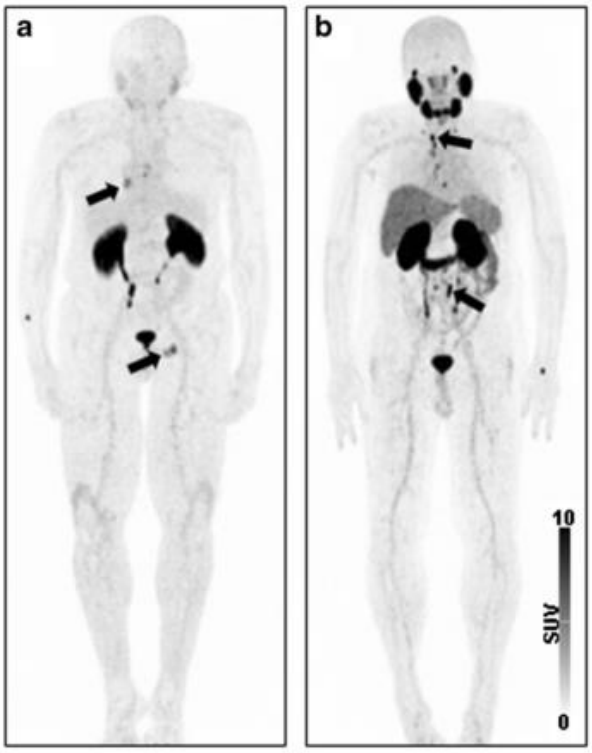

FIGURE 4.3: Images of two different patients with metastatic prostate cancer imaged at 1 hour post-injection with (A) [^{68}Ga]Ga-THP-PSMA and (B) [^{68}Ga]Ga-DOTAGA-PSMA(I&T). Reproduced with permission from (3).

4.2.4 Performance of [^{68}Ga]Ga-THP-PSMA in Biochemical Recurrence

These two studies show that [^{68}Ga]Ga-THP-PSMA is suitable for the detection of local recurrence, lymph node and bone metastasis in cases of rising PSA after radical prostatectomy.

In the smaller study, prostate cancer lesions were detected in 12 out of 25 patients and in the larger study, it was 52 out of 99 patients. A strong correlation was seen between detection rates and PSA blood levels as summarised in figure 4.4 with higher detection rates seen above 1 ng/mL.

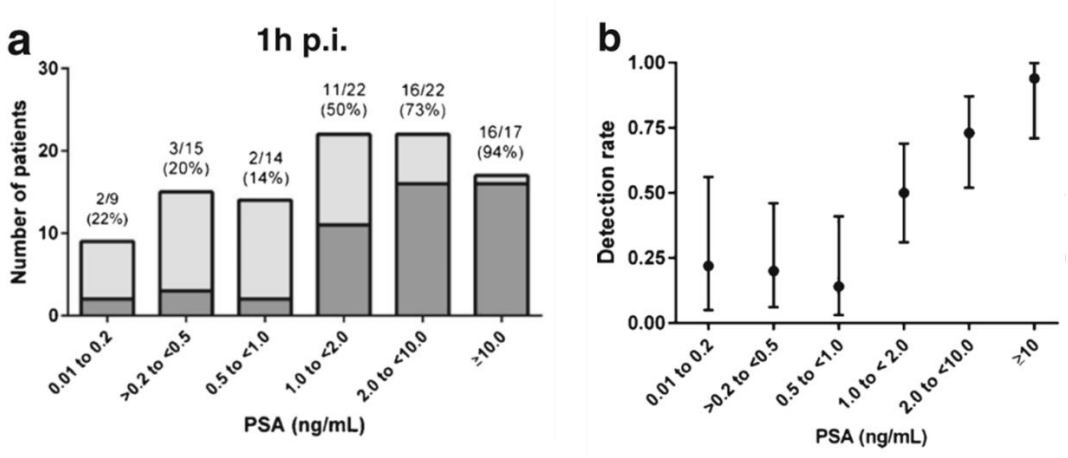

FIGURE 4.4: The number of patients with biochemical relapse scanned with [^{68}Ga]Ga-THP-PSMA PET/CT where the site of reoccurrence could be detected on the scan (A) Histogram of absolute numbers of positive and negative patients at 1 hour post-injection (B) Percentage detection. Error bars show 95% confidence intervals. Reproduced with permission from (4).

4.2.5 Conclusions from Studies at Hannover Medical School

These two studies showed [^{68}Ga]Ga-THP-PSMA can be used to identify GCP(II)/PSMA-expressing prostate cancer in biochemical recurrence. The detection rate correlated with the level of blood PSA, a proven biomarker for disease burden in biochemical recurrence (*16*). The tracer is able to distinguish lesions at much lower PSA levels than those where anatomical imaging and bone scans become clinically useful (20 ng/mL) (*12*).

4.3 Studies at Guy's and St Thomas' Hospital, London, UK

The work conducted at Guy's and St Thomas' hospital has been presented at the British Nuclear Medicine Society conference in April 2018 by Professor Gary Cook and the abstract published in Nuclear Medicine Communications (*5*). The results described here reference both the slide pack from this presentation and the published abstract.

4.3.1 Radiochemistry

[^{68}Ga]Ga-THP-PSMA was radiolabelled using the GalliProst™ kits. These were reconstructed by the elution of a Galliapharm gallium-68 generator (Eckert and Zeigler, Berlin, Germany, 5 mL,

0.1 M HCl) directly into the radiopharmaceutical kit in a one-step process and radiolabelling was assessed using two iTLC methods, with 95% radiochemical purity in both required to pass QC. This was the first [^{68}Ga]Ga-PSMA tracer to be produced within Guy's and St Thomas' radiopharmacy.

4.3.2 Patient Selection and Imaging Protocols

118 patients were included in this study and were analysed as two groups depending on whether the scan was conducted for primary staging (50 patients) or biochemical recurrence (68 patients). In this study biochemical recurrence was defined as a PSA >0.1 ng/mL. The study's aim was to determine the frequency of a clinical management change as a result of a [^{68}Ga]Ga-THP-PSMA PET/CT scan for these two populations. All patients had documented management plans before being included in the study, and information on PSA levels, Gleason scores, and PSA doubling times were available. Patients were administered 102-182 MBq of [^{68}Ga]Ga-THP-PSMA, and a dynamic PET scan was performed for the first 10 minutes post-injection followed by a static half body scan at 60 minutes.

4.3.3 Results in Initial Staging

[^{68}Ga]Ga-THP-PSMA PET/CT scans for all patients in the cohort undergoing initial staging, showed uptake of the tracer in the primary tumour, as expected. Some patients showed additional nodal and/or metastatic sites. As a result of having the scan, additional information was obtained for 24% of the patients and 24% of the patients had a change of management.

4.3.4 Results for Biochemical Recurrence

When [^{68}Ga]Ga-THP-PSMA PET/CT was used to image patients with biochemical recurrence, the site of recurrence was detected in 59% of scans. The distribution of these patients across the PSA range is shown in figure 4.5. No disease sites were detected for patients with a PSA of less than 0.5 ng/mL and the detection rate was between 80 and 90% in patients with PSA levels of 2 ng/mL or above. As a result of the scan, 34% of patients presenting with biochemical recurrence had a change to their management. The number of patients with a change in management within each PSA level is shown in figure 4.6. No patients with a PSA below 0.5 ng/mL had a change in management as the site of reoccurrence was not detected in any patient. However, a change in management was recorded for 42% of patients with PSA over 1 ng/mL.

4.3.5 Conclusions from Studies at Guy's and St Thomas'

[^{68}Ga]Ga-THP-PSMA was able to detect the site of prostate cancer in all patients imaged for primary staging and 59% of patients with biochemical recurrence. The data from the scan influenced patient management in both cohorts, however, the number of patients with a change in management was 24% in primary staging but 34% in patients with biochemical recurrence.

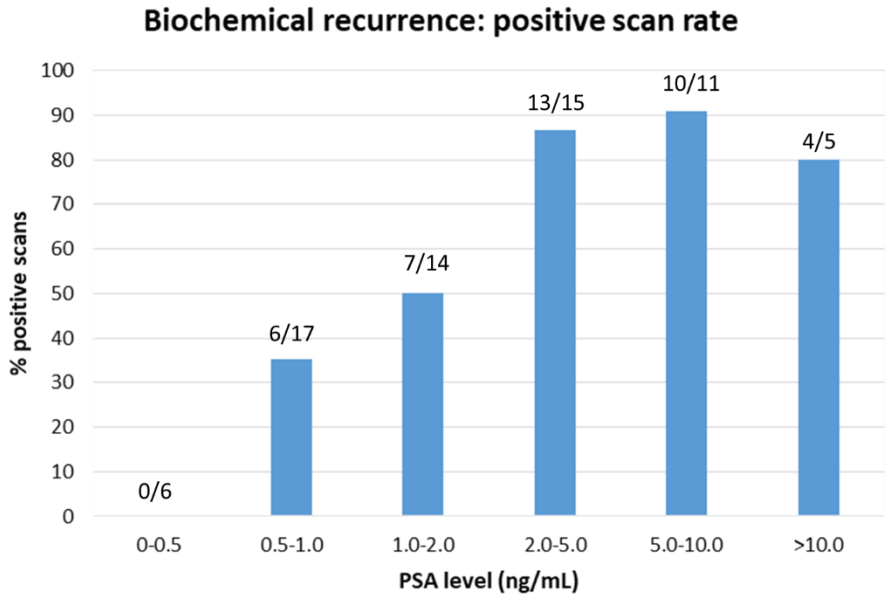

FIGURE 4.5: The number of patients where the site of recurrence was detectable on the [^{68}Ga]Ga-THP-PSMA PET/CT scan, at each PSA level (ng/mL). The numbers on top of the bars indicate the number of patients with detectable recurrence and the total number of patients scanned within this PSA range. Figure courtesy of Professor Gary Cook, presented at the British Nuclear Medicine Society conference in April 2018.

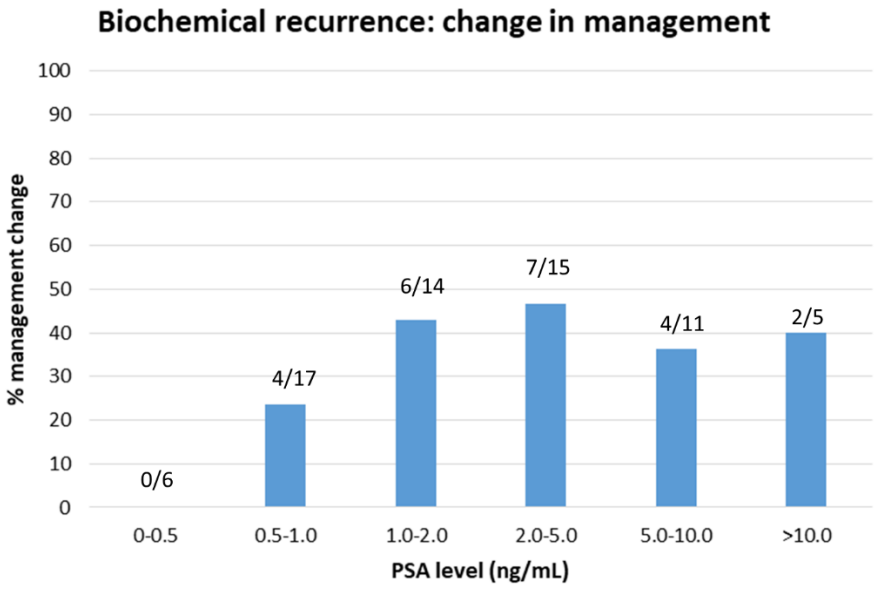

FIGURE 4.6: The number of patients with a change in management due to the results of the [^{68}Ga]Ga-THP-PSMA PET/CT scan, at each PSA level (ng/mL). The numbers on top of the bars indicate the number of patients with detectable recurrence and the total number of patients scanned within this PSA range. Figure courtesy of Professor Gary Cook and has been presented at the British Nuclear Medicine Society conference in April 2018.

4.4 Discussion

[^{68}Ga]Ga-THP-PSMA, has been found to be safe and to effectively detect prostate cancer in both initial staging and biochemical recurrence. However, differences in biodistribution are seen between [^{68}Ga]Ga-THP-PSMA, [^{68}Ga]Ga-HBED-CC-PSMA and [^{68}Ga]Ga-DOTAGA-PSMA(I&T). These include lower background uptake in non-target tissue for [^{68}Ga]Ga-THP-PSMA, as well as a higher rate of renal excretion, which produces some pooling of tracer in the urinary tract. This is combined with lower average SUV_{max} values in GCP(II)/PSMA positive prostate cancer. However, overall these tracers all give comparable tumour to background (liver) ratios.

The differences seen in the biodistribution of the tracers could be caused by a number of factors. These include: the affinity of the tracer for GCP(II)/PSMA (found in chapter 3 to be 361 ± 60 nM for Ga-THP-PSMA and 34.3 ± 4.1 nM for Ga-HBED-CC-PSMA); the ability of the tracers to differentiate between GCP(II)/PSMA and other similar receptors; the blood circulation time and excretion pathways (controlled by the hydrophilicity, charge, and size of the tracer); and the stability of the tracers *in vivo*. There are limited quantitative data available in the literature about the normal expression levels of GCP(II)/PSMA throughout the body and so it is difficult to know how accurately the uptake of a PSMA tracer reflects the distribution of GCP(II)/PSMA-expression. Immunohistochemistry studies have shown GCP(II)/PSMA-expression in the kidney, intestinal tract and the prostate but no expression in the liver, spleen and salivary glands (*17*)(*18*). This fits more closely with the biodistribution seen for [^{68}Ga]Ga-THP-PSMA than that of [^{68}Ga]Ga-HBED-CC-PSMA and [^{68}Ga]Ga-DOTAGA-PSMA(I&T). However, there are also mRNA studies which show expression of the GCP(II)/PSMA gene in the salivary glands, spleen and liver but protein expression was not confirmed (*19*). Further insight comes from the biodistribution of the zirconium-89 labelled GCP(II)/PSMA targeting humanised antibody J591 which does not show tracer uptake in the salivary and lacrimal glands of prostate cancer patients (*20*). See figure 4.7 for example [^{89}Zr]Zr-huJ591 PET scans up to 8 days post-injection.

Although it is interesting to consider which tracer's biodistribution most accurately correlates with GCP(II)/PSMA-expression, the scans purpose is to meet a clinical need: the identification of metastatic prostate cancer. Prostate cancer typically progresses from the primary tumour to lymph nodes within the pelvis (pelvic, hypogastric, iliac, sacral), then distant lymph nodes (aortic, common iliac, inguinal, supraclavicular, cervical) and to the skeleton, with other organs such as the lung and liver only involved at a very late stage (*21*). Therefore, it is most important that the tumour to background ratio is sufficient around these lymph nodes. The physiological uptake seen for [^{68}Ga]Ga-HBED-CC-PSMA and [^{68}Ga]Ga-DOTAGA-PSMA(I&T) in the liver, spleen and

salivary glands does not affect the ability to detect prostate cancer metastasis in either the pelvic or distant lymph nodes, and so this physiological uptake has little negative effect on the clinical utility of the scan. This in turn, means that the lack of the uptake with [^{68}Ga]Ga-THP-PSMA in these organs also brings little benefit. This is not true however, when molecular radiotherapy is being considered. Here uptake in salivary and lacrimal glands becomes very important to consider as these organs are particularly radiosensitive (*22*). In studies with [^{177}Lu]Lu-DOTA-PSMA(617) damage to these tissues due to the uptake of this tracer has caused xerostomia (dry mouth) and keratoconjunctivitis sicca (dry eyes) in a significant proportion of patients (87% experienced dry mouth and 17% dry eyes in a recent phase 2 study (*23*)). Therefore the lower uptake seen for [^{68}Ga]Ga-THP-PSMA in these glands may offer an advantage if the same bioconjugate could be radiolabelled with a therapeutic isotope and used for molecular radiotherapy. This idea will be explored further in chapter 5, where [^{67}Ga]Ga-THP-PSMA will be evaluated for molecular radiotherapy.

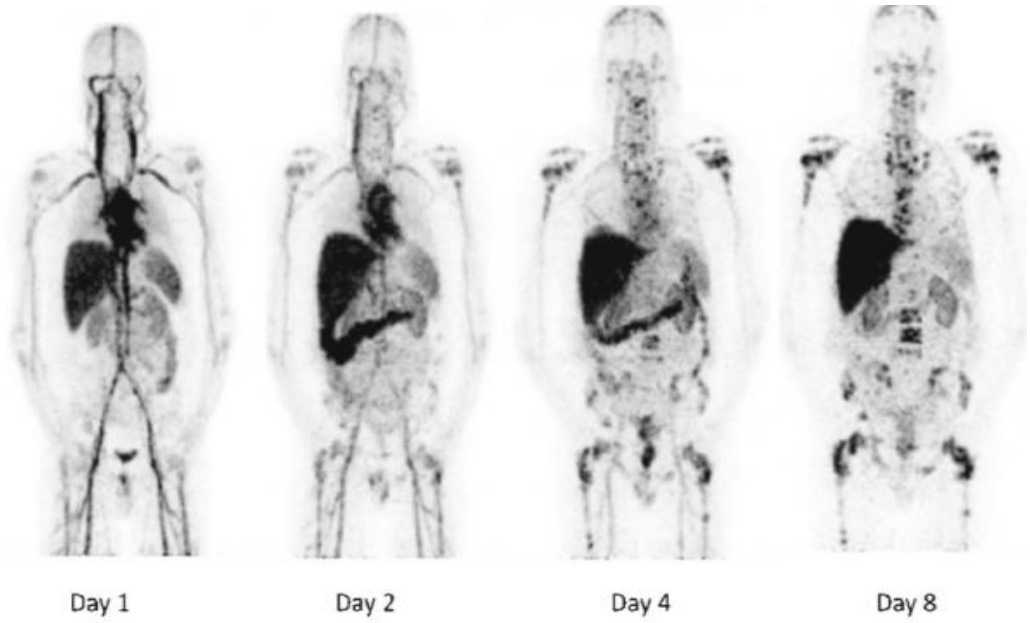

FIGURE 4.7: MIP images of a patient administered [^{89}Zr]Zr-huJ591 Images show physiological distribution in the cardiac and vascular blood pool, decreasing with time, in liver, spleen, kidneys, and gastrointestinal tract, but not in the salivary and lacrimal glands. Images show increased accumulation in bone lesions over time. (20)

In the studies conducted at Hannover Medical School and Guy's and St Thomas' Hospitals where [^{68}Ga]Ga-THP-PSMA was used in cases of biochemical recurrence, the detection rate was shown to be correlated with PSA level, and appears most effective when PSA is above 1 ng/mL. The definition of biochemical recurrence after prostatectomy is a PSA level greater than 0.2 ng/mL (*12*). However, imaging with bone scintigraphy or CT has only been shown effective in determining the site of relapse when patients have a PSA over 20 ng/mL (*12*). Therefore, patients

presenting with a PSA level in the range of 0.2 ng/mL – 20 ng/mL have biochemical recurrence but conventional imaging is not effective for them. All [^{68}Ga]Ga-PSMA tracers including [^{68}Ga]Ga-THP-PSMA allow detection in this vital range of PSA levels, however, it appears that [^{68}Ga]Ga-THP-PSMA may not have as good detection rate in patients presenting with a 0.2-1 ng/mL PSA as the alternative tracers, although a large comparative study in the same patients would be required to confirm this.

The study conducted at Guy's and St Thomas' Hospital showed that the results of a [^{68}Ga]Ga-THP-PSMA scan can affect patient management. In primary staging with [^{68}Ga]Ga-THP-PSMA 24% of patients showed a change in management, a very similar rate to the 21% determined for a multicentre prospective study conducted in Australia for [^{68}Ga]Ga-HBED-CC-PSMA (*24*). In patients with biochemical recurrence, 34% of patients imaged with [^{68}Ga]Ga-THP-PSMA had a change in treatment. This is lower than that value obtained for [^{68}Ga]Ga-HBED-CC-PSMA in an Australian prospective multicenter study, where management was changed in 62% of patients (*24*), but similar to the 39% of patients with biochemical recurrence that had there management changed in a retrospective study at University College London Hospital (*25*). With such variation between the results obtained in two different studies with [^{68}Ga]Ga-HBED-CC-PSMA, it is difficult to determine if the lower number of changes to patient management for [^{68}Ga]Ga-THP-PSMA in cases of biochemical recurrence is significant, and even a reflection on the [^{68}Ga]Ga-PSMA tracer used or instead due to differences in study design, the planned management before the scan which could vary between hospitals or clinicians, and how treatment changes are made at different hospitals.

As well as demonstrating the clinical utility of [^{68}Ga]Ga-THP-PSMA these studies have also demonstrated that its kit-based radiosynthesis offers advantages to the radiopharmacies producing the tracer and leads to a drop in synthesis time, from around 40 to less than 10 minutes. It was also the first [^{68}Ga]Ga-PSMA tracer to be produced at Guy's and St Thomas' Hospital and its validation procedure and clinical implementation was greatly expedited by the kit-based radiosynthesis.

4.5 Concluding Remarks

In conclusion, the one-step kit-based formation of [^{68}Ga]Ga-THP-PSMA provides advantages in the production of the tracer, while the use of the THP as the chelator does not affect the information derived from scans in patients. Effective detection of prostate cancer is possible with [^{68}Ga]Ga-THP-PSMA for both initial staging and in biochemical recurrence and the results of the scan have been shown to impact management of prostate cancer patients. To be able to accurately assess the performance of the tracers and the clinical impact of the tracer choice, more extensive comparative studies would be required. However, [^{68}Ga]Ga-THP-PSMA certainly provides advantages over conventional imaging and has the simplest radiolabelling procedure for any clinically tested PSMA radiotracer.

4.6 References

1. Hofman MS, Eu P, Jackson P, Hong E, Binns D, Iravani A, Murphy D, Mitchell C, Siva S, Hicks RJ, Young JD, Blower P, Mullen GE. Cold Kit PSMA PET Imaging: Phase I Study of 68Ga-THP-PSMA PET/CT in Patients with Prostate Cancer. *J Nucl Med*. 2018;59:625-631.
2. Hofman MS, Eu P, Mitchell C, Blower P, Iravani A, Murphy D, Young JD, Hicks RJ, Mullen GE. First In-Man Study of 68Ga-THP-PSMA PET in Patients with Primary Prostate Cancer: Initial Results. *Endocr Abstr*. 2016;47:OC31.
3. Derlin T, Schmuck S, Juhl C, Teichert S, Zörgiebel J, Wester H-J, Schneefeld SM, Walte ACA, Thackeray JT, Ross TL, Bengel FM. Imaging Characteristics and First Experience of [68Ga]THP-PSMA, a Novel Probe for Rapid Kit-Based Ga-68 Labeling and PET Imaging: Comparative Analysis with [68Ga]PSMA I&T. *Mol Imaging Biol*. 2018.
4. Derlin T, Schmuck S, Juhl C, Zorgiebel J, Schneefeld SM, Walte ACA, Hueper K, von Klot CA, Henkenberens C, Christiansen H, Thackeray JT, Ross TL, Bengel FM. PSA-Stratified Detection Rates for [68Ga]THP-PSMA, a Novel Probe for Rapid Kit-Based 68Ga-Labeling and PET Imaging, in Patients with Biochemical Recurrence after Primary Therapy for Prostate Cancer. *Eur J Nucl Med Mol Imaging*. 2018.
5. Cook G, Hughes S, Morris S, Challacombe B, Cathcart P, Popert R, Brown C, Dasgupta P, John J, Malliaa A, Young J, Gibson V, Mullen G, Warbey V. Management Impact of 68Ga-THP-PSMA in High-Risk and Biochemically Recurrent Prostate Cancer. *Nucl Med Commun*. 2018;39:346-395 Abstract 12.
6. Afshar-Oromieh A, Hetzheim H, Kübler W, Kratochwil C, Giesel FL, Hope TA, Eder M, Eisenhut M, Kopka K, Haberkorn U. Radiation Dosimetry of 68Ga-PSMA-11 (HBED-CC) and Preliminary Evaluation of Optimal Imaging Timing. *Eur J Nucl Med Mol Imaging*. 2016;43:1611-1620.
7. Afshar-Oromieh A, Hetzheim H, Kratochwil C, Benesova M, Eder M, Neels OC, Eisenhut M, Kubler W, Holland-Letz T, Giesel FL, Mier W, Kopka K, Haberkorn U. The Theranostic PSMA Ligand PSMA-617 in the Diagnosis of Prostate Cancer by PET/CT: Biodistribution in Humans, Radiation Dosimetry, and First Evaluation of Tumor Lesions. *J Nucl Med*. 2015;56:1697-1705.
8. Giesel FL, Hadaschik B, Cardinale J, Radtke J, Vinsensia M, Lehnert W, Kesch C, Tolstov Y, Singer S, Grabe N, Duensing S, Sch??fer M, Neels OC, Mier W, Haberkorn U, Kopka K, Kratochwil C. F-18 Labelled PSMA-1007: Biodistribution, Radiation Dosimetry and Histopathological Validation of Tumor Lesions in Prostate Cancer Patients. *Eur J Nucl Med Mol Imaging*. 2017;44:678-688.
9. Szabo Z, Mena E, Rowe SP, Plyku D, Nidal R, Eisenberger M a., Antonarakis ES, Fan H, Dannals RF, Chen Y, Mease RC, Vranesic M, Bhatnagar A, Sgouros G, Cho SY, Pomper MG. Initial Evaluation of [18F]DCFPyL for Prostate-Specific Membrane Antigen (PSMA)-Targeted PET Imaging of Prostate Cancer. *Mol Imaging Biol*. 2015;17:565-74.
10. Hövels AM, Heesakkers RAM, Adang EM, Jager GJ, Strum S, Hoogeveen YL, Severens JL, Barentsz JO. The Diagnostic Accuracy of CT and MRI in the Staging of Pelvic Lymph Nodes in Patients with Prostate Cancer: A Meta-Analysis. *Clin Radiol*. 2008;63:387-395.
11. Budäus L, Leyh-Bannurah SR, Salomon G, Michl U, Heinzer H, Huland H, Graefen M, Steuber T, Rosenbaum C. Initial Experience of 68Ga-PSMA PET/CT Imaging in High-Risk Prostate Cancer Patients Prior to Radical Prostatectomy. *Eur Urol*. 2016;69:393-396.
12. Heidenreich A, Bastian PJ, Bellmunt J, Bolla M, Joniau S, Van Der Kwast T, Mason M, Matveev V, Wiegel T, Zattoni F, Mottet N. EAU Guidelines on Prostate Cancer. Part II: Treatment of Advanced, Relapsing, and Castration-Resistant Prostate Cancer. *Eur Urol*. 2014;65:467-479.
13. Fendler WP, Eiber M, Beheshti M, Bomanji J, Ceci F, Cho S, Giesel F, Haberkorn U, Hope TA, Kopka K, Krause BJ, Mottaghy FM, Schöder H, Sunderland J, Wan S, Wester HJ, Fanti

S, Herrmann K. 68Ga-PSMA PET/CT: Joint EANM and SNMMI Procedure Guideline for Prostate Cancer Imaging: Version 1.0. *Eur J Nucl Med Mol Imaging*. 2017;44:1014-1024.

14. Fanti S, Minozzi S, Castellucci P, Balduzzi S, Herrmann K, Krause BJ, Oyen W, Chiti A. PET/CT with 11C-Choline for Evaluation of Prostate Cancer Patients with Biochemical Recurrence: Meta-Analysis and Critical Review of Available Data. *Eur J Nucl Med Mol Imaging*. 2016;43:55-69.
15. Eiber M, Maurer T, Souvatzoglou M, Beer a. J, Ruffani a., Haller B, Kubler H, Haberkorn U, Eisenhut M, Wester H-J, Gschwend JE, Schwaiger M. Evaluation of Hybrid 68Ga-PSMA-Ligand PET/CT in 248 Patients with Biochemical Recurrence after Radical Prostatectomy. *J Nucl Med*. 2015;56:668-674.
16. Thomas A. S, Norman Y, Alan R. H, John E. M, Fuad S. F, Elise R. Prostate-Specific Antigen as a Serum Marker for Adenocarcinoma of the Prostate. *N Engl J Med*. 1987;317:909-916.
17. Silver DA, Pellicer I, Fair WR, Heston WDW, Cordon-Cardo C. Prostate-Specific Membrane Antigen Expression in Normal and Malignant Human Tissues. *Clin Cancer Res*. 1997;3:81-85.
18. Mhawech-Fauceglia P, Zhang S, Terracciano L, Sauter G, Chadhuri A, Herrmann FR, Penetrante R. Prostate-Specific Membrane Antigen (PSMA) Protein Expression in Normal and Neoplastic Tissues and Its Sensitivity and Specificity in Prostate Adenocarcinoma: An Immunohistochemical Study Using Mutiple Tumour Tissue Microarray Technique. *Histopathology*. 2007;50:472-483.
19. O'Keefe DS, Bacich DJ, Heston WDW. Comparative Analysis of Prostate-Specific Membrane Antigen (PSMA) versus a Prostate-Specific Membrane Antigen-like Gene. *Prostate*. 2004;58:200-210.
20. Pandit-Taskar N, O'Donoghue JA, Beylergil V, Lyashchenko S, Ruan S, Solomon SB, Durack JC, Carrasquillo JA, Lefkowitz RA, Gonen M, Lewi JS, Holland JP, Cheal SM, Reuter VE, Osborne JR, Loda MF, Smith-Jones PM, Weber WA, Bander NH, et al. 89Zr-HuJ591 Immuno-PET Imaging in Patients with Advanced Metastatic Prostate Cancer. *Eur J Nucl Med Mol Imaging*. 2014;41:2093-2105.
21. American Joint Committee on Cancer. AJCC Cancer Staging Manual. Sixth Edit.; 2002.
22. Hohberg M, Eschner W, Schmidt M, Dietlein M, Kobe C, Fischer T, Drzezga A, Wild M. Lacrimal Glands May Represent Organs at Risk for Radionuclide Therapy of Prostate Cancer with [177Lu]DKFZ-PSMA-617. *Mol Imaging Biol*. 2016;18:437-445.
23. Hofman MS, Violet J, Hicks RJ, Ferdinandus J, Thang SP, Akhurst T, Iravani A, Kong G. Articles [^{177}Lu]-PSMA-617 Radionuclide Treatment in Patients with Metastatic Castration-Resistant Prostate Cancer (LuPSMA Trial): A Single-Centre , Single-Arm , Phase 2 Study. *Lancet Oncol*. 2018;2045:1-9.
24. Roach PJ, Francis R, Emmett L, Hsiao E, Kneebone A, Hruby G, Eade T, Nguyen Q, Thompson B, Cusick T, McCarthy M, Tang C, Ho B, Stricker P, Scott A. The Impact of 68 Ga-PSMA PET/CT on Management Intent in Prostate Cancer: Results of an Australian Prospective Multicenter Study. *J Nucl Med*. 2018;59:82-88.
25. Afaq A, Alahmed S, Chen S, Lengana T, Haroon A, Payne H, Ahmed H, Punwani S, Sathekge M, Bomanji J. 68 Ga-PSMA PET/CT Impact on Prostate Cancer Management. *J Nucl Med*. 2018;59:89-92.

5 Targeting Gallium-67 to Prostate Cancer with [^{67}Ga]Ga-THP-PSMA

5.1 Introduction

The clinical need to image metastatic prostate cancer more accurately, especially in hormone-resistant prostate cancer, is being met by small molecule GCP(II)/PSMA imaging. Unfortunately once the diagnosis has been confirmed, there are often limited therapeutic options available for these patients and so targeted molecular radiotherapy options are currently being investigated. This has been encouraged by the success of alpha-based therapy using radium-223 chloride ([^{223}Ra]$RaCl_2$) in men with castrate-resistant prostate cancer and bone metastases, which is now FDA-approved (*1*). A phase III study where patients received six injections of radium-223 chloride at a dose of 50 kBq per kilogram of body weight once every 4 weeks, showed improved overall survival compared to placebo, with the median survival increasing by 3.6 months (*2*). Cationic radium is naturally bone-seeking due to its ability to mimic calcium and gets incorporated into the newly forming inorganic matter of bone in areas of increased osteoblastic activity, such as bone metastases (*3*). The delivery mechanism of [^{223}Ra]$RaCl_2$ is therefore specific to bone-based metastases, meaning that soft tissue metastases do not receive radium-223 or its associated dose, and consequently do not respond. However, due to the targeting mechanism, there is also a lot of off-target uptake, as shown in figure 5.1 (*4*), and so it would be ideal if the targeting of therapeutic isotopes to prostate cancer metastases could be improved. As well as the possibility of imaging metastatic disease, GCP(II)/PSMA-expression provides a mechanism to specifically deliver radiotherapeutic isotopes to both bone and soft tissue metastases. Such targeting can be done using similar urea-based scaffolds, as utilised in the imaging agents, but replacing the radioisotope with one suitable for therapy; one which emits alpha particles, beta particles or Auger electrons.

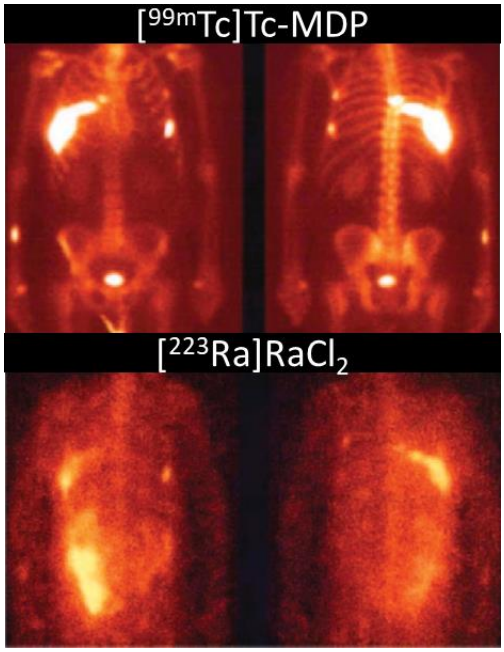

FIGURE 5.1: Gamma scintigraphy images of [^{99m}Tc]Tc-MDP(top) and [^{223}Ra]$RaCl_2$ (bottom) in a patient with skeletal metastases Note the non-specific uptake in the [^{223}Ra]$RaCl_2$ images including significant off-target gut uptake. Reproduced with permission from (4).

As reviewed in chapter 1, the most investigated options for GCP(II)/PSMA targeted molecular radiotherapy have been β^--based therapy using [^{131}I]I-MIP-1095 (*5*)(*6*), [^{177}Lu]Lu-DOTA-PSMA(617) (*7*)(*8*) or [^{177}Lu]Lu-DOTAGA-PSMA (I&T) (*9*). As shown in figure 5.2, all of these tracers use the same urea-based GCP(II)/PSMA targeting motif. [^{131}I]I-MIP-1095 was the first PSMA-based β^- therapy to be evaluated used this targeting structure and was administered to 28 men with metastatic resistant prostate cancer. It caused a significant reduction in PSA levels and bone pain (*5*). Studies investigating multiple doses of [^{131}I]I-MIP-1095 therapy have also been conducted, but show that although the first dose reduces tumour burden, there is little advantage in repeating doses, and doing so increases the likelihood and intensity of side effects (*6*). Compared to [^{131}I]I-MIP-1095, the lutetium-177-based GCP(II)/PSMA targeted therapies [^{177}Lu]Lu-DOTA-PSMA(617) (*10*)(*11*) and [^{177}Lu]Lu-DOTAGA-PSMA(I&T) (*12*)(*13*) have been performed in much higher patient numbers across a range of different sites. Like the iodine-131-based therapy, these have shown a reduction in tumour burden and blood PSA levels. Seven of these studies were included in a recent meta-analysis and which concluded that across the studies, 51% of patients administered [^{177}Lu]Lu-PSMA molecular radiotherapy had a reduction in PSA levels of 50% or more (*14*). This is therefore an extremely promising new therapeutic option.

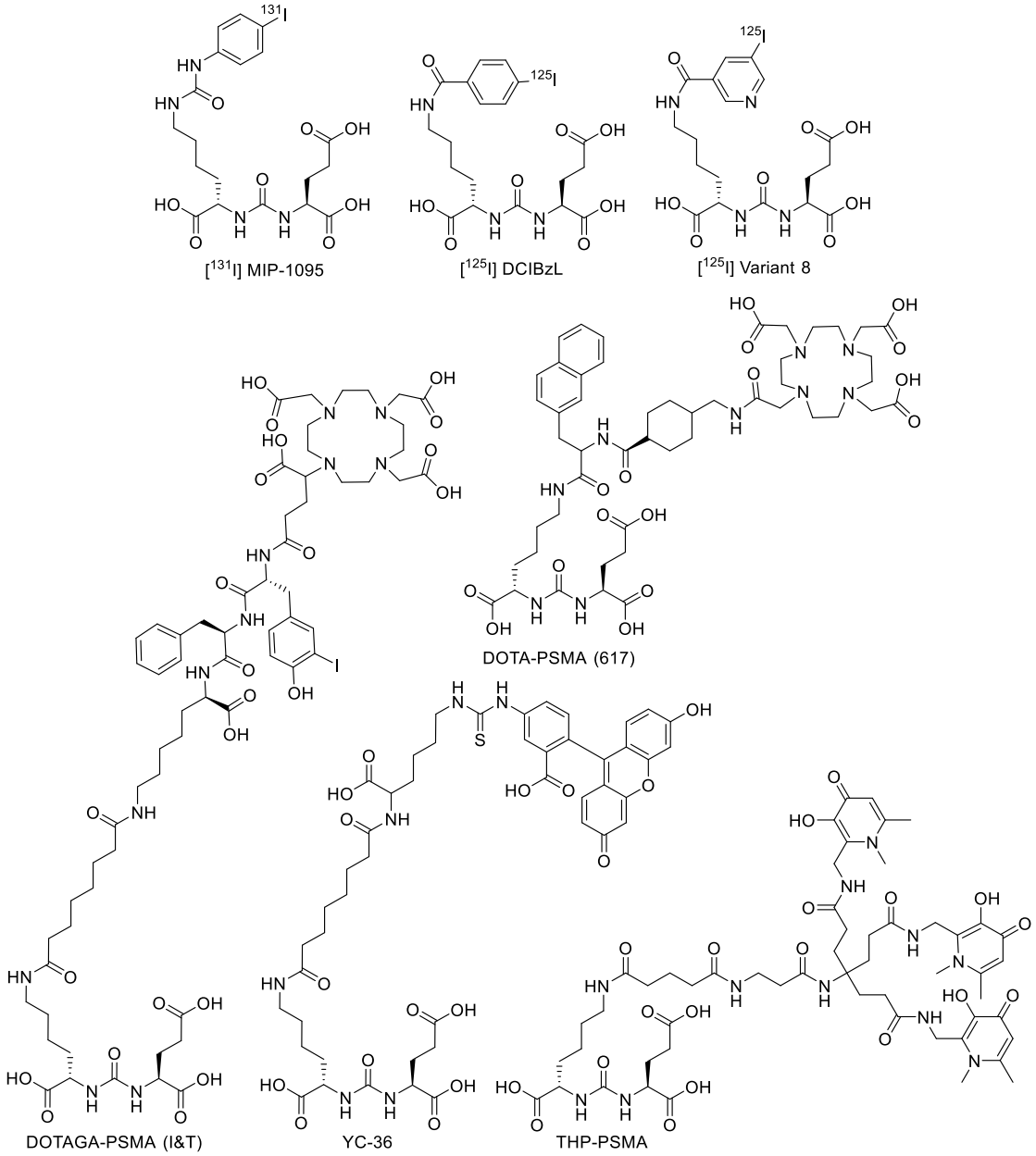

FIGURE 5.2: Structures of [^{131}I]I-MIP-1095 (5)(15), [^{125}I]I-DCIBzL (16), [^{125}I]I-variant 8 (17), DOTA-PSMA(617) (18), DOTAGA-PSMA(I&T) (19), YC-36 (16), THP-PSMA (20).

Tracers for GCP(II)/PSMA-targeted molecular radiotherapy, must possess favourable pharmacokinetics if they are to be translated into the clinic. It is paramount that the radiotracer accumulates rapidly in GCP(II)/PSMA-expressing tumours, where it should be retained for as long as possible, in order to deposit the maximum dose. In addition, it should have low uptake in non-target organs, preventing radiation damage. In non-cancerous tissues. where uptake is due to renal excretion (bladder, kidney) or mediated by GCP(II)/PSMA-expression (kidneys (*21*)), it would be ideal if the tracer washed out of these organs faster than from the tumour. Such properties have been shown in a preclinical model of prostate cancer for [^{177}Lu]Lu-DOTA-

PSMA(617) (*18*). In BALB/c *nu/nu* mice with LNCaP tumours, the uptake of [^{177}Lu]Lu-DOTA-PSMA(617) was 11.2 ± 4.17 %ID/g at 1 hour, and remained stable until 24 hours, when it was found to be 10.58 ± 4.5 %ID/g. Conversely, the washout from the kidneys was significant, changing from 137.5 ± 77.8 %ID/g at 1 hour, to 2.13 ± 1.36 %ID/g at 24 hours (*18*). Additionally, very high tumour to blood (1,058) and tumour to muscle values (529) were seen at 24 hours after injection. These observations held when the distribution of [^{177}Lu]Lu-DOTA-PSMA(617) was studied in prostate cancer patients (*8*), with the concentration of tracer in the tumour sustained for much longer than in the kidney, as shown in figure 5.3.

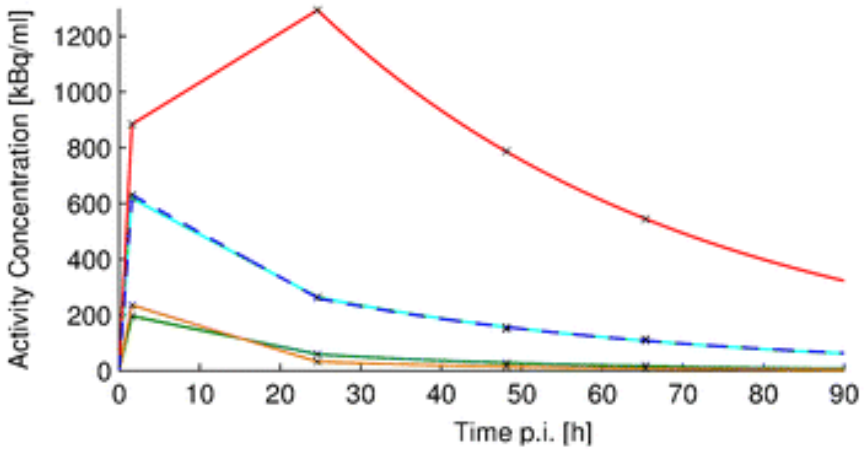

FIGURE 5.3: Time activity concentration curves in a representative patient. Tumour metastasis (red), kidneys (cyan and dashed blue), spleen (orange) and liver (green). This figure was reproduced with permission from (8).

However, these properties are not shared by all PSMA tracers that use the urea-based targeting motif. In fact, very small changes in the structure can affect the pharmacokinetics significantly. This has been demonstrated in a preclinical model (athymic nude mice with PC3-PIP tumours) with the iodine-based tracers [^{125}I]I-DCIBzL (*17*)(*22*) and [^{125}I]I-variant 8 (*17*), which had very similar structures (figure 5.4) and initial tumour uptake values (13.5 ± 2.1 %ID/g and 12.1 ± 4.9 %ID/g respectively at 1 hour). [^{125}I]I-DCIBzL was retained in both the tumour and the kidney for 48 hours whereas [^{125}I]I-variant 8 was washed out of both within 24 hours as shown in figure 5.4. The differences between [^{177}Lu]Lu-DOTA-PSMA(617), [^{125}I]I-DCIBzL and [^{125}I]I- variant 8 are stark, even though they all had the same targeting motif and subnanomolar K_i or IC_{50} values when measured with a NAALADase fluorescence-based assay (0.8 ± 0.3 nM (metal-free compound) (*23*), 0.010 ± 0.004 nM (*17*) and 0.557 ± 0.265 nM (*17*) respectively). This demonstrates there are more factors at play than the affinity for the target, and highlights the importance of assessing biodistribution properties experimentally.

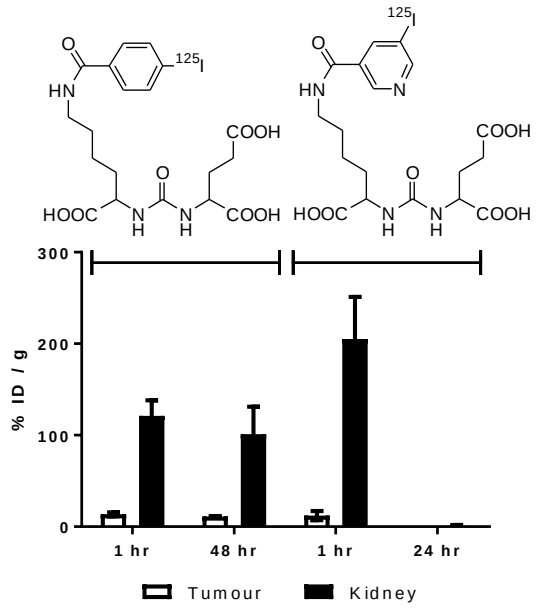

FIGURE 5.4: The tumour and kidney uptake of [^{125}I]I-DCIBzL, and [^{125}I]I-variant 8 at 1 hour and 48 hours and 24 hours. Data from reference (17).

When considering molecular radiotherapy it is important that the size of a tumour being treated is matched by the range over which a therapeutic radionuclide deposits its dose. Beta emitters have a range of 2-10 mm with a linear energy transfer (LET) of 0.1-1.0 keV/µm (*24*), and so are suitable for delivering a considerable dose to macroscopic tumours that are over 2 mm in diameter, without substantial "crossfire" to surrounding tissue. However, they are unlikely to be effective therapy for micro-metastases (0.2-2 mm in size (*25*)), isolated tumour cell clusters (< 0.2 mm in size or < 200 cancer cells (*25*)) or circulating individual tumour cells, as the majority of the energy from each decay would be deposited in non-target tissue rather than the cancer cell itself (*24*)(*26*). These smaller targets are of high importance as they are responsible for relapse in many patients and are very difficult to locate and treat (*27*)(*28*). Targeting them with molecular radiotherapy requires the radioactive decay to be deposited within a much shorter range, ideally within the cell itself or even just within the nucleus. This necessitates the use of therapeutic radionuclides with a short range but high enough LET to cause DNA damage. Auger electrons meet these criteria as they typically travel less than 0.5 µm and have a LET of 4-26 keV/µm (*26*). It is not only the emission of Auger electrons that causes therapeutic effects, additionally, a high positive charge is generated on the atom, due to the ejection of negatively charged electrons. This unstable positive charge has high potential energy and will be rapidly neutralised by stripping electrons from the surroundings (*29*). This effect is known as "the coulomb explosion" and is a highly localised phenomenon, which if located close enough to DNA

has been shown to contribute to irreparable double-strand breaks (*30*). Such double-strand breaks are hazardous to the cell and can trigger apoptosis (*31*).

The possibility of Auger electron-based PSMA therapy has been demonstrated with [^{125}I]I-DCIBzL, which uses the urea-based GCP(II)/PSMA targeting motif (figure 5.2)(*16*). This work showed that Auger-emitting [^{125}I]I-DCIBzL causes DNA damage *in vitro* as assessed by clonogenic assays and monitoring double-strand breaks using γH2AX staining. The study went on to show a significant reduction in tumour doubling time in a subcutaneous xenograft model in mice. Future work with more realistic models of micrometastases are ongoing, to validate its use for this type of disease, and any possible side effects before translation into the clinic (*32*). Particular issues are likely to be kidney toxicity, due to their natural GCP(II)/PSMA-expression (*21*)(*33*), and thyroid toxicity, as iodine naturally accumulates in the thyroid and therefore metabolites or autoradiolysis products of the tracer could build up in the thyroid, leading to a significant dose to this organ (*34*)(*35*). The 59.4 day half-life of iodine-125 (*26*) may also lead to challenges when attempting to block uptake to radiosensitive organs, due to the time over which it would need to be maintained. The long half-life also has an environmental impact, with any radioactive waste produced requiring long-term containment.

Gallium-67 has been proposed as an alternative Auger electron emitting radionuclide for molecular radiotherapy (*24*)(*36*)(*37*)(*38*)(*39*). Gallium-67 has a half-life of 78 hours (*26*) and decays by electron capture, producing a number gamma emissions (91-888 keV (*40*)) that can be used for SPECT studies, and an average of 4.7 Auger electrons per decay with a total energy of 6.3 keV (*26*). Recent evaluation of gallium-67 *in vitro* using viability and clonogenic assays has shown that it is able to induce cell death when cell surface-bound or internalised and that 1 Bq of gallium-67 per cancer cell is required to achieve 90% cell killing (*38*). In the study, gallium-67 was delivered to cells as a lipophilic gallium-8-hydroxyquinoline complex which entered cells by passive diffusion through the cell membrane. However, this makes it unspecific and therefore unsuitable for targeted molecular radiotherapy, as uptake needs to be receptor-mediated to ensure the therapy is targeted only to cancer cells. To date, gallium-67 has only been shown to have a targeting therapeutic effect in lymphoma cells (*39*)(*41*), myeloid leukemic blasts (*42*) and lymphoma xenograft mouse models (*43*). In those studies, targeting was achieved with gallium-67 citrate (*36*)(*42*) or anti-CD74 (*41*)(*43*) or anti-CD20 antibodies (*39*). Gallium-67-based molecular radiotherapy has not previously been considered for prostate cancer, nor utilised a peptide targeting motif. The work in this chapter aims to lay the groundwork for such therapeutic studies by determining the quantity of gallium-67 that can be delivered to GCP(II)/PSMA-expressing cells and tumours in a targeted manner, using [^{67}Ga]Ga-THP-PSMA.

A further advantage of using gallium-67 is that its isotope gallium-68 is suitable for PET imaging. Since gallium-67 and gallium-68 versions of the same complex will be chemically identical, they will have exactly the same behaviour *in vivo* (*44*). This means that gallium-68 PET imaging could be accurately used to assess patient suitability for therapy with gallium-67. It also means that any radiotracers or chelators that have been designed for imaging with gallium-68 can be labelled with gallium-67 through similar procedures. In particular, this means the specificity of the THP chelator for gallium, which underpins its excellent radiolabelling properties, should be suitable for radiolabelling of THP-PSMA with both radioisotopes of gallium.

This piece of work aims to assess the potential of [^{67}Ga]Ga-THP-PSMA to specifically deliver gallium-67 to prostate cancer. Radiolabelling of THP-PSMA tracer with gallium-67 will be optimised for high molar activity and stability over time. [^{67}Ga]Ga-THP-PSMA will then be assessed both *in vitro* and pre-clinically to determine uptake and retention over time. These results will provide the first insights into the potential of [^{67}Ga]Ga-THP-PSMA for molecular radiotherapy.

5.2 Experimental Aims

The above aims will be addressed through the following experimental objectives:

- Radiolabel [^{67}Ga]Ga-THP-PSMA at high molar activity
- Evaluate the serum stability of [^{67}Ga]Ga-THP-PSMA
- Evaluate the uptake and efflux of [^{67}Ga]Ga-THP-PSMA in GCP(II)/PSMA-expressing cells
- Evaluate the biodistribution and tumour uptake of [^{67}Ga]Ga-THP-PSMA over 7 days in a preclinical mouse model with a subcutaneous prostate cancer xenograft

5.3 Materials and Methods

All reagents and consumables were purchased from Sigma Aldrich or Fischer Scientific, with the following exceptions: DOTA-PSMA (PSMA 617) was purchased from ABX (Radeberg, Germany). THP-PSMA was synthesised as described in chapter 3 or purchased from Chematech-mdt (Dijon, France). Severe combined immunodeficient (SCID)/beige mice were purchased from Charles River (Margate, UK). DU145 and DU145-PSMA cell lines were provided by Dr Florian Kampmeier (*45*).

5.3.1 Gallium-67 Source

Gallium-67 was purchased from Nordion Inc. (Ottawa, ON, Canada), where it was produced by proton irradiation of enriched zinc-68, according to the nuclear reaction $^{68}Zn(p, 2n)^{67}Ga$. This gallium-67 was provided in 0.1 ± 0.05 M HCl. The levels of the trace metals Zn^{2+}, Cu^{2+}, and Fe^{3+} were all below 0.27 μg/GBq at batch release, and the molar activity was ≥ 37 TBq/g with a radionuclidic purity of over 99.9% (maximum level of Ga-66 detected at 0.04%). The activity concentration was 65.6 – 57.5 GBq/mL at the time of batch release. 2.5-2.8 GBq $[^{67}Ga]Ga^{3+}$ arrived in the lab in 70-79 μL of 0.1 M HCl, an activity concentration of 35-38 GBq/mL.

5.3.2 Instrumentation

HPLC and radio-HPLC: All high-performance liquid chromatography (HPLC) utilised an Agilent 1200 LC with in-line radio (sodium iodide gamma detector) and UV detection (254 nm). Data were analysed using Laura software (V.4.0.2.75 LabLogic Systems Ltd.). Radiolabelling of $[^{67}Ga]$Ga-THP-PSMA was assessed using an Agilent Eclipse XDB C_{18} 5 μm 4.6 x 150 mm column with an isocratic mobile phase (90% H_2O, 10% ACN, 0.05% TFA) and a flow rate of 1 mL/minute. Radiolabelling of $[^{67}Ga]$Ga-DOTA-PSMA(617) was assessed with the same HPLC equipment but an alternative mobile phase: A = H_2O with 0.05% TFA, B = ACN with 0.05% TFA, gradient: 0-5 minutes = 90% A, 5-15 minutes = ramp to 50% B (4%/min), 15-20 minutes = 90% A, with a flow rate of 1 mL/minute. Serum stability was assessed using size exclusion chromatography using a Phenomenex BioSep 5 μm SEC_s 2000 column (300 × 7.8 mm) with PBS and 2 mM EDTA as the mobile phase and a flow rate of 1 mL/minute.

iTLC methods: Radiolabelling of $[^{67}Ga]$Ga-THP-PSMA and $[^{67}Ga]$Ga-DOTA-PSMA(617) was assessed by iTLC utilising Varian ITLC SGI0001 strips (10 cm length) with a mobile phase of 1 M ammonium acetate in water/methanol (1:1). ITLC plates were scanned with a Lab-Logic mini-Scan TLC reader and analysed with Laura software.

Gamma counting: Radioactivity counting was performed with a γ-counter (LKB Wallac; PerkinElmer) for cell studies and *in vivo* biodistribution.

5.3.3 Radiolabelling

Initial radiolabelling [^{67}Ga]Ga-THP-PSMA: [^{67}Ga]Ga^{3+} in 0.1 M HCl (5-10 µL, 32-158 MBq) was added to THP-PSMA (0.25-5 µg, 1-10 µL) and neutralised with sodium bicarbonate solution to pH 6.5-7.5 (1 µL, 0.5-1 M) producing a range of THP-PSMA concentrations between 5 and 156 µM. Labelling was assessed after 5 minutes by HPLC and iTLC.

Highest molar activity radiolabelling [^{67}Ga]Ga-THP-PSMA: 1 µL THP-PSMA (0.5 mg/mL, 0.5 µg, 0.33 nmol) solution was added to 5 µL of [^{67}Ga]Ga^{3+} in 0.1 M HCl (115 MBq) and then neutralised to pH 7 by the addition of 5.5 µL 0.1 M sodium bicarbonate solution. After 5 minutes, radiolabelling was assessed by iTLC, and at 10 minutes by HPLC. 93% radiochemical purity (RCP) was achieved with a maximum molar activity of 326 MBq/nmol (213.9 MBq/µg).

5.3.4 Stability to Autoradiolysis [^{67}Ga]Ga-THP-PSMA

1 µL THP-PSMA (2 mg/mL, 2 µg, 1.3nmol) was added to 50 µL [^{67}Ga]Ga^{3+} (141 MBq) and neutralised to pH 6.5-7.5 with 6 µL 1 M sodium bicarbonate solution. ITLC was completed after 5 minutes (molar activity 108 MBq/nmol, >95% RCP, final concentration 2.5 MBq/µL, THP-PSMA 23 µM). The stability over time was monitored by iTLC. To assess the effect of ascorbic acid and dilution on the stability, this radiolabelling was repeated and then [^{67}Ga]Ga-THP-PSMA was diluted to 1 MBq/µL in PBS containing 12 µg ascorbic acid. Final concentrations were THP-PSMA 8 µM, ascorbic acid 488 µM. The stability over time was monitored by iTLC up to 18 hours.

5.3.5 Preparation of [^{67}Ga]Ga-PSMA Tracers for Biological Evaluation.

THP-PSMA for *in vitro* studies: 1 µL THP-PSMA (2 mg/mL, 2 µg, 1.3 nmol) was added to 50 µL [^{67}Ga]Ga^{3+} (180 MBq) in 0.1 M HCl, followed by neutralisation to pH 7 with 6 µL 1 M sodium bicarbonate solution (final concentration 3.2 MBq/µL, THP-PSMA 23 µM). Radiolabelling was assessed by HPLC and iTLC after 5 minutes. Over 99% RCP was achieved with a molar activity of 138.5 MBq/nmol. The solution was then diluted in PBS containing 12 µg ascorbic acid to a tracer concentration of 6.4 µM to produce solution A. Solution A was diluted 1 in 10 to give solution B (640 nM), and 1 in 100 to give solution C (64 nM).

DOTA-PSMA(617) for *in vitro* studies: 50 µL [^{67}Ga]Ga^{3+} in 0.1M HCl (145 MBq) was combined with 5 µL 1 M HCl and 20 µL 2.1 M HEPES buffer. After the pH was checked (pH 3.2, 2 µL reaction

solution), DOTA-PSMA(617) was added (1 µL, 1 mM, 1.5 µg, 1 nmol) followed by heating at 95 °C for 30 minutes. Radiolabelling was assessed by iTLC and HPLC. The resulting RCP was 98 %, and the molar activity was 120 MBq/nmol. On the day of the cell experiments, the molar activity had dropped to 76 MBq/nmol but the RCP was still 96%. This solution was diluted to a tracer concentration of 6.4 µM in PBS, to produce solution D. Solution D was diluted 1 in 10 to give solution E (640 nM) and 1 in 100 to give solution F (64 nM).

THP-PSMA for *in vivo* studies: 6 µL THP-PSMA (3 µg, 2 nmol) was added to 15 µL of $[^{67}Ga]Ga^{3+}$ in 0.1M HCl (360 MBq) followed by 3 µL of 0.5 M sodium bicarbonate to adjust the pH to 6.5-7.5 (final concentration 82 µM THP-PSMA). Radiolabelling was assessed by HPLC after 5 minutes. Over 95% RCP was achieved with a molar activity of 180 MBq/nmol. The solution was diluted in PBS to the concentration required for injection and monitored over time to ensure the administered radiotracer had a RCP of >90% at the point of injection.

5.3.6 Serum Stability

20 µL of $[^{67}Ga]$Ga-THP-PSMA with a molar activity of 25 MBq/nmol (7 MBq, 0.3 nmol) was added to 200 µL human serum. The following controls were also produced: $[^{67}Ga]$Ga-THP-PSMA without serum (20 µL $[^{67}Ga]$Ga-THP-PSMA diluted in 200 µL PBS, 7 MBq, 0.3 nmol) and unchelated $[^{67}Ga]Ga^{3+}$ incubated with serum (1.5 µL $[^{67}Ga]Ga^{3+}$ in 0.1M HCl, diluted in 18.5 µL PBS and then added to 200 µL human serum, 1.7-2.5 MBq). Samples were incubated at 37°C and monitored over 8 days by size exclusion HLPC. Chromatograms were decay-corrected and normalised to account for the activity used.

5.3.7 Cell Lines

The GCP(II)/PSMA-negative cell line chosen was DU145, a human carcinoma prostate cancer cell line derived from a brain metastatic site. The GCP(II)/PSMA-expressing cell line chosen was a genetically modified daughter cell line of DU145, DU145-PSMA. This cell line had previously been transduced to express full-length human GCP(II)/PSMA, with a published method (*45*) and has been shown to have 2.4 times higher expression levels than the naturally GCP(II)/PSMA expressing cell line LNCaP by saturation binding studies (*45*). These cells were cultured in RPMI 1640 medium supplemented with 10% fetal bovine serum, 2 mM L-glutamine, and penicillin/streptomycin (full RPMI 1640 medium). To prepare for experiments, cells were grown at 37°C in an incubator with humidified air equilibrated with 5% CO_2.

5.3.8 Cell Uptake and Efflux Studies

Cell uptake over time: To determine the cellular uptake of [^{67}Ga]Ga-THP-PSMA and [^{67}Ga]Ga-DOTA-PSMA(617) over time DU145 and DU145-PSMA cells were seeded in a 24 well plate (0.25 x 10^6 cells/well) 24 hours before the assay. Just before the assay, cell medium was replaced with 250 µL fresh full RPMI 1640 medium. 5 µL of [^{67}Ga]Ga-THP-PSMA or [^{67}Ga]Ga-DOTA-PSMA(617) diluted in PBS was added to the cells to give a final concentration of 12.5 nM. Cells were returned to the incubator (37 °C, 5% CO_2) and monitored up to 4 hours. At each time point, the medium was removed from the cells and cells were washed with PBS (0.25 mL x 3). The supernatant and washes were combined to determine the unbound fraction, followed by an acid wash (0.25 mL, 0.5 M glycine, pH 2.5, 5 minutes) to determine cell surface-bound activity. Finally, the cells were lysed with 1 M NaOH (0.25 mL) and the plates washed with PBS (0.25 mL) to determine the activity internalised by the cells. Fractions were gamma-counted and the percentage of activity in each environment at each time point was determined.

Cell efflux assay: To determine the cellular efflux of [^{67}Ga]Ga-THP-PSMA and [^{67}Ga]Ga-DOTA-PSMA(617) over time, DU145 and DU145-PSMA cells were seeded in a 24 well plate (0.25 x 10^6 cells/well) 24 hours before the assay. Just before the assay, the cell medium was replaced with 250 µL fresh RPMI 1640 medium. 5 µL of [^{67}Ga]Ga-THP-PSMA or [^{67}Ga]Ga-DOTA-PSMA(617) diluted in PBS was added to the cells to give a final concentration of 12.5 nM. Cells were returned to the incubator (37 °C, 5% CO_2) for 1 hour. After 1 hour the supernatant was removed from all wells and replaced with new RPMI 1640 medium (250 µL). Efflux was then measured for up to 4 hours. At each time point, the unbound, cell surface-bound and internalised fractions were determined using the same method as for cell uptake described above.

Cell uptake study with high molar activity [^{67}Ga]Ga-THP-PSMA and [^{67}Ga]Ga-DOTA-PSMA(617): DU145-PSMA cells, DU145 cells and medium-only controls were used for this experiment. Cells were prepared at 1 million cells/mL and 250 µL medium containing 0.25 million cells were added to sterile 1.5 mL centrifuge tubes. 5 µL of [^{67}Ga]Ga-THP-PSMA or [^{67}Ga]Ga-DOTA-PSMA(617) with molar activities of 138.5 MBq/nmol and 76 MBq/nmol respectively were added to each tube (final concentration and total activity added to cells: [^{67}Ga]Ga-THP-PSMA C: 1.25nM, 43 kBq; B: 12.5 nM, 430 kBq; A: 125 nM = 4300 kBq; [^{67}Ga]Ga-DOTA-PSMA(617) F: 1.25 nM = 24 kBq; E: 12.5 nM = 240 kBq). The cells were incubated with the tracer for 1 hour at 37°C, 5% CO_2. At each time point the unbound, cell surface-bound and internalised fractions were determined using the same method as for cell uptake described above.

5.3.9 Mouse Model of Prostate Cancer

Animal studies complied with UK Research Councils and Medical Research Charities guidelines on responsibility in the use of animals in bioscience research, under UK Home Office project and personal licences. Subcutaneous prostate cancer xenografts were produced in SCID/beige mice (male, 6-7 weeks) by injecting 4×10^6 DU145-PSMA cells in 50 µL non-supplemented RPMI medium into the flank. Injection of [^{67}Ga]Ga-THP-PSMA for imaging or biodistribution was undertaken once the tumour was palpable and had reached 5-10 mm in diameter (3-4 weeks after inoculation).

5.3.10 SPECT/CT Scanning

Mice bearing DU145-PSMA tumours (n = 3) were administered [^{67}Ga]Ga-THP-PSMA (40 MBq, 100 µL, 0.33 µg, 0.22 nmol) by tail vein injection. At each time-point, CT/SPECT imaging was performed under isoflurane anaesthesia with a BioScan nanoSPECT-CT®PLUS (Mediso, Hungary).

The SPECT/CT scans were performed on a BioScan nanoSPECT-CT®PLUS (Mediso, Hungary) machine and the acquisition software (Nucline 1.07). CT acquisition was performed using 65 kVp tube voltage, with an exposure time of 500 ms with 180° projections at a pitch of 1. One field of view was scanned, covering the whole body of the mouse apart from the tail, which required 12 minutes for completion. These settings had a CT dose index volume of 0.9 cGy and a dose length product of 79.8 cGy.mm and were chosen to minimise CT dose to the mouse.

The SPECT scanner has 4 heads which could be fitted with either a 1 mm or 2.5 mm multi-pinhole collimator. The collimator with 1 mm apertures (recommended for mouse imaging) was used for time-points 3 hours, 1 day and 4 days. However, the collimator with 2.5 mm apertures (recommended for rat imaging) was used for the 7 day scan due to the lower activity within the mice. The machine was calibrated with gallium-67 for each collimator used. The energy windows used were: primary 93.20 ± 20% keV, secondary 184.60 ± 20% keV and tertiary 300.00 ± 20% keV, as shown in figure 5.5. The SPECT scanning parameters were optimised depending on the activity remaining within the mouse to ensure at least 30,000 counts were detected per scan that could be used for image reconstruction. This meant varying the seconds per frame between 40 and 240 and the total number of projections between 30 and 45, resulting in the scan times ranging from 30 to 120 minutes. The parameters used for each scan are summarised in table 5.1.

Time point	Aperture size of collimator (mm)	Seconds per frame	Scan time (minutes)	Total projections
3 hour	1	40	30	45
1 day	1	80	53	40
4 day	1	120	80	40
7 day	2.5	240	120	30

TABLE 5.1: SPECT/CT acquisition parameters for each time point after [^{67}Ga]Ga-THP-PSMA injection.

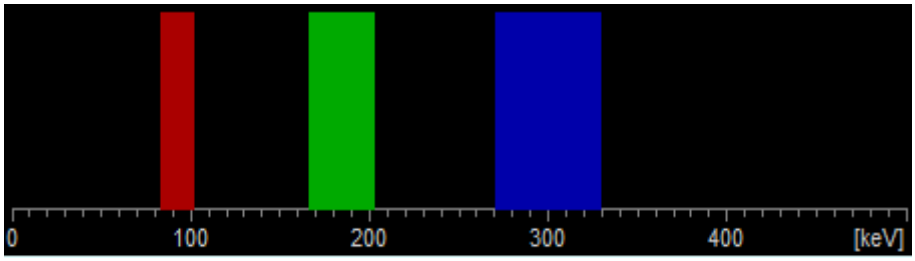

FIGURE 5.5: Energy windows used for SPECT imaging with gallium-67. Primary 93.20 ± 20% keV (red), secondary 184.60 ± 20% keV (green), and tertiary 300.00 ± 20% keV (blue).

5.3.11 Image Processing

The SPECT/CT data from each scan was reconstructed using Nucline software (v 2.00). The CT scans were reconstructed with a Ran Lak filter to produce a voxel size of 146 x 146 x 146 µm. SPECT data collected with each collimator type (1 mm or 2.5 mm aperture) were reconstructed using the gallium-67 calibration data acquired with the same collimator type. Images acquired with different collimators are therefore not directly comparable. Image processing and analysis were performed using Vivoquant software (v 1.23). Before analysis, both CT and PET images were realigned, processed to a voxel size of 0.16 mm^3 and the SPECT output calibrated to display MBq per voxel. Regions of interest (ROIs) for each data file were produced using freehand segmentation from the CT image. %ID/cm^3 values for each ROI were calculated using the activity and volume of the ROI and the injected dose as the decay corrected value administered at t = 0. During analysis, backscatter was accounted for by defining a background area within the field of view but outside of the mouse, and subtracting this value in MBq/mm^3 from values obtained for the ROIs.

5.3.12 *Ex vivo* Biodistribution Studies

Ex vivo biodistribution of [^{67}Ga]Ga-THP-PSMA was performed in mice bearing DU145-PSMA tumours without imaging. Three mice were used to assess radiotracer biodistribution at each time point post-injection: 1 hour, 3 hours, 1 day and 7 days. [^{67}Ga]Ga-THP-PSMA (100 µL, 1.5-10.9 MBq, 0.33 µg, 0.22 nmol THP-PSMA) was administered via tail vein injection under

isoflurane anaesthesia. After injection, anaesthesia ceased and the mice were returned to the animal house until the specified time-point, when they were culled by cervical dislocation and their organs harvested, weighed and counted.

5.3.13 Statistical Analysis

Data were analysed in GraphPad Prism 5 (version 5.04 or version 7.04) and expressed as mean ± standard deviation. Student t tests were used to determine statistical significance; a P value of less than 0.05 was considered significant.

5.4 Results

5.4.1 Radiolabelling

Radiochemical purity achieved after [^{67}Ga]Ga-THP-PSMA labelling over a range of concentrations is shown in figure 5.6. Radiochemical purity was consistently over 90% at concentrations of 23 µM or above. The highest molar activity achieved with 93% labelling was 326 MBq/nmol. In these conditions, the occupancy of gallium-67 in the THP chelator is 22.1%. This shows that there is potential for much higher occupancy levels than routinely achieved for gallium-68 (5 mL, 40 µg, THP-PSMA kits labelled with 1500 MBq would only have 0.005% occupancy). The highest molar activity achieved with [^{67}Ga]Ga-DOTA-PSMA was 120 MBq/nmol with 98% radiochemical purity. This is an occupancy of gallium-67 in the DOTA chelator of 8.1%. This was the highest molar activity attempted experimentally with DOTA-PSMA(617), so does not represent its upper limit.

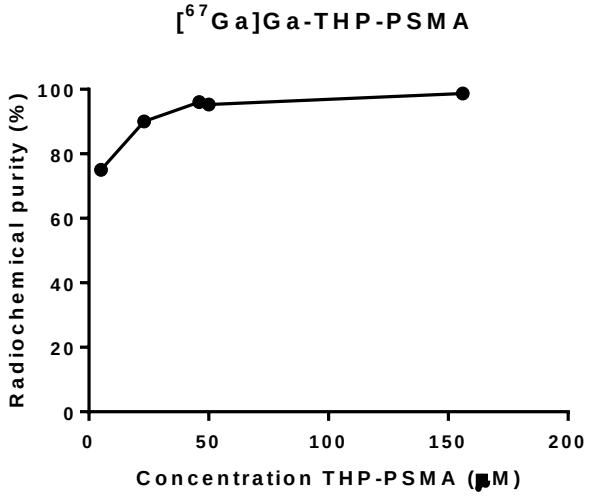

FIGURE 5.6: Dependence of radiochemical purity of [^{67}Ga]Ga-THP-PSMA on the concentration of THP-PSMA as measured by iTLC after 5 minutes pH 6.5-7.5.

5.4.2 Stability to Autoradiolysis

Radiolabelled [^{67}Ga]Ga-THP-PSMA (108 MBq/nmol, 2.5 MBq/µL, THP-PSMA 23 µM) was observed to undergo autoradiolysis with a drop to under 90% radiochemical purity in 2 hours. However, stability at this molar activity was extended to 18 hours by the addition of ascorbic acid accompanied by dilution in PBS to 1 MBq/µL (THP-PSMA 8 µM, ascorbic acid 488 µM) (figure 5.7).

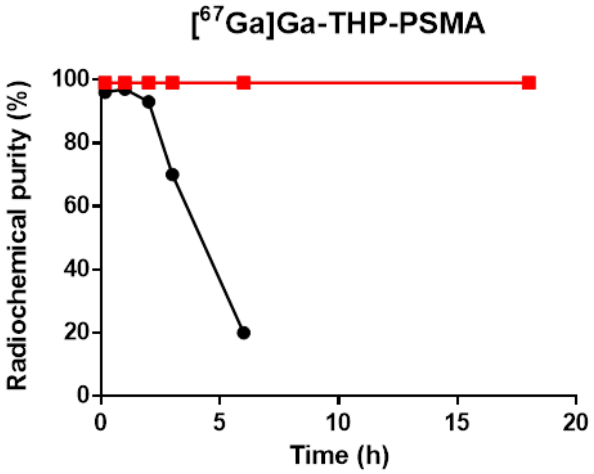

FIGURE 5.7: Stability over time of [^{67}Ga]Ga-THP-PSMA with (red) and without (black) the addition of ascorbic acid and dilution in PBS as monitored by iTLC.

5.4.3 Serum Stability

Human serum stability studies of [^{67}Ga]Ga-THP-PSMA (figure 5.8) showed minimal (< 5%) transchelation to serum proteins after 8 days incubation at 37°C.

5.4.4 Cell Uptake Over Time and Efflux Assays

Uptake over time of [^{67}Ga]Ga-THP-PSMA and [^{67}Ga]Ga-DOTA-PSMA(617), in DU145-PSMA and DU145 cells at 37°C are shown in figure 5.9. Both tracers showed time-dependent accumulation in GCP(II)/PSMA-expressing cells, but very low uptake (< 0.5 %) in non-GCP(II)/PSMA-expressing cells, confirming uptake is GCP(II)/PSMA-mediated. The uptake was higher at each time point for [^{67}Ga]Ga-DOTA-PSMA(617) compared to [^{67}Ga]Ga-THP-PSMA. Efflux studies (figure 5.10) show that both tracers are released from cells to the supernatant over time, but that the percentage of [^{67}Ga]Ga-THP-PSMA retained in the cell is half that of [^{67}Ga]Ga-DOTA-PSMA(617) across the time points studied. Therefore not only is less [^{67}Ga]Ga-THP-PSMA delivered to the cell over time but it also has faster efflux than [^{67}Ga]Ga-DOTA-PSMA(617).

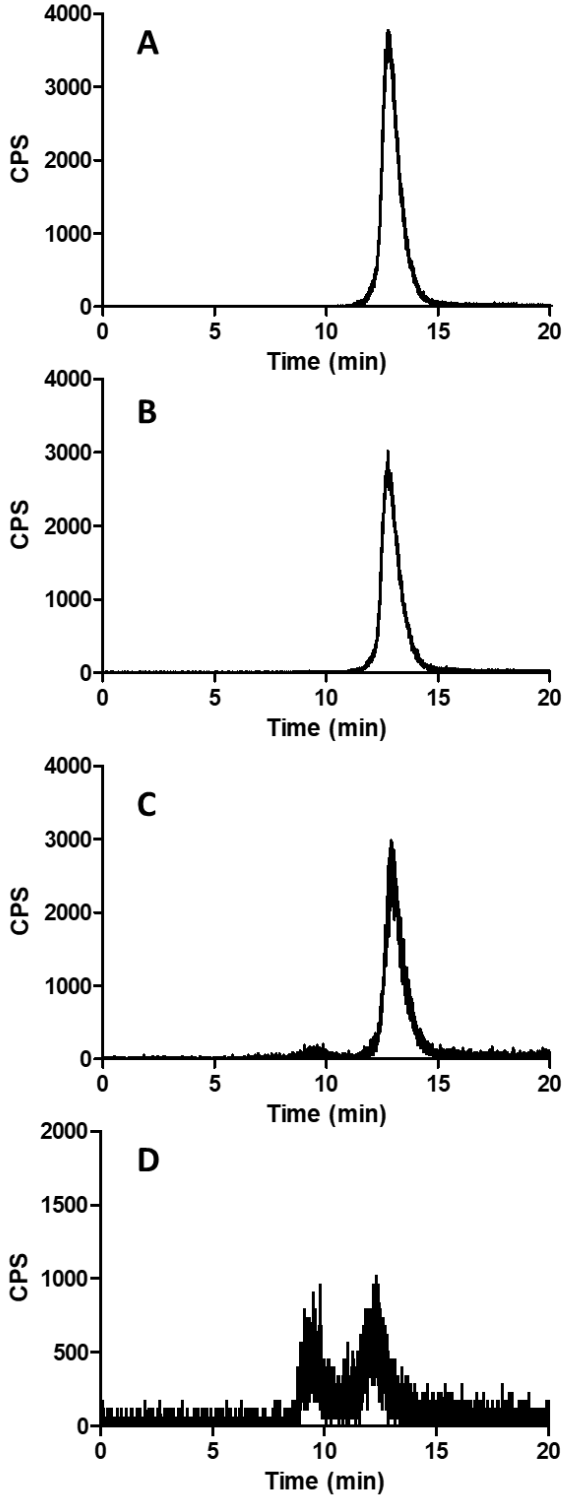

FIGURE 5.8: Size exclusion HPLC radiochromatograms of (A) [^{67}Ga]Ga-THP-PSMA; (B) [^{67}Ga]Ga-THP-PSMA after 1 hour incubation in human serum at 37°C, showing 0% transchelation to serum proteins; (C) [^{67}Ga]Ga-THP-PSMA after 8 days incubation in human serum at 37°C, showing < 5% transchelation to serum; (D) [^{67}Ga]Ga^{3+} incubated in human serum for 8 days showing [^{67}Ga]Ga^{3+} bound to serum protein and EDTA . All chromatograms are decay corrected, lower CPS for D due to a proportion of the gallium-67 sticking to the column.

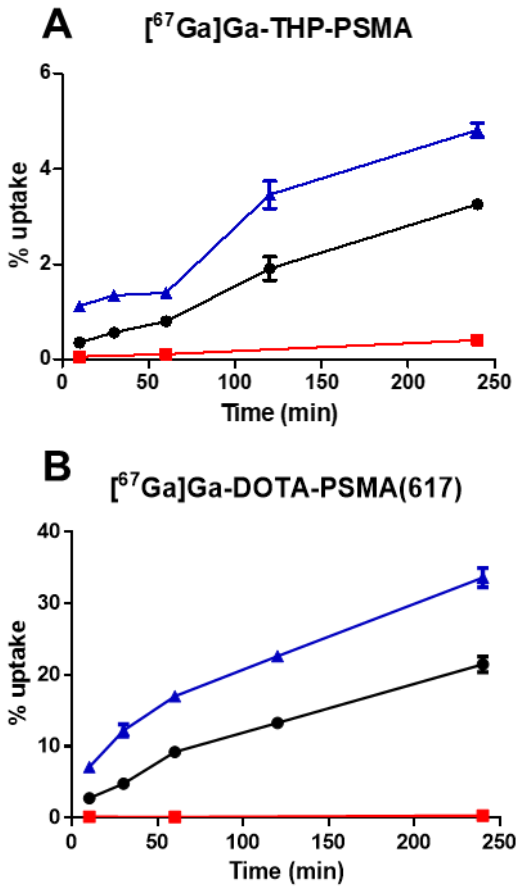

FIGURE 5.9: Uptake of 12.5 nM [^{67}Ga]Ga-THP-PSMA (A) and [^{67}Ga]Ga-DOTA-PSMA (B) over time at 37°C, 1×10^{6} cells/mL. Combined internalised and cell surface-bound activity DU145-PSMA cells (blue); internalised activity DU145-PSMA cells (black); internalised and cell surface-bound activity DU145 cells (red). Data points show mean ± SD (n = 4 [^{67}Ga]Ga-THP-PSMA) (n = 3 [^{67}Ga]Ga-DOTA-PSMA).

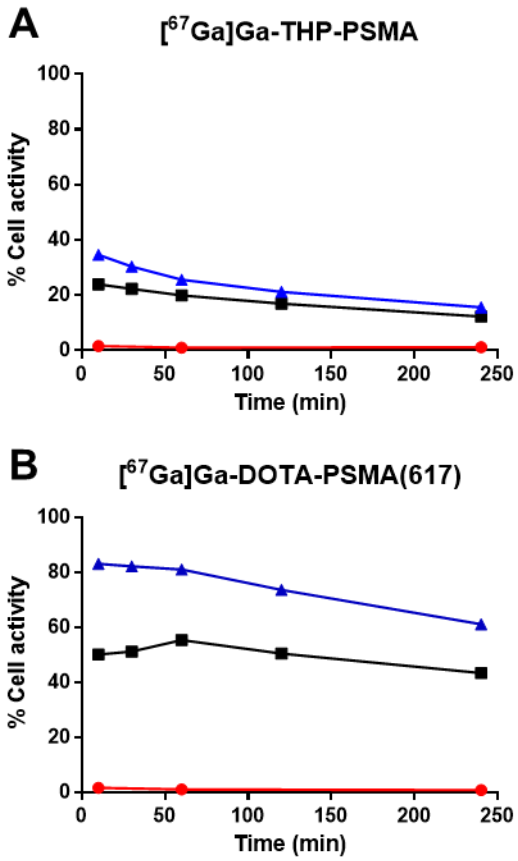

FIGURE 5.10: Efflux of [^{67}Ga]Ga-THP-PSMA (A) and [^{67}Ga]Ga-DOTA-PSMA (B) at 37°C, 1×10^{6} cells/mL. Prior to assay cells had been incubated for 1 hour at 37°C with of 12.5 nM tracer and then the supernatant was replaced. Combined internalised and cell surface-bound activity in DU145-PSMA cells (blue); internalised activity in DU145-PSMA cells (black); internalised and cell surface-bound activity in DU145 cells (red). Data points show mean ± SD (n = 4 for [^{67}Ga]Ga-THP-PSMA, n = 3 for [^{67}Ga]Ga-DOTA-PSMA).

5.4.5 Cell Uptake with High Molar Activity [^{67}Ga]Ga-THP-PSMA and [^{67}Ga]Ga-DOTA-PSMA(617)

The proportion of tracer bound to the cell surface and internalised into the cell after 1 hour incubation with a range of tracer concentrations are shown in figure 5.11. Both tracers showed low non-receptor-mediated uptake in non-GCP(II)/PSMA-expressing DU145 cells. The total activity associated with the cell surface and internalised after incubation (1 hour, 37°C) with [^{67}Ga]Ga-THP-PSMA (1.25 nM, 12.5 nM, or 125 nM) or [^{67}Ga]Ga-DOTA-PSMA(617) (1.25 nM, or 12.5 nM) is shown in figure 5.12. For both tracers the maximum value achieved was ~ 0.1 Bq/cell, however, for [^{67}Ga]Ga-DOTA-PSMA(617) this was achieved at a 10 fold lower concentration of tracer and at a lower molar activity (molar activity 76 MBq/nmol compared to a molar activity of 138.5 MBq/nmol for [^{67}Ga]Ga-THP-PSMA).

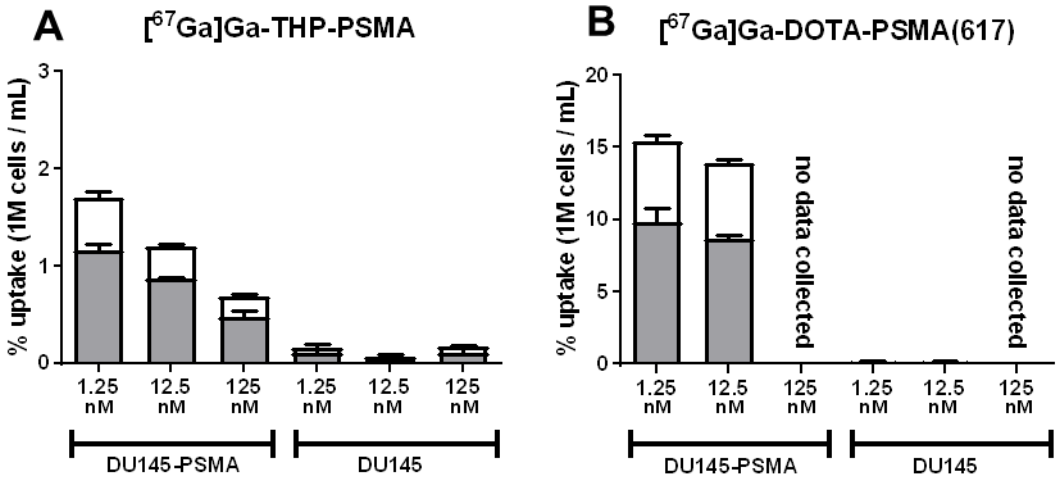

FIGURE 5.11: (A) Percentage uptake in DU145-PSMA cells of [^{67}Ga]Ga-THP-PSMA (molar activity 138.5 MBq/nmol) and (B) [^{67}Ga]Ga-DOTA-PSMA(617) (molar activity 76 MBq/nmol) after 1 hour at 37°C, 1×10^{6} cells/mL over a range of concentrations. Surface-bound activity (white) and internalised activity (grey) are shown (mean ± SD, n = 2).

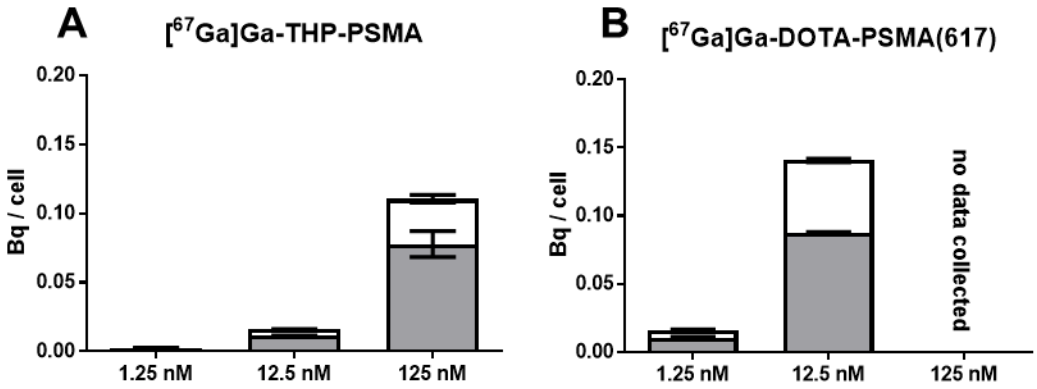

FIGURE 5.12: (A) Activity per cell of [^{67}Ga]Ga-THP-PSMA (molar activity 138.5 MBq/nmol) and (B) [^{67}Ga]Ga-DOTA-PSMA(617) (molar activity 76 MBq/nmol) after 1 hour at 37°C, 1×10^{6} cells/mL over a range of concentrations. Bars show surface-bound activity DU145-PSMA cells (white); internalised activity DU145-PSMA cells (grey) (mean ± SD, n = 2).

5.4.6 *Ex vivo* Biodistribution of [^{67}Ga]Ga-THP-PSMA

Biodistribution of [^{67}Ga]Ga-THP-PSMA at 1 hour showed that the majority of the tracer was no longer in circulation and that excretion was exclusively renal with the majority of the activity associated with the kidneys. Uptake in the GCP(II)/PSMA-expressing tumour was seen (3.5 ± 1.2 %ID/g). Over time, the activity in the whole body, including that associated with both the kidney and the tumour, decreased. The largest change occurred over the first 24 hour period, but activity was still detectable in the kidney and tumour 7 days post-injection. Tumour uptake of

[^{67}Ga]Ga-THP-PSMA was highest at 1 hour post-injection (3.47 ± 1.15 %ID/g), but then decreased over time, with a reduction to 1.12 ± 0.4 %ID/g in 3 hours, 0.2 ± 0.07 %ID/g in 24 hours and 0.16 ± 0.07 %ID/g in 7 days. The highest tumour to background ratios (tumour to muscle = 215, tumour to blood = 132) were observed at the 3 hour time-point. Table 5.2 and figure 5.13 summarise the biodistribution results.

	[^{67}Ga]Ga-THP-PSMA			
Tumour type	DU145-PSMA	DU145-PSMA	DU145-PSMA	DU145-PSMA
Time point	1 hour	3 hours	24 hours	7 days
	(n = 3)	(n = 3)	(n = 3)	(n = 3)
	%ID/g	%ID/g	%ID/g	%ID/g
Tumour	3.47 ± 1.15	1.12 ± 0.40	0.20 ± 0.07	0.16 ± 0.07
Blood	0.12 ± 0.04	0.01 ± 0.00	0.00 ± 0.00	0.01 ± 0.00
Small Intestines	0.06 ± 0.01	0.1 ± 0.12	0.02 ± 0.01	0.01 ± 0.00
Kidney	8.02 ± 3.22	1.83 ± 0.41	0.40 ± 0.10	0.20 ± 0.02
Liver	0.07 ± 0.02	0.09 ± 0.00	0.08 ± 0.01	0.07 ± 0.01
Lungs	0.20 ± 0.04	0.07 ± 0.04	0.03 ± 0.00	0.04 ± 0.02
Muscle	0.03 ± 0.01	0.01 ± 0.00	0.00 ± 0.00	0.00 ± 0.00
Pancreas	0.06 ± 0.02	0.01 ± 0.00	0.01 ± 0.01	0.01 ± 0.00
Spleen	1.54 ± 0.75	0.18 ± 0.04	0.05 ± 0.02	0.06 ± 0.05
Tumour to organ ratios				
Tumour to blood	28.6 ± 4	132 ± 95	107 ± 46	83 ± 81
Tumour to muscle	134 ± 18	215 ± 100	58 ± 34	49 ± 21
Tumour to spleen	2.6 ± 1.3	6.4 ± 1.9	4.1 ± 2.3	7.1 ± 9.7
Tumour to kidney	0.4 ± 0.0	0.6 ± 0.1	0.6 ± 0.3	0.7 ± 0.3

TABLE 5.2: *Ex vivo* biodistribution of [^{67}Ga]Ga-THP-PSMA in mice bearing DU145-PSMA tumours up to 7 days post-injection.

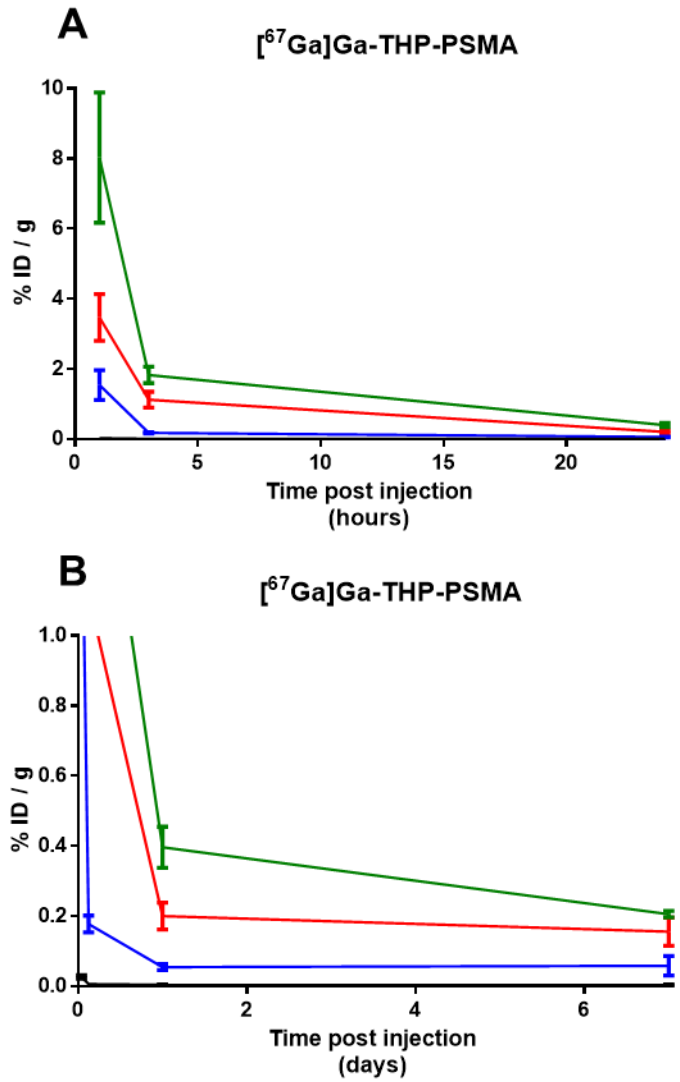

FIGURE 5.13: *Ex vivo* biodistribution-derived time-activity curves (%ID/g) of [^{67}Ga]Ga-THP-PSMA in mice bearing DU145-PSMA tumours: (A) shows first 24 hours; (B) shows up to 7 days. Kidney (green), tumour (red), spleen (blue), muscle (black) (mean ± SD, n = 3).

5.4.7 SPECT/CT Imaging Data

Gallium-67 imaging had not been performed previously on the nanoSPECT/CT system within the department and so the achievable image quality was unknown. The images produced were prone to high background scatter but the organs of interest (kidney, bladder and tumour) could still be delineated in the SPECT image (figure 5.14). The image analysis showed good alignment with the *ex vivo* biodistribution, with tracer distribution reflecting renal excretion and tumour uptake. In agreement with the biodistribution results, the total activity within the whole animal reduced over time, as well as the activity within the kidney and tumour (figure 5.15).

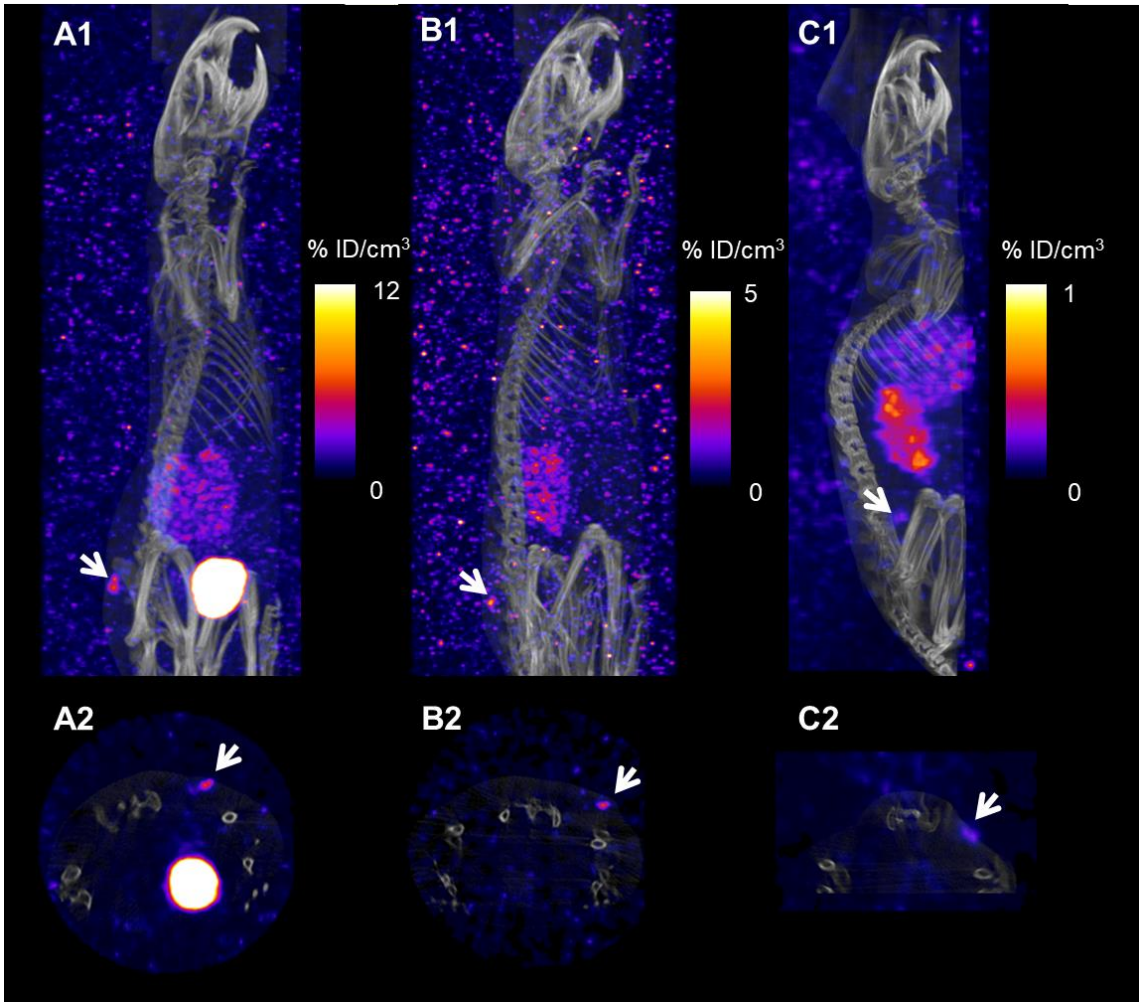

FIGURE 5.14: Representative SPECT/CT images of a SCID/beige mouse with DU145-PSMA tumours imaged with [^{67}Ga]Ga-THP-PSMA without scatter correction. The white arrows indicate the position of the tumour. For all images, the maximum intensity projection (1) and an axial slice (2) are shown. (A) 3 hour images scaled to 12 %ID/cm^3 (B) 24 hour images scaled to 5 %ID/cm^3 (C) 7 day images scaled to 1 %ID/cm^3.

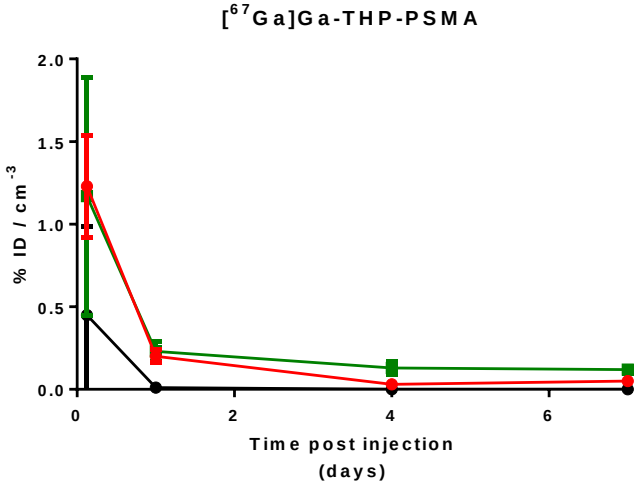

FIGURE 5.15: SPECT/CT derived time-activity curves of [^{67}Ga]Ga-THP-PSMA in mice bearing DU145-PSMA tumours: kidney (green), tumour (red), whole body (black). Results after scatter corrections (mean ± SD, n = 3).

5.5 Discussion

The aim of this study was to radiolabel [^{67}Ga]Ga-THP-PSMA at high molar activity and assess its ability to deliver gallium-67 to GCP(II)/PSMA-expressing cells. *In vitro* experiments were also completed with [^{67}Ga]Ga-DOTA-PSMA(617) for comparison as this radiotracer is known to have a higher affinity for GCP(II)/PSMA (*18*)(*20*)(*23*) (chapter 3) and its lutetium-177 analogue has been used for [^{177}Lu]Lu-DOTA-PSMA(617) therapy. It is not only the affinity for GCP(II)/PSMA that governs the activity delivered to each cell by a radiotracer and consequently the dose which that cell receives; molar activity is potentially just as critical, and should be as high as possible for therapeutic applications so that the highest possible target to background ratios can be obtained, without saturation of receptors. Therefore it was important to maximise the molar activity of the [^{67}Ga]Ga-PSMA tracers within this study. To achieve this, gallium-67 at a high activity concentration (35 GBq/mL) in 0.1 M HCl was used without the presence of any weakly coordinating ligands such as citrate. [^{67}Ga]Ga-THP-PSMA was labelled in one step at room temperature, with a radiochemical purity over 90%, within 10 minutes at pH 6-7 achieving a maximum molar activity of 326 MBq/nmol. In these conditions the occupancy of gallium-67 in the THP chelator was 22.1%. This is an extremely high value compared to most radiolabelled tracers and was achieved at room temperature within 10 minutes. This occupancy level for THP-PSMA is much higher than had previously been achieved with gallium-67 converted from citrate (0.4% occupancy (*20*)) or routinely achieved with gallium-68 (5 mL, 40 µg THP-PSMA kits labelled with 1500 MBq would only have 0.005% occupancy (*20*)). One factor allowing this increased occupancy is the higher activity concentration of the gallium-67 supplied/used (35 GBq/mL, 24 µM gallium-67) compared to gallium-67 in HCl converted from gallium-67 citrate (1.5 GBq/mL, 1 µM gallium-67 (*20*)) or gallium-68 from an Galliapharm (Eckert and Ziegler) generator (0.3 GBq/mL, 2.9 nM gallium-68 (*20*)). Another factor is likely to be the levels of contaminating trace-metals, and so it would have been interesting to have carried out ICP-MS on these samples to identify the all trace-metals in these different sources of gallium-67. However, it is known that iron and titanium are the trace metal contaminants that have the greatest impact on radiolabelling of THP (chapter 2, figure 2.20). The gallium-67 supplied by Nordion is likely to have had a lower concentration of these metal contaminants than, the gallium-67 converted from citrate or the gallium-68 from a generator. This is because, in the case of gallium-67, citrate buffers have been introduced (sodium citrate di-hydrate, sodium chloride) which are likely to contain trace-metals, and for gallium-68 the titanium-dioxide column of the generator is a major source of titanium in its eluate (*46*).

The occupancy level achieved for gallium-68 is therefore not limited by the chelator choice, the ability of THP to achieve excellent occupancy under the right conditions has been demonstrated here, but instead, it is most likely limited by the activity concentration of radioactive gallium-68 available and the levels of contaminating trace metals within it. Therefore further investigations into how these parameters could be improved for gallium-68 could be very valuable to the field.

After increasing the stability of [^{67}Ga]Ga-THP-PSMA by the addition of ascorbic acid in combination with dilution in PBS, to protect against autoradiolysis, *in vitro* experiments were performed to assess the tracer uptake and efflux over time. When compared to [^{67}Ga]Ga-DOTA-PSMA(617), [^{67}Ga]Ga-THP-PSMA showed almost 10 fold lower uptake and double the efflux rate; attributes that are unfavourable for a therapeutic radiotracer. It would be ideal to deliver a large amount of gallium-67 specifically to cells that express GCP(II)/PSMA, and for that gallium-67 to remain in that cell, even when the concentration drops in surrounding tissue/blood (as mimicked by the efflux assay), to deliver the maximum activity and consequently dose to the cell. The fate of [$^{67/68}$Ga]Ga-PSMA tracers after they enter the cell is unknown and this could greatly affect the rate of efflux. Of particular interest would be where the tracers localise, whether they are broken down intracellularly, and whether they release gallium. Current information about the intracellular location of PSMA compounds using the same urea-based scaffold can only be gleaned from fluorescent GCP(II)/PSMA imaging agents such as YC-36 (figure 5.2), which do show perinuclear accumulation (*16*). However, these results should be interpreted with caution as fluorescent agents require large, often lipophilic, substituents to be added to the GCP(II)/PSMA targeting moiety and so could have very different intracellular distribution to radiometal versions. Microautoradiography methods could provide insight into the location of the radiometal (within the resolution of this technique) and therefore could be used to help design tracers that not only have high affinity for GCP(II)/PSMA but also localise close to the nucleus, which is believed to induce the highest therapeutic effect (*20*)(*26*). However, the technique is limited as it is only possible to visualise the radiometal rather than specifically the radiometal complex, as it is not possible to differentiate between chelated and un-chelated radio-gallium within the cell.

With both [^{67}Ga]Ga-THP-PSMA and [^{67}Ga]Ga-DOTA-PSMA(617), with molar activities of 138.5 MBq/nmol and 76 MBq/nmol respectively, specific delivery of gallium-67 to GCP(II)/PSMA-expressing cells was possible. However, a maximum of only 0.1 Bq/cell was experimentally achieved within 1 hour. This is 10 times lower than the level of 1 Bq per cell shown to be required to achieve 90% cell killing with [^{67}Ga]Ga-8-hydroxyquinoline (*38*). Cell-associated activity of 0.1 Bq/cell was achieved at 125 nM for [^{67}Ga]Ga-THP-PSMA (138.5 MBq/nmol) and 12.5 nM for

[^{67}Ga]Ga-DOTA-PSMA(617) (76 MBq/nmol). [^{67}Ga]Ga-DOTA-PSMA(617) was not tested at 125 nM due to the limited quantity of gallium-67 available for radiolabelling at the time of this experiment. It is likely that the activity per cell would have increased further at this concentration, but as the IC_{50} of [^{67}Ga]Ga-DOTA-PSMA(617) is known to be in the range of 10-40 nM (*20*)(*23*) it is likely that blocking from unlabelled DOTA-PSMA(617) would occur and so it would be unrealistic to extrapolate this data to 125 nM. It would have been interesting to extend this work and establish whether 0.1 Bq per cell was high enough to see a therapeutic effect, as the [^{67}Ga]Ga-PSMA tracers may have different cellular distribution compared to that achieved by treatment with [^{67}Ga]Ga-8-hydroxyquinoline and so its dose could have been deposited in different cell areas. Also, it is important to consider that 0.1 Bq per cell is a mean value across 0.25 million cells. Studies looking into direct labelling of cells with [^{111}In]In-8-hydroxyquinoline have shown with microautoradiography that there are large differences in how heavily cells are labelled within the same population (*47*). Similarly, in this study, it is unlikely that each cell had the same uptake of gallium-67 and therefore received the same dose. Therefore a portion of the GCP(II)PSMA-expressing cells could have taken up enough gallium-67 for it to have a toxic effect which may have been detectable. The therapeutic effects of [^{67}Ga]Ga-THP-PSMA and [^{67}Ga]Ga-DOTA-PSMA(617) could have been monitored *in vitro* through, γ-H2AX staining for double-strand DNA breaks (*48*), and clonogenic assays which assess the level of cell reproductive death (*38*)(*49*). This was not possible within this project as the supplier of gallium-67 at high activity concentration (required to achieve these high molar activities) ceased its production and a suitable alternative could not be found. Additionally, these results suggested the affinity of [^{67}Ga]Ga-THP-PSMA was the factor limiting the uptake *in vitro*, rather than the molar activity, so this became the focus of future work. Chapter 6 provides a review of the GCP(II)/PSMA receptor which was used to propose higher affinity ligands and chapter 7 outlines the synthesis and evaluation of a new zinc ion binding motif designed to improve affinity for GCP(II)/PSMA.

Although these results suggest the affinity of [^{67}Ga]Ga-THP-PSMA is not ideal to continue *in vitro* studies, it was clear that the *in vitro* performance of the gallium-68 imaging agent [^{68}Ga]Ga-THP-PSMA had not limited its ability to delineate GCP(II)/PSMA-expressing tumours *in vivo* (chapter 3 & 4 (*20*)). As explored in the introduction, uptake and retention of radiotracers in tumours and other GCP(II)/PSMA-expressing organs are not well predicted by *in vitro* affinity values (IC_{50} or K_d), and so it was important to assess these parameters experimentally. Therefore *in vivo* studies were performed to monitor the uptake and retention of [^{67}Ga]Ga-THP-PSMA in GCP(II)/PSMA-expressing tumours. These results showed the biodistribution was similar to that seen for [^{68}Ga]Ga-THP-PSMA, with rapid renal excretion, low background uptake and specific uptake in

tumour (chapter 3 (*20*)). Biodistribution results showed decay-corrected tumour uptake of [^{67}Ga]Ga-THP-PSMA was highest at 1 hour post-injection (3.47 ± 1.15 %ID/g), but then fell over time, with a reduction to 1.12 ± 0.4 %ID/g in 3 hours, 0.2 ± 0.07 %ID/g in 24 hours and 0.16 ± 0.07 %ID/g in 7 days. These values can be extrapolated to gain an approximation of the amount of activity that could be delivered to the cells if [^{67}Ga]Ga-THP-PSMA at 326 MBq/nmol (maximum molar activity) had been administered. With this molar activity injecting 0.22 nmol of THP-PSMA per mouse (the level used in this study) would result in an injected activity of 72 MBq. As the average tumour mass in this study was 0.05 g and assuming this tumour contained 10^8 cells per gram (*50*), this tumour contained 5 million cells. Therefore using the experimentally derived %ID/g at 1 hour (3.47 %ID/g = 2.5 MBq/g), it could be assumed that 0.124 MBq would have been delivered to the tumour at this time-point, providing an average of 0.025 Bq/cell. This low value suggests that again improvements to affinity would be required to deliver an adequate therapeutic dose to tumours. There was also little difference between the rate of washout of [^{67}Ga]Ga-THP-PSMA from the tumour and the kidneys of the mice. This differs from published results for [^{177}Lu]Lu-DOTA-PSMA(617) which showed, a more favourable biodistribution for molecular radiotherapy, with high retention in the tumour but washout from the kidney (*18*). SPECT/CT data showed trends consistent with the biodistribution. However, the SPECT images had high background scatter, and so these were difficult to interpret without the CT to provide structural information. This also meant that the scatter had to be corrected for before quantitative data could be obtained from the scan. However, the quality of the images obtained would have been sufficient for dosimetry modelling: the main use of images from therapeutic radiotracers.

5.6 Conclusion

[^{67}Ga]Ga-THP-PSMA can be labelled at high molar activity and specifically accumulates within GCP(II)/PSMA-expressing cells and tumours. However, this uptake is lower than for [^{67}Ga]Ga-DOTA-PSMA(617) and [^{67}Ga]Ga-THP-PSMA is seen to have significant efflux from both cells and tumours over time, suggesting it is less suitable for therapeutic applications than other GCP(II)/PSMA tracers. High affinity [^{67}Ga]Ga-PSMA tracers, labelled at high molar activity would be required to deliver a therapeutic cellular activity *in vitro*. Currently [^{67}Ga]Ga-THP-PSMA does not meet this criterion due to its lower affinity and so improving this will be the focus for future work.

5.7 References

1. Kluetz PG, Pierce W, Maher VE, Zhang H, Tang S, Song P, Liu Q, Haber MT, Leutzinger EE, Al-Hakim A, Chen W, Palmby T, Alebachew E, Sridhara R, Ibrahim A, Justice R, Pazdur R. Radium Ra 223 Dichloride Injection: U.S. Food and Drug Administration Drug Approval Summary. *Clin Cancer Res*. 2014;20:9-14.
2. Parker C, Nilsson S, Heinrich D, Helle SI, O'Sullivan JM, Fosså SD, Chodacki A, Wiechno P, Logue J, Seke M, Widmark A, Johannessen DC, Hoskin P, Bottomley D, James ND, Solberg A, Syndikus I, Kliment J, Wedel S, et al. Alpha Emitter Radium-223 and Survival in Metastatic Prostate Cancer. *N Engl J Med*. 2013;369:213-223.
3. Henriksen G, Fisher DR, Roeske JC, Bruland ØS, Larsen RH. Targeting of Osseous Sites with Alpha-Emitting 223Ra: Comparison with the Beta-Emitter 89Sr in Mice. *J Nucl Med*. 2003;44:252-259.
4. Nilsson S, Larsen RH, Fosså SD, Balteskard L, Borch KW, Westlin J-E, Salberg G, Bruland OS. First Clinical Experience with Alpha-Emitting Radium-223 in the Treatment of Skeletal Metastases. *Clin Cancer Res*. 2005;11:4451-4459.
5. Zechmann CM, Afshar-Oromieh A, Armor T, Stubbs JB, Mier W, Hadaschik B, Joyal J, Kopka K, Debus J, Babich JW, Haberkorn U. Radiation Dosimetry and First Therapy Results with a 124I/ 131I-Labeled Small Molecule (MIP-1095) Targeting PSMA for Prostate Cancer Therapy. *Eur J Nucl Med Mol Imaging*. 2014;41:1280-1292.
6. Afshar-Oromieh A, Haberkorn U, Zechmann C, Armor T, Mier W, Spohn F, Debus N, Holland-Letz T, Babich J, Kratochwil C. Repeated PSMA-Targeting Radioligand Therapy of Metastatic Prostate Cancer with 131I-MIP-1095. *Eur J Nucl Med Mol Imaging*. 2017;44:950-959.
7. Kabasakal L, AbuQbeitah M, Aygün A, Yeyin N, Ocak M, Demirci E, Toklu T. Pre-Therapeutic Dosimetry of Normal Organs and Tissues of 177Lu-PSMA-617 Prostate-Specific Membrane Antigen (PSMA) Inhibitor in Patients with Castration-Resistant Prostate Cancer. *Eur J Nucl Med Mol Imaging*. 2015;42:1976-1983.
8. Delker A, Fendler WP, Kratochwil C, Brunegraf A, Gosewisch A, Gildehaus FJ, Tritschler S, Stief CG, Kopka K, Haberkorn U, Bartenstein P, Böning G. Dosimetry for 177Lu-DKFZ-PSMA-617: A New Radiopharmaceutical for the Treatment of Metastatic Prostate Cancer. *Eur J Nucl Med Mol Imaging*. 2016;43:42-51.
9. Herrmann K, Bluemel C, Weineisen M, Schottelius M, Wester H-J, Czernin J, Eberlein U, Beykan S, Lapa C, Riedmiller H, Krebs M, Kropf S, Schirbel A, Buck AK, Lassmann M. Biodistribution and Radiation Dosimetry for a Probe Targeting Prostate-Specific Membrane Antigen for Imaging and Therapy. *J Nucl Med*. 2015;56:855-861.
10. Ahmadzadehfar H, Rahbar K, Kürpig S, Bögemann M, Claesener M, Eppard E, Gärtner F, Rogenhofer S, Schäfers M, Essler M. Early Side Effects and First Results of Radioligand Therapy with 177Lu-DKFZ-617 PSMA of Castrate-Resistant Metastatic Prostate Cancer: A Two-Centre Study. *EJNMMI Res*. 2015;5:36.
11. Ahmadzadehfar H, Eppard E, Kürpig S, Fimmers R, Schlenkhoff CD, Gärtner F, Rogenhofer S, Essler M. Therapeutic Response and Side Effects of Repeated Radioligand Therapy with 177 Lu-PSMA-DKFZ-617 of Castrate-Resistant Metastatic Prostate Cancer. *Oncotarget*. 2016;7:12477-12488.
12. Heck MM, Retz M, D'Alessandria C, Rauscher I, Scheidhauer K, Maurer T, Storz E, Janssen F, Schottelius M, Wester HJ, Gschwend JE, Schwaiger M, Tauber R, Eiber M. Systemic Radioligand Therapy With177Lu Labeled Prostate Specific Membrane Antigen Ligand for Imaging and Therapy in Patients with Metastatic Castration Resistant Prostate Cancer. *J Urol*. 2016;196:382-391.
13. Kulkarni HR, Singh A, Schuchardt C, Niepsch K, Sayeg M, Leshch Y, Wester H, Baum RP. Castration-Resistant Prostate Cancer: The Bad Berka Experience since 2013. *J Nucl Med*.

2016;57:97S-104S.
14. Calopedos RJS, Chalasani V, Asher R, Emmett L, Woo HH. Lutetium-177-Labelled Anti-Prostate-Specific Membrane Antigen Antibody and Ligands for the Treatment of Metastatic Castrate-Resistant Prostate Cancer: A Systematic Review and Meta-Analysis. *Prostate Cancer Prostatic Dis*. 2017;20:352-360.
15. Babich W, Armor JT, Stubbs JB, Maresca KP, Stabin MG, Joyal JL, Eckelman WC, Barrett JA, Coleman RE, Goldsmith SJ, Vallabhajosula S, Petry NA, Cho S, Armor T, Babich JW. Prostate Cancer First-in-Man Evaluation of 2 High-Affinity PSMA-Avid Small Molecules for Imaging First-in-Man Evaluation of 2 High-Affinity PSMA-Avid Small Molecules for Imaging Prostate Cancer. *J Nucl Med*. 2013;54:380-387.
16. Kiess A, Minn I, Chen Y, Hobbs RF, Sgouros G, Mease RC, Pullambhatla M, Shen C, Foss C, Pomper M. Auger Radiopharmaceutical Therapy Targeting Prostate-Specific Membrane Antigen. *J Nucl Med*. 2015;56:1401-1407.
17. Chen Y, Foss C a, Byun Y, Nimmagadda S, Pullambhatla M, Fox JJ, Castanares M, Lupold SE, Babich JW, Mease RC, Pomper MG. Radiohalogenated Prostate-Specific Membrane Antigen (PSMA)-Based Ureas as Imaging Agents for Prostate Cancer. *J Med Chem*. 2008;51:7933-7943.
18. Benešová M, Schäfer M, Bauder-Wüst U, Afshar-Oromieh A, Kratochwil C, Mier W, Haberkorn U, Kopka K, Eder M. Preclinical Evaluation of a Tailor-Made DOTA-Conjugated PSMA Inhibitor with Optimized Linker Moiety for Imaging and Endoradiotherapy of Prostate Cancer. *J Nucl Med*. 2015;56:914-920.
19. Weineisen M, Schottelius M, Simecek J, Baum RP, Yildiz A, Beykan S, Kulkarni HR, Lassmann M, Klette I, Eiber M, Schwaiger M, Wester H-J, Rp-hplc A. 68Ga- and 177Lu-Labeled PSMA I&T: Optimization of a PSMA-Targeted Theranostic Concept and First Proof-of-Concept Human Studies. *J Nucl Med*. 2015;56:1169-1176.
20. Young JD, Abbate V, Imberti C, Meszaros LK, Ma MT, Terry SYAA, Hider RC, Mullen GE, Blower PJ. 68Ga-THP-PSMA: A PET Imaging Agent for Prostate Cancer Offering Rapid, Room-Temperature, 1-Step Kit-Based Radiolabeling. *J Nucl Med*. 2017;58:1270-1277.
21. Kinoshita Y, Kuratsukuri K, Landas S, Imaida K, Rovito PM, Wang CY, Haas GP. Expression of Prostate-Specific Membrane Antigen in Normal and Malignant Human Tissues. *World J Surg*. 2006;30:628-636.
22. Rowe SP, Drzezga A, Neumaier B, Dietlein M, Gorin MA, Zalutsky MR, Pomper MG. Prostate-Specific Membrane Antigen–targeted Radiohalogenated PET and Therapeutic Agents for Prostate Cancer. *J Nucl Med*. 2016;57:90S-97S.
23. Wüstemann T, Bauder-Wüst U, Schäfer M, Eder M, Benesova M, Leotta K, Kratochwil C, Haberkorn U, Kopka K, Mier W. Design of Internalizing PSMA-Specific Glu-Ureido-Based Radiotherapeuticals. *Theranostics*. 2016;6:1085-1095.
24. Aghevlian S, Boyle AJ, Reilly RM. Radioimmunotherapy of Cancer with High Linear Energy Transfer (LET) Radiation Delivered by Radionuclides Emitting α-Particles or Auger Electrons. *Adv Drug Deliv Rev*. 2017;109:102-118.
25. Naidoo K, Pinder SE. Micro- and Macro-Metastasis in the Axillary Lymph Node: A Review. *Surgeon*. 2017;15:76-82.
26. Buchegger F, Perillo-Adamer F, Dupertuis YM, Bischof Delaloye A. Auger Radiation Targeted into DNA: A Therapy Perspective. *Eur J Nucl Med Mol Imaging*. 2006;33:1352-1363.
27. Pantel K, Alix-Panabières C, Riethdorf S. Cancer Micrometastases. *Nat Rev Clin Oncol*. 2009;6:339-351.
28. Miller MC, Doyle G V, Terstappen LWMM. Significance of Circulating Tumor Cells Detected by the CellSearch System in Patients with Metastatic Breast Colorectal and Prostate Cancer. *J Oncol*. 2010;2010:1-8.
29. Kassis AI. Cancer Therapy with Auger Electrons: Are We Almost There? *J Nucl Med*.

2003;44:1479-1481.
30. Pomplun E, Sutmann G. Is Coulomb Explosion a Damaging Mechanism for 125IUdR? *Int J Radiat Biol*. 2004;80:855-860.
31. Khanna KK, Jackson SP. DNA Double-Strand Breaks: Signaling, Repair and the Cancer Connection. *Nat Genet*. 2001;27:247-254.
32. Shen C, Minn I, Chen Y, Mease RC, Brummet ME, Pomper MG, Kiess AP. Auger Radiopharmaceutical Therapy Targeting Prostate-Specific Membrane Antigen in a Micrometastatic Model of Prostate Cancer. *Int J Radiat Oncol*. 2016;96:S110.
33. Kratochwil C, Giesel FL, Leotta K, Eder M, Hoppe-Tich T, Youssoufian H, Kopka K, Babich JW, Haberkorn U. PMPA for Nephroprotection in PSMA-Targeted Radionuclide Therapy of Prostate Cancer. *J Nucl Med*. 2015;56:293-298.
34. Nayak TK, Brechbiel MW. Radioimmunoimaging with Longer-Lived Positron-Emitting Radionuclides: Potentials and Challenges. *Bioconjug Chem*. 2009;20:825-841.
35. Riesco-Eizaguirre G, Santisteban P. A Perspective View of Sodium Iodide Symporter Research and Its Clinical Implications. *Eur J Endocrinol*. 2006;155:495-512.
36. Jonkhoff AR, Huijgens PC, Versteegh RT, Martens HJM, Teule GJJ, Ossenkoppelel GJ. Gallium-67 Radiotoxicity in Human U937 Lymphoma Cells. *Br J Cancer*. 1993;67:693-700.
37. Jonkhoff AR, Plaizier MABD, Ossenkoppele GJ, Teule GJJ, Huijgens PC. High-Dose Gallium-67 Therapy in Patients with Relapsed Acute Leukaemia: A Feasibility Study. *Br J Cancer*. 1995;72:1541-1546.
38. Othman MF bin, Mitry NR, Lewington VJ, Blower PJ, Terry SYA. Re-Assessing Gallium-67 as a Therapeutic Radionuclide. *Nucl Med Biol*. 2017;46:12-18.
39. Michel RB, Brechbiel MW, Mattes MJ. A Comparison of 4 Radionuclides Conjugated to Antibodies for Single-Cell Kill. *J Nucl Med*. 2003;44:632-640.
40. Howell RW. Radiation Spectra for Auger-Electron Emitting Radionuclides: Report No 2 of AAPM Nuclear Medicine Task Group No.6. *Med Phys*. 1992:1371-1383.
41. Govindan S V, Goldenberg DM, Elsamra SE, Griffiths GL, Ong GL, Brechbiel MW, Burton J, Sgouros G, Mattes MJ. Radionuclides Linked to a CD74 Antibody as Therapeutic Agents for B-Cell Lymphoma: Comparison of Auger Electron Emitters with Beta-Particle Emitters. *J Nucl Med*. 2000;41:2089-97.
42. Jonkhoff AR, Huijgens PC, Versteegh RT, van Lingen A, Ossenkoppele GJ, Dräger AM, Teule GJJ. Radiotoxicity of 67-Gallium on Myeloid Leukemic Blasts. *Leuk Res*. 1995;19:169-174.
43. Ochakovskaya R, Osorio L, Goldenberg DM, Mattes MJ. Advances in Brief Therapy of Disseminated B-Cell Lymphoma Xenografts in Severe Combined Immunodeficient Mice with an Anti-CD74 Antibody Conjugated with 111 Indium, 67 Gallium, or 90 Yttrium. *Clin Cancer Res*. 2001;7:1505-1510.
44. Price EW, Orvig C. Matching Chelators to Radiometals for Radiopharmaceuticals. *Chem Soc Rev*. 2014;43:260-90.
45. Kampmeier F, Williams JD, Maher J, Mullen GE, Blower PJ. Design and Preclinical Evaluation of a 99mTc-Labelled Diabody of MAb J591 for SPECT Imaging of Prostate-Specific Membrane Antigen (PSMA). *EJNMMI Res*. 2014;4:13.
46. Tsionou MI, Knapp CE, Foley CA, Munteanu CR, Cakebread A, Imberti C, Eykyn TR, Young JD, Paterson BM, Blower PJ, Ma MT. Comparison of Macrocyclic and Acyclic Chelators for Gallium-68 Radiolabelling. *RSC Adv*. 2017;7:49586-49599.
47. Puncher MR, Blower PJ. Frozen Section Microautoradiography in the Study of Radionuclide Targeting: Application to Indium-111-Oxine-Labeled Leukocytes. *J Nucl Med*. 1995;36:499-505.
48. Kuo LJ, Yang L-X. Gamma-H2AX - a Novel Biomarker for DNA Double-Strand Breaks. *In Vivo (Brooklyn)*. 2008;22:305-9.
49. Franken NAP, Rodermond HM, Stap J, Haveman J, Bree C Van. Clonogenic Assay of Cells

in Vitro. *Nat Protoc*. 2006;1:2315-2319.
50. Del Monte U. Does the Cell Number 10^9 Still Really Fit One Gram of Tumor Tissue? *Cell Cycle*. 2009;8:505-506.

6 The Prostate Specific Membrane Antigen: Structure, Active Site and Interaction with Natural Substrates

The results in chapters 3, 4 and 5 indicate that there is an opportunity to re-design the THP-PSMA bioconjugate to have higher affinity for GCP(II)/PSMA. The following literature survey was conducted to inform this process and at the end of this chapter, my hypotheses for higher affinity variants of THP-PSMA will be presented. In this chapter, the major structural components of GCP(II)/PSMA will be described from the latest high-resolution crystal structures as well as the important interactions between GCP(II)/PSMA and its natural substrates. The interactions of inhibitors are also discussed, especially those used to determine the mechanism of enzymatic hydrolysis for GCP(II)/PSMA. The interactions that will be discussed govern the substrate's affinity and specificity. Of the two natural substrates N-acetyl-L-aspartyl-L-glutamate (NAAG) and poly-γ-glutamated folate, the latter has the most similar structure to the THP-PSMA bioconjugate that is the subject of optimisation. Therefore the interactions between GCP(II)/PSMA and poly-γ-glutamated folate will be focused on in this chapter.

6.1 Overview of GCP(II)/PSMA

The prostate specific membrane antigen (PSMA) is a transmembrane zinc-dependent metallo-enzyme formed of 750 residues, with a molecular weight of 110,000 daltons (1). The human PSMA gene was first cloned from the LNCaP prostate cancer cell line and is located in chromosome 11p11-12 (*2*). PSMA is known and referred to in the literature by multiple names: N-acetylated-α-linked acidic dipeptidase (NAALADase), folate hydrolase 1 (FOLH1), and glutamate carboxypeptidase II (GCP(II), EC 3.4.17.21) (*3*). This occurred due to the antigen being discovered independently in both prostate cancer, where it was named PSMA, and in the brain, where it was thought only to hydrolyse N-acetyl-L-aspartyl-L-glutamate (NAAG) and therefore named N-acetylated-α-linked acidic dipeptidase (NAALADase) (*4*). Separate names for this receptor prevailed until it was determined that these peptidases were in fact identical; found in multiple locations and had multiple functions. At this point, it was given the more general name glutamate carboxypeptidase II (GCP(II)) (*1*)(*3*).

Healthy human tissues that express GCP(II)/PSMA include the prostate gland (the cytoplasm and apical side of the epithelium surrounding prostatic ducts), the nervous system (astrocytes and Schwann cells), the kidney (proximal tubules) and the small intestine (jejunal brush border membranes) (*3*)(*5*)(*6*). The enzymatic activity of GCP(II)/PSMA is the cleavage of the terminal glutamate through the hydrolysis of a peptide bond; if a glutamate chain is present the

glutamates can be cleaved sequentially. GCP(II)/PSMA has two known natural substrates; N-acetyl-L-aspartyl-L-glutamate (NAAG) and poly-γ-glutamated folate. The structures of these compounds and their cleavage products are shown in figure 6.1. Note that in poly-γ-glutamated folate the glutamic acid chain is formed by a peptide bond between the side chain of one glutamic acid and the amino group of the next glutamic acid, rather than a traditional peptide backbone. GCP(II)/PSMA hydrolyses NAAG into glutamate and N-acetyl-aspartate (NAA) (*7*) and hydrolyses poly-γ-glutamated$_{(n)}$ folate into glutamate and poly-γ-glutamated$_{(n-1)}$ folate or folic acid (*8*). Kinetic studies have been used to determine the rate at which GCP(II)/PSMA can hydrolyse these compounds. The Michaelis constant (K_M) of NAAG was found to be 250 nM (*8*) (Michaelis constant (K_M) is equal to the concentration of the substrate when the rate is half of the maximum velocity). For poly-γ-glutamated folate the K_M was dependent on the number of glutamates in the poly-γ-glutamate chain. When only one cleavable glutamate was present the K_M was found to be 400-500 nM (*8*). The K_M value dropped to 50-100 nM with two cleavable glutamates and remained at this value for longer chain lengths (K_M was assessed with up to six cleavable glutamates) (*8*).

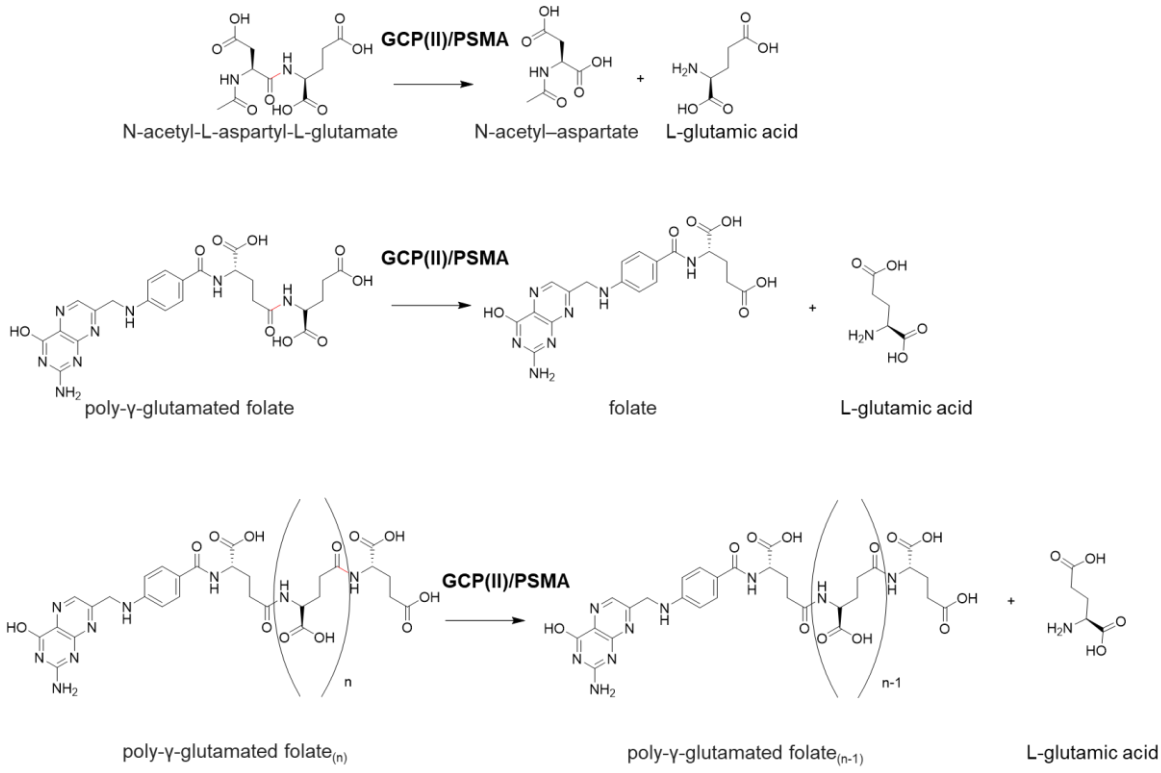

FIGURE 6.1: The structure of the natural substrates of GCP(II)/PSMA and their hydrolysis products. The cleaved bond is shown in red.

6.1.1 GCP(II)/PSMA in the Brain

NAAG is one of the three most prevalent neurotransmitters in the mammalian brain (*9*). The function of GCP(II)/PSMA in the brain in the glutamate signalling pathway has been well described and reviewed (*9*)(*10*), and so will not be discussed further here.

6.1.2 GCP(II)/PSMA in the Small Intestine

The cleavage of terminal glutamates from poly-γ-glutamated folate occurs in the small intestine, within the jejunal brush border. This is because poly-γ-glutamated folates present in food need to be hydrolysed to produce glutamate and folic acid before they can be transported in the blood and utilised by the body. Folic acid is integral to many metabolic processes in the body including DNA synthesis, DNA methylation and the formation of methionine (*2*). All of these processes are known to be important for cell proliferation. Glutamate, on the other hand, is a non-essential amino acid that can be synthesised by the body. It is an excitatory neurotransmitter in the central nervous system, and is also a precursor for the synthesis of many metabolites including δ-1-pyrroline-5-carboxylate, β-citrylglutamate, L-γ-glutamyl-L-cysteine, γ-aminobutyrate and glutathione (*11*).

6.1.3 GCP(II)/PSMA in the Prostate and Kidney

The role of GCP(II)/PSMA in the prostate and kidney is not fully understood, especially as neither NAAG, nor poly-γ-glutamated folate are present in the bloodstream under normal conditions. However, GCP(II)/PSMA does have receptor-like features, suggesting that GCP(II)/PSMA may be involved in transmembrane signalling or receptor-ligand interactions (*1*). These include its ability to undergo endocytic internalisation and the presence of a polyproline type II helix on its surface, which in other cells, is known to mediate protein-protein interactions (*1*). These functions, if confirmed, would give an explanation for the localisation of GCP(II)/PSMA at these sites and also further insight into its prevalence in prostate cancer (*1*)(*3*).

6.1.4 GCP(II)/PSMA in Prostate Cancer

GCP(II)/PSMA-expression levels are over one thousand times higher in malignant prostate cancer tissues than in normal/healthy tissues (*2*). GCP(II)/PSMA has also been detected in the neovasculature of a number of tumours including those of the kidney, bladder, thyroid, breast and colon (*12*)(*13*). In prostate cancer, GCP(II)/PSMA-expression level increases with cancer grade and the highest levels of expression are found in androgen-resistant prostate cancer (*14*).

This relationship suggests that GCP(II)/PSMA plays a role in cancer progression. However, biological mechanisms by which GCP(II)/PSMA aids malignant transformation or metastatic behaviour have not yet been determined (*15*). The expression of GCP(II)/PSMA is known to be negatively regulated by androgens, but its expression is increased by fibroblast, transforming, and epidermal growth factors (*16*). Increased GCP(II)/PSMA-expression has been shown *in vitro* to increase the metabolism of poly-γ-glutamated folates and folate uptake, and consequently proliferation in both physiological and low folate environments (*17*)(*18*). Blood typically contains folate but not poly-γ-glutamated folate, as this form is used for intracellular folate storage. However, in areas of necrosis poly-γ-glutamated folates could be released from dying cells. Therefore upregulation of GCP(II)/PSMA in prostate cancer and the neovasculature of other tumours may occur so that poly-γ-glutamated folates released from necrotic cells can be utilised. This additional folate could, in turn, increase the proliferation of the tumour (*2*). However, this is just a hypothesis; the physiological function of GCP(II)/PSMA in prostate cancer has not yet been determined and, as discussed above, it could also be upregulated on the cell surface because it provides a mechanism for transmembrane signalling.

6.1.5 GCP(II)/PSMA Internalisation

Membrane-bound GCP(II)/PSMA undergoes spontaneous internalisation, with 60% of the GCP(II)/PSMA internalised every hour (*19*). However, the internalisation rate can be increased by binding the monoclonal antibody J591 which increases the internalisation rate in a dose-dependent manner, to a maximum of three times the rate of spontaneous internalisation (*19*). Confocal microscopy and electron microscopy have been used to show that GCP(II)/PSMA-[mAb] complexes are endocytosed through clathrin-coated pits (*2*). The protein is then recycled to the cell membrane by the recycling endosomal compartment (REC) or transported to the lysosomes where it is degraded (*2*). The bound ligands may also be retained in the lysosomal compartments or may be released within the cell, where they could redistribute within the cell, or diffuse out of it (*15*). Conversely, small molecule substrates and inhibitors of the active site of GCP(II)/PSMA do not alter the rate of internalisation, showing that internalisation and enzymatic function are independent processes (*2*).

6.1.6 Structure of GCP(II)/PSMA

GCP(II)/PSMA is a typical type II transmembrane protein with three main parts: a short N-terminal cytoplasmic tail; a single helix that spans the membrane; and a large extracellular region. The N-terminal of the protein is important for internalisation and recycling of

GCP(II)/PSMA, through clathrin-coated pits (*2*). The membrane-spanning helix fixes the protein in the membrane and connects the intracellular and extracellular parts. It has been shown that GCP(II)/PSMA dimerises through interlinking the extracellular regions of two GCP(II)/PSMA enzymes and that it only has hydrolytic activity in this form (*1*). The extracellular region of GCP(II)/PSMA resembles the transferrin receptor and has 54% homology with it (*2*). Like transferrin, GCP(II)/PSMA is heavily glycosylated on nitrogen and oxygen sites. Its ten nitrogen glycosylation sites have been shown to be vital for: enzymatic activity, targeting GCP(II)/PSMA to the membrane and ensuring correct protein folding and stability (*20*)(*21*). Interestingly, the glycosylation profile varies between prostate cancer cell lines suggesting that different sugar epitopes may affect the metastatic potential of GCP(II)/PSMA-expressing prostate cancer (*2*).

The extracellular domain of GCP(II)/PSMA produces the enzymatic function of the protein and is comprised of three individual domains: the protease domain (domain I); the apical domain (domain II); and the C-terminal (domain III). All three are required for substrate binding and processing as residues from each domain contribute to the binding cavity and active site. An overview of the structure of GCP(II)/PSMA is shown in figure 6.2.

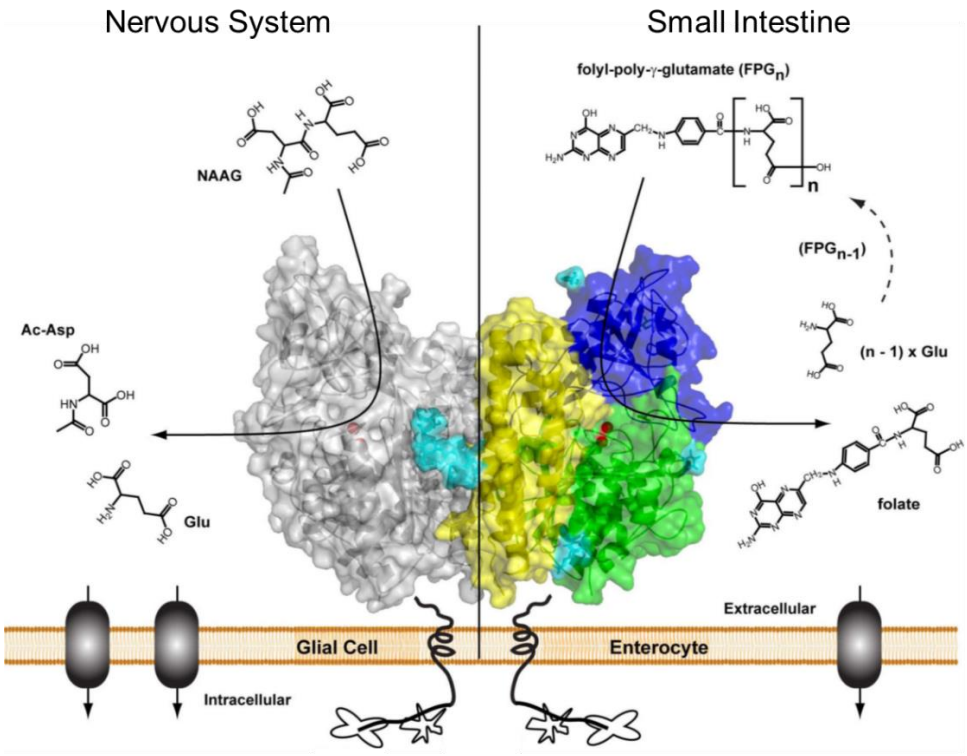

FIGURE 6.2: The overall structure of GCP(II)/PSMA dimer showing the short N-terminal cytoplasmic tail, a single membrane-spanning helix and a large extracellular region which is divided into 3 domains: domain (I) is shown in green, domain (II) is shown in dark blue and, domain (III) is shown in yellow. The zinc ions in the active site are represented as red spheres and the N-linked sugar moieties are coloured cyan. Reproduced with permission from (3).

6.2 Overview of the Active Site of GCP(II)/PSMA

GCP(II)/PSMA is a protease which cleaves terminal glutamates from its natural substrates NAAG and poly-γ-glutamated folate. The nomenclature used for the amino acid residues in protease substrates is P1 for the residue N-terminal to the cleavage site and P1' for the residue C-terminal to the cleavage site (*22*). The values of P then increase towards the N terminus and the values of P' increase towards the C terminus, as shown in figure 6.3. The protease binding pockets, which accommodate each residue, are named S1 and S1' at each side of the cleaved bond and increase in the same manner as the values for P or P'. For the natural substrates of GCP(II)/PSMA, NAAG and poly-γ-glutamated folate, the P1' residue is always the terminal glutamate and interacts with the S1' pocket. The other side of the cleavable peptide bond is the P1 residue which interacts with the S1 pocket (*1*). Figure 6.4 identifies the P1 and P1' regions of GCP(II)/PSMA's natural substrates and a number of its known inhibitors.

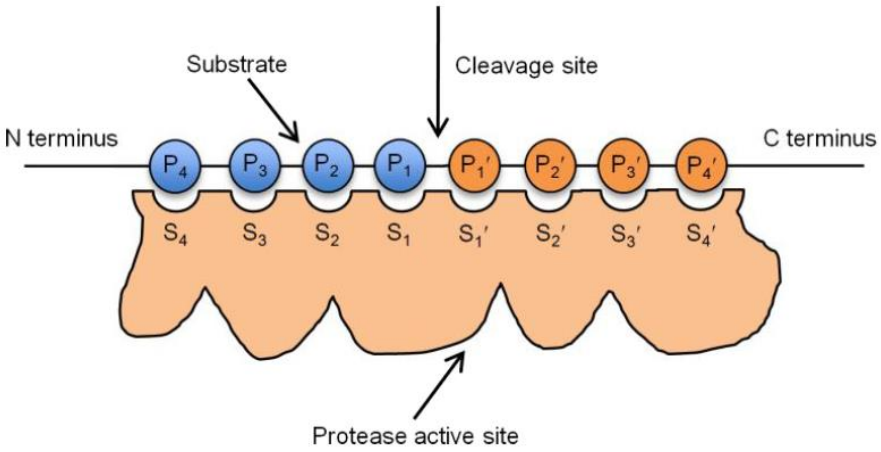

FIGURE 6.3: Nomenclature for naming substrate residues and binding pockets. Reproduced with permission from (22).

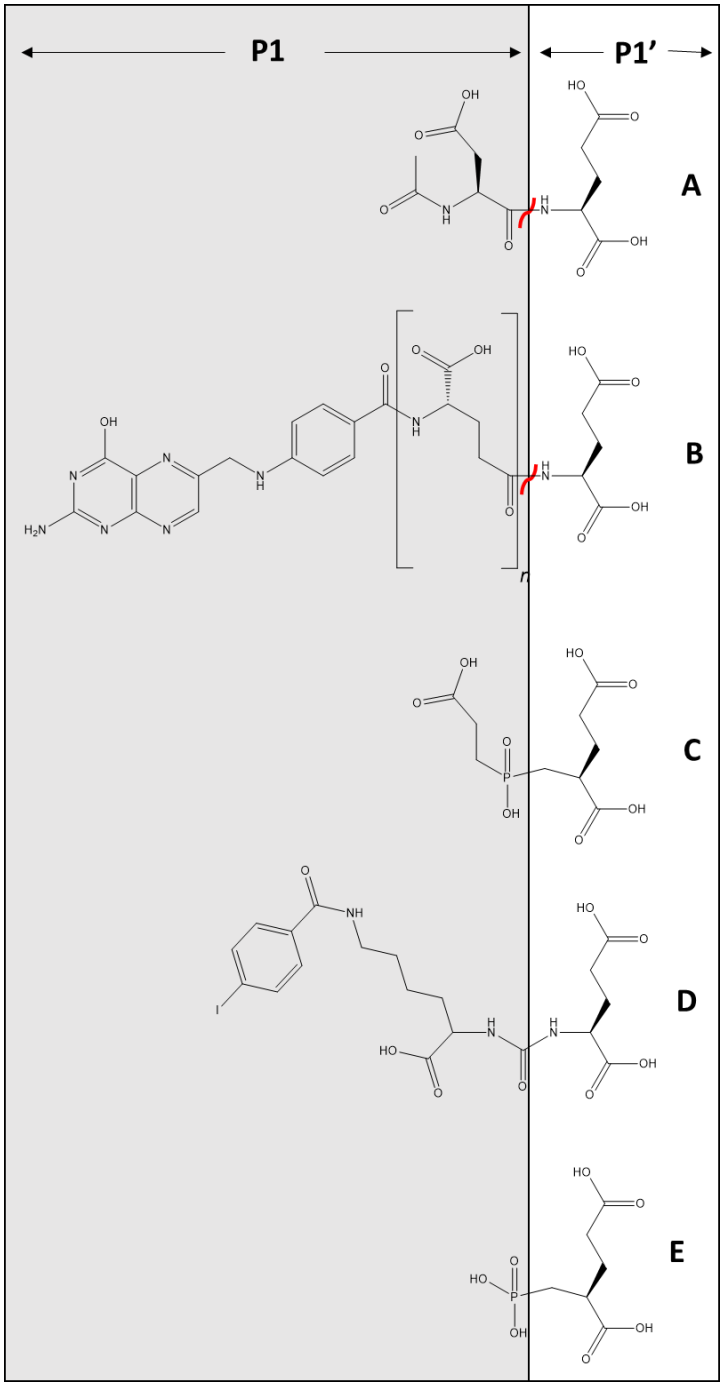

FIGURE 6.4: The structures of the natural substrates and inhibitors of GCP(II)/PSMA and their P1 and P1' regions. The red line denotes the bond that is broken through hydrolysis. (A) N-acetyl-L-aspartyl-L-glutamate (NAAG), (B) Poly-γ-glutamated folate, (C) Phosphinate-based inhibitor SPE ((2S)-2-{[(2-carboxy-ethyl)-hydroxy-phosphinoyl]methyl}-pentanedioic acid), (D) Urea-based inhibitor DCIBzL ((S)-2-(3-((S)-1-carboxy-(4-iodobenzamido)pentyl)ureido)pentanedioic acid), (E) Phosphonate-based inhibitor without a P1 region 2-PMPA (2-(phosphonomethyl)pentanedioic acid).

The binding pocket for GCP(II)/PSMA consists of a 20 Å entrance tunnel leading to the active site of the enzyme at the base of the cavity. The key active site components are: two zinc ions; an activated water molecule (or OH^-) which bridges the zinc ions; and a catalytic glutamic acid residue Glu424 which acts as a proton shuttle during hydrolysis. The importance of Glu424 has been evaluated with mutagenesis studies (*23*) where Glu424 was replaced with an alanine residue. This caused complete loss of hydrolytic activity, demonstrating that Glu424 is vital for the enzymatic mechanism (*23*). Deeper into the cavity, past the active site, is the S1' pocket which is specific for terminal glutamate residues. An overview of the structure is shown in figure 6.5. There is evidence that the hydrolysis of peptide bonds by GCP(II)/PSMA proceeds through an induced-fit mechanism. This requires that the substrate induces changes in the conformation of the enzyme upon binding and that this rearrangement stabilises a transition state with a lower activation energy for bond cleavage, allowing hydrolysis to occur. Evidence supporting an induced-fit mechanism will be discussed throughout this chapter.

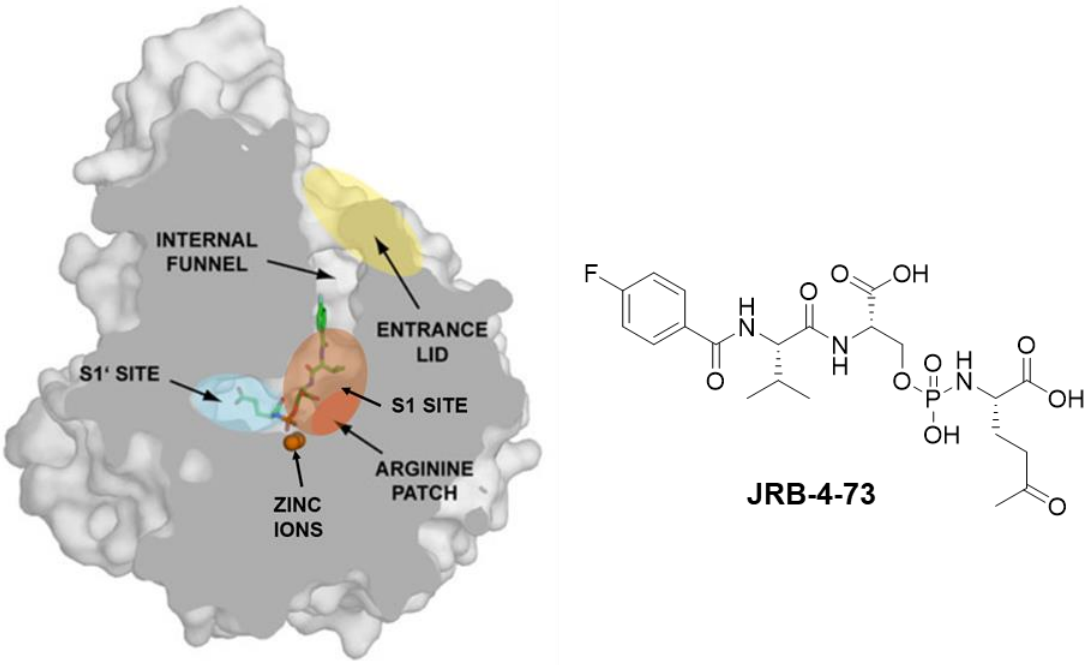

FIGURE 6.5: An overview of the substrate binding site of GCP(II)/PSMA showing the S1' site, S1 site, zinc ions, arginine patch, internal funnel and entrance lid. The inhibitor inside the enzyme is JRB-4-73. Modified with permission from (24).

6.2.1 Crystallographic Studies of the Active Site

High-resolution X-ray crystal structures (1.65-2.4 Å) of GCP(II)/PSMA are available and provide detailed information about the active site, S1, and S1' pockets of this enzyme. However, it should be noted that before these high-resolution crystal structures were obtained, the best available models suggested different substrate-pocket binding, and therefore a different mechanism of action (*25*)(*26*). Alongside this a number of different hydrolysis mechanisms have been proposed for GCP(II)/PSMA (*1*)(*27*) and consequently there continues to be some confusion in the literature. Here only the latest high-resolution structures will be discussed alongside the quantum and molecular mechanics (QM/MM) modelling that was used to propose a hydrolysis mechanism.

High-resolution crystal structures of GCP(II)/PSMA have been obtained ligand-free (*28*), and in complex with a number of substrates and inhibitors (*29*)(*30*)(*31*). Combining these findings with mutagenesis studies (*23*) has provided insight into how natural substrates and inhibitors sit within the enzyme and the mechanism of hydrolysis itself. There are four key crystal structures of GCP(II)/PSMA which have provided this insight: 1) the unbound state of GCP(II)/PSMA (*28*); 2) GCP(II)/PSMA in complex with a urea-based inhibitor DCIBzL (((S)-2-(3-((S)-1-carboxy-(4-iodobenzamido)pentyl)ureido)pentanedioic acid), which acts as a mimic of the cleavable peptide bond (*30*); 3) GCP(II)/PSMA in complex with SPE ((2S)-2-{[(2-carboxy-ethyl)-hydroxy-phosphinoyl]methyl}-pentanedioic acid), a phosphinate analogue of NAAG. The phosphinate group maintains its tetrahedral conformation when it binds the zinc ions of the active site mimicking the substrate transition state (*23*)(*31*); 4) a mutant of GCP(II)/PSMA where the catalytic residue Glu424 (E424) was replaced with an alanine (completely inhibiting its catalytic activity), in complex with the natural substrate NAAG. The chemical structures of these substrates and inhibitors are shown in figure 6.4.

These crystal structures all confirm the presence of the two zinc ions in the active site. Zn_1 is coordinated by His377 and Asp453. Zn_2 is coordinated by Glu425 and His553. The two zinc ions are bridged by Asp387 (*23*)(*28*)(*30*)(*31*)(*32*). Interestingly, the Asp387-Pro388 peptide bond is in the less common cis conformation, a feature often found in other zinc metalloenzymes (*1*). Mutagenesis studies have shown that if any of these five residues that bind the two zinc ions are substituted for alternative residues, loss of enzymatic activity occurs (His377 for Ala, Asp387 for Glu, Asp453 for Asn, Glu425 for Gln and His553 for Ala) (*32*). When no substrate is bound, the zinc ions are 3.3 Å apart and tetrahedrally coordinated to these residues plus a hydroxyl group (OH^-) which bridges the two zinc ions symmetrically (*28*). There has been some debate as

to whether a hydroxyl group or an activated water molecule bridges the two zinc ions; however, the shortened Zn-O bond lengths (2.01-2.03 Å (*28*)) compared to standard Zn-OH_2 distances (2.2-2.4 Å (*23*)) indicate it is a hydroxyl group. This has been confirmed through QM/MM calculations which revealed that as soon as a water molecule bridges the two zinc ions, one of its protons would be abstracted by the Glu424 residue (*23*). As the enzyme performs bond cleavage through hydrolysis, which is typically acid- or base-catalysed, it is logical that this hydroxyl molecule plays a key part in the mechanism.

In the mutant GCP(II)/PSMA(E424A) with NAAG in the active site, the hydroxyl molecule (OH^-) remains bound symmetrically between the two zinc ions, and the oxygen of the carbonyl group of the cleavable peptide bond interacts with Zn_1 (*23*). This same carbonyl group is both orientated and polarised by a hydrogen bond between it and a hydroxyl group on the side chain of the Try552 residue, which itself is polarised by the nearby positively charged Arg210 residue. At the other end of the cleavable peptide bond, the amide is shown to form a hydrogen bond to the backbone carbonyl oxygen between Gly518 and Asn519. In order to study the interactions of the Glu424 residue GCP(II)/PSMA, the urea inhibitor of DCIBzL can be used as a substrate mimic (*30*). These inhibitors utilise a urea bond in place of the peptide bond which makes them unsusceptible to cleavage by the enzyme. This allows them to be crystallised with the fully active enzyme forming GCP(II)/PSMA-[DCIBzL]. When the urea inhibitor sits within the active site of GCP(II)/PSMA, all of the interactions seen for GCP(II)/PSMA(E424A)-[NAAG] are conserved but in addition the N-H of the urea, which sits in the same place as the N-H of the peptide bond in the natural substrate, forms a hydrogen bond to Glu424. This provides further evidence that Glu424 acts as a proton shuttle, delivering a proton from the water molecule to this amine during hydrolysis.

In the crystal structure of GCP(II)/PSMA(E424A)-[NAAG], the cleavable peptide bond remained planar, because without the Glu424 residue, it could not pass into the transition state required to break the bond. This would not be the case if NAAG entered the fully functional GCP(II)/PSMA; instead of remaining planar, a tetrahedral intermediate will form. It is well known that acid/base-catalysed hydrolysis of peptide bonds proceeds through sp^3 hybridisation at the carbonyl carbon and therefore the active site of GCP(II)/PSMA must allow for a tetrahedral transition state. An understanding of how the active site changes when a tetrahedral intermediate is formed can be obtained from studying how inhibitors that mimic this transition state sit within the active site. A phosphonate group is a good mimic, as it will maintain its tetrahedral geometry upon binding and has two oxygens, one that can mimic the carbonyl oxygen of the peptide bond and one that can mimic the hydroxyl (OH^-) as it attacks the carbon

of the carbonyl. The crystal structure of GCP(II)/PSMA complexed with SPE (figure 6.4) shows that the phosphonate group displaces the bound water molecule and that it binds the two zinc ions using both oxygen groups. Another important observation is that that these two oxygen atoms sit in very similar positions to the carboxyl oxygen of the natural substrate and the oxygen of the hydroxyl (OH^-). By superimposing the GCP(II)/PSMA-[SPE] crystal structure with the GCP(II)/PSMA(E424A)-[NAAG] crystal structure as shown in figure 6.6, the key differences between the initial binding mode (Michaelis complex) and the phosphonate mimic of the transition state can be seen (*23*). The key differences observed are: in the GCP(II)/PSMA-[SPE] crystal structure the carbonyl carbon centre (mimicked by the phosphorus atom in SPE) is moved 1 Å towards Zn_2 and the nitrogen atom (mimicked by a carbon atom in SPE) is moved 0.7 Å towards the catalytic Glu424 residue (*23*). Such changes could not occur if the peptide bond remained planar and so it must be stabilised in a resonance form which allows the bonds to lengthen and twist. Such stabilisation comes from the hydrogen bond between the oxygen of the carbonyl and the Try552 residue (which itself is polarised by adjacent residues). The change in the substrate's conformation is complemented by changes in the active site itself with the zinc ions moving away from each other (the distance increases from 3.3 Å to 3.7 Å) and the histidine residues His377 and His533 moving with them (*23*). The changes to the active site stabilise the transition state and consequently catalyse hydrolysis. These are therefore one aspect of the induced-fit mechanism.

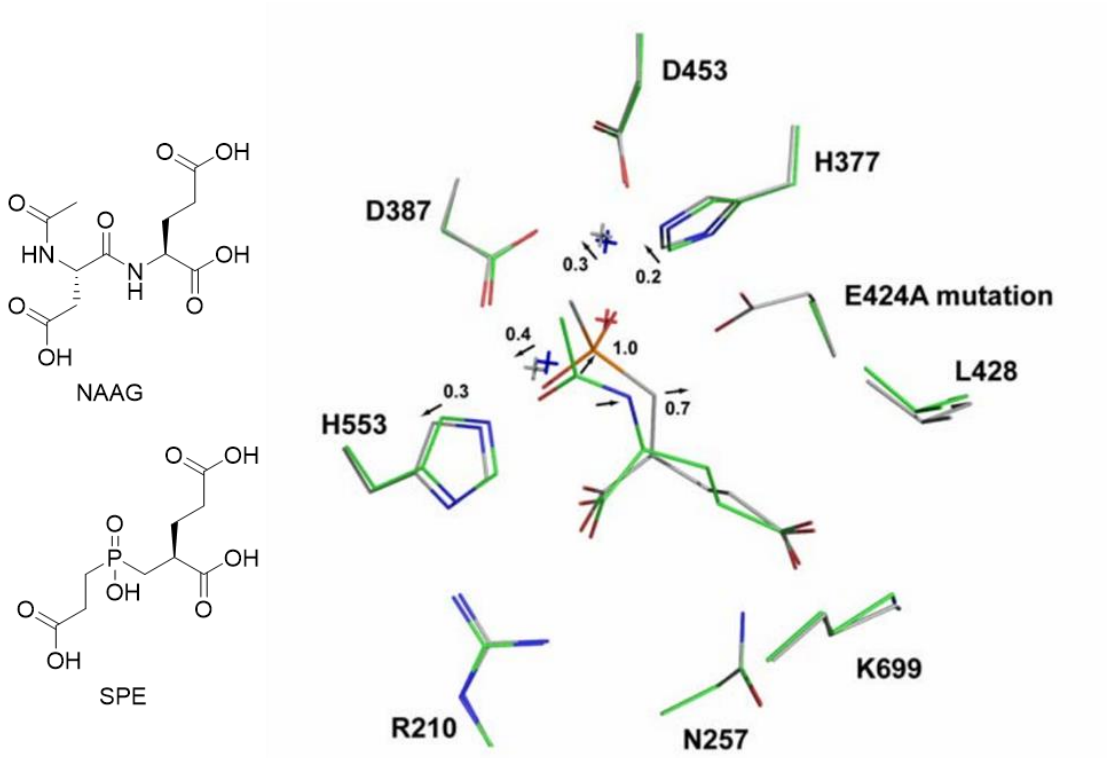

FIGURE 6.6: The structures of the GCP(II)/PSMA(E424A)-[NAAG] complex superimposed on the GCP(II)/PSMA-[SPE] complex on corresponding Cα atoms. Atoms are shown as: carbon (green, GCP(II)/PSMA(E424A)-[NAAG] complex; grey, GCP(II)/PSMA-[SPE] complex), nitrogen (blue), oxygen (red), and phosphate (orange). The Zn ions are shown as blue (GCP(II)/PSMA(E424A)-[NAAG] complex) and grey (GCP(II)/PSMA-[SPE] complex) crosses; the hydroxyl molecule (OH^-) is shown as a red cross. The direction of movement of GCP(II)/PSMA side chains and the substrate reaction intermediate is indicated by arrows with distances shown in Å. The P1 portion of the substrate/reaction intermediate (or transition state) was omitted for clarity. This figure is reproduced with permission from the supplementary information of (23).

6.2.2 Enzymatic Mechanism

The inferences that can be made about the enzymatic mechanism of GCP(II)/PSMA, from the four crystal structures discussed, have been further combined with QM/MM calculations to characterise the transition states (*23*). There are four equilibrium structures revealed by these models: the Michaelis complex (substrate bound in the active site); the first transition state; the reaction intermediate; and the second transition state (determined to be the rate-limiting step from calculated energy barriers). Each of these intermediates are shown in figure 6.7. All of these equilibrium structures confirm the important role of the two zinc ions, the hydroxyl molecule and the glutamic acid residue Glu424.

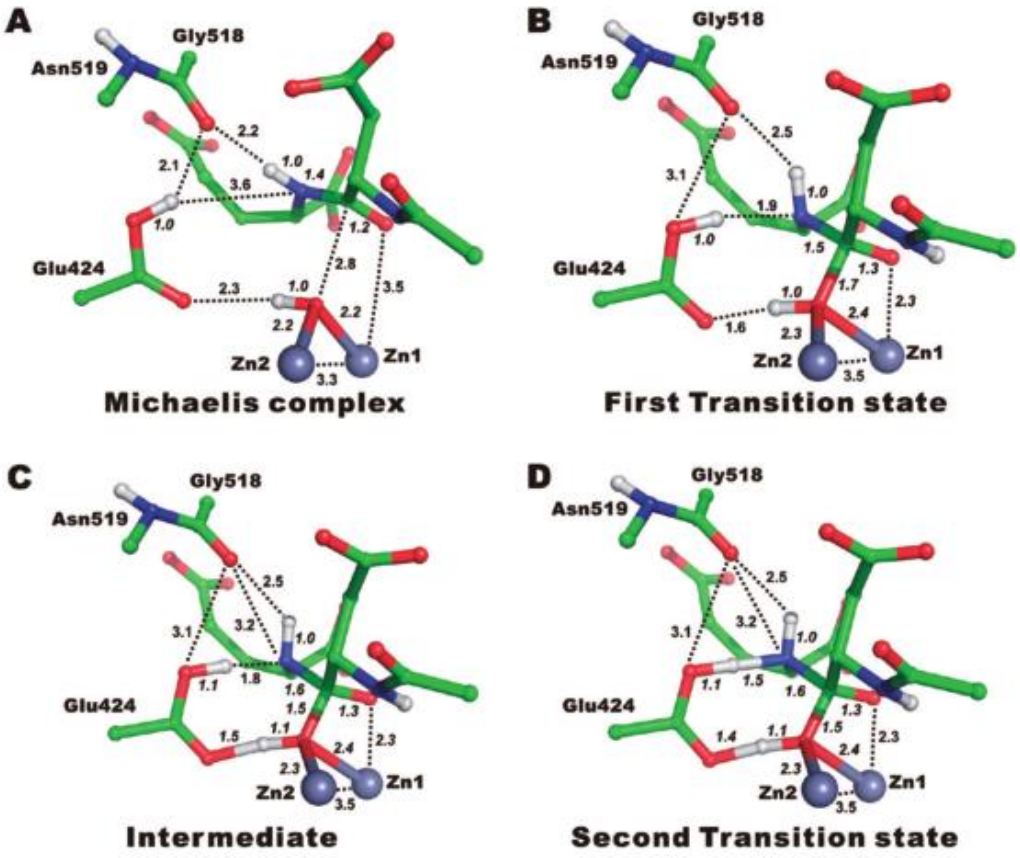

FIGURE 6.7: The QM/MM equilibrium structures of (A) the Michaelis complex (substrate bound in the active site), (B) the first transition state, (C) the reaction intermediate, (D) the second transition state, leading to the products. Reproduced with permission from (23)

The Michaelis complex shown in figure 6.7A has the same interactions as seen for GCP(II)/PSMA-[DCIBzL] and GCP(II)/PSMA(E424A)-[NAAG]. The key interactions can be summarised as follows: 1) a weak interaction between the carbonyl oxygen and $Zn_{(1)}$; 2) the same carbonyl oxygen, hydrogen bonding to the Try552 which controls its orientation; 3) the formation of a hydrogen bond between the N-H group of the peptide bond and the carbonyl oxygen between Gly518 and Asn519; 4) the Glu424 aligning itself so that its deprotonated oxygen is stabilizing the OH^- bridging the zinc ions.

In the first transition state (figure 6.7B) the key difference is that the carbonyl carbon adopts a tetrahedral geometry as it undergoes nucleophilic attack by the hydroxyl molecule (OH^-). This tetrahedral conformation at the carbonyl carbon creates increased negative charge on the carbonyl oxygen which is stabilised by the zinc ions and the catalytic glutamic acid. At the other end of the peptide bond, the conformation also shifts; the nitrogen atom moves towards the proton on the Glu424 residue. The reactive intermediate is shown in figure 6.7C and was identified by calculating the local energy minima between the two transitions states. Here the other end of the peptide bond moves into tetrahedral conformation as the lone pair on the nitrogen points towards the proton on the Glu424, ready for a subsequent N-H bond to form. This tetrahedral conformation at the nitrogen, is stabilised by the carbonyl between Gly518 and Asn519. In the second and final transition state, shown in figure 6.7D, a bond forms between the proton of Glu424 and the nitrogen atom. This bond formation will cause the subsequent cleavage of the peptide bond, which in this second transition state is no longer planar and has increased in length from 1.4 to 1.6 Å.

These transition states have provided enough evidence for a detailed reaction mechanism to be proposed for the hydrolysis of NAAG. This is shown in figure 6.8. Once NAA and glutamate have been formed, the NAA is pulled out of the active site by the positive charge of the arginine residues lining the S1 pocket, and the glutamate can exit the active site via a small hole at the back of the S1' pocket (*1*)(*15*)(*33*). This mechanism can also be applied to the serial removal of glutamate from poly-γ-glutamated folates as shown in figure 6.9 and figure 6.10.

It is not only the interaction described here that contributes to the induced-fit mechanism; the S1' pocket and to a lesser extent the S1 pocket also change conformation to aid binding, stabilise the transition state and consequently increase the rate of hydrolysis (*1*)(*31*). The structure of the S1 and S1' pockets, and their substrate recognition properties through the "glutarate sensor" within the S1' pocket and the arginine patch within the S1 pocket will be discussed in the next sections.

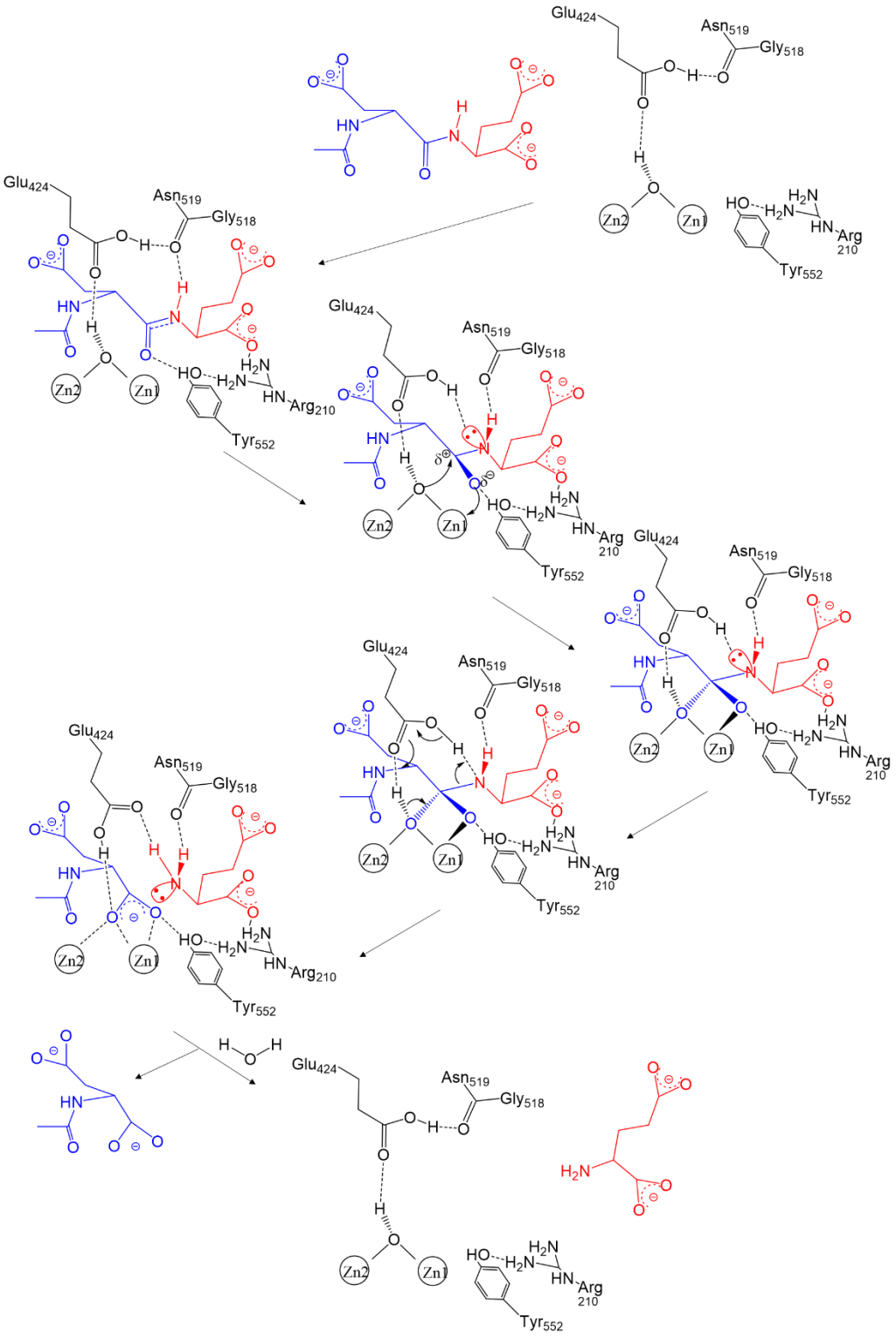

FIGURE 6.8: The GCP(II)/PSMA reaction cycle with NAAG. This cycle depicts important steps/structures throughout the reaction pathway. The suggested reaction mechanism was obtained by QM/MM calculations (23).

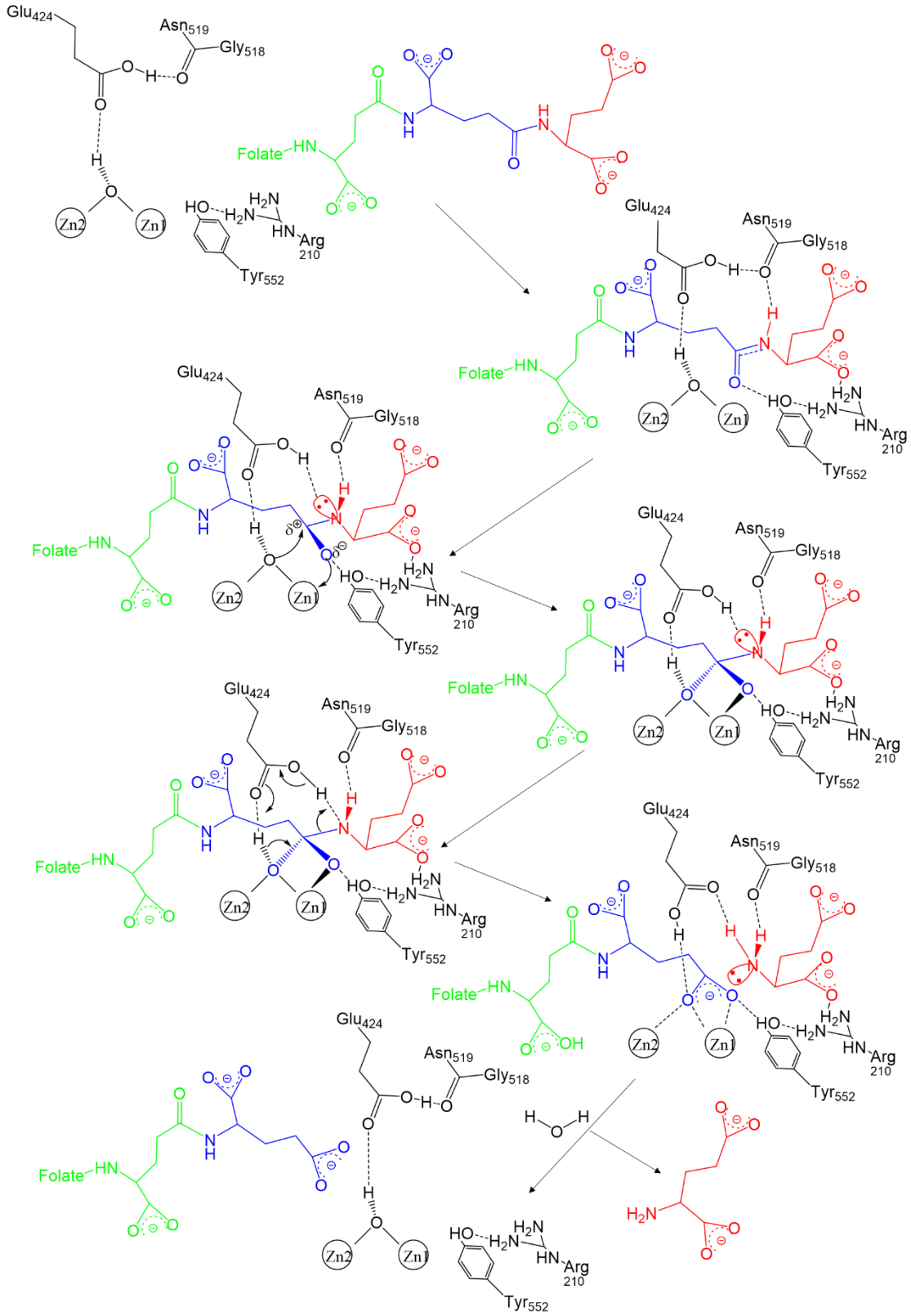

FIGURE 6.9: The GCP(II)/PSMA reaction cycle with poly-γ-glutamated$_{(n=2)}$ folate. This cycle depicts important steps/structures throughout the reaction pathway. The suggested reaction mechanism was obtained by QM/MM calculations (23).

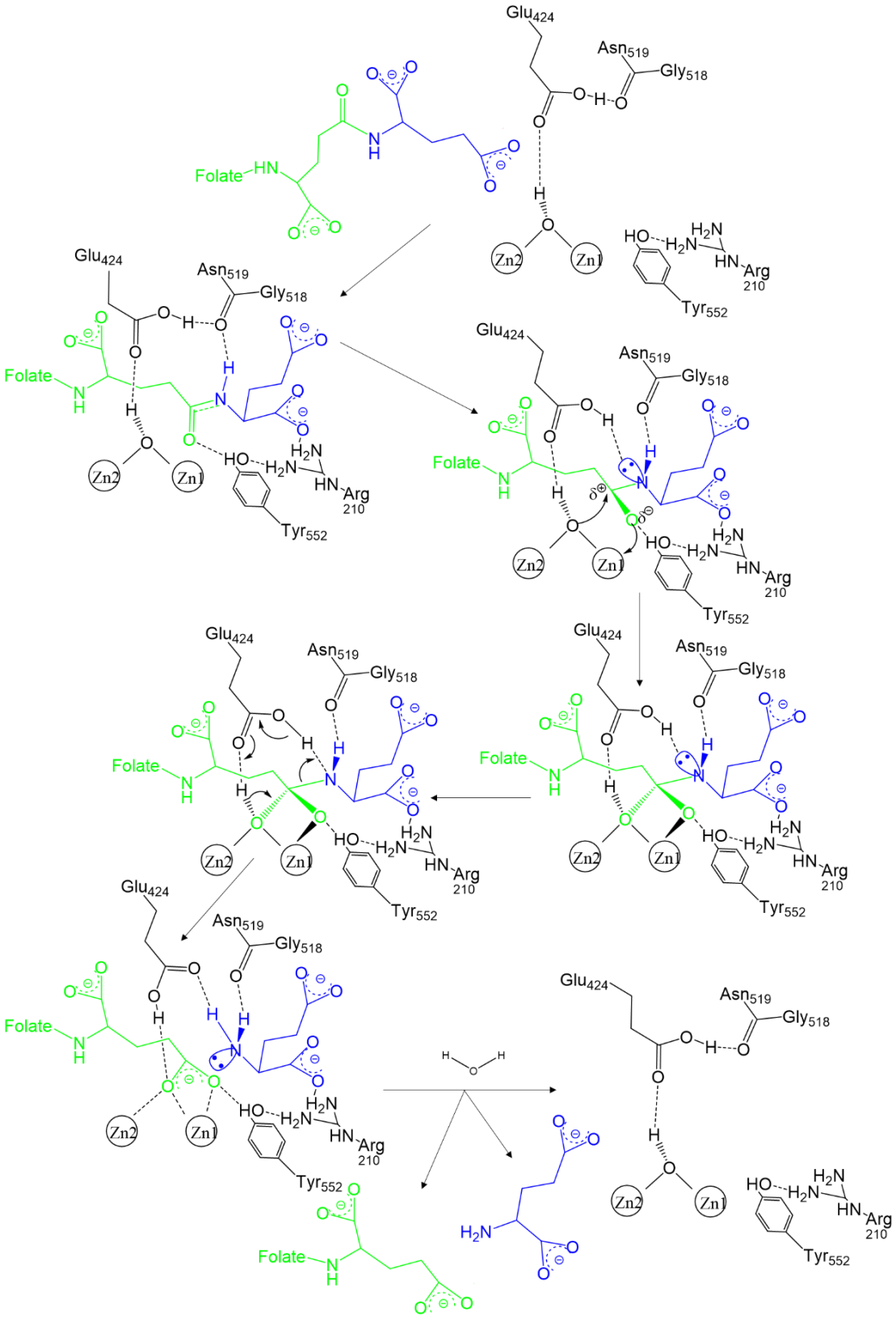

FIGURE 6.10: The GCP(II)/PSMA reaction cycle with poly-γ-glutamated$_{(n=1)}$ folate. This cycle depicts important steps/structures throughout the reaction pathway. The suggested reaction mechanism was obtained by QM/MM calculations (23).

6.3 Detail of S1' Pocket

The S1' pocket has been fully characterised through crystallographic studies (*1*). The important residues that interact with the P1' glutamate are Arg210, Tyr552, Tyr700, Lys699, and Asn257. Glutamate bound to the active site is shown in figure 6.11. Arg210, Tyr552 and Tyr700 all interact with the C-terminal carboxylate group of the glutamate rather than its side chain. Arg210 forms a strong ion pair between its positive charge on its guanidinium moiety and the negative charge on the substrate's carboxylate. The two tyrosine residues, Tyr552 and Try700, form hydrogen bonds to the substrate from their hydroxyl groups. Lys699 and Asn257 interact with the side chain of the glutamate, with Lys699 forming a salt bridge (a hydrogen bond and an electrostatic interaction between two ionised sites) and Asn257 forming a hydrogen bond. The majority of these residues are part of domain (II) but residues Lys699 and Try700 are an exception (*34*). These are part of domain (III) and also a series of residues (692-704) which have a different structure when the S1' pocket is substrate-free compared to when glutamate or a glutaric acid is bound in the pocket. For this reason, this series of residues (692-704) has been termed the "glutarate sensor". The choice of the name "glutarate" sensor rather than glutamate sensor was chosen by the original paper's author because this interaction does not require the presence of the amine group of a glutamic acid (glutamate) and so it was named accordingly (*1*). However, it is important to remember that for cleavage to occur there must be a glutamate in the S1' position.

When the S1' pocket is unoccupied the 692-704 chain forms flexible loops with multiple conformations, characterised by weak electron density in the crystal structure (*1*)(*28*). When this happens, a space is created between the active site and the main cup of the GCP(II)/PSMA dimer. When a substrate is bound this region forms a hairpin structure (strand 692-695, turn, strand 699-704) named the β15/β16 hairpin, which closes this gap, and Lys699 and Try700 bind directly to the glutamate/glutarate substrate as described above. There are significant structural changes between the bound and unbound state with the position of Tyr700 moving 4.7 Å and other residues in the chain moving as much as 7.6 Å. The two different positions of the sensor can be seen in figure 6.12. This hairpin region is directly involved in the specific binding of glutamate, demonstrating another attribute of the induced-fit mechanism.

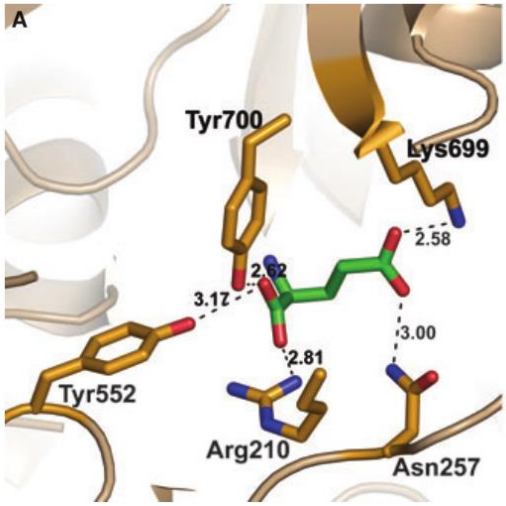

FIGURE 6.11: The binding mode of cleaved glutamate in the S1' portion of the GCP(II)/PSMA binding pocket. Reproduced with permission from (34).

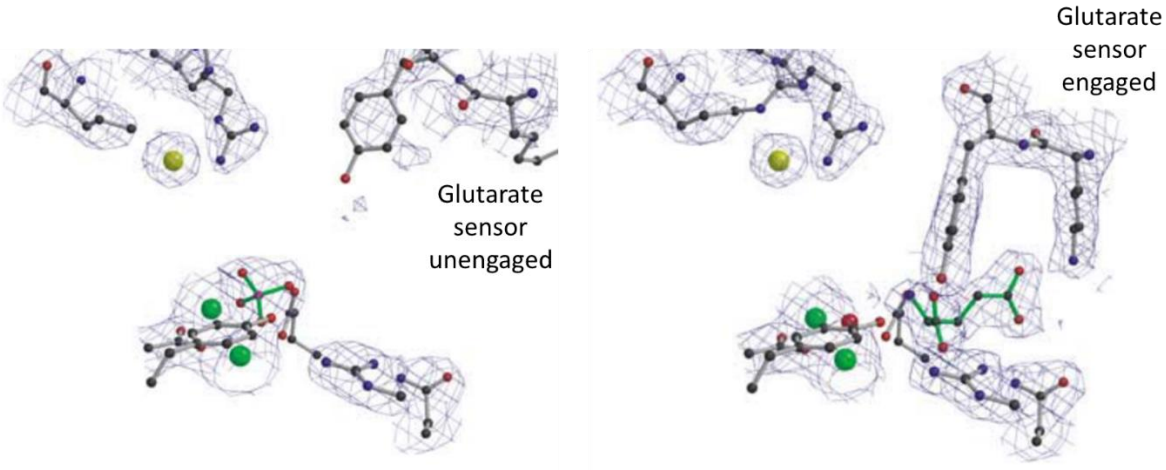

FIGURE 6.12: The two positions of the "glutarate sensor", the first when phosphate is within the active site and the second when glutamate is docked in S1'. Reproduced with permission from (1).

The "glutarate sensor" is also likely to play a role in the release of glutamate from the active site, via a small hole in the back of the S1' pocket. Such an exit route is of particular importance for the natural substrate poly-γ-glutamated folates. In this structure, there are multiple glutamates that could be cleaved sequentially from the substrate, and it would be inefficient to require the release of the cleaved poly-γ-glutamated$_{(n-1)}$ folate followed by the glutamate through the entrance tunnel before the poly-γ-glutamated$_{(n-1)}$ folate could re-bind the active site. Instead it has been proposed that the hole formed when the "glutarate sensor" (692-704 residue series) is disengaged from the S1' pocket would allow the cleaved terminal glutamate to pass out of the enzyme, and thus the poly-γ-glutamated$_{(n-1)}$ folate can move into the active site directly after cleavage and the next glutamate in the chain can be cleaved. This release mechanism would

require the hairpin to be able to discriminate between the binding of the natural substrates and the hydrolysis products, engaging this loop with the substrate and releasing it with the product. Evidence supporting the hypothesis that the enzyme can differentiate between the natural substrates and their hydrolysis products can be found by looking at differences in inhibition and enzymatic rate. The IC_{50} inhibition value for glutamate is in the micromolar range (30 μM (*35*)) whereas the K_M values for the natural inhibitors are in the nanomolar range (NAAG 250 nM, poly-γ-glutamated folates 50- 500 nM (*7*)(*8*)) showing that glutamate alone does not bind the active site as strongly as the natural substrates. This implies that although the interaction of the "glutarate sensor" with cleaved glutamate is observed in the crystal structure, it is not as strong as when the substrate also binds the zinc ions in the active site, probably due to the conditions required for crystallisation. Additional evidence to support this comes from the difference in IC_{50} values between 2-PMPA and glutamate. PMPA has a very similar structure to glutamate, but with an additional zinc ion binding phosphonate moiety (figure 6.4). This causes a dramatic improvement in affinity with the IC_{50} value dropping to just 0.3 nM (*35*). This implies that the GCP(II)/PSMA can discriminate between 2-PMPA and glutamate and that this is governed by the interaction with the zinc ion.

The important residues in the structure of the S1' pocket have been corroborated by a site-directed mutagenesis study (*34*). This showed that the S1' pocket is vital for high affinity substrate or inhibitor binding and that Arg210 is the most important residue within this pocket (figure 6.11). This is because it interacts directly with the carboxylate of the C-terminal of the glutamate and maintains the S1' pocket's conformation by controlling the positioning of the Tyr552 side chain. The importance of the S1' pocket in controlling affinity was also confirmed by studies where the P1' part of the inhibitor was changed, which caused 100-1000 fold decreases in binding affinity (*36*). From these studies it can be concluded that the P1' moiety is very sensitive to structural changes and it is the feature primarily responsible for tight GCP(II)/PSMA binding (*31*). Further studies have shown that the chirality of the glutamate residue is also crucial for high affinity binding, with L- glutamates being preferred over D-glutamates (*31*)(*37*)(*38*).

6.4 Detail of S1 Pocket

6.4.1 The Arginine Patch and the 'Binding' and 'Stacking' Conformations of the Arg536 Residue

The residues of the S1 pocket that interact with the substrate are Asn519, Arg534, Arg463 and Arg536 (*1*)(*31*)(*34*). The arginine residues form a positively charged area within the S1 pocket named "the arginine patch" which is responsible for the preference of GCP(II)/PSMA for acidic residues in the P1 position (*28*). A chloride ion is found within this arginine patch, and crystal structures show that it fixes the position of the Arg534 and Arg463 residues through ionic interactions (*28*) as shown in figure 6.13. Experiments where hydrolytic activity was measured under different chloride concentrations, showed activity was Cl^- dependent (*4*), and so it is believed that this chloride ion is also essential for enzymatic activity. When a natural substrate is present within the S1 pocket, the Asn519 and Arg534 form hydrogen bonds to the carboxylate oxygen of the substrate. This is the key interaction that determines affinity for the S1 pocket. However, there is also the potential for an additional hydrogen bonding interaction between Arg536 and the carboxylate oxygen to occur, which increases affinity further. This happens when the orientation of Arg536 changes from the "stacking" to the "binding" position (*31*). The change of preference from the stacking to the binding position requires the adjacent Arg463 to be repositioned by 2 Å, through interaction with a suitably positioned carboxyl oxygen on the substrate, which in turn prevents Arg536 from adopting the "stacking" conformation through steric hindrance. The "binding" position requires a 4.5 Å shift of the Arg536 residue's guanidinium group, which is stabilised by the S1 bound chloride atom. When in this "binding" position the Arg536 is able to form two hydrogen bonds to the γ-carboxylate of the P1 substrate. Substrates that promote the "binding" position of Arg536 by interacting with the Arg463 residue have significantly higher affinity than those which do not. It is claimed that this rearrangement is responsible for the 100-fold difference in IC_{50} between MPE (a phosphonate transition-state analogue of poly-γ-glutamated folate) and EPE (a phosphonate transition-state analogue of γ-glutamyl-glutamate) (0.12 ± 0.03 nM and 14.0 ± 4.2 nM respectively) (*31*). The structures of these two compounds are shown in figure 6.14.

The S1 pocket has been shown to accommodate more substrate diversity than the S1' pocket using both substrate inhibitor binding and mutagenesis studies (*34*). This includes variation in stereochemistry. However, it is favourable to have an acidic residue (either aspartic acid or glutamic acid) in the P1 position due to their interactions with the arginine patch (*34*). These

same studies also suggest that S1 interactions do not affect the affinity as strongly as S1' but instead are more important in controlling specificity and substrate turn-over (*34*).

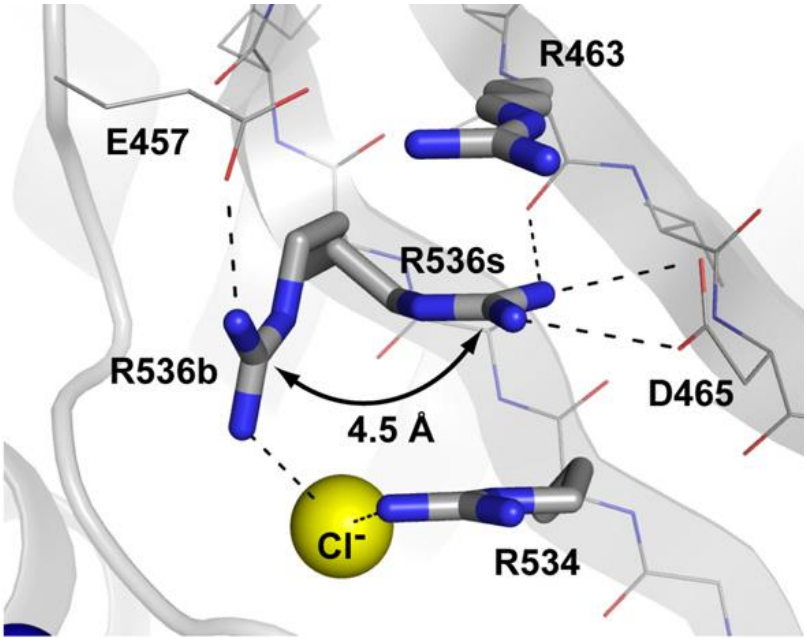

FIGURE 6.13: The residues of the arginine patch within the S1 pocket. The side chain of Arg536 can adopt two alternate conformations. (A) Arginine 536 can adopt two distinct conformations referred to as the "stacking" (R536s) and "binding" (R536b) conformation, respectively. A transition between the two conformations is associated with a 4.5 Å shift of the guanidinium group. The atoms are coloured blue (nitrogen), red (oxygen), grey (carbon), and yellow (chloride ion). Polar interactions stabilizing individual conformations of Arg536 are shown as broken lines. Figure reproduced with permission from (31).

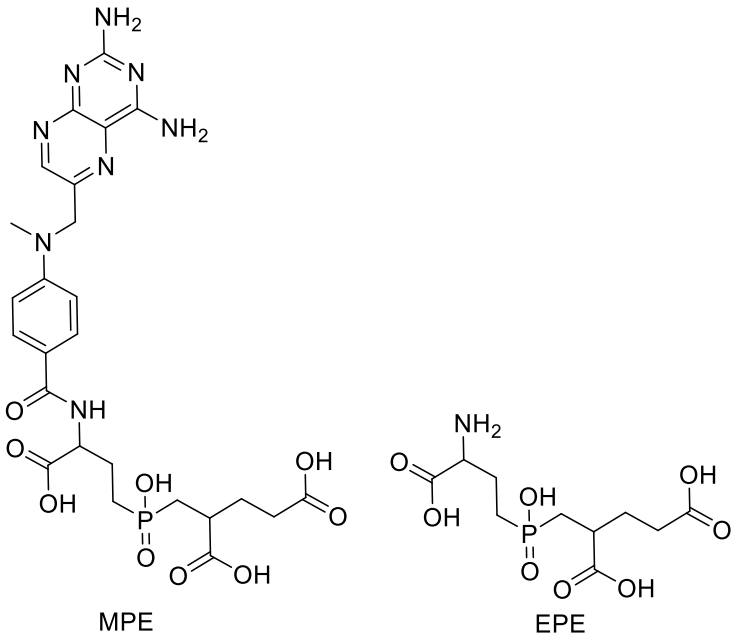

FIGURE 6.14: The structures of the inhibitors MPE and EPE phosphonate, which are transition state analogues of poly-γ-glutamated folate and γ-glutamyl-glutamate, respectively (31).

6.4.2 The Entrance Lid and the Arene-Binding Pocket

Crystallographic studies of GCP(II)/PSMA have revealed that the entrance tunnel to the active site has a lid, that can exist in an open or closed conformation, depending on the bound substrate (*8*)(*31*)(*39*). These two positions are shown in figure 6.15. This lid is made from the residues Trp541 to Gly548 and moves a distance of 9 Å between the open and closed states. In general, the lid is only open when larger substrates such as poly-γ-glutamated folate or its analogues are present. It is not possible for these substrates to bind with the lid closed due to steric hindrance. The motion of this lid is controlled by the peptide bond between Asn540 and Trp541 which acts as a hinge and flips between two conformations (*31*). The open conformation allows the enzyme to accommodate larger substrates and reveals an additional binding cleft named the "arene binding pocket". This site is formed of the indole group of Trp541 (the first residue of the entrance lid) and the guanidinium groups of Arg511 and Arg463 which allow for π-cation and π-stacking interactions with ligands containing aromatic groups (*39*). An increase in substrate affinity is observed if binding at the enzyme active site and also at the arene-binding cleft occurs (*8*)(*39*). However, it is important to note that, for poly-γ-glutamated folates, the interaction with the arene-binding cleft varies depending on the number of glutamate moieties in the structure, and that the molecule must contain at least two glutamates to allow it to reach the arene binding pocket at all (*8*). This same effect was seen for poly-γ-glutamated folate analogues, where there was a clear demonstration of an optimal linker length between the zinc ion binding moiety and the arene-binding region (*39*). Studies have also found that the properties of the aromatic group, which interacts with the arene-binding pocket, affect its affinity. The aromatic groups with the lowest LUMO (lowest unoccupied molecular orbital) energies had the strongest interactions with the arene binding pocket (a substrate with dinitrophenol had a higher affinity than ones with nitrophenol or phenol) (*39*). Mutagenic studies where the arene-binding site was altered showed a large impact on the crystallographic binding modes of poly-γ-glutamated folate but a much smaller effect on the hydrolysis rate of poly-γ-glutamated folates (*8*). This suggests that the substrate is likely to dock at the active site through the glutamate terminal first and then secondary interactions occur between the substrate and the arene-binding site (*8*). Therefore these interactions are more likely to be important for inhibitors than for natural substrates.

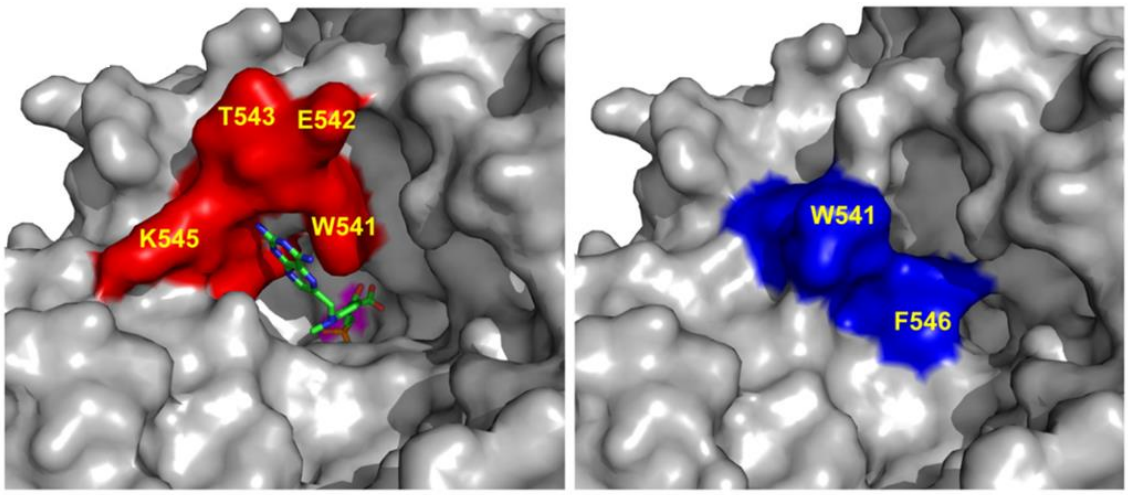

FIGURE 6.15: The open (left) and closed (right) conformations of the entrance lid to the active site of GCP(II)/PSMA. This lid is formed by the amino acids Trp541–Gly548 (highlighted red in the open conformation and blue in the closed). Reproduced with permission from (31).

6.5 Summary of All Interactions of GCP(II)/PSMA with its Natural Substrates

The previous sections revealed the features of the substrate binding pockets and active site which allow recognition and tight binding of the natural substrates and are involved in the induced-fit hydrolysis mechanism. These interactions can be summarised as follows: 1) the glutamate moiety binds within the S1' pocket, ensuring a tight fit and moves the "glutarate sensor" into its binding mode; 2) the coordination of the oxygen of the cleavable peptide bond, to the zinc ions in the active site; 3) the presence of a carboxylic acid residue in the P1 position, that is able to hydrogen bond to the positively charged arginine patch; 4) a carbonyl oxygen, that is able to interact with the Arg463 residue and causes the conformational change required for the Arg536 residue to move from its "stacking" to its "binding" mode; 5) larger substrates can cause the entrance lid to open, revealing the arene-binding region, that can form π-stacking interactions with substrates containing suitably aligned aromatic groups.

Figure 6.16 highlights the areas of the structure of the natural substrates poly-γ-glutamated folate and NAAG that interact with GCP(II)/PSMA. Figure 6.17 is a schematic highlighting the regions of the enzyme that interact with the substrate. The interactions within the S1' binding pocket, active site and S1 binding pocket are similar between the two substrates but the larger poly-γ-glutamated folate will require the opening of the entrance lid revealing the arene-binding pocket.

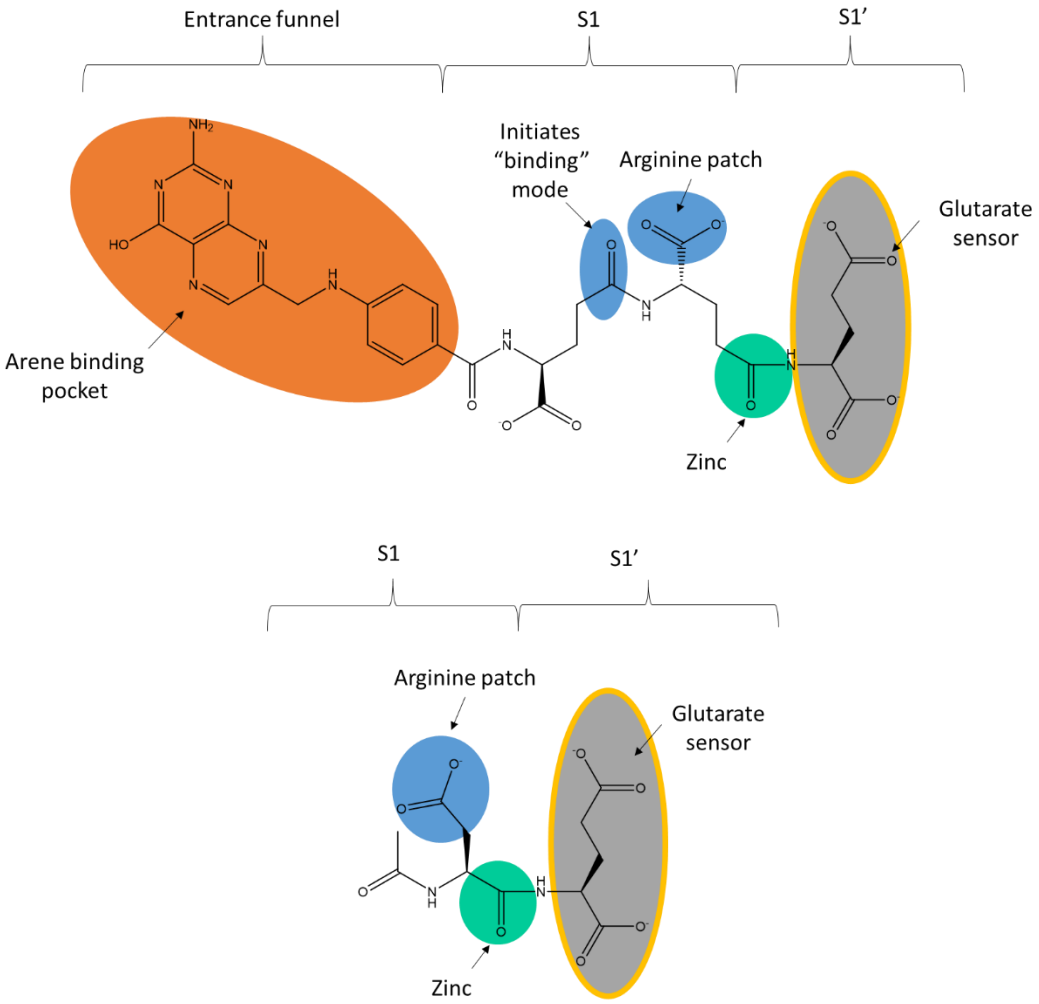

FIGURE 6.16: Summary of interactions of NAAG and poly-γ-glutamated folates with GCP(II)/PSMA active site. The colours used to allow you to locate the interaction within the active site of GCP(II)/PSMA shown in figure 6.17.

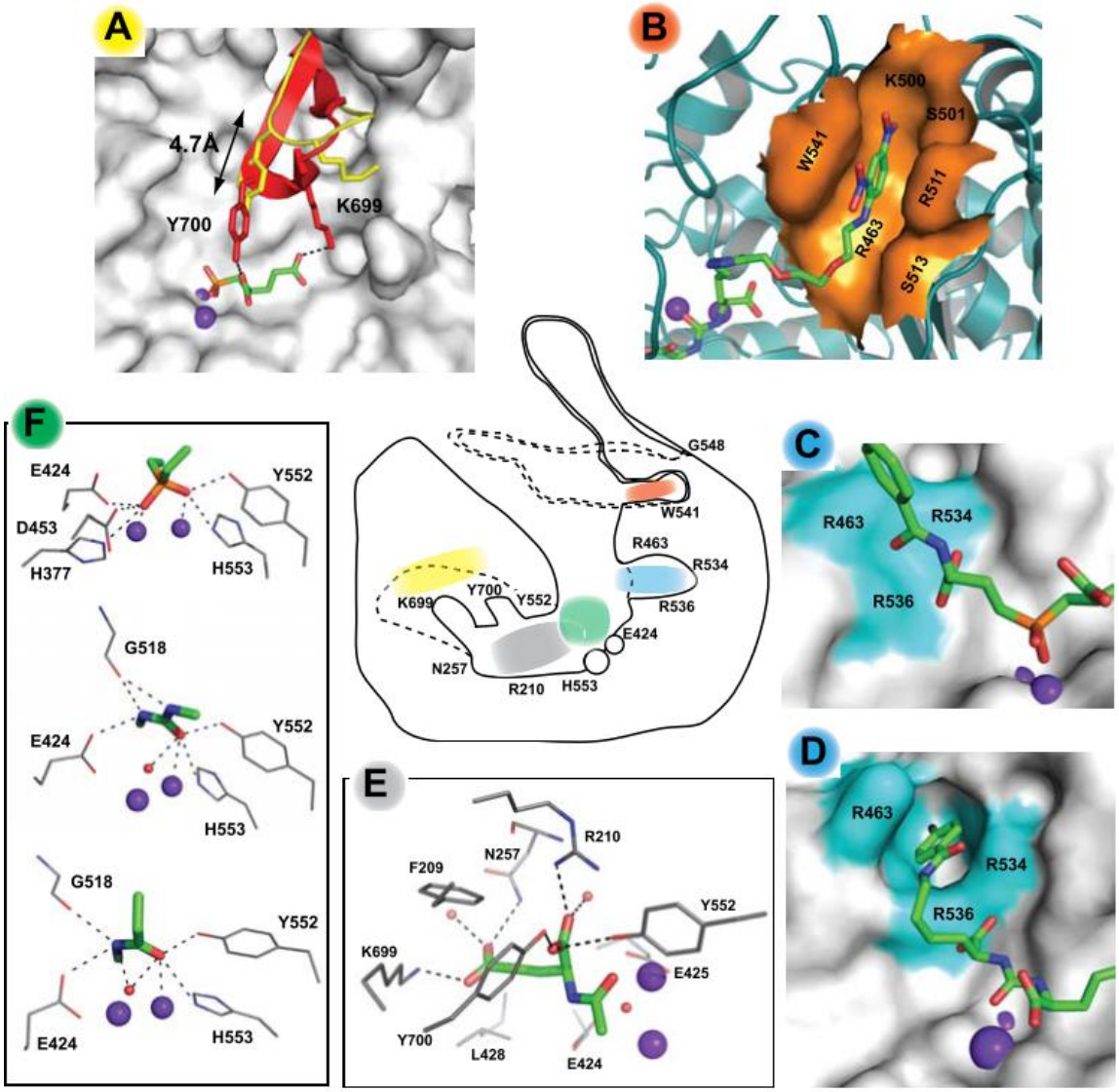

FIGURE 6.17: The internal cavity of human GCP(II)/PSMA. The schematic representation of GCP(II)/PSMA is in the centre of the figure. Flexible segments (the entrance lid, the arginine patch and the "glutarate sensor") are depicted in two conformations by solid and dashed lines, respectively. Residues lining the internal cavity are shown as one-letter codes and the zinc ions are depicted as circles. The coloured areas on this schematic show the location for each of the following binding interactions (A-yellow) the position of the "glutarate sensor", when the pharmacophore pocket is empty (yellow) or occupied by an inhibitor/substrate (red); (B-orange) the details of the arene-binding site occupied by the dinitrophenyl group of ARM-P2. The arene-binding site is coloured orange; (C-blue) the surface representation of the arginine patch (cyan) in the "stacking conformation"; (D-blue) the S1 accessory hydrophobic pocket is opened by simultaneous repositioning of the side chains of Arg463 and Arg536; (E-grey) hydrogen-bonding interactions between the S1' (pharmacophore) pocket-bound substrate and interacting GCP(II)/PSMA residues; (F-green) interactions in the vicinity of the active-site zinc ions. Phosphinate (top) and urea (middle) zinc ion binding groups. The peptide bond of NAAG (bottom) is shown for comparison. In all figures, zinc ions and water molecules are shown as purple and red spheres, respectively. Reproduced with permission from (29).

6.6 Design of Novel THP-PSMA Ligands for Higher Affinity

By reviewing the substrate inhibitor interactions for GCP(II)/PSMA with poly-γ-glutamated folate and NAAG, the features of the substrate that are likely to lead to higher affinity have been identified. This has formed the basis for my proposals for novel higher affinity variants of THP-PSMA which will be described below.

6.6.1 S1' Pocket

It is clear from the literature reviewed that conserving the terminal glutamate in any GCP(II)/PSMA targeting group is essential. This group is responsible for tight binding within the active site and so should not be altered in the design of a high-affinity tracer.

6.6.2 Zinc Ion Binding Group

The zinc ion binding group is the second most important feature of an inhibitor for GCP(II)/PSMA and it is resilient to more diversity than the S1' pocket. In the natural substrates, the zinc ion binding group is the carboxyl oxygen of the cleavable peptide bond. As reviewed above, this is replaceable by a urea group, which mimics the initial binding mode of the peptide bond, and with a phosphonate, phosphinate or phosphoramidate, all of which mimic the tetrahedral transition state through which the complex passes during bond cleavage. In these the zinc ion binds directly to the oxygen of the urea or two of the oxygens of the phosphonate/phosphinate/phosphoramidate, one mimicking the position of the carboxyl oxygen of the peptide bond and the other the position of the hydroxyl molecule (OH^-) which bridges the two zinc ions. The binding between the zinc ions and the substrate is very important and improving its strength could increase the affinity of the substrate for GCP(II)/PSMA. One way that this could be achieved is through replacing these oxygen atoms with sulfur atoms, as sulfur groups bind more strongly to zinc ions. The phosphonamidothionate, and phosphonamidodithionate zinc ion binding groups have previously been investigated (*40*) but no work has been published on thiourea-based zinc ion binding groups. This hypothesis will be explored in chapter 7 which describes the development and evaluation of a novel thiourea-PSMA inhibitor. Figure 6.18 shows the known zinc ion binding groups for GCP(II)/PSMA and alternatives that have been proposed.

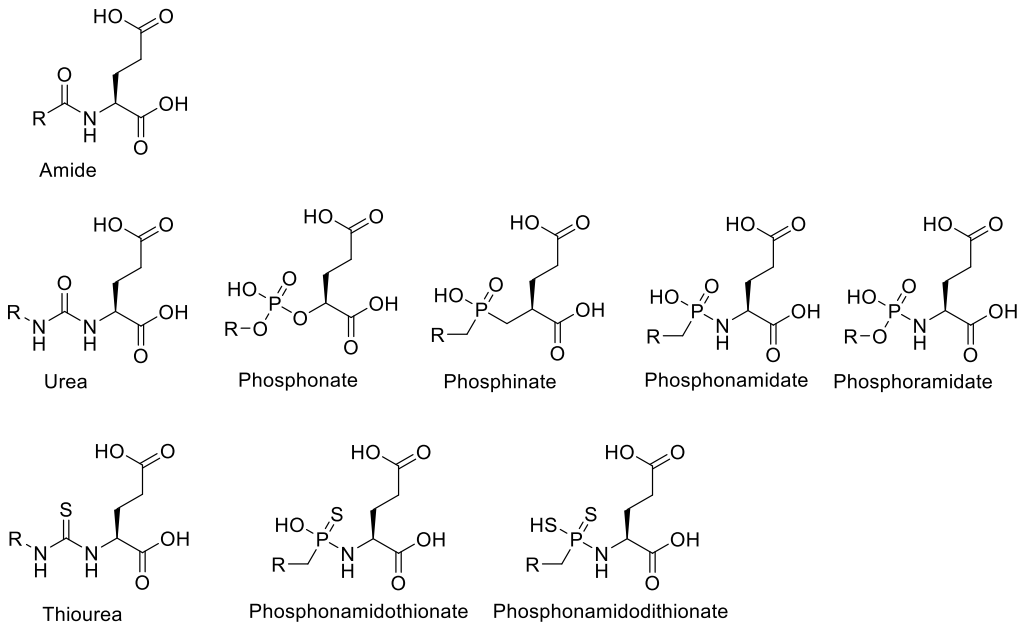

FIGURE 6.18: Structures of known and proposed zinc ion binding groups for GCP(II)/PSMA substrates and inhibitors. All except the thiourea have been synthesised previously (24)(40).

6.6.3 S1 Pocket

It is known that the S1 pocket can withstand much more structural diversity than the S1' pocket and that interactions in this region tend to have more effect on specificity than the affinity of inhibitors (*34*). Most enzymes have evolved to be very specific for their natural substrates and so it is logical to try to understand the interactions that the natural substrate has with this pocket and replicate these as closely as possible when designing a high-affinity inhibitor or tracer. In this discussion, poly-γ-glutamated folate will be the natural substrate focused on, due to its greater structural similarities with THP-PSMA. As described above poly-γ-glutamated folate has a carboxylic acid group in the P1 position which interacts with the positively charged arginine patch, and so we hypothesise this will be important to conserve. It also has a carbonyl oxygen which hydrogen bonds to Arg463 causing Arg536 to move into its "binding" mode. The position of this carboxyl group in the substrate is vital to ensure this interaction can occur, and so we hypothesise this should also be conserved. If the aim is to maintain the position of the carboxylic acid and carbonyl groups in the structure, then the most common GCP(II)/PSMA targeting motif used in PSMA radiotracers (Lys-C(O)-Glu) is unsuitable. This design places the carboxylic acid of the lysine in a slightly different position to the carboxylic acid in the natural substrate, while the lysine side chain extends the molecule past the position of the carboxyl group in the natural substrate, removing the opportunity for that interaction to occur. These differences are demonstrated in figure 6.19. However, the position of the carboxylic acid and the carboxyl group

could be conserved at the same time as introducing a urea group, in order to make the tracer resistant to enzymatic cleavage, if the Dap-C(O)-Glu motif was used instead. This structure is shown in figure 6.19. Dap or L-diaminopropanoic acid, is a non-proteinogenic amino acid, which can be made synthetically and is commercially available. Obtaining the structure shown in figure 6.19 would require the amine group at the end of the Dap side chain to form one half of the urea group rather than its α-amine. The concept of linking amino acids together using their side chains, came from studying the natural substrate poly-γ-glutamated folate. In this structure, the terminal carboxylic acids of the side chains are bound to the α-amine group of the next glutamic acid in the chain.

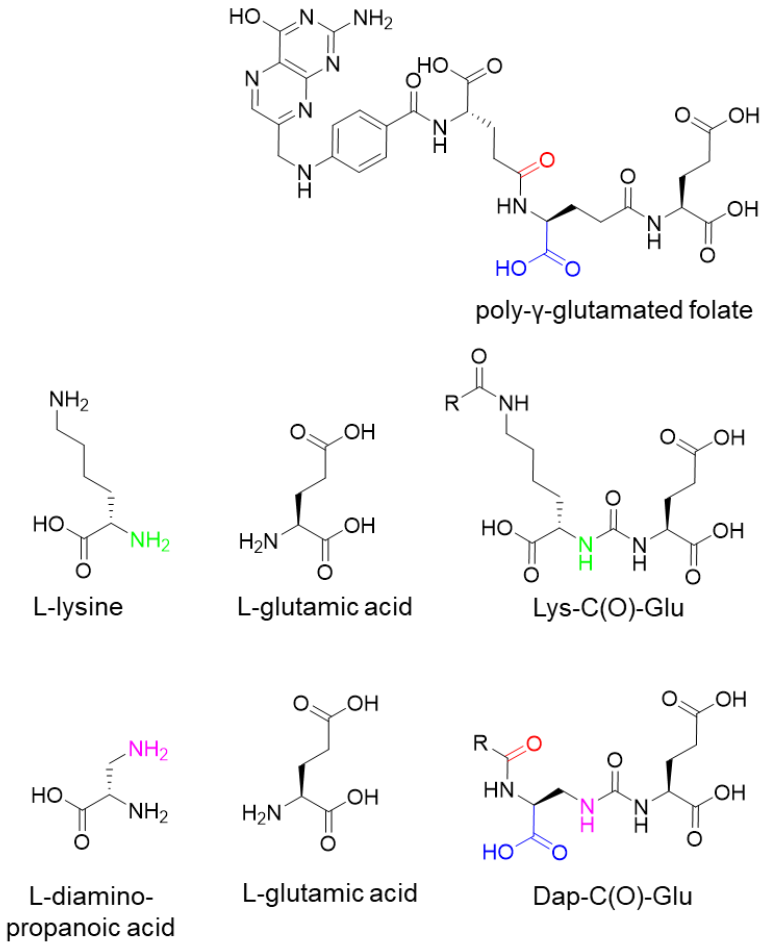

FIGURE 6.19: Modifications that could be used to make the urea-based mimic align more closely to the structure of the natural substrate. For poly-γ-glutamated folate the position of the carboxylic acid required to bind with the arginine patch is highlighted in blue and the position of the carbonyl which hydrogen bonds to Arg463 is shown in red. These features are preserved in the Dap-C(O)-Glu motif and highlighted in the same colours. The amine groups highlighted in green in the L-lysine is the amine that reacts to form the urea bond in the Lys-C(O)-Glu motif. The amine group highlighted in purple in the L-diaminopropanoic acid is the amine that reacts to form the urea bond in the Dap-C(O)-Glu motif.

It may also be beneficial to use the poly-γ-glutamate structure in the natural substrate as the linker between the motif that binds the active site and the THP chelator. The optimal length of the chain can also be determined from studies with poly-γ-glutamated folate. These suggest that there should be at least 3 glutamates in the chain before the aromatic groups of the folate; more may be beneficial (*8*). The final interaction that should be conserved occurs between the aromatic groups of the folate and the arene binding pocket. It is unlikely that the THP chelator itself would align correctly to interact with this arene binding pocket and so it would be beneficial to introduce an aromatic group before the chelator itself. There is already a bifunctional version of THP available which could be used to incorporate an aromatic group; THP-Ph-NCS (*41*) (figure 6.20). The phenol group could also be exchanged for a dinitrophenol which was found to have the strongest interaction with this region in inhibitor studies (*39*), although that would require developing a new synthetic pathway.

By combining all of the interactions present between poly-γ-glutamated folate and GCP(II))/PSMA with a non-cleavable zinc ion binding group and the THP-chelator, a hypothetical higher-affinity THP-PSMA tracer has been designed. The structure of a THP-PSMA bioconjugate which could form the basis of a family of ligands is shown in figure 6.21, with the features conserved from poly-γ-glutamated folate highlighted.

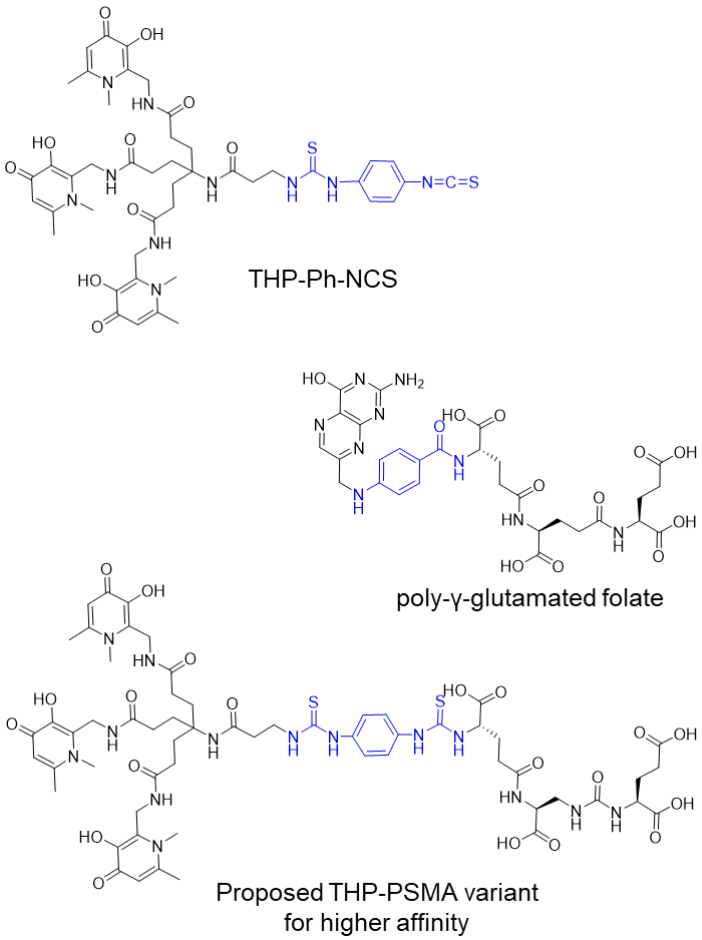

FIGURE 6.20: The structures of the bifunctional chelator THP-Ph-NCS, poly-γ-glutamated folate, and a proposed high-affinity THP-PSMA variant. The parts of the molecule highlighted in blue are the aromatic groups that will interact with the arene binding pocket in the natural inhibitor and the proposed mimic in the THP-PSMA variants.

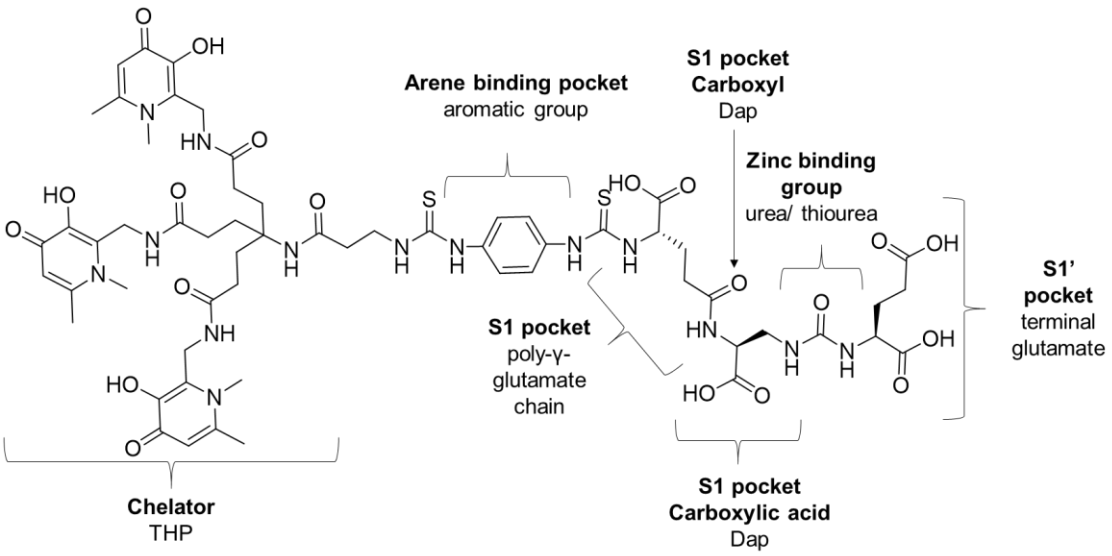

FIGURE 6.21: The structure of the proposed high affinity THP-PSMA variant.

6.7 Concluding Remarks

In this chapter, the important high-resolution crystal structures of GCP(II)/PSMA have been reviewed. This has provided insights into the important interactions between GCP(II)/PSMA and its natural substrates, including the hydrolysis mechanism. These learnings have been used to propose novel alterations to the structure of THP-PSMA which could improve the affinity of this tracer.

6.8 References

1. Mesters JR, Barinka C, Li W, Tsukamoto T, Majer P, Slusher BS, Konvalinka J, Hilgenfeld R. Structure of Glutamate Carboxypeptidase II, a Drug Target in Neuronal Damage and Prostate Cancer. *EMBO J*. 2006;25:1375-1384.
2. Ghosh A, Heston WDW. Tumor Target Prostate Specific Membrane Antigen (PSMA) and Its Regulation in Prostate Cancer. *J Cell Biochem*. 2004;91:528-539.
3. Bařinka C, Rojas C, Slusher B, Pomper M. Glutamate Carboxypeptidase II in Diagnosis and Treatment of Neurologic Disorders and Prostate Cancer. *Curr Med Chem*. 2012;19:856-870.
4. Robinson MB, Blakelys RD, Couto R, Coylenii JT. Hydrolysis of the Brain Dipeptide N-Acetyl-L-Aspartyl-L-Glutamate. *J Biol Chem*. 1987;262:14498-14506.
5. Silver DA, Pellicer I, Fair WR, Heston WDW, Cordon-Cardo C. Prostate-Specific Membrane Antigen Expression in Normal and Malignant Human Tissues. *Clin Cancer Res*. 1997;3:81-85.
6. Mhawech-Fauceglia P, Zhang S, Terracciano L, Sauter G, Chadhuri A, Herrmann FR, Penetrante R. Prostate-Specific Membrane Antigen (PSMA) Protein Expression in Normal and Neoplastic Tissues and Its Sensitivity and Specificity in Prostate Adenocarcinoma: An Immunohistochemical Study Using Mutiple Tumour Tissue Microarray Technique. *Histopathology*. 2007;50:472-483.
7. Luthi-Carter R, Barczak AK, Speno H, Coyle JT. Hydrolysis of the Neuropeptide N-Acetylaspartylglutamate (NAAG) by Cloned Human Glutamate Carboxypeptidase II. *Brain Res*. 1998;795:341-348.
8. Navrátil M, Ptáček J, Šácha P, Starková J, Lubkowski J, Bařinka C, Konvalinka J. Structural and Biochemical Characterization of the Folyl-Poly-Gamma-l-Glutamate Hydrolyzing Activity of Human Glutamate Carboxypeptidase II. *FEBS J*. 2014;281:3228-3242.
9. Zhou J, Neale JH, Pomper MG, Kozikowski AP. NAAG Peptidase Inhibitors and Their Potential for Diagnosis and Therapy. *Nat Rev Drug Discov*. 2005;4:1015-1026.
10. Vornov JJ, Hollinger KR, Jackson PF, Wozniak KM, Farah MH, Majer P, Rais R, Slusher BS. Still NAAG'ing after All These Years. The Continuing Pursuit of GCPII Inhibitors. Vol 76. 1st ed. Elsevier Inc.; 2016.
11. Yelamanchi SD, Jayaram S, Thomas JK, Gundimeda S, Khan AA, Singhal A, Keshava Prasad TS, Pandey A, Somani BL, Gowda H. A Pathway Map of Glutamate Metabolism. *J Cell Commun Signal*. 2016;10:69-75.
12. Ristau BT, O'Keefe DS, Bacich DJ. The Prostate-Specific Membrane Antigen: Lessons and Current Clinical Implications from 20 Years of Research. *Urol Oncol Semin Orig Investig*. 2014;32:272-279.
13. Rowe SP, Drzezga A, Neumaier B, Dietlein M, Gorin MA, Zalutsky MR, Pomper MG. Prostate-Specific Membrane Antigen–targeted Radiohalogenated PET and Therapeutic Agents for Prostate Cancer. *J Nucl Med*. 2016;57:90S-97S.
14. Evans MJ, Smith-Jones PM, Wongvipat J, Navarro V, Kim S, Bander NH. Noninvasive Measurement of Androgen Receptor Signaling with a Positron-Emitting Radiopharmaceutical That Targets Prostate-Specific Membrane Antigen. *Proc Natl Acad Sci*. 2011;108:9578-9582.
15. Mease RC, Foss C a, Pomper MG. PET Imaging in Prostate Cancer: Focus on Prostate-Specific Membrane Antigen. *Curr Top Med Chem*. 2014;13:951-962.
16. Driscoll CCO, Cork T, E-mail I, Evans JC. The Therapeutic and Diagnostic Potential of the Prostate Specific Membrane Antigen / Glutamate Carboxypeptidase II (PSMA/GCPII) in Cancer and Neurological Disease. *Br J Pharmacol*. 2016;173:3041-3079.
17. Veronica Yao and Dean J. Bacich. Prostate Specific Membrane Antigen (PSMA) Expression Gives Prostate Cancer Cells a Growth Advantage in a Physiologically Relevant Folate

Environment in Vitro. *Prostate*. 2006;66:867-875.
18. Yao V, Berkman CE, Choi JK, O'Keefe DS, Bacich DJ. Expression of Prostate-Specific Membrane Antigen (PSMA), Increases Cell Folate Uptake and Proliferation and Suggests a Novel Role for PSMA in the Uptake of the Non-Polyglutamated Folate, Folic Acid. *Prostate*. 2010;70:305-316.
19. Liu H, Rajasekaran AK, Moy P, Xia Y, Kim S, Navarro V, Bander NH. Constitutive and Antibody-Induced Internalization of Prostate-Specific Membrane Antigen. *Cancer Res*. 1998;58:4055-4060.
20. Barinka C, Sácha P, Sklenár J, Man P, Bezouska K, Slusher BS, Konvalinka J. Identification of the N-Glycosylation Sites on Glutamate Carboxypeptidase II Necessary for Proteolytic Activity. *Protein Sci*. 2004;13:1627-1635.
21. Ghosh A, Heston WDW. Effect of Carbohydrate Moieties on the Folate Hydrolysis Activity of the Prostate Specific Membrane Antigen. *Prostate*. 2003;57:140-151.
22. Song J, Boyd SE, Shen H, Mahmood K, Webb GI, Akutsu T, Whisstock JC, Pike RN. Bioinformatic Approaches for Predicting Substrates of Proteases. *J Bioinform Comput Biol*. 2011;9:149-178.
23. Klusák V, Bařinka C, Plechanovová A, Mlčochová P, Konvalinka J, Rulíšek L, Lubkowski J. Reaction Mechanism of Glutamate Carboxypeptidase II Revealed by Mutagenesis, X-Ray Crystallography, and Computational Methods. *Biochemistry*. 2009;48:4126-4138.
24. Novakova Z, Cerny J, Choy CJ, Nedrow JR, Choi JK, Lubkowski J, Berkman CE, Barinka C. Design of Composite Inhibitors Targeting Glutamate Carboxypeptidase II: The Importance of Effector Functionalities. *FEBS J*. 2016;283:130-143.
25. Davis MI, Bennett MJ, Thomas LM, Bjorkman PJ. Crystal Structure of Prostate-Specific Membrane Antigen, a Tumor Marker and Peptidase. *Proc Natl Acad Sci*. 2005;102:5981-5986.
26. Rong S-BB, Zhang J, Neale JH, Wroblewski JT, Wang S, Kozikowski AP. Molecular Modeling of the Interactions of Glutamate Carboxypeptidase II with Its Potent NAAG-Based Inhibitors. *J Med Chem*. 2002;45:4140-4152.
27. Holz RC, Bzymek KP, Swierczek SI. Co-Catalytic Metallopeptidases as Pharmaceutical Targets. *Curr Opin Chem Biol*. 2003;7:197-206.
28. Barinka C, Starkova J, Konvalinka J, Lubkowski J. A High-Resolution Structure of Ligand-Free Human Glutamate Carboxypeptidase II. *Acta Crystallogr Sect F Struct Biol Cryst Commun*. 2007;63:150-153.
29. Pavlicek J, Ptacek J, Barinka C. Glutamate Carboxypeptidase II: An Overview of Structural Studies and Their Importance for Structure-Based Drug Design and Deciphering the Reaction Mechanism of the Enzyme. *Curr Med Chem*. 2012;19:1300-1309.
30. Barinka C, Byun Y, Dusich CL, Banerjee SR, Chen Y, Castanares M, Kozikowski AP, Mease RC, Pomper MG, Lubkowski J. Interactions between Human Glutamate Carboxypeptidase II and Urea-Based Inhibitors: Structural Characterization. *J Med Chem*. 2008;51:7737-7743.
31. Barinka C, Hlouchova K, Rovenska M, Majer P, Dauter M, Hin N, Ko Y Sen, Tsukamoto T, Slusher BS, Konvalinka J, Lubkowski J. Structural Basis of Interactions between Human Glutamate Carboxypeptidase II and Its Substrate Analogs. *J Mol Biol*. 2008;376:1438-1450.
32. Speno HS, Luthi-Carter R, Macias WL, Valentine SL, Joshi ART, Coyle JT. Site-Directed Mutagenesis of Predicted Active Site Residues in Glutamate Carboxypeptidase II. *Mol Pharmacol*. 1999;55:179-185.
33. Hlouchova K, Barinka C, Konvalinka J, Lubkowski J. Structural Insight into the Evolutionary and Pharmacologic Homology of Glutamate Carboxypeptidases II and III. *FEBS J*. 2009;276:4448-4462.
34. Mlčochová P, Plechanovová A, Bařinka C, Mahadevan D, Saldanha JW, Rulíšek L,

Konvalinka J. Mapping of the Active Site of Glutamate Carboxypeptidase II by Site-Directed Mutagenesis. *FEBS J*. 2007;274:4731-4741.

35. Mesters JR, Henning K, Hilgenfeld R. Human Glutamate Carboxypeptidase II Inhibition: Structures of GCPII in Complex with Two Potent Inhibitors, Quisqualate and 2-PMPA. *Acta Crystallogr Sect D Biol Crystallogr*. 2007;63:508-513.
36. Pavlicek J, Ptacek J, Cerny J, Byun Y, Skultetyova L, Pomper MG, Lubkowski J, Barinka C. Structural Characterization of P1'-Diversified Urea-Based Inhibitors of Glutamate Carboxypeptidase II. *Bioorganic Med Chem Lett*. 2014;24:2340-2345.
37. Kozikowski AP, Nan F, Conti P, Zhang J, Ramadan E, Bzdega T, Wroblewska B, Neale JH, Pshenichkin S, Wroblewski JT. Design of Remarkably Simple, yet Potent Urea-Based Inhibitors of Glutamate Carboxypeptidase II (NAALADase). *J Med Chem*. 2001;44:298-301.
38. Kozikowski AP, Zhang J, Nan F, Petukhov PA, Grajkowska E, Wroblewski JT, Yamamoto T, Bzdega T, Wroblewska B, Neale JH. Synthesis of Urea-Based Inhibitors as Active Site Probes of Glutamate Carboxypeptidase II: Efficacy as Analgesic Agents. *J Med Chem*. 2004;47:1729-1738.
39. Zhang AX, Murelli RP, Barinka C, Michel J, Cocleaza A, Jorgensen WL, Lubkowski J, Spiegel DA. A Remote Arene-Binding Site on Prostate Specific Membrane Antigen Revealed by Antibody-Recruiting Small Molecules. *J Am Chem Soc*. 2010;132:12711-12716.
40. Mallari JP, Choy CJ, Hu Y, Martinez AR, Hosaka M, Toriyabe Y, Maung J, Blecha JE, Pavkovic SF, Berkman CE. Stereoselective Inhibition of Glutamate Carboxypeptidase by Organophosphorus Derivatives of Glutamic Acid. *Bioorganic Med Chem*. 2004;12:6011-6020.
41. Ma MT, Cullinane C, Imberti C, Baguna Torres J, Terry SY a., Roselt P, Hicks RJ, Blower PJ, Bagunya Torres J, Terry SY a., Roselt P, Hicks RJ, Blower PJ. New Tris (Hydroxypyridinone) Bifunctional Chelators Containing Isothiocyanate Groups Provide a Versatile Platform for Rapid One-Step Labeling and PET Imaging with 68Ga3+. *Bioconjug Chem*. 2015;27:309-318.

7 Development of a Thiourea-Based Inhibitor of PSMA

7.1 Introduction

Results from chapters 3 and 4 have shown that [^{68}Ga]Ga-THP-PSMA is a successful imaging agent for GCP(II)/PSMA-expressing prostate cancer. This has been demonstrated *in vitro*, in a mouse model of prostate cancer (*1*), and in clinical studies, in which primary tumours, cancerous lymph nodes and bone metastases could be detected (*2*)(*3*)(*4*). The results of these scans also had an impact on patient management (*2*)(*4*). However, as discussed in chapter 5, the current tracer is not ideal for molecular radiotherapy with the Auger emitting isotope gallium-67, despite the exceptionally high molar activity that can be achieved (326 MBq/nmol, 22% occupancy of THP-PSMA). The *in vitro* results show that even with high molar activity the amount of gallium-67 that can be delivered to cells is limited by the uptake of the tracer into GCP(II)/PSMA-expressing cells. Additionally, in a xenograft mouse model of GCP(II)/PSMA-expressing prostate cancer the tracer has been shown to washout of solid tumours over the first 24 hours: a much faster rate than seen for the clinically tested therapeutic PSMA-tracers [^{177}Lu]Lu-DOTA-PSMA(617) (*5*) and [^{125}I]I-DCIBzL (*6*). One factor contributing to these *in vitro* and *in vivo* properties is likely to be the affinity of Ga-THP-PSMA for GCP(II)/PSMA. This was shown to be 10.4 ± 3.4 and 8.6 ± 3.4 fold lower than for Ga-HBED-CC-PSMA and Ga-DOTA-PSMA(617) respectively (data from chapter 3 (*1*)). Affinity is related to the targeting and uptake in GCP(II)/PSMA-expressing cells as well as contributing to internalisation of tracers (*7*). Therefore improving the affinity for GCP(II)/PSMA is one strategy that could have a big impact on the uptake and retention of this tracer in prostate cancer.

As explored in chapter 6, there are at least 5 important interactions between GCP(II)/PSMA and its natural substrates. Conservation of these features in inhibitor and radiotracer design could lead to higher affinity. Both the conservation of the terminal glutamic acid, and having a suitable binding group for the zinc ion within the active site, are known to be the most vital features of an inhibitor (*8*). Of these two, the only one amenable to change is the zinc ion binding group, and small changes to this group are known to have a large impact on the affinity of inhibitors (*9*)(*10*)(*11*)(*12*). When the natural substrates (NAAG and poly-γ-glutamated folate) bind to GCP(II)/PSMA, the group that interacts with the zinc ions is the carbonyl oxygen of the cleaved peptide bond, between the terminal glutamate and the remainder of the molecule (*13*). In designing an inhibitor or tracer, this peptide bond needs to be replaced with a peptide bond mimic (*8*) that is resistant to enzymatic cleavage but binds the active site tightly including maintaining this interaction with the zinc ion. Figure 7.1 shows the structures of previously

investigated zinc ion binding groups. All have the conserved glutamic acid or pentanedioic acid for binding the S1' pocket. The most utilised peptide bond mimic for GCP(II)/PSMA tracers is a urea bond. Replacing a peptide bond with a urea reduces the electrophilicity of the carbonyl carbon and so this bond is no longer cleavable by the enzyme. This urea motif, in which oxygen is the zinc ion binding ligand, is used in [^{68}Ga]Ga-THP-PSMA but also in all of the other PSMA-based tracers discussed in chapter 1 ([^{11}C]MCG, [^{123}I]I-MIP-1095, [^{99m}Tc]Tc-MIP-1404, [^{18}F]DCFPyL, [^{18}F]F-PSMA-1007, [^{68}Ga]Ga-HBED-CC-PSMA, [^{68}Ga]Ga-DOTA-PSMA(617) and [^{68}Ga]Ga-DOTAGA-PSMA (I&T)). Thiols and a range of phosphoryl-based groups have also been investigated (*9*)(*10*)(*11*). These included phosphonates (*10*), phosphinates (*10*), phosphoramidates (*11*). In these structures, the phosphoryl group mimics the tetrahedral transition state/intermediate (with an sp^3 hybridised carbon) through which the substrate passes during enzymatic cleavage (*13*), and the oxygens of the phosphoryl groups bind to the zinc ion (*14*). There are no crystal structures available for the thiol-based inhibitors in the active site of GCP(II)/PSMA and so the exact positioning of this group is unknown. However, the number of methylene units between the thiol group and pentanedioic acid (figure 7.1) affects the binding to GCP(II)/PSMA and is optimal when there are three methylene groups present, suggesting this length allows for the greatest interaction between the thiol and the zinc ions (*9*). Crystal structures are available for urea, phosphonate, phosphinate, and phosphoramidate inhibitors within GCP(II)/PSMA and their binding modes are shown in figure 7.2 and figure 7.3. Additionally, phosphonamidothionate and phosphonamidodithionate analogues have been synthesised where one or two oxygens are replaced with a sulfur atom as shown in figure 7.1 (*15*). Unfortunately, these have only been assessed as inhibitors for the enzyme carboxypeptidase-G and not with GCP(II)/PSMA. This enzyme is closely related to GCP(II)/PSMA and is also a zinc metalloenzyme which cleaves terminal glutamates. This study found that the affinity of phosphoramidate-, phosphonamidothionate-, or phosphonamidodithionate-based inhibitors was greatly affected by the group in the P1 position, but that in some cases the presence of sulfur improved the K_i value measured. The results of this study are shown in table 7.1.

The rationale for replacing oxygen with sulfur in an inhibitor for a zinc-based metalloenzyme is that zinc and sulfur are a better matched Lewis acid/Lewis base pair (as they are both borderline soft/hard) than zinc and oxygen (a hard Lewis base) (*16*). Zinc ions and sulfur-based ligands have a strong affinity for each other and typically form highly stable complexes (*17*)(*18*). This stronger interaction could improve the affinity of an inhibitor and may also increase the residence time within the active site, in turn affecting internalisation. Internalisation is a key feature when

designing radiotracers for molecular radiotherapy (particularly with Auger electron emissions) as this maximises the quantity of therapeutic isotope that accumulates in GCP(II)/PSMA-expressing cells.

Although the concept of exchanging an oxygen within a zinc ion binding group for a sulfur has been explored for phosphonyl derivatives, (albeit not tested with GCP(II)/PSMA itself), this has not been studied for the urea-based inhibitors. Therefore this study was designed to investigate the impact of using thiourea-based inhibitors in place of the successful urea-based inhibitors currently employed in PSMA radiotracers. The only change required in the structure is the replacement of the urea group in the existing inhibitor with its thiourea analogue. This should be synthetically achievable through the generation of an isothiocyanate intermediate, with existing well-characterised chemistry (*19*)(*20*)(*21*). Thiourea variants would be expected to act as inhibitors for GCP(II)/PSMA as all of the interactions present in the urea version should be conserved and the interaction with the zinc ion should be enhanced by the presence of the sulfur group. In addition, like the urea bond, the less electrophilic carbonyl of the thiourea (compared to that of a peptide bond) should make it resistant to cleavage by GCP(II)/PSMA. In order to investigate the consequences of this change, a simple model was used as a starting point: the symmetrical inhibitor Glu-C(O)-Glu, named urea-PSMA. This inhibitor has been reported to have a K_i value for GCP(II)/PSMA of 8 nM, and can be made by a simple solution-based synthetic route (*22*). The novel thiourea analogue of this inhibitor thiourea-PSMA (Glu-C(S)-Glu) will be synthesised and characterised and the IC_{50} values of these inhibitors will be compared alongside the widely used inhibitor PMPA (with a phosphonate zinc ion binding group) as a control. The structures of these three compounds are shown in figure 7.4. The names urea-PSMA/thiourea-PSMA and Glu-C(O)-Glu/Glu-C(S)-Glu will be used interchangeably, depending on whether synthesis or PSMA-targeting is being discussed.

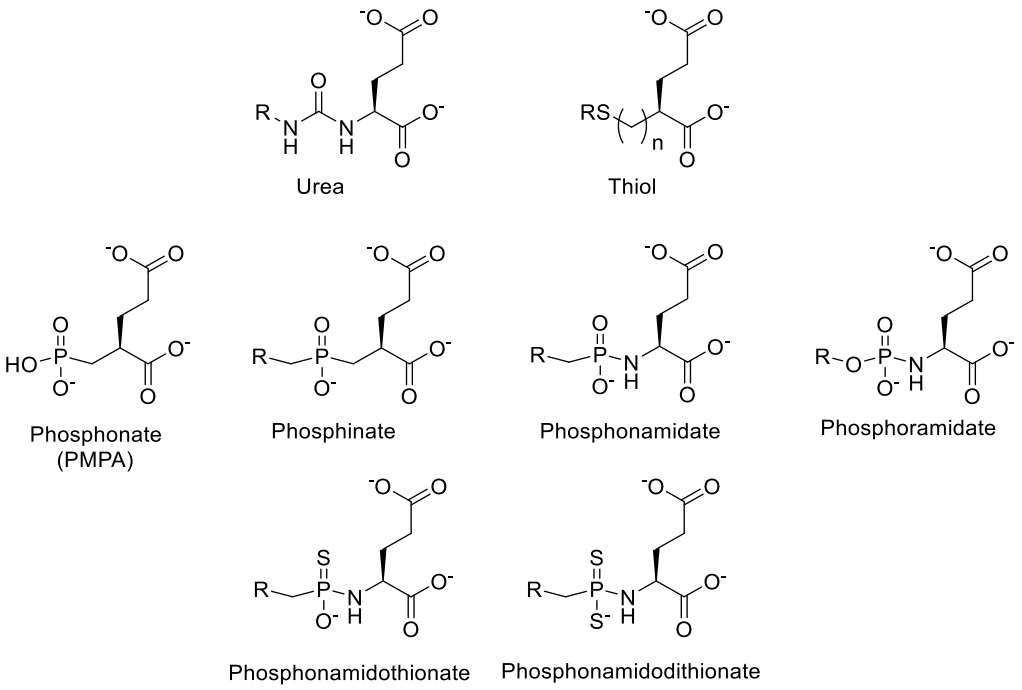

FIGURE 7.1: The structures of a range of zinc ion binding moieties that have been investigated as inhibitors for GCP(II)/PSMA or carboxy-peptidase-G. Note the conserved terminal glutamate or pentanedioic acid. These structures have been shown with their charge at physiological pH.

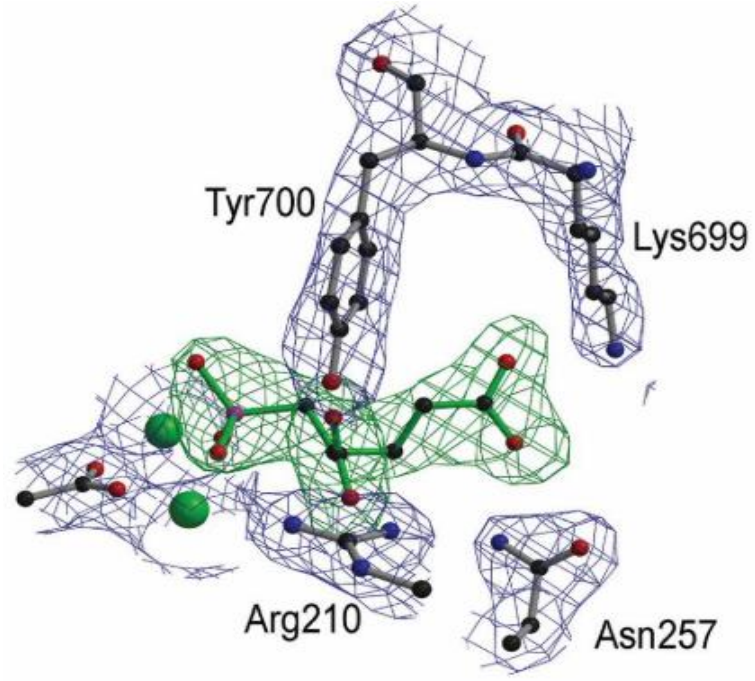

FIGURE 7.2: Electron density map of the active site of GCP(II)/PSMA (blue contours) with the PMPA inhibitor (green contours) bound. Zinc ions are shown as green spheres. Reproduced with permission from (14).

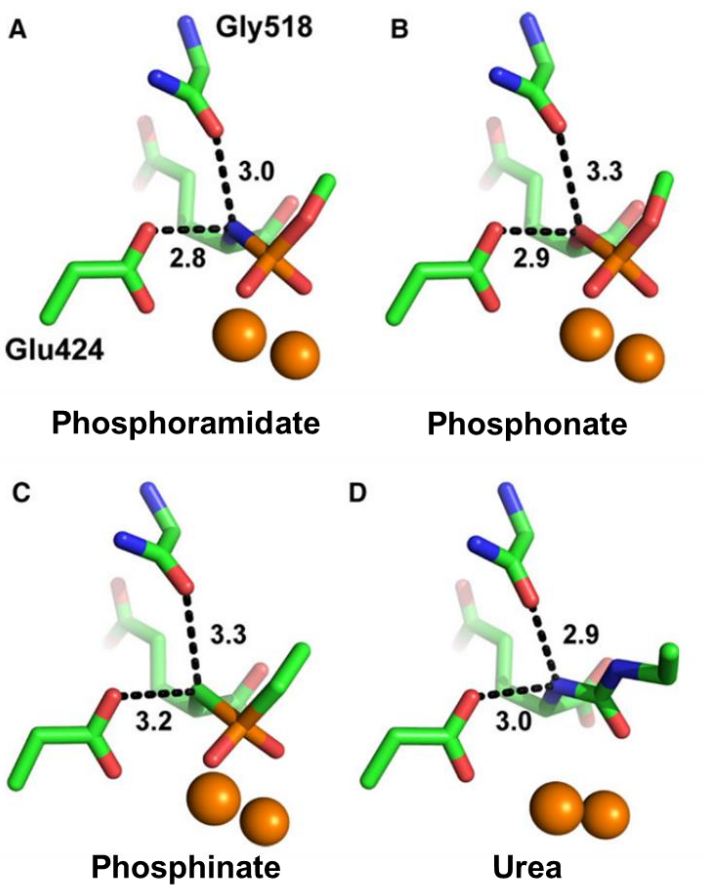

FIGURE 7.3: Interactions of phosphorus- and urea-based zinc ion binding moieties of inhibitors within the active site of GCP(II)/PSMA. Individual atoms are coloured red (oxygen), blue (nitrogen), orange (phosphorus), and green (carbon). The active-site zinc ions are shown as orange spheres. Reproduced with permission from (12).

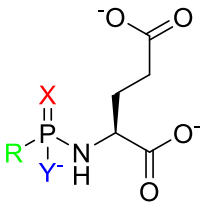

R	X	Y-	Phosphorus configuration	Ki (µM) (± SD)
Et	O	O	-	63 ± 1.1
Et	S	O	R	2.2 ± 0.13
Et	S	O	S	20 ± 1.6
Et	S	S	-	25 ± 1.3
n-Bu	O	O	-	0.63 ± 0.15
n-Bu	S	O	R	1.2 ± 0.11
n-Bu	S	O	S	3.7 ± 0.17
n-Bu	S	S	-	22 ± 1.4
Ph	O	O	-	24 ± 1.2
Ph	S	O	R	13 ± 0.65
Ph	S	O	S	46 ± 2.0
Ph	S	S	-	530 ± 71

TABLE 7.1: A range of inhibitors and their experimentally obtained K_i values with carboxy-peptidase G (15).

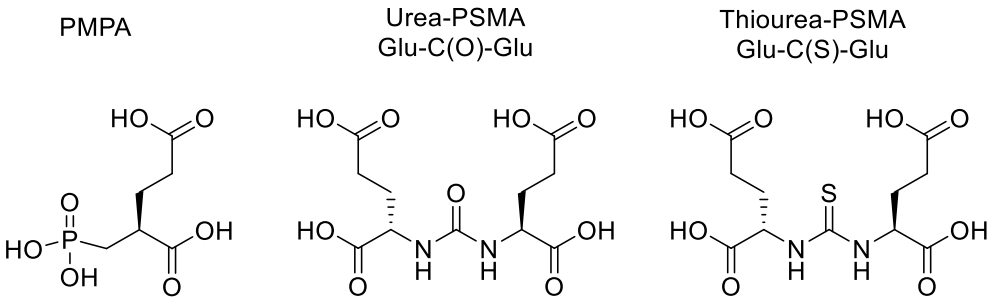

FIGURE 7.4: The structures of PMPA, urea-PSMA (Glu-C(O)-Glu) and thiourea-PSMA (Glu-C(S)-Glu), the inhibitors to be compared in this study.

7.2 Experimental Aims

The above aims will be addressed through the following experimental objectives:

- Synthesis and characterisation of urea-PSMA (Glu-C(O)-Glu) (synthesised previously (*22*)) and the novel inhibitor thiourea-PSMA (Glu-C(S)-Glu)
- Stability studies under the conditions required for cell-based inhibition assays
- Evaluation of these compounds as GCP(II)/PSMA inhibitors using an IC_{50} assay

7.3 Materials and Methods

All reagents and consumables were purchased from Sigma Aldrich (Gillingham, UK) or Fischer Scientific (Loughborough, UK), with the exception of DOTA-PSMA (PSMA 617) which was purchased from ABX (Radeberg, Germany). DU145 and DU145-PSMA cells were grown from stocks provided by Dr Florian Kampmeier (*1*).

7.3.1 Instrumentation

NMR: ^{1}H- and ^{13}C-NMR spectra were acquired on either a Bruker Avance III 400 spectrometer operating at 400 MHz (^{1}H frequency) equipped with a QNP probe, or a Bruker Ascend 800 spectrometer operating at 800 MHz (^{1}H frequency) equipped with a TCI cyroprobe.

Infrared spectroscopy: IR was conducted with solid sample on a Perkin Elmer Spectrum 100 FT-IR Spectrometer using a universal ATR sampling accessory.

Mass spectrometry: Routine direct injection mass spectrometry was conducted on a Waters Quadruple MS in positive ion mode. LC-MS results were produced with an Agilent ion-trap LC-MS in positive ion mode, with an in-line photodiode array. The high-resolution mass spectrometry results were produced on a Thermo Scientific Exactive in positive ion mode.

HPLC: Analytical and semi-preparative HPLC utilised an Agilent 1200 LC with in-line ultraviolet detection (220 nm, 240 nm or 254 nm). Two HPLC methods were used to monitor reactions, both with an Agilent Eclipse XDB C_{18} 5 µm 4.6 × 150 mm column and the same mobile phases (A = H_2O 0.1% TFA, B = acetonitrile 0.1% TFA). Method 1: 1 mL/minute with the following gradient: 0-5 minutes 100% A, 5-15 minutes 0-50% B, 15-20 minutes 100% A. Method 2: 1 mL/minute with the following gradient: 0-5 minutes 98% A, 5-20 minutes 2-98% B, 20-25 minutes 98% B, 25-30 minutes 98% A. Semi-preparative reversed-phase HPLC was conducted using an Agilent Eclipse XDB C_{18} 5 µm 21.2 × 150 mm column with the concentration of mobile phase B increasing at a rate of 1%/minute (A = H_2O with 0.2% TFA, B = acetonitrile with 0.2% TFA, starting from 100% A at time 0; flow rate, 3 mL/min).

7.3.2 Synthesis of Tertiary Butyl Protected Urea-PSMA; $Glu(tBu)_2$-C(O)-$Glu(tBu)_2$

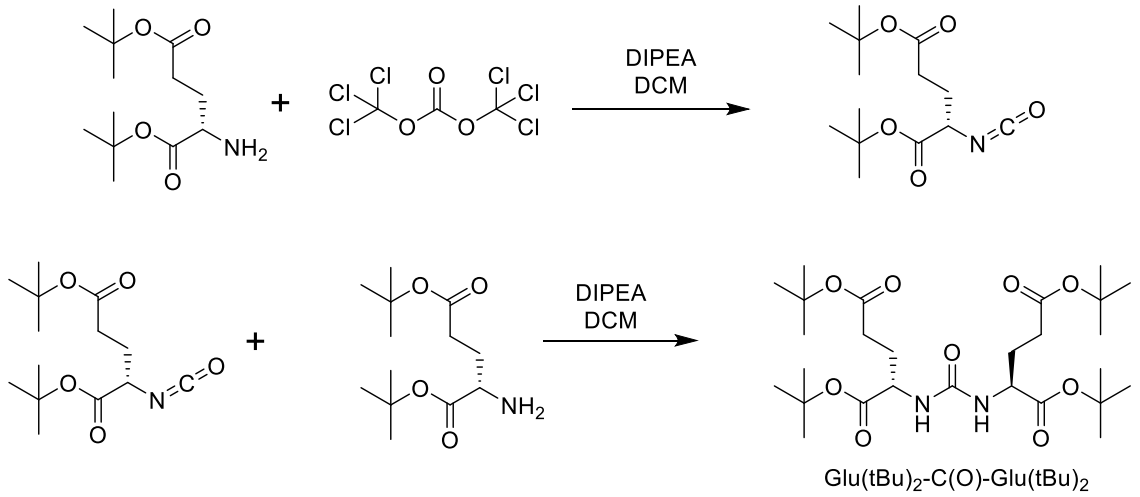

REACTION SCHEME 7.1: Synthesis route for the production of tertiary butyl protected urea-PSMA – $Glu(tBu)_2$-C(O)-$Glu(tBu)_2$.

An oven dried three-necked round-bottomed flask with a dropping funnel, was attached to a Schlenk line and cycled with vacuum and nitrogen gas three times. Triphosgene (0.53 mmol, 156 mg, MW 296.75) was added to the flask which was then cooled to 0°C in an ice bath. L-glutamic acid di-tert-butyl ester (1.6 mmol, 459 mg, HCl salt, MW 295.8) was dissolved in 20 mL anhydrous DCM containing two equivalents of DIPEA (550 µL, 3.2 mmol, MW 129.2, density 0.742 g/mL). This solution was added dropwise to the reaction flask over 45 minutes using the dropping funnel whilst the flask remained under nitrogen. The solution was stirred throughout addition and some fuming occurred. The ice bath was then removed and the reaction mixture left to warm to room temperature for 1 hour. Then a further 600 mg L-glutamic acid di-tert-butyl ester (2 mmol, HCl salt, MW 295.8) dissolved in 20 mL of DCM and 600 µL DIPEA (3.5 mmol, MW 129.2, density 0.742 g/mL) was added to the dropping funnel and added slowly to the flask over 45 minutes. The flask remained under nitrogen for 30 minutes post-addition and was then sealed and left to stir overnight. The next day the reaction mixture was washed with water (50 mL x 3) and brine (50 mL x 1), dried over magnesium sulfate and the solvent removed by rotary evaporation. The product was identified using TLC with 80:20 DCM:ethyl acetate (starting material $R_F = 0$, product $R_F = 0.65$). The crude product was purified using flash chromatography (Biotage Isolaera™ Four) using a 10 g KP SNAP silica column with a DCM and ethyl acetate gradient (100% DCM to 60% DCM, 40% ethyl acetate) and then dried under vacuum to produce $Glu(tBu)_2$-C(O)-$Glu(tBu)_2$ as a white solid (562 mg, 1.03 mmol (MW = 544.69), yield 64%). ^{1}H NMR: ($CDCl_3$, 400 MHz, normalised to chloroform solvent peak (*23*)): δ 1.39 (s, 18H), 1.42 (s, 18H), 1.83 (m, 2H), 2.02 (m, 2H), 2.27 (m, 4H), 4.30 (dd, *J*= 6.8, 12, 2H), 5.25 (broad s, 2H). ^{13}C

NMR: ($CDCl_3$, 100 MHz, normalised to chloroform solvent peak (*23*)): δ 28.07 (s, 6C), 28.14 (s, 6C), 28.52 (s, 2C), 31.64 (s, 2C), 53.13 (s, 2C), 80.53 (s, 2C), 82.03 (s, 2C) 156.94 (s, 1C) 172.13 (s, 2C), 172.50 (s, 2C). High-resolution mass spectrometry: $[C_{27}H_{48}N_2O_9+H]^+$: observed m/z 545.3426, theoretical m/z 545.3433,$[C_{27}H_{48}N_2O_9+Na]^+$: observed m/z 567.3241, theoretical m/z 567.3252.

7.3.3 Synthesis of Urea-PSMA; Glu-C(O)-Glu.

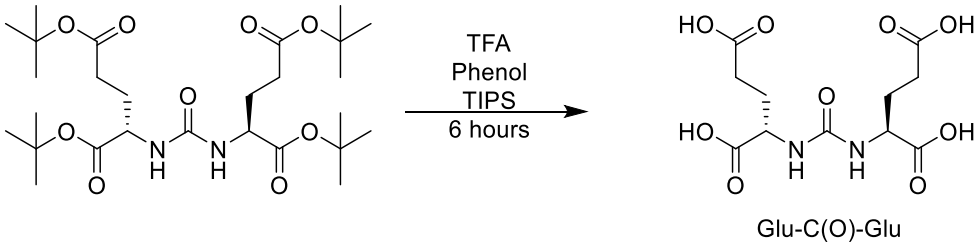

REACTION SCHEME 7.2: Synthesis route for the production of urea-PSMA – Glu-C(O)-Glu.

A solution containing 75 mg phenol (0.8 mmol, MW 94.11), 75 µL H_2O, 35.5 µL TIPS (0.17 mmol, MW 158.36, density 0.773 g/mL) and 1.5 mL TFA (19.6 mmol, MW 114.02, density 1.489 g/mL) was added to 66 mg of $Glu(tBu)_2$-C(O)-$Glu(tBu)_2$ (0.12 mmol, MW = 544.69) and the mixture stirred at room temperature for 6 hours. After this time 5 mL DCM was added and then the solution was evaporated to ~0.5 mL under a stream of nitrogen gas, and 15 mL of ice-cold diethylether was added, whereupon a white solid precipitated. The solid was separated from the diethyl ether by centrifugation, dried overnight at room temperature, dissolved in 7 mL water containing 0.1% TFA and then purified by semi-preparative HPLC. The purified sample was freeze-dried, forming a white solid. 18.6 mg (48% yield) of Glu-C(O)-Glu (50 µmol, MW 320.25) was produced. ^{1}H NMR: (D_2O plus drop of MeOD, 400 MHz, normalised to methanol solvent peak (*23*)) δ 1.97 (m, 2H), 2.16 (m, 2H), 2.50 (t, *J* = 7.6, 4H), 4.26 (dd, *J* = 5.2, 9.2, 2H). ^{13}C NMR: (D_2O plus drop of MeOD, 100 MHz, normalised to methanol solvent peak (*23*)) δ 27.82 (s, 2C), 31.50 (s, 2C), 160.65 (s, 1C), 177.60 (s, 2C), 178.57 (s, 2C). High-resolution mass spectrometry: $[C_{11}H_{16}N_2O_9+H]^+$: observed m/z 321.0924, theoretical m/z 321.0929, $[C_{11}H_{16}N_2O_9+Na]^+$: observed m/z 343.0743, theoretical m/z 343.0748.

7.3.4 Synthesis of Tertiary Butyl Protected Thiourea PSMA; $Glu(tBu)_2$-C(O)-$Glu(tBu)_2$

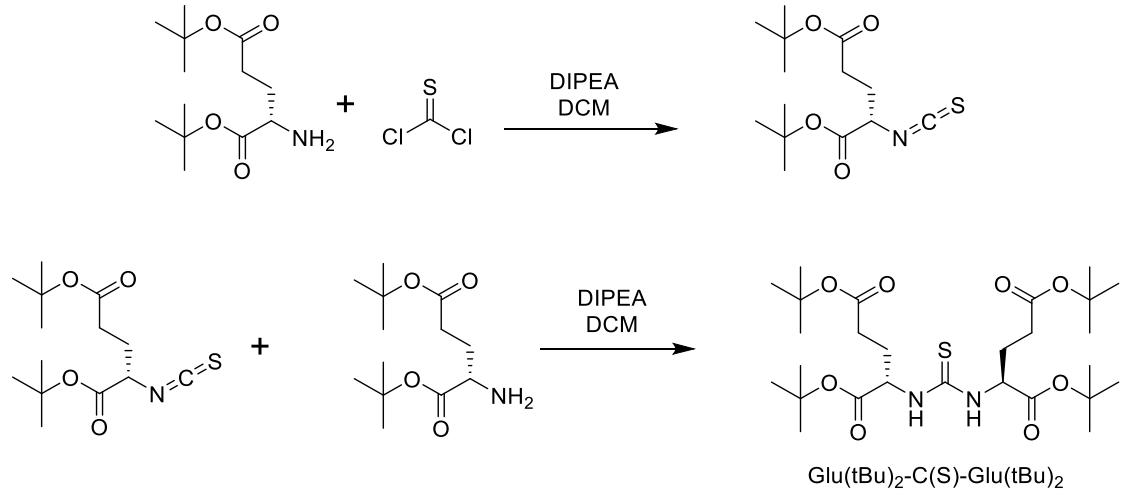

REACTION SCHEME 7.3: Synthesis route for the production of tertiary butyl protected thiourea-PSMA – $Glu(tBu)_2$-C(S)-$Glu(tBu)_2$.

An oven-dried three-necked round-bottomed flask with a dropping funnel was attached to a Schlenk line and cycled with vacuum and nitrogen gas three times. 5 mL DCM was added to the round-bottomed flask, followed by 260 µL of thiophosgene (3.4 mmol, MW 114.98, density 1.5, bright orange liquid). The flask was then cooled to 0°C in an ice bath. L-glutamic acid di-tert-butly ester (1 g, 3.4 mmol, HCl salt, MW 295.8) was dissolved in 20 mL anhydrous DCM and 1.1 mL DIPEA (6.3 mmol, MW 129.2, density 0.742 g/mL) was added dropwise to the flask over 45 minutes using the dropping funnel whilst the flask remained under nitrogen. The solution was stirred throughout the addition and some fuming occurred. The ice bath was then removed and the reaction mixture was left to warm to room temperature for 1 hour. Then a further 1.1 g L-glutamic acid di-tert-butyl ester (3.7 mmol, HCl salt, MW 295.8) dissolved in 20 mL of DCM and 1.1 mL DIPEA (6.3 mmol, MW 129.2, density 0.742 g/mL) was added dropwise to the flask over 45 minutes using the dropping funnel. The flask was left under nitrogen for a further 30 minutes, then sealed and left to stir overnight. The next day the reaction mixture was washed with water (50 mL x 3) and brine (50 mL x 1), dried over magnesium sulfate and then the solvent removed by rotary evaporation. The product was identified using silica TLC with 95:5 DCM:ethyl acetate (starting material R_F = 0, product R_F = 0.4). The crude product was purified using flash chromatography (Biotage Isolaera™ Four) using a 25 g SNAP KP silica column with a DCM and ethyl acetate gradient (100% DCM to 90% DCM, 10% ethyl acetate) and then dried under vacuum to produce $Glu(tBu)_2$-C(S)-$Glu(tBu)_2$ as a light yellow oil which solidified upon standing. 260 mg, 0.46 mmol, a 14% yield (MW 560.75). ^{1}H NMR: ($CDCl_3$, 400 MHz, normalised to chloroform solvent peak (*23*)): δ 1.41 (s, 18H), 1.43 (s, 18H), 1.98 (m, 2H), 2.09 (m, 2H), 2.31 (m,

4H), 4.84 (broad s, 2H), 6.79 (broad s, 2H). ^{13}C NMR: ($CDCl_3$, 100 MHz, normalised to chloroform solvent peak (*23*)): δ 27.75 (s, 2C), 28.06 (s, 6C), 28.13 (s, 6C), 31.39 (s, 2C), 56.93 (s, 2C), 80.84 (s, 2C), 82.53 (s, 2C) 171.38 (s, 2C) 172.51 (s, 2C), 182.50 (s, 1C). High-resolution mass spectrometry: $[C_{27}H_{48}N_2O_8S+H]^+$: observed m/z 561.3195, theoretical m/z 561.3204, $[C_{27}H_{48}N_2O_8S+Na]^+$: observed m/z 583.3010, theoretical m/z 583.3024

7.3.5 Synthesis of Thiourea-PSMA; Glu-C(S)-Glu

A number of different deprotection strategies were employed to obtain Glu-C(S)-Glu. The details of each will be described here. The method used to produce the Glu-C(S)-Glu used for characterisation, stability and cell studies was method C2.

7.3.5.1 Deprotection Method A – Trifluoroacetic Acid

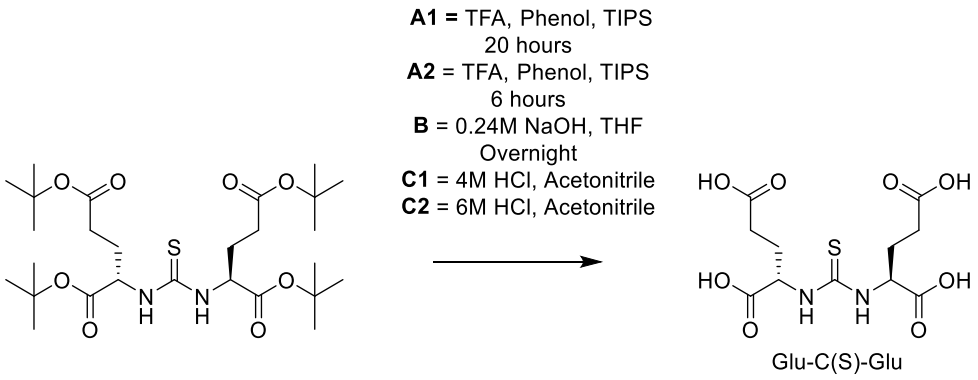

REACTION SCHEME 7.4: Synthesis routes for the production of thiourea-PSMA – $Glu(tBu)_2$-C(S)-$Glu(tBu)_2$.

Method A1 - 20 hour deprotection: A solution containing, 150 mg phenol (1.6 mmol MW 94.11), 150 µL H_2O, 75 µL TIPS (0.35 mmol, MW 158.36, density 0.773 g/mL) and 3 mL TFA (39 mmol, MW 114.02, density 1.489 g/mL) was added to 300 mg of $Glu(tBu)_2$-C(S)-$Glu(tBu)_2$ (0.53 mmol, MW = 560.75) and the mixture stirred at room temperature for 20 hours. After this time 2 mL DCM was added and then the solution was evaporated down under a stream of nitrogen gas. Once only ~0.5 mL remained 15 mL of ice-cold diethyl ether was added, and the resulting white solid was separated from the diethyl ether by centrifugation, dissolved in water and dried overnight in the freeze drier. Analysis of this crude mixture was carried out by analytical HPLC method 1. Purification was carried out with a 2 g C_{18} cartridge preconditioned with acetonitrile/0.1% TFA followed by water/0.1% TFA. The reaction mixture was loaded in water/0.1% TFA and the reaction products eluted with increasing concentrations of acetonitrile. Each fraction was analysed by MS with direct injection in positive ion mode, data are provided in the results section along with the identity of the compounds produced.

Method A2 - 6 hour deprotection: A solution containing 150 mg phenol (1.6 mmol, MW 94.11), 150 µL H_2O, 75 µL TIPS (0.35 mmol, MW 158.36, density 0.773 g/mL) and 4 mL TFA (52 mmol, MW 114.02, density 1.489 g/mL) was added to 200 mg of $Glu(tBu)_2$-C(S)-$Glu(tBu)_2$ (0.35 mmol, MW = 560.75) and the mixture stirred at room temperature for 6 hours. After this time 2 mL DCM was added and then the solution was evaporated down under a stream of nitrogen gas. Once only ~0.5 mL remained 15 mL of ice-cold diethyl ether was added, and the resulting white solid separated from the diethyl ether by centrifugation, dissolved in water and dried overnight in the freeze drier. Analysis of this crude mixture was carried out by analytical HPLC method 1. Purification was carried out with a 2 g C_{18} cartridge preconditioned with acetonitrile/0.1% TFA followed by water/0.1% TFA. The reaction mixture was loaded in water/0.1% TFA and the reaction products eluted with increasing concentrations of acetonitrile. Each fraction was analysed by direct injection low-resolution MS. Purification on the other half of the solid mixture was also carried out with semi-preparative HPLC, the desired fractions were freeze-dried and then analysed by MS, direct injection in positive ion mode, data are provided in the results section along with the identity of the compounds produced.

7.3.5.2 Deprotection Method B – Sodium Hydroxide and Tetrahydrofuran

$Glu(tBu)_2$-C(S)-$Glu(tBu)_2$ (100 mg, 178 µmol, MW 560.75) was dissolved in 7.5 mL of tetrahydrofuran and 7.5 mL of a 0.24 M NaOH solution. This solution was refluxed overnight at 85°C. The next day the solution had turned orange-yellow. The reaction mixture was cooled to room temperature and neutralised to pH 5 with 4 M HCl. The colour faded upon neutralisation. The solvents were removed by rotary evaporation and then the product was separated from the salt of neutralisation and purified using a 2 g C_{18} cartridge preconditioned with acetonitrile 0.1% TFA followed by water 0.1% TFA. The reaction mixture was loaded in water/0.1% TFA and the reaction products eluted with increasing concentrations of acetonitrile. The crude product and each fraction from this purification method was analysed by MS, direct injection in positive ion mode, data are provided in the results section along with the identity of the compounds produced.

7.3.5.3 Deprotection Method C – Hydrochloric Acid and Acetonitrile

Deprotection method C1: $Glu(tBu)_2$-C(S)-$Glu(tBu)_2$ (5 mg, 9 µmol, MW 560.75) was dissolved in 1 mL acetonitrile and 0.5 mL 4 M HCl. The reaction was stirred at room temperature and samples were taken for HPLC and LC-MS analysis at 18 hours, 90 hours and 138 hours. After this time the

reaction solution was reduced to less than 0.5 mL on the rotary evaporator and then diluted to 5 mL in H_2O. This solution was purified using semi-preparative HPLC and the desired fraction freeze-dried and dissolved in D_2O and analysed by NMR. Data are provided in the results section along with the identity of the compounds produced.

Deprotection method C2: $Glu(tBu)_2$-C(S)-$Glu(tBu)_2$ (30 mg, 53.5 µmol, MW 560.75) was dissolved in 4 mL acetonitrile and 2 mL 6 M HCl (final concentration 5 mg/mL) and stirred at room temperature for 8 hours. The reaction was monitored by HPLC. Figure 7.23 shows the HPLC results at the point that the reaction was quenched. After 8 hours the solution was neutralised to pH 3-7 with NaOH (4 M ~3330 µL), frozen and then freeze-dried to form a white powder. The solid was dissolved in 6 mL H_2O containing 0.1% TFA and then purified by semi-preparative HPLC and freeze-dried forming a white solid. 7.7 mg (43%) of (Glu-C(S)-Glu) (22.8 µmol, MW 336.32). ^{1}H NMR: ($(CD_3)_2SO$, 400 MHz, normalised to DMSO solvent peak (*23*)): δ 1.85 (m, 2H), 2.01 (m, 2H), 2.25 (m, 4H), 4.79 (dd, *J*=7.2, 12.8, 2H), 7.82 (d, *J*=8, 2H), 12.45 (broad s, 4H). ^{1}H NMR: (D_2O PBS, 400 MHz, normalised to H_2O solvent peak (*23*)) δ 2.10 (m, 2H), 2.24 (m, 2H), 2.48 (t, *J*=8 4H). It is assumed that the additional expected CH peak resides under the H_2O solvent peak. High-resolution mass spectrometry: $[C_{11}H_{16}N_2O_8S+H]^+$: observed m/z 337.0697, theoretical m/z 337.0700, $[C_{11}H_{16}N_2O_8S+Na]^+$ observed m/z 359.0515, theoretical m/z 359.0520.

7.3.6 Alternative Protection Strategy: Synthesis of Benzyl-Ester Protected Thiourea-PSMA; Glu(Bn)2-C(S)-$Glu(Bn)_2$

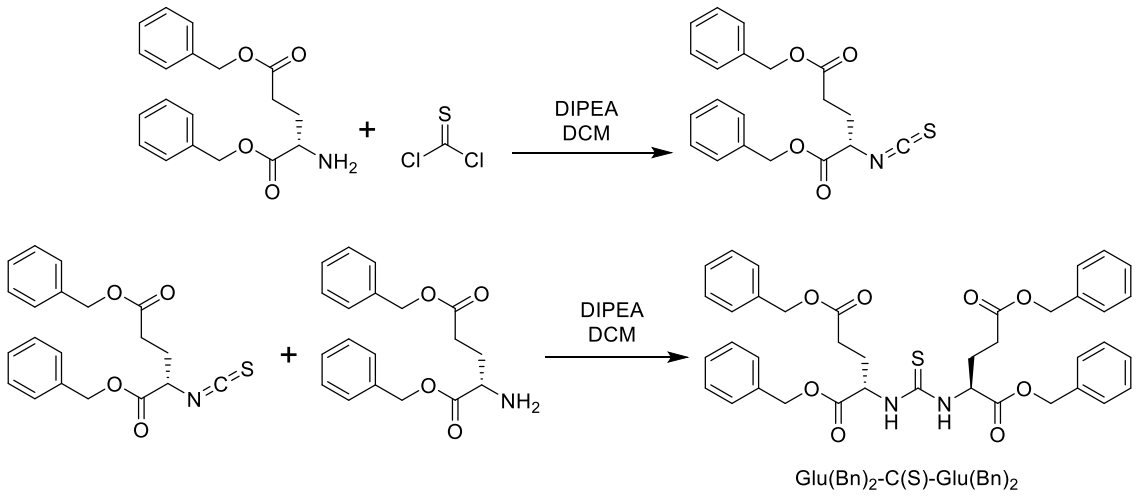

REACTION SCHEME 7.5: Synthesis route for the production of benzyl-ester protected thiourea-PSMA – $Glu(Bn)_2$-C(S)-$Glu(Bn)_2$.

As well as different deprotection strategies, different protection methods were investigated.

Method 1 – standard DIPEA levels: An oven-dried 3-necked round-bottomed flask with a dropping funnel was attached to a Schlenk line and cycled with vacuum and nitrogen gas three times. 5 mL DCM was added to the round-bottomed flask, followed by 250 µL of thiophosgene (3 mmol, MW 114.98, density 1.5, bright orange liquid) the flask was then cooled to 0°C in an ice bath. L-glutamic acid di-benzyl-ester (1 g, 2.75 mmol, HCl salt, MW 363.8) was dissolved in 20 mL anhydrous DCM and 1 mL DIPEA (5.7 mmol, MW 129.2, density 0.742 g/mL) was added dropwise to the flask over 45 minutes using the dropping funnel whilst the flask remained under nitrogen. The yellow solution was stirred throughout the addition and some fuming occurred. The ice bath was then removed and the reaction mixture left to warm to room temperature for 1 hour. Then a further 1.1 g L-glutamic acid di-benzyl-ester (3.0 mmol, HCl salt, MW 363.8) dissolved in 20 mL of DCM and 1 mL DIPEA (5.7 mmol, MW 129.2, density 0.742 g/mL) was added dropwise to the flask over 1 hour using the dropping funnel and the solution turned yellow. The flask was left under nitrogen for a further 30 minutes, then sealed and left to stir overnight. The reaction mixture was washed with water (50 mL x 3) and brine (50 mL x 1), dried over magnesium sulfate and then the solvent removed by rotary evaporation. The product was identified using silica TLC with 50:50 hexane:ethyl acetate (starting material R_F = 0, product R_F=0.9). The crude product was purified using flash chromatography (Biotage Isolaera™ Four) using a 25 g SNAP KP silica column with a hexane and ethyl acetate gradient (100% hexane to 20% ethyl acetate). The collected fractions were dried under vacuum and analysed by MS, direct injection in positive ion mode. Data are provided in the results section along with the identity of the compounds produced.

Method 2- increased DIPEA levels: An oven-dried 3-necked round-bottomed flask, with a dropping funnel was attached to a Schlenk line and cycled with vacuum and nitrogen gas three times. 5 mL DCM was added to the round-bottomed flask, followed by 240 µL of thiophosgene (2.75 mmol, MW 114.98, density 1.5, bright orange liquid). The flask was then cooled to 0°C in an ice bath. L-glutamic acid di-benzyl-ester (1 g, 2.75 mmol, HCl salt, MW 363.8) was dissolved in 20 mL anhydrous DCM and 1.1 mL DIPEA (6.3 mmol, MW 129.2, density 0.742 g/mL) was added dropwise to the flask over 30 minutes using the dropping funnel whilst the flask remained under nitrogen. The yellow solution was stirred throughout the addition and some fuming occurred. The ice bath was then removed and the reaction mixture left to warm to room temperature for 1 hour. Then a further 1 g L-glutamic acid di-benzyl-ester (2.75 mmol, HCl salt, MW 363.8) dissolved in 20 mL of DCM and 2 mL DIPEA (11.4 mmol, MW 129.2, density 0.742 g/mL) was added dropwise to the flask over 1 hour using the dropping funnel and the solution turned red-brown. The flask was left under nitrogen for a further 30 minutes, then sealed and

left to stir overnight at room temperature. The reaction mixture was washed with water (50 mL x 3) and brine (50 mL x 1), dried over magnesium sulfate and then the solvent removed by rotary evaporation. The product was identified using silica TLC with 95:5 DCM:ethyl acetate (starting material R_F = 0, product R_F = 0.2, side-product R_F = 0.6). 500mg of the crude product was purified using flash chromatography (Biotage Isolaera™ Four) using a 10 g SNAP KP silica column with a hexane and ethyl acetate gradient (100% DCM to 100% ethyl acetate) which produced 3 different peaks, although peaks 2 and 3 were not well-separated by the gradient. The collected fractions were dried under vacuum and analysed by LC-MS in positive ion mode. Data are provided in the results section along with the identity of the compounds produced.

7.3.7 Stability Studies

These studies have shown that the cyclisation of Glu-C(S)-Glu to Glu-C(S)-pyroGlu occurs at both high and low pH, and that this cyclisation is detectable by NMR. Therefore it was important to ensure that the product was stable at pH 7, the pH at which cell studies would be carried out. In order to ensure that Glu-C(S)-Glu was stable at near neutral pH the compound was dissolved in D_2O containing ten times the standard concentration of PBS (NaCl 1.37M, KCl 27 mM, Na_2HPO_4 100 mM, KH_2PO_4 18 mM). This only brought the pH to 4 and so ammonium acetate was used to raise the pH to at least 6.5 (final concentration 1 M ammonium acetate). This mixture was then monitored by ^1H NMR (400 MHz) at time points up to 48 hours to look for any evidence of cyclisation. The same experiment was also carried out with Glu-C(O)-Glu over 48 hours.

7.3.8 Concentration Determination by NMR

In order to determine the relative concentration of the two inhibitors urea-PSMA (Glu-C(O)-Glu) and thiourea-PSMA (Glu-C(S)-Glu), quantitative NMR studies were performed. Here, equal volumes (200 µL) of the two stability samples (~25 mM) containing Glu-C(O)-Glu and Glu-C(S)-Glu were mixed and then a further 200 µL of a 125 mM NMR standard, maleic acid, was added. This sample was analysed in a shaped NMR tube with an oval rather than a circular cross-section (Bruker Z106898). This shaped tube reduces the negative impact that the conductivity of high salt solutions (< 60 mM) has on the signal-to-noise ratio by reducing the resistance of the sample to radio frequency penetration (*24*). Analysis was conducted on an 800 MHz NMR with a relaxation time (D_1) of 20 seconds, long enough to ensure that the spectrum was quantitative. The 800 MHz machine gave improved resolution and separation between the peaks of interest compared to the 400 MHz. The integration of these peaks was used to confirm the concentration

of each solution that had been mixed to produce this NMR sample. These solutions of known concentrations were used to prepare the inhibitor solutions for future cell assays.

7.3.9 Cell Studies

The GCP(II)/PSMA-negative cell line chosen was DU145, a human carcinoma prostate cancer cell line derived from a brain metastatic site, which does not express GCP(II)/PSMA. The GCP(II)/PSMA-expressing cell line chosen was a genetically modified daughter cell line of DU145, DU145-PSMA. This cell line had previously been transduced to express full-length human GCP(II)/PSMA, with a published method (*25*). These cells were cultured in RMPI 1640 medium supplemented with 10% foetal bovine serum, 2 mM L-glutamine, and penicillin/streptomycin. To prepare for experiments, cells were grown at 37°C in an incubator equilibrated with humidified air and 5% CO_2.

IC_{50}: To determine the IC_{50}, competitive binding studies were performed with DU145-PSMA cells with 1 nM [^{68}Ga]Ga-DOTA-PSMA as the probe and blocking with Glu-C(O)-Glu, Glu-C(S)-Glu and PMPA over a range of concentrations (1 nM - 400 µM). As both Glu-C(O)-Glu and Glu-C(S)-Glu had been dissolved in 10 x PBS and 1 M ammonium acetate to maintain pH at 7 for the stability and quantification NMR studies, care was taken to ensure that the same amount of these reagents were added into every well used in this assay. Cells (0.25×10^6 per well) were seeded in a 24-well plate, 1 day before the assay. At the time of the assay, the medium was removed and replaced with 240 µL of complete RMPI medium at 37°C. Increasing concentrations of Glu-C(O)-Glu, Glu-C(S)-Glu or PMPA (5 µL dissolved in 1 M ammonium acetate and 10 x PBS) followed by 1 nM [^{67}Ga]Ga-DOTA-PSMA (5 µL, molar activity 5–10 MBq/nmol, diluted in PBS) were added to the cells (total volume, 250 µL). A control was also included to account for non-specific binding where non-GCP(II)/PSMA-expressing cells (DU145) prepared in the same way were also incubated with 1 nM [^{67}Ga]Ga-DOTA-PSMA. After 1 hour incubation at 37°C, the supernatant was removed and the cells were washed with PBS (2 × 0.25 mL), lysed with NaOH (1 M, 0.25 mL), and the wells washed with PBS (0.25 mL). The activity present in supernatant and lysate was measured by γ-counting. Data were analysed using GraphPad Prism (version 7.04 GraphPad Software) and a 1-site–fit log IC_{50} algorithm.

Stability of Glu-C(S)-Glu in the presence of cells: NMR spectroscopy was used to determine if cyclisation of Glu-C(S)-Glu to Glu-C(S)-pyroGlu occurred whilst the blocking agent was incubated with cells. DU145-PSMA cells (1×10^6 per well) were seeded in a 6-well plate, 1 day before the assay. At the time of the assay, the medium was removed and replaced with 980 µL of PBS at

37°C. Then 20 µL of Glu-C(S)-Glu was added (dissolved in 1 M ammonium acetate and 10 x PBS) to give a final concentration of 400 µM on the cells. The cells were then incubated at 37°C for 1 hour. As a control, wells without any cells were incubated with Glu-C(S)-Glu in the same way. After 1 hour the supernatant was removed from the wells (containing cells or with no cells), centrifuged to remove any cell debris or particulates, then analysed by ^{1}H NMR spectroscopy at 400 MHz.

7.3.10 Statistical Analysis

Data were analysed in GraphPad Prism 5 (version 5.04 or version 7.04) and expressed as mean ± standard deviation. Student t tests were used to determine statistical significance; a P value of less than 0.05 was considered significant.

7.4 Results

7.4.1 Synthesis of Urea-PSMA; Glu-C(O)-Glu

Urea-PSMA (Glu-C(O)-Glu) was successfully synthesised in two steps. In the first, the tertiary butyl-protected form ($Glu(tBu)_2$-C(O)-$Glu(tBu)_2$) was produced by the reaction of tertiary butyl-protected glutamic acid with triphosgene in the presence of DIPEA base to form an isocyanate intermediate. This was then reacted with a further protected glutamic acid in the presence of excess DIPEA base. This formed a urea bond between these two amino acids producing the symmetrical product $Glu(tBu)_2$-C(O)-$Glu(tBu)_2$. After purification with flash column chromatography, this product was deprotected using trifluoroacetic acid in the presence of phenol and TIPS as scavengers. The final product was then purified by semi-preparative HPLC and characterised. The NMR spectroscopy and high-resolution mass spectrometry results are detailed in the methods section and the IR spectra of the two compounds are shown in figure 7.5 and figure 7.6.

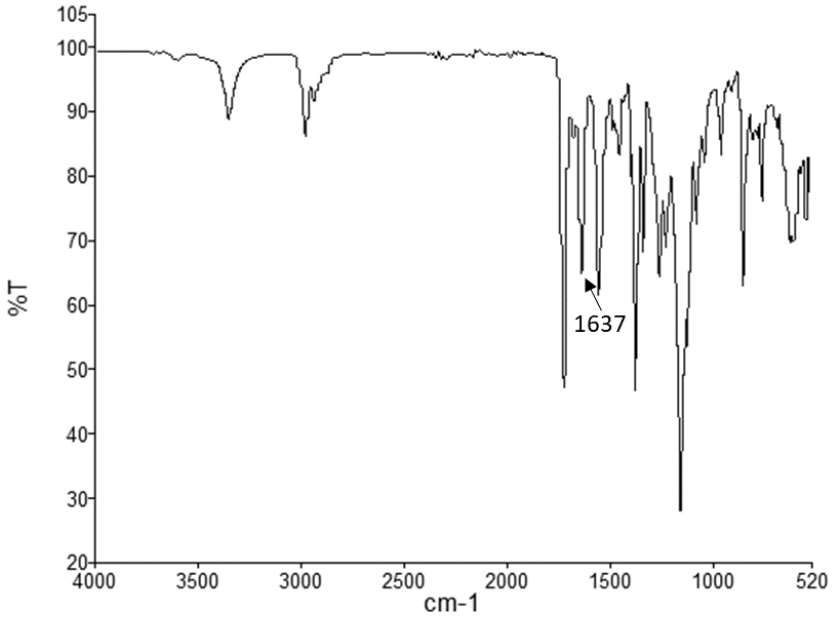

FIGURE 7.5: IR spectrum for tertiary butyl-protected urea-PSMA $Glu(tBu)_2$-C(O)-$Glu(tBu)_2$: a characteristic urea C=O stretch is seen at 1637 cm^{-1} (26).

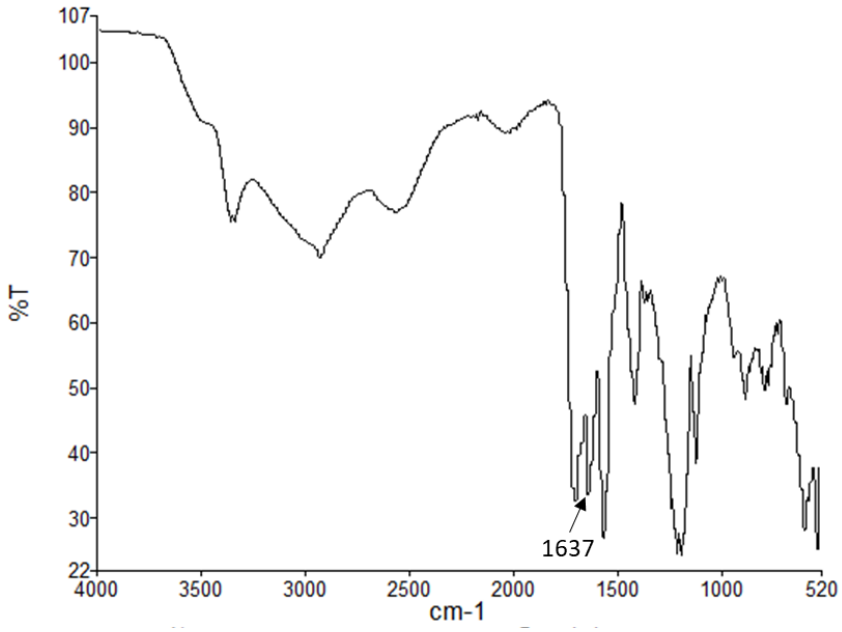

FIGURE 7.6: IR spectrum for Glu-C(O)-Glu: a characteristic urea C=O stretch is seen at 1637 cm^{-1} (26).

7.4.2 Synthesis of Tertiary Butyl Protected Thiourea-PSMA; $Glu(tBu)_2$-C(S)-$Glu(tBu)_2$

The t-butyl-protected thiourea-PSMA ($Glu(tBu)_2$-C(S)-$Glu(tBu)_2$) was produced by the reaction of t-butyl protected glutamic acid with thiophosgene in the presence of DIPEA base to form an isothiocyanate intermediate which was then reacted with t-butyl-protected glutamic acid in the presence of excess DIPEA base. This formed a thiourea bond between these two amino acids producing the symmetrical product $Glu(tBu)_2$-C(S)-$Glu(tBu)_2$. The protected thiourea intermediate was purified by flash column chromatography and characterised. The NMR spectroscopy and high-resolution mass spectrometry results are detailed in the methods section and the IR spectrum of the compound is shown in figure 7.7.

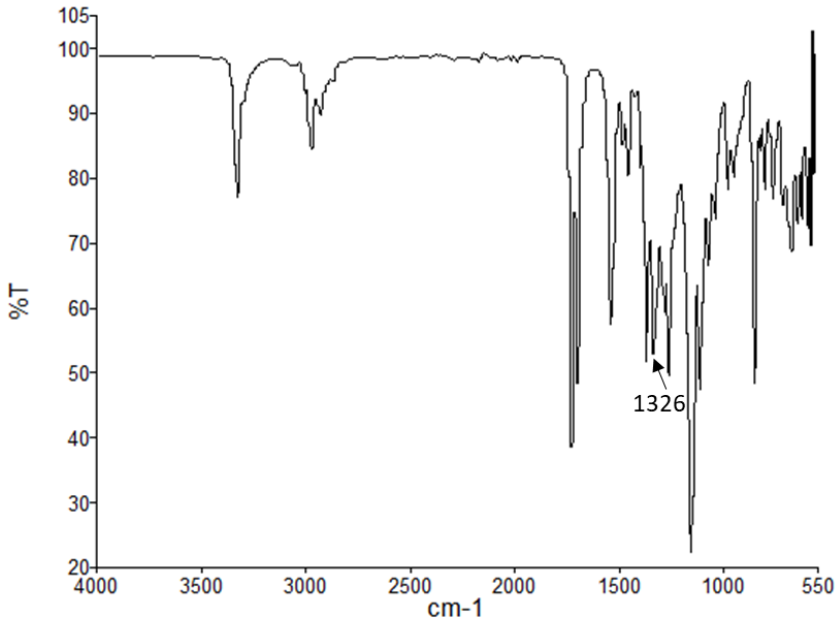

FIGURE 7.7: IR spectrum for tertiary butyl-protected thiourea-PSMA Glu(tBu)$_2$-C(S)-Glu(tBu)$_2$: a characteristic thiourea C=S stretch is seen at 1326 cm^{-1} (26).

7.4.3 Synthesis of Thiourea-PSMA; Glu-C(S)-Glu

A number of different strategies were investigated for the deprotection of the t-butyl protected thiourea-PSMA in order to produce thiourea-PSMA (Glu-C(S)-Glu). This was required due to the formation of side-products when deprotection was carried out with the same method as used for the preparation of urea-PSMA. After optimisation experiments, method C2, which used acetonitrile and 6 M HCl for deprotection, was used to isolate enough thiourea-PSMA (Glu-C(S)-Glu) for thorough characterisation and cell studies.

7.4.3.1 Deprotection Method A1 – TFA 20 hours

When deprotection of thiourea-PSMA with TFA was carried out for 20 hours, the crude product contained a mixture of products, as determined by analytical HPLC (method 1 figure 7.8). This was then purified using a C_{18} cartridge eluted with increasing concentrations of acetonitrile. The mass spectra were determined for these fractions and the 9:1 water: acetonitrile fraction showed a major peak with of 319 m/z (figure 7.9). This mass corresponds to the desired product ([Glu-C(S)-Glu+H]$^+$ m/z = 337.06) minus 18 mass units, which is likely to correspond to the loss of a water molecule (exact mass = 18.01), suggesting a dehydration reaction had occurred. Further investigation was required to determine whether this dehydration was occurring in the mass spectrometer or during the deprotection process.

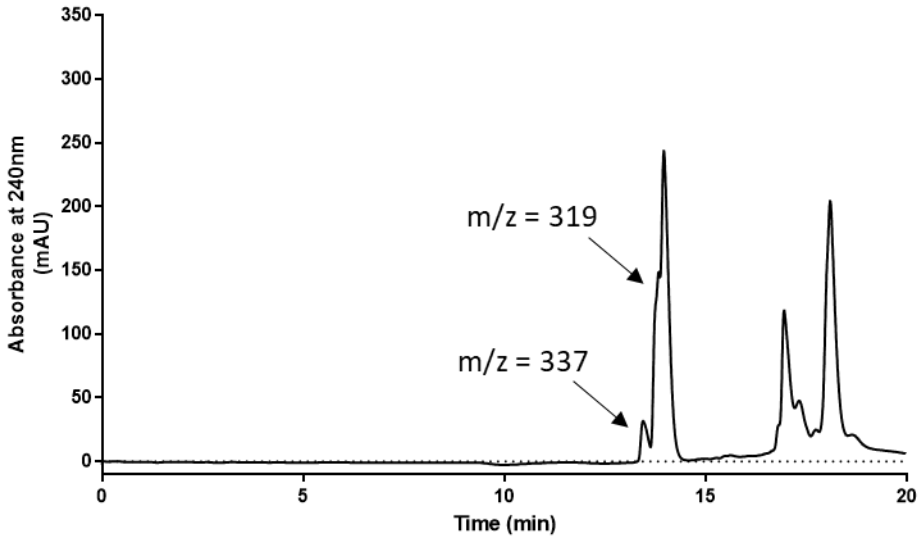

FIGURE 7.8: HPLC analysis of the crude deprotection mixture, after Glu(tBu)$_2$-C(S)-Glu(tBu)$_2$ was reacted with TFA for 20 hours, method A1. HPLC method 1.

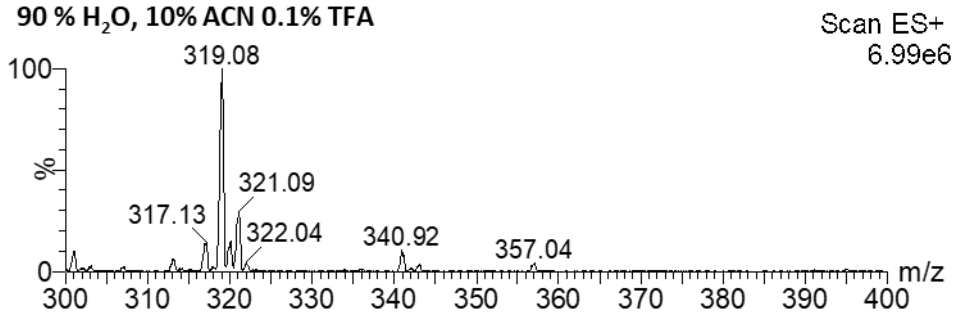

FIGURE 7.9: MS analysis of C_{18} purified product, after Glu(tBu)$_2$-C(S)-Glu(tBu)$_2$ was reacted with TFA for 20 hours. The major signal at 319.08 m/z corresponds to the mass of Glu-C(S)-Glu minus 18 mass units, suggesting the loss of water.

7.4.3.2 Deprotection Method A2 – TFA 6 hours

When the deprotection time was reduced from 20 hours to 6 hours, the analytical HPLC (method 1) of the crude product still showed multiple peaks, but a larger peak was observed at a retention time of 13.5 minutes as shown in figure 7.10. This crude mixture was purified by two different methods, C_{18} cartridge and semi-preparative HPLC. The MS analysis of the fractions from the C_{18} cartridge showed major peaks with an m/z of 301, 319 and 337 in the 5% and 10% acetonitrile washes as shown in figure 7.11 and figure 7.12. The peak at m/z 337 corresponds to the value of the desired product [Glu-C(S)-Glu+H]$^+$ demonstrating it was detectable in the MS and therefore the peak at 319 is unlikely to be a MS artefact or product of a gas phase reaction. The signal at 319 has 18 fewer mass units than [Glu-C(S)-Glu+H]$^+$, and the signal at 301 has a further loss of 18 mass units suggesting the sequential loss of water from the molecule. Semi-

preparative HPLC was used to isolate the major peaks produced upon deprotection and determine their identity. The MS of the first peak isolated by preparative HPLC showed a major peak at 337 m/z corresponding to the desired product, and a small peak at 319 m/z (figure 7.13). The second isolated peak showed a major product at 337 m/z but also a peak at 319 m/z (figure 7.14). This suggests that semi-preparative HPLC could separate these two products, but of course, it would be ideal to only produce Glu-C(S)-Glu during deprotection by avoiding production of this dehydrated side product.

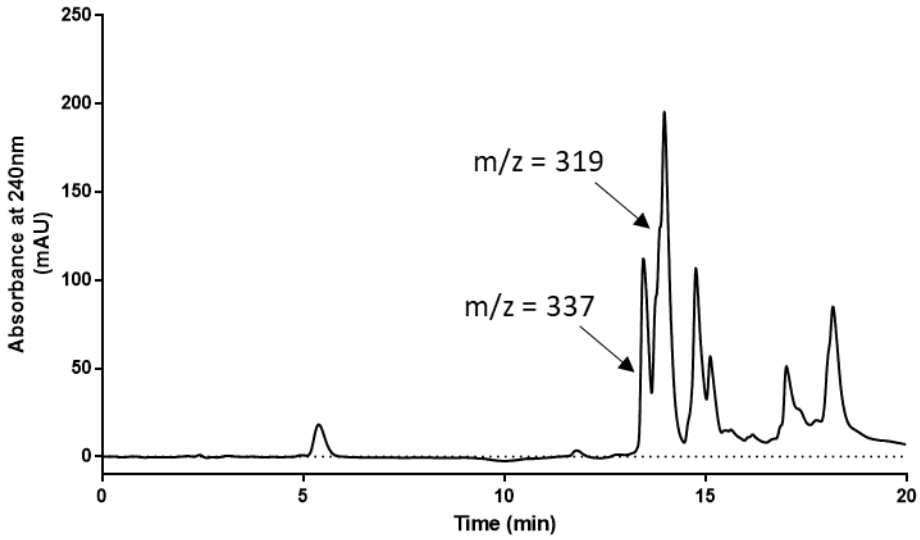

FIGURE 7.10: HPLC analysis of the crude deprotection mixture, after $Glu(tBu)_2$-C(S)-$Glu(tBu)_2$ was reacted with TFA for 6 hours, method A2. HPLC method 1.

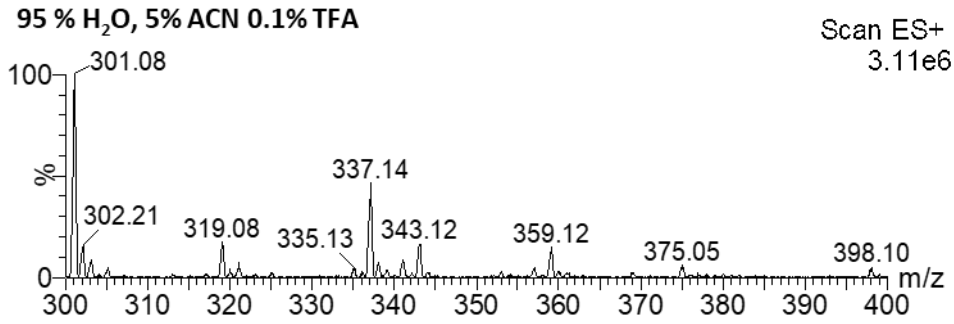

FIGURE 7.11: MS analysis of the C_{18} purified product, after $Glu(tBu)_2$-C(S)-$Glu(tBu)_2$ was reacted with TFA for 6 hours method A2 . The major peak at 337 m/z corresponds to the mass of Glu-C(S)-Glu, and the signal at m/z =319.08 corresponds to the mass of Glu-C(S)-Glu minus 18 mass units, suggesting the loss of water.

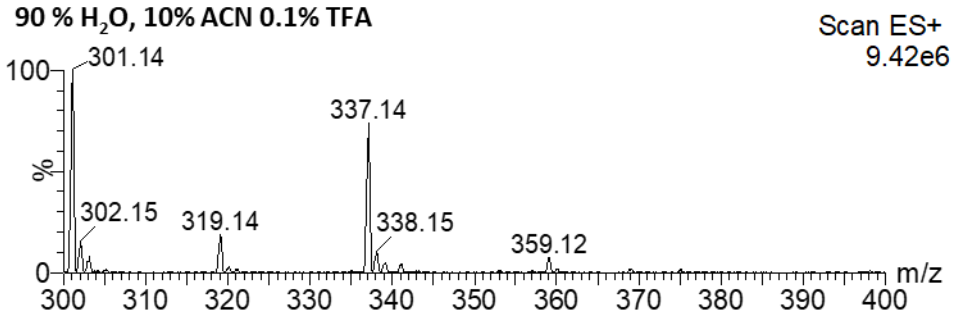

FIGURE 7.12: MS analysis of C_{18} purified product, after Glu(tBu)$_2$-C(S)-Glu(tBu)$_2$ was reacted with TFA for 6 hours method A2. The major signal at 337 m/z corresponds to the mass of Glu-C(S)-Glu. The signal at 319 m/z =319.08 corresponds to the mass of Glu-C(S)-Glu minus 18 mass units, suggesting the loss of water.

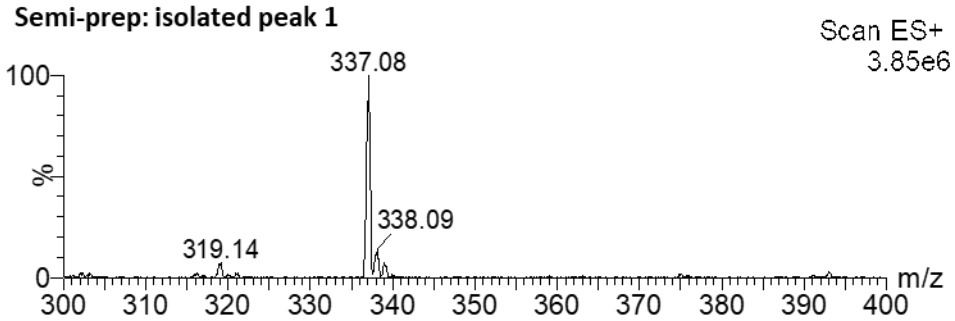

FIGURE 7.13: MS analysis of reaction products purified by semi-preparative HPLC, after Glu(tBu)$_2$-C(S)-Glu(tBu)$_2$ was reacted with TFA for 6 hours method A2. The major signal at 337 m/z corresponds to the mass of Glu-C(S)-Glu.

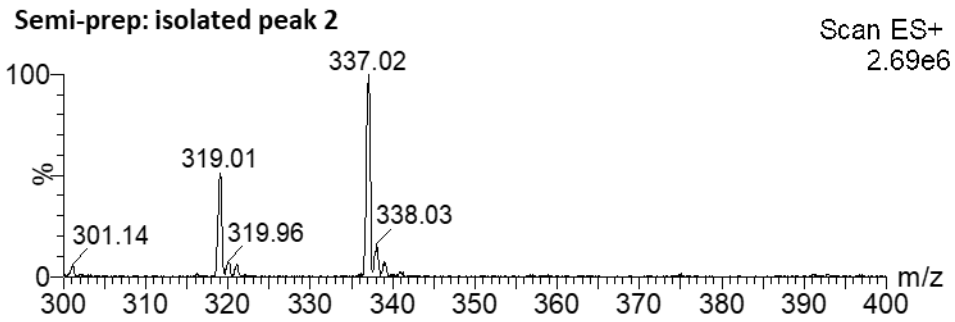

FIGURE 7.14: MS analysis of reaction products purified by semi-preparative HPLC, after Glu(tBu)$_2$-C(S)-Glu(tBu)$_2$ was reacted with TFA for 6 hours, method A2. The major signal at 337 m/z corresponds to the mass of Glu-C(S)-Glu. The signal at 319.08 m/z corresponds to the mass of Glu-C(S)-Glu minus 18 mass units, suggesting the loss of water.

7.4.3.3 Deprotection Method B.

As the undesired side product in methods A1 and A2 appeared to be a dehydration product that was formed under low water but highly acidic conditions, an alternative method was tested in

which an aqueous base was used to deprotect the tertiary butyl groups. A disadvantage of this method was that at the end of the reaction the sodium hydroxide was neutralised to pH 5 with hydrochloric acid, which produced a large excess of salt. This had to be removed from the solution before the product could be isolated and impeded analysis of the crude mixture by MS. However, MS signals were observed in a highly diluted sample of the crude mixture as shown in figure 7.15. The signals differ by a mass of 22 and were therefore most likely sodium adducts. It was therefore assumed that the same side product, a dehydrated form of Glu-C(S)-Glu, had formed (336 – 18 (H_2O) + 23 (Na) = 341). This was confirmed by removing the salt and purifying the crude mixture with a C_{18} cartridge. The 9:1 water:acetonitrile/0.1% TFA fraction was analysed by MS and showed a signal at m/z = 319 corresponding to the same dehydrated side-product observed for previous deprotections (figure 7.16). This suggests that the highly basic conditions of this reaction caused this dehydration to occur, even in the presence of water. Heating of the reaction mixture is also likely to have accelerated the formation of this undesired dehydrated product.

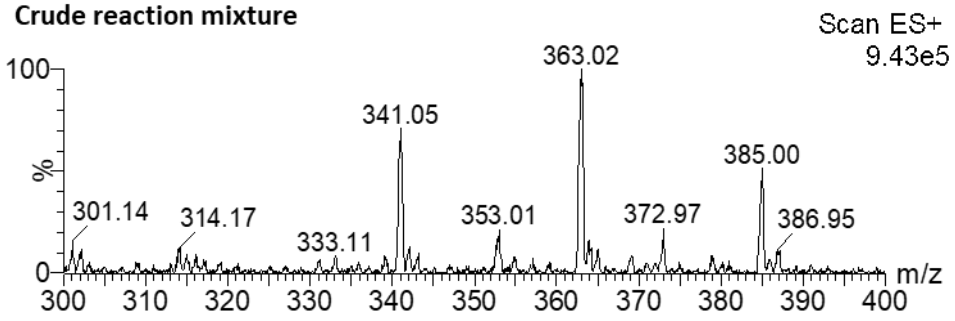

FIGURE 7.15: MS analysis of the crude reaction mixture, after Glu(tBu)$_2$-C(S)-Glu(tBu)$_2$ was deprotected by method B. The major signal at 341 m/z corresponds to the mass of the dehydrated Glu-C(S)-Glu plus sodium.

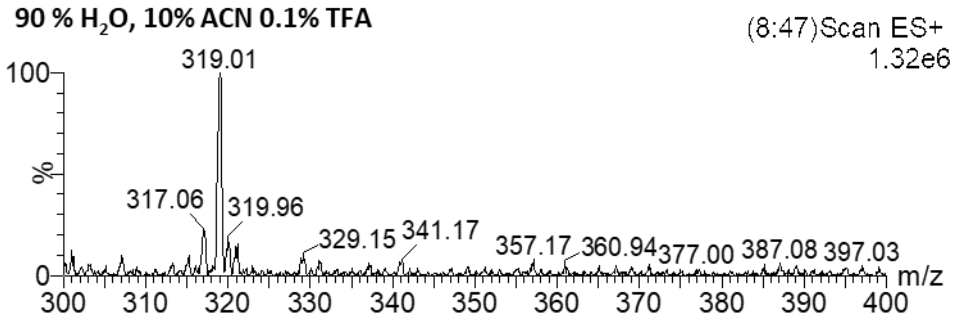

FIGURE 7.16: MS analysis of the crude reaction mixture, after Glu(tBu)$_2$-C(S)-Glu(tBu)$_2$ was deprotected by method B. The major signal at 319 m/z corresponds to the mass of the dehydrated Glu-C(S)-Glu.

7.4.3.4 Deprotection Method C1

In an attempt to avoid the dehydration of Glu-C(S)-Glu, reaction conditions C1 were chosen to slow down the deprotection and allow the formation of the different species in solution to be observed over time. The conditions chosen were 1 mL acetonitrile to ensure the $Glu(tBu)_2$-C(S)-$Glu(tBu)_2$ was fully dissolved, and 0.5 mL 4 M HCl to provide the acidic conditions for deprotection but also enough water to reduce dehydration. The reaction was then monitored by analytical HPLC method 2 and LC-MS. The combined analytical HPLC and LC-MS results after 18 hours of reaction can be seen in figure 7.17A. The fully protected $Glu(tBu)_2$-C(S)-$Glu(tBu)_2$ was still observed, plus each of the partially deprotected species (Glu(tBu)-C(S)-$Glu(tBu)_2$, Glu-C(S)-$Glu(tBu)_2$/Glu(tBu)-C(S)-Glu(tBu), Glu-C(S)-Glu(tBu)), and the desired final product Glu-C(S)-Glu. This demonstrates that deprotection happens sequentially and that under these conditions the desired product Glu-C(S)-Glu was produced before the dehydrated side-product. Note also that there are 2 signals with masses corresponding to Glu-C(S)-$Glu(tBu)_2$, suggesting a mixture of constitutive isomers gives rise to different retention behaviours on the C_{18} column. After 90 hours the majority of the deprotection reaction was completed with only a small peak observed corresponding to Glu-C(S)-Glu(tBu) at a retention time of 16 minutes as shown in figure 7.17B. The LC-MS of this sample confirmed that the major peak was Glu-C(S)-Glu and that the second peak was the dehydrated side product with an m/z of 319. After 138 hours, the sample was fully deprotected and the major species had become the dehydrated side-product (figure 7.17C). In order to understand more about this side-product and to isolate as much Glu-C(S)-Glu as possible. This sample was purified by semi-preparative HPLC, the fractions containing the 2 peaks were freeze-dried and then analysed by HPLC and NMR. Figure 7.18 shows the analytical HPLC (method 2) for each peak isolated by semi-preparative HPLC, demonstrating there is no interconversion during this separation/purification.

The ^1H NMR spectra of the dehydrated side-product is shown in figure 7.19 and the corresponding COSY is shown in figure 7.20. These results suggest that Glu-C(S)-Glu has been dehydrated under the reaction conditions and has cyclised to form Glu-C(S)-pyroGlu. The integration of each peak matches this cyclised structure as does the evidence from the COSY spectrum, as the peak at 5.28 ppm is only coupled to the peak at 2.47 ppm. The NMR spectra for the isolated Glu-C(S)-Glu peak (figure 7.21) shows that the major product is the desired compound but there is also some cyclised material present. This cyclisation could have occurred after purification as the product was stored in acidic conditions (HPLC buffer containing 0.1% TFA) and suggests that this product is sensitive to low pH and should only be stored as a solid or at near-neutral pH. This investigation has revealed that the deprotection is sequential, and that

the cyclised product is only produced after the desired product. The different species produced under these reaction conditions and the order in which they are produced are shown in figure 7.22.

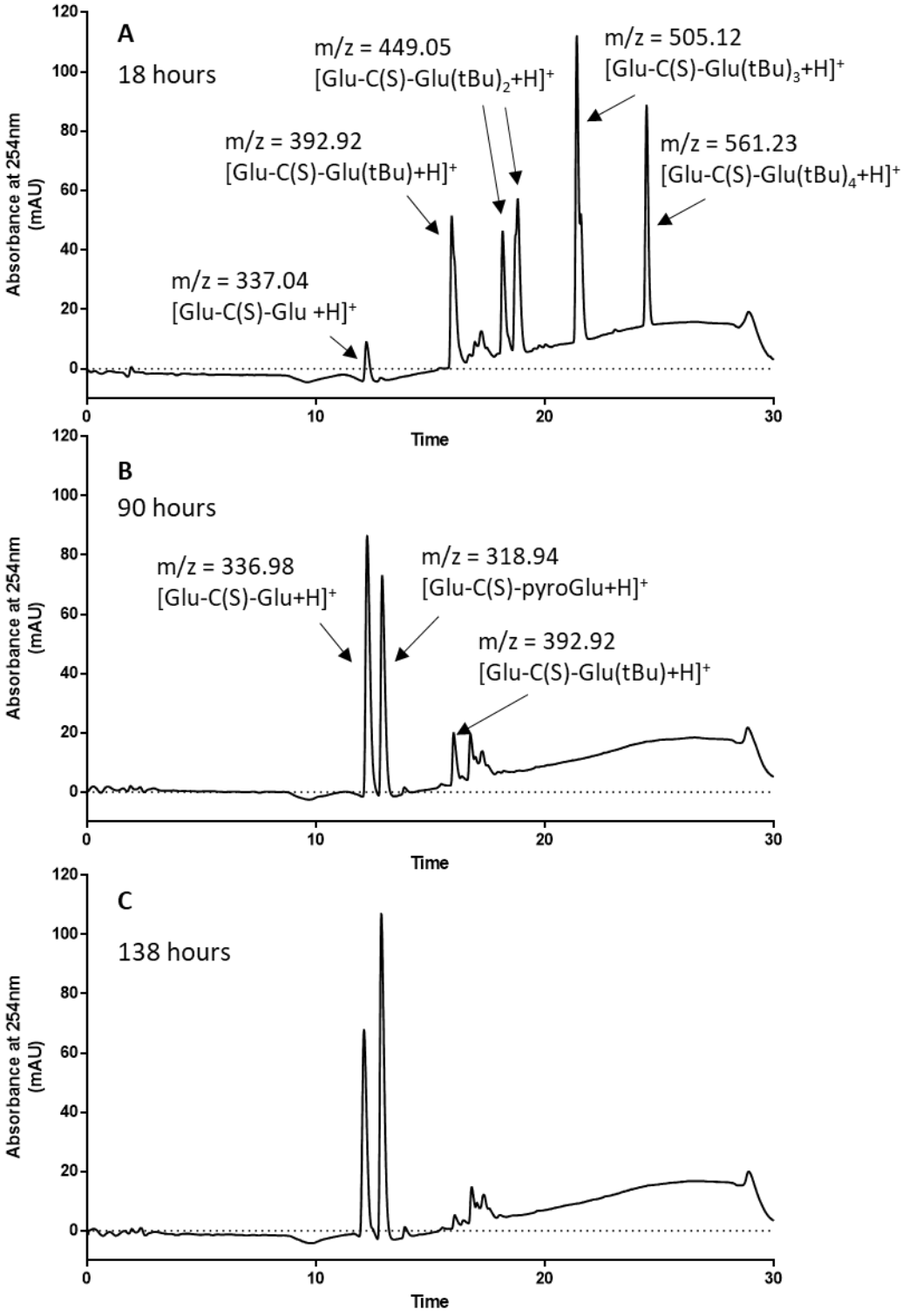

FIGURE 7.17: HPLC chromatograms of deprotection reaction method C1 over time. (A) HPLC of the reaction mixture after 18 hours, with peaks identified from LC-MS data. (B) HPLC of the reaction mixture after 90 hours, with peaks identified from LC-MS data. (C) HPLC of the reaction mixture after 138 hours.

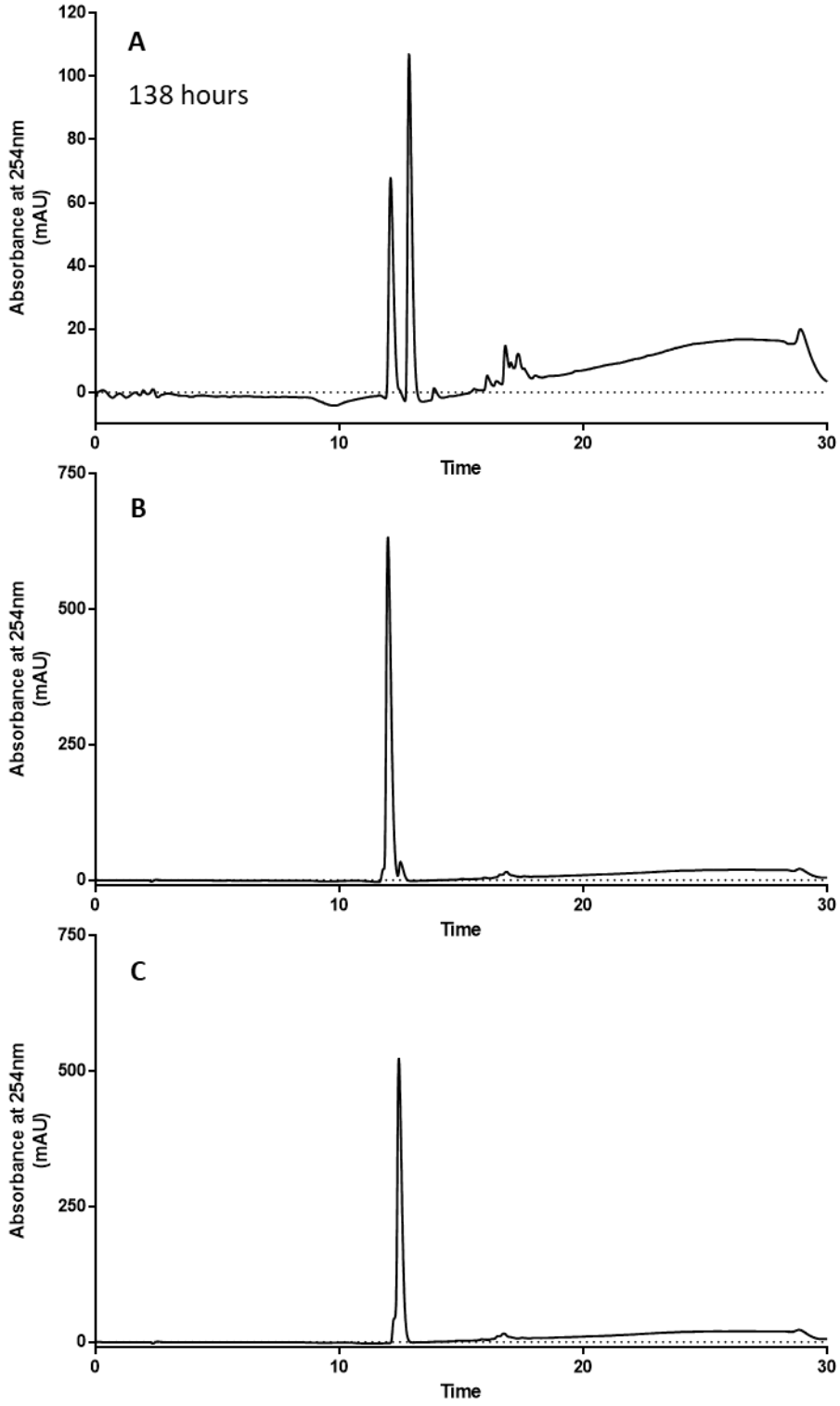

FIGURE 7.18: (A) HPLC of the reaction solution after 138 hours of deprotection though method C1. The two major product peaks were separated by semi-preparative HPLC. These isolated fractions, corresponding to (B)

peak 1; (C) peak 2; were then reinjected on the HPLC. This shows the peaks do not interconvert on this time frame and demonstrates the purity of products used for NMR analysis.

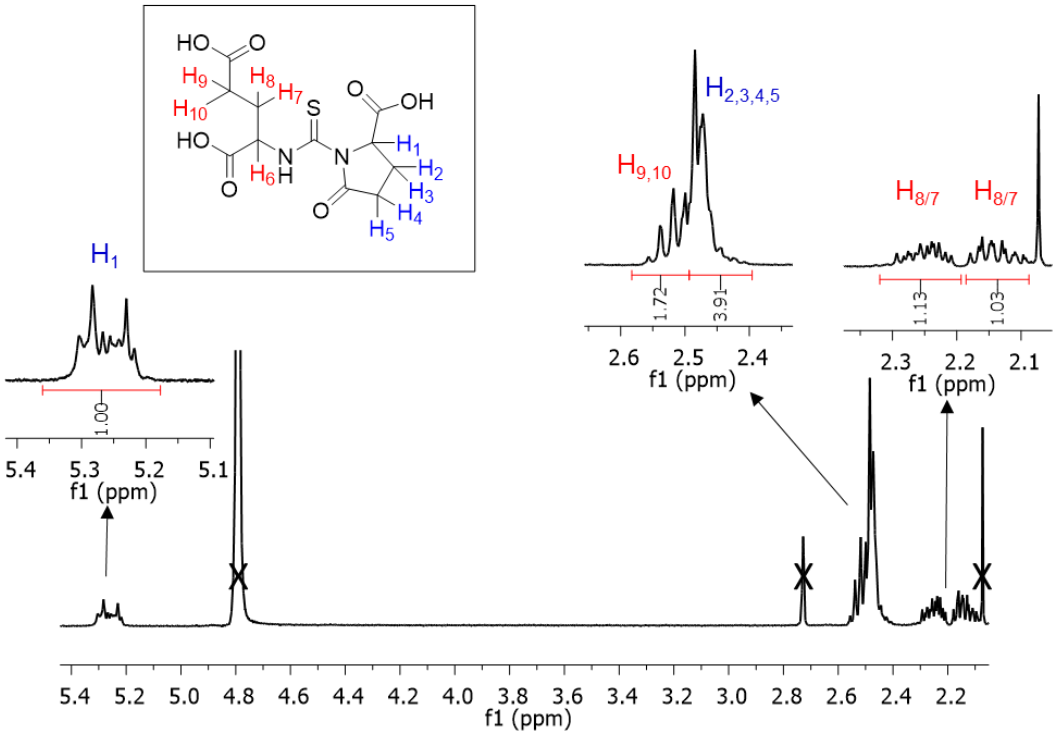

FIGURE 7.19: 400 MHz ^{1}H NMR spectra of cyclised side-product Glu-C(S)-pyroGlu. ^{1}H NMR: (D_2O, 400 MHz, normalised to H_2O solvent peak(23)): δ 2.15 (m, 1H), 2.25 (m, 1H), 2.47 (m, 4H), 2.52 (t, 2H), 5.28 (m, 1H).

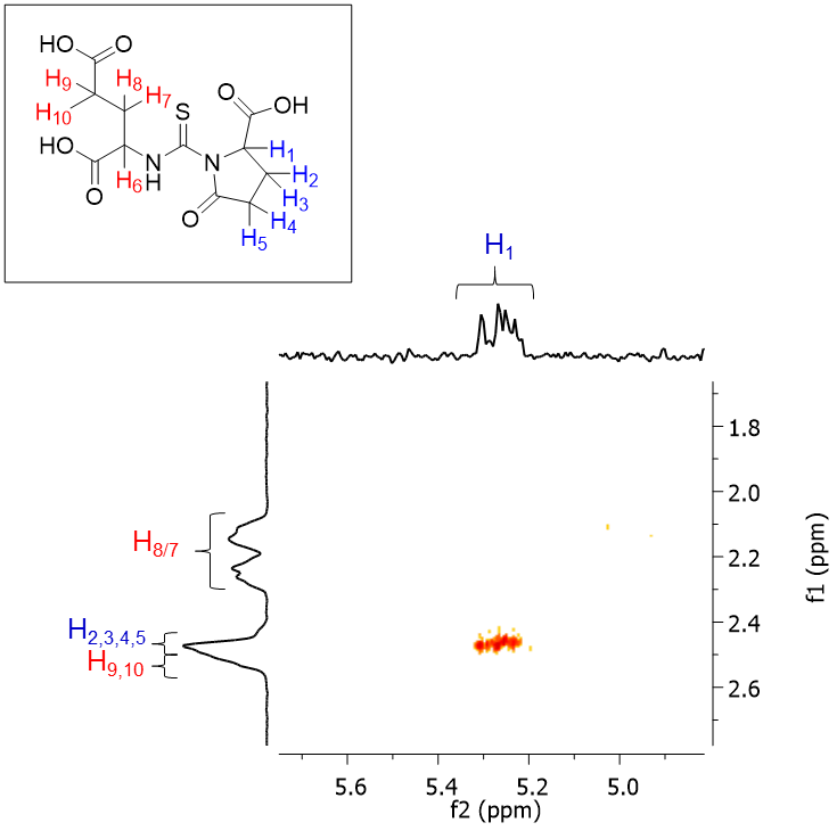

FIGURE 7.20: 400 MHz ^{1}H COSY NMR spectra of cyclised side-product Glu-C(S)-pyroGlu. This demonstrates the coupling between the proton in position H_1 and those in positions $H_{2\text{-}5}$.

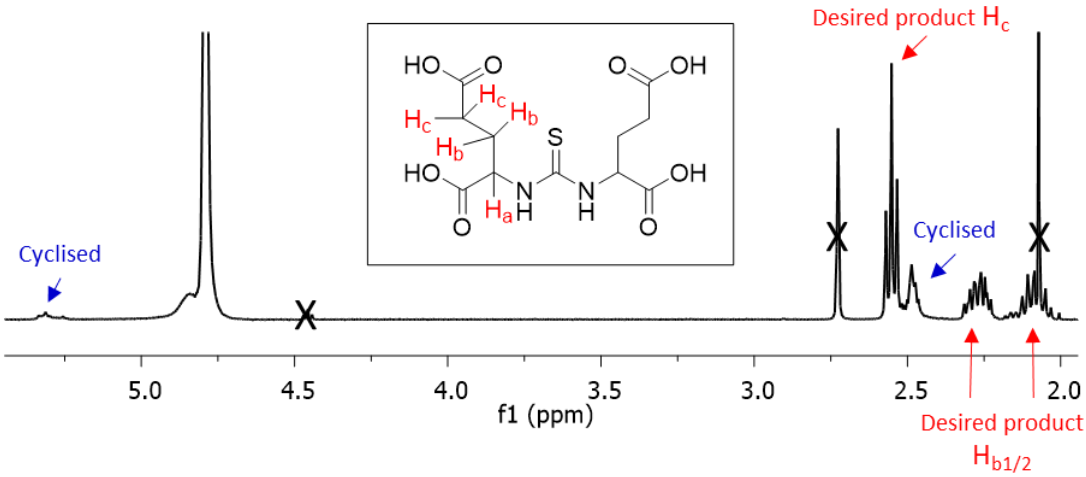

FIGURE 7.21: 400 MHz ^{1}H NMR spectra of Glu-C(S)-Glu, purified after 138 hour deprotection by method C1 by semi-preparative HPLC.

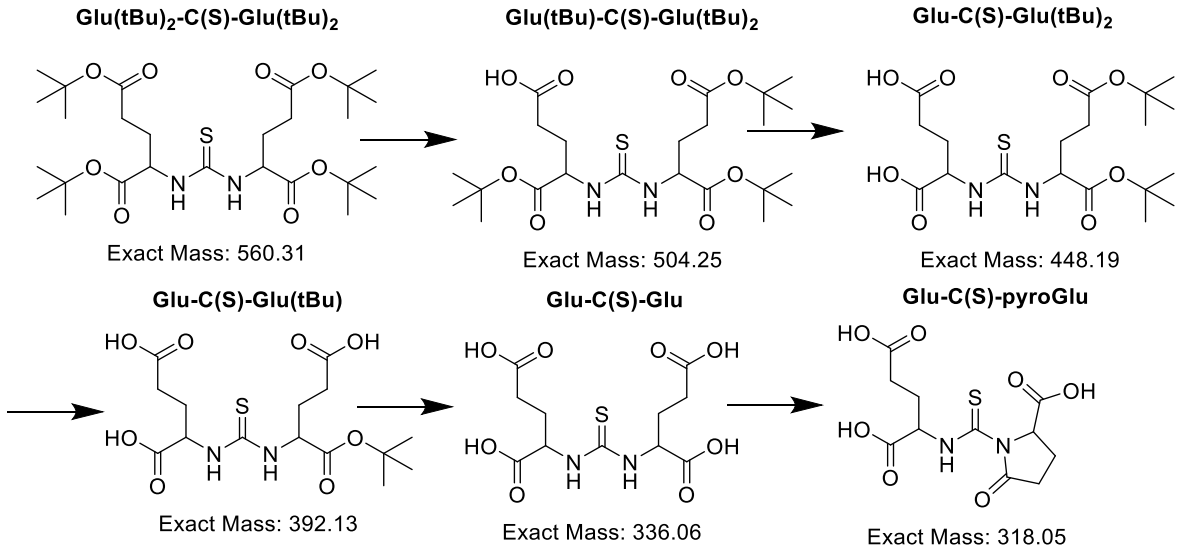

FIGURE 7.22: Species detected during the deprotection of Glu(tBu)$_2$-C(S)-Glu(tBu)$_2$ over 138 hours and the order in which they are produced. Note that it is not clear in which order the carboxylic acids are deprotected, only that this happens sequentially, and so the specific structures shown are only illustrative.

7.4.3.5 Deprotection Method C2

This method was used to isolate the final product in sufficient quantities to characterise and carry out cell studies. Method C2 was very similar to method C1 except that the acid concentration was increased to 6 M to accelerate the reaction so the deprotection could be carried out in 8 hours. The reaction was monitored by analytical HPLC method 2 until the

production of Glu-C(S)-pyroGlu was just detectable as shown in figure 7.23. Then the reaction was neutralised, frozen, freeze-dried and purified by semi-preparative HPLC. When the fractions were collected from the semi-prep system they were immediately frozen in liquid nitrogen and freeze-dried to avoid unnecessary exposure of the product to the acidic HPLC solvent. The solid produced was analysed by ^{1}H NMR in both DMSO-d_6 and D_2O and showed a pure product. The compound was further characterised by IR and high-resolution MS. See results section and figure 7.24, figure 7.25 and figure 7.26.

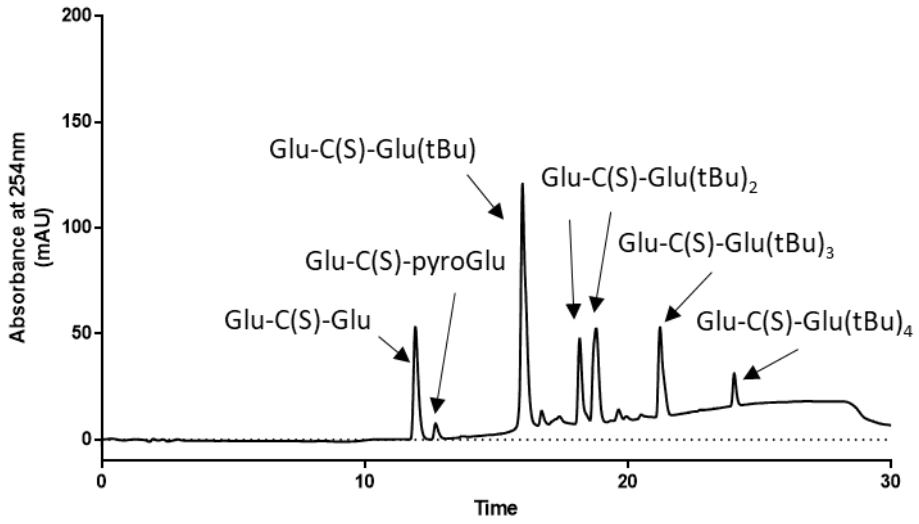

FIGURE 7.23: HPLC of deprotection mixture C2 after 8 hours. At this time-point, the reaction was neutralised and freeze-dried ready for purification. HPLC method 2.

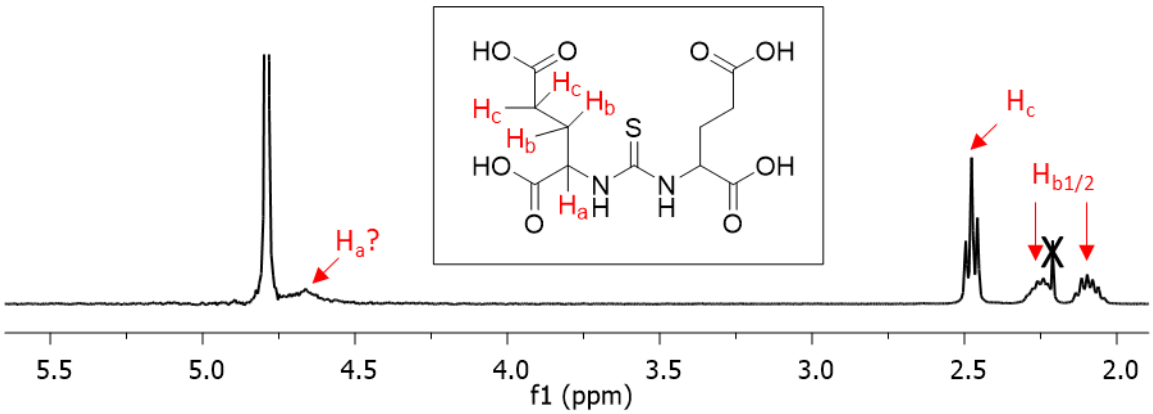

FIGURE 7.24: 400 MHz ^{1}H NMR (D_2O pH ~3) spectra of Glu-C(S)-Glu, purified after 8 hour deprotection with method C2 followed by purification by semi-preparative HPLC.

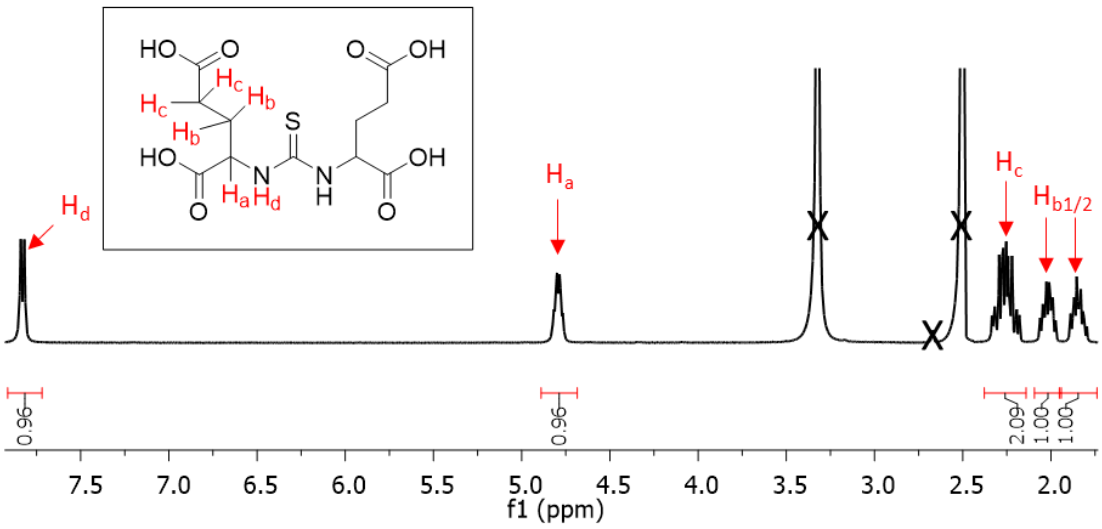

FIGURE 7.25: 400 MHz ^{1}H NMR ($(CD_3)_2SO$) spectra of Glu-C(S)-Glu, purified after 8 hour deprotection with method C2 followed by purification by semi-preparative HPLC.

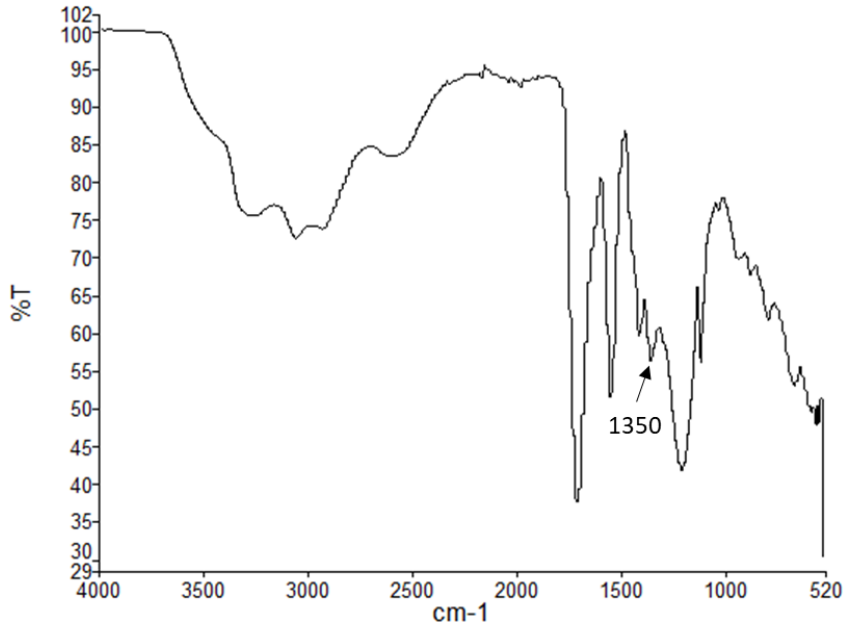

FIGURE 7.26: IR spectra for thiourea-PSMA Glu-C(S)-Glu. Characteristic thiourea C=S stretch seen at 1350 cm^{-1} (26).

7.4.4 Alternative Protection Strategy: Synthesis of Benzyl-Ester Protected Thiourea-PSMA; $Glu(Bn)_2$-C(S)-$Glu(Bn)_2$

As the deprotection strategies described above all had low yield due to the formation of Glu-C(S)-pyroGlu, or the requirement to stop the reaction before the deprotection was complete to avoid its formation, alternative protection strategies were considered to avoid this. The benzyl protecting group was chosen as a viable alternative as it can be removed by hydrogenation in

the presence of a palladium catalyst (*22*), avoiding the need for the highly acidic or basic conditions. Therefore the reaction was carried out by the same method as used for tertiary butyl protected glutamic acid but replacing this with benzyl-ester protected glutamic acid. This strategy caused the formation of the isothiocyanate intermediate $(Bn)_2$Glu-NCS ([$(Bn)_2$Glu-NCS+H]$^+$ m/z-= 370) but not the formation of the desired product Glu-C(S)-Glu$(Bn)_4$. The mass spectrum of this reaction mixture is shown in figure 7.27. This suggests there was insufficient base present to deprotonate the primary amine of the glutamic acid and therefore it could not react with the isothiocyanate to form the thiourea. The reaction was therefore repeated with higher levels of DIPEA. Although this overcame the original issue and the thiourea formed, a side reaction also occurred; the cyclisation of the desired product to form $(Bn)_2$Glu-C(S)-pyroGlu(Bn) with an m/z of 589 (

figure 7.28). The LC-MS data for this reaction is shown in figure 7.29. As this protection strategy caused the cyclisation to occur in the protected state, rather than at the later deprotection step, this avenue was not pursued further.

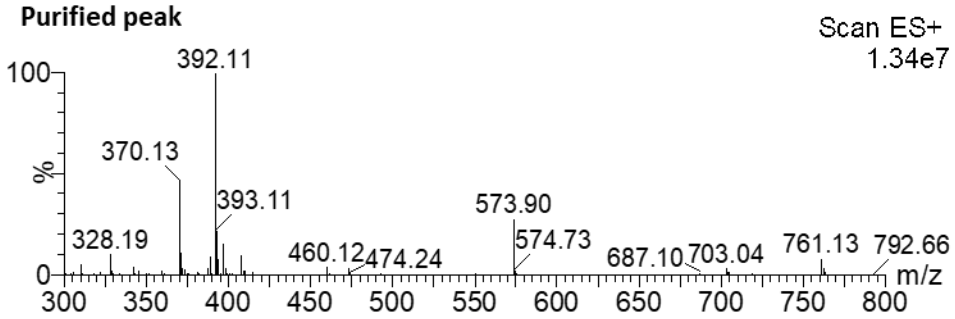

FIGURE 7.27: MS analysis of the crude reaction mixture for the synthesis of benzyl-ester protected thiourea-PSMA method 1, showing the desired product 370 m/z [$(Bn)_2$Glu-NCS+H]$^+$ and the unreacted isothiocyanate intermediate 392 m/z [$(Bn)_2$Glu-NCS+Na]$^+$.

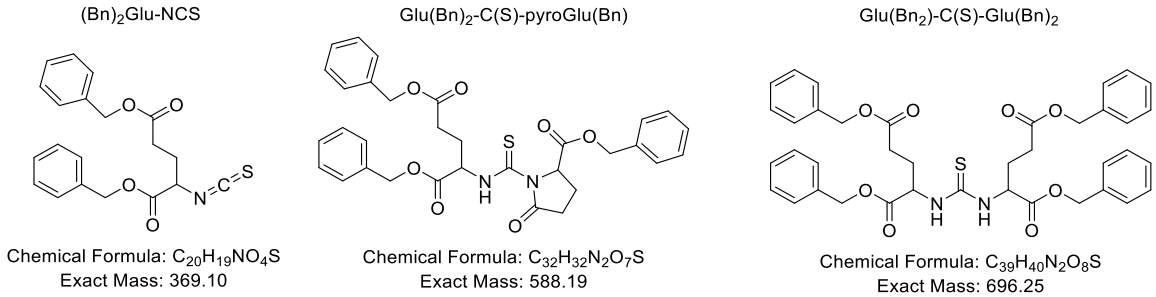

FIGURE 7.28: Structures of the products formed after reacting benzyl-ester protected glutamic acid with thiophosgene in the presence of DIPEA base.

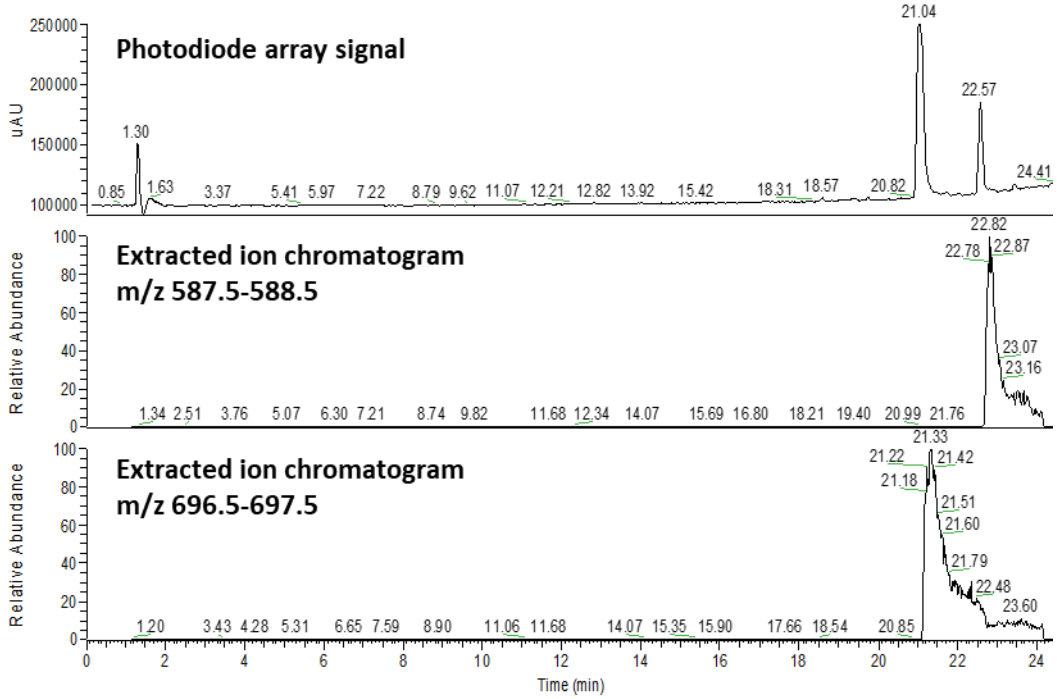

FIGURE 7.29: LC-MS data for the reaction products of the synthesis of benzyl-ester protected thiourea-PSMA method 2. This spectrum shows the presence of two species $[(Bn)_2Glu\text{-}C(S)\text{-}pyroGlu(Bn)+H]^+$ (m/z = 589) and $[(Bn)_2Glu\text{-}C(S)\text{-}Glu(Bn)_2+H]^+$ (m/z = 697). The delay between detectors was 0.3 minutes.

7.4.5 Stability Studies

In order to ensure that thiourea-PSMA (Glu-C(S)-Glu) did not cyclise over time at pH 7, NMR studies were conducted for 48 hours after solution preparation to assess stability. From the NMR spectra obtain previously for both (Glu-C(S)-Glu) and the cyclised side product (Glu-C(S)-pyroGlu) (figure 7.19 and figure 7.24) it was evident that the best signal to monitor was the triplet at 2.3 ppm from the 4 H_c protons. Upon cyclisation this triplet decreases in intensity and a mutliplet signal at lower chemical shift appears as shown in figure 7.21. It was not possible to also monitor the signals from the 4 $H_{b1/2}$ protons due to the signal from the ammonium acetate used to neutralise the solution overlapping with them. Figure 7.30 shows the ^1H NMR spectra for each of the time-points monitored and demonstrates that the molecule is stable under these conditions. The same study was conducted for urea-PSMA (Glu-C(O)-Glu), and showed that the compound was stable under these conditions.

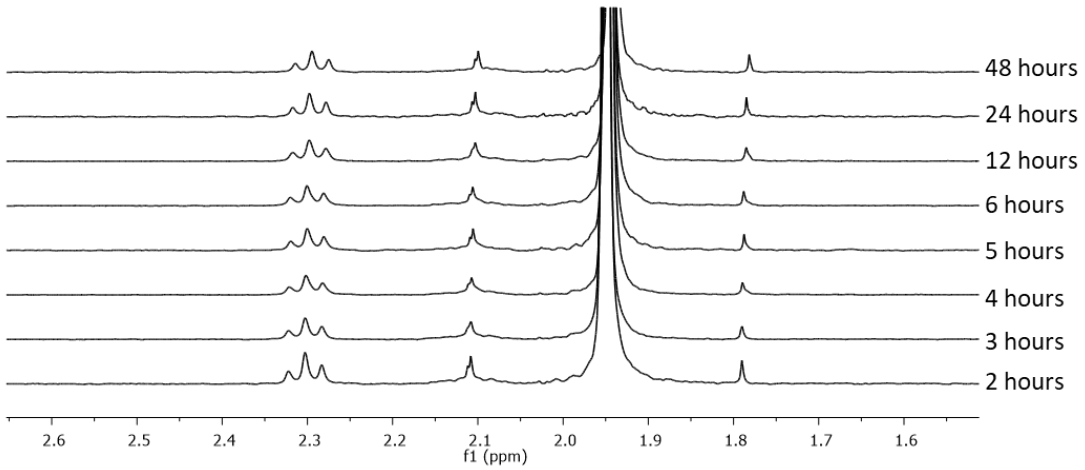

FIGURE 7.30: Stability study for Glu-C(S)-Glu monitored by ^{1}H NMR spectroscopy (400 MHz). No change in the spectra over the time-course confirms the compound is stable under these conditions for up to 48 hours.

7.4.6 Confirming Concentration of Inhibitors through Quantitative NMR

In order to prepare for future cell studies, it was important to quantify the concentration of the inhibitor compounds present in solution. NMR spectroscopy was chosen as the most appropriate quantification method. Equal volumes of a solution containing ~24 mM thiourea-PSMA (Glu-C(S)-Glu), a solution containing ~25 mM urea-PSMA (Glu-C(O)-Glu) and a 125 nM standard of maleic acid were mixed together and the NMR spectrum of the resulting solution measured at 800 MHz. This spectrum is shown in figure 7.31. The peak at 2.30 ppm was confirmed to be from urea-PSMA as the integration of this peak matched the signal at 4.00 ppm known from earlier NMR studies to derive from the protons highlighted in green, and gave the expected 2:4 ratio. Therefore the peak at 2.33 ppm was identified as deriving from the Glu-C(S)-Glu and so the ratio of this triplet and the triplet at 2.30 ppm was used to obtain the ratio of these two components in solution. As the two signals slightly overlapped, the central peak of each triplet was integrated rather than the whole triplet. This gave a ratio of 1:1.4 (thiourea-PSMA:urea-PSMA). The quantity of these two compounds relative to the maleic acid present was calculated using the peak at 6.10 ppm and the combined integration of the triplets from the thiourea-PSMA and urea-PSMA. This gave a ratio of 1:0.92 (maleic acid: thiourea-PSMA + urea-PSMA). As the signal at 6.10 ppm from the maleic acid only came from 2 protons per molecule, but the signal at 2.30 and 2.33 came from 4 protons per molecule this needed to be accounted for when calculating the concentration. Therefore the total concentration of thiourea-PSMA plus urea-PSMA was 125 mM / 2 x 0.92 = 57.5 mM. The ratio of the thiourea and urea peaks is 1:1.4 and so the final concentrations were determined as 24 mM for thiourea-PSMA and 33.5

mM for urea-PSMA. The remaining solutions from this study were then diluted to 20 mM in the same ammonium acetate PBS buffer for use in cell studies.

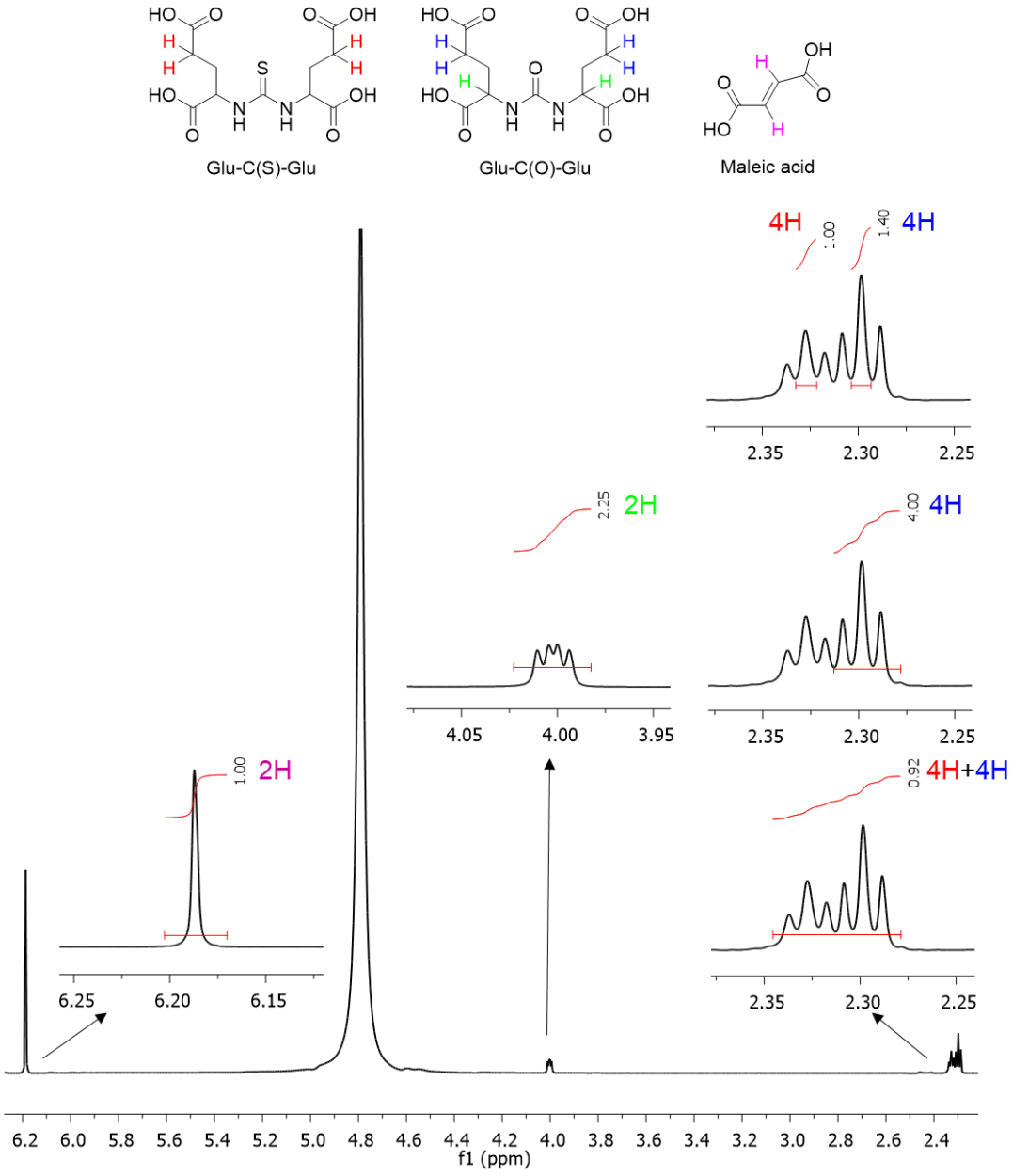

FIGURE 7.31: ^{1}H NMR spectrum (800 MHz) of a mixture of thiourea-PSMA (Glu-C(S)-Glu), urea-PSMA (Glu-C(O)-Glu) and maleic acid. Each integration used to identify the peaks or to calculate the concentration of each compound present in the solution is highlighted. The identity of the protons producing each signal has been shown on the corresponding structures using a colour coding system.

7.4.7 Cell Studies

IC_{50} assays were carried out in triplicate for each inhibitor (PMPA, urea-PSMA, thiourea-PSMA) over a range of 1 nM to 400000 nM (final concentration in the cell suspensions). For all assays the probe used was [^{67}Ga]Ga-DOTA-PSMA at a concentration of 1 nM DOTA-PSMA. Good agreement was seen between repeats of this assay conducted with the same inhibitor, which allowed differences in the performance of the inhibitors to be clearly established. The results are shown in figure 7.32. Of the three inhibitors used PMPA had the best IC_{50} value of 94 ± 4.3 nM. Urea-PSMA had a ten-fold higher IC_{50} value than PMPA, (1340 ± 70 nM), however, the thiourea-PSMA showed a further hundred-fold higher IC_{50} value than the urea-PSMA (135000 ± 6600 nM). In order to validate these results and ascertain whether or not the thiourea-PSMA was cyclising during incubation with the cells, a further NMR stability study was conducted. Here the thiourea-PSMA was incubated with 1 million cells for 1 hour in 1 mL of PBS at 37°C and the supernatant analysed by NMR (figure 7.33). This study showed that there is no detectable change in the thiourea-PSMA NMR signal after incubation under these conditions. Lactate, pyruvate and alanine excreted by the cells were also detected in the NMR spectrum. This result shows that thiourea-PSMA is stable when incubated with cells, and that the IC_{50} results were not affected by cyclisation of the thiourea-PSMA.

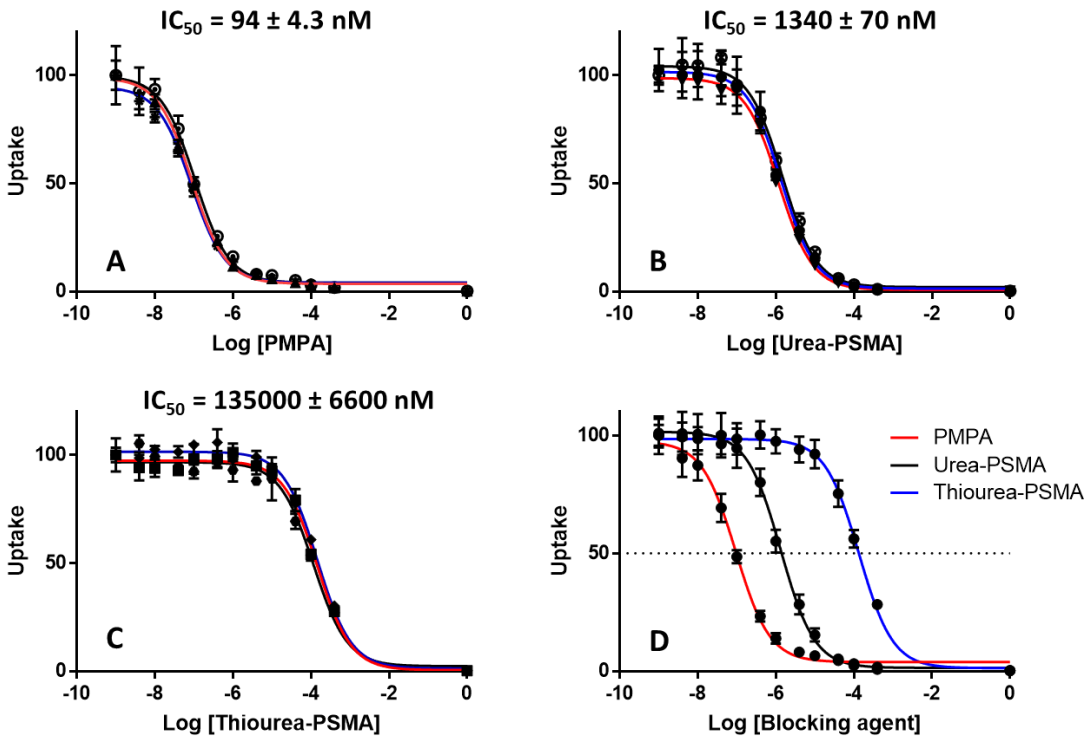

FIGURE 7.32: Inhibition curves for (A) PMPA, (B) urea-PSMA (Glu-C(O)-Glu) and (C) thiourea-PSMA (Glu-C(S)-Glu). Each assay repeat is represented by a different coloured curve. For each assay n = 4 wells at each concentration and error bars show SD values. (D) Average values across triplicate assays for each blocking agent. Note that non-specific binding of [^{67}Ga]Ga-DOTA-PSMA with non-GCP(II)PSMA-expressing cells (DU145) was input for all the assays as the nominal value at 1 M inhibitor.

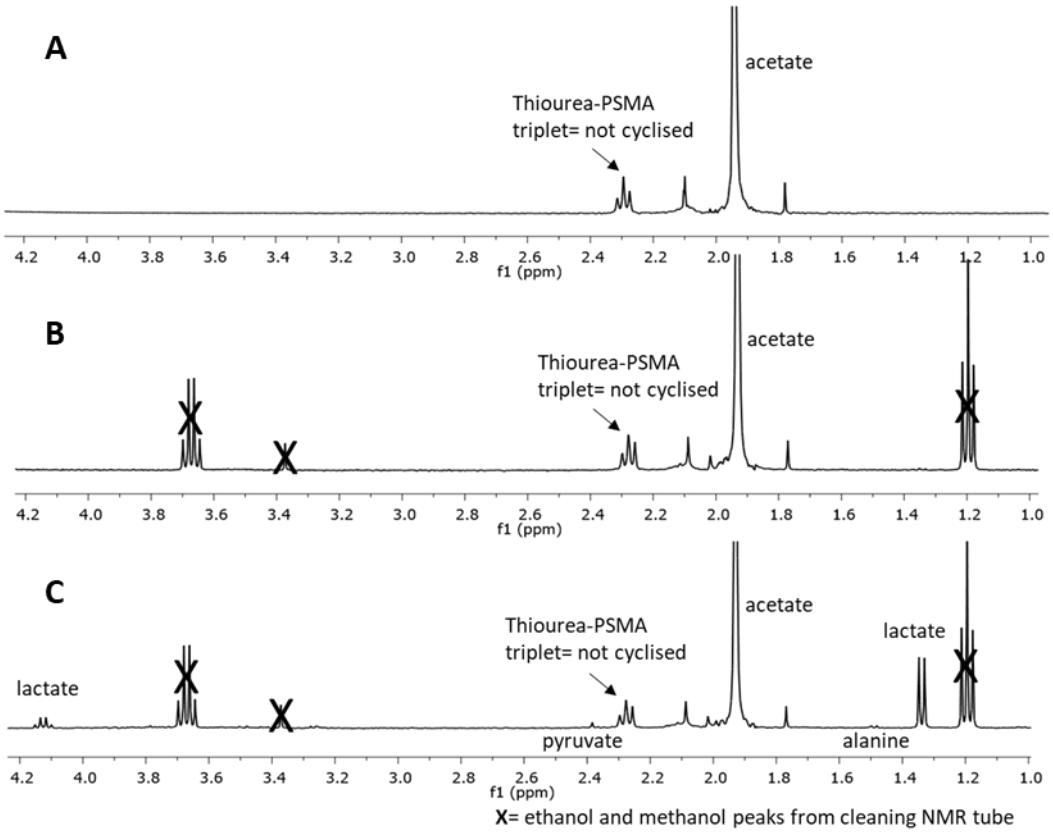

FIGURE 7.33: ^{1}H NMR (400 MHz) spectrum of: (A) a sample of the thiourea-PSMA compound solution added to the cells for the IC_{50} assay. The signal at 2.2 ppm looks identical to that of the stability study. (B) thiourea-PSMA after incubation at 400 μM in an empty 6 well plate in 1 mL PBS for 1 hour. (C) thiourea-PSMA after incubation at 400 μM with 1 million cells in a 6 well plate in 1 mL PBS for 1 hour. Peaks corresponding to the release of lactic acid, pyruvate and alanine from the cell can be detected, but the signal coming from the thiourea-PSMA at 2.3 ppm does not change showing it is stable under these conditions.

7.5 Discussion

The synthesis and characterisation of both urea-PSMA (Glu-C(O)-Glu) (synthesised previously (*22*)) and the novel inhibitor thiourea-PSMA (Glu-C(S)-Glu) have been successfully completed. However, thiourea-PSMA posed synthetic challenges due to its propensity to undergo intramolecular dehydration. The evidence available from the ^{1}H and COSY NMR spectra suggests that the product formed is the γ-lactam, 5-oxopyrrolidine-2-carboxylic acid or pyroglutamic acid (figure 7.19). This has a five-membered ring closure between the nitrogen of the thiourea and the carbonyl carbon at the end of the glutamic acid side chain, with the loss of water. Similar cyclisation reactions are well-known with the formation of a pyroglutamic acid by dehydration of glutamic acid first discovered in 1882 when glutamic acid was heated to 180°C (*27*). Additionally, many peptides and proteins have pyroglutamic acid at their N-terminus, as shown in table 7.1. This has been shown to protect proteins from degradation, particularly by aminopeptidases (*28*)(*29*)(*30*). These pyroglutamic acids can form from either an N-terminal glutamic acid or glutamine residue, and this is catalysed *in vivo* by the enzyme glutaminyl cyclase as shown in figure 7.34 (*28*)(*30*)(*31*). Such cyclisation has also been shown to occur in the absence of this enzyme (*30*)(*32*) and it is known that pH affects the formation rate as shown in figure 7.35. In these literature examples the carbonyl carbon reacts with a primary amine, but in this study it reacted with one of the secondary amines of a thiourea. These amines therefore have different characteristics, and although the reactions are related, they are not identical. Like the formation of pyroglutamic acid from N-terminal glutamic acids, the cyclisation seen in this study is pH dependent, with cyclisation occurring at low and high pH but not when the pH was maintained between 6.5 and 7.5. Evidence for this was obtained by conducting ^{1}H NMR spectroscopy stability studies (figure 7.30). A mechanism for such cyclisation at both high and low pH has been proposed in figure 7.36. Low pH would encourage cyclisation by promoting the protonation of the carboxylic acid so that water becomes the leaving group. At high pH the conditions will reach the pK_a of the thiourea amine proton, with its loss facilitating cyclisation. It is interesting that cyclisation occurred to a greater extent in the thiourea-PSMA synthesis than in the urea-PSMA synthesis and shows that the presence of this sulfur greatly alters the behaviour of the system, in particular lowering the pK_a of the amine protons. This observation can be explained by considering the resonance structures of urea and thiourea as shown in figure 7.37. It is likely that the enol resonance form would be more preferred for the thiourea than the urea due to its better stabilisation of the negative charge. Therefore it would have been ideal to have a deprotection strategy for thiourea-PSMA that avoided the use of either high or low pH. An existing method that may have been able to avoid extremes of pH is the removal of

t-butyl groups by reacting the protected compound with zinc bromide (500 mol% $ZnBr_2$) in DCM at room temperature for 24 hours (*33*). However, this was not attempted, as an acceptable separation technique of deprotected thiourea-PSMA (Glu-C(S)-Glu) from $ZnBr_2$ could not be conceived. Instead, an alternative strategy was attempted using benzyl-esters as the protecting group known to be removable by hydrogenation in the presence of a palladium catalyst (*22*). When t-butyl groups were used, no cyclisation was observed under the conditions required to form the protected thiourea. However, when this was conducted with benzyl protecting groups cyclisation occurred whilst the protecting groups were still intact. This can be explained by considering the electronic properties of these two protecting groups. A benzyl-ester is more electron withdrawing than a t-butyl ester and so it causes the carbon of the carboxyl group to become more electronegative, and therefore more prone to cyclisation under the basic reaction conditions (excess DIPEA). Additionally, the benzyl-ester is a good leaving group and forms toluene upon deprotection. There are alternative protection strategies possible for carboxylic acids, yet to be explored in this system, which could avoid high or low pH. An example is the "supersilyl" group which can be removed with just UV light (254 nm) (*34*).

Instead of these alternatives methods, a method which could produce sufficient product for the required studies was adopted. By understanding that the processes of deprotection and then cyclisation were sequential, a deprotection method that slowed down the formation of Glu-C(S)-pyroGlu was developed. This involved deprotecting $(tBu)_2$Glu-C-(S)-Glu$(tBu)_2$ in 6 M HCl and acetonitrile, over 8 hours and then neutralising the reaction to halt both the deprotection and cyclisation, followed by purification by semi-preparative HPLC. These are mild conditions which avoid the use of concentrated acid or a heating step, which are both likely to accelerate dehydration to pyroglutamic acid. However, this is not a suitable strategy for larger scale production and would be further complicated if the thiourea-PSMA motif was to be functionalised with a chelator in order to develop a radiotracer or other bioconjugate. In such cases, alternative synthetic strategies would need to be developed. Although the use of this motif for targeting GCP(II)/PSMA is unlikely in light of the IC_{50} results, this information is useful for others in this area, particularly as thioureas are routinely used in bioconjugate chemistry.

PMPA, urea-PSMA and thiourea-PSMA were assessed in an IC_{50} cell assay to assess their ability to bind GCP(II)/PSMA. PMPA has been reported to have a K_i value of 0.3 nM (*10*) and urea-PSMA (Glu-C(O)-Glu) a K_i value of 8 nM (*22*). The IC_{50} studies conducted here were not designed to give the same values but instead to obtain the relative affinities for the inhibitors in this study and ascertain the size of affinity change upon substituting a urea with a thiourea. The IC_{50} values obtained in this study were 94 ± 4.3 nM for PMPA and 1340 ± 70 nM for urea-PSMA. Although

the absolute values are much higher for this assay than in previous literature, the difference between the two inhibitors is of the same order of magnitude as seen for the literature values. At the outset of this study, it was postulated that thiourea-PSMA would have higher affinity than its urea-PSMA analogue due to the importance of zinc binding within the GCP(II)/PSMA active site and the strong interaction between zinc ions and sulfur ligands. However, this was not seen in the experimental results. Instead, the opposite was observed: the thiourea-PSMA was a much weaker inhibitor, producing a high IC_{50} value of 135000 ± 6600 nM, 100 fold higher than that of the urea-PSMA derivative. The quantification and stability tests performed confirmed that thiourea-PSMA was at a known concentration during the assay and that it was stable for its duration. Therefore, this value is a true reflection of the difference in affinity caused by the replacement of a urea with a thiourea. This unexpected difference could be due to the larger radius of sulfur and the longer bond length of the C=S bond of thiourea groups compared to the C=O bond of urea groups (1.71 Å (*35*) and 1.26 Å (*36*) respectively). Such changes could cause the rest of the molecule to fit more poorly within the active site, reducing those interactions and counteracting any gain in affinity caused by the strength of the bond between the zinc ion and the sulfur ligand. This is not inconsistent with previous findings that suggest that the success of a zinc ion binding group is dependent on maintaining the interactions of the glutamate with the S1' pocket.

Protein or peptide	Sequence
Thyrotropin-releasing hormone	pGlu-His-Pro-NH2
Thyrotropin-releasing hormone-like peptide (prostate)	pGlu-Glu-Pro-NH2
Anorexigenic peptide	pGlu-His-Gly-OH
Eisenine	pGlu-Glu-Ala-OH
Colon mitosis-inhibitory peptide	pGlu-Glu-His-Gly-OH
Peptide-inhibiting epidermal mitosis	pGlu-Glu-asp-Cys-Lys-OH
Vasoactive polypeptide	pGlu-Val-Pro-Gln-Trp
Luteinizing hormone-releasing hormone	pGlu-His-Trp-Ser-Tyr-Gly-Leu-Gln-Pro-Gly-NH_2
GnRH-II	pGlu-His-Trp-Ser-His-Gly-Trp-Tyr-Pro-Gly-NH_2
Eledoisin	pGlu-Pro-Ser-Lys-Asp-Ala-Phe-Ile-Gly-Leu-Met-NH_2
Neurotensin	pGlu-Leu-Tyr-Glu-Asn-Lys-Pro-Arg-Arg-Pro-Tyr-Ile-Leu-NH_2
Fibrinopeptide B	pGlu-Gly-Val-Asn-Asp-Asn-Glu-Glu-Gly-Phe-Phe-Ser-Ala-Arg
Gastrin	pGlu-Gly-Pro-Trp-Leu-Glu-Glu-Glu-Glu-Glu-Ala-Tyr-Gly-Trp-Met-
Orexin A	pGlu-Pro-Leu-Pro-Asp-Cys-Cys-Arg-Gln-Lys-Thr-Cys-Ser-Cys-Arg-Leu-
Apelin	pGlu-Arg-Pro-Arg-Leu-Ser-His-Lys-Gly-Pro-Met-Pro-Phe

TABLE 7.2: Naturally occurring peptides and proteins which have pyro-glutamic acid at their N-terminus (28).

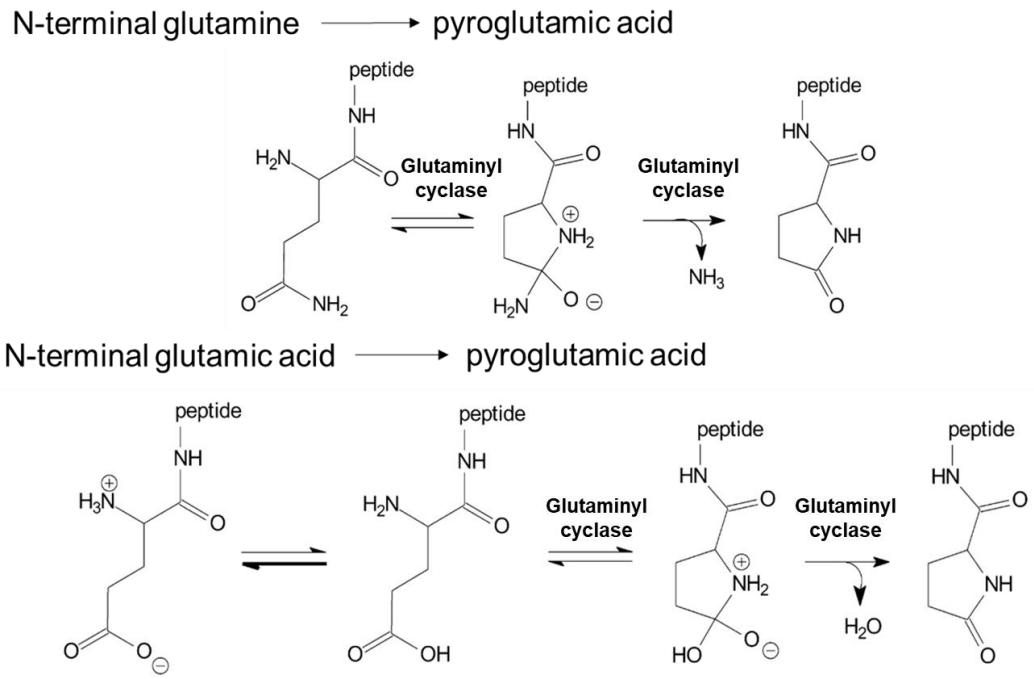

FIGURE 7.34: N-terminal cyclization of peptides with terminal glutamine and glutamic acid residues by the enzyme glutaminyl cyclase. Modified with permission from (30).

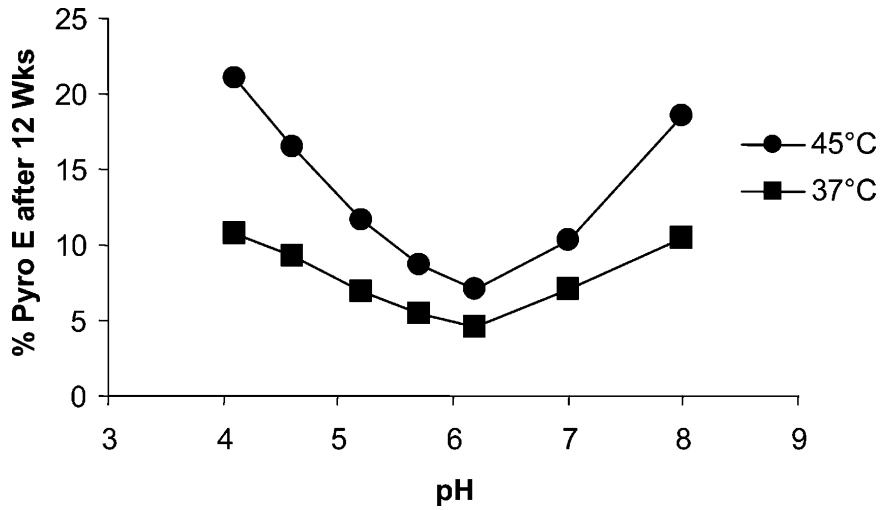

FIGURE 7.35: The formation of pyroglutamic acid after 12 weeks over a range of pH. An antibody with the terminal sequence EIVMTQSPATLSVSPGER (light chain) was incubated at pH 4.1, 4.6, 5.2, 5.7, 6.2, 7.0, and 8.0 at 37 and 45 °C for 12 weeks. The percentage of pyroglutamic acid was calculated based on the peak areas of the light chain and the post light chain from the reversed-phase chromatogram. The minimum was found to be at pH 6.2. Reproduced with permission from (32).

Acid Catalysed

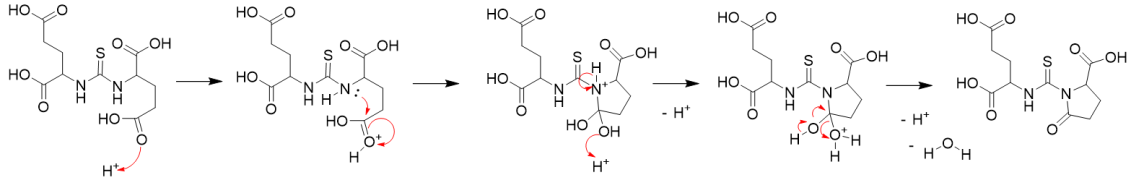

Base Catalysed

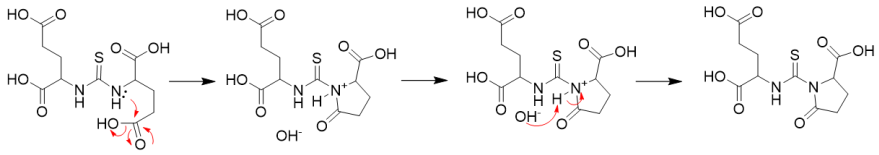

FIGURE 7.36: Proposed mechanisms for the formation of pyroglutamic acid

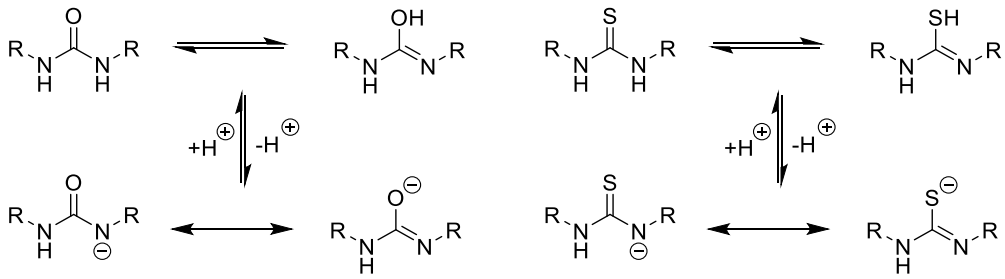

FIGURE 7.37: The resonance structures of urea and thiourea.

7.6 Conclusion

Thiourea-PSMA (Glu-C(S)-Glu) has been successfully synthesised in quantities sufficient for inhibitor studies to be performed. Despite its propensity to cyclise in low or high pH its stability at pH 6.5-7.5 has been confirmed and cell studies have been performed to determine its inhibition constant (IC_{50}). This was found, unexpectedly, to be much higher for thiourea-PSMA than urea-PSMA and PMPA. This suggests that this functional group is not suitable for making higher affinity tracers and therefore other interactions must govern the affinity more than the strength of the substrate-zinc bond.

7.7 References

1. Young JD, Abbate V, Imberti C, Meszaros LK, Ma MT, Terry SYAA, Hider RC, Mullen GE, Blower PJ. 68Ga-THP-PSMA: A PET Imaging Agent for Prostate Cancer Offering Rapid, Room-Temperature, 1-Step Kit-Based Radiolabeling. *J Nucl Med*. 2017;58:1270-1277.
2. Hofman MS, Eu P, Jackson P, Hong E, Binns D, Iravani A, Murphy D, Mitchell C, Siva S, Hicks RJ, Young JD, Blower P, Mullen GE. Cold Kit PSMA PET Imaging: Phase I Study of 68Ga-THP-PSMA PET/CT in Patients with Prostate Cancer. *J Nucl Med*. 2018;59:625-631.
3. Derlin T, Schmuck S, Juhl C, Teichert S, Zörgiebel J, Wester H-J, Schneefeld SM, Walte ACA, Thackeray JT, Ross TL, Bengel FM. Imaging Characteristics and First Experience of [68Ga]THP-PSMA, a Novel Probe for Rapid Kit-Based Ga-68 Labeling and PET Imaging: Comparative Analysis with [68Ga]PSMA I&T. *Mol Imaging Biol*. 2018.
4. Cook G, Hughes S, Morris S, Challacombe B, Cathcart P, Popert R, Brown C, Dasgupta P, John J, Malliaa A, Young J, Gibson V, Mullen G, Warbey V. Management Impact of 68Ga-THP-PSMA in High-Risk and Biochemically Recurrent Prostate Cancer. *Nucl Med Commun*. 2018;39:346-395 Abstract 12.
5. Benešová M, Schäfer M, Bauder-Wüst U, Afshar-Oromieh A, Kratochwil C, Mier W, Haberkorn U, Kopka K, Eder M. Preclinical Evaluation of a Tailor-Made DOTA-Conjugated PSMA Inhibitor with Optimized Linker Moiety for Imaging and Endoradiotherapy of Prostate Cancer. *J Nucl Med*. 2015;56:914-920.
6. Kiess A, Minn I, Chen Y, Hobbs RF, Sgouros G, Mease RC, Pullambhatla M, Shen C, Foss C, Pomper M. Auger Radiopharmaceutical Therapy Targeting Prostate-Specific Membrane Antigen. *J Nucl Med*. 2015;56:1401-1407.
7. Wüstemann T, Bauder-Wüst U, Schäfer M, Eder M, Benesova M, Leotta K, Kratochwil C, Haberkorn U, Kopka K, Mier W. Design of Internalizing PSMA-Specific Glu-Ureido-Based Radiotherapeuticals. *Theranostics*. 2016;6:1085-1095.
8. Pavlicek J, Ptacek J, Barinka C. Glutamate Carboxypeptidase II: An Overview of Structural Studies and Their Importance for Structure-Based Drug Design and Deciphering the Reaction Mechanism of the Enzyme. *Curr Med Chem*. 2012;19:1300-1309.
9. Majer P, Jackson PF, Delahanty G, Grella BS, Ko Y, Li W, Liu Q, Maclin KM, Pola J, Shaffer KA, Stoermer D, Vitharana D, Wang EY, Zakrzewski A, Rojas C, Slusher BS, Wozniak KM, Burak E. Synthesis and Biological Evaluation of Thiol-Based Inhibitors of Glutamate Carboxypeptidase II : Discovery of an Orally Active GCP II Inhibitor. *J Med Chem*. 2003;46:1989-1996.
10. Jackson PF, Slusher BS. Design of NAALADase Inhibitors: A Novel Neuroprotective Strategy. *CurrMedChem*. 2001;8:949-957.
11. Wu LY, Anderson MO, Toriyabe Y, Maung J, Campbell TY, Tajon C, Kazak M, Moser J, Berkman CE. The Molecular Pruning of a Phosphoramidate Peptidomimetic Inhibitor of Prostate-Specific Membrane Antigen. *Bioorganic Med Chem*. 2007;15:7434-7443.
12. Novakova Z, Cerny J, Choy CJ, Nedrow JR, Choi JK, Lubkowski J, Berkman CE, Barinka C. Design of Composite Inhibitors Targeting Glutamate Carboxypeptidase II: The Importance of Effector Functionalities. *FEBS J*. 2016;283:130-143.
13. Klusák V, Bařinka C, Plechanovová A, Mlčochová P, Konvalinka J, Rulíšek L, Lubkowski J. Reaction Mechanism of Glutamate Carboxypeptidase II Revealed by Mutagenesis, X-Ray Crystallography, and Computational Methods. *Biochemistry*. 2009;48:4126-4138.
14. Mesters JR, Henning K, Hilgenfeld R. Human Glutamate Carboxypeptidase II Inhibition: Structures of GCPII in Complex with Two Potent Inhibitors, Quisqualate and 2-PMPA. *Acta Crystallogr Sect D Biol Crystallogr*. 2007;63:508-513.
15. Mallari JP, Choy CJ, Hu Y, Martinez AR, Hosaka M, Toriyabe Y, Maung J, Blecha JE, Pavkovic SF, Berkman CE. Stereoselective Inhibition of Glutamate Carboxypeptidase by Organophosphorus Derivatives of Glutamic Acid. *Bioorganic Med Chem*. 2004;12:6011-

6020.
16. Overton T, Rourke JP, Weller M, Armstrong F. *Shriver & Atkins' Inorganic Chemistry*. Oxford, UK: Oxford University Press; 2010.
17. Maret W. Zinc and Sulfur: A Critical Biological Partnership. *Biochemistry*. 2004;43:3301-3309.
18. Krężel A, Maret W. The Biological Inorganic Chemistry of Zinc Ions. *Arch Biochem Biophys*. 2016;611:3-19.
19. Maddani MR, Prabhu KR. A Concise Synthesis of Substituted Thiourea Derivatives in Aqueous Medium. *J Org Chem*. 2010;75:2327-2332.
20. Dyson GM, George HJ. The Reactions of Thiocarbonyl Chloride. Part I. Reaction with Aromatic Primary Amino-Compounds. *J Chem Soc*. 1924;125:1702-1708.
21. Munch H, Hansen JS, Pittelkow M, Christensen JB, Boas U. A New Efficient Synthesis of Isothiocyanates from Amines Using Di-Tert-Butyl Dicarbonate. *Tetrahedron Lett*. 2008;49:3117-3119.
22. Kularatne SA, Zhou Z, Yang J, Post CB, Low PS. Design, Synthesis, and Preclinical Evaluation of Prostate-Specific Membrane Antigen Targeted 99mTc-Radioimaging Agents. *Mol Pharm*. 2009;6:790-800.
23. Fulmer GR, Miller AJM, Sherden NH, Gottlieb HE, Nudelman A, Stoltz BM, Bercaw JE, Goldberg KI. NMR Chemical Shifts of Trace Impurities: Common Laboratory Solvents, Organics, and Gases in Deuterated Solvents Relevant to the Organometallic Chemist. *Organometallics*. 2010;29:2176-2179.
24. Robosky LC, Reily MD, Avizonis D. Improving NMR Sensitivity by Use of Salt-Tolerant Cryogenically Cooled Probes. *Anal Bioanal Chem*. 2007;387:529-532.
25. Kampmeier F, Williams JD, Maher J, Mullen GE, Blower PJ. Design and Preclinical Evaluation of a 99mTc-Labelled Diabody of MAb J591 for SPECT Imaging of Prostate-Specific Membrane Antigen (PSMA). *EJNMMI Res*. 2014;4:13.
26. Williams DH, Flemming I. *Spectroscopic methods in organic chemistry 5th Edit.* London, UK: McGraw-Hill; 1995.
27. Haitinger L. Vorläufige Mittheilung Über Glutaminsäure Und Pyrrol. *Monatshefte für Chemie und verwandte Teile anderer Wissenschaften*. 1882;3:228–229.
28. Kumar A, Bachhawat AK. Pyroglutamic Acid: Throwing Light on a Lightly Studied Metabolite. *Curr Sci*. 2012;102:288-297.
29. Fietzek PP, Breitkreutz D, Kohn K. Amino Acid Sequence of the Amino-Terminal Region of Calf Skin Collagen. *Biochim Biophys Acta*. 1974;365:305-310.
30. Schilling S, Hoffmann T, Manhart S, Hoffmann M, Demuth HU. Glutaminyl Cyclases Unfold Glutamyl Cyclase Activity under Mild Acid Conditions. *FEBS Lett*. 2004;563:191-196.
31. Huang K-F, Liu Y-L, Cheng W-J, Ko T-P, Wang AH-J. Crystal Structures of Human Glutaminyl Cyclase, an Enzyme Responsible for Protein N-Terminal Pyroglutamate Formation. *Proc Natl Acad Sci*. 2005;102:13117-13122.
32. Chelius D, Jing K, Lueras A, Rehder DS, Dillon TM, Vizel A, Rajan RS, Li T, Treuheit MJ, Bondarenko PV. Formation of Pyroglutamic Acid from N-Terminal Glutamic Acid in Immunoglobulin Gamma Antibodies. *Anal Chem*. 2006;78:2370-2376.
33. Kaul R, Brouillette Y, Sajjadi Z, Hansford KA, Lubell WD. Selective Tert-Butyl Ester Deprotection in the Presence of Acid Labile Protecting Groups with Use of ZnBr2. *J Org Chem*. 2004;69:6131-6133.
34. Tan J, Akakura M, Yamamoto H. "Supersilyl" Group as Novel Carboxylic Acid Protecting Group: Application to Highly Stereoselective Aldol and Mannich Reactions. *Angew Chemie - Int Ed*. 2013;8:28.
35. Kunchur NR, Truter MR. 517. A Detailed Refinement of the Crystal and Molecular Structure of Thiourea. *J Chem Soc*. 1958:2551-2557.
36. Laboratories C, La- C, Brunswick N. The Structure of Urea. Interatomic Distances and

Resonance in Urea and Related Compounds. *Acta Crystallogr*. 1952:530-535.

8 Future Works

In this section opportunities for future work will be discussed. Some of these are natural extensions of the work presented in this thesis, others are challenges that exist in the field as a whole that would be valuable to explore

8.1 The Gallium-THP Complex

THP displays outstanding radiolabelling properties with gallium isotopes and so it would be advantageous to understand what properties of THP confer these properties. Information about how THP coordinates gallium has been obtained from the NMR studies carried out in chapter 3. This work suggested that only a 1:1 complex was formed upon the coordination of gallium ions, and this complex remained the same when the THP-PSMA was at a higher concentration than the gallium ions and when gallium ions were in excess. It also showed that the complex was stable over time (3 weeks), and resistant to heating (70°C). Upon binding gallium, the proton signals from the THP section of the molecule split into 3 equal intensity signals, suggesting just one complex is formed, but that it does not have C_3 symmetry and each arm of this tripodal chelator is in a different environment. This could be caused by hydrogen bonding between 2 of the arms of coordinated THP. More conclusive and extensive investigations were impeded by the poor solubility of Ga-THP-PSMA and the overlap of signals from the rest of the molecule (the linker and PSMA motif). It would be advantageous to develop more soluble variants of THP, functionalised with hydrophilic groups, which could be used for further NMR studies. X-ray crystallography studies would also be extremely informative, but again are likely to require a more soluble derivative of THP to facilitate crystal growth. In the absence of a crystal structure, it would be interesting to study this complex with X-ray absorption fine structure spectroscopy, which is able to provide information on the coordination environment and three-dimensional geometry around the metal centre (*1*). These results could all be combined with molecular modelling to gain a better understanding of the gallium binding properties of THP, allowing further improvements to be made to the THP ligand, which in turn could result in better tolerance to contaminating metals and high molar activity radiolabelling.

8.2 Modifications to the THP Chelator

The choice of chelator is known to influence the *in vivo* properties of radiotracers including biodistribution, circulation time, affinity, and targeting (*2*). These observations have also been reported for [^{68}Ga]Ga-PSMA tracers (*3*)(*4*). Therefore it would be ideal to develop a library of THP chelators with different properties, such as lipophilicity, solubility and charge. This would

allow the most appropriate THP variant to be selected during radiotracer design, according to the *in vivo* properties required. Work towards this aim has already begun in this group, which has focused on ways of modifying the nitrogen substituent of the 3,4-hydroxypyridinone groups of THP. Additionally, as the THP chelator was originally designed as an iron scavenger it may also be fruitful and informative to screen a wide range of existing of iron chelators for their ability to chelate gallium under radiolabelling conditions, compared to THP. Studies of this nature have already begun (*5*), and there is particular interest in the potential of siderophores, which naturally occur as iron transporters in bacteria, fungi, and some plants (*6*)(*7*)(*8*).

8.3 Modifications to THP-PSMA

Hypotheses about how THP-PSMA could be modified to make higher affinity variants, after studying the interactions between poly-γ-glutamated folate and GCP(II)/PSMA, have already been discussed in chapter 6. These can be split into modifications to the GCP(II)/PSMA-binding motif and changes to linker design. The first modification proposed to the GCP(II)/PSMA-binding motif, a thiourea zinc binding group, was studied in chapter 7 but was found to result in 100-fold weaker affinity than its urea analogue. This result is of interest to the scientific community as it suggests that if the zinc binding group is too large this will impede binding in other areas, reducing affinity. From this, it can be inferred that other bulky peptide bond mimics are also unlikely to be successful GCP(II)/PSMA inhibitors, for example, triazol-, squarate- or phosphonamido-dithionate-based inhibitors. The other proposal was the use of a Dap-C(O)-Glu motif instead of Lys-C(O)-Glu to target GCP(II)/PSMA as hopefully, this would conserve the interactions with arginine patch in the S1 pocket of the receptor, present when the natural substrate, poly-γ-glutamated folate, binds the active site. Further ideas for modifications to the linker include the use of a poly-γ-glutamate chain of optimal length (greater than 2 glutamates), and the introduction of an aromatic group at the end of the linker before the chelator is attached, which could pi-stack with the arene-binding group of the entrance lid. Therefore the synthesis of a library of novel THP-PSMA variants incorporating these features, followed by evaluation *in vitro* and *in vivo* for their specific targeting of GCP(II)/PSMA would be valuable future work. Many of these insights have been obtained by studying the high-resolution X-ray crystal structures of GCP(II)/PSMA and the interactions observed between it and its natural substrates, therefore this approach should be encouraged when designing any future GCP(II)/PSMA targeted tracers or tracers for alternative receptors.

8.4 Opportunities for Gallium-67

The selectivity of THP for gallium, and the development of the THP-PSMA conjugate provided

the opportunity for gallium-67 to be explored as a targeted therapeutic radionuclide. The interest in Auger electron-emitting radionuclides is due to their high linear energy transfer and the very short range (< 2 μm) of Auger electrons in tissue (*9*)(*10*). It has been hypothesised that Auger electrons would be effective in treating micro-metastases or circulating tumour cells, therefore slowing disease progression (*11*)(*12*). The work in chapter 3 showed that despite the exceptionally high molar activity of the labelled complex, [^{67}Ga]Ga-THP-PSMA did not deliver a sufficient quantity of gallium to cells or tumours, and the activity that was delivered had poor retention, suggesting that [^{67}Ga]Ga-THP-PSMA is not ideal for a therapeutic application. Therefore higher affinity bioconjugates with better retention need to be developed before the radiobiological effects of these tracers are investigated. There are still many questions that remain unanswered about the potential of gallium-67 itself as a therapeutic radionuclide. In order to provide more concrete evidence for the use of gallium-67 as a therapeutic radionuclide, the biological effects of its Auger electrons and the coinciding "coulomb explosion" effect should be explored more deeply along with their mechanism for cellular toxicity. This would be bolstered by a better understanding of how the subcellular distribution of gallium-67 impacts on its therapeutic effect, and whether cell membrane-bound gallium-67 can also lead to cell death. Such information would make it easier to design experiments to evaluate and screen radiotracers *in vitro* but also to design tracers that are able to deliver the radionuclide in the right form, to the right (subcellular) location, for the right duration. A consistent and affordable source of gallium-67 chloride, that facilitates the radiolabelling at high molar activity, will be essential for such studies to be carried out. Unfortunately, such commercial sources are becoming rarer and this is likely to limit the study of gallium-67 going forward.

8.5 Opportunities for Gallium-68

The recent popularity of gallium-68 has been driven by both the marketing authorisation in Europe of the Galliapharm (Eckert & Ziegler) generator (*13*), as well as its clinical application in PET imaging for both neuroendocrine tumours (*14*) and prostate cancer (*15*) becoming established. Now that the majority of research hospitals have access to a germanium-68/gallium-68 generator, gallium-68 is likely to continue to be the PET radiometal utilised for translational studies, encouraged by its availability from generators, at modest cost, and the ease by which it can be incorporated into a radiotracer. Now that the advantages of THP have been proven in a clinical setting, THP may even become the chelator of choice for gallium-68 radiolabelling with novel targeting vectors. Utilising THP would allow extremely simple labelling

for peptides and small molecules, but also for heat- and pH-sensitive proteins because of the mild chelation conditions of THP.

8.6 One-Step Kits

The THP chelator has made one-step kits possible for gallium-68 tracers, and this has been demonstrated for the first time through one-step kit labelling of [^{68}Ga]Ga-THP-PSMA. Simple radiolabelling has also been demonstrated for other THP bio-conjugates including [^{68}Ga]Ga-THP-mal-J591c-scFv (*16*), [^{68}Ga]Ga-THP-TATE (*17*), and [^{68}Ga]Ga-THP-RDG (*18*). The next challenge will be for the THP technology to be leveraged further and come into widespread use, either as a translational tool or in commercial radiopharmaceutical kits. The concept of developing one-step kits for gallium-68 was inspired by the prevalence of technetium-99m kit-based radiolabelling. However, the radiolabelling now demonstrated for [^{68}Ga]Ga-THP-PSMA is much simpler than the methods being used for [^{99m}Tc]Tc-PSMA and other technetium-99m-based bioconjugates. As described in chapter 2 these are still multistep processes, which typically involve heating to 100°C and take over 1 hour to perform (*19*)(*20*). Therefore it would be advantageous to develop ways to turn radiolabelling for these technetium-99m radiotracers into one-step kits. In fact, the desire for simple, rapid, single-step radiolabelling exists for all clinically relevant radiometals, not just those produced by a generator. The demonstration that such radiolabelling is achievable for gallium-68 should inspire the design novel chelators for all clinically relevant radiometals, with properties amenable to single-step radiolabelling. Of course, this is not a trivial task, but the benefits to the nuclear medicine community would be far-reaching.

8.7 References

1. Gaur A, Shrivastava BD, Nigam HL. X-Ray Absorption Fine Structure (XAFS) Spectroscopy – a Review. *Proc Indian Natn Sci Acad Spl Issue, Part B*. 2013;79:921-966.
2. Banerjee SR, Pullambhatla M, Foss C a, Falk A, Byun Y, Nimmagadda S, Mease RC, Pomper MG. Effect of Chelators on the Pharmacokinetics of 99mTc-Labeled Imaging Agents for the Prostate-Specific Membrane Antigen (PSMA). *J Med Chem*. 2013;56:6108-6121.
3. Wüstemann T, Bauder-Wüst U, Schäfer M, Eder M, Benesova M, Leotta K, Kratochwil C, Haberkorn U, Kopka K, Mier W. Design of Internalizing PSMA-Specific Glu-Ureido-Based Radiotherapeuticals. *Theranostics*. 2016;6:1085-1095.
4. Eder M, Schäfer M, Bauder-Wüst U, Hull W-E, Wängler C, Mier W, Haberkorn U, Eisenhut M. 68Ga-Complex Lipophilicity and the Targeting Property of a Urea-Based PSMA Inhibitor for PET Imaging. *Bioconjug Chem*. 2012;23:688-697.
5. Tsionou MI, Knapp CE, Foley CA, Munteanu CR, Cakebread A, Imberti C, Eykyn TR, Young JD, Paterson BM, Blower PJ, Ma MT. Comparison of Macrocyclic and Acyclic Chelators for Gallium-68 Radiolabelling. *RSC Adv*. 2017;7:49586-49599.
6. Petrik M, Haas H, Dobrozemsky G. Ga68-Siderophores for PET Imaging of Invasive Pulmonary Aspergillosis: Proof of Principle. *J Nucl Med*. 2010;51:639-645.
7. Petrik M, Zhai C, Novy Z, Urbanek L, Haas H, Decristoforo C. In Vitro and in Vivo Comparison of Selected Ga-68 and Zr-89 Labelled Siderophores. *Mol Imaging Biol*. 2016;18:344-352.
8. Ioppolo JA, Caldwell D, Beiraghi O, Llano L, Blacker M, Valliant JF, Berti PJ. 67Ga-Labeled Deferoxamine Derivatives for Imaging Bacterial Infection: Preparation and Screening of Functionalized Siderophore Complexes. *Nucl Med Biol*. 2017;52:32-41.
9. Buchegger F, Perillo-Adamer F, Dupertuis YM, Bischof Delaloye A. Auger Radiation Targeted into DNA: A Therapy Perspective. *Eur J Nucl Med Mol Imaging*. 2006;33:1352-1363.
10. Kassis AI. Cancer Therapy with Auger Electrons: Are We Almost There? *J Nucl Med*. 2003;44:1479-1481.
11. Kiess A, Minn I, Chen Y, Hobbs RF, Sgouros G, Mease RC, Pullambhatla M, Shen C, Foss C, Pomper M. Auger Radiopharmaceutical Therapy Targeting Prostate-Specific Membrane Antigen. *J Nucl Med*. 2015;56:1401-1407.
12. Aghevlian S, Boyle AJ, Reilly RM. Radioimmunotherapy of Cancer with High Linear Energy Transfer (LET) Radiation Delivered by Radionuclides Emitting α-Particles or Auger Electrons. *Adv Drug Deliv Rev*. 2017;109:102-118.
13. European Medicines Agency website. List of Nationally Authorised Medicinal Products. Active Substance: Germanium (68Ge) Chloride / Gallium (68Ga) Chloride. Procedure No.: PSUSA/00010364/201603. http://www.ema.europa.eu/docs/en_GB/document_library/Periodic_safety_update_single_assessment/2016/11/WC500216013.pdf. Updated Oct 27, 2016. Accessed Jun 25, 2018.
14. FDA Approves 18F-Fluciclovine and 68Ga-DOTATATE Products. *J Nucl Med*. 2016;57:9N.
15. Fendler WP, Eiber M, Beheshti M, Bomanji J, Ceci F, Cho S, Giesel F, Haberkorn U, Hope TA, Kopka K, Krause BJ, Mottaghy FM, Schöder H, Sunderland J, Wan S, Wester HJ, Fanti S, Herrmann K. 68Ga-PSMA PET/CT: Joint EANM and SNMMI Procedure Guideline for Prostate Cancer Imaging: Version 1.0. *Eur J Nucl Med Mol Imaging*. 2017;44:1014-1024.
16. Nawaz S, Mullen GED, Sunassee K, Bordoloi J, Blower PJ, Ballinger JR. Simple, Mild, One-Step Labelling of Proteins with Gallium-68 Using a Tris(Hydroxypyridinone) Bifunctional Chelator: A 68Ga-THP-ScFv Targeting the Prostate-Specific Membrane Antigen. *EJNMMI Res*. 2017;7:86.
17. Ma MT, Cullinane C, Waldeck K, Roselt P, Hicks RJ, Blower PJ. Rapid Kit-Based (68)Ga-

Labelling and PET Imaging with THP-Tyr(3)-Octreotate: A Preliminary Comparison with DOTA-Tyr(3)-Octreotate. *EJNMMI Res*. 2015;5:52.

18. Ma MT, Cullinane C, Imberti C, Baguna Torres J, Terry SY a., Roselt P, Hicks RJ, Blower PJ, Bagunya Torres J, Terry SY a., Roselt P, Hicks RJ, Blower PJ. New Tris (Hydroxypyridinone) Bifunctional Chelators Containing Isothiocyanate Groups Provide a Versatile Platform for Rapid One-Step Labeling and PET Imaging with 68Ga3+. *Bioconjug Chem*. 2015;27:309-318.
19. Badar A, Williams J, de Rosales RTM, Tavaré R, Kampmeier F, Blower PJ, Mullen GED. Optimising the Radiolabelling Properties of Technetium Tricarbonyl and His-Tagged Proteins. *EJNMMI Res*. 2014;4:1-8.
20. Vallabhajosula S, Nikolopoulou A, Babich JW, Osborne JR, Tagawa ST, Lipai I, Solnes L, Maresca KP, Armor T, Joyal JL, Crummet R, Stubbs JB, Goldsmith SJ. 99mTc-Labeled Small-Molecule Inhibitors of Prostate-Specific Membrane Antigen: Pharmacokinetics and Biodistribution Studies in Healthy Subjects and Patients with Metastatic Prostate Cancer. *J Nucl Med*. 2014;55:1791-1798.

9 Table of Figures

10 Table of Tables

11 Table of Reaction Schemes